Fluvial and alluvial system response to rift basin evolution

David James Philip Somerville

Submitted in accordance with the requirements for the degree of Doctor of Philosophy

University of Leeds

Institute of Applied Geosciences

School of Earth and Environment

November, 2020

The candidate confirms that the work submitted is their own, except where work which has formed part of jointly authored publications has been included. The contribution of the candidate and the other authors to this work has been explicitly indicated below. The candidate confirms that appropriate credit has been given within the thesis where reference has been made to the work of others.

Chapter 3 – Prepared for submission for publication

Somerville, D.J.P. – Main author. Data collection, data analysis, manuscript preparation and figure illustrations.

Mountney, N.P. – Manuscript review and edits, discussion.

Colombera, L. – Manuscript review and edits, discussion.

Collier, R.E.Ll. – Manuscript review and edits, discussion.

Chapter 4 – Published

Somerville, D.J.P., Mountney, N.P., Colombera, L. & Collier, R.E.Ll. (2020) Impact of a pre-existing transverse drainage system on active rift stratigraphy: An example from the Corinth Rift, Greece. Basin Research, 32(4), 764-788. DOI: 10.1111/bre.12396 (Appendix 1)

Somerville, D.J.P. – Main author. Data collection, data analysis, manuscript preparation and figure illustrations.

Mountney, N.P. – Manuscript review and edits, discussion.

Colombera, L. – Manuscript review and edits, discussion.

Collier, R.E.Ll. – Field area introduction, manuscript review and edits, discussion.

Chapter 5 – Prepared for submission for publication

Somerville, D.J.P. – Main author. Data collection, data analysis, manuscript preparation and figure illustrations.

Mountney, N.P. – Manuscript review and edits, discussion.

Colombera, L. – Manuscript review and edits, discussion.

Collier, R.E.Ll. – Field area introduction, manuscript review and edits, discussion.

Acknowledgements

I would firstly like to express my gratitude to my supervisors, Nigel Mountney, Luca Colombera, and Richard Collier. Nige, thank you for always making time for me and your countless pointers in science and the English language – and over the last few weeks in particular, being a guiding voice toward the end of this project. Luca, thank you for your help with statistics and the legendary efficiency with which you have given feedback on posters and manuscripts - it has been greatly appreciated over the last four years. Richard, thank you for introducing me to the wonders of the Gulf of Corinth, and the teaching opportunities you have given me over my time at Leeds. All three of you have steered me over the finish line while allowing me to drive this research in my own direction, and I am indebted to you for it. I would also like to express my thanks to the FRG sponsors who funded this project; Aker BP, Cairn India, Chevron, CNOOC, Equinor, Occidental, Saudi Aramco, Shell, Woodside, and YPF.

I never would have survived Greece without my field assistants Ben and Rob, or without Dan, who has been a great friend during this process – we'll go back for spanakopita one day! Road trips in the US after conferences has been a particular highlight of the last few years, thank you to Dan and Tim for checking out rocks and gators with me. Huge thanks to all of the other seddys (and others!) in the office, especially Bonnie, Grace, Dave, Bassam, Andy, Issy, Ben, and Laura – I've appreciated all our conversations to help break up the monotony of the working day. Special thanks go to Sam Haynes for all of her help over the years. Thank you to past and present members of FRG for your support and guidance over the last few years, but particularly to Roman and José – I'm not sure I've ever said a serious word to either of you! Outside of Leeds, thank you to Mike, Rich, and Clare – our games nights and chats about Fantasy Football have helped keep me going.

To my family – Mum, Dad, Katy, Robbie, and Ali (and Ambrose...!) – words will never express how much you all mean to me, and how grateful I am to have had your love and support (or indifference, in Ambrose's case) since this project began. Thank you.

Finally, to my 'rock', Charley. We met at the start of this journey and have stuck by each other every step of the way. Your unwavering belief in me has always uplifted me, and even writing a 265-page thesis with you during a global pandemic has been manageable! I owe it all to you – thank you for everything.

Abstract

The accumulated stratigraphy of alluvial and fluvial successions constitutes a significant proportion of the fill of many continental rift basins. Subsurface studies commonly fail to adequately account for sedimentological complexity, and field-based and remote sensing studies typically focus on a single scale of observation. Detailed analyses of alluvial and fluvial sedimentary successions across multiple scales are required to examine the roles played by extrinsic and intrinsic depositional controls, and to determine response to ongoing basin evolution.

Three studies have been undertaken to improve understanding of alluvial fan and fluvial system response to rift evolution. First, three modern-day tilt-block crests from active rifts are analysed through the measurement of their developed catchment and associated fan system morphometrics. Comparisons are made of systems sourced over the footwall slope and those sourced over the hangingwall dipslope. Moreover, comparisons are made of each rift setting and their climatic regimes. The importance of system scale is examined: as catchment size decreases, so fan size decreases, though at a markedly reduced rate. Alluvial fan systems are especially important in smaller rift zones.

Second, a 600 m-thick conglomerate-dominated alluvial synrift succession from the Gulf of Corinth, Greece, is analysed through interpretations of facies elements and architectural elements within the context of a spatially and temporally complex framework of rift basin evolution. The system developed as an alluvial fan sourced externally from the rift over the hangingwall dipslope. Rift sedimentation led to overfilled basin conditions, which transitioned rapidly to underfilled conditions following the onset of intrabasinal faulting, which induced rapid subsidence. Results demonstrate the importance of rift evolution as a control on the distribution of depositional environments.

Third, 1,531 conglomerate clasts from eight conglomerate lithofacies of a single synrift succession are examined in terms of their qualitative (roundness, composition, shape) and directional (axis lengths, dips, orientations) characteristics. Comparisons between facies enable detailed reconstructions of formative depositional process.

The results are integrated to develop a suite of models that improve our understanding of the links between basin-scale dynamics and resultant synrift alluvial stratigraphy, notably allowing for enhanced subsurface prediction of their character.

Table of Contents

List of Tables

List of Figures

List of Abbreviations

3D – three-dimensional

ALOS - Advanced Land Observing Satellite

ASTER - Advanced Spaceborne Thermal Emission and Reflection Radiometer

AW3D30 - ALOS World 3D-30 m, digital surface model

DEM – Digital Elevation Model

DF – degrees of freedom

DFS – Distributive Fluvial System

EARS – East African Rift System

Fm. – Formation

GIS – Geographic Information System

ITCZ – Inter-Tropical Convergence Zone

JAXA – Japan Aerospace eXploration Agency

ka – thousands of years ago

Ma – millions of years ago

MIS – Marine Isotope Stage

RMSE – Root Mean Square Error

SRTM - Shuttle Radar Topography Mission

USA – United States of America

USGS – United States Geological Survey

WMO – World Meteorological Organization

“That’s just a stupid boulder!”

“It’s not just a boulder. It’s a rock! A rock! A ro-ho-hua-ha-hua-ock! It’s a big, beautiful, old rock. Oh the pioneers used to ride these babies for miles! And it’s in great shape.”

- Spongebob Squarepants, Season 1, Episode 5A (1999)

1. Introduction

Alluvial and fluvial systems in continental rift settings reveal important relationships between active tectonics and ongoing sedimentation. The resultant preserved sedimentary successions provide an important record of the past tectonic events that have shaped our planet. By studying the sedimentology of active alluvial and fluvial systems in present-day basins, and their deposits in basin fills in the rock record, we can hope to reconstruct an important part of earth system behaviour in considerable detail. This thesis examines these relationships and the issues associated with their interpretation.

This chapter provides an overview of continental rift basins and their sedimentary systems, and the rationale underpinning the research presented in this thesis. The overarching aim and research objectives are introduced, as are the Research Questions that are answered by achieving those objectives. Specific objectives for each data chapter and how they can be applied to the Research Questions are outlined, and the main methods of data collection used in subsequent chapters are introduced.

1.1. Overview and rationale

1.1.1. Overview

Large-scale rift systems are ruptures in surface of the Earth that occur where two tectonic plates are pulling apart, or where a tectonic plate is commencing break-up into smaller pieces. Such rifts are typically expressed as an extensive system of normal faults, bounding depressions of subsiding crust that form basin depocentres (named grabens or half-grabens) with variable accommodation. Over time, developing rift basins become filled with sequences of sediments (the basin acts as a sediment sink). Sediment is sourced in part via the erosion of newly developed topography associated with fault

uplifts and is delivered into the adjacent basins via source-to-sink delivery pathways. Sediment delivery may also be provided from sources external to the rift basin by large-scale drainage systems drawn towards the newly developed topographic lows. In this manner, complex and interlinked source-to-sink sedimentary systems develop in response to rifting (Gawthorpe & Leeder, 2000; Allen, 2008a; Hinderer, 2012; Pechlivanidou et al., 2018).

Where rift systems are developed in continental lithosphere, and are not subsequently inundated by rising sea level, continental rift systems are formed. Over time they can initiate continental break-up, causing the generation of new sections of the Earth's crust, and the formation of new oceans and seas (a 'successful' rift, e.g. the Atlantic Ocean; McHone, 2000; Tucholke et al., 2007). If the stresses driving the extension diminish, rift activity will cease, and any generated surface features will be degraded over time by the erosion and deposition of sediment, by which parts of the system are preserved in the rock record (a 'failed' rift, e.g. the North Sea Rift; Rattey & Hayward, 1993, Erratt et al., 1997). Rift settings are highly variable in terms of both their structure and the nature of their sediment infill at a variety of scales both prior to continental break-up, and during the life of a failed rift.

At the **system and basin scale** (Figure 1.1A), different structural geometries can form through the complex interplay of local and regional stress fields, induced by lithosphere dynamics or plate tectonics. These include: (i) half-grabens, where one major extensional fault forms on one side of an asymmetric basin (Morley, 1990); (ii) full grabens, where a major extensional fault forms on each side of a symmetrical basin (Morley, 1990); and (iii) transtensional basins, where extensional basins form as kinks in strike-slip faults,

induced as sinistral (left) or dextral (right) movement in the Earth's rigid crust (Mann, 1997; Wu et al., 2009).

Within each basin, multiple different **depositional environment** settings (Figure 1.1B) can form. A combination of external controls (such as climate, far-field tectonics, bedrock lithology, base-level change, and sea-level change in the case of marine-influenced rifts) and internal controls (such as local drainage development, the presence of endorheic [internally-draining] and exorheic [externally-draining] basins within the system, and the stage and magnitude of rift evolution) govern the presence and distribution of continental and marine environments within the generated individual basin depocentres, and how they vary and interact in space and time.

These depositional environments are comprised of different geomorphic elements which are represented in the rock record by sedimentary deposits. These deposits can be assigned to building blocks of different scales, of which the largest are defined as **depositional elements** (Figure 1.1C). These elements form as sediment is transported through, and deposited by, a variety of different processes (for example, forming river channel deposits or floodplain deposits). These elements will be juxtaposed against one another across the basin and will vary in location through time as competing environments respond to basin evolution and external factors such as climate change. As the basin develops, subsidence generates the necessary accommodation to enable the progressive accumulation of a thick sedimentary pile. In this way, a sedimentary succession is accumulated; the preservation of stacked elements comprises the sedimentary fill of the basin. Each depositional element will be made up of different **architectural elements** (Figure 1.1D), representing the sedimentary record of individual morphological features of depositional environments (such as high-sinuosity

meandering river deposits). Each architectural element is itself made up internally of one or a series of **facies** (Figure 1.1E) (typically represented by beds or sets of differing lithology; sandstone or mudstone, for example). Different facies units might typically occur together as a commonly occurring **facies association**. Such associations are commonly made of facies that are deposited in a specific order to form distinctive vertical **facies successions**. Facies analysis is the study of the detailed sedimentology of these units, which is applied to develop diagnostic tools for the recognition of depositional sub-environments from their preserved deposits (Miall, 1978, 1985; Walker, 1979; Reading, 2006).

As such, the sedimentary infill of a rift basin can be considered across many hierarchical scales, whereby small-scale building blocks are nested within larger ones – which are themselves nested within even larger elements. The distributions of features present at any of these scales will change spatially and temporally through the basin fill, as a function of the extrinsic and intrinsic controls outlined above; the variability of these controls in space and time will drive variations in the different building blocks of rift basin sediment fill.

Figure 1.1 (next two pages) *Schematic 3D block models displaying the observable hierarchical scales of sedimentary systems developed within continental rift settings. Further detail is provided in the main text. (A) System and basin scale; the rift forms a series of linked or isolated depressions (basins) in the Earth's surface across its length, bounded by extensional faults. (B) Depositional environment scale: within those basins, different environmental conditions occur in different parts of the basin. Their form, location, and extent vary spatially and temporally depending on external factors. (C) Depositional element scale: the preserved expression of each environment in the rock record is made up of stacked depositional elements representing different parts of the environmental system. (D) Architectural element scale: in turn, those depositional elements comprise variable architectural elements representing morphological features or events of the depositional system. (E) Facies element scale: different facies made up of different sediment calibres and compositions are preserved in stacked sections, which when occurring in repeatable patterns can be described as facies associations, which in turn are the building blocks of architectural elements.*

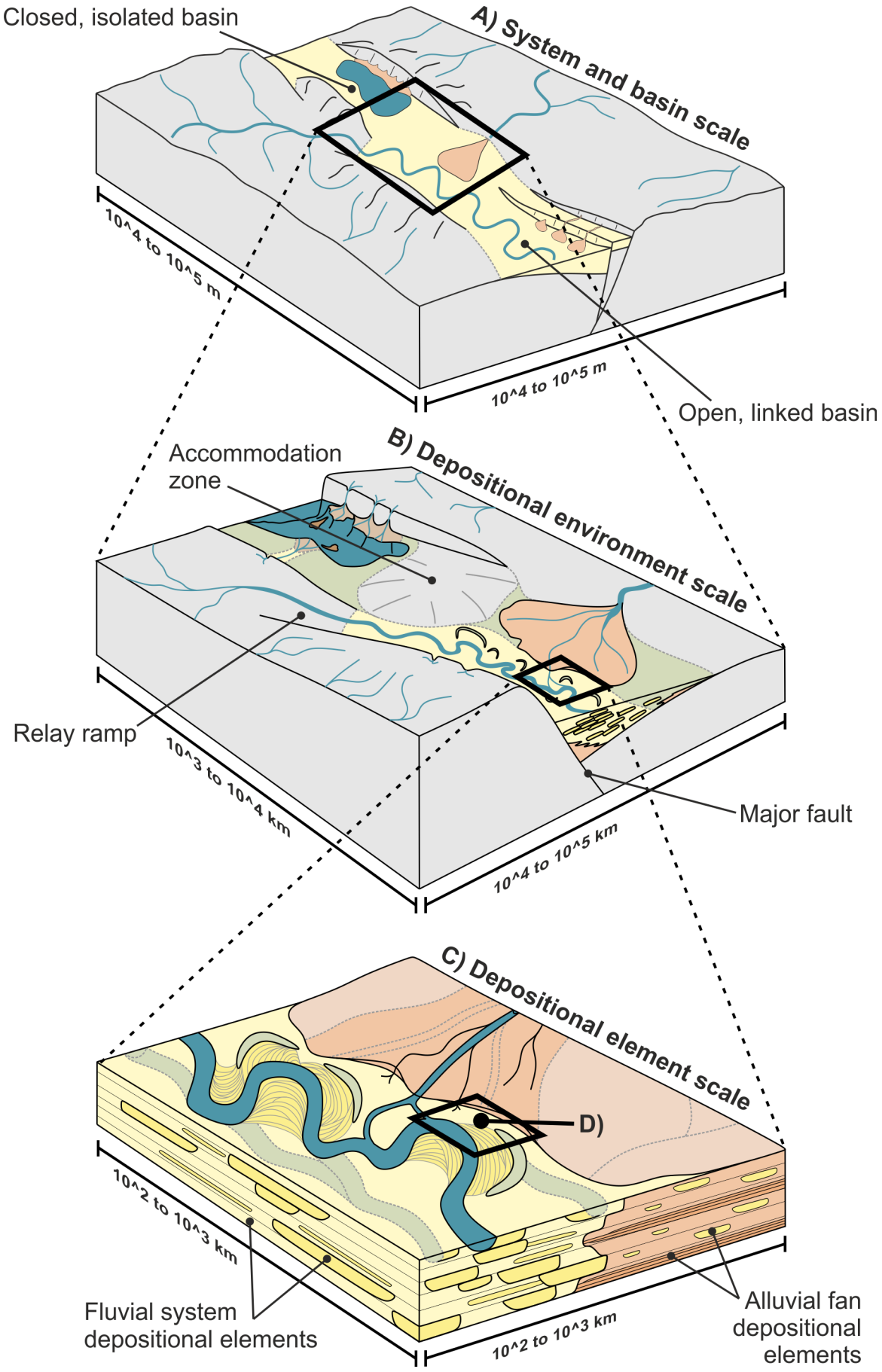
Closed, isolated basin
A) System and basin scale
10^4 to 10^5 m
10^4 to 10^5 m
Open, linked basin
Accommodation zone
B) Depositional environment scale
Relay ramp
10^3 to 10^4 km
10^4 to 10^5 km
Major fault
C) Depositional element scale
D)
10^2 to 10^3 km
10^2 to 10^3 km
Fluvial system depositional elements
Alluvial fan depositional elements

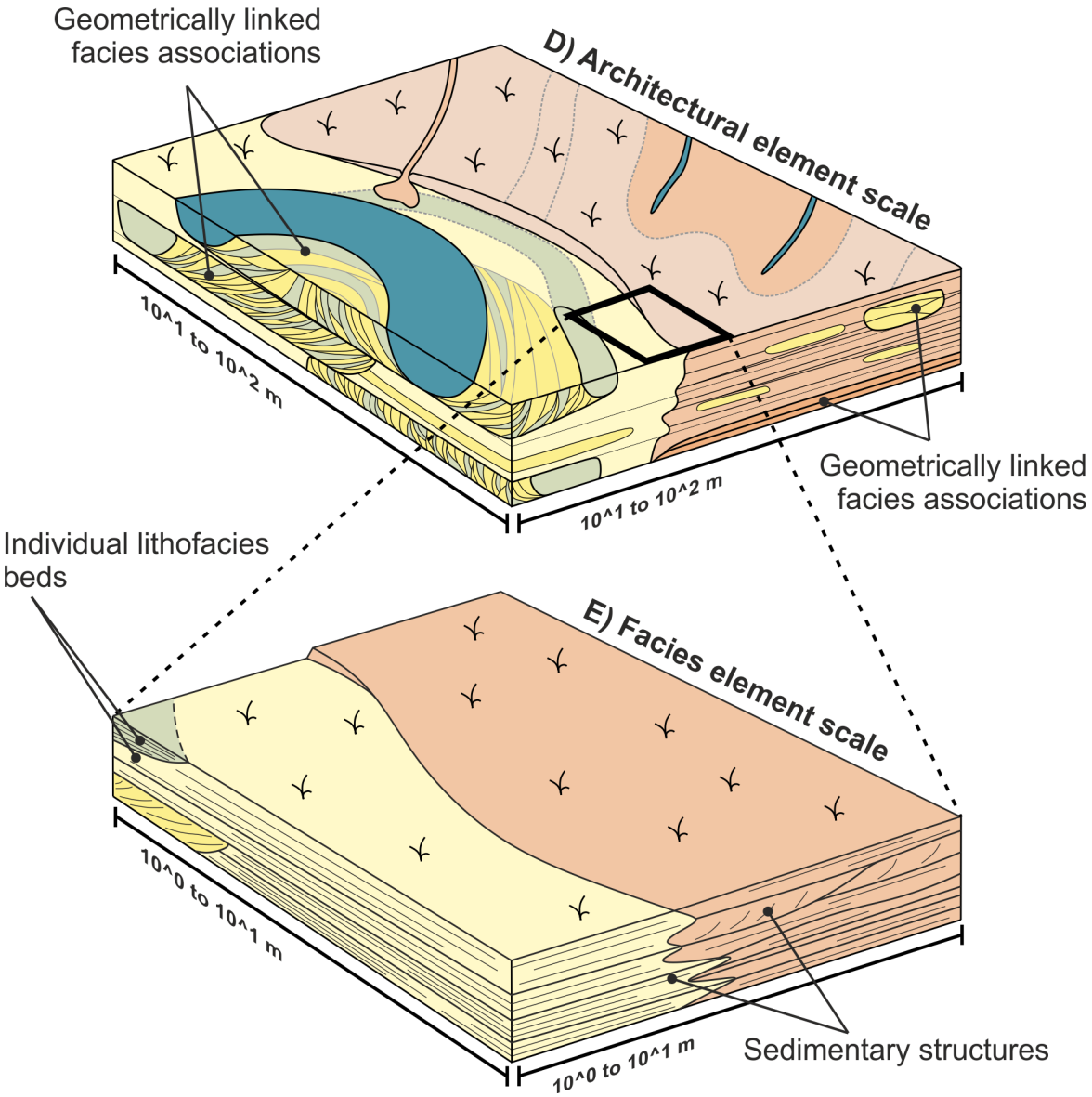

An understanding of the complex interplay of these different hierarchical scales through space and time during the evolution of a rift system is paramount when making inferences about the presence and distribution of potential resources. Since the early 20th century, this has included the presence and size of hydrocarbon reservoirs held in buried rift deposits; Mann et al. (2001) classify 271 of the known 877 giant oil and gas accumulations as occurring in rift-related deposits. More recently, water-bearing aquifers within ancient rifts could provide water sources to areas of the world where

other surface water sources are more difficult to develop due to environmental constraints. This has been applied in the Middle East related to the Red Sea rift systems (Sultan et al., 2011) and those of the Jordan Rift Valley in Israel and Jordan (El-Naqa et al., 2009). The development of geothermal resources from ancient rift systems is currently being driven by a worldwide need to identify and develop sustainable geo-energy sources, such as developed resources related to the extensional Wessex Basin of south England (Gluyas et al., 2018). Improving our understanding of the structural and sedimentological evolution of rift systems will allow for more accurate predictions of the presence, size, and potential of these different resources, and allow for their safe and efficient extraction.

1.1.2. Research rationale

Fundamental to understanding the stratigraphic development of the sedimentary infill of rift basins is an understanding of the relative impacts of different sediment transport pathways. Sediment sources can either be inherited by the rift system from pre-existing drainage, else can be formed by the erosion of newly developed topographical highs caused by the surface rupture, linkage, and displacement of extensional faults. By sourcing sediments into the rift basins which are then buried and preserved, linked sediment source-to-sink systems are formed. Their distribution, size, and transport mechanism constitute major controls on the presence, distribution and types of sediment deposited in different depositional environments within the rift.

Within many rift systems, continental sedimentation typically comprises a significant proportion of the basin fill, either entirely filling a basin's accommodation (e.g. de Almeida et al., 2009) or sourcing early syn-rift stratigraphy (as observed in the Italian Apennines; Martini & Sagri, 1993, and Gulf of Corinth; Dart et al., 1994, Ford et al., 2013).

Decades of study on the development of continental rift basins has led to multiple landmark studies on the initiation and the evolution of both their structure and their depositional environments (e.g. Hooke, 1972; Wernicke & Burchfiel, 1982; Leeder & Alexander, 1987; Leeder & Gawthorpe, 1987; Prosser, 1993; Anders & Schlische, 1994; Gawthorpe & Leeder, 2000). Consequently, these studies have been used to underpin analyses of the effects of rift evolution on sediment deposition, through studies of the rock record (e.g. Hemelsdaël et al., 2017; Barrett et al., 2019; Cullen et al., 2020), modern-day systems (e.g. Weissmann et al., 2010, 2015) and numerical and computational modelling (e.g. Alexander & Leeder, 1987; Cowie et al., 2006; Yan et al., 2020).

Alluvial and fluvial systems in continental rift basins are an integral part of the source-to-sink sedimentary system. These environments serve as major sediment transport routes via different fluidal flows, such as a streamflows forming a fluvial system. These environments can also form long-lived sediment accumulations, for example as the preserved deposits of meander point bars, braid bars and alluvial fan lobes (Leeder & Gawthorpe, 1987; Leeder, 2011). Of these systems, alluvial fans are widespread in many continental rift settings, forming as streams exiting catchments developed on uplifted hinterlands reach the basin floor and become unconfined (Ventra & Clarke, 2018). Consequently, alluvial fans act as recorders of both environmental (e.g. Fordham et al., 2010; Meek et al., 2020) and tectonic (e.g. Mack & Leeder, 1999; Whittaker et al., 2007) processes that govern their formation; through observation and interpretation of their modern-day formation, and their preserved sediments, tectonostratigraphic models for their evolution can be developed.

Previous studies of alluvial fans in rift settings and their associated fluvial systems are typically focussed on a variety of relationships including: (i) their relationship with

feeding catchments, described in terms of their morphometric parameters (e.g. Whittaker et al., 2007; Densmore et al., 2007); (ii) the sedimentological response to allogenic (e.g. climate and tectonics; Allen & Densmore, 2000) or autogenic (e.g. incisional and aggradational cycles; Ventra & Nichols, 2014) forcing; or (iii) their relationship to sedimentary environments within the associated basin (e.g. to axial fluvial systems; Leeder & Mack, 2001). Studies of these relationships commonly focus on a single sub-basin within which an alluvial fan has formed (e.g. Santos et al., 2014) with some recent studies illustrating the effect of further rift development on alluvial systems (e.g. Leleu & Hartley, 2016; Hemelsdaël et al., 2017). Where studies are focussed on isolated sub-basin examples, identifiable links between basin-scale dynamics and resultant stratigraphy, and its constituent sedimentological components, remain elusive. Understanding this interplay requires the integration and comparison of datasets across a variety of scales to elucidate the response of alluvial and fluvial systems to ongoing rifting.

1.2. Research aim and objectives

The aim of this thesis is to analyse the effect of rift evolution on fluvial and alluvial sedimentation within rift basins, and to explain the sedimentological response recorded in synrift stratigraphy at different depositional scales.

This will be achieved through the following set of research objectives, designed to consider the environmental and sedimentological response of alluvial fan systems to rift evolution:

(i) Quantify attributes of modern-day rift environments and preserved sedimentary deposits to determine the different sources of alluvial fans in continental rifts and detail their response to ongoing rift evolution.

(ii) Classify the developmental response of intrabasinal tilt-block crest structures to their formation and uplift, in terms of sediment supply to adjacent basins and the sediment flows that will form linked alluvial fans.

(iii) Develop novel models with which to account for the evolution of an alluvial fan system formed in a rift sub-basin during one evolutionary stage of the rift cycle, investigating how sedimentological character varies both spatially and temporally, before determining its response to the initiation of the next rifting phase.

(iv) Assess the impact of extrinsic and intrinsic controls on the development of the sub-basin chosen as the case study, and determine whether signatures of those controls can be derived from detailed sedimentological observations at the scale of individual facies beds and their depositional features.

1.3. Research Questions

The aim and objectives outlined above can be distilled down into three main Research Questions, which will be used to drive the data studies and achieve the study objectives.

1.3.1. Research Question 1: What are the impacts of pre-existing and rift-formed drainage catchments on the presence of underfilled and overfilled rift basin conditions, and consequent alluvial syn-rift sedimentation?

The presence of antecedent drainage systems (or pre-existing drainage systems) is a major controlling factor on the distribution, type and volume of sediments delivered into continental rift basins as they initiate and develop into a fully-fledged rift system (Leeder & Gawthorpe, 1987; Gawthorpe & Leeder, 2000; Leeder, 2011). Typically, antecedent drainage systems have been considered in conjunction with a rift system axis forming

parallel to the main flow direction, whereby the fluvial flow pathways will be maintained and adopted into the newly formed depocentre as an axial fluvial system leading to intrabasinal lacustrine or marine deltas (Prosser, 1993; Gawthorpe & Leeder, 2000). More recently, increasing consideration has been given to antecedent systems that are cut obliquely by rift systems, including those where drainage is consequently diverted around new fault tips (e.g. Barrett et al., 2019) or drawn into new depocentres over the hangingwall dipslope of half-grabens (e.g. Santos et al., 2014). Key to this has been the study of relay zones between adjacent faults and their exploitation by antecedent drainage pathways as routes into adjacent hangingwall depocentres, with consideration given to subsequent relay zone breaching and the impact on sediment transport pathways (e.g. Jackson et al., 2002; Trudgill, 2002).

To date, less consideration has been given to the impact of subsequent faulting on antecedent drainage systems that have been drawn into rift systems, where the transfer of displacement onto synthetic and antithetic faults alters the location of maximum accommodation within a basin. This intrabasinal faulting consequently acts as either a barrier or conduit to sediment pathways, allowing different stratigraphy to develop in other parts of the basin (Hemelsdaël et al., 2017, provide one example). Existing models of basin evolution (e.g., Gawthorpe & Leeder, 2000) envisage intrabasinal faulting as an integral part of the rift evolution but provide only limited detail of the controls that act to influence the distribution of depositional environments and representative sedimentary bodies that fill the generated accommodation.

In conjunction with antecedent drainage systems, the formation of new topography as a consequence of rifting triggers the formation of new sediment source areas, forming catchments that link to fluvial and alluvial fan systems on the basin floor (Leeder &

Gawthorpe, 1987; Cowie et al., 2006; Densmore et al., 2007). These systems are typically limited to the basin margins but can be the dominant sediment source for both isolated rift basins and endorheic rift basins (Fordham et al., 2010), where antecedent drainage has not been adopted by the new depocentres. Studies of these degradational hinterlands and their linked depositional systems are common, and include those of both (i) modern-day fan systems in extensional settings like the Basin and Range province, USA and the Gulf of Corinth, Greece (see Leeder & Jackson, 1993, for one such review), and (ii) outcrop examples from the same locations (e.g. Fordham et al., 2010; Rohais et al., 2007a, 2007b).

Predicting the influence of intrabasinal faulting on alluvial fan systems in rift basins is important to better understand the variation in the ratio between accommodation generation rate to sediment supply rate ($\delta A/\delta S$) at any given point in the rift. Depending on this ratio, the basin can be described as becoming overfilled, filled, or underfilled (concepts explored further in Chapter 2, section 2.1.3.), whereby higher ratios indicate an increasingly underfilled basin (Schlische & Anders, 1996; Withjack et al., 2002). In turn, these conditions control the stacking patterns of different alluvial fan units within the basin, and consequently the distribution of different depositional, architectural and facies elements. Recent studies have considered the impacts of polyphase rifting on antecedent catchment-derived and rift-adjacent catchment-derived sediment distributions (see Henstra et al, 2017, for one such subsurface example) but few have considered the effects on continental stratigraphy (see Leleu & Hartley, 2016, for one such example). This is despite the near omnipresence of interpretations of alluvial and fluvial sedimentation in the earliest syn-rift sedimentation phase (reviewed by Anders & Schlische, 1994; Gawthorpe & Leeder, 2000) where the rupture and development of intrabasinal faulting will have its largest impact on these sediment pathways as the rift becomes established. Chapters 4 and 5 explore an example of the response of a pre-

existing drainage system to rift initiation and subsequent fault development. From these data and wider considerations, a set of scenarios can be constructed displaying the possible responses of sediment source pathways to rift initiation and evolution (provided in Chapter 6).

1.3.2. Research Question 2: How does evolving rift fault development control the scale, stacking patterns, and sedimentary facies of alluvial fans in rift basins?

As discussed in Research Question 1, intrabasinal faulting and further fault propagation has a direct influence on the presence and distribution of sediments within their adjacent basins (Jackson et al., 2002; Henstra et al., 2017; Hemelsdaël et al., 2017; Barrett et al, 2019, 2020). The study of continental rift systems has been synonymous with the analysis of catchments formed on uplifted footwalls and tilt-block crests and their linked alluvial fan, fluvial, and fan delta sedimentary sinks in order to interpret their sensitivity to external controls (e.g. Jackson et al., 2002; Whittaker et al., 2007) and intrinsic factors governing sediment deposition (e.g. Ventra & Nichols, 2014). These catchments are a major source of sediment into rift basins, forming a large transverse component that can limit the extent of other basin floor environments such as aeolian, lacustrine or fluvial systems.

Typically, in both studies of modern and ancient systems, focus has been given to individual basins fed from either side by sediment pathways over footwall slopes (for full-graben structural morphologies) and hangingwall dipslopes (for half-graben structural morphologies). Comparison of catchment morphometrics, depositional styles and constituent sedimentary facies result in depositional models that are specific to localised allogenic and autogenic controls, for example an arid to semi-arid half-graben system (Fordham et al., 2010) or a humid half-graben system (Nichols & Uttamo, 2005).

A frequently overlooked aspect of sedimentary system development in rift settings is the consideration of strike-parallel basins that share an intermediate separating hinterland (formed by the crest of a tilted fault block) that sources sediment over each flank into depocentres on either side. These settings are commonly seen in generic models reviewing continental syn-rift sedimentation (Gawthorpe & Leeder, 2000) but comparisons between their competing depositional systems are poorly represented. Catchments formed over the footwall crest side and hangingwall dipslope side of an intrabasinal tilt-block crest will interact and compete, leading to different stacking patterns and sedimentary facies distributions in adjacent basins.

Different climatic regimes influence flow behaviour and give rise to different depositional flow types on alluvial fans. Climate controls the spatial and temporal variability of erosion in a catchment, by controlling the hydrological regime and subsequently flow discharge and stream power (Ventra & Clarke, 2018). This in turn alters the occurrence and magnitude of different depositional flow types that occur on the fan surface. Further to these interpretations, other factors such as bedrock lithology (e.g. Blair, 1999c) and catchment morphometrics (e.g. ruggedness; Wilford, 2004; de Scally et al., 2010; Welsh & Davies, 2011) have been identified as major influences on flow type. Consequently, by considering the overall setting of different interpreted tilt-blocks, predictions can be made on the different depositional processes that may occur on either side, as a function of the competing catchments on the tilt-block crest. As such, these rift-formed sediment source pathways become major sediment entryways into the depositional basin. Data derived from modern-day rifts in Chapter 3 analyses these major inputs, whilst their wider impact on syn-rift sedimentation and the distribution of alluvial fan deposits in synrift sedimentary packages is summarised in Chapter 6.

1.3.3. Research Question 3: How can alluvial fan facies and their constituent components be used to determine depositional flow types, and their variable temporal and spatial locations within rift basins?

Alluvial fan sedimentary systems can be formed by a variety of rheologically distinct fluvial flows, existing on a continuum from viscous cohesive debris flows, carrying high concentrations of sediment, to low viscosity streamflows with minimal sediment concentration (Nemec & Steel, 1984; Pierson & Scott 1985; Pierson & Costa, 1987). Flows may also be described as confined or unconfined depending on their degree of channelisation, resulting in spatial and temporal variation in flow velocity and local shear stress, subsequently impacting sediment carrying capacity of that flow (North & Davidson, 2012).

Three dominant depositional flow types are typically described when considering alluvial fan construction, consisting of debris flows (of cohesive and non-cohesive types), hyperconcentrated flows and stream flows (Benvenuti & Martini, 2002). Debris floods have been introduced as a separate rheological flow type, which remobilise part of the entire stream bed during flood conditions (Hungr et al., 2001; proposed definition from Church & Jakob, 2020). The calibre and volume of sediment that a flow is able to transport is a function of flow velocity, shear stress, and sediment availability (Pierson & Costa, 1987). Alluvial fan deposits comprise a wide variety of lithofacies including conglomerates, sandstones, siltstones and claystones. As they are usually short-range, closed systems (as opposed to far reaching, tens of kilometres scale fluvial fans; Harvey et al., 2005; Ventra & Clarke, 2018), it is possible to find all these different sediment types in close proximity within the same fan body (Blair & McPherson, 1994; Ventra & Clarke, 2018). This stratigraphic variability means alluvial fans can be particularly sensitive to

tectonic and climatic forcing, and small fluctuations in these controls can be preserved within the stratigraphic record.

Field-based studies of alluvial fan deposits in rift settings are the primary method for obtaining detailed lithofacies information, and how their specific stacking patterns comprise different facies associations that in turn form different architectural and depositional elements (e.g. Blair, 1999c; Mack & Leeder, 1999; Leleu et al., 2016; Hemelsdaël et al., 2017). This information is then placed in a framework of the interpreted structural and climatic settings at the time of deposition in order to derive palaeogeographic models to detail the evolution of the rift system. The measurement of depositional features can provide key insights into the specific formative processes of those sediments, and lead to an improved understanding of the response of depositional environments to external forcing. Conglomeratic deposits are particularly difficult to decipher, as coarse grain sizes are indicative of high magnitude flows whose high erosive power could potentially remove previous deposits from the stratigraphic record (DeCelles et al., 1991; Moscariello, 2018). Further analysis of the identifiable signals of extrinsic and intrinsic forcing on facies textures is required: conglomerate clast shapes, sizes and orientations are tested extensively in Chapter 5 for this purpose.

1.4. Chapter-specific objectives

Three studies have been undertaken, utilising both field-based and remote sensing methodologies in order to address the outlined research questions; specific objectives, and research question(s) they address, are outlined below:

Chapter 3: Development of alluvial fans associated with uplifted tilt-block crests; a comparative study from present-day extensional regimes **(addresses Research Questions 1, 2, 3)**

1. Map the extent of alluvial fans and their catchments sourced from four modern-day intrabasinal uplifted tilt-block crests (Hammar Range; East African Rift System, Barguzin Range; Baikal Rift System, Toiyabe and Toquima Ranges; Basin and Range province). Identify and measure key morphometric parameters to establish similarities and differences in morphological form between sets of fans occurring on either side of the same hinterland, and across different rift systems **(Research Questions 1, 2)**

2. Link the measured morphologies to potential depositional flow types, and elucidate the dominant processes present on footwall slope-sourced fans, hangingwall dipslope fans, and between different rift systems **(Research Questions 2, 3)**

Chapter 4: Impact of a pre-existing transverse drainage system on active rift stratigraphy: An example from the Corinth Rift, Greece **(addresses Research Questions 1, 2, 3)**

1. Map the lithofacies variations of the Rodini Fm., a synrift conglomeratic succession located in the Gulf of Corinth, Greece, and define architectural elements that forms the stratigraphy **(Research Question 3)**

2. Determine flow processes active when the Rodini Fm. was deposited, and examine spatial and temporal variation **(Research Question 3)**

3. Determine how active depositional systems interacted with evolving uplifted footwall regions and the inception and displacement of new intrabasinal faults **(Research Questions 2, 3)**

4. Propose new palaeogeographic models describing deposition of the Rodini Fm., and predict how the system evolved to its present-day configuration **(Research Questions 1, 2, 3)**

Chapter 5: Conglomerate clast morphometrics to determine palaeogeographic evolution within a rift basin fill, Gulf of Corinth, Greece **(addresses Research Questions 1, 2, 3)**

1. Identify and measure the fabrics and textures of conglomeratic clasts of the Rodini Fm., based on the derived lithofacies from Chapter 4 **(Research Question 3)**

2. Investigate the similarities and differences in clast fabric through the stratigraphy and across the basin to refine the determined lithofacies and palaeogeographies of Chapter 4 **(Research Questions 1, 2, 3)**

3. Predict how these similarities and differences may have been affected by ongoing rift evolution **(Research Questions 2, 3)**

4. Verify the applicability of detailed conglomeratic clast data in determining depositional flow processes **(Research Question 3)**

1.5. Study methodologies

This section provides a summary of the methods employed for data collection and the data sets collected for study, in relation to Chapters 3, 4 and 5. These datasets allow for the interpretation and analysis of alluvial fan deposits within rift basins across a variety of scales, and under the influence of different extrinsic and intrinsic controls. Detailed coverage of the specific methods used in data collection and analyses are outlined in the methodology sections of each chapter.

1.5.1. Field-based data collection

The Gulf of Corinth, Greece, was chosen as a suitable study area for synrift alluvial fan deposition; as an actively extending rift system, exposed synrift deposits deposited over the last 5 Ma are relatively recent, and not overprinted by further structuration. This allows for clearer links to be established between depositional and structural events. The Gulf lies between mainland Europe to the north, and the Peloponnesus peninsula to the south. Across the northern coast of the Peloponnesus peninsula, early stage synrift deposits crop out, forming large cliffs and mountainous terrain. These deposits were exhumed by footwall uplift as displacement on older, more southerly faults was reduced and was accommodated on new faults further to the north, forming much of the present-day coastline of the Peloponnese.

The Rodini Fm., located on the northernmost tip of the peninsula, was analysed as recent studies indicated the sediments had a fluvio-alluvial origin (Palyvos et al., 2007; Esu & Gerotti, 2015). Consequently, two field seasons totalling 8 weeks were undertaken in the Spring-Summer and Autumn of 2017. Field-based data collection methods employed included outcrop reconnaissance and geological mapping, collection of large-scale (hundreds of metres) vertical profiles, acquisition of small-scale (decimetres to metres) vertical profiles, and the measurement of detailed clast morphometrics.

1.5.2. Remote-sensing data collection

Remotely sensed data was utilised to study present-day rift systems at a large scale. Google Earth satellite imagery was used to make general observations on the sedimentary processes occurring within rift basins of the East African Rift, Baikal Rift and Basin and Range province extensional systems. Initial data collection of alluvial fan

catchments and associated fans was completed on Google Earth using the inbuilt polygon tool, to provide basic outlines of the extent of fans and associated catchments.

These frameworks were then saved as individual shape files and imported into ArcGIS. DEM imagery of the study locations was obtained from the ALOS Global Digital Surface Model, or ALOS World 3D – 30m (AW3D30), provided for free online by the Japanese Space Agency, JAXA (https://www.eorc.jaxa.jp/ALOS/en/aw3d30/index.htm). These data provide a global dataset of DEM imagery with a horizontal resolution of 1 arcsecond (~30 m). Individual GeoTIFF files were georeferenced according to their latitude and longitude and stitched together using the Mosaic to Raster tool. Imported Google Earth shapefiles where then referenced to the new combined raster, according to predetermined localities present on both the shapefile and the raster (such as fault tips). The ArcGIS polygon and polyline tools were then used to define catchment and fan morphometrics, using the imported Google Earth shapefile as a rough guide.

1.6. Thesis outline

This thesis comprises seven chapters, each of which address different aspects of the thesis aim and objectives, and research questions outlined above.

Chapter 1: Introduction

This chapter provides a general overview of alluvial and fluvial system development in continental rift settings, before introducing the thesis aim and objectives. The three research questions are justified, and the specific objectives of each data chapter are presented. Finally, the research methods employed in the thesis are outlined.

Chapter 2: Research context

This chapter provides an overview of the previously published literature on the research areas covered by this thesis. Particular focus is given to: (i) the geodynamic formation of continental rift systems and the spatial and temporal evolution of their structure and sedimentary systems; (ii) the extrinsic and intrinsic controls of alluvial fan formation in rift basins and their formative depositional processes; and (iii) the tectonic evolution of the three study areas analysed in the presented data chapters.

Chapter 3: Development of alluvial fans associated with uplifted tilt-block crests; a comparative study from present-day extensional regimes

This chapter presents a satellite imagery and DEM imagery-based study of alluvial fan systems from modern-day continental rifts. Data on the morphometric parameters of linked alluvial fans and catchments are presented from three uplifted tilt-block crests from the East African Rift (Ethiopia), Baikal Rift (Russia), and Basin and Range province (USA). Comparisons of the quantitative data are drawn to understand the similarities and differences between depositional systems formed over the footwall slope and hangingwall dipslope, and between systems formed at different scales and under different climatic regimes.

This chapter is presented in a format suitable for submission as a journal publication.

Chapter 4: Impact of a pre-existing transverse drainage system on active rift stratigraphy: An example from the Corinth Rift, Greece

This chapter presents a field-based study of a synrift conglomeratic succession from the Gulf of Corinth, Greece. Interpretations of the observed lithofacies and of the architectural elements that they build are summarised. Palaeogeographic maps are constructed outlining the evolution of the alluvial fan system that formed the preserved sediments,

and the response of the depositional system to ongoing rift evolution. The deposits are then placed into the wider context of the evolution of the Gulf of Corinth since its formation.

A published version of this chapter exists as:

Somerville, D.J.P., Mountney, N.P., Colombera, L. & Collier, R.E.Ll. (2020) Impact of a pre-existing transverse drainage system on active rift stratigraphy: An example from the Corinth Rift, Greece. Basin Research, 32(4), 764-788. DOI: 10.1111/bre.12396 (Appendix 1)

Chapter 5: Conglomerate clast morphometrics to determine palaeogeographic evolution within a rift basin fill, Gulf of Corinth, Greece

This chapter analyses morphometric data recorded from clasts constituting the conglomeratic lithofacies outlined in Chapter 4. A total of 1,531 clasts are described in terms of their composition, shape, size and directional data. These data are used to supplement interpretations of the lithofacies and architectural elements outlined in Chapter 4, and construct updated palaeogeographic maps of the temporal and spatial evolution of the alluvial system. The applicability of detailed clast measurements in understanding depositional flow processes is then considered in detail.

This chapter is presented in a format suitable for submission as a journal publication.

Chapter 6: Discussion

This chapter integrates the results of Chapters 3-5 of this thesis in the context of the three stated research questions. The wider implications of the presented data are considered, and interpretations of the varying responses of alluvial and fluvial systems to rift evolution are provided.

Chapter 7: Conclusions and future work

The final chapter summarises the conclusions of each chapter with regard to the overarching aim of the thesis and the stated research questions. Three recommendations for possible areas of future research are outlined.

2. Research context

This chapter provides an overview of prior research pertaining to the geological evolution of continental rift systems and their sedimentary fill, providing context for the research – including approaches to data collection and analysis, and surrounding discussion – contained within this thesis. Developments in the understanding of how rift systems initiate and evolve, and how sediment is routed into these basins to accumulate as the infill are outlined. The formation of alluvial fan systems within rift basins and their typical formative flow processes and resultant deposits are summarised. Finally, geodynamic introductions to each of the four main study areas provide further context to specific contextual reviews in the following chapters.

2.1. The formation of continental rifts and their deposits

2.1.1. On the occurrence and development of rift basins

Continental rift systems manifest as the surface expression of tensional stresses in the Earth's crust. Continental rift provinces comprise a series of linked or unlinked sedimentary basins bounded by normal faults; many evolve as the precursor to continental breakup and the formation of new ocean basins. The driving mechanisms behind the tensional stresses forming these basins can be broadly assigned to two categories: *active rifting* and *passive rifting* (Keen, 1985). *Active rifting* (Figure 2.1) is caused by thermal pluming in the deeper mantle, which acts to drive the upwelling of the asthenosphere and leads to the stretching of the relatively more brittle overlying lithosphere, initiating tensional stress and subsequent fracture (Sengör & Burke, 1978; White & McKenzie, 1989; Allen & Allen, 2013). *Passive rifting* (Figure 2.1) relies on pre-

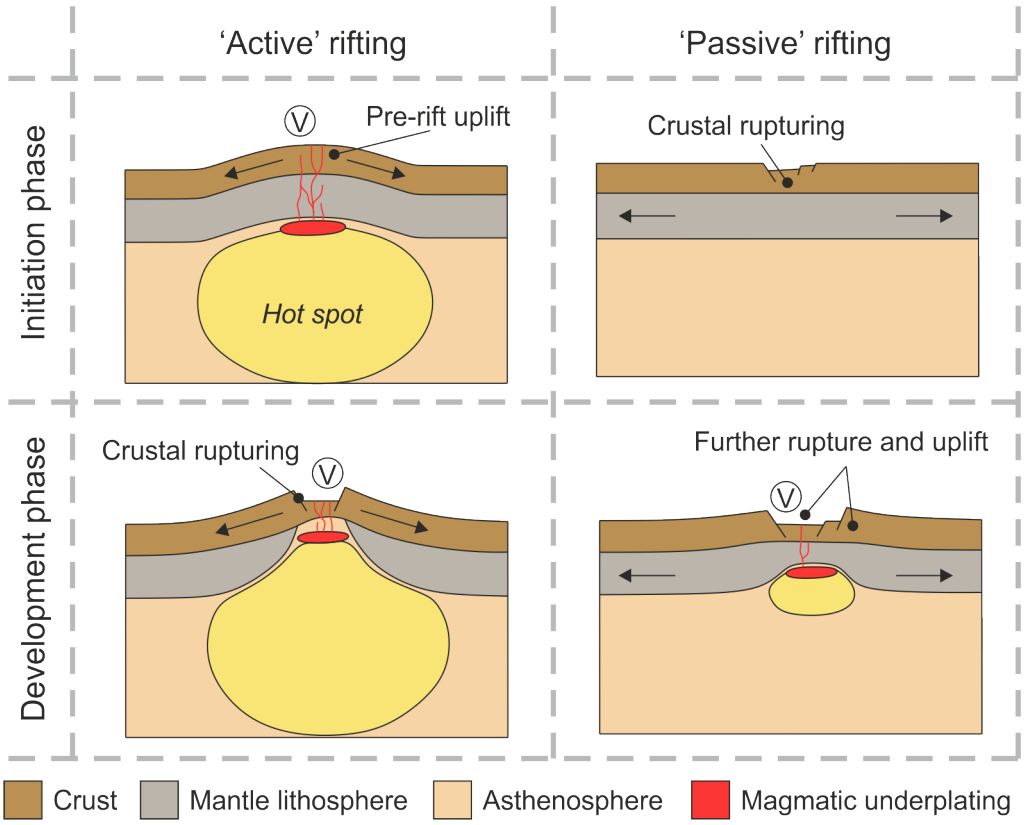

Figure 2.1 *Schematic diagrams displaying the 'active' and 'passive' hypotheses driving the initiation and development of continental rifting. The 'active' mechanism relies on the ascent and emplacement of a low-density mantle body, driving surface uplift and volcanism (V) before surface rupture. The 'passive' mechanism relies on regional stress fields derived from plate boundary forces, leading to crustal stretching and the formation of a sublithospheric mantle body that undergoes decompression melting. After Corti et al. (2003).*

existing, far-field tensional stresses acting simultaneously on the lithosphere and upper asthenosphere, laterally stretching and thinning them, driving fracturing and leading to basin generation (McKenzie, 1978; McKenzie & Bickle, 1988). A consequence of *passive rifting* is the doming and partial melting of the upper asthenosphere; the important distinction is that this is not caused by an actively upwelling mantle 'hotspot' (Mutter et al., 1988; McKenzie & Bickle, 1988). Subsequent rift basins have traditionally been described as magma-poor or magma-rich (e.g. Reston 2009; Stab et al., 2016), depending on the amount of decompression melting occurring as a result of the upwelling asthenosphere, and the presence of fractures in the lithosphere through which magma

can flow (see Corti et al., 2003, for review). This rigid classification has been disputed in the last two decades (see Ziegler & Cloetingh, 2004 and Tugend et al., 2018 for review), with recent studies detailing the temporal evolution of magma-poor to magma-rich systems, and magma-rich to magma-poor rifts. Typically, this evolution would occur over the life cycle of a rifting system, from initiation through to lithospheric and continental breakup (e.g. Shillington et al., 2009). Courtillot et al. (1999) determined that, in the event of continental breakup, a combination of both *active* magma-rich rifting, and *passive* lithospheric stress-driven rifting, would be the likely driver of rift evolution.

Extension of the crust and mantle lithosphere in this manner manifests itself in one of three ways (Figure 2.2):

(i) a pure shear model, where the crust and its underlying mantle lithosphere undergo similar instantaneous stretching, accommodated by brittle fracturing of the crust and ductile stretching of the lithosphere (McKenzie, 1978). This results in symmetrical deformation and lithospheric thinning across any vertical line through those layers.

(ii) a simple shear model, where extension is controlled by a throughgoing shallow detachment fault, cutting through both layers, causing brittle fracturing and subsidence on the crustal surface (Wernicke, 1985). This results in asymmetrical deformation that is non-uniform across any vertical line through those layers.

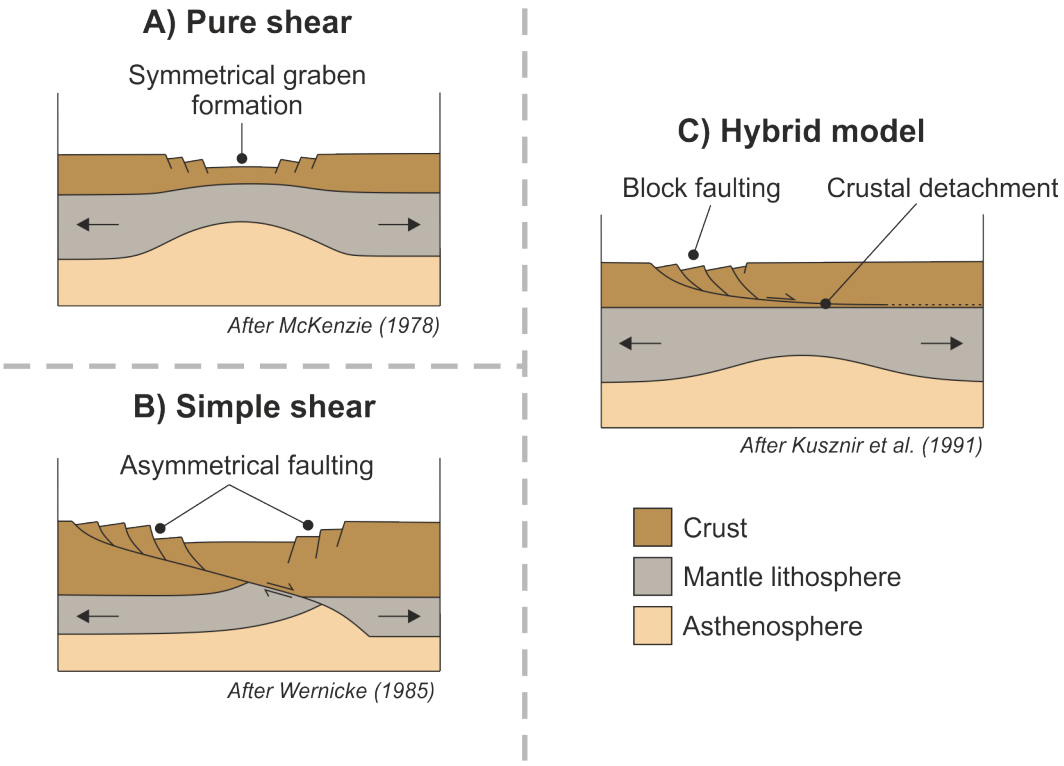

Figure 2.2 *Schematic diagrams displaying (A) the extension of the lithosphere through pure shear, whereby the brittle crust and ductile upper lithosphere have the same stretching factor and deform uniformly; (B) the extension of the lithosphere through simple shear, whereby deformation between the brittle crust and ductile upper lithosphere occurs asymmetrically, forming a throughgoing low angle detachment fault; (C) the extension of the lithosphere through a hybrid model, whereby the brittle crust is deformed through fracturing and forms a detachment fault boundary at its juxtaposition to the more ductile upper lithosphere. After McKenzie (1978), Wernicke (1985), Buck (1988) and Kusznir et al. (1991).*

(iii) a hybrid model, where the crust and lithosphere are sufficiently detached to allow brittle fracturing and simple shearing of the crust, and the stretching of an unfractured mantle lithosphere (Kusznir et al., 1991).

The method of formation of a rift will govern potential heat flow variations along its axis (Buck et al., 1988), its structural character (half-graben vs. full graben formation), and the development of features such as accommodation zones in response to basin subsidence (see Faulds & Varga, 1998, for review), which in turn will control the distribution and type of sediments deposited therein (Gawthorpe & Leeder, 2000).

Further controls on the distribution, size and orientation of depocentres (and subsequently on the pattern of rift sedimentation) include: (i) changes in the rate of extension; (ii) changes in stress orientations; (iii) the orientation and type of pre-existing structural features in the crust and mantle lithosphere; and (iv) the lithologies present in both pre-rift basement and syn-rift basin-fill sediments (Ziegler & Cloetingh, 2004). The result is a wide array of possible combinations and a unique mode of formation for each individual rift system, where the magnitude of influence of each control on its development varies in both space and time.

2.1.2. Initiation, growth and linkage of normal faults

At the Earth's surface, extension causes the rupture of the crust and subsidence occurs. Basins are bounded by normal faults, which initiate and grow over time as extension continues (Gawthorpe et al., 1994; Allen & Allen, 2013). Initial subsidence of the crust without surface rupture may occur as a precursor to surface fault development (e.g. Martins-Neto, 2000). Cowie et al. (2000) and Gawthorpe & Leeder (2000) describe normal fault development in detail based on numerical models and field observations; faults are initially small and unlinked, leading to a broad region characterised by relatively small, shallow depocentres. These initial ruptures serve as weak points in the crust which accommodate additional strain, which drives further extension and deepening of adjacent depocentres, and which causes faults to increase in length such that they begin to link together. Coherent fault networks commence development, and form in a way whereby major faults vary in dip orientations (i.e. they exhibit distinct *polarities*) along the length of the overall fault zone (McClay & White, 1995). Intermediary transfer zones (Faulds & Varga, 1998) and related structural features such as relay zones additionally develop. The latter are the slopes between two parallel faults and provide a

link between the newly uplifted hinterland, a sediment source, and the newly formed hangingwall depocentre, a sediment sink (McClay & White, 1995; Gupta et al., 1999). Wider rift zones may also form fault-bounded *rotational tilt-blocks* of crust and mantle lithosphere, as extension is accommodated on multiple parallel faults separated by an uplifted tilt-block crest and adjacent depositional basin (Anders et al., 1993).

The mechanisms driving the growth of individual faults, both prior to and following their linkage, is a point of contention in the literature. Watterson (1986) and Dawers et al. (1993) determined that normal fault displacement and length displayed a linear correlation, and early studies provided evidence for an *isolated fault growth model* (Watterson, 1986; Walsh & Watterson, 1988; Childs et al., 2017), the basis of which is that as a fault grows, its length and displacement increase at similar rates (Figure 2.3). More recently, however, observations have been made of a *constant length model* (Morley, 2002; Walsh et al., 2002; Jackson & Rotevatn, 2013), whereby a fault extends to its final or near-final length early on in its life, and displacement then continues to increase despite no further increase in fault length (Figure 2.3). However a fault grows, impacts are felt on the subsequent early rift sedimentation into the newly formed depocentre. Notably, the location of sediment input points (e.g. fault tips, relay zones) and rates of sediment supply (e.g. from uplifting footwalls) are affected (Gawthorpe et al., 2000). Furthermore, the linking of established faults results in those faults being under-displaced relative to their combined length (Gawthorpe & Leeder, 2000; Gawthorpe et al., 2003). This can act to divert sediment away from the previously exploited relay zones, as uplift on the breached ramp may form an impassable topographic high. Overlapping faults can also lead to the formation of temporary topographic highs in the hangingwall, diverting sediment away from the centre of the basin (Figure 2.4) (Schlische & Anders,

1996; Jackson et al., 2002; Densmore et al., 2003; Cowie et al., 2006; Fossen & Rotevatn, 2016).

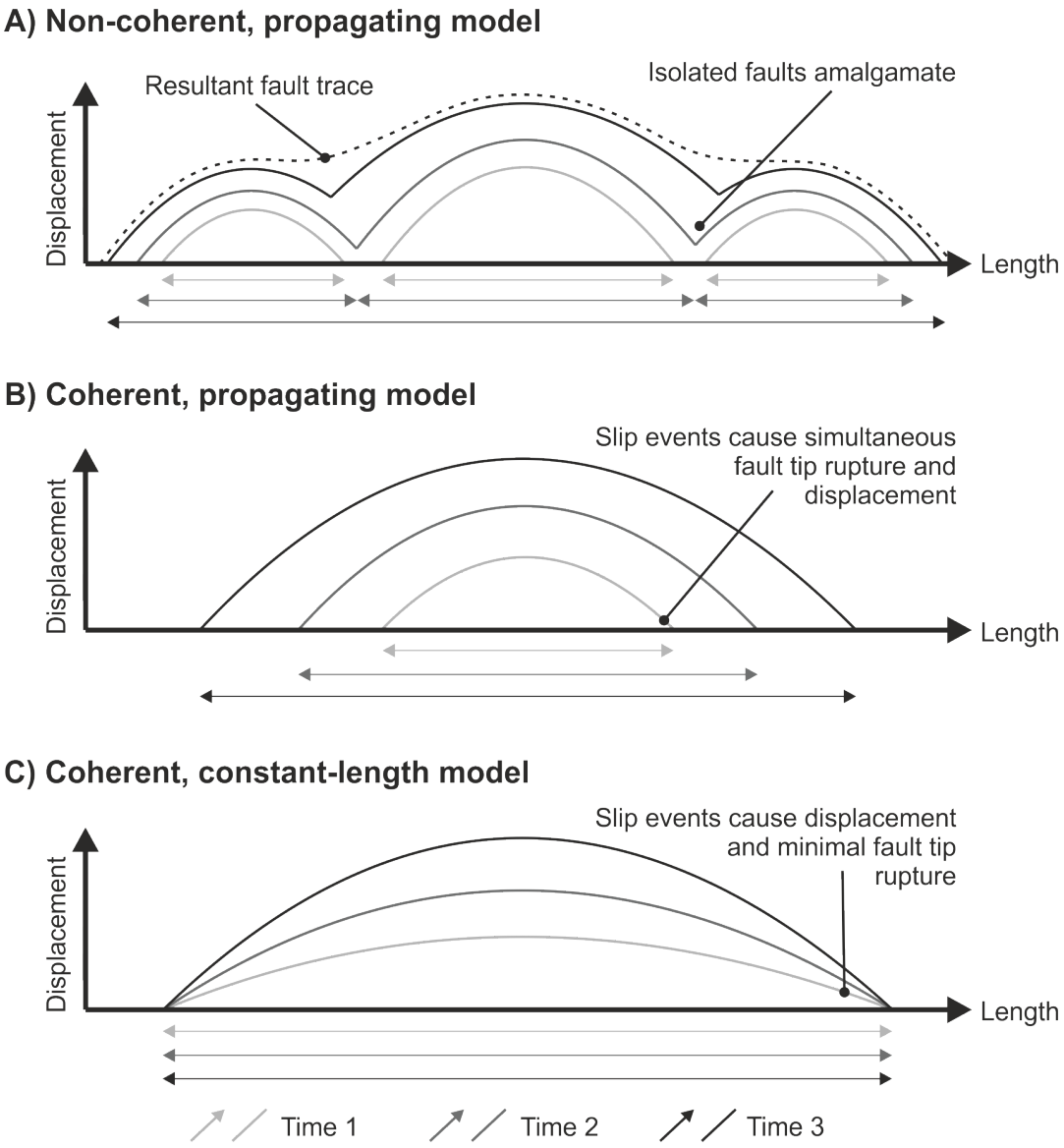

Figure 2.3 *Displacement-length profiles displaying the fault growth through time of (A) the non-coherent, propagating case, or 'isolated' model, whereby individual faults propagate and displace at constant rates before linking; (B) the coherent, propagating case, or individual 'isolated' model, whereby a single fault propagates and displaces at constant rates; (C) the coherent case, or 'constant-length' model, whereby a fault rapidly reaches it maximum length before extensive displacement occurs. After Childs et al. (2017).*

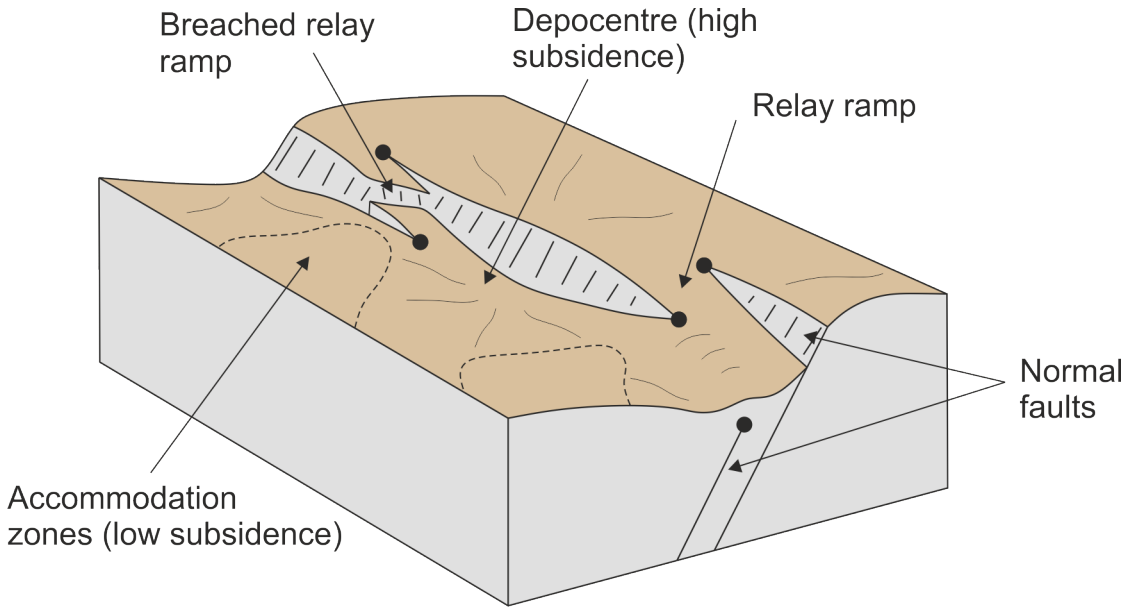

Figure 2.4 *Schematic diagram of a rift setting showing examples of differential topography formed within major depocentres. Where fault tips overlap one another, subsidence is reduced compared to subsidence loci adjacent to the centres of faults. If relay ramps become breached, the faults will link, and displacement will begin to correct the intrabasinal topography. After Jackson et al. (2002), modified from Larsen (1988), Trudgill & Cartwright (1994) and Schlische (1995).*

As faults grow and form arrays, and the rift zone becomes established, half-graben or full graben morphologies may form. Half-grabens are asymmetric basins, bounded on one side by a master normal fault, whereas full grabens are symmetrical basins, bounded on both sides by master normal faults (Morley, 1990; Morley, 2002). The predominance of one type over the other depends on the presence and orientation of pre-existing basement structures (Morley et al., 2004), mechanical and thermogenic properties of the extended crust (including the impact of volcanism) (Buck, 1991), and the length of time over which extension has been ongoing (Lambiase & Bosworth, 1995). In the early rift phase, when continental sedimentation is more common, half-graben morphologies forming an asymmetric rift are common (Leeder & Gawthorpe, 1987; Lambiase & Bosworth, 1995). These settings are a focus of this study. Half graben basins are mostly represented by a major basin-bounding fault, which generates an uplifted footwall on one

side of the basin. By contrast, a directly adjacent hangingwall depocentre and a hangingwall dipslope (affected by flexure or intrabasinal faulting) develop in the centre and on the far side of the basin, respectively (see Figure 2.5). The supply of sediment into the basin is affected by these structures, which may develop as upstanding highs from which sediment is sourced, else may act as barriers that influence sediment transport pathways (Gawthorpe & Leeder, 2000). The role of fault-related basin surface topography in controlling sediment distribution has remained a key focus of study since the 1980s and through to the time of this present work (see Figure 2.6, e.g. Leeder & Gawthorpe, 1987; Martini & Sagri, 1993; Schlische & Anders, 1996; Connell et al., 2012; Henstra et al., 2017; Hemelsdaël et al., 2017; Cullen et al., 2020; Somerville et al., 2020; Barrett et al., 2020).

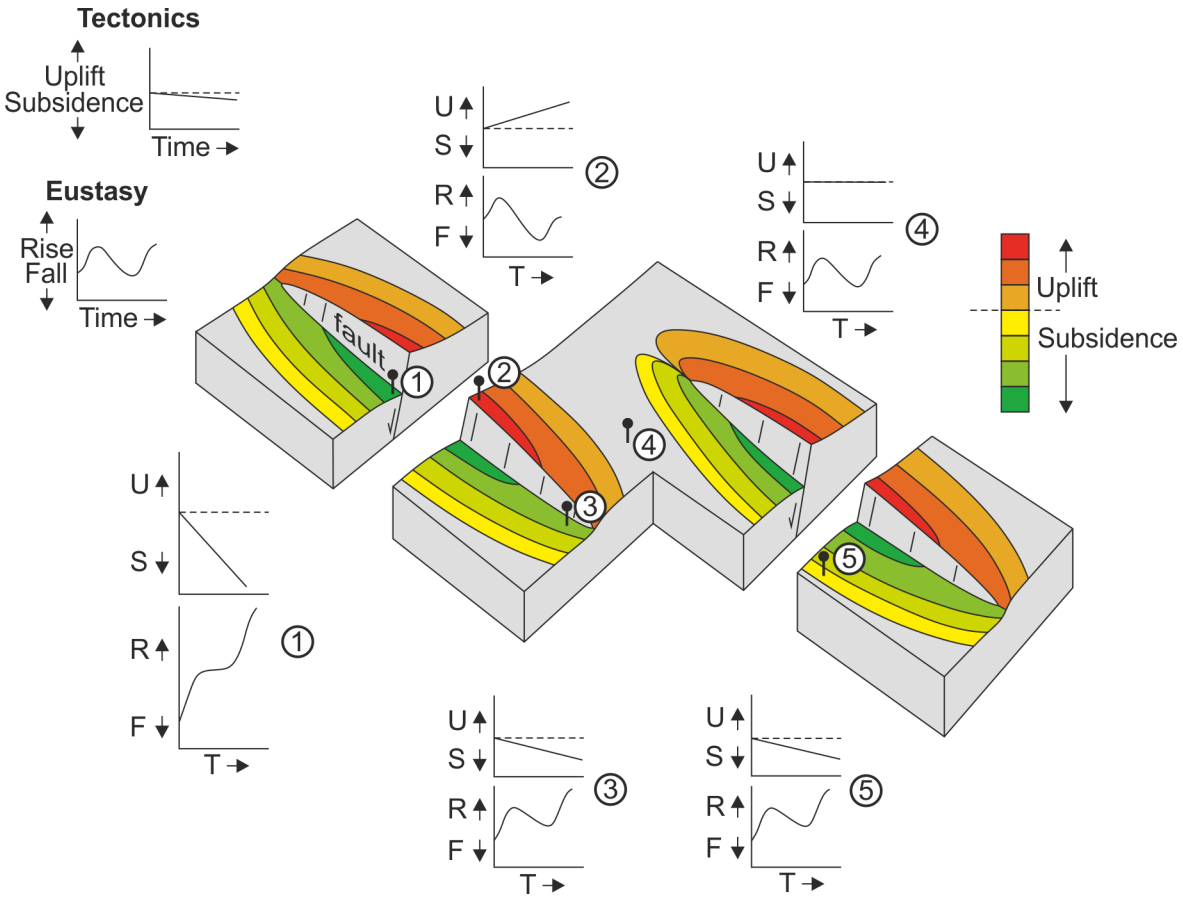

Figure 2.5 *Schematic diagram showing differential subsidence and uplift, and resulting base level changes, from multiple locations in adjacent half-graben basins. Overlapping basin bounding faults form a relay zone (location 4) that experiences net zero uplift or subsidence as a consequence of extension. After Gawthorpe et al. (1994).*

Figure 2.6 (next page) *3D block models displaying the predicted depositional environments that develop within continental rift basins and resultant depositional architectures. Fluvial and alluvial system response to ongoing rift evolution varies drastically between (A) the initiation stage, (B) the interaction and linkage stage, (C) the throughgoing fault stage, and (D) the "fault death" stage. From Bridge (2006), originally after Gawthorpe & Leeder (2000).*

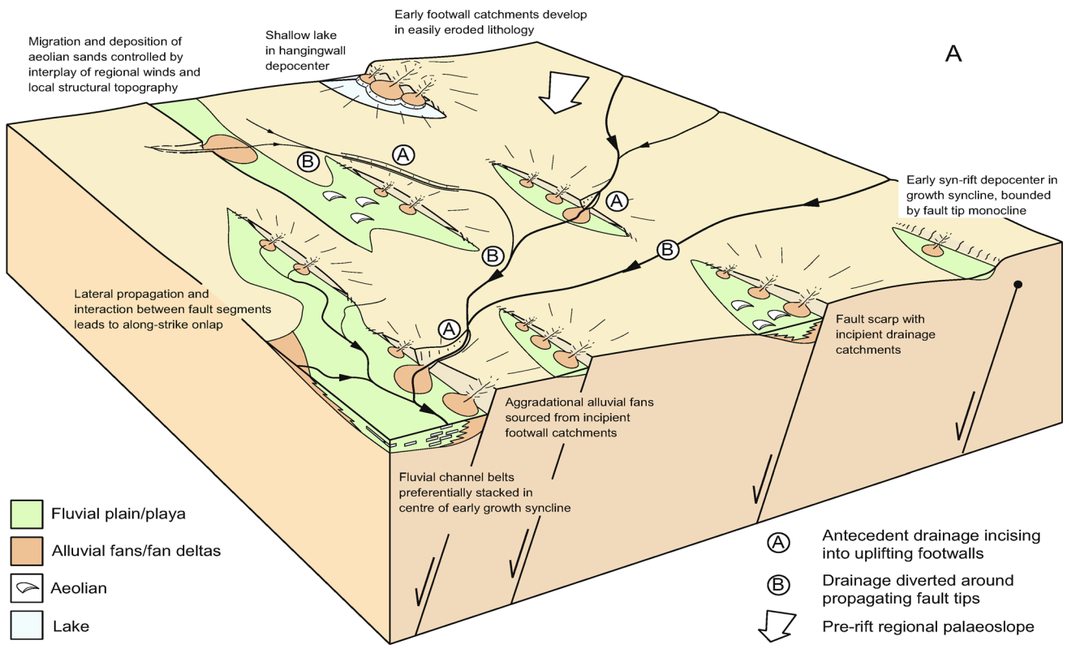
A
Migration and deposition of aeolian sands controlled by interplay of regional winds and local structural topography
Shallow lake in hangingwall depocenter
Early footwall catchments develop in easily eroded lithology
Early syn-rift depocenter in growth syncline, bounded by fault tip monocline
Lateral propagation and interaction between fault segments leads to along-strike onlap
Fault scarp with incipient drainage catchments
Aggradational alluvial fans sourced from incipient footwall catchments
Fluvial channel belts preferentially stacked in centre of early growth syncline
Fluvial plain/playa
Alluvial fans/fan deltas
Aeolian
Lake
Ⓐ Antecedent drainage incising into uplifting footwalls
Ⓑ Drainage diverted around propagating fault tips
Pre-rift regional palaeoslope

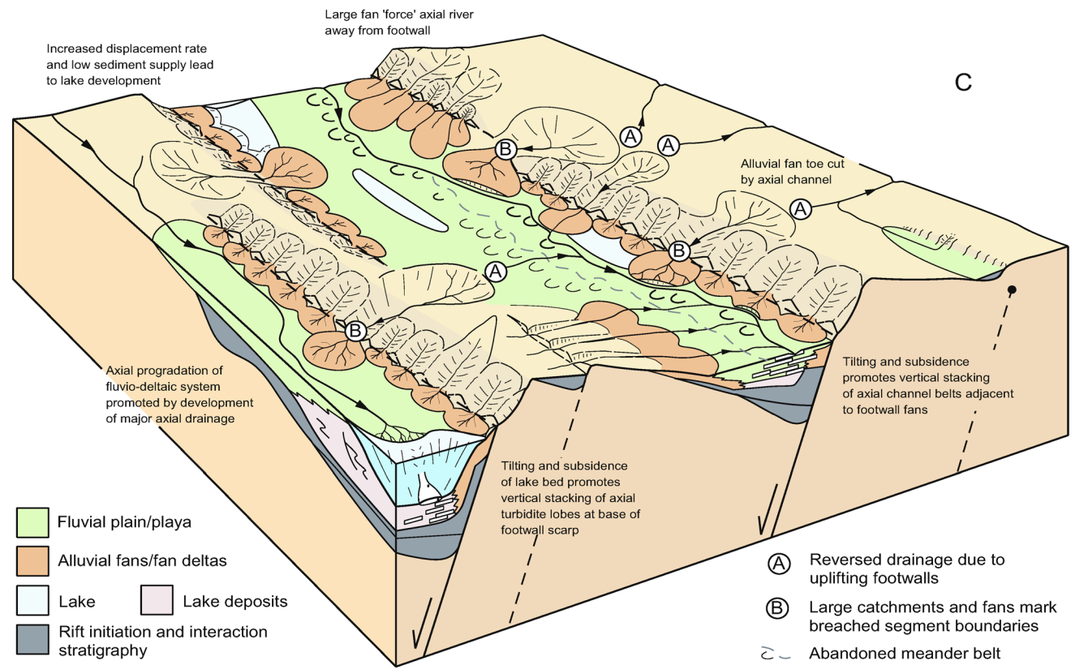
C
Large fan 'force' axial river away from footwall
Increased displacement rate and low sediment supply lead to lake development
Alluvial fan toe cut by axial channel
Axial progradation of fluvio-deltaic system promoted by development of major axial drainage
Tilting and subsidence promotes vertical stacking of axial channel belts adjacent to footwall fans
Tilting and subsidence of lake bed promotes vertical stacking of axial turbidite lobes at base of footwall scarp
Fluvial plain/playa
Alluvial fans/fan deltas
Lake
Lake deposits
Rift initiation and interaction stratigraphy
Ⓐ Reversed drainage due to uplifting footwalls
Ⓑ Large catchments and fans mark breached segment boundaries
Abandoned meander belt

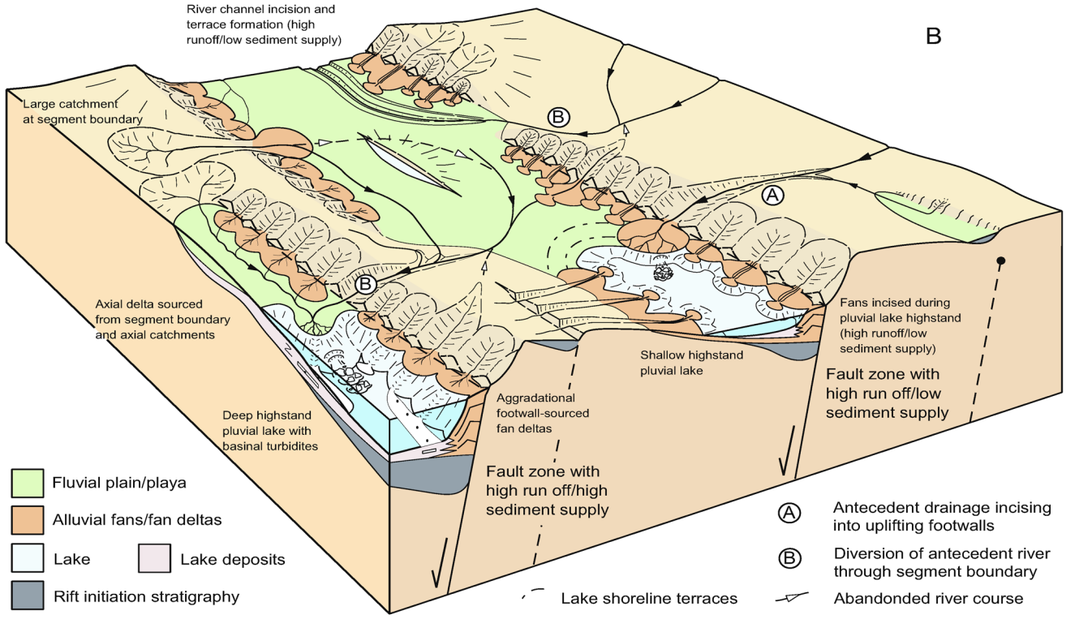
B
River channel incision and terrace formation (high runoff/low sediment supply)
Large catchment at segment boundary
Axial delta sourced from segment boundary and axial catchments
Deep highstand pluvial lake with basinal turbidites
Aggradational footwall-sourced fan deltas
Shallow highstand pluvial lake
Fans incised during pluvial lake highstand (high runoff/low sediment supply)
Fault zone with high run off/low sediment supply
Fault zone with high run off/high sediment supply
Fluvial plain/playa
Alluvial fans/fan deltas
Lake
Lake deposits
Rift initiation stratigraphy
Lake shoreline terraces
Ⓐ Antecedent drainage incising into uplifting footwalls
Ⓑ Diversion of antecedent river through segment boundary
Abandonded river course

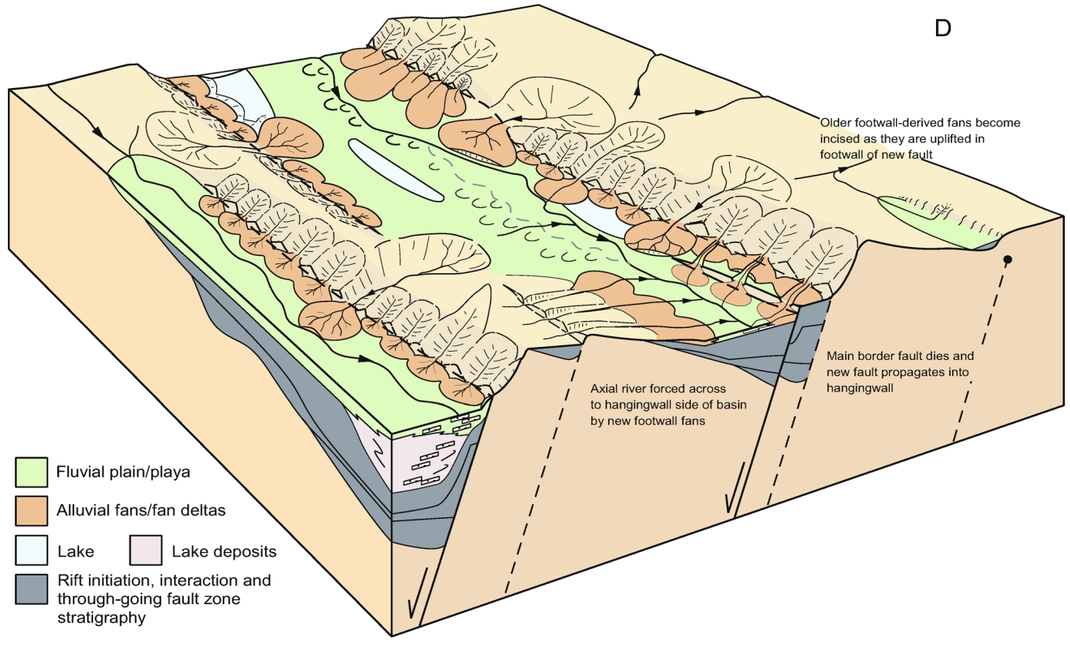
D
Older footwall-derived fans become incised as they are uplifted in footwall of new fault
Axial river forced across to hangingwall side of basin by new footwall fans
Main border fault dies and new fault propagates into hangingwall
Fluvial plain/playa
Alluvial fans/fan deltas
Lake
Lake deposits
Rift initiation, interaction and through-going fault zone stratigraphy

2.1.3. The response of sediment delivery and preservation to newly formed rifts

As subsidence occurs and accommodation forms, drainage pathways and their sediment will be drawn to them by gravitational forces. This, in conjunction with the asymmetric morphology of new basins (described above) and the overall structure of the rift zone, controls the *tectonostratigraphy* that forms during ongoing extension (Figure 2.7). The disruption of existing drainage pathways by faulting can result in numerous different responses:

(i) The diversion of flow *away* from the new depocentres by newly uplifted topography (e.g. Frostick & Reid, 1989; Henstra et al., 2017), resulting in an initially sediment-starved basin prior to the development of basin margin sediment sources as a consequence of rift margin uplift (for example, linked catchment and alluvial fan systems).

(ii) The diversion of flow *towards* new depocentres over the hangingwall dipslope (e.g. Eliet & Gawthorpe, 1995; McCarthy, 2013), resulting in sediment supply to the basin at a rate that is rapid relative to the rate of generation of accommodation space.

(iii) The diversion of flow *around* newly uplifted footwalls and their associated fault tips (e.g. Young et al., 2000; Henstra et al., 2017) resulting in axial sediment deposition in the basin. This may be through aforementioned relay zones, depending on the density of faulting.

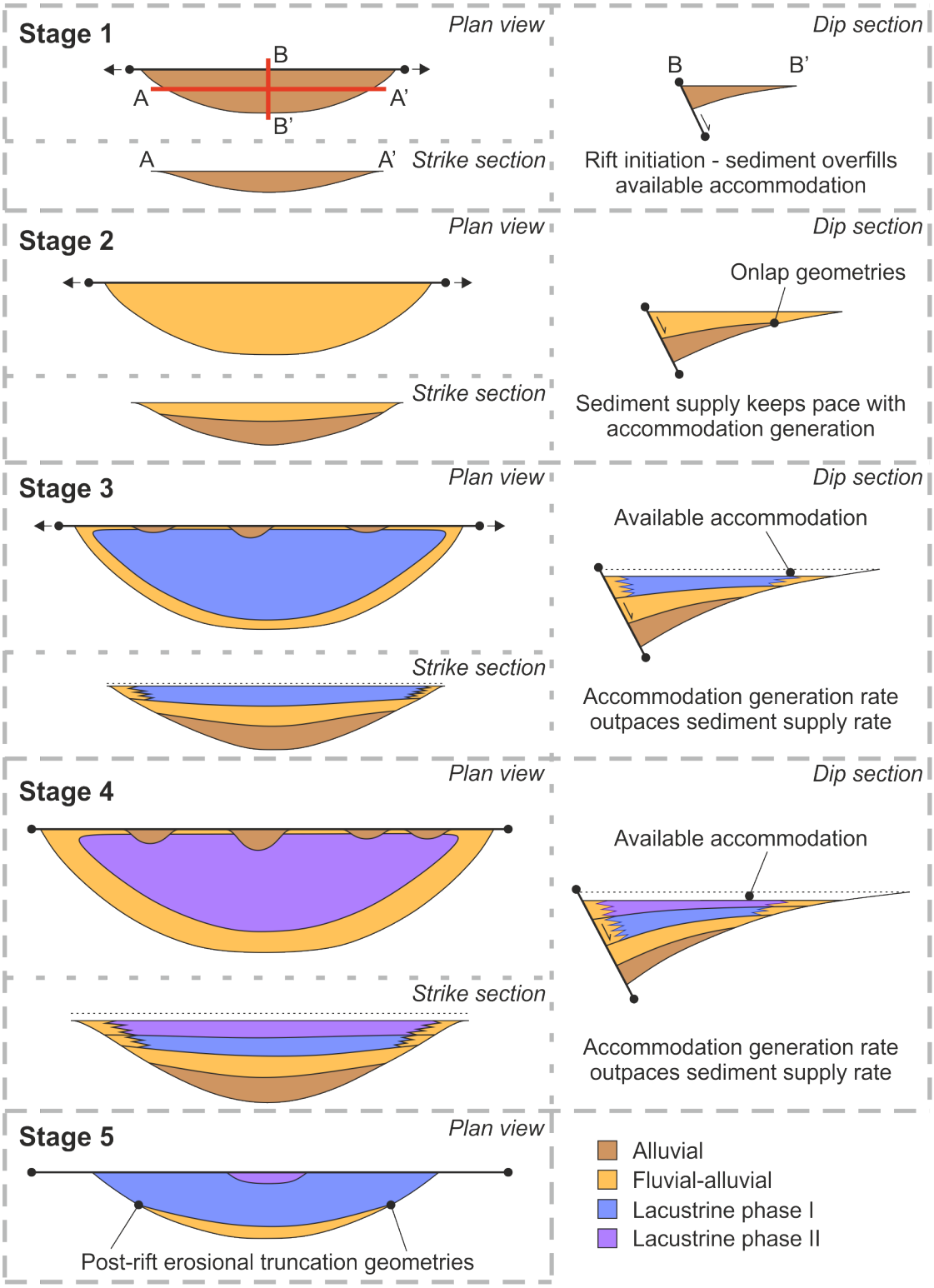

Figure 2.7 *Example predicted syn-rift stratigraphy of a continental rift basin from basin formation through to the developed rift stage. Little consideration is given to the variability of external sediment sources. After Schlische & Anders (1996).*

(iv) The *erosion* of a system through the newly uplifting footwall (Hemelsdaël et

al., 2017; Barrett et al., 2019) as the incisional strength of the fluvial system keeps pace with active footwall uplift and delivers vast amounts of sediment over the footwall slope.

(v) The *overfilling* of available accommodation by high rates of sediment delivery, resulting in no topographic expression of faults at the surface and the bypass of excess sediment to other areas (Hemelsdaël et al., 2017).

Further to these mechanisms, sediment can also be delivered to the basin directly from the newly uplifted footwall. As the uplift occurs, small catchments form as erosion begins, leading to sediment being shed off the new topographical high in both directions, supplying sediment directly into the adjacent hangingwall over the footwall slope (see Figure 2.6; Leeder & Gawthorpe, 1987; Gawthorpe et al., 1994; Densmore et al., 2003). In this hangingwall depocentre, between the uplifted footwall and the *fulcrum* of the hangingwall dipslope (where there is net zero uplift or subsidence), a syn-tectonic wedge of sediment is deposited (Leeder & Gawthorpe, 1987). This is commonly termed the *syn-rift megasequence* (Gawthorpe et al., 1994) and is the setting for and focus of much of the research described in this thesis. The syn-rift megasequence is a major part of the tectonostratigraphy (the deposits formed as a function of tectonics) of the rift zone.

Studies of tectonostratigraphy have generated models of sediment supply rates from rift initiation to the end of fault activity (e.g. Prosser, 1993; Lambiase & Bosworth, 1995; Martins-Neto & Catuneanu, 2010). At different stages of the basin's life cycle, the depocentre can be described as being either *underfilled*, *filled*, or *overfilled* (Schlische & Anders, 1996; Ravnås & Steel, 1998; Withjack et al., 2002), where a spill point from which excess sediment can by transferred out of the system accounts for what constitutes a filled basin (e.g. Mack et al., 1997); these are defined depending on the ratio between the

rate of sediment supply and the rate of accommodation generation, which will determine the fill state of the basin (Ravnås & Steel, 1998; Withjack et al., 2002). For *underfilled* conditions, the rate of sediment supply is less than the rate of accommodation generation, and vice versa for *overfilled* conditions (Figure 2.8). Where these rates are in perfect balance, the basin may be described as *filled,* a rare basin state that would typically only occur in a relatively limited spatial and temporal domain. The occurrence of *underfilled* or *overfilled* conditions at different times determines the distribution and type of sediment that is deposited in the basin, and also affects the preservation potential of those sediments. During episodes of *underfilled* conditions, preservation potential is enhanced; lake environments may develop, and sediment accumulation occurs below a datum level (defined by a spill point). This creates favourable conditions for long-term sediment storage (Schlische & Anders, 1996; Withjack et al., 2002). During *overfilled* conditions, preservation potential is limited by a lack of available accommodation, which tends to lead to the repeated reworking of transient sedimentary deposits, especially in fluvial and alluvial environments (Schlische & Anders, 1996; Hemelsdaël et al., 2017). Depending on the amount of sediment supplied into the basin, sediment loading may alter the rate of basin subsidence (and subsequently accommodation generation) (Kusznir et al., 1995) affecting the formation of sedimentary environments therein, and the tectonics of the rift system (such as altering seismicity; e.g., the Okavango delta, Gumbricht et al., 2001). Sediment loading typically has a larger impact in post-rift settings, where the influence of active tectonism is reduced (Cochran, 1983; Watts & Burov, 2003).

Much of the focus of this thesis is the sedimentary geology of alluvial fan systems in continental rift settings. Such alluvial environments are commonly present throughout the continental life cycle of a rift and form a variety of different depositional facies in different parts of basins at different times, depending on all of the above factors.

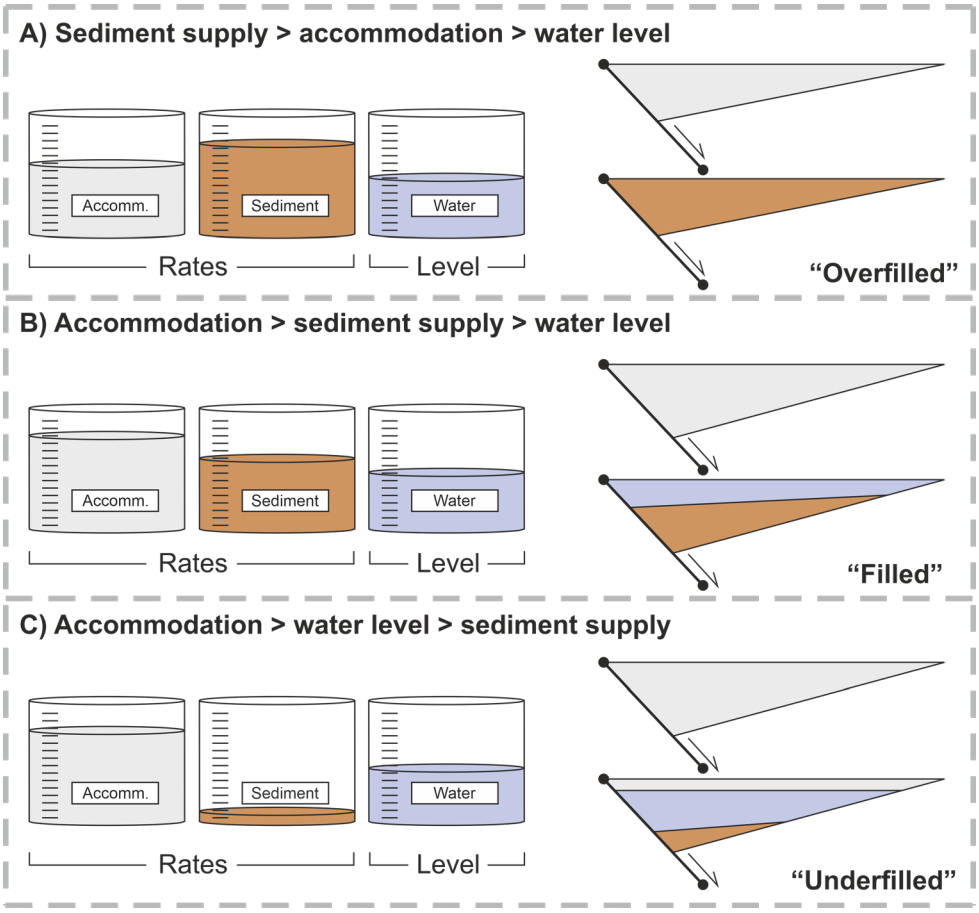

Figure 2.8 *Schematic diagram displaying the relationships of syn-rift sedimentation with the ratios of accommodation generation rates, sediment supply rates, and available water. For a given amount of water available to the rift system, different basin fill states (labelled) will occur according to the ratio of accommodation generation rate to sediment supply rate. Where water is freely available, lacustrine systems will develop in filled and underfilled basins; otherwise, continental depositional systems will dominate the basin floor. After Withjack et al. (2002).*

2.2. The development of alluvial fan systems in continental rifts

2.2.1. Sediment sources and basin locations

An alluvial fan system is a depositional environment forming a cone of clastic sediment from a point source and develops along the margins of sedimentary basins (Ventra & Clarke, 2018). In continental rifts, alluvial fan systems can be categorised as being *axial systems* or *transverse systems,* according to their routing orientations relative to the

orientation of the rift axis (broadly parallel and perpendicular, respectively) (Blair, 1987; Gawthorpe & Leeder, 2000; Weissmann et al., 2015). Typically, there will always be a component of transverse sediment input present over the uplifting footwall, as any degradation of that footwall will cause sediment to be shed from both sides of the new topography, and partly transported into the adjacent hangingwall (Leeder & Gawthorpe, 1987; Whittaker et al., 2010; Barrett et al., 2020). The presence of an axial system or major transverse system is dependent on the diversion of drainage systems into the depocentre. It will also be affected by whether a major sediment source can be established from the adjacent uplifted footwall. The alluvial fan systems of the Basin and Range province (USA) have been studied for many decades in an attempt to analyse the links between tilt-block crest uplift and the fan systems they form (Denny, 1965; Christenson & Purcell, 1985; Allen & Hovius, 1998; Dade & Verdeyen, 2007), with particular focus on the links between the dynamics and morphology of the drainage catchments and their associated fans (Allen, 2008). In the Gulf of Corinth (Greece), observations of syn-rift units have shown ancient alluvial and fan-delta successions to be the deposits of inherited transverse systems. The erosive power of these large pre-rift fluvial systems drove incision through the newly uplifting footwalls, leading to deposition of sediments directly into the adjacent hangingwall (Rohais et al., 2007a; Hemelsdaël et al., 2017; Barrett et al., 2019). Relay zones can also provide key transverse sediment input points and alluvial fans can form at their juncture with the basin floor, as interpreted from both ancient successions and modern systems (e.g. Schlische 1992; Eliet & Gawthorpe, 1995; Braathen et al., 2011).

Extensive transverse systems are known to develop over the hangingwall dipslope of half-grabens (Gawthorpe et al., 1994) where the impact of uplifted barriers to flow (such as uplifted footwall crests) is significantly reduced. These arise from either (i) inherited

drainage systems diverted from their original flow pathways into the new basin (Eliet & Gawthorpe, 1995), where such systems are typically long lived compared to their uplifted footwall-sourced counterparts and they generate wide, low gradient features; or (ii) the development of catchments on the hangingwall side of concurrently uplifting hinterlands forming the uplifted footwall of a parallel basin (Cowie et al., 2006). Through time, as further extension occurs, new faults may grow on the hangingwall dipslope, being either *antithetic* or *synthetic* to the main basin bounding fault (Higgs, 1988; McLeod et al., 2000; Morley et al., 2004). These will alter the structure of the basin floor and generate new local topography within the original basin, thereby acting to influence alluvial fan deposition over the hangingwall dipslope and either diverting sediment into new depocentres, or away from the rift entirely (Frostick & Reid, 1989).

Where the rift axis develops parallel to pre-existing drainage routes, axial alluvial fan systems can form in rare circumstances; typically, the system will preferentially form an axial fluvial system, either traversing the length of the basin or forming deltas feeding lacustrine environments (Cohen et al., 1995; Mack & Leeder, 1999; Gawthorpe & Leeder, 2000). An alluvial fan will preferentially form when a drainage system transitions from being laterally confined to unconfined, leading to a loss of flow competence and the formation of a cone- or fan-shaped body (McCarthy & Cadle, 1995; North & Warwick, 2007; Ventra & Clarke, 2018). Consequently, alluvial fans form an important environment for the delivery of sediment into continental rift basins, commonly forming a margin (apron or bajada) around the edges of syn-rift infill. Such fan aprons can occupy varying proportions of the developing basin floor. Alluvial fan systems compete with other major basin floor environments, including lakes, aeolian dune fields and axial fluvial systems. Types of interaction between alluvial fans and axial fluvial systems occupying the basin floor are varied but commonly include (i) the cutting and erosion of the front (toe) of the

fan by the axial system (Mack & Leeder, 1999; Leeder & Mack, 2001), or (ii) the lateral shifting of the axial fluvial system in response to fan growth and progradation over the basin floor (Cohen et al., 1995). Where alluvial fan systems compete with lacustrine systems (which is especially common in underfilled basins), fan deltas of different types may develop (Scholz et al., 1990; Gawthorpe & Colella, 1990; Rohais et al., 2007a). These interactions are controlled by the type of alluvial fan that forms, which is itself governed by both autogenic fan processes (e.g., Beuhler et al., 2011; Ventra & Nichols, 2014), and a variety of allogenic factors (e.g., Blair, 1999a, b, c; Allen & Densmore, 2000; Meek et al., 2020) that act to govern fan development. These will be discussed in detail in the following sections.

2.2.2. Typical fan types and their controls

Alluvial fans can be formed by either continual fluvial processes (leading to the development of systems commonly called fluvial fans) or by processes linked to depositional events or short duration flows with various types of run-off events occurring over the fan surface (including debris flows, debris floods, hyperconcentrated flows, stream flows). The distinction between fluvial fans and alluvial fans has long been discussed in the literature (Stanistreet & McCarthy, 1993; Blair & McPherson, 1994; Kim, 1995; McCarthy & Cadle, 1995; Hartley et al., 2010; Moscariello, 2018), with little agreement on their definition as distinct sedimentary systems, or as parts of a continuous spectrum of fan forms. This has been further complicated with the introduction of the term Distributive Fluvial Systems (DFS) by Weissmann et al. (2010; 2015) used to describe fluvial fans displaying a radial pattern of laterally unconfined channels that decrease in size downstream. Ventra and Clarke (2018) argue that the two fan types are adequately distinct based on observations of present-day and recent systems; the

defining characteristic of which are the different sizes typical of each fan type (tens to hundreds of km radii for fluvial fans, hundreds of metres to several kilometres for alluvial fans, e.g. de Scally & Owens, 2004; Fontana et al., 2014). Alluvial fans will typically form cone shapes, with slopes reaching multiple degrees when compared to the larger, shallower gradients of fluvial fans reaching fractions of a degree (Ventra & Clarke, 2018).

In this thesis, alluvial fans refer to features described in Moscariello (2018) as cone-shaped accumulations of clastic material of length scales up to 10 km. Deposits are dominated by sediment mass flows and high-energy, typically non-channelised water flows (Figure 2.9). The presence of fluvial fans in modern and ancient continental rifts is well documented (Weissmann et al., 2010; McCarthy, 2013; Weissmann et al., 2015), as it is in other tectonically active basin settings (e.g., Cain and Mountney, 2009, Coronel et al., 2020).

It is common for medium to large size catchments to form ephemeral fluvial systems resulting in some channelisation and braided stream deposition on the fan surface (e.g. Coronel et al., 2020); the size of the resultant depositional or architectural elements is typically limited, however, and the establishment of a long-lived fluvial system on the fan surface is prevented, inhibiting the development of a true fluvial fan or DFS (Distributed Fluvial System). Importantly, the common interpretations of terminal fluvial fan systems represented by simultaneously active downstream bifurcating channels as a result of discharge reduction have been shown to be flawed by observations of surface processes in the modern day. North and Warwick (2007) detail contrasting evidence from modern fluvial fans in Australia, Mongolia, India and Sudan of single-thread channels developed on fan surfaces, misinterpreted as coeval bifurcating channels in previous studies and applied to models of fluvial fan formation.

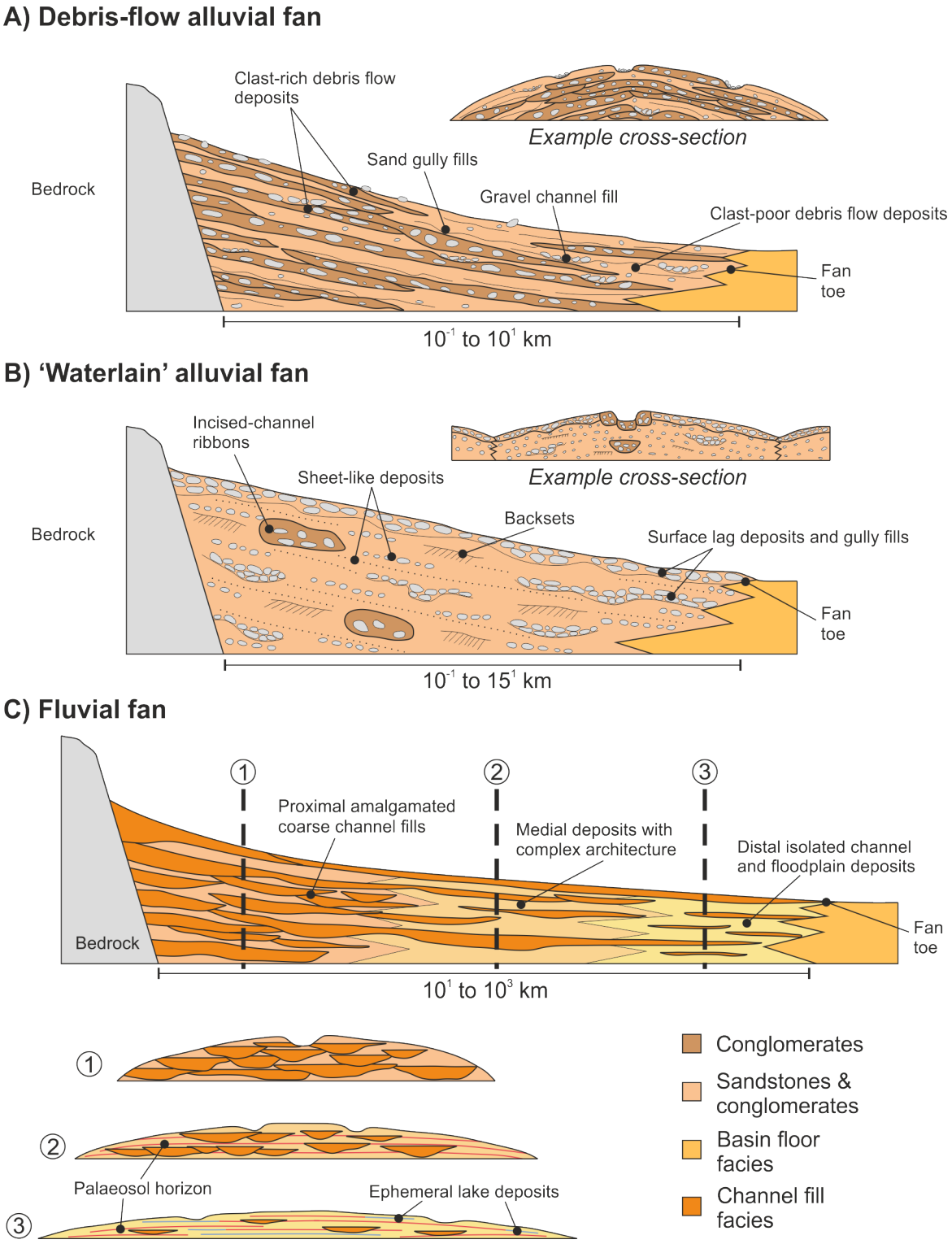

Figure 2.9 *Cross-sectional models displaying the key sedimentological features of (A) an alluvial fan formed through debris-flow processes; (B) and alluvial fan formed through 'waterlain' (hyperconcentrated flow, stream flow, unconfined flow) processes; (C) a fluvial fan. After Moscariello (2018).*

The type of alluvial fan that develops in a continental rift is influenced by allogenic controls of tectonics, climate and base-level changes (Harvey et al., 2005; Ventra & Clarke, 2018). Tectonic factors influence catchment geometries, subsidence rates, and the impact of uplift on erosion and sediment supply rates. Climatic factors govern the regional climatic setting (e.g. arid or humid), vegetation cover, and precipitation rates and subsequent discharge. Base-level changes govern fan surface gradients, equilibrium profiles, lake and sea-level variations. Global drivers such as glacioeustasy will exert control over base-level variations in open (exorheic) rift basins, whereas climate will exert the dominant control in closed (endorheic) basins.

In entirely subaerial settings – which is the setting of particular interest in this thesis – tectonics and climate are the primary allogenic drivers; many authors include the controls of sediment supply and bedrock lithology as allogenic controls too (e.g. Eliet & Gawthorpe, 1995). Sediment supply rates are themselves controlled by climate, tectonics and bedrock lithology (determining the rates of erosion of a source area), and bedrock lithology is partly controlled by the overall tectonics (determining which pre-rift strata are exhumed). Consequently, these factors are all interrelated and influence each other both spatially and temporally, generating the resultant stratigraphic architecture of the developed fans. As a result, both stratigraphic architecture and the overall fan form have the potential to preserve a record of climatic, tectonic and base-level changes over time and space for a basin or broader province (e.g. Quigley et al., 2007).

Autogenic factors are intrinsic processes that govern the flow pathways and development of depositional features on alluvial fan surfaces, and the resultant sedimentary deposits. As such, these factors also influence the stratigraphic architecture of accumulated fan deposits. Autogenic controls include fan head trenching and migration, surface channel

avulsions, depositional lobe switching, channel backfilling and aggradational-incisional cycles (Clarke et al., 2010; Ventra & Nichols, 2014). These have been studied in detail through laboratory modelling over the last three decades (e.g. Whipple et al., 1998; Clarke et al., 2010; Reitz & Jerolmack, 2012; Van Dijk et al., 2012; see Clarke et al., 2015 for review).

The complex interplay of extrinsic and intrinsic forcing described here, and how they are interrelated (for example, climatic variations altering flow conditions and changing the frequency of avulsions that occur on the fan surface; de Haas et al., 2018) control the stratigraphic architectures preserved in alluvial fan deposits. Fan surfaces are typically dynamic features; indicators of high-resolution climatic and tectonic variability (e.g. palaeosol development) can be lost due to signal shredding whereby erosive and post-depositional processes driven by autogenic processes overprint allogenic signatures (Ventra & Nichols, 2014; de Haas et al., 2014). Where they are present, allogenic signatures can be used to interpret cyclicity of external forcing responsible for driving fan sedimentation (Harvey et al., 2005; Ventra & Nichols, 2014; Meek et al., 2020).

As they develop, alluvial fans can be described as *progradational*, *aggradational* or *retrogradational* features (Figure 2.10), based on the interplay between the rate of accommodation generation (controlled by tectonics and base level changes) and sediment supply (controlled by climate, bedrock lithology, and autogenic factors) (Viseras et al., 2003). *Progradational* fans (fans that deposit sediment progressively further into the basin through time) form when sediment supply outpaces the rate of accommodation generation, or when base level falls. Typically, progradation occurs through telescopic nesting, whereby the active depositional segment of a fan cuts through older fan deposits, forming relic terraces and depositing sediment further downstream

(Bowman, 1978; Harvey, 2002). When sediment supply rates and accommodation generation rates are in equilibrium, and particularly when a fan is limited laterally by other features, such as axial rivers or other alluvial fans, fan systems may preferentially *aggrade* such that facies belts remain in approximately the same positions through time (Viseras et al., 2003; Ventra & Nichols, 2014). *Retrogradation* typically occurs when the rate of accommodation generation is greater than the rate of sediment supply. This form is typically reserved for fans with low slope profiles where the rate of sediment delivery diminishes over time (Viseras et al., 2003; Cain & Mountney, 2009). By contrast, the impact of gravity on alluvial fans with high surface gradients leads to deposition on the fan front and the overall enlargement of the fan through time. This occurs where fans are formed of coarse material leading to increased angles of repose or form adjacent to basin margins with a high topographic difference between the sourcing catchment and basin floor (e.g. Chun & Chough, 1995; Patranabis-Deb & Chaudhuri, 2007). Alluvial fans can experience combinations of progradation, aggradation, and retrogradation throughout their life cycle, entirely dependent on the development of the controlling factors outlined above. Whether fans prograde, aggrade, or retrograde, can have a major impact on their morphological development through time and space. Such evolutionary behaviour impacts the location and distribution of different facies belts within the accumulated fan deposits that characterize the basin fill. In this way, preserved alluvial-fan successions within rift-basin stratigraphies can be used to reconstruct both basin and fan development and controls thereon.

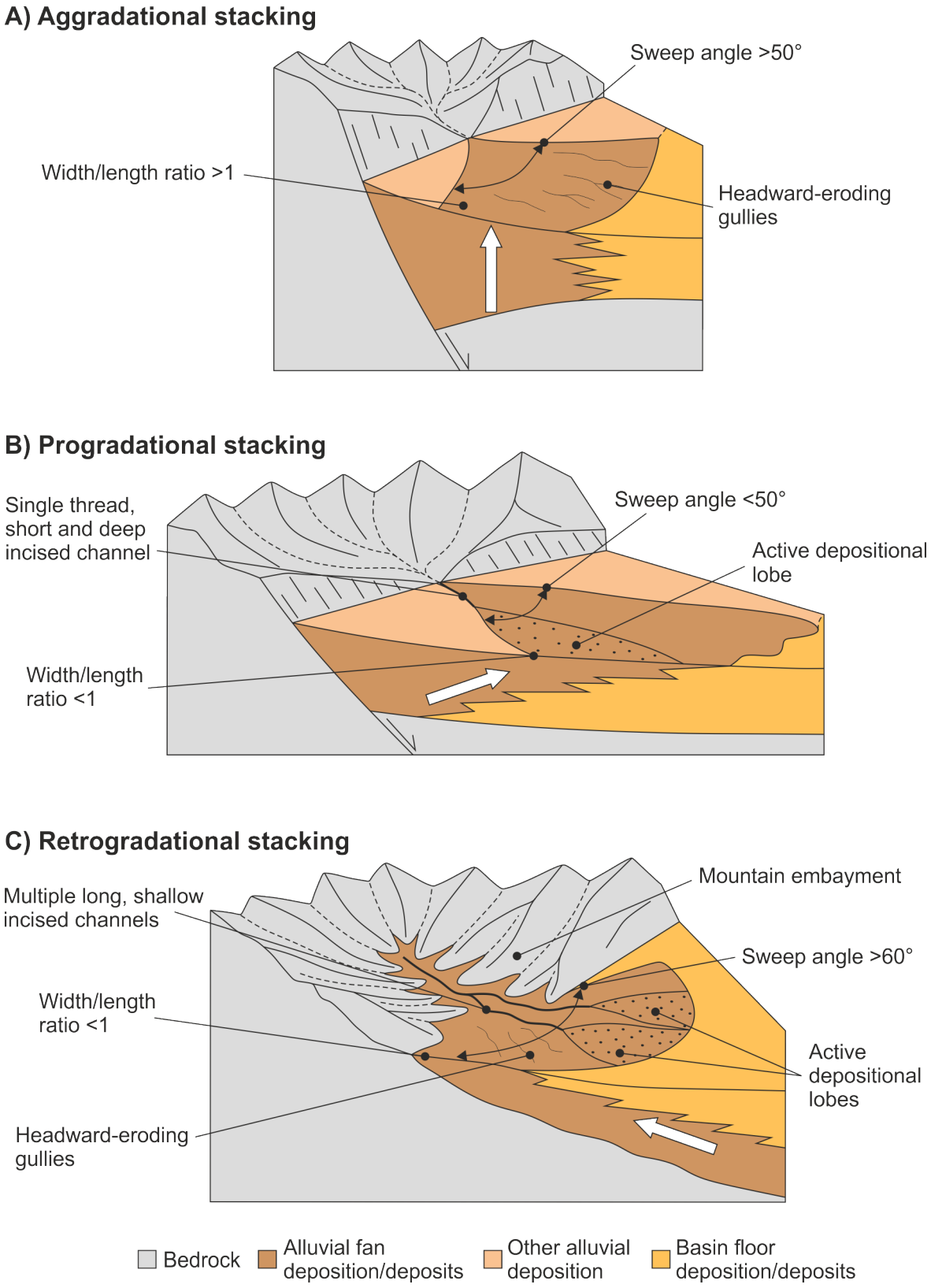

Figure 2.10 *Predicted stratigraphic stacking patterns of alluvial fans formed at basin margins including (A) aggradational stacking through high tectonic subsidence; (B) progradational stacking through low tectonic subsidence; (C) retrogradational stacking through base level rise. After Viseras et al. (2003).*

2.2.3. Dominant flow processes and their sedimentary response

Sediment mass flows (or mass wasting) are mixtures of water and sediment particles at varying concentrations to one another that move under the influence of gravity. They are dominant depositional processes on alluvial fans, forming a continuum of flow types depending on the availability of water for sediment transport, and the grain size of the transport material (Blackwelder, 1928; Pierson & Costa, 1987; Blair & McPherson, 1994; Iverson, 1997; Major, 1997). Flows can be described as Newtonian or non-Newtonian, related to the relationship of that flow's viscosity to applied shear stress; a Newtonian flow has a constant velocity no matter the shear stress applied, whereas a non-Newtonian flow has a variable viscosity when shear stress is applied (Pierson & Costa, 1987; Collinson & Mountney, 2019). The flows can also be described as cohesive or non-cohesive, where a cohesive flow forms as a rigid flow body with reduced particle near-boundary shear and inhibited streamflow miscibility, and a non-cohesive flow forms a less viscous, fluidal body with a higher streamflow miscibility (Scott et al., 1995).

The development of one flow type over another is dependent on the viscosity of the flow and typically a function of the proportion of clay in the transported sediment (Pierson & Scott, 1985; Scott et al., 1995). Increased clay content provides a barrier between grains, reducing their interaction (Scott et al., 1995) and increasing the impact of shear forces near flow boundaries (Hooke, 1967). Increased clay material also reduces the tendency of coarse grains to settle towards the bottom of the flow (and applies a buoyancy force to those coarse grain particles (Hooke, 1967; Hampton, 1979). This prevents the full mixing of sediment and associated water (Scott et al., 1995). The typical flow types by their relative water and sediment concentrations are outlined in Figure 2.11; deposits can be formed of clay through to boulder grade grains, with a wide range of sorting and textural

maturity, making alluvial fan facies some of the most variable in continental successions (Blair, 1999a, b; Moscariello, 2018).

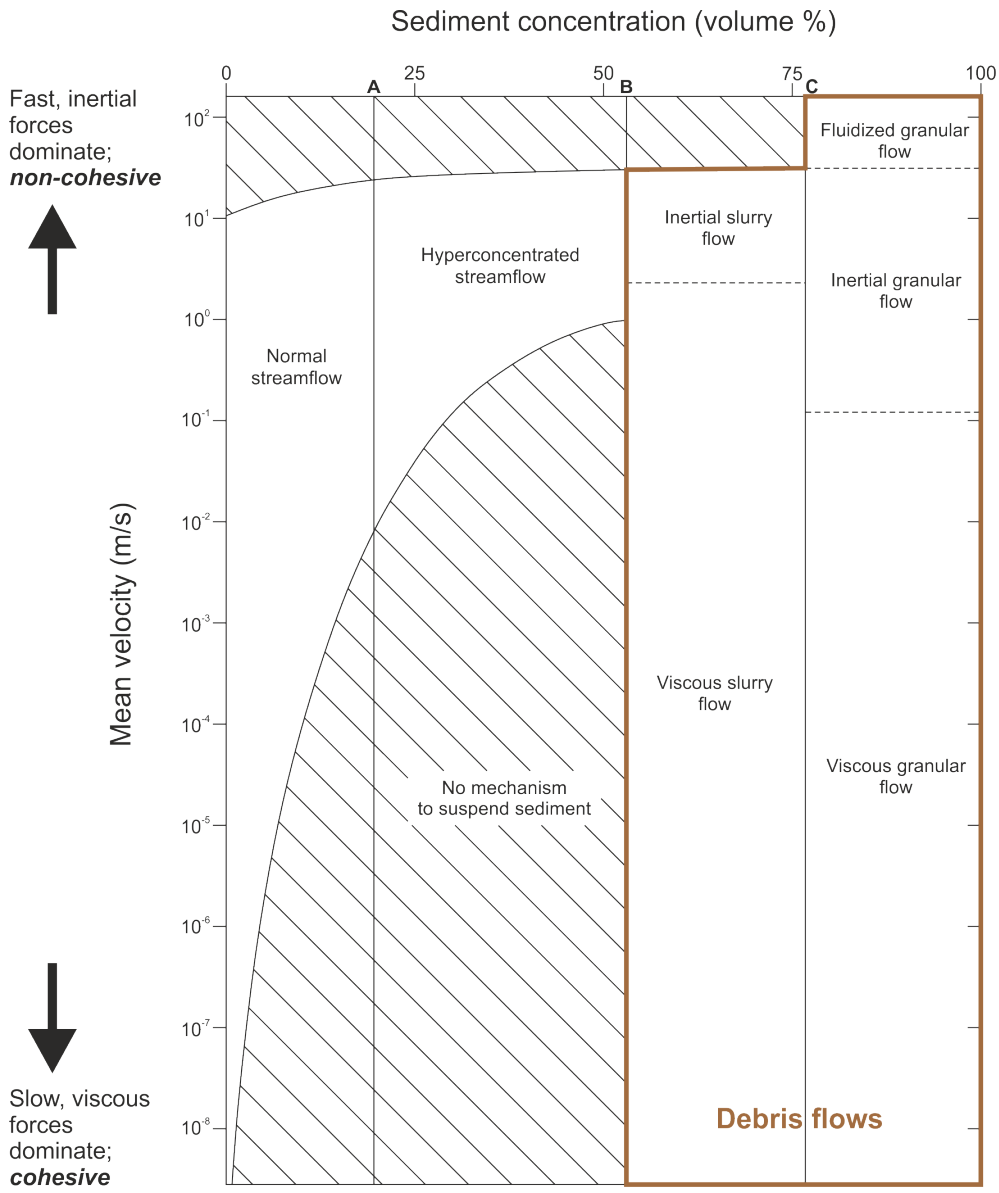

Fluid type	Newtonian	Non-newtonian	
Interstitial fluid	Water	Water + fines	Water + air + fines
Flow category	Streamflow	Slurry flow	Granular flow
Flow behaviour	Liquid	Plastic	

Figure 2.11 *Rheologic classification of different sediment-water flows. Boundaries A, B and C indicate flow rheology thresholds defined by the grain-size distribution of the flow sediment where (A) indicates the onset of yield strength; (B) indicates a rapid increase in yield strength; (C) indicates the cessation of liquefaction behaviour. After Pierson & Costa (1987).*

Mixtures of sediment and water with high sediment concentrations can lead to the formation of hyperconcentrated flows. These can form individual flow events, or can form as either a precursor to a trailing debris flow, or immediately following a debris flow, where that debris flow is non-cohesive with a reduced clay content (Pierson & Scott, 1985; Scott et al., 1995; Sohn et al., 1999; Benvenuti & Martini, 2002; Pierson, 2005). Consequently, they form similar deposits to what are termed hybrid event beds in the world of submarine channels (Talling, 2013) of linked coarse-grained and fine-grained facies which vary laterally in proportion and sediment character. Increasing the water content further will result in high-energy flood deposits, leading to the rapid deposition of either structureless sediment or well-sorted lenses of similar grade sediment, and the winnowing of fine material further down-fan (Pierson & Scott, 1985; Pierson & Costa, 1987). The term 'sheetflood' (first described by McGee, 1987) has commonly been employed by many authors (e.g. Blair & McPherson, 1994; Miall, 1996; Bull, 1997; Hampton & Horton, 2007) as a depositional process to describe thin, laterally extensive sandstone units. North & Davidson (2012) have shown this terminology to be unrepresentative of depositional process, however, due to its vague definition and inconsistent application in the interpretation of different deposits; further, it does not accurately portray the flow rheology leading to the preserved sediments, due to the variability of unconfined flows (for example, the non-uniformity of their velocities across lateral space).

The dominant flow processes that operate on the fan, in combination with the available space for deposition, controls the pattern of sedimentation across the fan surface. This in turn controls the evolution of the shape of the fan body as it grows and the interplay between the fan and coeval processes operating in neighbouring sedimentary environments present on the basin floor. Coarse grained sediments deposited through

mass flows (in particular, rock fall and cohesive debris flows) will form cone-shaped fans with higher surface gradients (Blair & McPherson, 1994), resulting from rapid deposition of their coarse-grained fraction (Stock et al., 2008), than their waterlain counterparts, which will preferentially form lower gradient fans with a greater width-to-length ratio (Mascariello, 2018; Ventra & Clarke, 2018). Fans may be isolated, or amalgamate to form a bajada (or apron), depending on the proximity of adjacent fan apices (where the top of the fan meets its feeding catchment), the shape of their catchment (where catchments with a decreased width-to-length ratio will feed fans that typically amalgamate) and their dominant depositional flow types. From proximal to distal areas over a fan surface, a reduction in mean grain size and increase in the sorting and textural maturity of grains is common for all depositional flow types (Stock et al., 2008; Miller et al., 2014; Harries et al., 2019) with an increase in the water quantity of a flow typically corresponding to a longer runout distance (e.g. rock fall only occurring at the fan apex) (Blair & McPherson, 1994; de Haas et al., 2015). Figure 2.12 displays the key features of the dominant depositional flow types mentioned in this study (debris flows, hyperconcentrated flows, debris floods and water or stream flows) from which their sedimentological signature is derived.

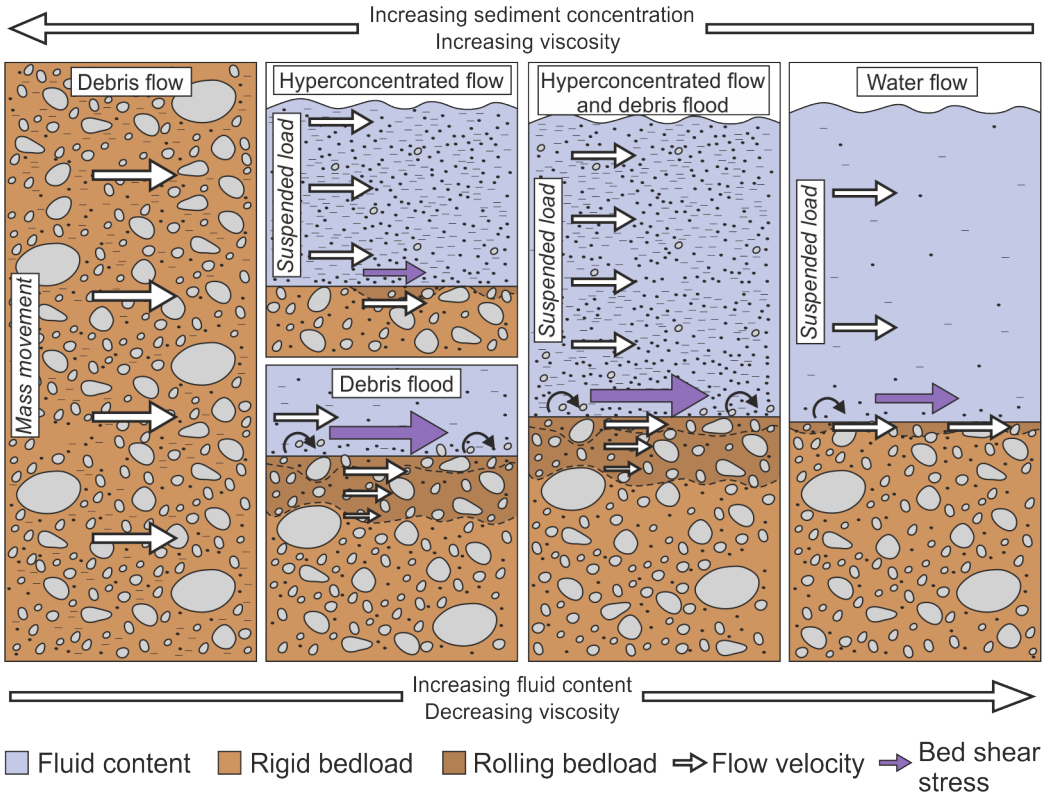

Figure 2.12 *Schematic images displaying the features of sediment-water flows described in this study. Note the proportions of bedload mobilized by the overlying flowing water-sediment body, and the density of suspended sediment in water flows of different types. After Brenna et al. (2020).*

2.3. General background on the study areas

The material presented here provides further information on the proposed geodynamic formation and consequent evolution of the four main study areas utilised in the following chapters.

2.3.1. The Gulf of Corinth

The Corinth rift, located at the Gulf of Corinth, Greece, is part of the Aegean tectonic domain (Figure 2.13). It represents a region that is currently extending as a result of back-arc extension caused by the subduction of the African Plate underneath the European

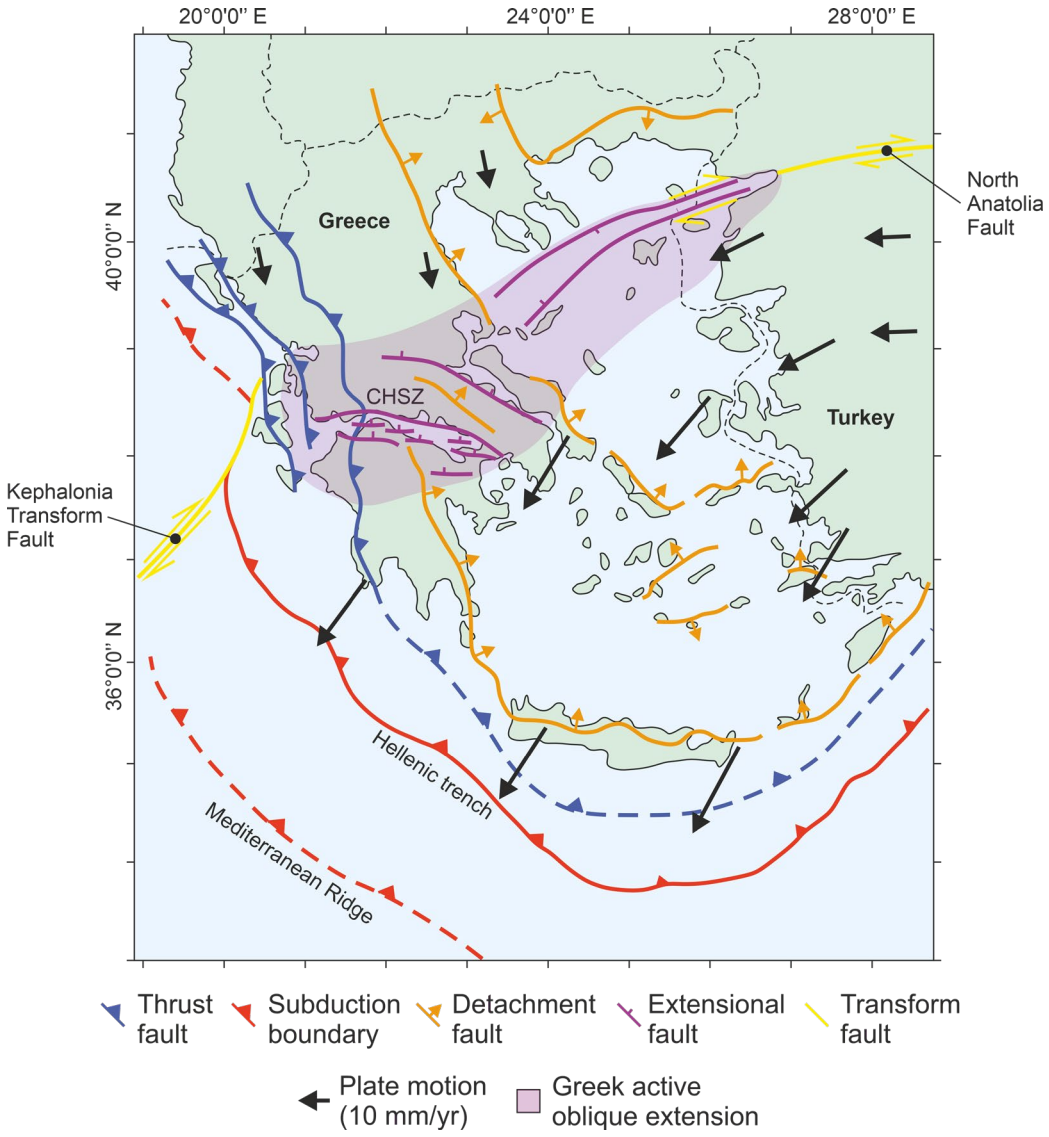

Figure 2.13 *Present-day tectonic setting of the Greek Aegean extensional domain (pink colour). The Gulf of Corinth strikes E-W in the southwest portion of this zone. CHSZ = Central Hellenic Shear Zone. After Vassilakis et al. (2011) and Royden & Papanikolaou (2011).*

Plate (Le Pichon & Angelier, 1979; Jolivet et al., 2013). The pre-rift stratigraphy is made up of a several kilometres-thick succession comprising hemipelagic carbonates with interbedded chert deposits (Pindos unit; Triassic-Jurassic, Tripolitza unit; Mesozoic-Eocene, Apulian Carbonates; Mesozoic-Eocene), and sandy turbidites (Pindos unit; Cretaceous-Eocene, Ionian and Tripolitza units; Oligocene). This succession accumulated in a foreland basin setting resulting from the ongoing evolution of the Hellenide mountain

belt to the east (Skourlis & Doutsos, 2003; Van Hinsbergen et al., 2005; Piper, 2006; Ford et al; 2016). The collision of the African and European plates, initiated in the late Mesozoic, caused nappe emplacement which generated NNW to SSE fold and thrust sheets, creating topographic highs and exposing the aforementioned rock units at the surface in roughly similar NNW/SSE trending ridges and troughs (Doutsos et al., 1988, 1993; Jolivet et al., 2013).

Following the collision of the African and European plates, subduction of the former commenced to the NNE and continues today at a rate of 5-35 mm a^{-1} (increasing from north to south), with a rate of 5-12 mm a^{-1} in the Late Miocene when rifting began (McClusky et al., 2000; Royden & Papanikolaou, 2011; Vassilakis et al., 2011). This originally formed the Aegean Sea at 30 Ma through the aforementioned back-arc extension caused by slab rollback. Slab rollback pulled down the denser subducting plate African Plate into the asthenosphere and dragged forward the overriding European Plate causing back-arc extension (Jolivet et al., 2013). Many geodynamic models for the occurrence of slab rollback in the Aegean have been proposed. Such models invoke slab retreat (Royden & Papnikolou, 2011), slab tearing (Wortel & Spakman, 2000; Govers & Wortel, 2005; Jolivet et al., 2013), and mantle flow (Faccenna et al., 2014). Sachpazi et al (2015) outline new geophysical data interpreting the subduction of the African Plate by the mapping of the Moho layers of both tectonic plates, implying that rollback has occurred in this region in a segmented manner. Common transform faults along the subduction boundary generate multiple zones of deformation in the crust, resulting in the different structures found in the adjacent tectonic regimes of the North Anatolia Fault zone, Gulf of Corinth, Kephalonia Transform Fault and Ionian subduction system. The locus of this geodynamic activity moved from east to west through time, where at approximately 5 Ma the North Anatolia Fault propagated west to southwest into the

Aegean Sea, coinciding with the termination of extension in the central Aegean Sea and the transfer of deformation to the east and west (Jolivet et al., 2013). Since 5 Ma, the zone between the SW tip of the North Anatolia Fault and the Kephalonia Transform Fault (located to the north-west of the Peloponnese) has accommodated the north-south extension, forming the Corinth rift and Gulf of Evia rift to the north (Ford et al., 2016) through the initiation of a north-dipping, low-angle inclined detachment fault followed by successive synthetic higher angle faults through time (Sorel, 2000).

Today, the Gulf of Corinth serves as a natural laboratory for rift-focused sedimentological, structural and geodynamic studies; extension continues to the present day. Chapter 4 outlines in further detail the structural and sedimentological history of the rift since its initiation at 5 Ma.

2.3.2. The East African Rift System

Rift propagation between the African and Somalian Plates began at approximately 30 Ma, originally forming open fractures at the present day Afar triangle due to hot spot activity (Figure 2.14) (Bastow et al., 2008). The African superplume, a result of chemical anomalies in the mantle asthenosphere below southern Africa (Ritsema et al., 1999; Park & Nyblade, 2006; Bastow et al., 2008), extended to the north-east generating surface uplift and the thinning of the lithosphere beneath the present-day rift (Hansen et al., 2012; Hansen & Nyblade, 2013). This was identified by analyses of low P-wave velocity anomalies and low shear velocities in the upper and lower mantle beneath eastern and southern Africa (Montelli et al., 2006; Simmons et al., 2007, 2009; Ritsema et al., 2011) compared to equivalent values from neighbouring areas. This consequently caused tensional stress in the overlying continental lithosphere. Initial extension in the brittle

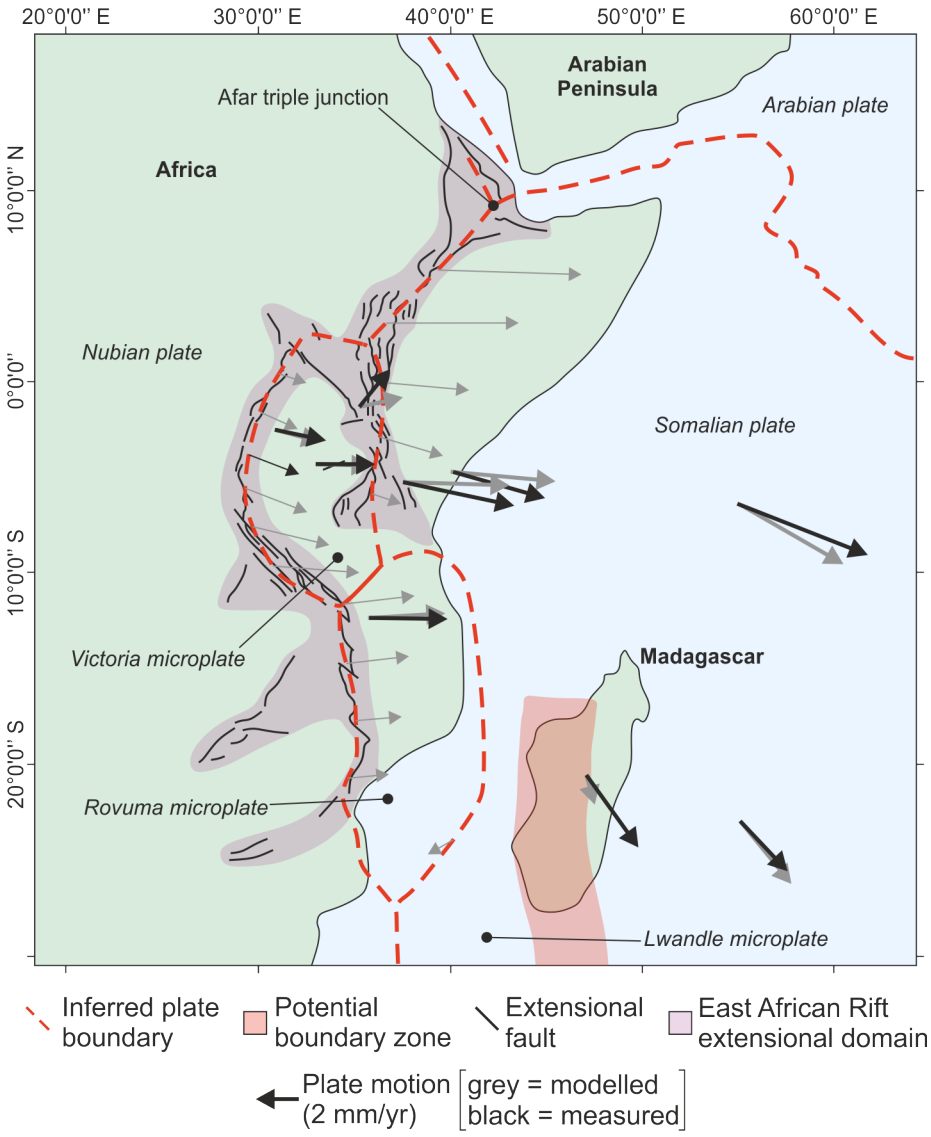

Figure 2.14 *Present-day tectonic setting of the East African Rift extensional domain (pink colour). The continental expression of the rift traces the boundary of the Nubian, Somalia, Victoria and Rovuma tectonic plates before terminating to the north at the Afar triple junction. After Chorowicz (2005) and Corti (2009).*

crust was accommodated by faulting in the Gulf of Aden (29.9 to 28.7 Ma) and then the southern Red Sea (27.5 to 23.8 Ma) (Bosworth et al., 2005) before the formation of a triple junction in the vicinity of the Afar triangle (Wolfenden et al., 2004). Further surface rifting of the major Ethiopian rift and the introduction of the modern Eastern branch to the East African Rift occurred at 11 Ma; this followed Oligo-Miocene-age volcanic events (Chernet et al., 1998; Wolfenden et al., 2004) between two loci of volcanism, the Afar triangle in

the north and the junction of the northern Kenyan, central Kenyan and Nyanza rifts in the south (Bonini et al., 2005; Corti, 2009). This trend of volcanism preceding surface rupturing continued in the northern part of the present-day Western branch, with eruptions at 12.6 Ma preceding surface fault displacement from 12.6 to 10 Ma (Ebinger, 1989). A western branch formed via the 'unzipping' model described by Ebinger (1989), whereby opening occurred from north to south with significantly reduced associated volcanism. Importantly, for both branches, rifting does not directly overlie proposed locations of mantle pluming (Chang & Van der Lee, 2011) leading to an interpreted simple shear or hybrid pure-simple shear model for lithospheric extension (Chorowicz, 2005).

Rifting is accommodated by half-graben and full graben morphologies of switching polarities (east to west) along its length (Ebinger, 1989; e.g. Dunkelman et al., 1989; Woldegabriel et al., 1990). Major transform zones at the Tanganyika-Rukwa-Malawi rifts, Aswa through to Ethiopia, and the Omo-Turkana region of the Eastern branch, accommodate large amounts of extension through both dextral and sinistral movement (Chorowicz, 2005). Presently, the East African Rift can be described as the best-developed example of a modern-day complete rift system containing basins of oceanic rift stage (Afar triangle), advanced rift stage (Ethiopian rift), typical rift stage (Tanganyika rift), initial rift stage (Malawi rift) and pre-rift stage (Limpopo area) (Chorowicz, 2005), making it an ideal location to study active and ancient sedimentological, structural, and volcanic processes in a major extensional province.

2.3.3. The Baikal Rift

Extension in the Baikal region has been ongoing since the Late Cretaceous (~70 Ma) with active rifting since ~30 Ma (Zonenshain & Savostin, 1981; Petit & Déverchère, 2006; Mats & Perepelova, 2011) over the boundary between the Siberian continental craton and the

Amurian plate to the east, which today is shown at the surface as the Sayan-Baikal fold belt (Figure 2.15). These structures represent the accretion of Proterozoic microcontinents and volcanic arcs that accreted against the Siberian craton during the early Paleozoic, which were then reactivated and enhanced in the Mesozoic (Ren et al., 2002; Mats & Perepelova, 2011). This forms the NE-SW structural fabric exploited by the extensional basins of the Baikal Rift, offset from the main Siberian craton suture (Logatchev & Florensov, 1978; Petit & Déverchère, 2006).

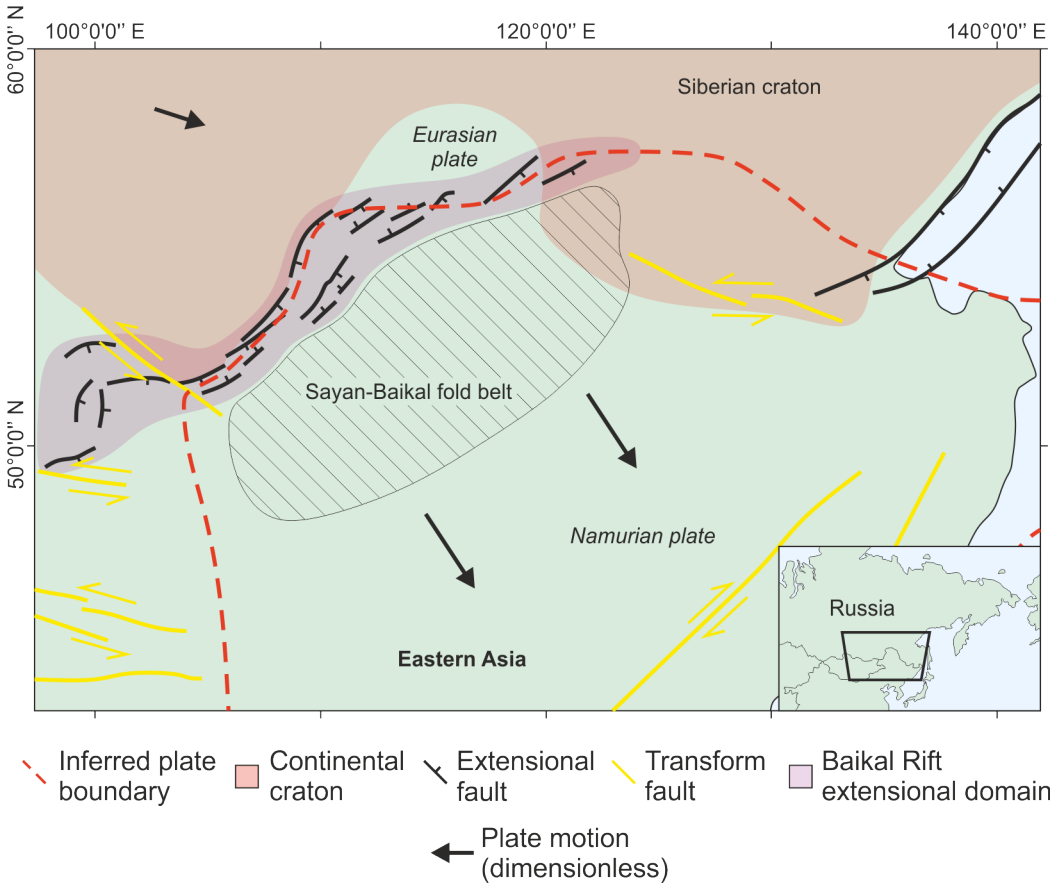

Figure 2.15 *Present-day tectonic setting of the Baikal extensional domain (pink colour). The Eurasian plate and Namurian plate are moving east-southeast at different rates, further driving extension at their boundary. After Petit & Déverchere (2006) and Ivanov et al. (2015).*

The formation of the rift zone has been associated with a variety of different processes, and no single mechanism of formation has been agreed upon to date:

(i) The presence of a mantle plume, identified by low seismic P-wave velocities and located presently to the south-west of the main Lake Baikal (Zorin et al., 2003; Zhao et al., 2006), leading to lithospheric thinning and active rifting with associated volcanism from the Late Cretaceous (Zorin et al., 2003; Mats & Perepelova, 2011).

(ii) Brittle failure associated with movement of rigid lithosphere, as a result of the collision of India and Eurasia, causing the splitting and breakup of continental lithosphere into a series of microplates to the south of, and adjoining, the present-day rift. This led to local tensional stresses caused by far-field stress regimes and surface rupture with associated transform faults (Zonenshain & Savostin, 1981; Petit & Déverchère, 2006).

(iii) A combination of both the 'active' scenario (i) above and 'passive' scenario (ii), whereby the lithospheric heterogeneity of the Siberian craton and Sayan-Baikal zone altered deep heat flow and caused a transition from scenario 1 to scenario 2 (see Popov, 1990; Ivanov et al., 2015 for review).

Volcanism associated with the Baikal Rift makes its history difficult to unravel, as activity began in the Late Cretaceous with a dominant episode occurring from the Miocene through to 600 Ka but limited in rift location to the Tunka basin (south-west tip of Lake Baikal) (Rasskasov, 1994; Rasskasov et al., 2003b). Volcanism has also occurred away from the main rift, to the north-east and the east of the largest rift basins at Lake Baikal (Ivanov et al., 2015). This would typically represent a lithospheric anomaly or mantle plume off-axis to a simple shear rift, as described above for parts of the East African Rift. However, the presence of chemically similar basaltic eruptions in the Tibet area indicate a more regional volcanic episode (Petit & Déverchère, 2006).

Surface rifting has been typically split into two stages of slow and fast extension, beginning with the slower formation of the South Baikal and Tunka basins and deposition of fine-grained lacustrine sediments during the Oligo-Miocene, (Zonenshain & Savostin, 1981; Logatchev & Zorin, 1987) followed by an increase in extension rates and the formation of the central and northern rift basins since the Pliocene (Zonenshain & Savostin, 1981). More recently, further divisions of evolution have been proposed including the reclassification of proto-rift areas to a full rift stage (Mats & Perepelova, 2011). Petit & Déverchère (2006) outlined the main formational history in three key stages: (i) lacustrine conditions and associated sedimentation in early south, central and Tunka basins at 30 to 27 Ma (slow stage); (ii) increased subsidence of south and central basins, and initiation of northern basins at 10 to 4 Ma (fast stage I); and (iii) pervasive subsidence through most of the system at 2.5 to 0 Ma (fast stage II).

The driving forces behind the formation of the Baikal Rift (and the relative timing of individual basin formation) is still a topic of intense debate today, with evidence pointing toward numerous mechanisms combining to cause the present-day rift structure.

2.3.4. The Basin and Range province

Extension of the Basin and Range province has been ongoing since the Late Eocene (Dickinson, 2002; Bahadori & Holt, 2019) and forms one of the most recent tectonic phases of the American Cordillera (Figure 2.16), overprinting the earlier Sevier-Laramide orogeny of the Mesozoic to early Cenozoic eras (DeCelles, 2004; Dickinson, 2006).

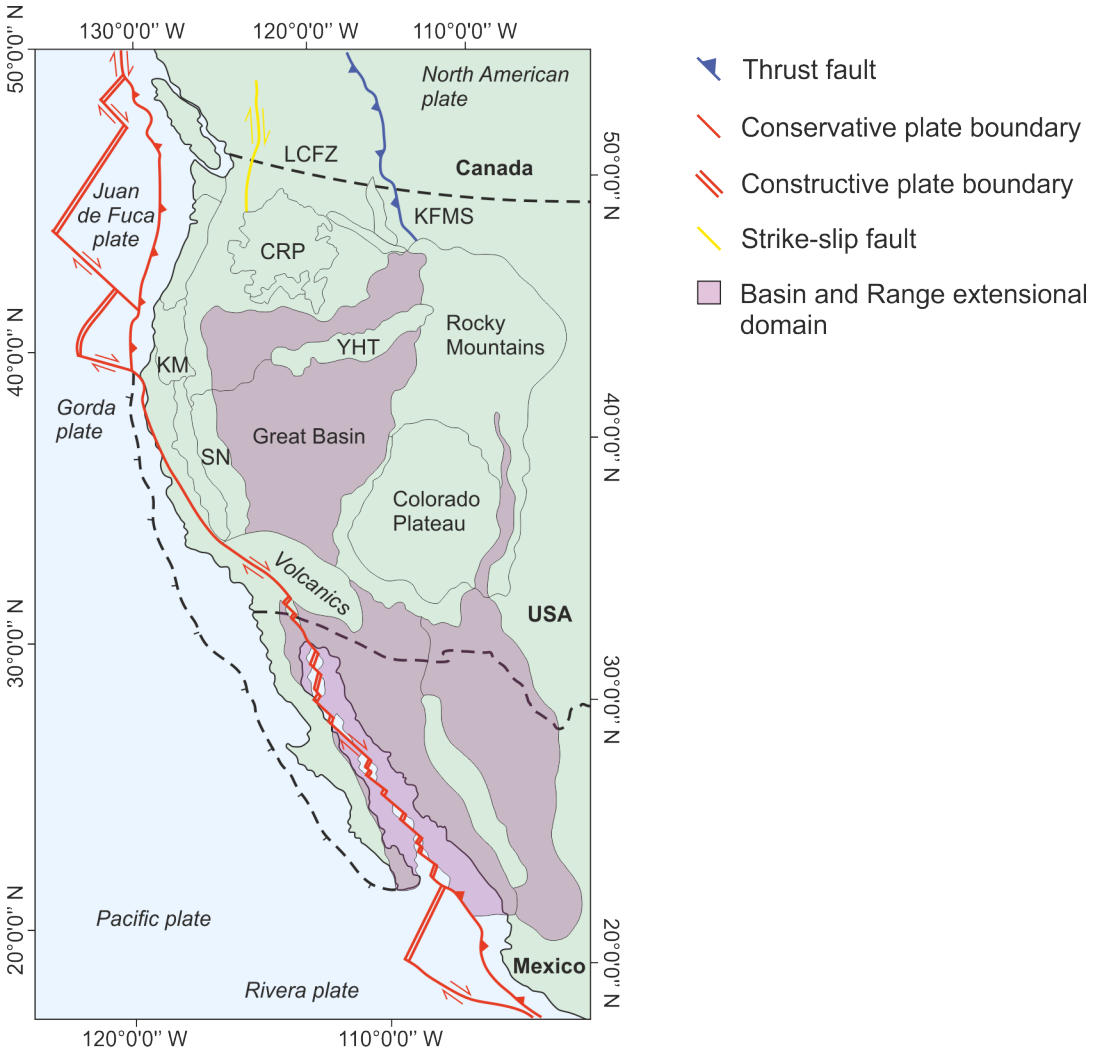

Figure 2.16 *Present-day tectonic setting of the Basin and Range extensional domain (pink colour). The Great Basin and other subregions form a large extensional province surrounded by different tectonic features of the western Cordillera. LCFZ = Lewis and Clark Fault Zone, CRP = Columbia River Plateau (igneous province), KM = Klamath Mountains, YHT = Yellowstone Hotspot Track, SN = Sierra Nevada. After Dickinson (2006).*

Following the collision of the Farallon and North American plates forming the orogen, the Farallon Plate began to rapidly subduct underneath the less dense North American Plate (Humphreys, 1995; McQuarrie & Wernicke, 2005), causing slab rollback to occur and the initial extension of the lithosphere accommodated by back-arc basin formation (Dickinson, 2002). Slab rollback progressively occurred from 55 to 17 Ma across the province (Bahadori & Holt, 2019) causing the exhumation of metamorphic core

complexes of the deep lithospheric crust as extension was accommodated on crustal scale shallow listric faults (Wernicke & Burchfiel, 1982; Hamilton, 1987). Associated widespread volcanism occurred (Hamilton, 1987; Armstrong & Ward, 1991; Colgan et al., 2006) as the underlying asthenosphere underwent partial decompression melting in response to the thinning lithosphere. Simultaneous (~Eocene) transrotational extension occurred in the Pacific Northwest, the effects of which were incorporated in the Basin and Range by rotational block faulting in the north of the province (Dickinson, 2002). Major syn-transform extension has subsequently occurred from the mid-Miocene as the transfer of oblique shear from the Pacific and North American plates moved inland both along the evolving San Andreas transform and the further south at the Mexican coast (McQuarrie & Wernicke, 2005). Further hypotheses for the occurrence of extension include asthenospheric mantle flow (Moucha et al., 2008; Forte et al., 2010), upper mantle density variabilities (Best et al., 2016), and lithosphere delamination (Wells & Hoisch, 2008). It is likely that many of these processes have occurred to varying degrees through the time of extension of the region.

As a result, the province is a wide zone of extension whose topography is dominated by a series of horst and graben structures, and asymmetrical half-grabens with uplifted footwalls, which form rotational blocks over a detachment surface driven by the action of larger, crustal-scale listric normal faults (Wernicke & Burchfiel, 1982; Hamilton, 1987; Dickinson, 2002). The extensional style here provided the initial study sites that led to the development of the simple shear model described by Wernicke (1985) and have provided a key location to study the development of continental rift stratigraphy and its associated effect on the surrounding landscape.

2.4. Summary

Understanding the formation of a continental rift province, from its phase of initiation through to its development into a large-scale surface feature, allows for the interpretation of the different structural morphologies that constitute the system. When combined with knowledge of the surrounding climate and the lithological composition of the ruptured surface, these extrinsic factors provide the framework from which sediments are delivered into the newly formed basins to form alluvial fans. Detailed observations of the rock record preserved within those basins, and of present-day fan bodies, can be used to deconstruct the extrinsic and intrinsic controls that may have formed them.

In Chapter 3, the development of intrabasinal faulting in three modern-day rift systems is considered in order to identify structurally similar basin morphologies to attempt to isolate the allogenic controls (climate, bedrock lithology) that drive differences in their depositional environment-scale alluvial fan systems. In Chapters 4 and 5, detailed observations of synrift alluvial fan sediments from the Gulf of Corinth region allow for the development of palaeogeographic models to depict the depositional response of a fan system to known ongoing tectonic and climatic variations. This is done at a variety of scales, from the larger, depositional element and architectural element scale, through to the facies element and individual sediment fabric scale.

3. Development of alluvial fans associated with uplifted tilt-block crests; a comparative study from present-day extensional regimes

3.1. Introduction

The geomorphologic and sedimentary development of alluvial fans in extensional basin settings is well documented by examples from both presently active systems and ancient preserved counterparts. Numerous studies document fan development from uplifted footwalls directly into the adjacent hangingwalls of graben and half-graben basins (Cohen et al., 1995; Leeder et al., 1991; Eliet & Gawthorpe, 1995; Alçiçek et al., 2007). Alluvial fans forming aprons over hangingwall dipslopes are typically larger and are sourced from catchments that provide a greater volume of sediment to the basin, compared to their footwall-sourced counterparts (Martini & Sagri, 1993; Friedmann & Burbank, 1995; Frostick & Reid, 1987). To date, relatively few studies have attempted quantitative comparisons of the morphologies of footwall slope fans and those formed over the hangingwall dipslope (Gumbricht et al., 2001; Mack et al., 2008). No prior published studies have explicitly sought to directly compare formation processes for footwall- and hangingwall-derived fans from the same uplifted hinterland source area.

The respective roles of tectonics, climate, sediment supply, and bedrock lithology in controlling alluvial-fan deposition are well documented in both modern systems (Ritter et al., 1995; Blair, 1999a, b, c; Kumar Singh et al., 2001; Crosta & Frattini, 2004) and ancient successions (Frostick & Reid, 1989; Waresback & Turbeville, 1990; Jolivet et al., 2017). However, studies of the influence of each of these factors typically focus on one control (D'Arcy et al., 2017), or on isolated deposits or systems (Frostick & Reid, 1989; Amorosi et al., 1996). Although some studies of isolated systems review multiple

allogenic controls affecting syn-rift deposition (e.g., Waresback & Turbeville, 1990; Whipple & Trayler, 1996; Quigley et al., 2007), few comparative analyses have been undertaken between different rift systems as part of a single study (Allen & Hovius, 1998). Direct linkage of observable geomorphic processes to resultant preserved facies in continental environments is not commonly achieved (Davidson et al., 2011); yet it is usually possible to predict the areal and length scales of environments, and the expected sediment distributions within them (for example, 'distributive fluvial systems' outlined by Hartley et al., 2010 & Weissmann et al., 2010), even if the occurrence of specific facies types cannot be predicted in detail.

This study examines and characterises examples of uplifted tilt-block crests in presently active extensional regimes where deposition of dipslope fan aprons, and fans sourced directly from the footwall slope, occur simultaneously from the same hinterland into neighbouring depocentres. Through such an approach, comparisons can be drawn regarding sedimentological and morphometric differences between related hangingwall- and footwall-derived fan systems. Such an analysis can provide insight into potential scaling relationships and can provide estimates for the expected lateral extent and distribution of alluvial-fan facies in continental rift settings. The results of this study are important for the predictive interpretation of ancient successions, including those known only from subsurface seismic datasets (Figure 3.1).

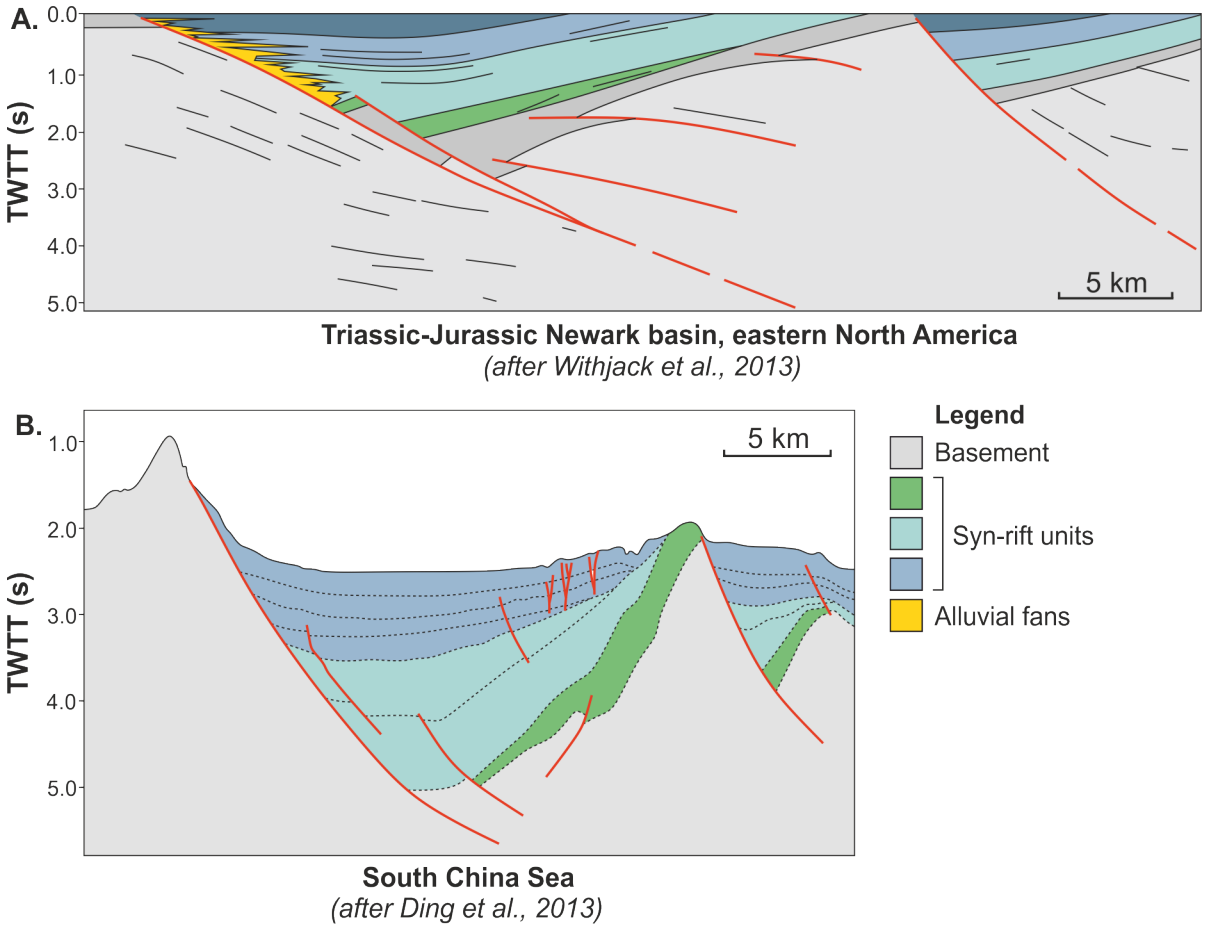

Figure 3.1 *(A) An example of continental syn-rift subsurface interpretation where alluvial fan units have been interpreted, with little known evidence of their extent or variation in time. (B) An example of continental syn-rift subsurface interpretation where it would be beneficial to predict the distribution of facies belts.*

The aim of this study is to identify the similarities and differences between measurable morphological parameters of alluvial fans and their catchments formed over the hangingwall dipslope, and those formed directly from the footwall slope (uplifted and eroded fault scarps), of a single uplifted tilt-block crest in extensional settings. These differences are directly compared between half-grabens from different extensional regimes to infer the relative impact of different allogenic controls; notably tectonic style and climatic setting. Specific objectives of this research are as follows: (i) to map the extent of alluvial fans and their catchments sourced from four hinterlands (one from each

of the East African and Baikal rifts, and two from the Basin and Range province), that are presently undergoing uplift in three separate modern rift systems; (ii) to identify and measure key morphometric parameters (e.g., fan area, active depositional area, fan slope, catchment area, and both fan and catchment width-to-length ratios) using DEM data to establish area, slope and differences in morphological form; (iii) to link these morphometric parameters to evidence of formative processes on the fan surfaces; and (iv) to compare these processes both between different rift settings, and between fans formed over the footwall slope and those formed over the hangingwall dipslope.

This study is of broad appeal because it: (i) improves understanding of the relative impact of different allogenic controls on alluvial-fan development in rift settings; (ii) establishes predictive empirical relationships between different morphometric aspects of alluvial fans in rifts; and (iii) enables the development of models that can be used to predict the extent of alluvial-fan facies belts in subsurface rift deposits in cases where other data are not available.

3.2. Data and methods

To enable detailed study of presently active alluvial fans, remotely sensed data were acquired from two open sources: Google Earth satellite imagery (imagery from 2016) and the AW3D30 DEM database (provided by the Japan Aerospace Exploration Agency, JAXA). The spatial distribution of fans and their catchments were defined (see sections 3.2.1., 3.2.2. and 3.2.3. for detail); morphometric parameters were then extracted using GIS-based analysis (Figure 3.2).

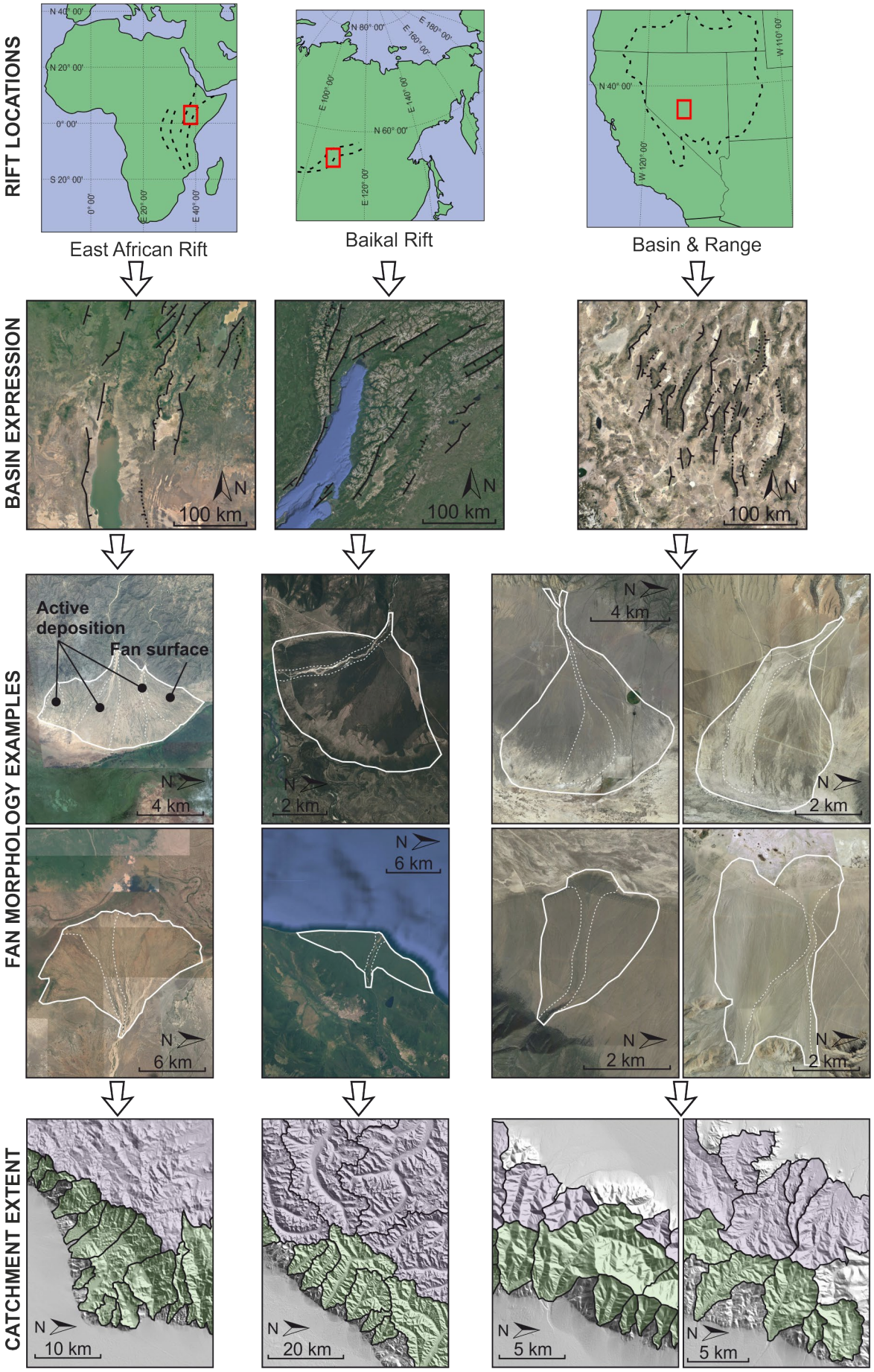
RIFT LOCATIONS
East African Rift
Baikal Rift
Basin & Range
BASIN EXPRESSION
100 km
FAN MORPHOLOGY EXAMPLES
Active deposition
Fan surface
4 km
2 km
6 km
CATCHMENT EXTENT
10 km
20 km
5 km

Figure 3.2 (previous page) *Images detailing the three study areas within the East African Rift, the Baikal Rift, and the Basin and Range Province, their major fault and basin system. Satellite imagery data and DEM imagery data is utilised to derive alluvial fan and associated catchment morphometrics.*

Study sites were selected on the basis of structural settings that are similar for each of the three identified study regions; each tilt-block crest that divides adjacent sub-basins has a basin-bounding normal fault on one side, and a hangingwall dipslope on the opposing side. As such, neighbouring basins form either a pair of half-grabens with the same polarity, or a pair of half-graben and full graben. Study of alluvial systems developed within basins with similar structural styles effectively minimises the role of structural setting in governing alluvial fan formation; therefore, differences in the formation of the fans will likely be linked to other controls.

Study areas with a similar structural setting were chosen based on the examination of candidate examples for which the presence of a rotated and uplifted tilt-block crest with a hangingwall dipslope on one side of the structural high, and a footwall scarp (or fault plane) on the opposing side could be demonstrated. Notwithstanding, whilst the overall structures of each basin may be similar, faulting is highly variable between different extensional systems for a variety of reasons (e.g. the impact of stratigraphy on the type of faulting, the overall stress regime, and the impact of pre-existing basement structures). Structural differences between each study area include overall fault length, fault throw (e.g. 3-6 km for the eastern fault of the Hammar Range [Asrat et al., 2009] and 2-4 km for the eastern fault of the Barguzin Range [Epov et al., 2007; Krivonogov & Safonova, 2017]), but the overall structural style of each is similar. These differences may be affecting alluvial fan formation indirectly (e.g. because of varying fault throws causing different

rates of accommodation generation, in turn affecting fan surface area) but are assumed to be negligible for the study areas.

3.2.1. Satellite imagery

Google Earth satellite imagery was used to define the spatial limits of the alluvial fans and their catchments. Bounding co-ordinates of individual fan surfaces and their catchments were used to identify the same features in ArcGIS on the georeferenced AW3D30 DEM data. In particular, Google Earth was used to define the surface extent of alluvial fan deposits within depocentres; this identification, based on the fan slope (described in section 3.2.3., and used to identify a change in depositional process on the fan surface), was combined with observations of the surface expression of the fan (for example, the position of the fan toe) which could then be overlain onto the georeferenced DEM.

3.2.2. AW3D30 DEM data

The AW3D30 global DEM (obtained from http://www.eorc.jaxa.jp/ALOS/en/aw3d30/index.htm) released in 2016 and subsequently updated in 2017 consists of a worldwide DEM with a 30 m horizontal resolution, covering 82° N to 82° S latitude (Boulton & Stokes, 2018). The high resolution of this public dataset allows for accurate measurements of relief between catchments and associated alluvial fans (Boulton & Stokes, 2018). This global DEM was generated from the Advanced Land Observing Satellite (ALOS) with optical stereoscopic observation during its active time from 2006 to 2011 (Takaku et al., 2014). All images were processed in 2016, generating a dataset with a vertical accuracy ranging from under 5 m (Takaku et al., 2014; Tadono et al., 2016) to 5.68 m Root Mean Square Error (RMSE) (Santillan & Makinano-Santillan, 2016). The AW3D30 dataset was chosen for three main reasons over counterpart global DEMs (for example, the ASTER Global DEM Version 2 (GDEM2) and SRTM-30m): (i) its vertical accuracy being higher

than that of other data sources (values are 11.98 m and 8.28m for SRTM-30 m and GDEM2, respectively; cf. Santillan & Makinano-Santillan, 2016); (ii) its ability to provide the closest fit to true drainage network configurations in mountainous regions (Boulton & Stokes, 2018); and (iii) its accessibility. For this study, the 'average' DEM was used; this was produced by averaging the value of elevation of 49 pixels (7 x 7) to obtain a final pixel value. This was used in place of the 'median' value, also produced for the AW3D30 dataset (Tadono et al., 2016). Comparative tests run by Boulton & Stokes (2018) analysing the accuracy of different DEM datasets found the AW3D30 data to be the most accurate at that time. By utilising projected coordinate systems, elevation could be measured more accurately, between catchment and fan morphologies in each of the study areas. DEM subsets were extracted for each of the three study areas and imported into ArcMAP 10.4.1, where measurements were made (described in sections 3.3.2., 3.4.2., and 3.5.2.).

3.2.3. Definition of alluvial fans and catchments

Identification of alluvial features for both fans and catchments was undertaken using Google Earth satellite imagery (Figure 3.2). In this study, fans and catchments were considered from their most recent available satellite and DEM imagery. Catchments were mapped based on drainage divides visible in the studied mountain ranges. Drainage divides bordering each catchment were mapped across the ranges based on manual assessment of visible water courses. The downstream extent of the catchment was determined by identifying a drainage 'chokepoint', where the catchment was narrowest at its lowest elevation. This location defined the start of the deposited alluvial fan feature for each measured example. Many fans may partly backfill their feeder gulleys (and part of the measured catchment), but recognition of this on the imagery was not possible and is therefore ignored in all cases for consistency. Alluvial fans were identified through a combination of their visible shapes (e.g., cone-shaped or lobate forms), their slope

measurements derived from Google Earth elevations and DEM data, and colour variations on the imagery relative to that of adjoining environments. Figure 3.2 shows the criteria used to qualitatively determine the following attributes: (i) catchment areas between drainage divides using a combination of elevation and stream profiles, and (ii) the down-system length and area of alluvial fans in the sedimentary basins, based on the presence and morphology of a relatively finer-grained apron at the toe of the fans. These attributes were identified by observing a clear break in slope (transition to flat gradient) and by marked colour variation (typically darker browns) relative to surrounding environments (D'Arcy et al., 2017; Delorme et al., 2018). In the case of fan deltas (Holmes, 1965; McPherson et al., 1987), which in this study are exclusive to the Baikal rift example, only their subaerial delta-top portion is considered and measured. A direct comparison of the fan-delta tops and alluvial fans is not a like-for-like comparison and is a limitation of this study.

3.2.4. Data collection and analyses

The polygon tool in ArcGIS was used to measure and define the morphometric parameters outlined in Table 3.1 for the defined catchments and associated fans. These parameters quantify the size of fans and associated catchments (planimetric area, width, length, and width/length ratio), allowing for any relationships between those parameters to be determined and compared to both previous studies of fan-catchment systems, and to other study areas. Hypsometric curves and Melton's ratio values were derived for each catchment to infer the erosive and depositional processes taking place in the catchments and on the fans, respectively, and to link those processes to the tectonic, climatic and lithological setting of each study area.

Morphometric parameter	Description	Units
Fan area	Planimetric area of the visible fan surface	km^2
Catchment area	Planimetric area of the visible drainage catchment	km^2
Active depositional area	Planimetric area of the visible fan surface undergoing active deposition	km^2
Fan slope	Inclination of the fan surface taken from fan apex to the fan toe	km/km
Fan width	Planimetric distance of the widest section of the fan surface	km
Fan length	Planimetric distance between the fan apex and the most distal point of the fan surface	km
Catchment width	Planimetric distance of the widest section of the drainage catchment	km
Catchment length	Planimetric distance between the fan apex and the most distal point of the drainage catchment	km
Catchment relief	Elevation difference between the highest and lowest points of the drainage catchment	km
Melton's ratio	Catchment relief (km) divided by the square root of catchment area (km^2)	km/km

Table 3.1 *List of morphometric parameters used in the analysis of the proposed rift settings. After Wilford et al. (2004), de Scally et al. (2010), and Kain et al. (2018).*

In total, 51 hypsometric curves and Melton's ratios were determined for the Hammar Range of the East African Rift System, 26 for the Barguzin Range of the Baikal Rift, and 56 for the Toiyabe and Toquima Ranges of the Basin and Range, for a total of 133.

Hypsometric curves

Hypsometric curves are generated by plotting the cumulative proportion of the catchment area against the relative elevations in that catchment (Strahler, 1952; Schumm, 1956). One curve has been plotted for each catchment. The shape of the

generated curves acts as a proxy for the amount of erosion that a catchment has undergone, whereby a higher proportion of relatively high elevations indicates a lower amount of total erosion, and vice versa. This observation can then be used to indicate potential catchment age, based on the assumption that an older catchment will have undergone more erosion than a younger one in the same mountain range (Strahler, 1952).

Ohmori (1993) examined hypsometric curves in actively uplifting areas, a situation that is relevant to this study, since hypsometric curves are applied here to catchments developed on uplifting tilt-block crests. As a catchment is uplifted, the proportion of higher relative elevations within that catchment increases, altering the shape of the curve (Giaconia et al., 2012; Maroukian et al., 2008; Delcaillau et al., 2011). This can be identified when multiple curves, from multiple catchments on the same tilt-block crest, are directly compared in terms of their shapes; it allows for interpretations of the rate of uplift occurring on different sections of a fault, and of the erodibility of the catchment as a function of climate and bedrock lithologies (Ohmori, 1993). Slope contrasts between the footwall slope and hangingwall dipslope of the uplifted tilt block may also be represented by changes in the shape of the curves.

To analyse hypsometric curves for each of the studied catchments (as a proxy for their relative ages), the plugin CalHypso for ArcGIS was used (see Pérez-Peña et al., 2009). This allowed for the automatic calculation and comparison of the hypsometric curves compiled in this study, thereby aiding identification of catchment differences.

Melton's Ratio

The Melton's ratio (Melton, 1957) is a metric that quantifies the ruggedness of a drainage area. It is calculated as the ratio between the catchment relief (i.e. its total range in

elevation) and the square root of the catchment area. Higher ratios correspond to more rugged catchments (Melton, 1957).

The Melton's ratio has been used and adapted in numerous previous studies of alluvial fans or fan deltas and their catchments (Sorriso-Valvo et al., 1998; de Scally et al., 2010; Welsh & Davies, 2011; de Haas & Densmore, 2019), and has been taken as a proxy for different flow types downstream of the studied catchments. For increasing values of Melton's ratio, flows tend to be dominated by debris-flow conditions, displaying increasingly cohesive non-Newtonian plastic rheology; as the ratio decreases, flows tend to be dominated by fluvial stream flow (Jackson et al., 1987; Wilford et al., 2004; Welsh, 2008). This allows for inferences to be made of the depositional processes operating on the alluvial-fan surface at the time of catchment morphometry measurement. Welsh & Davies (2011) describe ranges of ratios (between 0 and 1) for different fan surface flow types (indicated by dashed lines in Figures 3.5, 3.8 and 3.11) of 0 – 0.3, 0.3 – 0.6 and 0.6 – 1.0. These ranges, ground-truthed by field observations, indicate dominant depositional flow types of fluvial flows, transitional flow types, and debris flows, respectively. Fans derived from the hangingwall dipslope and footwall slope can be directly compared in terms of their Melton's ratios so as to determine similarities and differences in likely flow types; results can be compared between each structurally similar rift setting to determine the impact of other allogenic controls, such as climate, bedrock lithology, and basin scale.

Values of Melton's ratio were calculated from the extracted elevation and area data derived from catchment polygons mapped across uplifted footwall slopes of the study areas.

3.3. The East African Rift System (EARS)

3.3.1. Geological setting

The East African Rift system is one of the most extensive and well-developed extensional provinces active today; it exhibits a range of half-graben and full graben basin structures along its ~4,300 km length (Chorowicz, 2005; Macgregor, 2015). In the section of the rift extending through Kenya and Ethiopia (colloquially named the Eastern Branch), alluvial fans have developed at the basin flanks, sourced from river networks cutting into newly formed footwall scarps up to the Afar Triangle (Tiercelin, 1990). Further fan development occurs locally adjacent to volcanic features forming topographical highs on the basin floor, and form extensive external drainage networks with outflow over flexural basin margins into depocentres (Frostick & Reid, 1987; Tiercelin, 1990). This study focuses on the Chew Bahir and South Omo basins (Figure 3.3), which are separated by an uplifted tilt-block crest named the Hammar Range. Half-graben formation and subsequent fault block rotation generated accommodation forming the South Omo basin (Ebinger et al., 2000), with subsequent sedimentation dominated by fluvio-lacustrine deposits on the basin floor (de Heinzelin, 1983; Howell et al., 1987), and alluvial-fan facies towards the basin margins (Howell et al., 1987). The syn-rift stratigraphy reaches a maximum thickness of ~4,500 m on the western side of the basin (Mammo, 2012), and thins towards the east before onlapping onto the western side of the Hammar Range.

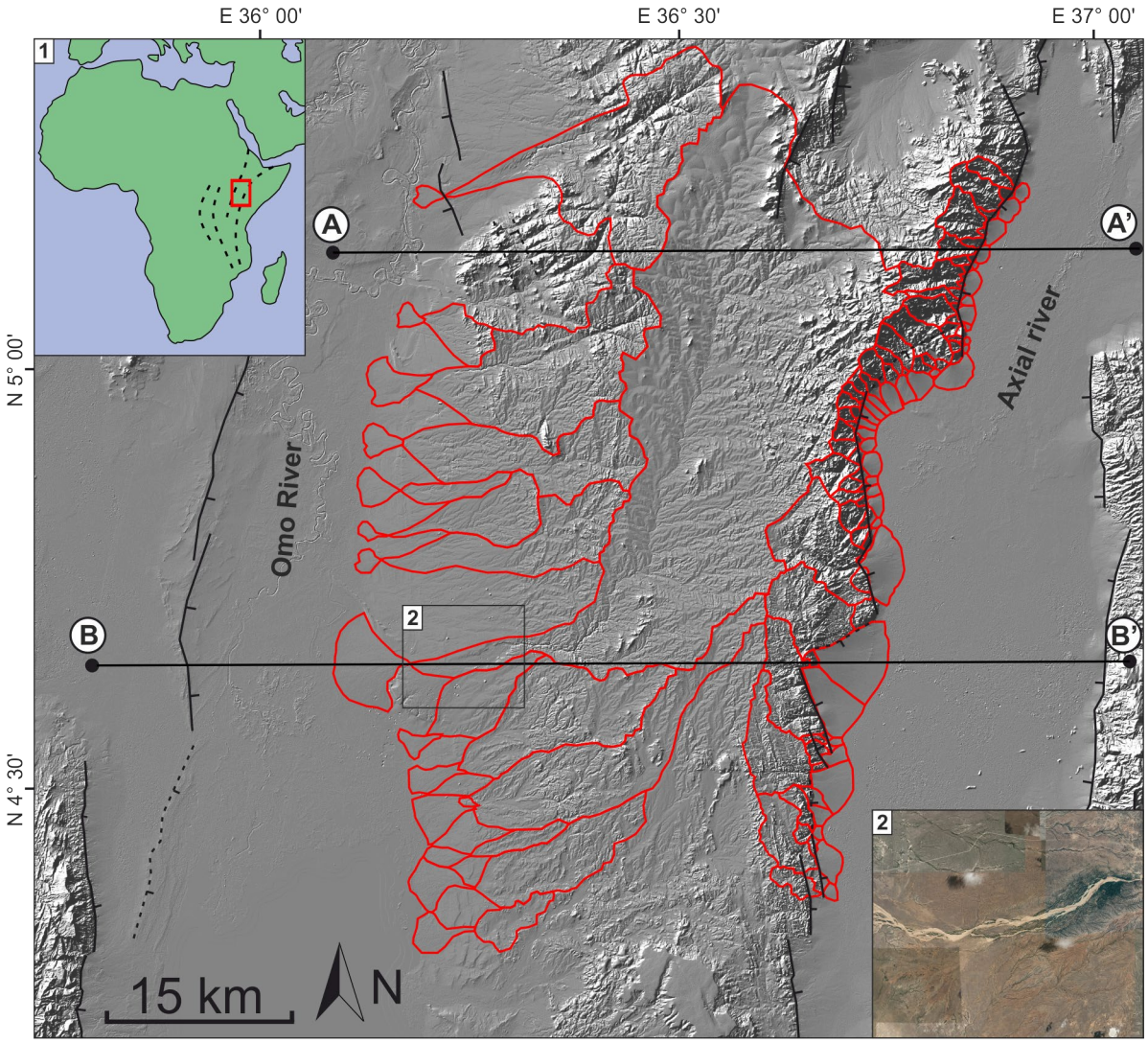

Figure 3.3 *DEM imagery of the Hammar Range and surrounding basins, Ethiopia, East African Rift. Studied fan bodies and drainage catchments are outlined in red. Inset 2 displays an example of a short-range stream formed near the terminus of a hangingwall dipslope drainage catchment. Lines A – A' and B – B' represent cross sections displayed in Figure 3.4.*

A steep footwall scarp on the eastern side of the Hammar Range associated with a major east-dipping normal fault forms a boundary to the Chew Bahir Basin (Figure 3.4) and dictates the position of alluvial fans growing directly over the footwall slope into the hangingwall. The basin-bounding fault here is heavily influenced by the pre-existing basement structure, leading to multiple kinks in the fault profile (Corti, 2009). Pre-

existing basement fabrics heavily influence the surface faulting visible today, and likely impacts the size and scales of the basins themselves (Corti et al., 2019).

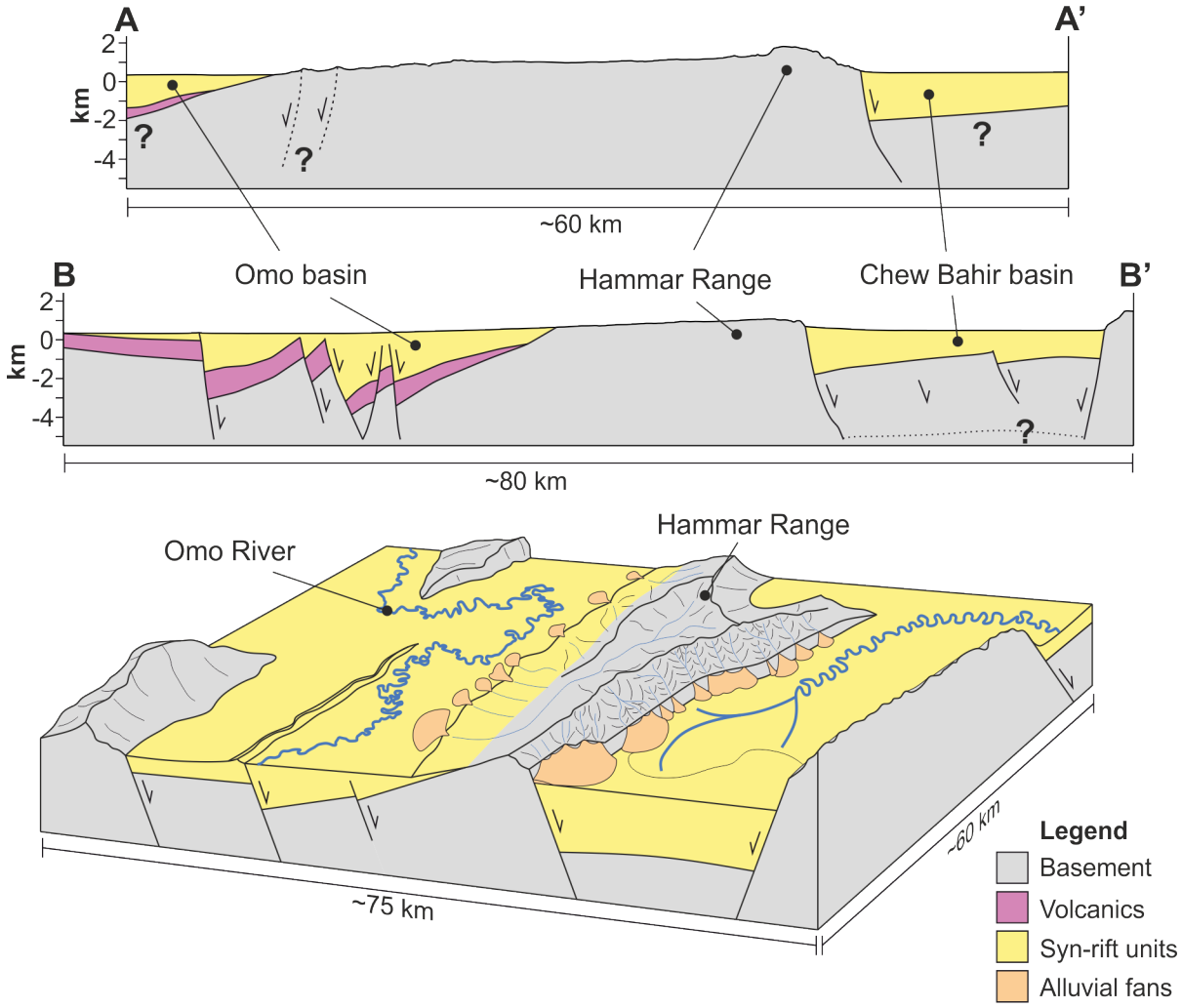

Figure 3.4 *Cross sections (locations shown on Figure 3.3) and a 3D block model of the Hammar Range and its adjacent basins. Major present-day basin environments are displayed, in conjunction with alluvial fan bodies and associated catchments formed on the Hammar Range. Subsurface information is after Ebinger et al. (2000), Mammo (2012).*

The studied subaerial alluvial fans extend into depocentres on both sides of the uplifted block (Hammar Range), into the realm of an axial fluvial system in the west (the Omo river, which terminates to the south in Lake Turakana) and into an axial terminal-fan and mudflat system in the Chew Bahir basin (Foerster et al., 2012). Key to this system is the geology of the Hammar Range: in the south, Oligocene Fejej (or Nabwal) basalts (Ebinger et al., 2000) correspond to the earliest extension-influenced rock formation in the Ethiopia-Kenya area. In the centre and northern parts of the range, the bedrock is dominated by undivided Precambrian gneisses and remnant metamorphosed Permian sandstones (Davidson & Rex, 1980; Foerster et al., 2012), which form the dominant source lithology to alluvial fans on both the footwall slope and hangingwall dipslope. The alluvial fans studied here are largely unconfined; high rates of accommodation generation have enabled growth on both sides of the Hammar Range. There is only very limited human impact on fan development on both sides of the hinterland.

The hinterland itself is dominated by a combination of igneous basalts to the very south, transitioning to metamorphosed sandstones and Proterozoic basement lithologies that include volcanics, gneisses and metasediments (Davidson & Rex, 1980; Ebinger et al., 2000). The current climate within the basin itself is a seasonal tropical wet and dry climate, with two annual periods of rainfall introduced by the ITCZ (Intertropical Convergence Zone) feeding catchments on the Hammar Range, which itself has a cooler, transitional climate between tropical and summer monsoon (Foerster et al., 2012; Beck et al., 2018).

3.3.2. Results and interpretations

Over the Hammar Range and its associated uplifted hinterland, 37 catchments and their fans were identified forming directly over the footwall slope side (eastward draining) of

the range, and 14 catchments and their fans were identified on the hangingwall dipslope side (westward draining) (Figure 3.3). On the footwall slope side, alluvial fans typically form part of the same debris 'apron' directly adjacent to the range. As a result, although some isolated fan geometries exist, most fans are amalgamated to form a bajada fed by multiple catchments. On the hangingwall dipslope side, catchments are typically larger and each feeds one distinct fan body. Relic fan surfaces visible updip of the active fans present on the hangingwall dipslope indicate the influence of autogenic processes leading to fan channel entrenchment, and the transport of sediment downdip, leading to the abandonment and progradation of the fan system (Ventra & Nichols, 2013). Notably, one catchment dominates the uplifted area suggesting potential drainage capture through time.

Figure 3.5 shows a comparison between morphometric parameters for fans and catchments of the footwall slope and hangingwall dipslope. For footwall slope features, catchment areas vary from 1.41 km^2 to 109.26 km^2 (mean = 18.8 km^2). Catchment areas are larger for hangingwall dipslope features (with a range of 24.61 km^2 to 382.65 km^2; mean = 157.32 km^2, excluding a single anomalously large catchment of area 1760.87 km^2), corresponding to fan surface areas being significantly different for both sides of the range with means of 8.08 km^2 vs. 15.11 km^2 for footwall slope and dipslope fans, respectively (a 2-sample t-test yields a T statistic of -2.18, a DF [degrees of freedom] of 30, and p-value of 0.0372; in this study, these values will be stated wherever a t-test is run). The active depositional area of the fan surface (identified from a lack of erosional features visible on satellite imagery) has a strong linear relationship with the overall fan surface area (R = 0.98 and 0.90 for footwall slope and hangingwall dipslope fans,

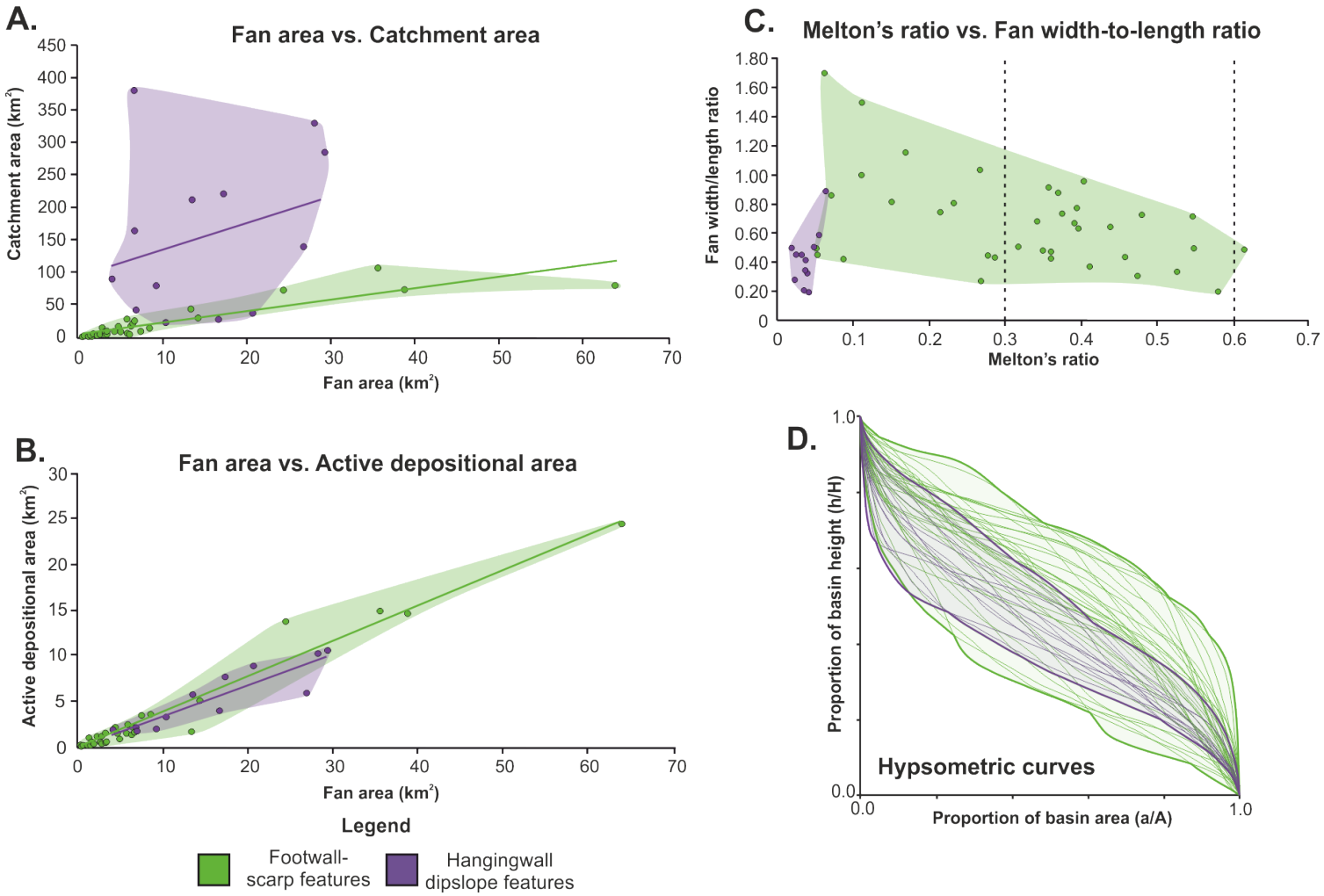

Figure 3.5 *Plots of select measured morphometric parameters, Melton's ratios and hypsometric curves from the Hammar Range dataset. (A) Plot of fan area vs. catchment area. (B) Plot of fan area vs. active depositional area. (C) Plot of Melton's ratio vs. fan width-to-length ratios (for dashed line definition, see section 3.2.4., Melton's Ratio). (D) Plot of hypsometric curve variability for both footwall slope and hangingwall dipslope catchments. See text for details.*

respectively) despite potential differences in depositional style (see discussion of Melton's ratio below). Measurements of fan slopes vary from 0.014 to 0.063 for footwall slope fans, and 0.008 to 0.013 for hangingwall dipslope fans, indicating a prevalence of steep-sided talus cones for fans forming directly from the footwall slope into the adjacent depocentre.

Hypsometric curves derived for all 51 catchments are outlined in Figure 3.5. The range of curves shown by this diagram indicates that relative elevations within footwall slope catchments are more variable than in their hangingwall dipslope counterparts. As described in section 3.2.4., the shape of the curve is typically used as a proxy for the age of a basin, whereby an increasingly concave-up curve represents an older drainage catchment (Strahler, 1952). Consequently, if the major normal fault on the east side of the Hammar Range grew via the isolated fault growth model, it would be expected that the predicted 'oldest' catchments would be located at the fault centre, and the 'youngest' at the fault tips. In this example however, there is no spatial relationship between location on the fault and hypsometric curve shape (and predicted catchment age). The fragmented nature of the faulting, itself a function of pre-existing basement fabrics (Ebinger et al., 2000), likely results in sporadic magnitudes of fault activity affecting the catchment curves, where uplift of the hinterland creates a catchment curve profile expressed as a convex-up curve with higher relative elevations.

A comparison of relations between the Melton's ratio and fan width-to-length ratios is provided in Figure 3.5, allowing a comparison between potential flow types on the fan surface. For footwall slope catchments, the ratio varies from 0.05 to 0.61, whereas for the dipslope catchments it never exceeds 0.04. In this example, footwall slope fans are inferred to be dominated by debris-flow conditions, whereas streamflow conditions are

interpreted as dominating the hangingwall dipslope fans. This is further evidenced by the development of short-range stream conditions near the mouth of catchments on the dipslope side, which extend onto the fan surface and into the adjacent basin (see Figure 3.3, inset 2). Fan width-to-length ratios are influenced by the formation of bajadas, confining fan lateral expansion and elongating the fan body. Multiple bajadas form on the footwall slope side of the tilt-block crest, and their constituent fans have an average width-to-length ratio of 0.73. The other studied fans, here called isolated fans to distinguish them from their bajada-forming counterparts, have an average width-to-length ratio of 1.09.

3.4. The Baikal Rift

3.4.1. Geological setting

Focussed on the eastern edge of the northern parts of Lake Baikal, the Barguzin Range is an uplifted tilt-block crest (orientated NNE-SSW) over 80 km wide and 250 km long (Figure 3.6). It acts as a source to alluvial fans accreting to the west as a fan delta apron over a half-graben hangingwall dipslope, and to the east directly into the hangingwall of the adjacent Barguzin basin. The Baikal Rift covers 2,000 km in eastern Siberia and is the deepest modern active continental rift system (Moore et al., 1997) with its major depocentres (covered by Lake Baikal) more than 1.5 km deep (Mats, 2012). Beneath the sediment cover of the northern lake basin, basement units representing the top of a fault block shallow to the east, displaying a strong degree of asymmetry (Moore et al., 1997) and exposing the uplifted footwall of the Barguzin Range. Present-day extension in the region is caused by the eastward motion of the Amurian tectonic plate (<10 mm/yr with respect to the Eurasian plate) (Heki et al., 1999). Several hypotheses have been

postulated to explain the cause of extension: (i) the presence of a sub-lithospheric "hotspot" (Thybo & Nielsen, 2009); (ii) extension as a side-effect of the India-Eurasia collision (Yin, 2000); (iii) the exploitation of structures associated with previous long-lived transtensional regimes (Ren et al., 2002).

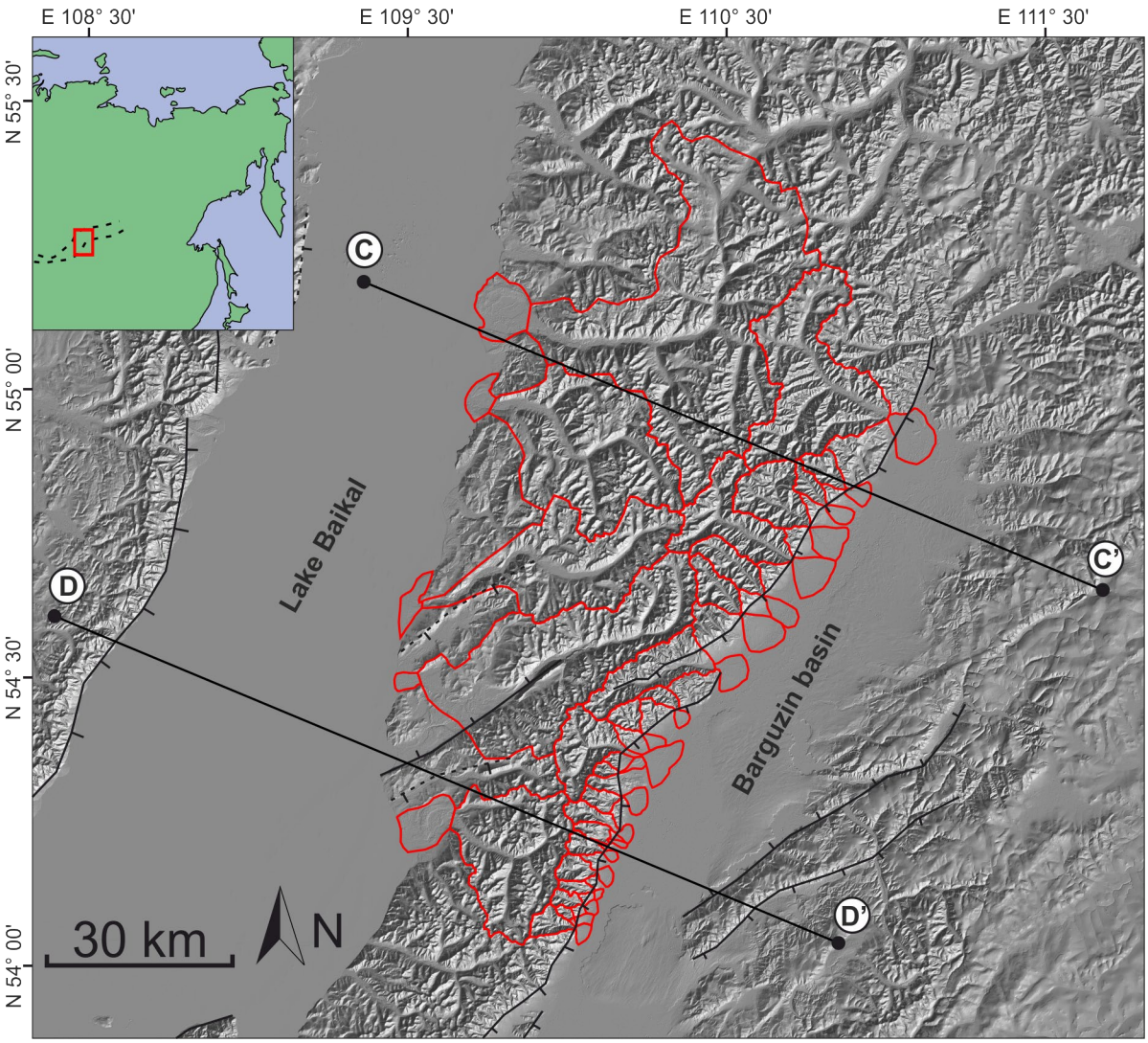

Figure 3.6 *DEM imagery of the Barguzin Range and surrounding basins, Russia, Baikal Rift. Studied fan bodies and drainage catchments are outlined in red. Lines C – C' and D – D' represent cross sections displayed in Figure 3.7.*

The Barguzin Range has delivered sediment to the Barguzin and North Baikal basins intermittently since its exhumation at 65 Ma, and during uplift over the last 5 Ma (Logatchev & Florensov, 1978; Mats, 1993; Buslov, 2012). Faulted and partially uplifted fan deltas extend into northern Lake Baikal feeding delta slopes and possible turbiditic systems (Nelson et al., 1999). Sediment thicknesses reach their maximum on the lake bed; early studies predicted a sediment thickness up to 4,500 m (Zonenshain & Savostin, 1981), later increased to 8,000 m (Moore et al., 1997), though with more recent conservative estimates predicting 1,000 to 2,000 m (Mats, 2012) (Figure 3.7). On the eastern edge in the Barguzin basin, sediments are of Middle Pliocene-Quaternary age (Buslov, 2012) and are typically dominated by non-lacustrine continental units (Kolomiets & Budaev, 2015; Krivonogov & Safonova, 2017). Multiple small-scale drainage catchments feed individual alluvial fans that compete for accommodation with the axial meandering Barguzin River. The total sediment thickness in the Barguzin basin is approximately ~1,500 to 1,800 m along the deeper western edge, with a maximum thickness up to 2,500 m (Epov et al., 2007; Krivonogov & Safonova, 2017). The range and its surrounding rift system lie in a subarctic-humid climatic setting (Brunello et al., 2006), which is currently warming due to the onset of human-induced climate change (Törnqvist et al., 2014). The catchments have been influenced by the activity of glaciers since the initiation of rifting (Osipov et al., 2003).

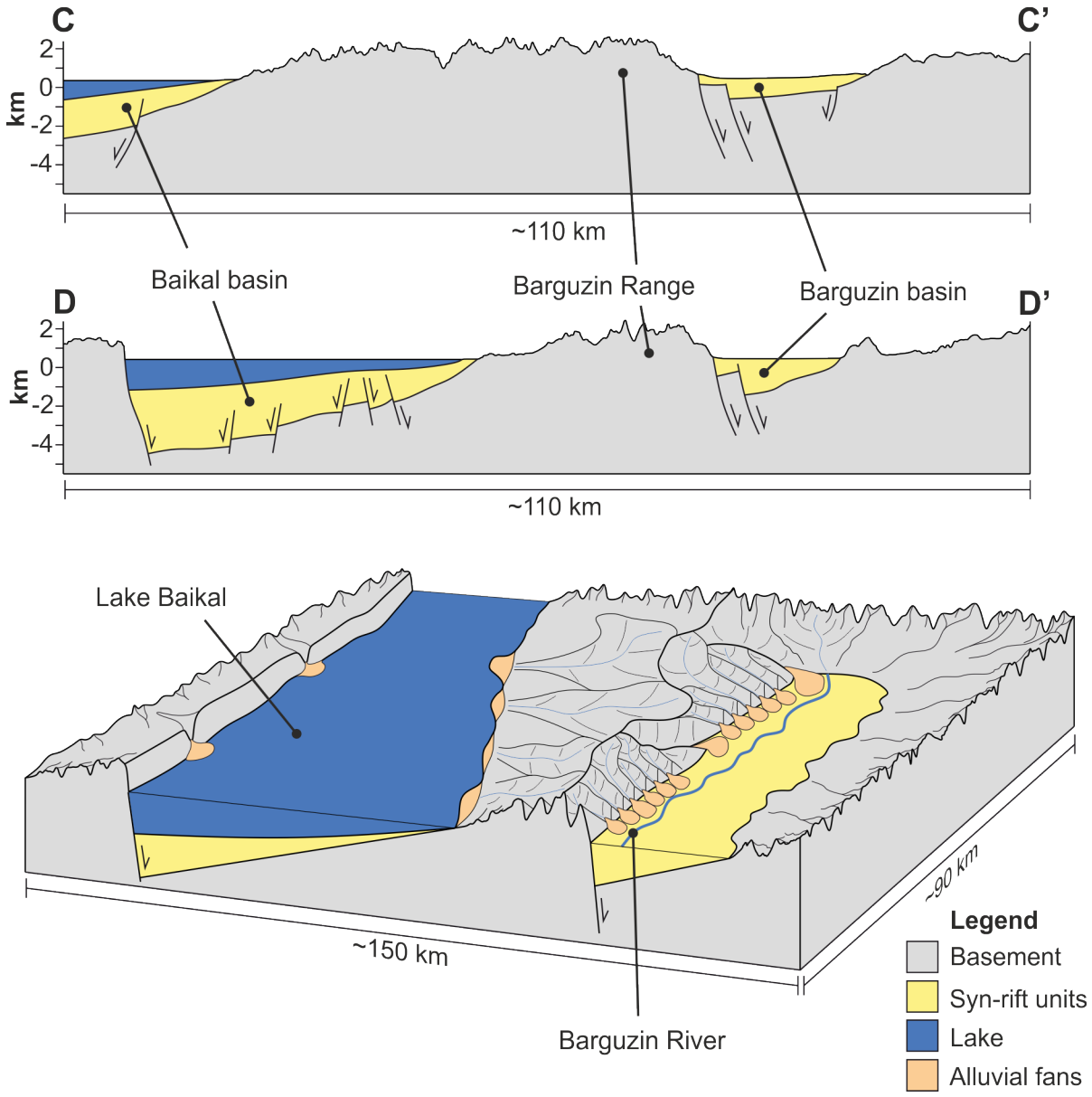

Figure 3.7 *Cross sections (locations shown on Figure 3.6) and a 3D block model of the Barguzin Range and its adjacent basins. Major present-day basin environments are displayed, in conjunction with alluvial fan bodies and associated catchments formed on the Barguzin Range. Subsurface information is after Epov et al. (2007), Plyusnin et al. (2008), Krivonogov & Safonova (2017).*

3.4.2. Results and interpretations

In the Barguzin Range, 26 catchments were identified that provided sediment to fans in adjacent basins (21 on the footwall slope side to the east, and 5 on the hangingwall

dipslope side to the west) (Figure 3.6). On the footwall slope, fans take the form of mostly isolated landforms adjacent to the steep-sided range, and compete for space with the Barguzin River, an axially orientated fluvial system that flows southwest toward Lake Baikal. On the hangingwall dipslope, fan deltas prograding into the eastern part of Lake Baikal have formed at the mouths of hinterland catchments, with a clear delta plain visible on satellite imagery (further discussed in section 3.2.3.). The lithology of the Barguzin Range is dominated by granites and gneisses related to Proterozoic activity (Epov et al., 2007; Plyusnin et al., 2008) with some metasediments, mostly Ordovician (Jolivet et al., 2009) and late Proterozoic Riphean rift deposits (Plyusnin et al., 2008).

Figure 3.8 shows comparative details between morphometric parameters for the footwall slope and hangingwall dipslope fans and catchments. For footwall slope features, catchment areas range from 6.80 km^2 to 607.36 km^2 (mean = 86.18 km^2). Catchment areas of dipslope features are larger than their footwall slope counterparts, ranging from 498.59 km^2 to 1855.56 km^2 (mean = 947.26 km^2). Despite this difference, visible fan surface areas on the dipslope side are only marginally larger than their footwall counterparts (a range of 15.19 km^2 to 110.55 km^2, and 2.76 km^2 to 71.70 km^2, respectively). Fan-surface area and active depositional area display a strong linear relationship (R = 0.92 and 0.82 for footwall slope and hangingwall dipslope fans, respectively), despite key differences in depositional style between subaerial and lacustrine settings. Measurements of fan slopes vary from 0.013 to 0.110 for footwall slope fans, and 0.004 to 0.013 for hangingwall dipslope fans, again showing an increased tendency towards steeper-sided fans forming next to the uplifted footwalls present in the Baikal Rift.

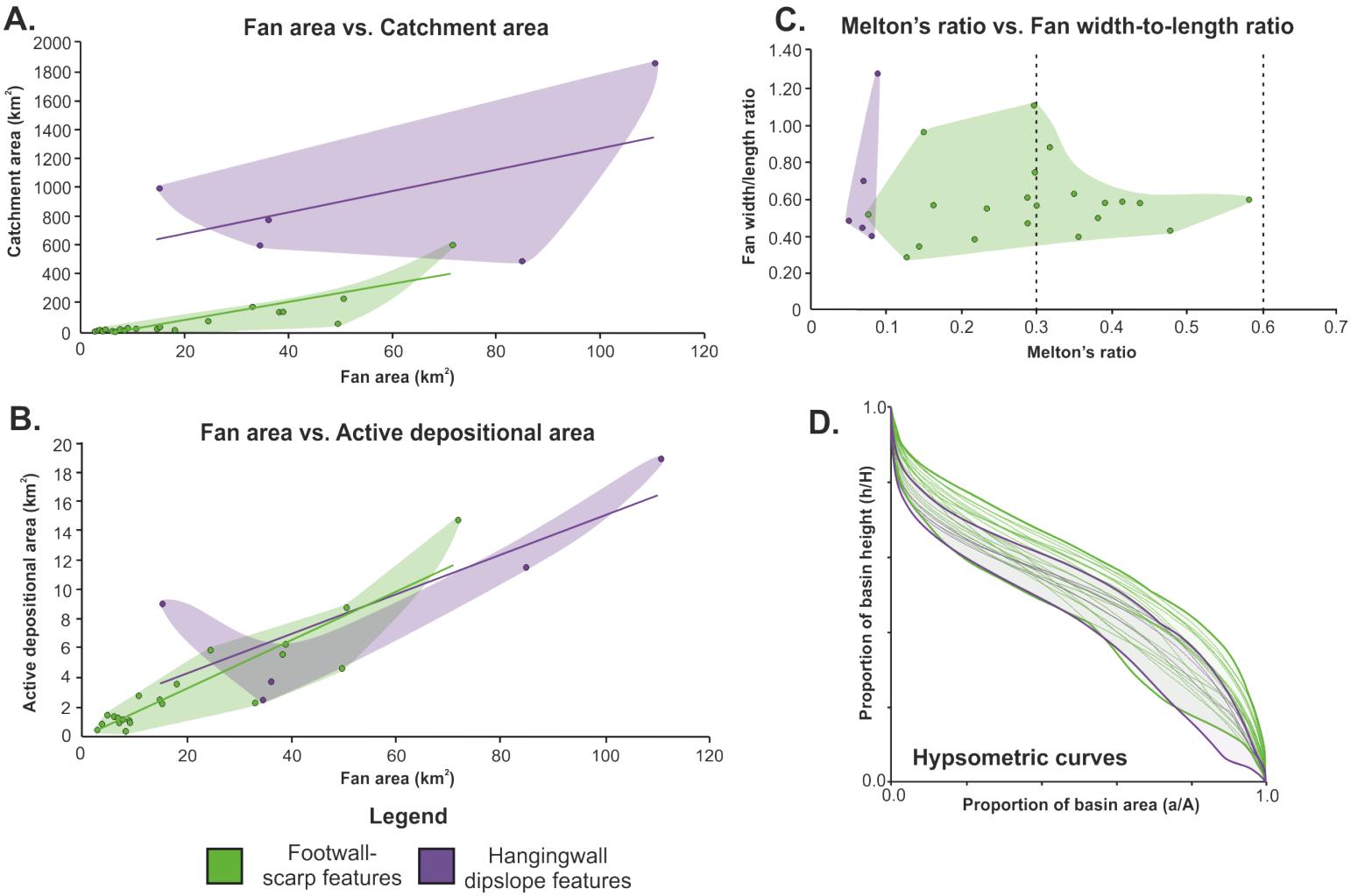

Figure 3.8 *Plots of select measured morphometric parameters, Melton's ratios and hypsometric curves from the Barguzin Range dataset. (A) Plot of fan area vs. catchment area. (B) Plot of fan area vs. active depositional area. (C) Plot of Melton's ratio vs. fan width-to-length ratios (for dashed line definition, see section 3.2.4., Melton's Ratio). (D) Plot of hypsometric curve variability for both footwall slope and hangingwall dipslope catchments. See text for details.*

Figure 3.8 depicts hypsometric curves for the studied catchments of the Barguzin Range. Overall, the curves display a tendency towards concave-down profiles (ergo, larger proportions of catchment areas retaining higher relative elevations), which may be caused by ongoing fault activity leading to the present-day uplift of the entire hinterland. The lack of variation in profiles both within each footwall slope and hangingwall dipslope set, and between the sets themselves, indicates a particular similarity in erosion of the catchments on both the footwall slope and hangingwall dipslope; unlike the Hammar Range example, it appears that the influence of slope, lithology or climate has been subdued here leading to similar responses to uplift. It should be noted that these curves may have been affected by glaciation, occurring as recently as the Late Pleistocene (MIS 2; Osipov et al, 2003), which would likely have caused an increase in the proportion of lower topographic relief within each catchment as a result of glacial erosion being more rapid than alluvial erosion (Shuster et al., 2005). Despite this, the curves are still dominated by higher relative elevations, with 40 to 70% of the catchment area being higher than 50% of the difference between the minimum and maximum elevations of the catchment.

A comparison of the Melton's ratio and of the fan width-to-length ratios is provided in Figure 3.8. Ratios vary from 0.08 to 0.58 for footwall slope catchments, and from 0.05 to 0.09 for hangingwall dipslope catchments. Despite the increased range of values for footwall slope fans, values do not typically extend beyond 0.50, indicating a likely mixture of streamflow processes and sediment-laden debris floods dominating depositional flows on the fan surface (Wilford et al., 2004; Welsh & Davies, 2011). This can be seen on the satellite imagery, with clear alluvial channels forming on the fan surfaces. On the delta plains on the dipslope side of the range, meandering fluvial systems are well developed with channel morphologies visible; flood and fluvial deposition likely dominates in the

generation of these features, in agreement with the observed low Melton's ratio values. From the data in this example, there is no clear relationship between the ratio and the catchment width-to-length ratio; this may be due to the influence of glacial systems on basin ruggedness.

3.5. The Basin and Range province

3.5.1. Geological setting

The Basin and Range province in North America is a 600-km wide extensional domain (Dickinson, 2006) that covers much of western North America, reaching Mexico on its southern fringes. This study focuses on the internally draining Great Basin, a part of the province that occupies large parts of Nevada and Colorado, transitions to the west into the Walker Lane Belt, and is bordered to the east by the Wasatch and Sevier fault systems (Long, 2018). The Great Basin comprises a suite of grabens and half-grabens forming basins with interspersed mountain ranges west of the Colorado Plateau (Stewart, 1980). Extension through time has been attributed to a variety of causes, including backarc extension, and transrotational and syn-transform extension (Dickinson, 2002). Over the last 30 Ma, the rollback of the subducting Farallon tectonic slab led to extensive magmatism and extension across the southern Great Basin (Best et al., 2013). A wide mixture of faulting styles and basin morphologies are present across the province, including early listric faulting (Stewart, 1980; Anderson et al., 1980), graben-horst structuration (Stewart, 1980; Dickinson, 2006) and widespread half-graben development (Proffet, 1977; Stewart, 1980; Leeder & Gawthorpe, 1987). Despite the province being one of the most studied extensional areas in the world (Dickinson, 2002; Dickinson, 2006) questions remain about its formation and evolution over the last 20 Ma.

The Toiyabe and Toquima Ranges are concurrent uplifted tilt-block crests within these partially rotated fault blocks (Figure 3.9), shedding alluvial material to the east and west of each respective range, into the Monitor Valley basin, Big Smoky Valley basin and Reese River Valley basin from east to west. The geology of these two ranges and their adjacent sedimentary basins remain relatively poorly documented in the literature; however geological maps (USGS maps GQ-770 and GQ-1307; McKee 1968, 1976) outline normal faulting on the east side of the ranges (Figure 3.10), and display westward dipping exposed basement forming large parts of the ranges themselves, indicating likely half-graben basin morphologies. The Big Smoky Valley may be influenced by small amounts of local faulting on its eastern side (based on small imaged surface scarp morphologies) indicating the initiation of the transition to a full-graben morphology. As a result – and similarly to nearby basins (Proffet, 1977; Oldow & Bartel, 1987; Camilleri, 2013) within the Great Basin – these basins are likely to be westward-deepening depocentres, allowing for the study of footwall slope and hangingwall dipslope alluvial fan morphologies. Lithologies in the ranges include marine carbonates and siliceous rocks with granodiorite plutons and tuff deposits in the Toquima Range (McKee, 1976) and Paleozoic metasediments (dominated by limestones (containing cherts and pelites) and shales), pillow basalts and quartz latite in the Toiyabe Range (Babaie, 1987). The two ranges described here are located in an arid to semi-arid climatic system (up to 300 mm of rainfall per year) (Osborn, 1989).

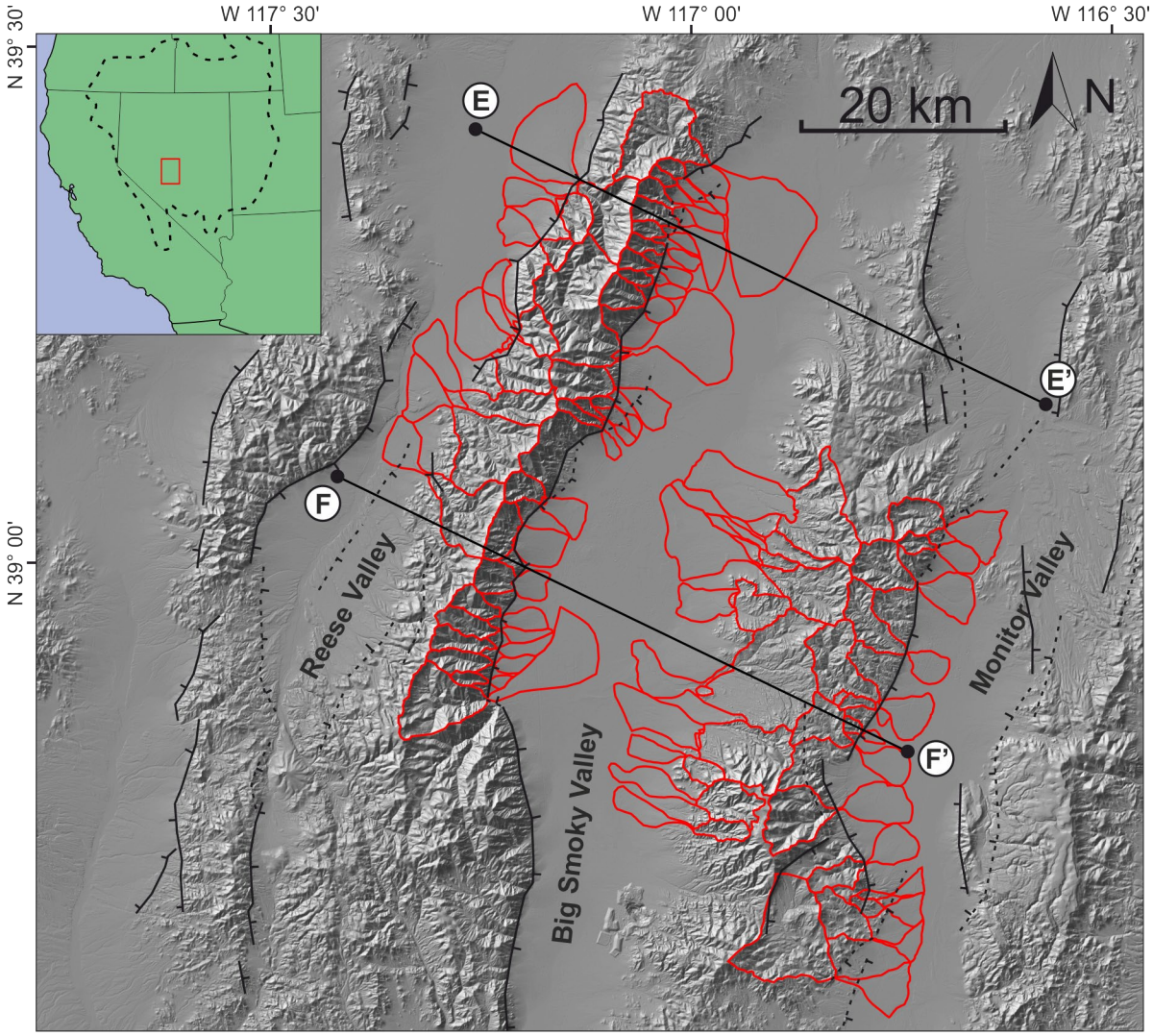

Figure 3.9 *DEM imagery of the Toiyabe (left) and Toquima (right) Ranges and surrounding basins, Basin and Range province, USA. Studied fan bodies and drainage catchments are outlined in red. Lines E – E' and F – F' represent cross sections displayed in Figure 3.10.*

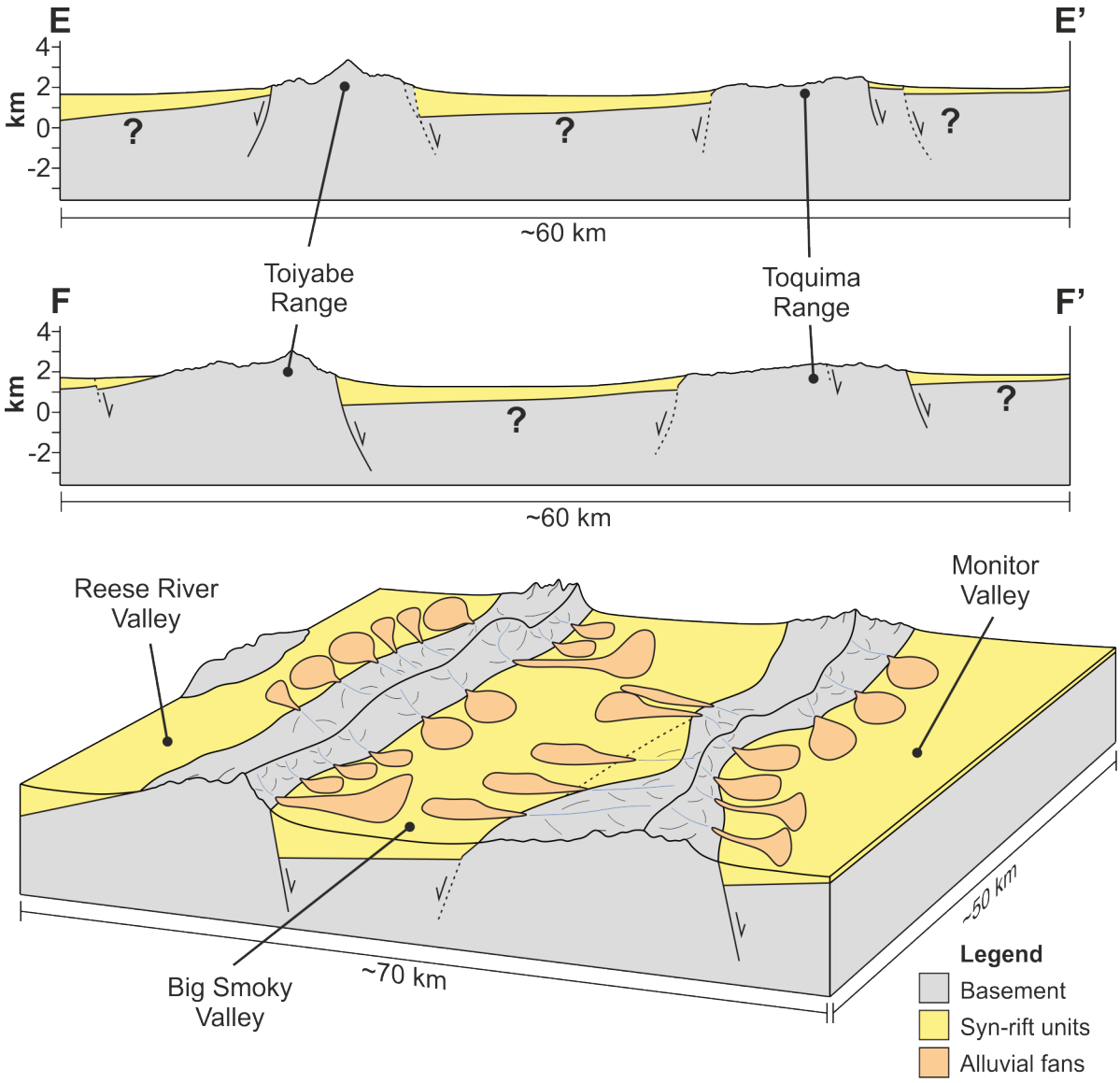

Figure 3.10 *Cross sections (locations shown on Figure 3.9) and a 3D block model of the Toiyabe and Toquima Ranges and their surrounding basins. Major present-day basin environments are displayed, in conjunction with alluvial fan bodies and associated catchments formed on the ranges. Subsurface information is after McKee (1968), McKee (1976), Stewart (1980).*

3.5.2. Results and interpretations

In the Toiyabe Range, 32 catchments were identified (Figure 3.9) as providing sediment to fans in adjacent basins (24 on the footwall slope side, and 8 on the hangingwall dipslope side); this is combined with the 24 catchments studied over the Toquima Range to the east (of which 14 provide sediment sourced from the footwall slope, and 10 provide

sediment over the opposing dipslope). Here, the details of two separate ranges are measured to provide a larger suite of data with which to enable comparison to the EARS and Baikal examples (Figure 3.11). Fans on either side of the asymmetric half-grabens include isolated forms and laterally extensive bajada and compete for space on the basin floor with ephemeral axial rivers (for example, the Reese River), and with fans forming on the opposite side of the basin.

Details of the measured features morphometric parameters are outlined in Figure 3.11. For footwall slope catchments across both ranges, areas range from 2.10 km^2 to 71.78 km^2 (mean = 15.32 km^2). For dipslope catchments, the areas range from 4.64 km^2 to 86.14 km^2 (mean = 26.75 km^2); consequently, there is limited difference in catchment size (T-statistic = -2.01, DF = 27, p-value = 0.054). Similarly, the fan surface area does not vary greatly across the two groups, with average areas of 12.19 km^2 and 19.26 km^2 for footwall slope and dipslope located fans, respectively (T-statistic = -1.79, DF = 38, p-value = 0.081). Again, as for the previous two examples, the active depositional area of the fan surface displays a strong linear relationship with the total fan surface area (R = 0.80 and 0.85 for footwall slope and hangingwall dipslope fans, respectively). The fan slopes vary from 0.013 to 0.090 for footwall slope fans, and from 0.022 to 0.054 for dipslope fans; compared to the other two studied examples, there is greater similarity in fan gradient between the footwall slope and hangingwall dipslope sides.

The hypsometric curves of the studied catchments are depicted in Figure 3.11, with data relating to footwall slope catchments and hangingwall dipslope catchments combined from both ranges. In this example, catchments on the hangingwall dipslope side of the ranges show curves that take a convex-down shape more frequently than those for the footwall slope side; similarly to the previous examples, ongoing fault activity may be

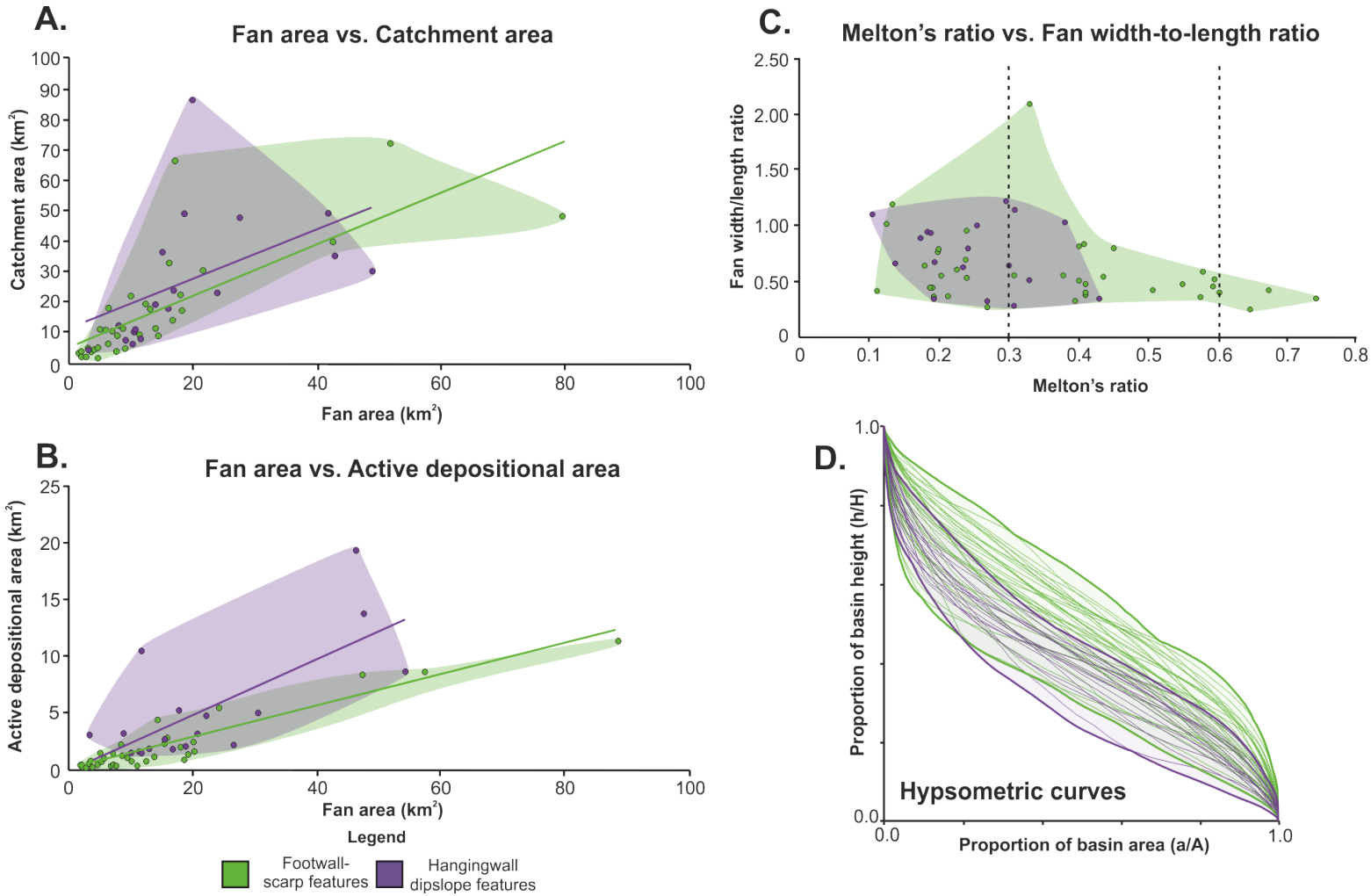

Figure 3.11 *Plots of select measured morphometric parameters, Melton's ratios and hypsometric curves from the Toiyabe and Toquima Ranges datasets. (A) Plot of fan area vs. catchment area. (B) Plot of fan area vs. active depositional area. (C) Plot of Melton's ratio vs. fan width-to-length ratios (for dashed line definition, see section 3.2.4., Melton's Ratio). (D) Plot of hypsometric curve variability for both footwall slope and hangingwall dipslope catchments. See text for details.*

contributing to the higher proportions of higher elevations for footwall slope catchments due to their proximity to the active fault, and increased catchment slope gradient. Importantly, the range of profiles is larger for the footwall slope catchments, indicating that there is variable ongoing fault slip activity affecting catchment elevations along-strike. This would be related to the presence of multiple normal border faults slipping at different rates.

Figure 3.11 shows a comparison of the Melton's ratio and of the width-to-length ratio of all the catchments studied. The distribution of Melton's ratios between footwall slope catchments (range: 0.11 to 0.74) and hangingwall dipslope catchments (range: 0.10 to 0.43) is more similar in this example (T-statistic = 3.33) than the Hammar or Barguzin examples (T-statistics of 10.73 and 8.75, respectively), indicating increasing similarity of depositional flow types occurring on the surfaces of each of the fan sets. The low ratio values indicate a tendency towards low viscosity flows (high water content compared to sediment content), represented by visible channels on the fan observed from satellite imagery.

3.6. Results of the comparison of fan surface areas and catchment areas

Figure 3.12 displays the relationships between all footwall slope catchment and fan pairs (green colour) and all hangingwall dipslope catchment and fan pairs (purple colour). Superimposed on the graph are boundaries for different values of ϕ, a term describing the ratio between catchment area and fan area (Allen & Densmore, 2000). Values for footwall slope pairs show a clear trend; ϕ values of 0.6 to 0.2 display a weak power law relationship (R = 0.34 between ϕ and log10[catchment area]) with catchment areas of 10 to 1,000 km^2 (where higher values of ϕ are associated with smaller catchments, and vice

versa). For hangingwall dipslope features, values of ϕ are more variable (1.0 to 0.03 for catchment areas of 10 to 1,000 km^2, respectively) and display a stronger power law relationship (R = 0.78 between ϕ and log10[catchment area]) than their footwall slope counterparts.

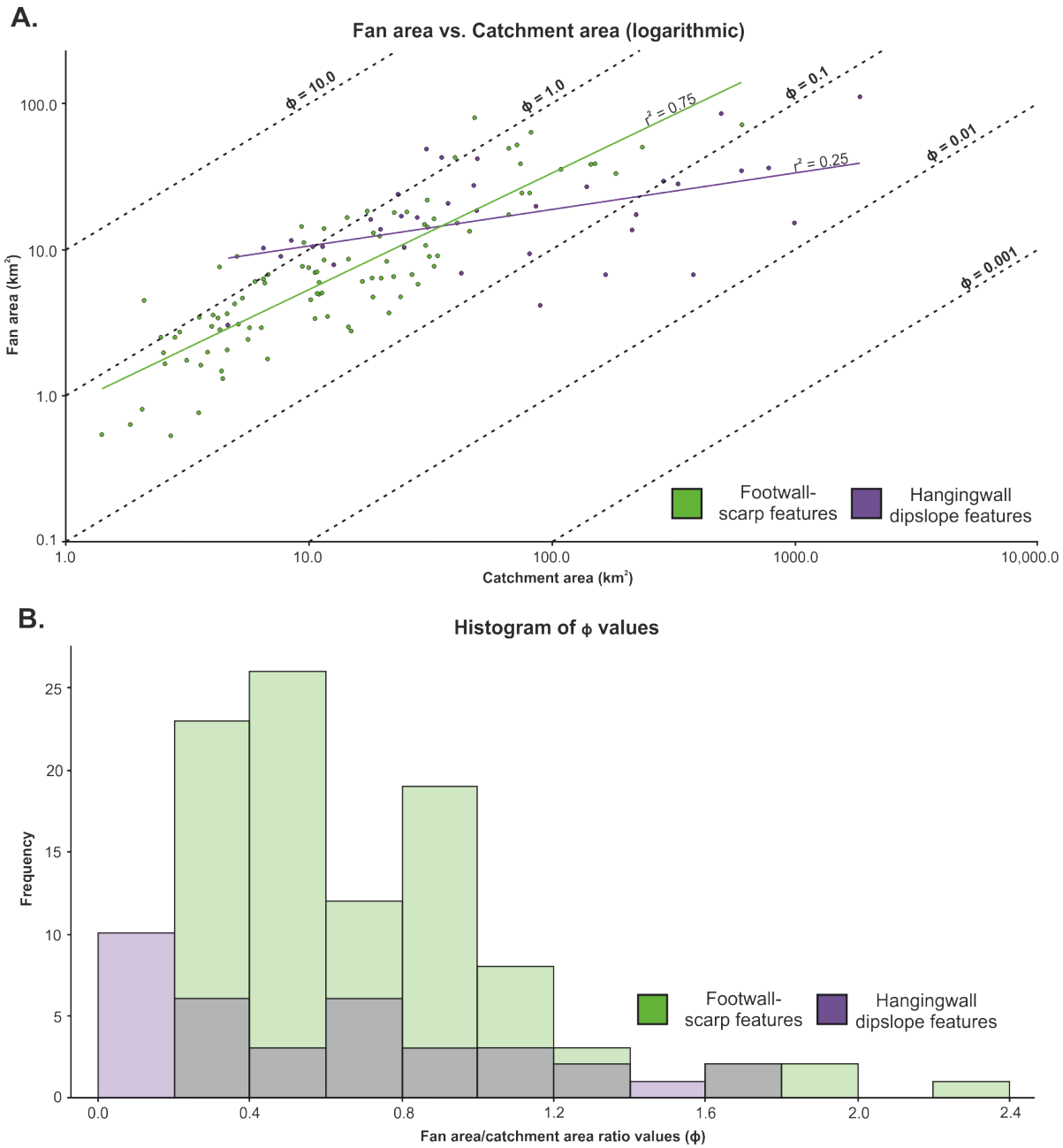

Figure 3.12 *(A) Plot of fan area vs. catchment area, on logarithmic axes, displaying key variations in ϕ between footwall slope and hangingwall dipslope features. (B) Histogram showing the distributions of ϕ values for footwall slope and hangingwall dipslope features. Bar colours are transparent.*

3.7. Discussion

3.7.1. Comparisons between different studied examples

The application of data derived from observations of modern-day environments to subsurface continental successions is dominated by discussions on the specific depositional environments involved, and their resultant deposits (cf. Hartley et al., 2010; Weissmann et al., 2010). In the case of alluvial-fan systems in rifts, the identification of similarities and differences across environments of this type in a variety of settings allows for: (i) the prediction of the lateral extent of alluvial-fan facies belts in the subsurface; (ii) the estimation of deposit thicknesses (and subsequently, fan body volumes) within different settings; and (iii) potential facies variations to be inferred from the basin structural style, bedrock lithologies and climate estimations, where detailed information on the sedimentary infill itself is lacking.

The most pertinent similarities between the examples of this study exist between the Barguzin Range (Baikal Rift) and Hammar Range (East African Rift) catchment and fan systems: (i) fans formed over the footwall slope are smaller on average than those on the hangingwall dipslope; (ii) a large difference in catchment size is observed between the hangingwall dipslope (larger) and footwall slope (smaller) sides of the range; (iii) power law relationships exist between overall alluvial fan areas and inferred areas of active deposition on the fan surface for both hangingwall dipslope and footwall slope fans; (iv) flows that tend to be dominated by streamflow on the hangingwall dipslope fans, and by debris flows on the footwall slope fans. Major differences between the two study areas are related to the absolute values of catchment and fan areas, active depositional areas, and fan surface gradients, as opposed to their relationships to each other. Typically, larger drainage catchments over the Hammar Range: (i) generate larger alluvial fans; (ii)

with a higher proportion of that area undergoing active deposition; and (iii) with a lower fan-surface gradient than their Barguzin Range counterparts.

The climate of each studied system varies significantly. The Hammar Range is dominantly cool, with temperatures and aridity increasing into the adjacent basins (Foerster et al, 2012). Seasonal rainfall provided by the ITCZ is up to 1,000 mm per year in the upper ranges but < 500 mm in adjacent basins (Segele & Lamb, 2005; Foerster et al., 2012); this leads to seasonal flooding of the Omo river and deposition on alluvial fan surfaces. The Baikal Rift experiences a high-latitude, persistently humid climate, with between 400-800 mm of rainfall per year (WMO 1981). These differences in climate are expected to have an influence on the differences outlined above with regards to fan area, active depositional area, and overall gradient. Similarly, these parameters will be affected by differences in bedrock lithology; a larger proportion of igneous basement lithotypes and metamorphosed sandstones in the Hammar Range (Davidson & Rex, 1980; Ebinger et al., 2000), compared to the metasediments and metamorphosed fine-grained material that form part of the Barguzin Range (Plyusnin et al., 2008; Jolivet et al., 2009), is likely to impact the dominant depositional flow types observed on the fan surfaces of both settings (Moscariello et al., 2002). The combination of increased humidity and fine-grained erodible material in the catchments of the Barguzin Range is a possible cause for the overall lower Melton's ratios for the footwall slope side (Figure 3.8), likely associated with an increase of stream-flow processes (Welsh & Davies, 2011). In Figure 3.5, the typically higher values of Melton's ratio for the Hammar Range may reflect the combined effect of increased climate seasonality and less erodible bedrock.

Although the Baikal Rift and EARS examples display many key similarities, the Basin & Range study is largely different from these; this example is characterised by limited

variation between dipslope and footwall slope features. This corresponds to a pronounced symmetry of the Toquima and Toiyabe systems along the tilt-block crest drainage divides, and by a linear correlation between catchment area and fan surface area (Figure 3.11). These major differences are unlikely to be solely caused by variations in bedrock lithology (indeed, granitic rocks dominate swathes of the Barguzin, Toquima and Toiyabe Ranges) or in climatic setting (since the Hammar Range experiences semi-arid climatic periods). Despite draining much smaller ranges, the fans of the Basin & Range case study are comparable in planform size to those seen in the EARS example, with footwall slope features reaching average fan areas of 12.02 km^2 and 8.08 km^2, respectively, and with dipslope fans averaging at 19.23 km^2 and 15.11 km^2, respectively. This is despite the significantly larger drainage catchments observed in hangingwall dipslope of the Hammar Range (157.32 km^2 average compared to 26.51 km^2). Here it is important to recognise the occlusion of the largest hangingwall dipslope drainage catchment of the Hammar Range from the dataset (see Figure 3.3); this catchment is likely influenced by either structural heterogeneities on the fault block generating a larger catchment, or it is the remnants of inherited drainage basins from pre-rift topography. By removing this data from the presented study (except where explicitly stated otherwise), average values are not 'dragged up' by anomalous datapoints directly influenced by external catchment-influencing processes. Had this catchment not formed, it is likely that the bordering downdip catchments (on the western side of the large catchment) would have larger areas, extending up to the drainage divide with the footwall slope catchments.

An important difference between the Hammar Range and Barguzin Range examples, and the Toiyabe and Toquima Range examples, is the spread of Melton's Ratios. For the Hammar and Barguzin Ranges, there is a clear split between the footwall slope and hangingwall dipslope catchments (see Figures 3.5 and 3.8) with lower viscosity flows

predicted on the hangingwall dipslope side. For the Basin and Range examples, the spread of Melton's ratios is similar between the footwall slope and hangingwall dipslope sides. This is likely due to the scale of the systems, and the resultant catchment slopes: the smaller (< 20 km scale width) tilt-block crests of the Basin and Range result in the drainage divide between the footwall slope and hangingwall dipslope catchments to be more central on the crest, leading to similar catchment slope angles, catchment areas, and catchment lengths. As a result, depositional processes resulting from these catchments are likely to be similar. Conversely, for larger tilt-block crests (> 20 km wide) the drainage divide is skewed heavily towards the footwall slope side. This increases the average slope of footwall slope catchments, decreasing the average slope of the opposite side and increasing hangingwall dipslope catchment areas and lengths. Increased maximum transport distance results in flows requiring higher water content in order to reach the fan surface, leading to the dominance of low viscosity flows causing deposition. As mentioned in section 3.3.1., the formation of rifts at different scales could be affected by the exploitation of pre-existing basement fabrics and structures by normal faulting, and the stretching factor of the lithosphere.

It is beneficial to consider here that data for the hangingwall dipslope fans of the Barguzin Range is measured from visible delta plains feeding into Lake Baikal. These features are sedimentologically and morphometrically different to the subaerial fans measured in the rest of the dataset. Importantly, their true extent (including delta front features) cannot be determined from the DEM and satellite imagery data used in this study, meaning that data recorded of their areas is likely significantly smaller than their true depositional surface areas. Despite this, their inclusion in Figure 3.12A does not produce any observable data outliers of the plotted hangingwall dipslope catchment and fan pairs. As fan deltas, their formation, size, and surface area will be affected by the base level control

introduced by Lake Baikal; base level fall may invoke increased catchment erosion and distal fan deposition, whereas base level rise may invoke the formation of radial surface channels and the sediment backfilling of part of the catchment chokepoint (Fernández et al., 1993). Overall, these data have been included in this study as the low sample size of these features (5) indicates that comparisons crossing all three study areas between hangingwall dipslope features are still valid.

3.7.2. Variations in the relationship between fan surface area and catchment size between hangingwall dipslope and footwall slope features

In each of these examples, larger catchments are seen on the hangingwall dipslope than over the footwall slope (Leeder & Jackson, 1993), but both sets of catchments feed alluvial fans of similar areas within adjacent subsiding basins. Previous studies (Allen & Hovius, 1998; Allen & Densmore, 2000) have identified a power law relationship between catchment area and fan surface area (the ratio of which is defined as ϕ); this ratio is influenced by active tectonism (Allen, 2008b) which affects each of the studied examples. The actively uplifting Barguzin and Hammar Ranges display distinct drainage divides at the height of the tilt-block crests, resulting in typically smaller footwall slope catchments (Leeder & Jackson, 1993) and subsequent headward expansion into catchments on the hangingwall dipslope side (Leeder & Jackson, 1993). Consequently, the ratio that describes the power-law relationship between catchment area and fan area will be different between the footwall slope and hangingwall dipslope sides of an uplifted block.

Allen & Densmore (2000) investigated the response of catchment-fan systems, established across a normal fault, to a variety of climatic and tectonic slip rate conditions. Typically, values for ϕ fall between 0.01 and 10.0 for actively uplifting areas (Figures 4 and 6, Allen & Densmore 2000) with high slip rates leading to lower ϕ values; the values for fan-catchment pairs in this study (Figure 3.12) predominantly range from 0.1-1.0.

This indicates high slip rates on associated faults, which is to be expected as all three areas are undergoing active extensional tectonism. As described in section 3.6., the power law relationships between measured fan and catchment areas vary between the footwall slope and hangingwall dipslope features. For footwall slope features, increasing catchment size has an increased effect on fan area, with a power law exponent of 0.797 indicating a near-linear relationship between the two parameters. Conversely, the relationship between hangingwall dipslope catchments and fans is less linear, with a power law exponent of 0.250. The observed difference is likely a combination of: (i) increased competition for space for catchment formation on the footwall slope side of a tilt-block crest, and for fan formation immediately in the adjacent basin, resulting in more similarly sized features and similar ϕ values; (ii) a gentler gradient on the dipslope side of the tilt-block crest, generating larger catchments which may not provide substantially more eroded sediment to their fans depending on the dominant flow processes transporting that sediment (reducing ϕ values); and (iii) the process of fan abandonment and progradation on the hangingwall dipslope side of large scale systems, resulting in new fan formation before the fan becomes too large (reducing ϕ values). Typically, in half-grabens, fan formation on the hangingwall dipslope side will be occurring in the down-dip direction, allowing this process to occur. For footwall slope fans, they are fighting to expand in an up-dip direction (in conjunction with competing with axial fluvial systems on the basin floor for depositional space).

In this study, half-graben structural morphologies and their associated tilt-block crests are considered. The tilt-block crests are asymmetrical, as a function of having a major basin bounding on only one side of the crest. For graben morphologies, their associated horsts are more symmetrical with major faults on both sides of the uplifted crest. This would subsequently lead to similar catchment area to associated fan area ratios on each

side of the horst, depending on any potential climatic and bedrock lithology variations (e.g., one side of the horst preferentially receiving rainfall).

3.7.3. Applications of the data in this study

The study of modern-day depositional environments for guiding interpretations and predictions of subsurface successions has been attempted in a variety of settings. This approach is particularly important for resource discovery and production allowing for increased confidence in interpretations and reducing associated risks (e.g. Johannessen et al., 2010).

The analyses outlined in this study provide a basis for attempting quantitative predictions of the extent of alluvial-fan deposits in early rift basin fills, typically within asymmetric half-graben basins. This in turn allows for inferences to be made about the distribution of hydrocarbon-reservoir facies (for example, fluvial sands) within the syn-rift sedimentary fill. Specifically, subsurface seismic datasets collected over an area undergoing exploration detail the structural setting and the shape of the sedimentary basin fill but are limited to interpretations of seismic attributes in determining lithological variations and facies (e.g. Strecker et al., 1999; Pigott et al., 2013). Predictive studies such as this can help lead to better decisions being made on subsequent data collection (wireline log data, core data) for detailing facies distributions within the basin. Wider knowledge of the scale of the system, the lithologies of the basement rocks, and the potential climatic setting of the studied time interval, can also lead to more confident predictions of the extent of alluvial-fan units based on the results of this research.

3.8. Conclusions

Four pairs of adjacent basins, from three separate present-day rift settings each possessing similar structural styles, have been analysed to demonstrate the effect of climate, bedrock lithology, and system scale on the deposition of alluvial fans either side of an uplifted tilt-block crest. Rotated fault blocks forming asymmetric half-grabens allow for the differences between the morphometrics of drainage catchments and subsequent alluvial fans deposited over footwall slopes and hangingwall dipslopes to be determined.

The following key outcomes are demonstrated: (i) in the studied settings, catchment area and fan surface area are linked in a power law relationship (given the ratio ϕ), similar to that described by previous studies (Whipple & Trayler, 1996; Guzzetti et al., 1997; Sorriso-Valvo et al., 1998; Allen & Densmore, 2000; Crosta & Frattini, 2004; Volker et al., 2007; Mirabella et al., 2018) with variable relationships between both the footwall slope and hangingwall dipslope sides of mountain ranges; (ii) there is a decrease in the ratio between fan area and catchment area (ϕ) with increasing catchment size which is much more pronounced on the hangingwall dipslope side of tilt-block crests, as described by power law exponents of 0.797 for footwall slope features, and 0.250 hangingwall dipslope features; (iii) as half-graben basins trend towards smaller sizes, alluvial fan bodies will dominate larger proportions of the basin floor depositional environments, with an increasing tendency toward higher-viscosity flows dominating deposition on both sides of a tilt-block crest.

Results of this study indicate the importance of considering system size in the prediction of facies distributions in syn-rift basin fill and underline the value of using satellite imagery analyses of present-day depositional environments to better understand the sedimentary evolution of rift basins.

4. Impact of a pre-existing transverse drainage system on active rift stratigraphy: An example from the Corinth Rift, Greece

4.1. Introduction

The onset of extensional faulting and associated rift-basin subsidence commonly trigger the accumulation of conglomerate and sandstone bodies, many of alluvial origin (Graham et al., 2001; Martins-Neto & Catuneanu, 2010; Zaghloul et al., 2010; Hemelsdaël et al., 2017; Teixeira et al., 2018). In the continental realm, conglomerate bodies that form the initial fill of evolving rift basins typically record sedimentation from alluvial fans, and commonly transition up-section into fluvio-lacustrine deposits (cf. Sinclair et al., 1994; Graham et al., 2001; Zaghloul et al., 2010; Turner, 2010). Newly uplifted footwalls are prone to denudation by erosional processes and source these earliest syn-rift deposits (Mack & Leeder, 1999). This denudation is most notable where the impact of antecedent drainage is relatively subdued, and either rifting does not crosscut major drainage networks or fluvial systems are diverted away from the rift zone, for example by growing rift shoulders (Gawthorpe and Leeder, 2000). Where extensional regimes evolve at a high angle relative to pre-existing drainage networks, coarse-grained sedimentary deposits typically accumulate downstream of the point where drainage networks are sourced over, or deflected around, the newly uplifted footwall (cf. Gupta et al., 1999; Hemelsdaël et al., 2017; Hopkins & Dawers, 2018). Although newly developed normal faults are known to act as buffers to drainage over the hangingwall dipslope (Leeder & Jackson, 1993; Gawthorpe & Leeder, 2000), limited research has been undertaken to date to compare subsequent deposition on the hangingwall dipslope to their footwall-sourced counterparts.

The Corinth rift, Greece (Figure 4.1), provides a location to study the impact of antecedent drainage on deposition over the hangingwall dipslope during the onset of rifting. Alluvial-fan deposits dominated by coarse grained, clast- to matrix-supported conglomeratic bodies are exposed in cliff faces – notably along valley sides – as part of an uplifted footwall block on the northern coast of the Peloponnese (Ford et al., 2013; Ford et al., 2016; Gawthorpe et al., 2018). Exposures of sedimentary successions juxtaposed against normal faults allows for the detailed examination of sedimentary processes in a single fault block during the early syn-rift, and the impact of intra-basinal faulting on the prevalence of "overfilled" and "underfilled" depositional conditions (Gawthorpe & Leeder, 2000).

The aim of this study is to establish a depositional model to account for the generation of the early syn-rift conglomerate units deposited from antecedent drainage flowing over a hangingwall dipslope, and to describe the sedimentological variations that occur across the newly formed depocentre. Specific objectives of this research are as follows: (i) to map lithofacies variations of an alluvial fan sourced over the hangingwall dipslope of an evolving rift basin through space and time; (ii) to determine the processes by which sediment was transported and deposited by an alluvial fan present in the rift basin; (iii) to show how the alluvial-fan system responded to fault block rotation and local uplifted footwall blocks; and (iv) to propose palaeogeographic models that describe the depositional processes occurring in the basin from rift initiation to the present day.

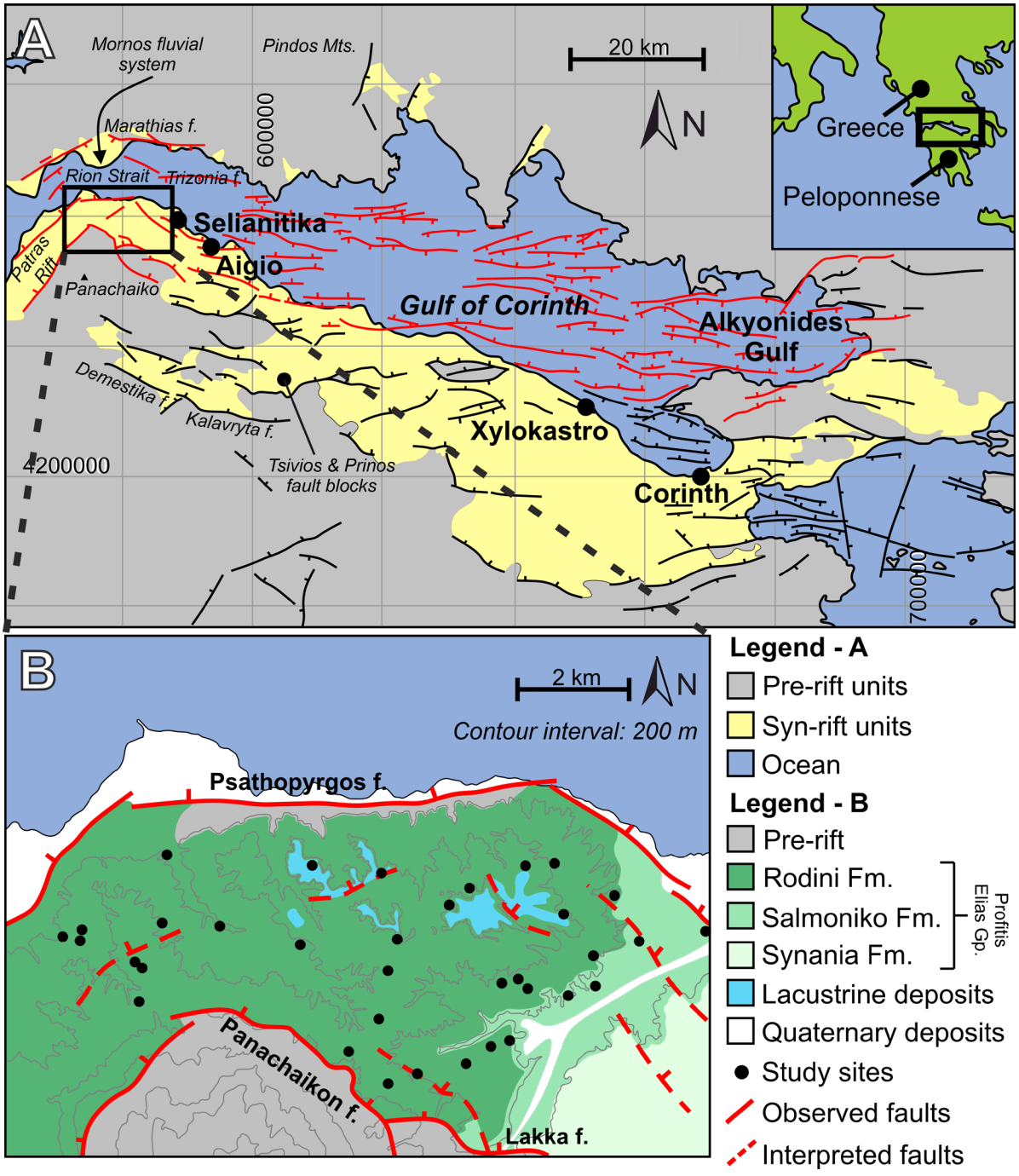

Figure 4.1 *Map of the study area and the Gulf of Corinth rift, adapted from Gawthorpe et al. (2018). (A) Map of the entire Corinth Rift detailing distributions of syn-rift sediments and pre-rift basement. Active faults and inactive faults are represented in red and black colours respectively. Fault mapping is defined from Rohais et al. (2007a), Ford et al. (2013, 2016), Gawthorpe et al., (2018). (B) Detailed map of the study area for this chapter showing the mapped extent of the Rodini, Salmoniko and Synania Fms., and study sites used in this research.*

These analyses are novel, significant and of broad appeal because they allow for the sedimentological history of a developing rift basin to be reconstructed in detail. The outcome of this study demonstrates the following key insights: (i) the benefits of underpinning tectonostratigraphic analyses with detailed sedimentological observations; (ii) the importance of antecedent drainage direction in the prediction of the distributions of alluvial facies and architectures in a single extensionally faulted block; (iii) the influence of subsequent intra-basinal faulting in the switching between high sediment supply to accommodation ratios, and low sediment supply to accommodation ratios (i.e. "overfilled" and "underfilled" scenarios).

4.2. Geological setting

4.2.1. The Gulf of Corinth

The Gulf of Corinth is an area of active extension between the Peloponnese and mainland Greece. It formed as a result of extension associated with the subduction of the African tectonic plate underneath the Aegean Sea plate (forming the Hellenic Arc) to the west and south of the gulf (Doutsos et al., 1988; Bell et al., 2009). Prior to the onset of extension, a NNW-SSE trending fold-and-thrust belt, the Pindos thrust sheet, formed during the Late Eocene (Skourlis & Doutsos, 2003). This feature now forms the pre-rift basement, and the associated tectonic evolution originally separated the pre-existing drainage into a series of north-south orientated catchments that drained predominantly towards the north (Seger & Alexander, 1993; Zelilidis, 2000). The present-day Mornos catchment, situated at the western edge of the gulf (see Figure 4.1A), has persistently flowed from north to south as a result of local gradient variations. Each catchment eroded the same Pindos thrust sheet, which is composed of Mesozoic carbonates and sandy clastic turbidites

deposited on a passive margin and orogenic wedge (Degnan & Robertson, 1998). Rifting commenced in the Pliocene (Ford et al., 2016; Nixon et al., 2016) with the principal trend of the developing rift striking east-west, at high angle to the direction of antecedent drainage (Figure 4.1; Collier & Gawthorpe, 1995). Rifting has continued to the present day and covers an area of approximately 105 km x 30 km (Figure 4.1). Current extension rates vary from 10 to 16 mm/yr (Nixon et al., 2016), with higher rates in the west of the rift (Ford et al., 2016). Initial rifting led to the development of northward-dipping extensional faults on the northern coast of the Peloponnese. Extension has progressively migrated to the north, with more recent faulting in the last 400 kyr (Gawthorpe et al., 2018) having occurred in the hangingwalls of older structures to form the morphology of the present-day Gulf (Ori, 1989; Ford et al., 2013). As a result, Plio-Pleistocene syn-rift successions up to 3 km thick, and of mixed continental and marine origin, are now exposed onshore as uplifted footwalls (Gawthorpe et al., 2018). Offshore in the present-day Gulf, sedimentary successions up to 2.5 km thick have accumulated as the Late Pleistocene and Holocene fill of rift basins. Both sets of successions record sedimentation in a variety of environmental settings, including continental, shallow-marine and deep marine environments (Nixon et al., 2016). Due to the relatively short extensional history of the rift and the lack of subsequent overprinting by other structural regimes, this area is especially well suited to the study of both onshore and offshore syn-rift sedimentation in settings adjacent to active extensional faults (Bell et al., 2009).

Syn-rift sedimentation occurred in two distinct phases: the first from the Pliocene to the Middle Pleistocene (400 ka), and the second from the Middle Pleistocene to the Present (Esu & Gerotti, 2015). This study focuses on the nature of sedimentation in the latter part of the first phase, during which depocentres hosted deep-water lacustrine systems with water depths of 300-600 m, indicated by deltaic foreset stratal packages that are several

hundred metres thick (Gawthorpe et al., 2018) in the east (from the Alkonyides Gulf extending to the town of Selianitika; Figure 4.1). These deltaic deposits pass into continental environments to the west (west of Selianitika) (Ford et al., 2013; Ford et al., 2016; Gawthorpe et al., 2018). The sedimentology of these palaeoenvironmental settings provides a record of both axially derived deposits that fed into Lake Corinth to the east (Ford et al., 2016; Gawthorpe et al., 2018), and transverse drainage systems that resulted in deposition of sediment over relic uplifted footwalls (Collier & Dart, 1991).

As extension progressively migrated northward, the oldest stratigraphic intervals recording syn-rift sedimentation were progressively uplifted into the footwalls of younger faults, thereby resulting in the exhumation and exposure of older sedimentary successions of deep-water, deltaic and alluvial origin – from east to west, respectively (Dart et al., 1994; Ford et al., 2016). Large, Gilbert-type deltaic deposits are present across exposed cliff sections from Xylokastro to Aigio (Figure 4.1; Collier & Dart, 1991; Dart et al., 1994). These fan deltas were sourced from feeder valleys that cut down through uplifting footwalls, or which exploited topographic lows between fault tips (Leeder & Jackson, 1993). Presently, over 1000 m of continental syn-rift deposits are exposed in a series of cliff faces up to 600-m high and hills in the footwall of the Psathopyrgos fault, directly west of Aigio (Figure 4.1) (Bell et al., 2009).

4.2.2. The Profitis Elias Group

The early-rift deposits at the northernmost tip of the Peloponnese between Aigio and the Patras Rift (see Figure 4.1A for location) are dominantly represented by the older Profitis Elias Gp. and the younger Galada Gp., both of which are well preserved in the Panachaikon fault block, a 7-8 km-wide unit between the Rion Strait and the Panachaiko mountain, where these two groups attain a combined thickness of 1.4 km (Palyvos et al., 2007; Ford

et al., 2016). The Profitis Elias Gp. contains three formations of similar age: the Rodini Formation (west), the Salmoniko Formation and the Synania Formation (east), which are interpreted by Ford et al. (2016) to represent alluvial fan, braided stream and lacustrine environments, respectively. These formations record a progressive fining in mean sediment calibre from west to east (Palyvos et al., 2007, Palyvos et al., 2010). The main focus of this study is the Rodini Fm., deposited furthest to the west on the northern tip of the Peloponnese.

Together, the three formations represent the major proportion of the Profitis Elias massif and attain a preserved (post-uplift) thickness of up to 600 m (Esu & Gerotti, 2015), with original depositional thickness estimated at over 1000 m (Ford et al., 2016). Multiple wadis expose the formations, where erosion over the last 400 kyr has left a reduced thickness (~10 m) of sandy siltstone of the Synania Fm. at the highest points of the massif, overlying large cliff faces that are 50 to 120 m high and which expose sections of the underlying Rodini Fm.

The Rodini Formation has not been the focus of prior detailed study; the majority of prior research efforts in the Gulf of Corinth region have focussed on the eastern parts of the rift (see Collier & Dart, 1991; Collier & Gawthorpe, 1995; Rohais et al., 2007). Previous studies of the Rodini Fm. are based on limited and fundamental observations of lithology over the area (see Doutsos et al., 1988; Esu & Gerotti, 2015; Ford et al., 2016), where the Rodini Fm. is present in the form of reddish to grey conglomerates dominated by cobbles and boulders. These deposits have previously been interpreted as the depositional record of an alluvial or fluvial system sourced from the north (Doutsos et al., 1988; Gawthorpe et al., 2018). However, this general interpretation needs to be refined through the development of a detailed palaeoenvironmental reconstruction based on analysis of

lithofacies, sedimentary architectures, and on analysis of the spatial and temporal distribution of palaeocurrent data. These interpretations are the focus of this study, which is based on a detailed field-acquired data set.

4.3. Data and methods

4.3.1. Lithological mapping

Mapping was undertaken to document lithological variations across the study area, based on the three main rock types present: conglomerate, sandstone and siltstone. In addition to regional mapping, 37 sites were selected for detailed study; for these sites proportions of lithologies were recorded as percentages. Two hundred dip and strike readings (from 20 of the 37 sites), ranging from 04-40° dip angle, were separated into three groups of equal size based on their relative elevations and their magnitudes. This allowed the relative chronostratigraphic positions of the different sites to be determined; in conjunction with lithological data, a tectonostratigraphic framework was then established (see section 4.3.3. for detail).

For conglomerate lithologies, the percentage volume of both matrix and clasts was recorded to map subtle variations in lithofacies across the study area. The matrix of conglomerate lithofacies is defined as grains from clay to medium-sand size (similar to the procedures implemented by Steel & Thompson 1983; Sohn et al., 1999; Kim & Lowe, 2004; Puy-Alquiza et al., 2017, in their studies of alluvial deposits). The maximum grain size of the matrix, and minimum clast size of the overall deposit, define a bimodality in grainsize.

4.3.2. Vertical profiles

Twenty of the 37 locations were chosen for detailed sedimentological analysis based on the description of vertical profiles at the decimetre scale (Figure 4.2). Special attention was dedicated to detailing clast fabric and texture variations in conglomeratic bodies by tabulating individual clast features. Lithofacies were tabulated recording their thicknesses and key sedimentological features (e.g., grading, sedimentary structures, clast-to-matrix proportions). Profiles were placed in their approximate chronostratigraphic positions through extrapolation by combining observations of tectonic dip and topographic data (see below). There is no biostratigraphic control within the Rodini Fm., and there is no clear opportunity to establish an event stratigraphy, for example via radiometric dating. In total, twenty vertical profiles with a cumulative thickness of 250 m were recorded in detail.

These data were supplemented by an additional six large-scale log profiles recorded to capture larger-scale stratigraphic variations in lithology, through 533 m of the approximately 600-m-thick formation. These vertical profiles enabled the construction of a tectonostratigraphic framework for the area by combining them with data used for lithological mapping and structural data, as outlined above.

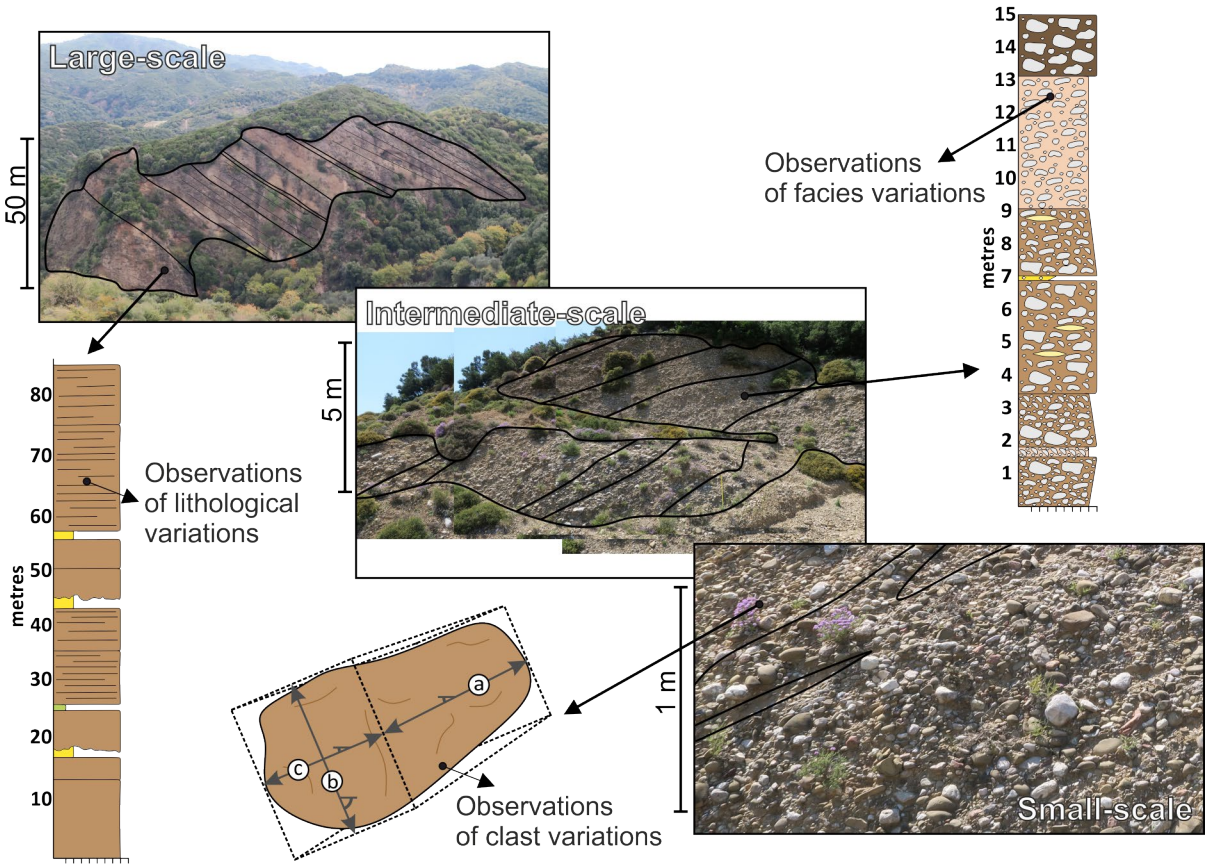

Figure 4.2 *Images detailing data collection methods at 3 different scales (tens of metres, metres, and centimetre scale). Integration of datasets in this study allows for the underpinning of larger scale regional variations by higher-resolution facies and individual clast analyses (where 'a', 'b' and 'c' represent clast long, intermediate, and short axes respectively).*

4.3.3. Tectonostratigraphy definitions

Establishment of the chronostratigraphy of the studied succession is problematic due to a lack of biostratigraphic control or of datable ash deposits similar to those found in syn-rift sediments to the east (Gawthorpe et al., 2018). To develop a well-defined tectonostratigraphy for the study area, bedding dip and strike data and topographic elevation were combined to determine the relative ages of deposits at different localities across the study area, as a function of varying amounts of rift-induced differential tilting (Figure 4.3). Depositional gradients are likely to have been low, given the absence of high-angle inclined foresets. Small-scale intra-basinal faulting is also assumed to have minimal

effect, with the few observed post-depositional faults experiencing throws of <5 m. This approach has allowed a tentative chronology of the deposits and has enabled establishment of a tectonostratigraphy with which to support interpretations of depositional environment, and of the influence of active faulting on palaeogeography.

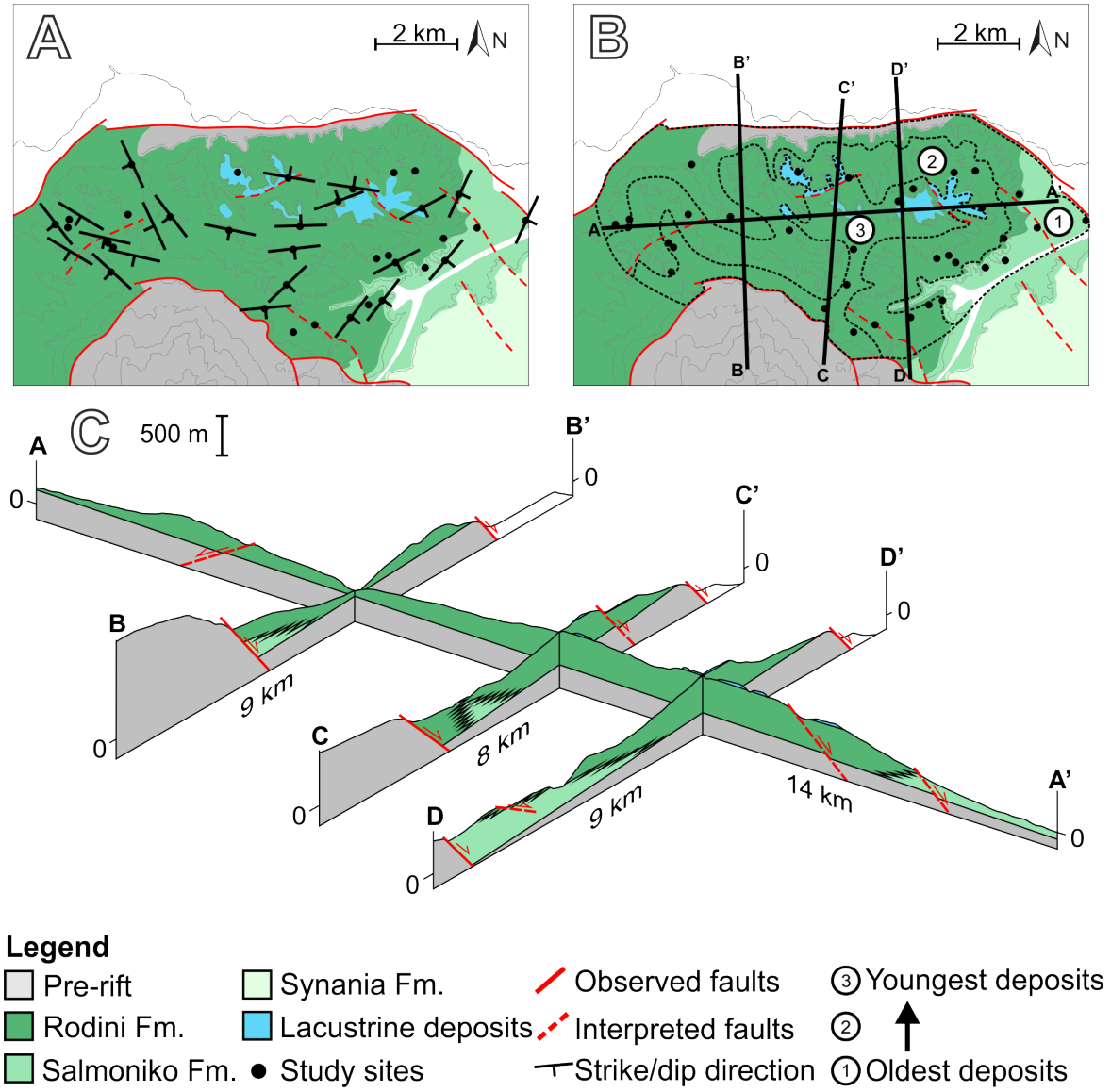

Figure 4.3 *(A) Study area map displaying regional variations in stratigraphic dip and dip direction. Note the approximate radial pattern of dips away from the north of the study area. (B) Approximate areas of time slices through the study area between relatively older, middle-aged and younger stratigraphy. Lines of section A-A', B-B', C-C', D-D' are located. (C) Fence diagram of structural cross sections through study area.*

The initiation of sediment accumulation is considered to have commenced in response to the onset of movement on the Panachaikon fault at 2.2 – 1.8 Ma (Figure 4.4) (Gawthorpe et al., 2018). For this study, the rate of sediment supply is assumed constant, leading to the definitions of the three stratigraphic intervals outlined in this study. This is necessary in order to define approximate times of deposition (relative to other recorded deposits in the Rodini Fm.) for each recorded sedimentary succession (see section 4.4.3.).

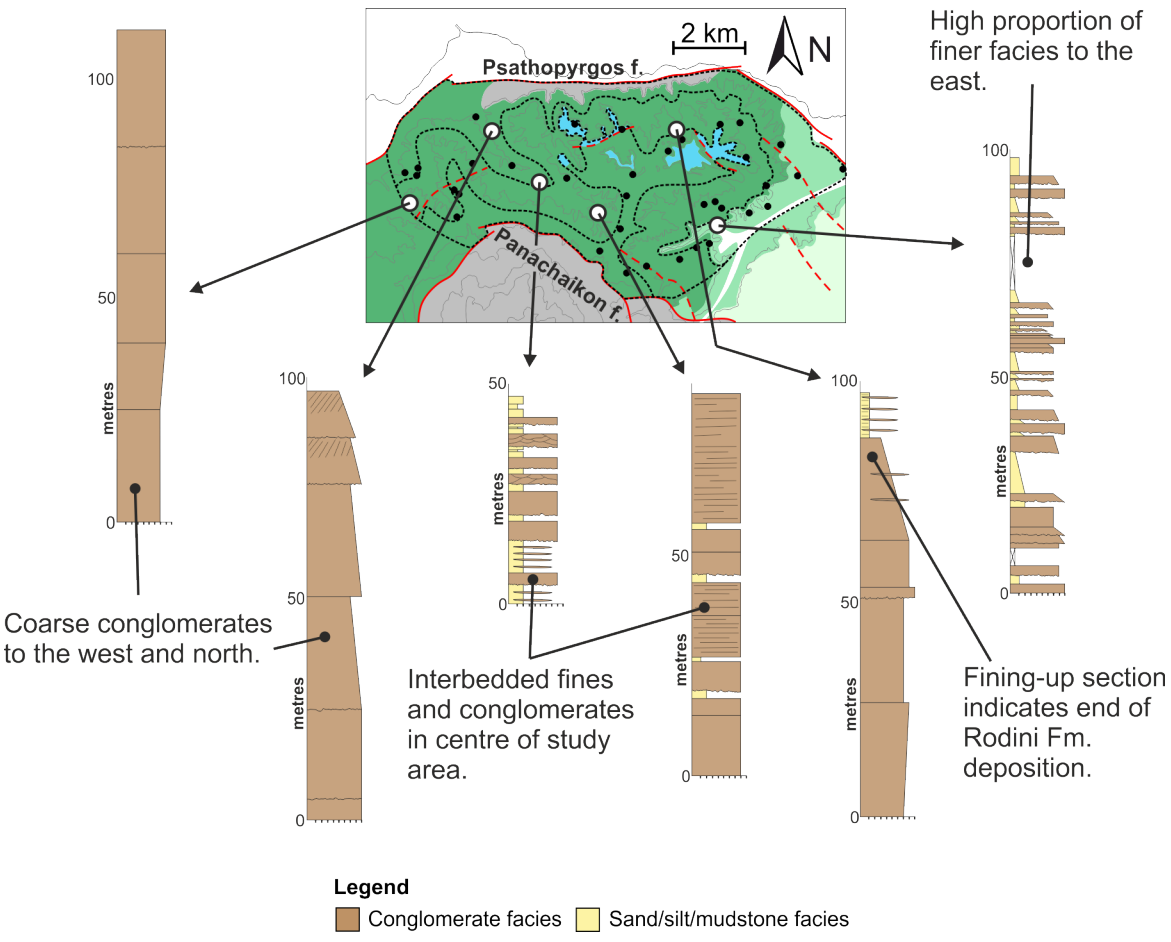

Figure 4.4 *Regional logs detailing lithological variations over the study area. Note the increase of conglomeratic facies both up-section (towards the end of the deposition of the Rodini Fm.) and towards the west and north.*

4.3.4. Clast fabric and texture description

At each of the 20 sites where vertical profiles were recorded, conglomeratic facies were subject to detailed clast-fabric and texture analysis. At each site, up to two facies were chosen for clast measurements, and a square grid of 1 m^2 in area was placed on the outcrop surface (see Chapter 5, section 5.3.2. for more detail). The 50 largest clasts within that square were characterised with respect to three qualitative attributes (composition, shape, roundness) and ten quantitative features (length, plunge and azimuth of three axes, from which palaeocurrent direction was inferred based on identification of types of clast imbrication). These features were later corrected for bedding strike and dip. This approach was taken to randomise the clasts chosen for measurement, to obtain data in a systematic fashion, and to collect data for future studies on clast metrics. In total, 1,531 clasts were measured for these features from 10 conglomerate facies types; in addition, 1,001 palaeocurrent indicators were derived from patterns of clast imbrication. In this chapter, focus is given to clast axis orientation data, composition data, and palaeocurrent data for the purpose of determining flow processes, sediment input sources and sediment flow directions over the basin. From clast composition alone, the detailed provenance cannot be determined given the presence of similar lithologies in the basement rocks on both sides of the basin. However, where information on clast composition is combined with clast-fabric analysis, an indication of palaeotransport direction (as indicated by clast imbrication) can be used to deduce the likely provenance for the basin-filling conglomerates.

4.4. Results

4.4.1. Lithofacies

Fifteen distinct lithofacies types are identified within the Rodini Fm: ten types of conglomerate and five types of sandstone and siltstone (Table 4.1; Figure 4.5). In the conglomerate facies, clast composition is dominated by a mixture of well-sorted sandstone, well-cemented limestone, and coloured cherts. All clasts were apparently sourced from basement units (dominated by limestone and flysch deposits; Skourlis & Doutsos, 2003) uplifted in nearby footwalls. The distribution of lithofacies and architectural elements through the formation is represented by twenty vertical profiles (Figures 4.6A, 4.6B, 4.6C) taken from across the study area (Figure 4.1).

Code	Lithofacies	Description	Interpretation
B-wtm	Well-sorted boulder conglomerate	Clearly bedded, clast-supported (90-100%), with granule matrix. Tightly packed with sub-rounded to sub-angular clasts up to 50 cm in diameter. Form massive beds with erosional bases.	Conglomeratic debris-flow deposits proximal to the sediment source at the apex of an alluvial fan. More consistent, high-energy flows represented by tight packing of boulders and their large sizes (Puy-Alquiza et al., 2017, Teixeira et al., 2018).
B-rlf	Moderately-sorted normally graded boulder conglomerate	Clearly bedded, clast-supported (80-100%), with medium-coarse sand matrix. Loosely packed with rounded-sub-rounded clasts up to 30 cm in diameter. Normally grade to granule-pebble clasts and have erosive bases.	Bedload stream deposits in the upper-fan to mid-fan transition, close to fan apex, with discrete units formed by stream avulsions Fining upward grain-size trend and imbrication indicate turbulent nature of flow. (Moscariello et al., 2002; Reitz & Jerolmack, 2012).
B-plm	Poorly-sorted boulder conglomerate	Clearly bedded, clast-supported (80-90%), with medium sand-granule matrix. Loosely packed with sub-rounded to sub-angular clasts up to 50 cm in diameter. Form massive beds, may have erosive bases.	Non-cohesive debris flow deposits in the mid-fan represented by an increased matrix proportion and lack of sorting, indicating single event deposits. Further supported by erosive bases to units. (Murcia et al., 2008, Colombera & Bersezio, 2011).
B-pll	Poorly-sorted boulder conglomerate with sand lenses	Crudely bedded, clast-supported (70-90%) with medium-coarse sand matrix. Loosely packed with rounded to sub-angular clasts up to 30 cm in diameter. Beds contain medium sand lenses.	Non-cohesive debris flow deposits close to the fan toe. Higher matrix proportions and sand lenses represent a decrease in energy, either in distal locations or as trails behind transported clasts. (Kim et al., 2009; Shukla, 2009).

B-plc	Poorly-sorted boulder conglomerate with strong cement	Crudely bedded, clast-supported (70-90%) with well cemented medium sand-granule matrix. Loosely packed with sub-rounded to sub-angular clasts up to 30 cm in diameter. Form massive beds.	Cemented debris flow deposits (see B-plm interpretation), predicted to have experienced dissolution of carbonate clasts and subsequent reprecipitation, common in other areas of the Gulf of Corinth. (Backert et al., 2010; Gawthorpe et al., 2017).
B-ple	Poorly-sorted, polymodal boulder conglomerate	Crudely bedded, clast-supported (90%) with medium sand-granule matrix. Loosely packed with rounded to sub-angular clasts up to 30 cm in diameter. Contains coarser and finer discontinuous lenses in each unit.	Streamflow deposits represented by highly variable flows leading to the interbedding of finer and coarser clast-supported, clean conglomerate lenses, forming low-relief bars. (Karpeta, 1993; Kim et al., 2009).
C-rll	Moderately-sorted cobble conglomerate	Clearly bedded, clast supported (80-90%) with medium-coarse sand matrix. Loosely packed with rounded-sub-angular clasts up to 15 cm in diameter. Form massive beds. Some discontinuous sand lenses.	Debris-flow deposits close to the fan toes, finer grain sizes represent lower energy compared to B-pll. Sand lenses represent poorly developed flood dune bar deposits. (Lindsey et al., 2005; Chakraborty & Ghosh, 2010).
C-pth	Poorly-sorted, horizontally stratified cobble conglomerate	Crudely bedded, clast-supported (80-90%) with medium-coarse sand matrix. Tightly packed with rounded to sub-angular clasts up to 15 cm in diameter. Beds are horizontally stratified.	Cobble bedload sheet deposits in the upper-fan to mid-fan transition as a result of turbulent flash flood flows, creating horizontal stratification. (Moscariello et al., 2002; Teixeira et al., 2018).
P-wtm	Well-sorted pebble conglomerate	Clearly bedded, clast-supported (90-100%) with medium sand matrix. Tightly packed with sub-rounded clasts up to 5 cm in diameter. Form massive beds of texturally mature clasts.	Relatively low-energy streamflow bedload deposits. Flow is consistent leading to clean, well-sorted fine grained conglomerates. Deposited away from large fan toe, or more proximally on a smaller alluvial fan. (Steel & Thompson, 1983; Ford et al., 2016).

G-wtm	Well-sorted granule conglomerate	Clearly bedded, clast-supported (90-100%) with medium sand matrix. Tightly packed with sub-rounded clasts up to 1 cm in diameter. Form massive beds of texturally mature clasts.	Relatively very low energy streamflow bedload deposits. Flows wash away silt and clay particulates, leading to clean, very well-sorted fine-grained conglomerates. (Steel & Thompson, 1983; Ford et al., 2016).
S-l	Massive silty sandstone with granule-cobble lenses	Crudely bedded, poorly-sorted silt to coarse grade sand. Intermittent well-sorted granule to cobble grade lenses throughout.	Rapid finer-grained sediment dumping from suspension in flows, with periods of high energy allowing upper plane-bed conglomerate deposition. (Lindsey et al., 2005; Franke et al., 2015).
S-s	Massive silty sandstone with intermittent clasts	Crudely bedded, poorly-sorted silt to coarse grade sand. Single clasts present randomly throughout massive beds, up to 2 cm in diameter.	Deposited in the most distal portions of a hyperconcentrated flow, where energy can only sustain rare small clasts. Rapid deposition from suspension. (Wells, 1984, Franke et al., 2015)
S-h	Silty sandstone with horizontal laminations	Crudely bedded, poorly-sorted silt to coarse grade sand. Horizontally laminated picking out fine grained sections, laminations typically 3-5 mm apart and increase in frequency up-section.	Waning debris flows or streamflow deposit laminated sands and silts away from main channel flow locations. (Allen, 1982; Colombera & Bersezio, 2011).
S-sh	Massive silty sandstone with shell fragments	Crudely bedded, poorly-sorted silt to coarse grade sand. Contain shell fragments up to 0.5-1 cm diameter that are present randomly or in thin < 15 cm laterally discontinuous lenses.	Low-moderate energy shallow lacustrine deposits where fragile shells are broken up by small amounts of current and wave action. (Alvarez-Zarikian et al., 2008; Ford et al., 2016).

F	Fine grained mudstone	Clearly bedded, well sorted clay-mud grade unit. Light to dark grey, brown, and cream colours present. Highly fissile with no structure, form laterally continuous beds up to 10 cm thick.	Overbank palaeosol development representing areas away from the influence of floods and channel processes. (Lindsey et al., 2005; Franke et al., 2015).

Table 4.1 *Descriptions and interpretations of studied lithofacies. Facies codes are based on the following pattern; (largest grain size; B, C, P, G, S, F) – (sorting; w – well, r – moderate, p – poor)(clast packing; t – tight, l – loose)(structures; m – massive, f – fining up, l – sand lenses, c – cement, e – conglom. lenses, h – horizontal stratification).*

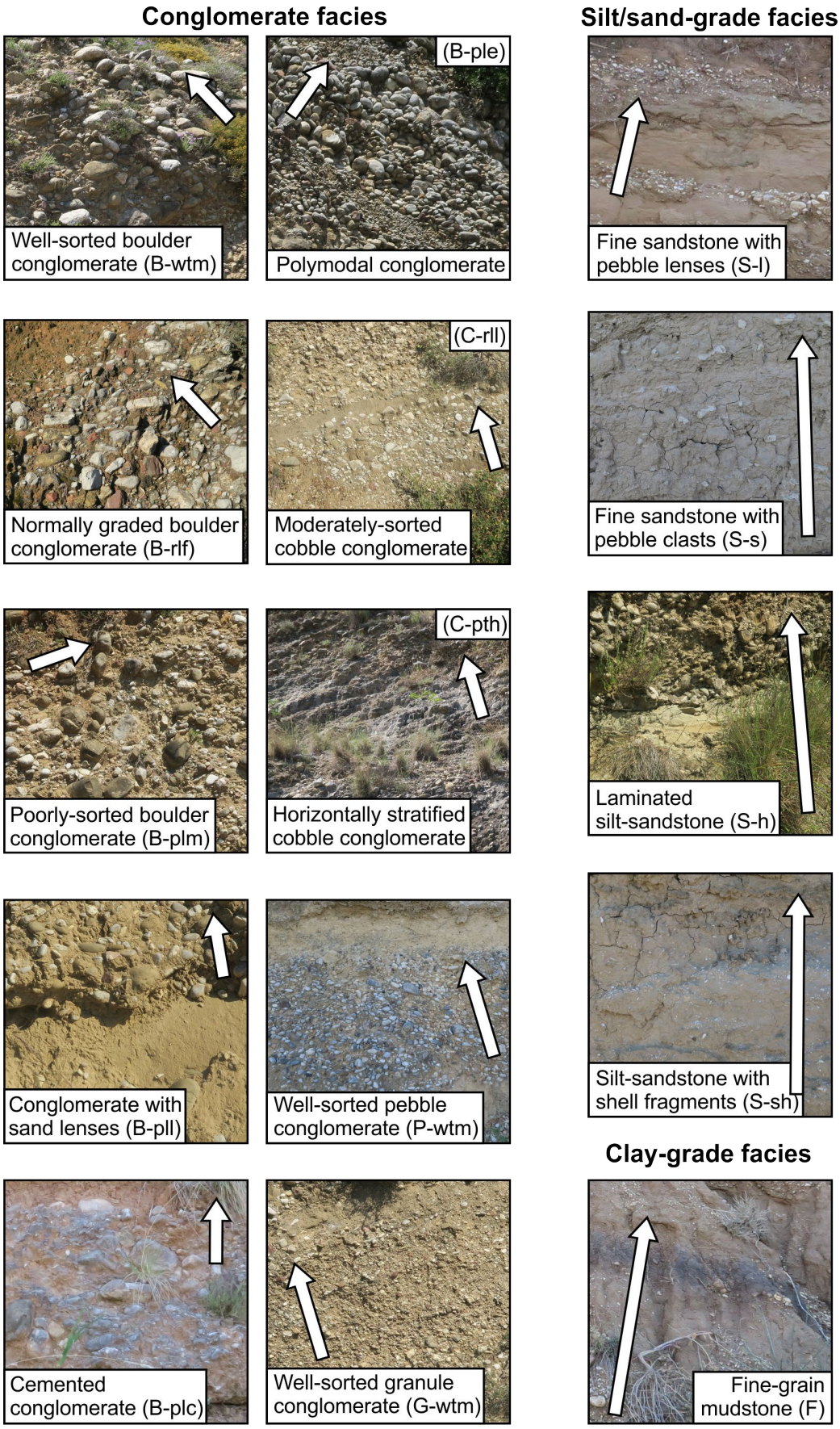

Figure 4.5 *Outcrop images of each of the 15 facies detailed in Table 4.1. Arrows represent 1 m scale and indicate younging direction.*

Figure 4.6A
Stratigraphic interval 1: Rodini Fm.

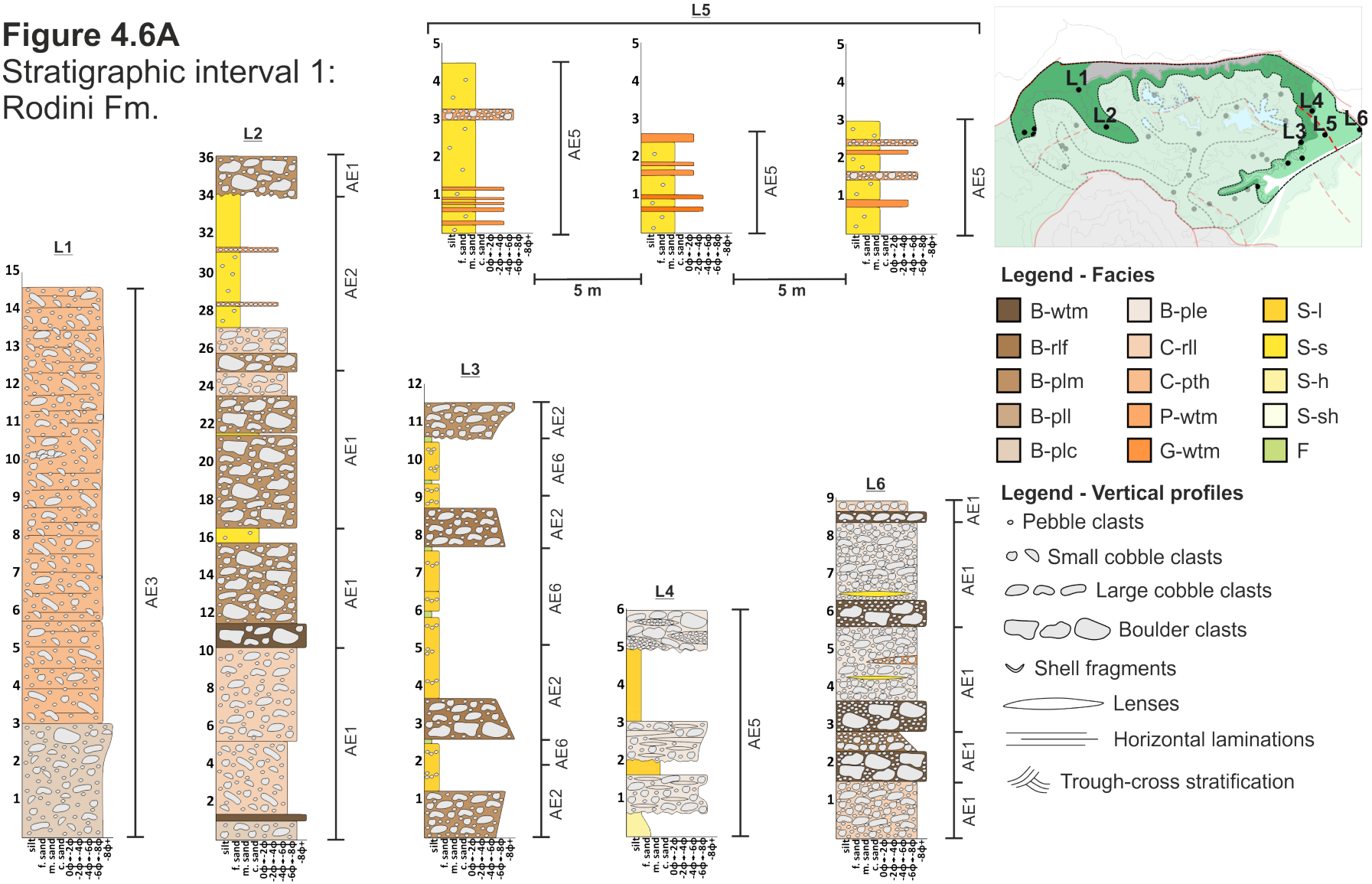

Figure 4.6B
Stratigraphic interval 2:
Rodini Fm.

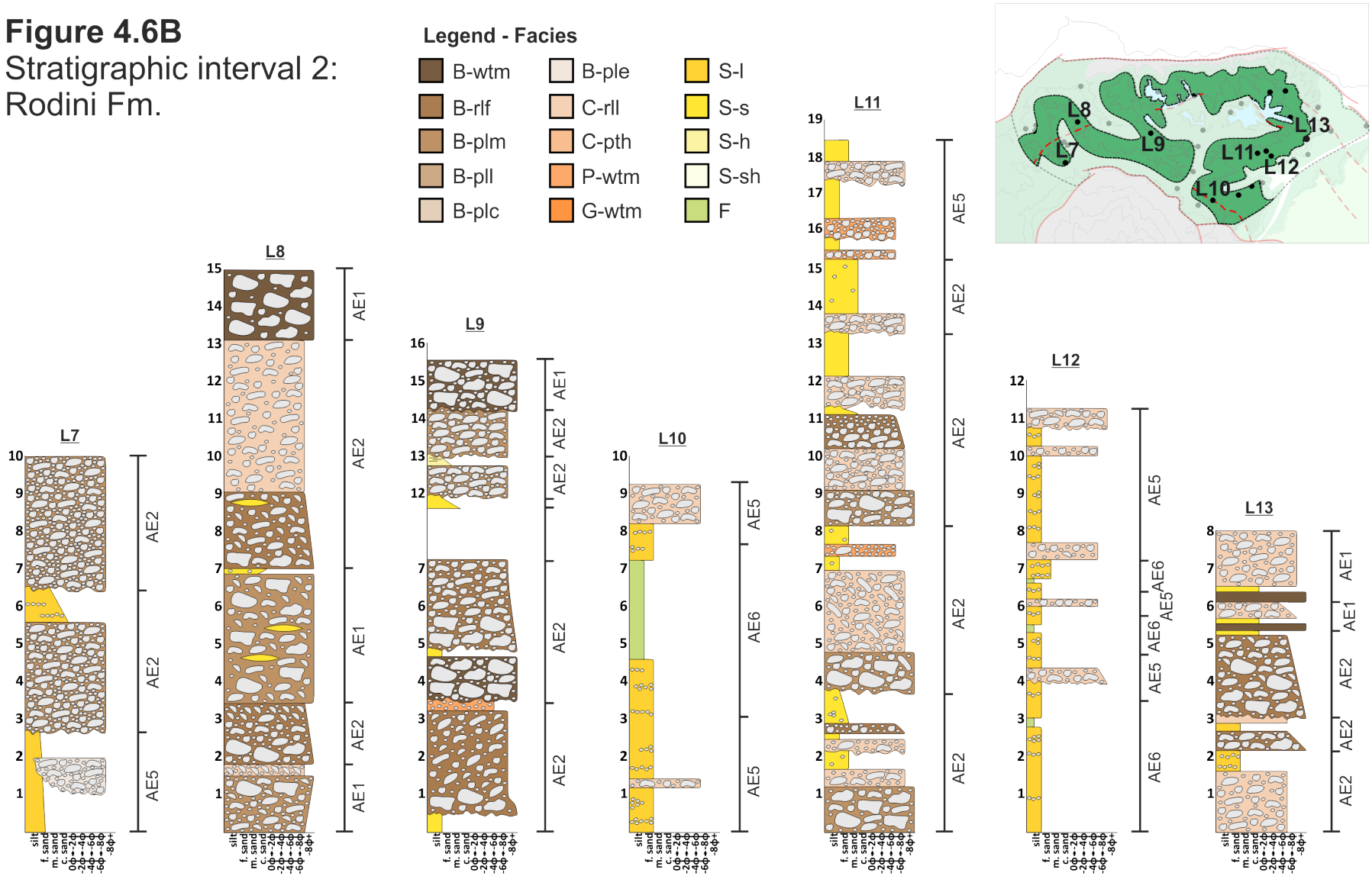

Figure 4.6C
Stratigraphic interval 3:
Rodini Fm. & Lacustrine Sands

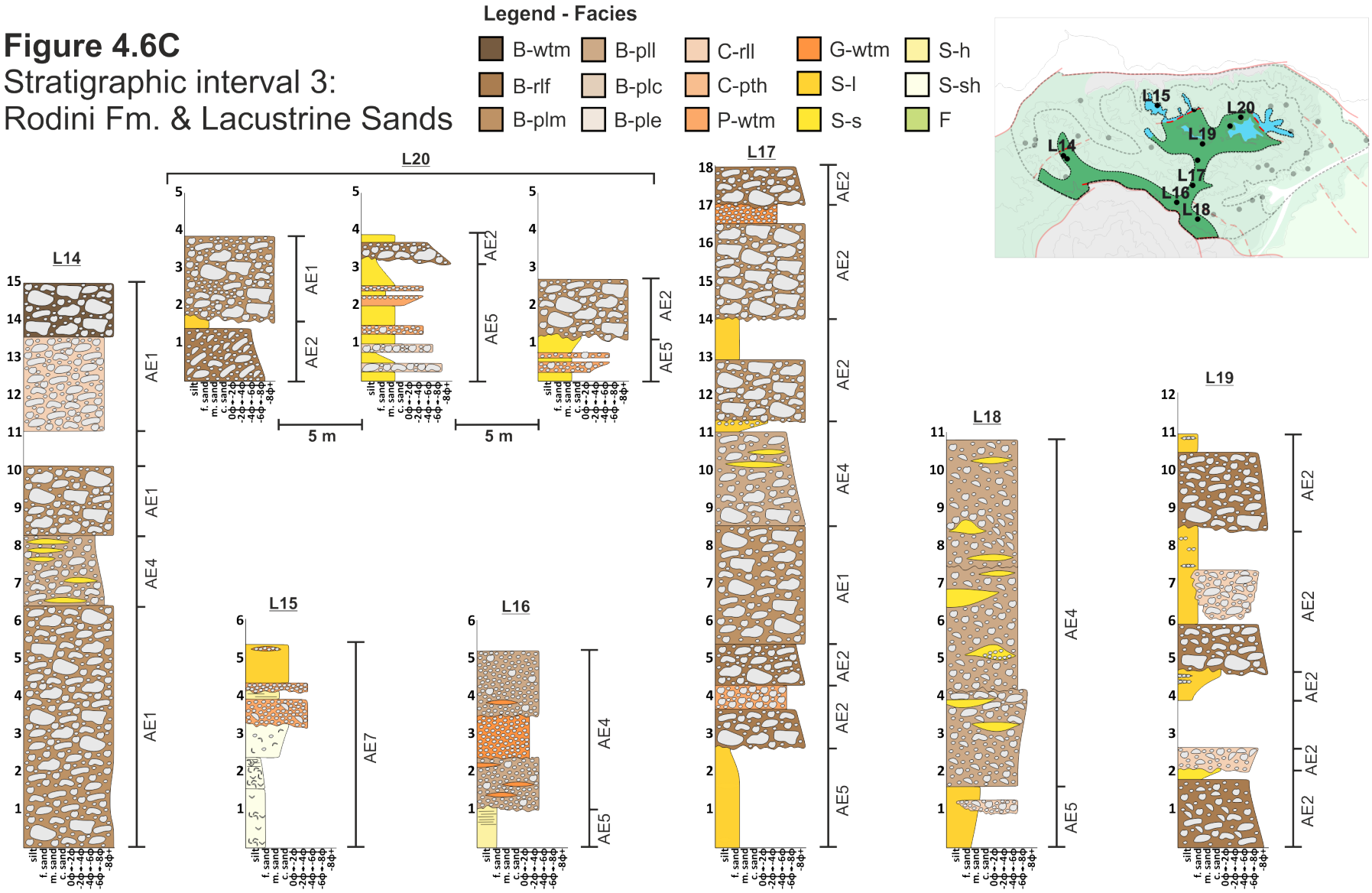

Figure 4.6A (page 126) *Sedimentary logs of the Rodini Fm. and Salmoniko Fm. deposited during rift initiation (vertical scale in metres). Initial sheet-like mass flows (AE3 in L1) close to the fan apex transition downstream into persistent non-cohesive debris flows and intermittent sand-laden hyperconcentrated flows (AE1 and AE2 in L2). Further to the east, finer grained facies dominate in distal locations (L3, L4, L5) with intermittent active lobe deposition represented by coarse debris-flow conglomerates (L6). See Figure 4.3 for inset map definition.*

Figure 4.6B (page 127) *Sedimentary logs of the Rodini Fm. deposited after rift initiation (vertical scale in metres). Coarse conglomerates close to the fan apex (L7, L8, L9) extend further into the basin than during rift initiation. These transition laterally into finer grained facies on inactive lobes (L10) and recently active lobes (L11, L12, L13). Pedogenic development in L12 combined with frequent conglomerate horizons (formed under upper flow regime) indicate frequent lobe switching. See Figure 4.3 for inset map definition.*

Figure 4.6C (previous page) *Sedimentary logs of the Rodini Fm. during its final phase of deposition before lacustrine transgression (vertical scale in metres). Coarse debris-flow conglomerates sourced from the north dominate deposition across the study area (L14, L19, L20) with smaller fans sourced from the uplifted footwall in the south developed (L16, L18, L19). L15 represents the lacustrine transgression and prolonged activity on the Psathopyrgos fault. See Figure 4.3 for inset map definition.*

4.4.2. Architectural elements

Architectural elements are defined here as discrete packages of sediment with a measurable lateral and vertical extent (and associated 3D geometry), deposited as a result of a specific depositional process and its associated processes (for example, a braided fluvial channel deposit and its associated overbank sediments). Their comprising facies, in conjuncture with the elements themselves, form a specific set of arrangements (facies associations) leading to the interpreted natural progression of depositional environments described in sections 4.4.3. and 4.4.4. The architectural elements detailed here are displayed in Figure 4.7 at the end of the section.

AE1: Coarse non-cohesive debris flow elements

Description: This element type comprises 25.7% of the measured succession. Sedimentary units of this type range from 3 to 10 m thick and are dominated by beds that are laterally extensive over tens of metres, themselves each from 0.5 m to 5 m thick. Compared with other associations, beds exhibit lateral variations in thickness up to 0.5 m. The base of each element of AE1 is strongly erosional with 10 – 20 cm persistent relief. Basal erosion surfaces of these elements are overlain by a coarse boulder conglomerate bed (B-wtm, B-plm). Up-section, stacked beds of finer conglomerates (typically cobble to boulder grade) dominate. All beds are massive with no discernible internal stratification (B-wtm, B-plm, B-ple, C-rll). Beds contain a higher proportion of matrix (15 - 20%) than other architectural elements. Thin beds of finer facies (S-s) may be present within the element, and are laterally extensive with a maximum thickness of 0.2 m. AE1 units may be stacked vertically, resulting in amalgamated conglomerate packages, or may occur as isolated elements separated by other types of architectural elements (AE3, AE4, AE5).

Interpretation: Structureless, matrix- to clast-supported conglomerates are most commonly the result of rapid deposition by non-cohesive debris flows that typically wane over time to deposit relatively more well-sorted and fining-up conglomerate beds up-section from hyperconcentrated flows (Nemec & Steel, 1984; Costa, 1988; Sohn et al., 1999; Went, 2005; Calhoun & Clague, 2018). Poorly sorted units with isolated boulders and a wide range of clast sizes are interpreted as the rapid freezing of coarse clasts within flows, with stacked sets and erosional bases to each bed. This indicates that flow events were frequent and initially erosive (Miall, 1996), and representative of more turbulent flow types (Blair & McPherson, 1994; Jo et al., 1997). These types of elements and their constituent lithofacies are typical of proximal alluvial-fan environments, notably in locations close to their feeder valley (Gloppen & Steel, 1981).

AE2: Coarse, poorly channelized streamflow units and associated waning-flood elements

Description: This element type comprises 35.0% of the measured succession. These associations are 2 to 17 m thick and are dominated by conglomerates and silty sandstones arranged into two or more beds, each of which is 0.2 to 3 m thick. Conglomerate beds are lenticular over distances of 5 to 10 m where outcrop extent permits characterisation, with finer-grained facies being more laterally extensive. Coarse-grained conglomerates with erosional bases (B-wtm, B-rlf) are overlain by normally graded conglomerates, either forming a single bed (B-rlf) or fining-upward bedsets with multiple beds (B-rlf, C-rll, P-wtm, G-wtm), which may be sharply overlain up-section by silt- and sand-grade facies (S-l, S-s, S-h). Conglomerates are compositionally and texturally mature, with a high (90-100%) clast proportion by volume. Fine grained units are dominantly massive. AE2 typically occur as stacked sets of

unknown maximum thickness (due to outcrop limitations), but observed to be over 50 m, or interbedded with elements AE5 and AE1.

Interpretation: Moderately to well-sorted conglomerate units of texturally and compositionally mature clasts that fine upward are typical of bedload transport processes (Miall, 1996); deposits are subsequently represented up-section by sand and silt deposits representing the waning of floods (Maizels, 1993; Sohn et al., 1999). Decimetre- to metre-scale infilled scours show these events to be highly erosive and often rapid in nature (Jo & Chough, 2001; Collinson et al., 2006) where each element is taken as a single, or stacked set, of depositional events. In places, fine-grained facies show horizontal lamination picked out by subtle grain-size variations from silt to fine-sand, here speculatively interpreted as the expression of waning deposits during flood events (Gloppen & Steel, 1981; Sohn et al., 1999). The lozenge shape of the conglomerate beds in cross section, in conjunction with their stacking style, indicate elements of weak channelization (Khadkikar, 1999; Collinson et al., 2006) of coarse-grained bedload conglomerates (Miall, 1996). AE2 is interpreted as occurring on the medial section of an alluvial fan, and likely as a downstream expression of AE1. Based on clast morphometric data detailed in Chapter 5, these elements are reinterpreted to represent hyperconcentrated flow deposits based on a lack of identifiable sedimentary structures typical of streamflow deposits (such as inclined cross-bedding) and pebble clasts contained within sandstone and siltstone beds (see Chapter 5, section 5.4.1.).

AE3: Coarse, unchannelised flow elements

Description: This element type comprises 6.14% of the measured succession. These elements are at least 10 – 15 m thick and are composed of one sheet-like coset of conglomerate, divided internally into 0.5 m-thick horizontal beds delineated by traceable

surfaces (marked by a change in matrix grain size from fine sand to silt grade, and a reduction in clast frequency to 50% 10 cm either side of the surface) and clast orientation variations between beds. The elements are laterally extensive across outcrops and cliff sections at a minimum of 20 m, and have flat, sharp bases. Cobbles dominate and reach up to 15 cm in diameter, with a medium-sand-grade matrix (C-pth) forming up to 20% of the beds. Within horizontally stratified sets, clast long axes are typically flat-lying, parallel to stratification. Although AE3 elements are not common over the study area, where present they are bounded by AE1 elements at their base and top.

Interpretation: Repeated non-channelised flows lead to multiple stacked horizons of cobble-grade conglomerates being deposited (Gloppen & Steel, 1981; Mack & Leeder, 1999) where lateral continuity of units, a lack of grading, and lack of erosional bases, indicate a highly viscous rheology (Todd, 1989; Kim & Lowe, 2004). Deposition occurred in a relatively proximal setting within the fluvial system, likely close to a primary feeder valley of the alluvial fan, as indicated by the large cobble clast sizes that dominate throughout (North & Davidson, 2012). A high sediment load led to a traction carpet of clasts being deposited (Todd, 1989) and preferentially orientated with long axes parallel to bedding surfaces. A lack of fine-grained deposits in AE3 indicates that repeated events were of high magnitude and possibly of high frequency, allowing for consistent coarse-grained deposition with no time for the settling of sediment from suspension (Wells, 1984; Hwang et al., 1995).

AE4: Medial fan debris-flow elements

Description: This element type comprises 7.61% of the measured succession. These elements are typically 1.5 to 9 m thick, but may be thicker locally. They are formed by 1.5 to 4 m thick conglomerate beds which are laterally extensive across outcrops (~50 m).

The thickness of each bed varies laterally by up to 50 cm, but does not pinch out. Each bed has an erosional base to underlying deposits of poorly sorted boulder conglomerates containing sand lenses (B-pll) or moderately sorted cobble conglomerate (C-rll), which together form the element. Repeated sandy-silt lenses are common throughout elements. Conglomerates are clast supported, varying from pebble to boulder grade (up to 30 cm in diameter) and have a fine silty-sand matrix making up 5-20% of the lithology. Beds in the element are massive; however, silty-sand lenses within B-pll and C-rll beds locally demonstrate trough cross-stratification on the decimetre scale with sets up to 20 cm thick. AE4 elements are typically deposited in association with AE1 and AE5 elements; larger AE4 elements are deposited subsequent to AE5 elements with a transitional boundary over several metres as the proportion of B-pll and C-rll facies increases. In some cases, smaller examples of AE4 elements occur nested within successions otherwise dominated by AE1 elements.

Interpretation: Ungraded conglomerates of poorly to moderately sorted clasts are commonly formed by cohesive debris flows (Lowe, 1979; Suresh, 2007) as sediment undergoes frictional freezing, subduing settling processes (Cronin et al., 2000). Sandstone formation displays rare weakly developed sets of trough cross-stratification possibly representative of juvenile unit bar development (as stratification does not extend through entire sand units where present) or 3D dune development (Gloppen & Steel, 1981; Reading 1996) during the later stages of flows. These units are largely reworked and partially eroded by further mass-flow events (Lindsey et al., 2005) leading to limited preservation.

AE5: Fan-toe sandstones settled from suspension (with upper plane-bed conglomerate lenses) elements

Description: This element type comprises 17.2% of the measured succession. These elements are 1 to 6 m thick and laterally persistent between outcrops. Internally, they are composed of sets of sandstones that are 0.2 – 2 m thick and conglomerate units that are 0.1 to 1 m thick. Fine-grained facies extend laterally for up to tens of metres (S-l, S-s), whereas conglomerate facies (B-ple, C-rll, P-wtm, G-wtm) are 2 to 5 m in width. Boundaries between sets (and the elements themselves) are sharp but not erosional. Fine-grained units are moderately sorted, whereas conglomerate facies are well sorted with little to no matrix (typically <5%) and contain texturally and compositionally mature (well-rounded) clasts; 98% of clasts are <5 cm in diameter (but up to 15 cm at certain locations). All beds are internally massive. Rare in-situ calcrete nodules are found close to the tops of some sandstone beds, and are typically 2 cm in diameter. These elements are interbedded with AE2, AE5, AE7, and rarely AE1 units, and are common across the study area.

Interpretation: Massive, structureless sands and silts are most commonly deposited from rapid suspension during waning hyperconcentrated flows (Nichols & Fisher, 2007; Köykkä 2011; Lewis et al., 2017) commonly observed on the distal sections of an alluvial fan. Pebble-grade conglomerate lenses within the units represent higher-energy upper plane-bed deposition (Jo & Chough, 2001) forming channelized pebble streams (Croci et al., 2016). The maturity of the clasts, both texturally and compositionally, are representative of their increased distance from the sediment input source (Miall, 1996). Rare calcrete nodules in AE5 units are indicative of an arid or semi-arid climatic setting (Retallack, 2001; Alonso-Zarza, 2003), and a prolonged period of stability allowing calcrete formation in a silt-prone substrate (Alonso-Zarza, 2003).

AE6: Fan-toe overbank elements

Description: This element type comprises 6.18% of the measured succession. These elements are 0.5 to 5 m thick and laterally persistent between outcrops. They are composed internally of silty sandstone (S-s, S-h) and predominantly clayey lithologies (F) that are 0.2 to 2 m and 0.05 to 0.1 m thick respectively. Silty sandstones (S-s, S-h) are laterally extensive by tens of metres; however clayey units vary in thickness from 5 cm to 10 cm within the same bed. Bed boundaries are sharp, and the two lithologies alternate through the element. Silty sandstone beds are moderately sorted ranging up to medium sand; a marked colour change and sharp increase in clay proportions denotes change to finer lithology. Beds are dominantly massive, though with some millimetre-thick horizontal laminations at the top of some silty sandstone beds. These elements occur in larger packages tens of metres thick, in association with AE5 and AE2 elements.

Interpretation: Similar to AE5, sand and siltstone units represent deposition from suspension of waning flows (Nichols & Fisher, 2007; Köykkä 2011; Lewis et al, 2017). Thin clay horizons represent the end-of-flow deposition (both from tractional and suspension processes), and the development of palaeosols identified by their lateral continuity and a lack of further structure (Platt & Keller, 1992; Mack et al., 1993). Where AE6 and AE2 elements are found together, potential active channels are interpreted to have been abandoned through time and subsequently subject to low sedimentation rates, as active deposition occurs elsewhere on the fan (Davies & Gibling, 2010).

AE7: Shallow-lacustrine elements

Description: This element type comprises 2.21% of the measured succession. These elements attain thicknesses of 4 to 10 m and are laterally extensive for up to 20 m. Elements are composed internally of 0.5 to 1 m beds of silty sandstone and conglomerate lithologies. Finer-grained units (S-sh) are laterally extensive over tens of metres, whereas

conglomerates (P-wtm, G-wtm) typically pinch out laterally over 2 to 10 m. Silty sandstone beds contain small shell fragments such as *Melanopsis synaniae* and *Goniochilus achaiae*, freshwater gastropods (Esu & Gerotti, 2015); shell fossils are less than 2 cm in length and occur as shell beds intermittently within the element or single dispersed shells amongst the finer-grained lithofacies. Conglomerate facies are characterised by 1 to 5 cm diameter, well-rounded clasts and contain no matrix. Beds are mostly massive, but some contain shell horizons within beds and horizontal laminations. These elements do not appear to be preferentially associated with other architectural elements.

Interpretation: These elements are similar in origin to deposits of AE6; however, the presence of laterally persistent laminae deposited during steady suspension fallout conditions and the occurrence of freshwater shell fragments (outlined in Esu & Gerotti, 2015) testifies to the development of potential shallow lacustrine conditions (Abdul Aziz et al., 2003; Ford et al., 2016), associated with the inundation of the depocentre by Lake Corinth to the east and, later, the opening of the Rion Strait to the west (Gawthorpe et al., 2018).

Figure 4.7 (next page) *3D architectural element models displaying vertical and lateral nature of individual elements, and interpretations of their depositional processes. Yellow arrows indicate dominant sediment transport direction.*

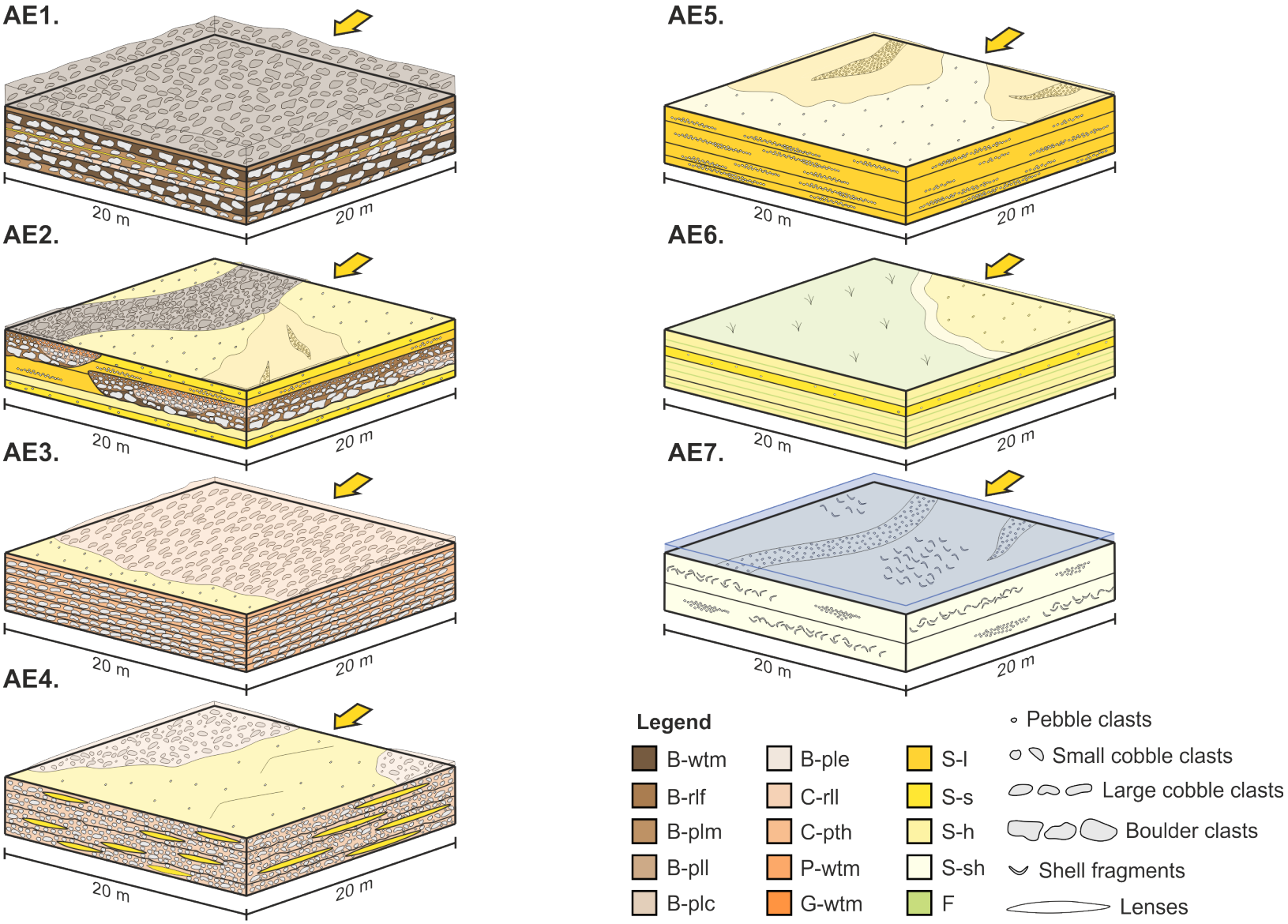
AE1.
20 m
20 m
AE2.
20 m
20 m
AE3.
20 m
20 m
AE4.
20 m
20 m
AE5.
20 m
20 m
AE6.
20 m
20 m
AE7.
20 m
20 m
Legend
B-wtm
B-rlf
B-plm
B-pll
B-plc
B-ple
C-rll
C-pth
P-wtm
G-wtm
S-l
S-s
S-h
S-sh
F
Pebble clasts
Small cobble clasts
Large cobble clasts
Boulder clasts
Shell fragments
Lenses

4.4.3. Chronostratigraphy

As a result of the Rodini Fm. being dominated by rapidly deposited conglomeratic units, absolute dating within the sediments is difficult due to a lack of potential data sources (Gawthorpe et al., 2018). Movement on major bounding faults to the south of the depocentre initiated at approximately 2.2 – 1.8 Ma (Gawthorpe et al., 2018) and this activity likely generated the initial accommodation to allow for the onset of accumulation of the conglomerates of the Rodini Fm. Corals and shells found in the overlying Synania Fm. siltstones provide a biostratigraphic age of approximately 420-400 ka (biozone MNN20) (Palyvos et al., 2010; Esu & Gerotti, 2015) that delimits the end of the episode of accumulation of the Rodini conglomerates. Thus, the total time available for accumulation of the Rodini Fm. is 1.8 – 1.4 Myr and the proposed relative time periods in this study would each represent one third of that value (approximately 600 – 470 Kyr each, assuming constant accumulation rates). Thirds were chosen in order to show a clear chronostratigraphic progression of sedimentological features, while retaining as much accuracy as possible in the relative geological ages of each study site.

Bedding dips reflect both tectonic and sedimentological factors: (i) original rotation of the palaeotopography as activity on the main bounding fault to the south occurred, forming shallower dips up-section, (ii) post-depositional fault block rotation as extension became accommodated by new north-dipping faults to the north, increasing the dips of beds towards the south, and (iii) deposition predominantly occurred in an alluvial-fan setting, which results in a general decrease in depositional dip angles away from the fan-apex feeder valley. Dip angles vary between 6 and 40 degrees across the study area, with maximum dips recorded in the west and south (corresponding with lower elevations and earlier stratigraphy that has been subject to greater fault-induced post-depositional rotation), and minimum dips recorded to the east and in the centre of the study area

(corresponding with higher elevations and later stratigraphy, with less fault-induced post-depositional rotation).

The integration of structural and topographic data allow for the definition of three relative time slices through the Rodini Fm. into which the study sites can be grouped (based on their locations within the study area). Sedimentological variations through both time and space can subsequently be defined and used to create an overall tectonostratigraphy in both dip and strike orientations (Figure 4.8). A relative increase in the proportion of conglomerate deposits towards the margins of the depocentre through time, in conjunction with an increase in AE1 and AE2 architectural elements across the study area, indicates that the fan system prograded across the basin.

Figure 4.8 (next page) *Diagram displaying lithological variations across the study area through time. The tectonostratigraphic record shows the progradational nature of the hangingwall-sourced fan and of smaller, footwall-sourced fans through times before lacustrine transgression. Relative timings are detailed in Palyvos et al. (2007).*

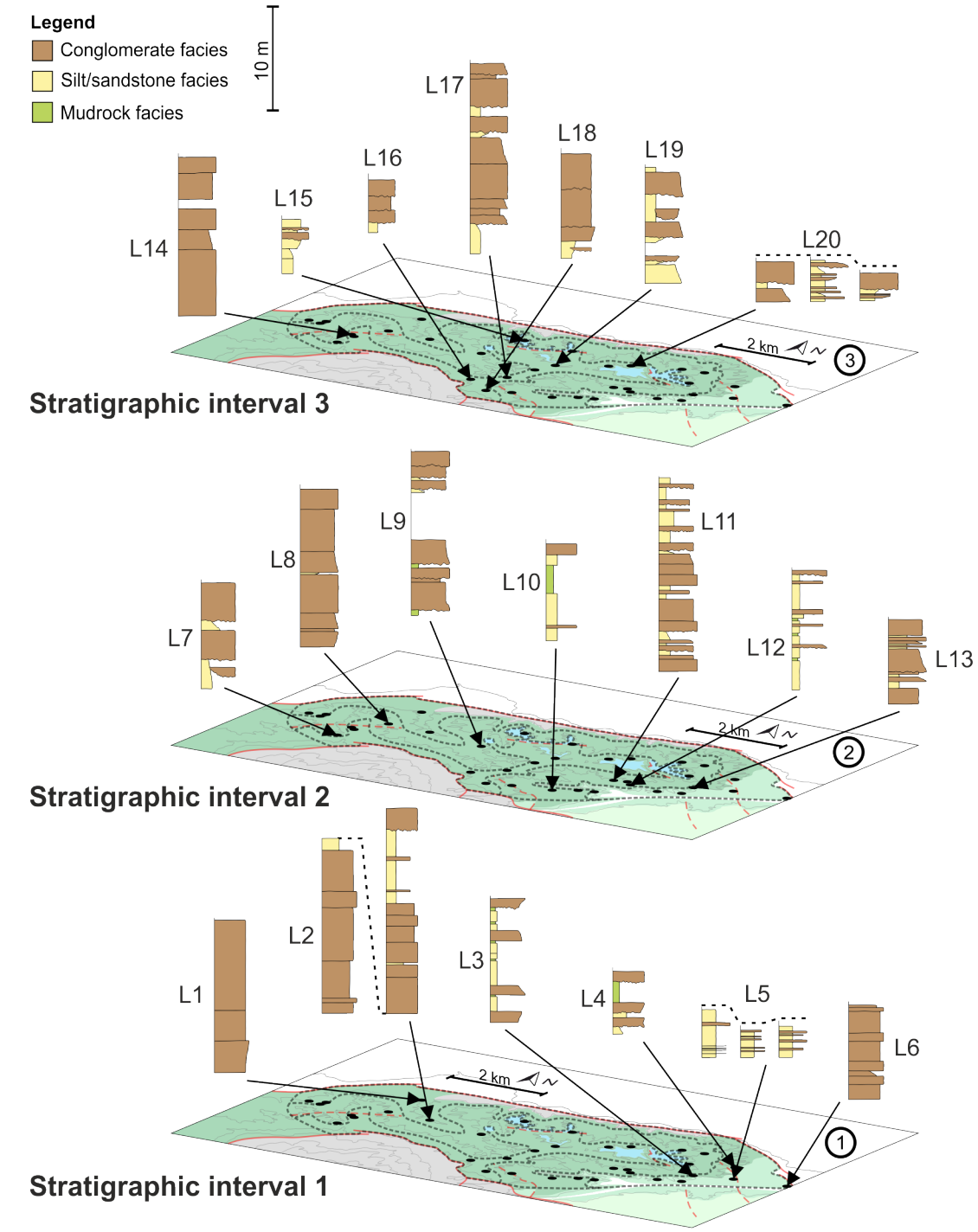
Legend
Conglomerate facies
Silt/sandstone facies
Mudrock facies
10 m
L14
L15
L16
L17
L18
L19
L20
2 km
3
Stratigraphic interval 3
L7
L8
L9
L10
L11
L12
L13
2 km
2
Stratigraphic interval 2
L1
L2
L3
L4
L5
L6
2 km
1
Stratigraphic interval 1

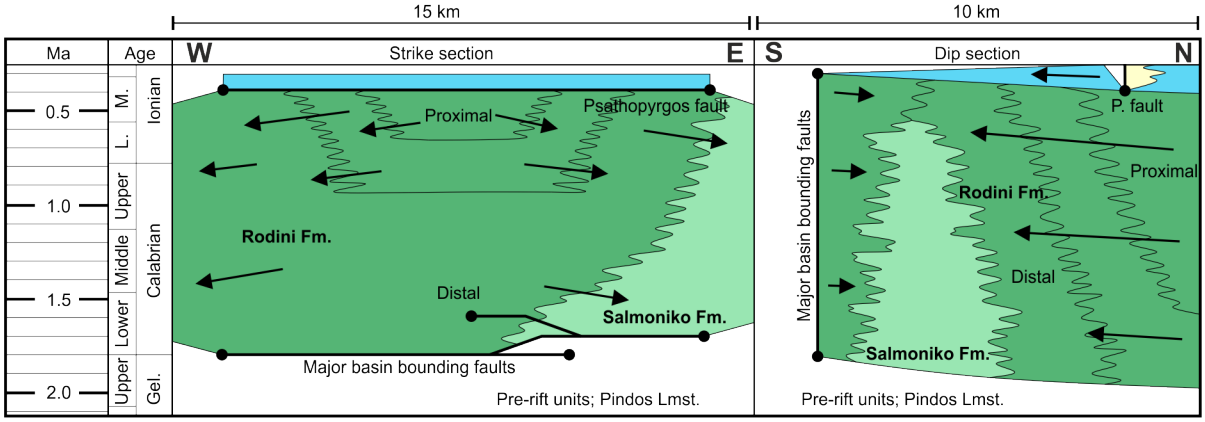
15 km
10 km
Ma
Age
W
Strike section
E
S
Dip section
N
0.5
1.0
1.5
2.0
M.
L.
Upper
Middle
Lower
Upper
Ionian
Calabrian
Gel.
Proximal
Psathopyrgos fault
Rodini Fm.
Distal
Salmoniko Fm.
Major basin bounding faults
Pre-rift units; Pindos Lmst.
Major basin bounding faults
P. fault
Proximal
Rodini Fm.
Distal
Salmoniko Fm.
Pre-rift units; Pindos Lmst.

4.4.4. Definition of tectonostratigraphy and the use of clast-fabric analysis

The prevalence of dominantly debris flow and flood-sourced architectural elements across the study area, as outlined in Figures 4.6A, 4.6B and 4.6C, is consistent with the development of an alluvial fan. This is further supported by the facies themselves, with the fabric of many structureless, coarse conglomeratic units indicative of alluvial-fan flow processes (Table 4.1). The lack of well-developed sandy mesoforms of fluvial origin is notable.

Sedimentological data derived from vertical profiles, when placed within the outlined relative time frame, allow for tectonostratigraphic definition as outlined in Figure 4.8. Clast orientations with respect to palaeoflow directions indicates flow processes: long axes parallel to palaeoflow suggest the rapid deposition of coarse sediment load, whereas intermediate axes parallel to palaeoflow suggest deposition by tractional rolling as bedload (Major, 1998). On this basis, non-cohesive debris-flow deposition (clast long-axes parallel to palaeoflow) in an alluvial-fan environment apparently prevailed in the north of the study area and extended into the depocentre towards the south and east as extension progressed. Hyperconcentrated or streamflow processes (AE2) are predominantly recorded in the east and south (clast intermediate-axes parallel to palaeoflow), and their prevalence lessens through time as the alluvial fan prograded and subdued their depositional environment.

The nature of the hangingwall dipslope alluvial fan was progradational in a radial manner; to the west into the Patras Rift, to the south (towards smaller-scale alluvial fans sourced from the uplifted footwall of the depocenter), and towards lacustrine-dominated depocentres to the east (represented by Synania Fm. deposits) (Figure 4.9). A south-flowing fluvial drainage system that existed prior to rift initiation is interpreted as the

probable source of most of the sediment that formed the hangingwall dipslope alluvial fan, as it was inherited by the newly formed depocentre. The progradation is represented by the advancement of facies belts away from the sediment input point in the north of the basin with time, interpretable from the overall coarsening up of facies in distal locations. As the basin cut the pre-rift drainage direction at high angle, the northward dipping Panachaikon fault (see Figure 4.1A for reference) developed small north-flowing drainage catchments as uplift occurred, developing juvenile alluvial fans. These footwall-derived alluvial fans (indicated by larger relative clast sizes, increased clast angularity, and northward palaeoflow directions) were smaller than their hangingwall counterpart.. Due to increased amounts of present-day erosion of syn-rift units close to the Panachaikon footwall scarp, it is difficult to recognise the development of these smaller fans through time; it is likely that these alluvial fans increased in size due to continued denudation of the associated uplifted footwall (cf. Densmore et al., 2007; Mirabella et al., 2018; Pechlivanidou et al., 2018).

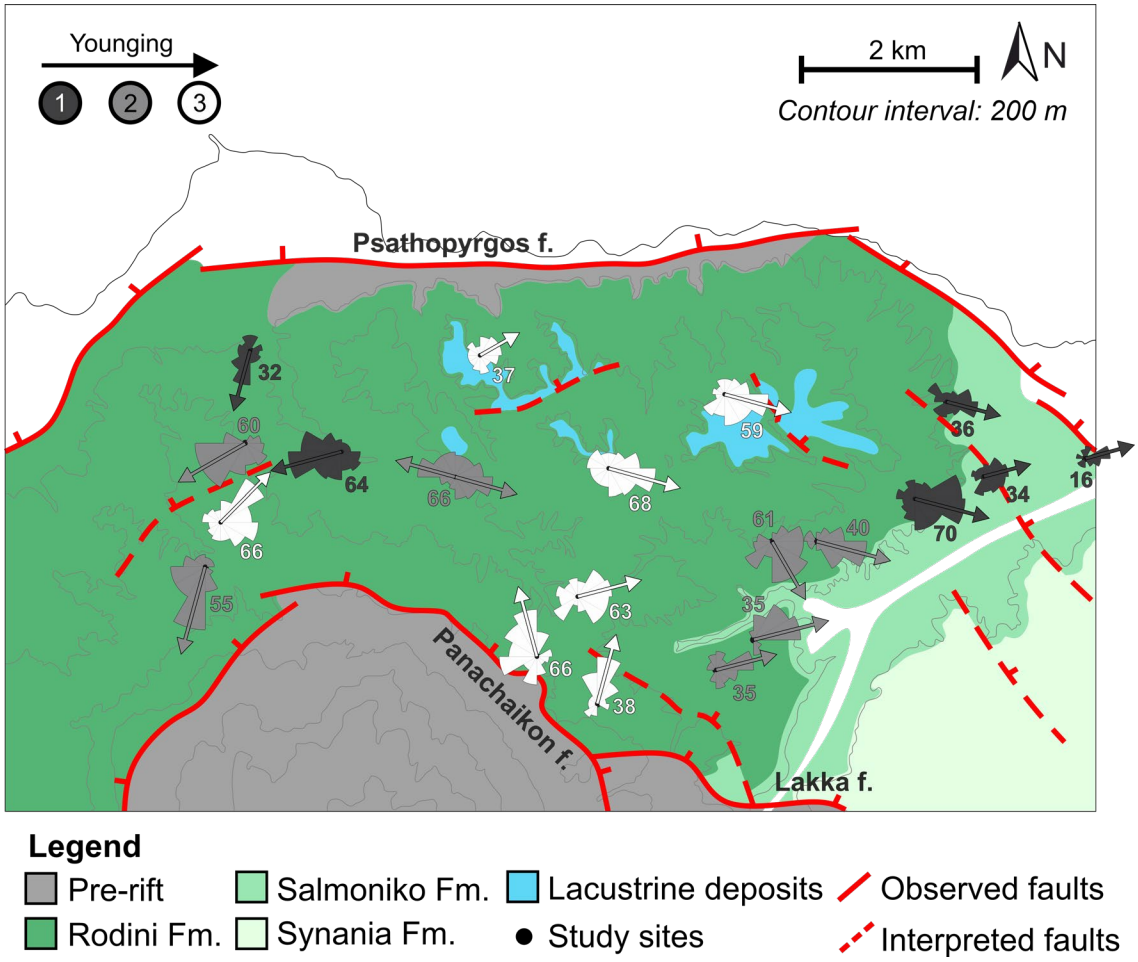

Figure 4.9 (previous page) *Palaeocurrent map showing directions of palaeoflow across the study area through time. Persistent flow to the west and east (with a southerly influence) indicate diversion of the alluvial system into axial depocentres in the rift. Small-scale fans sourced over the uplifted footwall are indicated by northerly dominated flow during late-phase deposition.*

The sand and silt deposits of the Synania Fm., which overlies the Rodini Fm., are interpreted to represent a lacustrine incursion caused by the northward migration of faulting and accommodation generation (Ford et al., 2016). Observations of shells and shell horizons within the unit (Palyvos et al., 2007; Esu & Gerotti, 2015), and extensive deposits interpreted as shallow-lacustrine deposition (see AE7) support this. The major sediment source from the north was eventually cut off by the formation of new normal

faults, causing key sediment routeways from the north to be blocked, thereby shutting down the depositional system before the basin began to uplift over the last 400 Kyr.

4.5. Discussion

4.5.1. The impact of rifting on fluvial drainage

The architectural elements detailed in this study represent different parts of the gradual transition (from proximal to distal locations) down-system of a large alluvial fan; massive debris flows lead into normally-graded bedload conglomerates that decrease in frequency away from major sediment source points, counterbalanced by an increase in fine-grained facies. Towards the east, fine-grained units containing shell fragments represent the lateral facies transition to lacustrine-dominated systems.

Placing the detailed sedimentological vertical profiles in the context of relative time slices allows for the creation of palaeogeographic models detailing the evolution of the depocentre (Figure 4.10). To the north of the present-day Gulf of Corinth, the River Mornos catchment drains the structurally quiescent Pindos Mountains (Piper et al., 1990) and forms an 8 x 4 km southward-prograding modern delta. This system is likely to be the ancestral fluvial system described in this study (the catchment of which has been inherited in the present day), and acted as the principal sediment source that fed the alluvial fan represented by the Rodini Fm. The fluvial system is interpreted to have flowed south–west, following the alignment of east to west propagating fold-and-thrust structures with a NNW-SSE strike. These were formed during the Early Oligocene to Late Eocene (Underhill 1989; Skourlis & Doutsos, 2003), and were also exploited by other antecedent drainage systems in the Gulf (Gawthorpe et al., 1994). As the fold-and-thrust structures form topographic highs between catchments, subtle variation in topographic

dips between structures allow for the switching of dominant drainage direction from north to south across the elevated highs (Gawthorpe et al., 2018).

Rifting propagated through the catchment at high angle, with the major northward-dipping master fault uplifting pre-rift basement to the south of the study area and forming a barrier to flow. As the hangingwall subsided, accommodation was created and an alluvial fan began to build out into the depocentre as flows spread radially to fill the available accommodation and attain an equilibrium profile. This process is interpreted to have continued until a new master fault developed in the north and acted to uplift the depocentre, and as a new footwall created a barrier to sediment pathways, sediment supply ceased and caused the exposure and erosion of the Rodini Fm. to the present day.

Figure 4.10 (next page) *Palaeoenvironmental reconstruction of the Panachaikon-Psathopyrgos fault block through time, from 2.2 Ma to present day. Faulting initially cut through the pre-rift Hellenide thrust-and-fold belt, with uplifted footwalls blocking fluvial flow to the southwest and forming an alluvial fan and associated axial fluvial systems (Rodini Fm. and Salmoniko Fm.). Initiation of the Psathopyrgos fault cut off sediment supply from the north, causing a lacustrine transgression and the backstepping of a major delta up the hangingwall dipslope. 'Interval' labels represent the stratigraphic intervals defined in Figure 4.3.*

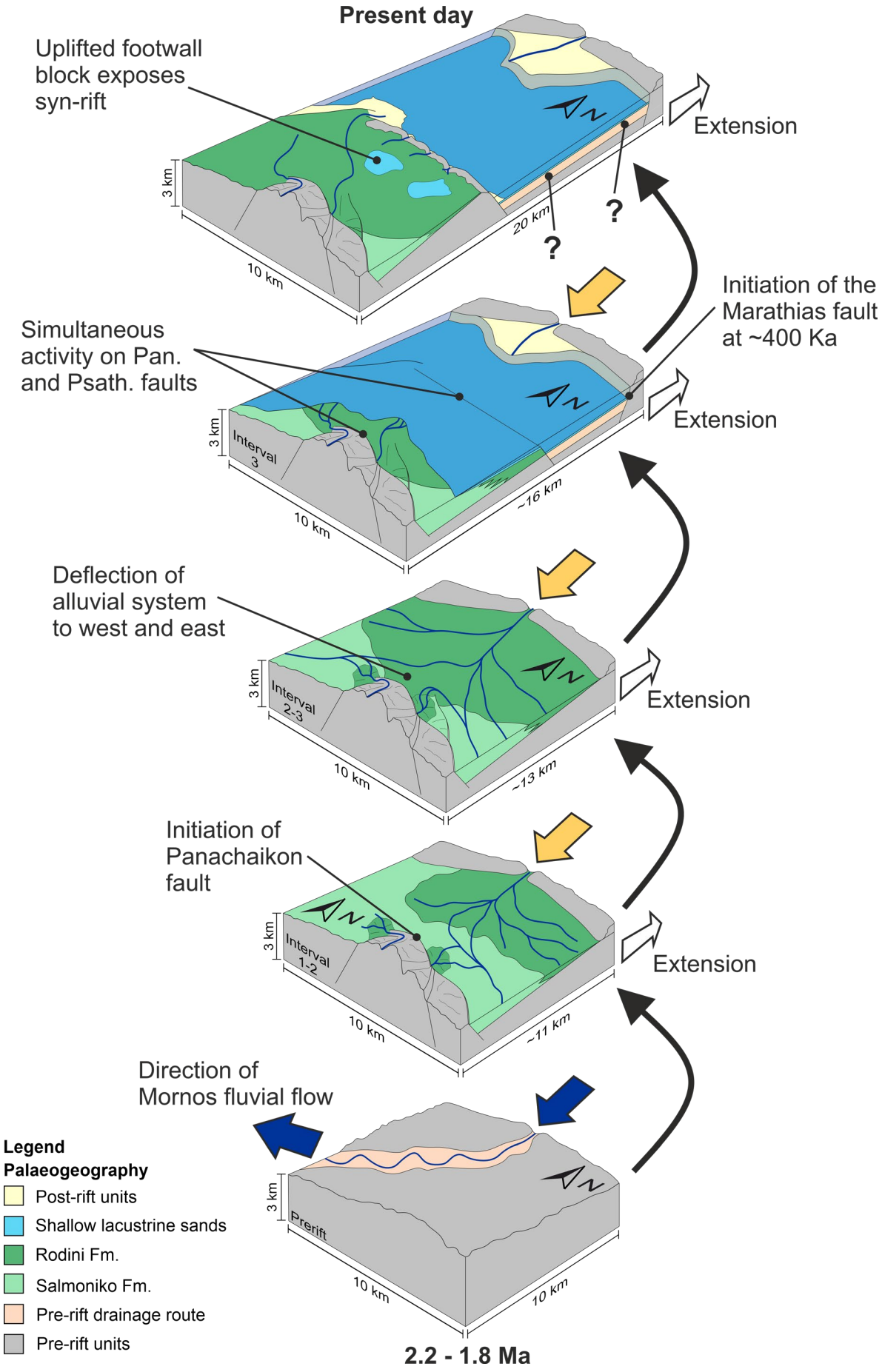
Present day
Uplifted footwall block exposes syn-rift
Extension
3 km
10 km
20 km
?
?
Initiation of the Marathias fault at ~400 Ka
Simultaneous activity on Pan. and Psath. faults
Extension
3 km
Interval 3
10 km
~16 km
Deflection of alluvial system to west and east
Extension
3 km
Interval 2-3
10 km
~13 km
Initiation of Panachaikon fault
Extension
3 km
Interval 1-2
10 km
~11 km
Direction of Mornos fluvial flow
3 km
Prerift
10 km
10 km
Legend
Palaeogeography
Post-rift units
Shallow lacustrine sands
Rodini Fm.
Salmoniko Fm.
Pre-rift drainage route
Pre-rift units
2.2 - 1.8 Ma

This interpretation represents one of three possible end-member scenarios whereby a rift system half-graben basin cuts a large-scale drainage catchment, examples of which are found across the Gulf of Corinth. The three evolutionary scenarios are explained below.

(i) Drainage incision keeps pace with footwall uplift; flow is orientated perpendicular to major normal faults and flows directly over the new footwall into the deepest part of the hangingwall. Erosion down into the bedrock lithology forms valleys in the footwall and eroded sediment is deposited directly into the newly formed depocentre (see Bentham et al., 1991; Backert et al., 2010; Leeder et al., 2012; Hemelsdaël et al., 2017).

(ii) Drainage is diverted away from the uplifting footwall; flow is orientated in the same direction as the dip of major normal faults, however a combination of low erosive power and bedrock resistance to erosion (Allen & Densmore, 2000) results in the diversion or complete reversal of drainage away from uplifted sections (see Rohais, 2007a; Gawthorpe et al., 2018). Small catchments form on the uplifted footwall close to the fault face, forming relatively small, high-gradient fans and fan deltas along the length of the fault (Gawthorpe et al., 1994).

(iii) Drainage flows over the hangingwall dipslope; flow is orientated perpendicular to major normal faults and flows over the hangingwall dipslope towards the major fault plane. This causes wider, lower-gradient fans and deltas. Sediment yield is influenced by antecendent catchment parameters (in conjunction with a dominant tectonic uplift control), such as bedrock lithology and climate, which are not influenced by the evolving rift system (described in detail in this study; see further examples in Mack & Seager, 1990; Martini & Sagri, 1993). Experimental work by Clarke et al. (2010) studying alluvial fan development with a downstream boundary condition (such as a fluvial system preventing

progradation, or structural barrier) found that initial deposition from sheet-like (i.e. non-confined) flows developed to channelized flows with time and advancement of the fan. In this study, the Panachaikon fault provides a boundary condition, and early deposits of the Rodini Fm. representing possible sheet-like flows (see Figure 4.6A, log L1) transitioning up-section into proposed channelized flow sediments (see Figure 4.6A, log L3) indicating a subduing of autogenic fan cycles of deposition (van Dijk, 2012).

These end-members have been explored previously (Gawthorpe et al., 1994; Gawthorpe & Colella, 2009); however few studies focus on intrabasinal faulting acting as barriers to hangingwall dipslope routes of sediment transport. Although scenario (iii) is described in detail in this study (and can be supported by the pattern of local sedimentation within the depocentre), Figure 4.10 shows that conditions allowing for scenarios (i) and (ii) to occur were present between the initiation of extension and the present day if considering this sub-basin in a regional context. The Trizonia fault to the northeast (see Figure 4.1A), located under the present day Gulf and likely active at the same time as the Panachaikon fault (Ford et al., 2016) may have provided a barrier to the Mornos drainage and diverted the system over the hangingwall dipslope of the Panachaikon fault – scenario (ii). Following deposition of the Rodini conglomerates, initiation of the Marathias (see Figure 4.1A) and Psathopyrgos faults at approximately 400 ka (Palyvos et al., 2010) has led to a marked increase in extension rates in the modern Western Gulf (Ford et al., 2016; Gawthorpe et al., 2018). This has developed more pronounced graben conditions with a northern basin-bounding fault (the Marathias fault, see Figure 4.10) (Beckers et al., 2015) of which the uplifted footwall is eroded sufficiently by the Mornos fluvial system to allow the formation of a modern fan-delta depositing directly into the hangingwall – representing scenario (i). A significant novel outcome of this study is that the succession

records evidence that all three scenarios can be present during the life cycle of a single fault block depending on the presence and activity of intrabasinal faulting.

The results of this study demonstrate the effect of a downstream boundary condition (in this case, an uplifted footwall) on alluvial-fan deposition. Numerical modelling studies (e.g. Van Dijk et al., 2012; Clarke et al., 2010; Clarke, 2015) commonly focus on the autogenic development of fan systems and surface depositional processes. Results from this study can be incorporated into future models to provide more realistic structural settings for alluvial-fan development, which will aid in the study of alluvial system response to fault development and basin subsidence for a variety of scenarios (e.g., analysis of the effect of differing rift and drainage orientations). Comparing results from such modelling efforts to real-world studies of ancient outcropping successions (this study), and similar modern analogues (e.g., the Okavango delta located in Botswana, Africa – a large alluvial fan oriented perpendicular to the trend of active rifting) will markedly increase our understanding of sedimentary system response to active faulting at a variety of scales.

4.5.2. The Rodini Fm. in the wider context of the Gulf of Corinth

Across the uplifted footwall exposures of the northern Peloponnesos, multiple different syn-rift depositional environments are represented. In the east near Corinth, sediments are dominated by fan deltas and deep-marine deposits of the ancient Lake Corinth, within the depocentre of the now uplifted footwall (Doutsos & Piper, 1990); these deposits transition up-section into shallow-marine sands related to the transition from the lake to the modern day Gulf (Rohais et al., 2007a; Ford et al., 2016). Further to the west towards the study area, the influence of continental sedimentation becomes apparent in the hangingwalls of the Kalavryta and Demestika Faults (Hemelsdaël et al., 2017) and in the

study area of this chapter, where conglomeratic deposition represents alluvial-fan and possible braided-stream environments. Gawthorpe et al. (2018) show that the uplifted sections exposed today can be separated into two distinct rift phases; the first where extension is localised around Corinth and extends as far west as Aigio (5.0-3.6 Ma to 2.2-1.8 Ma), and the second where extension has begun in the study area on the Lakka and Panachaikon faults (allowing the deposition of the Rodini Fm.; see Figure 4.1), north of Corinth (2.2-1.8 Ma to present). Within this second phase, the initiation of the Psathopyrgos fault on the present-day coastline uplifts the Rodini Fm. and causes the opening of the Rion Strait. This period has been narrowed down to approximately 400 ka by dating of overlying shell fauna in the Synania Fm. (Palyvos et al., 2007; Esu & Gerotti, 2015) which was deposited during a period of simultaneous activity on both the major Panachaikon Fault and Psathopyrgos Fault (Figure 4.10).

In the outlined first rifting phase, similar deposits to those found of the Rodini Fm. are found in the hangingwalls of the Kalavryta and Demestika Faults. Hemelsdaël et al. (2017) outlined the tectonosedimentary evolution of these deposits and found multiple similar facies and facies associations to those outlined in this chapter; similar units of coarse boulder conglomerates deposited close to a dominant sediment input source, transitioned distally to finer-grained sands and siltstones. The drainage system leading to the deposition of the facies described by Hemelsdaël et al. (2017) differs from the one described herein in two key ways; (i) although orientated at high angle to fault strike, antecedent drainage and flow is over the footwall and keeps pace with the uplifting bedrock, depositing sediment directly into the newly formed depocentres, and (ii) the drainage system as a result cuts across multiple fault blocks, where older normal faults to the north are buried by syn-rift sediments. It is inferred that similarly high sediment supply through one dominant sediment input source prevailed. This, in combination with

both drainage catchments eroding similar bedrock (due to the inherited palaeotopography around Kalavryta being dominated by the same Pindos Units forming the bedrock lithologies of the Mordos catchment; Degnan & Robertson, 1998), leads to strikingly similar deposits in these two depocentres at different times. In the Prinos and Tsivios fault blocks, the early syn-rift sediments are coarse basal conglomerate units of interpreted alluvial origin. These units infill the palaeotopography, in a very similar manner to the sediments of the Rodini Fm. documented in this study.

To the west of the Panachaikon fault hangingwall, the Patras rift extends towards the south-west, having initiated on an extensive low angle listric fault which underpins extension in the Gulf of Corinth (Sorel, 2000). The rifts are linked by two transfer fault zones trending towards the north-east, on the western end of the Panachaikon fault (Flotté et al., 2005). Imbricated cobbles within the Rodini Fm. indicate that part of the river drainage was directed into the Patras rift axially, as the uplifted footwall of the Panachaikon fault acted as a buffer to flow. The sediment supply likely outpaced the formation of an accommodation zone between the differently orientated rift segments (Morley et al., 1990) allowing for the continued progradation and deposition of fluvio-alluvial deposits into the Patras rift (Doutsos et al., 1988). This is similar to other locations in the Gulf of Corinth where steep-sided Gilbert fan deltas would build into both the ancient Lake Corinth and the more recent Gulf (Rohais et al., 2007a; Rohais et al., 2008; Backert et al., 2010), across multiple hangingwall depocentres each with varying amounts of accommodation space.

Following the formation of the radially prograding alluvial fan within the hangingwall of the Panachaikon fault, the initiation of the north-dipping Psathopyrgos fault (Figure 4.1A) formed a second hangingwall sub-basin further to the north. Sediment supply into the

hangingwall of the Panachaikon fault was subsequently shut off; hence during the period of simultaneous tectonic activity on the Panachaikon and Psathopyrgos faults, sediment-bearing flows were directed into the newly formed sub-basin of the Psathopyrgos fault. This is a direct result of antecedent drainage flowing over the hangingwall dipslope as opposed to across the uplifted footwall.

4.6. Conclusions

1. The Rodini Fm. is characterised by a 600 to 800 m-thick succession of upward coarsening conglomerates (up to ~75 cm clast sizes) with subordinate finer-grained lithologies. The succession represents the accumulated deposits of a major prograding alluvial-fan system. In western locations, stacked elements of boulder-to-cobble grade conglomerates represent proximal debris-flow and hyperconcentrated-flow deposits. In central and southern locations, distal to sites of major sediment input, conglomerates fine to pebble- and granule-grade, and the proportion of sand-grade and silt-grade facies increases significantly. Further to the east and up-section, a lacustrine influence is recorded by the occurrence of siltstone units containing a lacustrine shelly fauna.

2. Palaeocurrent data collected from 20 study sites (1,001 measurements total) indicate a dominant major sediment input source from the north of the study area flowing south over the hangingwall dipslope of the Panachaikon fault, a major basin-bounding fault. This alluvial system likely inherited the ancient course of the Mornos River and its catchment.

3. The uplifted footwall of the Panachaikon fault acted as a barrier to the Mornos catchment, and subsequently diverted drainage into adjacent depocentres to the east (ancient Lake Corinth) and west (Patras rift).

4. Palaeocurrent data indicating northerly flow, close to the uplifted footwall of the Panachaikon fault, indicate footwall-derived sediment deposition occurred in the basin on a small scale at both the fault tip of the Panachaikon fault to the west, and the point of hard linkage between the Panachaikon and Lakka faults (see Figure 4.1). These areas were exploited by small drainage catchments eroding the uplifted footwall.

5. The initiation of the Psathopyrgos fault to the north at approximately 400 ka provided a barrier to flow over the Panachaikon fault hangingwall. Simultaneous extension on both of these faults induced an episode of rapid basin subsidence that resulted in an initially lacustrine transgression over the recently deposited conglomerates, prior to the opening of the Rion Strait shortly after 400 ka (Gawthorpe et al., 2018).

6. Original fluvial flow of the pre-rift Mornos river to the south-south-west was blocked and buttressed by the newly formed Panachaikon fault and associated uplifted footwall, leading to the formation of the described alluvial fan and the diversion of drainage to the west and east into newly formed rift depocentres. In the present day, the south-flowing Mornos river forms a large delta that progrades south into the Gulf of Corinth.

7. Results from this research record the sedimentological expression of rift-basin evolution that cross-cuts an antecedent drainage network at a high angle. Three depositional models for this exist: (i) erosion through an uplifted footwall; (ii) diversion away from an uplifted footwall; (iii) deposition over the hangingwall dip-slope. While examples of each scenario can be found around the Gulf in the present day, here we show that intrabasinal faulting allows for the development of each scenario within the same basin segment as it evolves through time.

5. Application of conglomerate clast morphometrics to determine palaeogeographic evolution within a rift basin fill, Gulf of Corinth, Greece

5.1. Introduction

Alluvial fan systems in continental rift settings are a dominant depositional environment in incipient depocentres following the initiation of normal faulting (Blair, 1987; Ingersoll et al., 1990; Cohen et al., 1995; Schlische & Anders, 1996; Espinoza et al., 2019; Smyrak-Sikora et al., 2019). Typically, the stratigraphic record of these environments comprises a mix of conglomerate and sandstone facies, exposures of which can be studied using lithofacies and clast-fabric analyses to determine variations in palaeogeography, environmental conditions, depositional processes, and palaeocurrent directions through space and time (Allen, 1982). Sedimentological analyses are important for helping to understand the variations in climate, tectonics, and sediment supply through time (Blair & McPherson, 1998; Meek et al., 2020), and for improving our understanding of the response of depositional processes to ongoing crustal extension (Leeder & Gawthorpe, 1987; Gawthorpe & Leeder, 2000). Consequently, they can also be used to identify analogues for subsurface deposits in similar settings and predict facies distributions within subsurface depocentres (Prosser, 1993). In basins where conglomerates of fluvial or alluvial origin form the initial sedimentary fill of newly generated accommodation, that sedimentary package may be formed as a result of the redirection of pre-existing drainage (Jackson et al., 2006; de Almeida et al., 2009; Hemelsdaël et al., 2017; Espinoza et al., 2019). For such systems, subtle differences in sedimentological characteristics (including texture, clast fabric, and stacking patterns of stratal units) can be attributed to variations in both autogenic controls (e.g., fan-head entrenchment, channel avulsion, lobe

switching), and external allogenic controls including ongoing fault development, climatic variations and catchment dynamics (e.g. Meek et al., 2020). Importantly, through detailed lithofacies and clast-fabric analyses of conglomerate deposits, characteristics and controls of early syn-rift alluvial environments present in different parts of a rift basin can be inferred and palaeoenvironmental and palaeogeographic conditions can be reconstructed (e.g. Mack & Leeder, 1999; Hemelsdaël et al., 2017; Meek et al., 2020). However, these studies typically focus on qualitative observations of conglomeratic textures and fabrics (e.g. Hemelsdaël et al., 2017) or are limited to quantitative measurements of grain size variations (e.g. Brooke et al., 2018) without considering wider clast-fabric parameters (e.g. clast plunge and azimuth).

The size, composition, shape and orientation of conglomerate clasts, and their sorting, packing and arrangement relative to each other (i.e. sediment fabric) result from processes of sediment transport and deposition, and from post-depositional processes including settling, reworking and resultant clast degradation (Bertran et al., 1997). The types of flow that transport sediment vary depending on their ratio of suspended sediment to fluid content, where < 3 - 10% sediment by volume indicates streamflows, ~10 – 60% sediment by volume indicates hyperconcentrated flows, and ~ 60 – 100% sediment by volume indicates debris flows (Beverage & Culbertson, 1964; Pierson, 2005). Rheological criteria are applied to discriminate between these flow types, whereby: (i) a streamflow is defined as a Newtonian fluid (constant viscosity) with no yield strength; (ii) a hyperconcentrated flow contains sufficient suspended clay to add measurable yield strength and mark the transition to a non-Newtonian (variable viscosity) fluid; and (iii) a debris flow has sufficient yield strength and buoyancy force to suspend gravel particles, regardless of flow movement (Pierson & Costa, 1987; Rickenmann, 1991; Pierson, 2005). This increase in viscoplasticity will alter the dominant mode of sediment deposition from

settling processes to an increase in frictional freezing of flows and an increased impact of grain-grain interactions (Iverson, 1997; Sohn et al., 1999; Benvenuti & Martini, 2002; Pierson, 2005).

Identification of the processes that underpin the development of fabrics in debris-flow deposits was pioneered by Lindsay (1968), who identified the preferred alignment of clast long axes parallel to flow direction, through modelling based on the theoretical work of Jeffery (1922) and field-based study. Allen (1982) summarises further early studies (e.g. Harrison, 1957; Rapp, 1960a; Allen, 1969) and concludes that clast fabrics developed in mass flows are commonly highly variable, and are dependent on the distance they have travelled, grain size (and distribution thereof) and clast shape, as well as the vertical position of the clasts in the flow and the part of the flow they are in (such as lobe front, lobe fringe, or rigid plug body).

The study of conglomerate clast fabrics has been applied widely in many sedimentary environments previously, most notably in glacial (Eyles & Kocsis, 1988; Millar, 2006) and volcaniclastic (Suzuki & Ui, 1982; Mills, 1984; Kohlbeck et al., 1994; Karátson et al., 2002) settings where coarse grained colluvium is common in the accumulated sedimentary record. Statistical modelling of clast orientations (Mark, 1973) preceded laboratory modelling of subaerial mass-flows leading to advancements in the understanding of the response of clast geometries to flow dynamics (Major, 1998; approach used in examples including Miao et al. 2008; Ventra et al., 2013; Chen et al., 2016). Despite this, studies are lacking that integrate clast-fabric data in a detailed stratigraphic framework in order to interpret the response of flow dynamics to syn-depositional tectonism, and in particular the response to continental rift development.

The westernmost part of the Corinth Rift, Greece, contains an uplifted footwall on the northern tip of the Peloponnese. This uplifted footwall exposes syn-rift sediments which were deposited after the initiation of extension and initial accommodation generation associated with the uplifting of the Panachaikon range (Ford et al., 2016; Gawthorpe et al., 2018). These exposures provide a unique opportunity to study alluvial conglomeratic units deposited over a hangingwall dipslope in response to the first stage of accommodation generation (Somerville et al. 2020).

The aim of this study is to determine the detailed palaeogeography of the early rift sub-basin of the Panachaikon fault (Figure 5.1) and its relationship to ongoing faulting through detailed conglomerate clast texture and fabric analyses. This will test the hypothesis that there is a predictable relationship between (i) depositional flow type and associated conglomerate clast fabrics, and (ii) spatially and temporally variable fault activity. The specific research objectives of this study are to: (i) identify and measure the fabrics of clasts of the different conglomerate lithofacies according to their composition, shapes, sizes, and orientations; (ii) detail the similarities and differences in clast fabric through the stratigraphy and across the basin, in order to refine the local palaeogeography; (iii) determine the value of data on clast orientations and shapes for inferring depositional flow processes; and (iv) to evaluate the relationship between the structural evolution of the basin and the conglomerate clast fabrics preserved in the synrift stratigraphy.

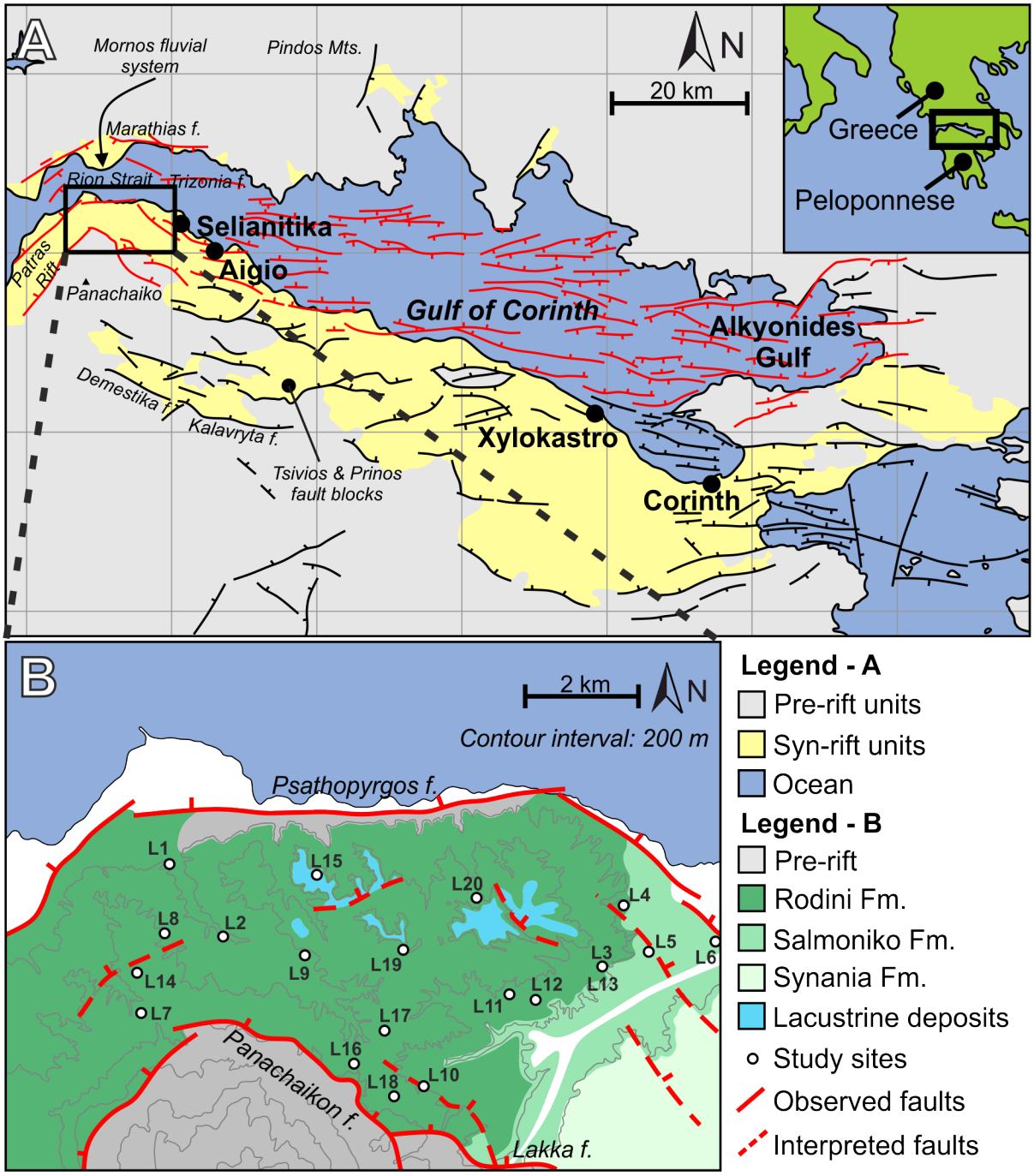

Figure 5.1 *Map of the study area of the Rodini Fm. in the wider western Corinth Rift, adapted from Gawthorpe et al. (2018). (A) Map of the entire Corinth Rift showing distributions of exposed syn-rift strata and pre-rift basement. Fault mapping defined from Rohais et al. (2007a), Ford et al. (2016) and Gawthorpe et al. (2018). (B) Detailed map of the study area showing the main study sites utilised for this research.*

5.2. Geological setting

5.2.1. The Gulf of Corinth

The Gulf of Corinth was formed by the initiation and extension of the Corinth Rift that lies beneath it (Figure 5.1). The rift has undergone multiple phases of extension (Ford et al., 2016; Gawthorpe et al., 2018), beginning in the Pliocene with a trend toward increasing rates of extension to the present day (Bell et al., 2011), resulting in the development of a range of continental environments, deposits of which have accumulated as the infill of progressively generated accommodation, with preserved successions representing lacustrine, fluvial, alluvial-fan and fan-delta environments (Rohais et al., 2007a; Rohais et al., 2007b; Ford et al., 2013; Ford et al., 2016; Rohais & Moretti, 2017; Gawthorpe et al., 2018). During the earliest rift phase (Phase 1, as described by Gawthorpe et al., 2018) north-dipping normal faults formed across the present-day northern Peloponnese, cutting through pre-existing NNW-SSE orientated drainage catchments. These catchments were orientated according to a pre-rift topography controlled by NNW-SSE striking fold-and-thrust structures (Skourlis & Doutsos, 2003), and typically drained from south to north (Seger & Alexander, 1993; Zelilidis, 2000). As a result, subsequent deposition into the Corinth Rift was markedly influenced by these pre-existing drainages, with streams either cutting through, or flowing around, the newly uplifted footwalls of the major depocentres (Hemelsdaël et al., 2017).

On the western edge of the present-day Gulf of Corinth, the Mornos River and its catchment are orientated east to west. Flow is then directed towards the south around the present day Marathias fault (Figure 5.1) (Piper et al., 1990), as a consequence of forming as part of the original set of NNW-SSE orientated catchments in the region. It is difficult to determine whether the Mornos originally flowed to the south, opposite to the regular S-N flow direction of other antecedent systems (Hemelsdaël et al., 2017;

Gawthorpe et al., 2018) as a result of subtle differences in palaeovalley gradients crossing the Hellenide fold and thrust belt. It may be that the initiation of the Panachaikon fault, striking transverse to the catchment, reversed the main flow direction of the system. The river terminates in a large 28 km^2 delta directly north of an exposed uplifted footwall crest on the northern Peloponnese. The early syn-rift units exposed at the northern tip of the Peloponnese on the southern side of the Gulf of Corinth (the Rodini Fm., the Salmoniko Fm., and Synania Fm.) are dominated by alluvial-fan conglomerate facies (Rodini Fm.) transitioning eastward into finer grained sandstones and siltstones deposited in the shallow reaches of a lacustrine environment (Salmoniko and Synania Fms.) (Ford et al., 2016). Somerville et al. (2020) outlined evidence for the sediment source of the Rodini Fm. and linked it to the present-day Mornos catchment, based on: (i) similarities between the catchment bedrock of the Mornos River and conglomerate clast compositions in the Rodini Fm.; (ii) palaeocurrent evidence of southerly, westerly and easterly flow within the basin indicating a northerly sediment source; and (iii) a lack of present day N-flowing fluvial systems to the south of the basin.

Consequently, the likely depositional setting of the basin during its early syn-rift stage (2.2-1.8 Ma, to 400 Ka; Gawthorpe et al., 2018) was an E-W striking half-graben with a major basin bounding fault to the south (the Panachaikon Fault), associated with a prograding alluvial fan depositing sediment over the hangingwall dipslope. A high rate of sediment supply relative to the rate of accommodation generation resulted in an overfilled basin when the sub-basin initially formed (Schlische & Anders, 1996; Gawthorpe et al., 2018). Fluvial and alluvial systems passed eastward into the lacustrine setting of the Corinth Lake near the town of Selianitika (Figure 5.1; Ford et al., 2016; Gawthorpe et al., 2018), before further extension led to the opening of the Rion Strait (at about 400 Ka; Palyvos et al., 2007; Esu & Girotti, 2015) and a shift in the locus of

sedimentation from the Mornos catchment to its present-day position on the north side of the Gulf of Corinth.

5.2.2. The Rodini Formation

The focus of this study are the conglomerate deposits of the Rodini Fm. The unit is approximately 600-800 m thick and forms the earliest syn-rift deposits in the hanging wall of the Panachaikon fault on the northern tip of the Peloponnese. Somerville et al. (2020) outline the facies and architectural elements present in the formation and detail the palaeogeographic evolution up until the initiation of the Psathopyrgos fault, which forms part of the northern coast of the Peloponnese today. Non-cohesive debris flows, weakly channelised hyperconcentrated flows and potential streamflows delivered coarse-grained (up to boulder clast size) sediment into the more proximal parts of the basin, transitioning downstream to predominantly cobble- and pebble-grade sediment before reaching the lacustrine system to the east. The conglomeratic facies examined in detail in the clast-fabric analysis that forms the focus of this study are outlined in Figures 5.2A and 5.2B.

Following the initiation of the Psathopyrgos fault, the dominant sediment source to the north (Somerville et al., 2020) was cut off from the basin by the resulting footwall uplift. The basin transitioned from overfilled conditions (where rates of sediment supply outpaced rates of accommodation generation; Withjack et al., 2002) to underfilled conditions (where rates of accommodation generation outpaced rates of sediment supply). The studied basin and stratigraphic unit provide a valuable opportunity to examine in detail the exposed rock record of a hangingwall dipslope-sourced alluvial system, and to analyse variations in depositional flow processes and locations through time and space.

A **Facies B-wtm** - well-sorted tightly packed boulder conglomerate

i) Facies picture

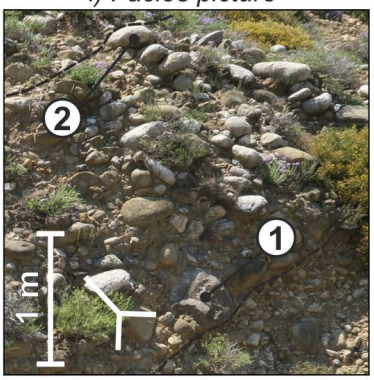

ii) Log expression

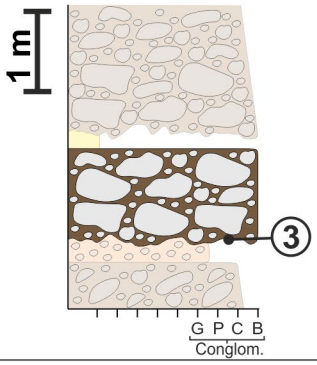

iii) Specific details

1. Rare large (40 cm) boulders near base of beds
2. Boulder and large cobble clasts present throughout the bed - massive structure
3. Typically have erosive bases, identified by large intrusive boulder clasts into underlying beds

B **Facies B-rlf** - normally graded boulder conglomerate

i) Facies picture

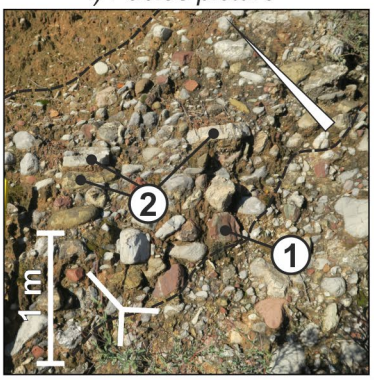

ii) Log expression

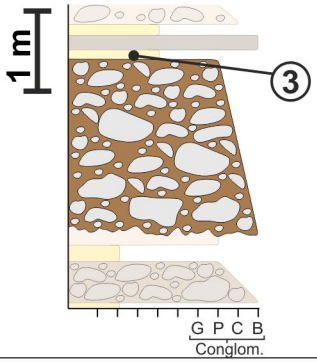

iii) Specific details

1. Well- to moderately-sorted boulder and large cobble clasts at base of bed
2. Common cobble and pebble clast imbrication
3. Frequently succeeded by finer sand facies up-section

C **Facies B-plm** - poorly-sorted loosely packed, massive boulder conglomerate

i) Facies picture

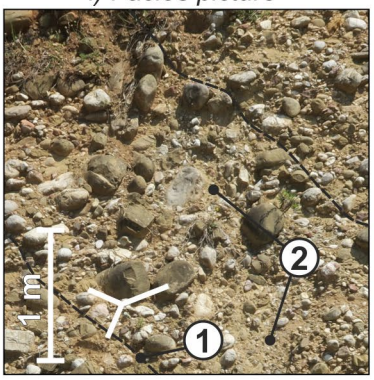

ii) Log expression

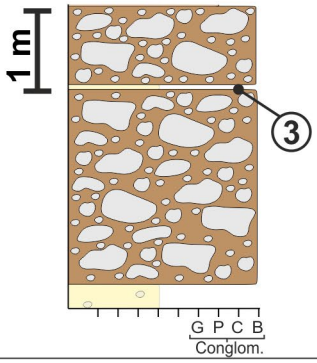

iii) Specific details

1. Bed boundaries typically identified by introduction of boulder clasts, or thin sand facies interbeds
2. Higher matrix proportion of sand and gravel mix
3. Sharp boundary at the top of beds to sand and conglomerate facies

D **Facies B-pll** - poorly sorted conglomerate with sand lenses

i) Facies picture

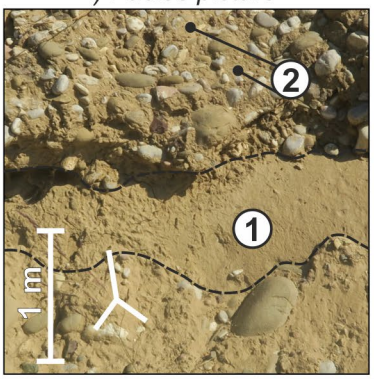

ii) Log expression

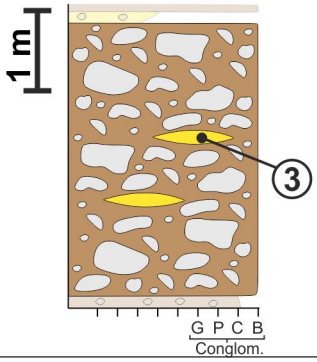

iii) Specific details

1. Typically massive fine-medium sand lenses, often with intermittent pebble / gravel clasts
2. Fine-medium sand matrix, same material as lenses
3. Lenses laterally discontinuous and typically tens of cm thick

E **Facies B-ple** - polymodal conglomerate with clast lenses

i) Facies picture

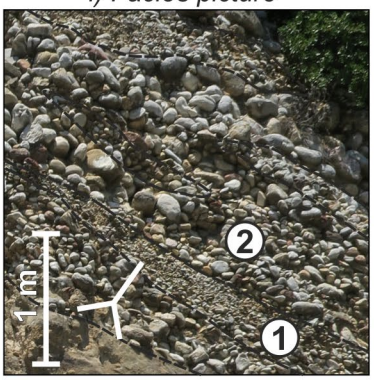

ii) Log expression

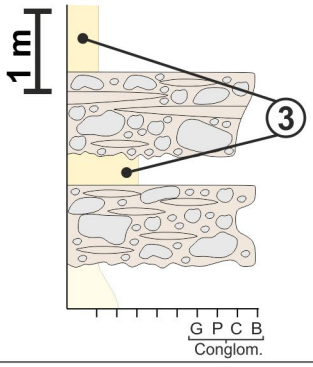

iii) Specific details

1. Stacked lenses of coarser and finer, well-sorted conglomerates
2. Small amount of sand / silt matrix
3. Typically interbedded with sand and silt facies

F **Facies C-rll** - relatively-sorted cobble conglomerate with sand lenses

i) Facies picture

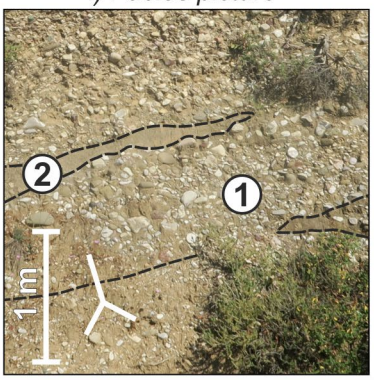

ii) Log expression

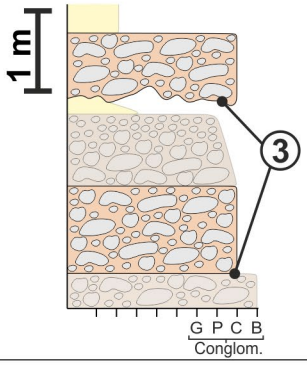

iii) Specific details

1. Relatively sorted cobble and pebble clasts in a fine sand matrix
2. Lenses of fine sand up to 25 cm thick, sometimes contain rare gravel clasts
3. Mixture of erosive bases and sharp bed contacts

G **Facies C-pth** - poorly-sorted, horizontally stratified cobble conglomerate

i) Facies picture

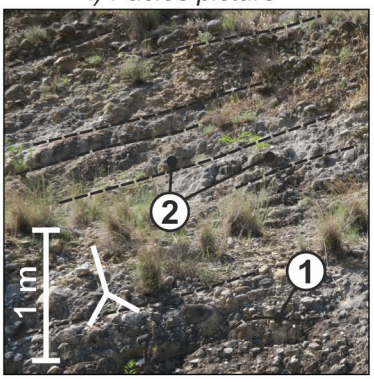

ii) Log expression

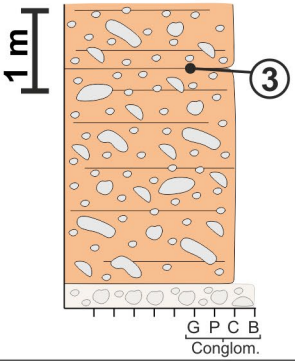

iii) Specific details

1. Horizontal to sub-horizontal stratification through facies
2. Typically flat-lying large cobble clasts with some imbrication present
3. Bed boundaries are sharp and identified from facies changes and outcrop weathering

H **Facies P-wtm** - well-sorted tightly packed pebble conglomerate

i) Facies picture

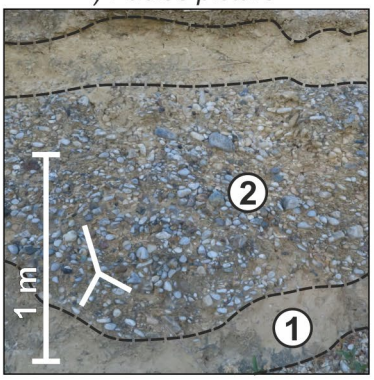

ii) Log expression

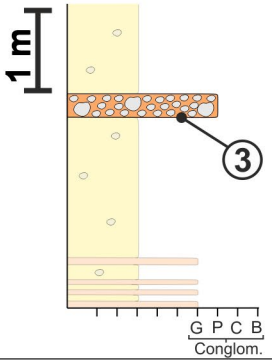

iii) Specific details

1. Well-sorted, massive fine sand / silt facies dominate deposition
2. Form channel-shaped (concave up base) beds or laterally continuous, thin (<25 cm) lenses
3. Channel-shape bodies have erosive bases, extensive lenses have sharp contacts

Figure 5.2A and 5.2B *Details and photo examples of the 8 conglomerate facies from which clast measurements were taken. Conglomerate facies are a mixture of clast-supported and matrix-supported, with drawn sedimentary logs displaying representative clasts from each facies bed. Adapted from Somerville et al. (2020).*

5.3. Methodology

5.3.1. Facies identification

In total, data were collected from 21 locations. For each, vertical profiles were measured from the exposed outcrops. Fifteen lithofacies were identified. Of these, 10 are conglomerate lithofacies, occurring in seven types of architectural elements (as outlined in Chapter 4; 79 total measured architectural elements). Eight of the ten conglomerate lithofacies were studied for detailed clast fabric and texture analyses; two were omitted due to their rare occurrence and difficulty in reaching a measurable facies surface. Conglomerate clast fabrics are documented in terms of packing style, degree of sorting and preferred orientations of groups of clasts; clast textures are documented in terms of size, shape and roundness of individual conglomerate clasts. Facies identification and classification were based on field observations of these features, and this study details the in-depth measurements that describe them quantitatively.

5.3.2. Clast data collection

From each of the 21 visited locations, up to two conglomerate facies were chosen for clast data collection and analysis; typically, in each site only two facies could be sampled due to access issues. Data were collected by (1) identifying an area of 1 x 1 m (1 m^2) where the facies being investigated crops out, (2) identifying the 50 largest visible clasts on the outcrop surface, and (3) measuring and recording data for these 50 clasts. Where a 1 x 1 m section could not be selected because a bedset comprising a conglomerate facies was

less than 1 m thick, or because the only reachable exposed surface for study was less than 1 m^2 in area, the largest measurable conglomerate clast was chosen and 50 total clasts were measured progressively away from this designated start point. In this scenario, measured clasts were chosen based on their size and proximity to the initial clast; larger, closer clasts were prioritised. This may have led to the representation of bias within the data of this secondary measurement method, as it relies on clast prioritisation as opposed to purely the largest 50 clasts within a given area. Nevertheless, only three clast sets (out of a total of 31 collected) employed this secondary method, and are important for data pertaining to facies P-wtm. These methods are similar to those of Nieuwenhuijzen & van Steijn (1990), Yagishita (1997), Miao et al. (2008) and Chen et al. (2016).

In all cases, a lack of 3D outcrop exposure resulted in clast analysis performed on a 2D plane; orientation bias outlined in Chandler & Hubbard (2008) as a result of this was mitigated as much as possible by (i) remaining true to the designated 1 m^2 measurement planes and (ii) not omitting clasts suitable for measurement based on difficulty. Jerram & Higgins (2007) outlined the difficulty in identifying 3D clast or grain sizes from a 2D plane where only a small surface area of a larger object may be exposed. This bias was reduced in part by the preferential erosion of poorly consolidated conglomerate matrix allowing for the exposure of larger parts of clasts helping to better determine their shape, and by removing and replacing clasts in order to measure their sizes and in-situ orientations. Despite these mitigating measures, unintentional bias may be present as a result. Figure 5.3 outlines the sampling strategy in graphical form; this approach was repeated for every set of measurements to ensure systematic data collection and to enable comparisons between the conglomerate facies.

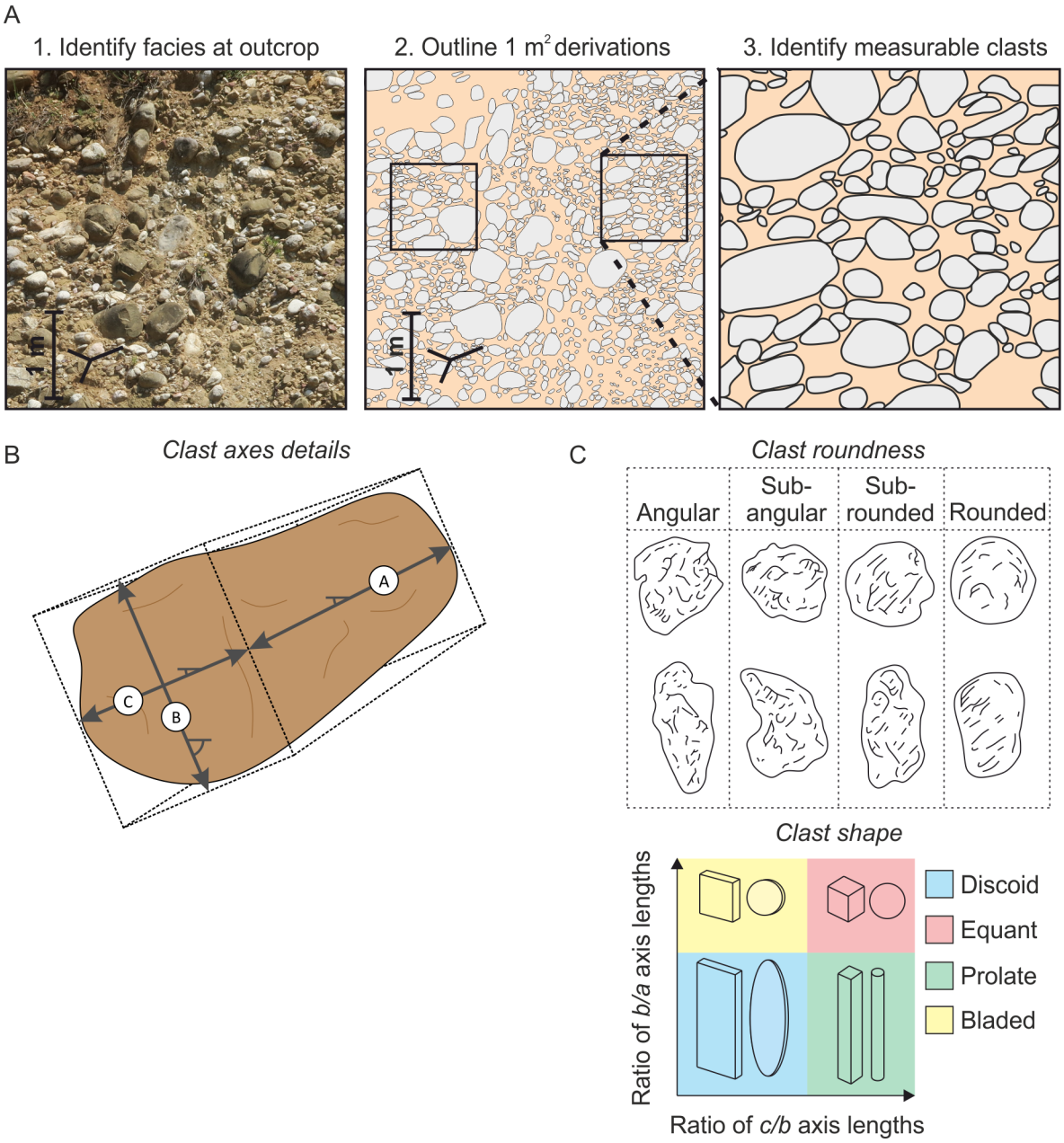

Figure 5.3 *Visual definitions of the clast morphometric, compositional and textural parameters measured for this study. (A) Identification of facies surfaces for detailed clast measurements. (B) Identification of clast axes lengths, dip angles and dip directions. (C) Classification of clast roundness and shapes, after Powers (1953); Collinson & Mountney (2019).*

From the eight conglomerate facies, a total of 1,531 clasts were measured for three qualitative and 10 quantitative parameters. The number of clasts measured per facies is outlined in Table 5.1, whereas the parameters measured for each clast are outlined in Table 5.2. These data are analysed in order to achieve some understanding of: (i) depositional flow processes occurring on the ancient fan surface (orientations of clast axes); (ii) the effect of transport distance and formative-flow type on clast texture (clast shape and roundness) and fabric (clast packing and sorting); (iii) the potential provenance of clasts (clast composition); and (iv) flow directions at time of deposition (palaeocurrent). Palaeocurrent directions have been determined by imbrication measurements from clasts; where a clast was seen to be resting at an angle over another, with respect to the depositional plane, the updip direction was measured as the palaeocurrent reading for that clast (Potter & Pettijohn, 1977). No further palaeocurrent indicators (e.g. inclined cross stratification, sole marks) were identifiable in the conglomeratic succession. Axes lengths were measured by defining the longest axis of the clast first, followed by identification of intermediate and shortest axes, and measuring those lengths with a tape measure. A compass clinometer was then used to measure the orientations and plunges of those axes, resting it adjacent to the clast at the chosen axis. If that axis corresponded to a surface on the clast, the compass clinometer was rested on that surface.

Axis orientation when compared to inferred palaeocurrent direction is referred to in the text in the form 'a(t)b(i)' (as an example) where 'a', 'b' and 'c' correspond to clast long, intermediate and short axes respectively, and the following brackets represent the orientation of that axis (where 'p' is parallel, 't' is transverse and 'i' is imbricated). Distributions in axis lengths have been presented as boxplots, and clast shapes, roundness and compositions have been presented as bar charts.

Facies code	Number of measured clasts
B-wtm	100
B-rlf	300
B-plm	400
B-pll	100
B-ple	81
C-rll	350
C-pth	50
P-wtm	150

Table 5.1 *Number of measured clasts per facies, measured in sets of 50 (one set of 31 clasts). Sets of 50 were recorded where possible, similar to previous studies (Hubbard & Glasser, 2005; Chandler & Hubbard, 2008), as this leads to statistically robust results that are representative of the studied section.*

Parameter	Description
Shape	Defined as discoid, bladed, prolate or equant initially qualitatively in the field, and then by comparison of clast axes lengths.
Roundness	Qualitative measurement recorded in the field based on the diagrams displayed in Figure 5.3.
Composition	Determined by field observations and based on previous studies of the geology of the uplifted Pindos mountains to the north.
Clast long axis (A) length	Measurement in cm (to one decimal place) of the longest axis of an individual clast.
Clast intermediate axis (B) length	Measurement in cm (to one decimal place) of the intermediate axis of an individual clast.
Clast short axis (C) length	Measurement in cm (to one decimal place) of the shortest axis of an individual clast.
Clast A-axis dip	Measurement in degrees of the maximum dip of the longest axis of an individual clast.
Clast B-axis dip	Measurement in degrees of the maximum dip of the intermediate axis of an individual clast.
Clast C-axis dip	Measurement in degrees of the maximum dip of the shortest axis of an individual clast.
Clast A-axis dip direction	Azimuth of the longest axis of an individual clast.
Clast B-axis dip direction	Azimuth of the intermediate axis of an individual clast.
Clast C-axis dip direction	Azimuth of the shortest axis of an individual clast.
Palaeocurrent direction	Bearing measurement of the updip axis of imbricated clasts.

Table 5.2 *Details of the different clast measurements taken in this study.*

5.4. Results

Comparisons between the collected clast data are made in four ways: (i) identifying relationships between clast size, composition, roundness, and shape, and spatial location in the study area; (ii) by interpreted depositional process derived from facies analysis, compared with the orientations of constituent clasts with respect to imbrication and associated interpretations of depositional flow processes; (iii) vertically through the stratigraphy, to determine the evolution of the palaeogeographic environment through time; and (iv) laterally across the basin fill, to determine variations in interpreted depositional flow conditions from relatively more proximal to more distal locations. Graphical displays of the measured data (relating to Figures cited in the text) in section 5.4.2. are displayed in order after each subsection.

5.4.1. Relationships between spatial location and clast size, composition, roundness, and shape

Clast size variations

Clast sizes, in this study represented by clast A-axis lengths, have been used in previous studies to infer the locations of sediment input sources to a basin, and define flow pathways of alluvial fans, based on the interpretation that clast size will decrease downstream as a flow wanes (Blair, 1987; Mack et al., 2002). Figure 5.4 displays the average and maximum A-axis lengths recorded at each of the study sites where clast data was measured. These data give a relative indication of the maximum flow strength that reached that part of the basin (indicated by maximum A-axis length) and of the typical flow strength in that location (indicated by average A-axis length, which may include data from different facies types).

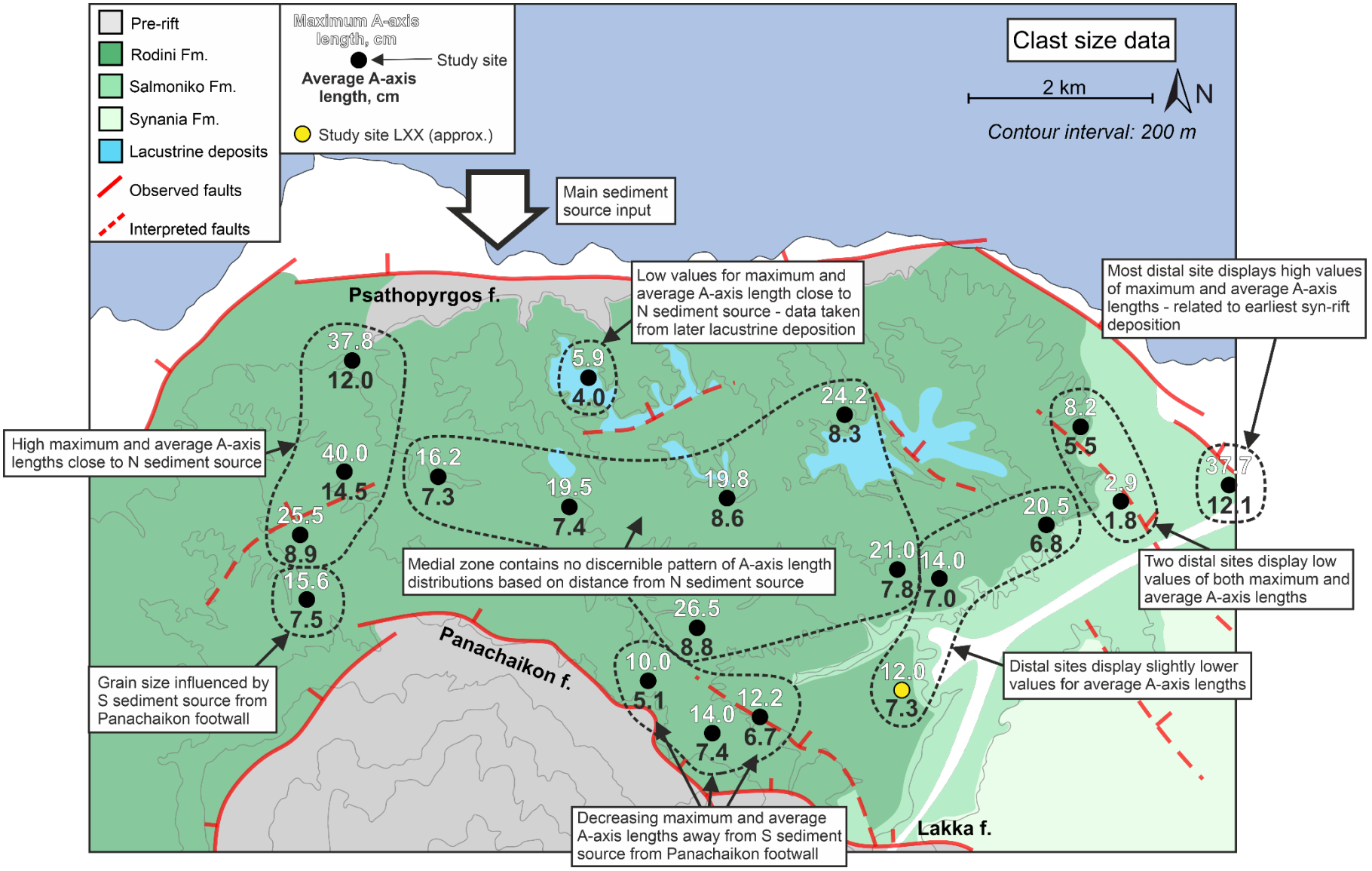
Pre-rift
Rodini Fm.
Salmoniko Fm.
Synania Fm.
Lacustrine deposits
Observed faults
Interpreted faults
Maximum A-axis length, cm
Study site
Average A-axis length, cm
Study site LXX (approx.)
Clast size data
2 km
N
Contour interval: 200 m
Main sediment source input
Psathopyrgos f.
Low values for maximum and average A-axis length close to N sediment source - data taken from later lacustrine deposition
Most distal site displays high values of maximum and average A-axis lengths - related to earliest syn-rift deposition
High maximum and average A-axis lengths close to N sediment source
Medial zone contains no discernible pattern of A-axis length distributions based on distance from N sediment source
Two distal sites display low values of both maximum and average A-axis lengths
Distal sites display slightly lower values for average A-axis lengths
Grain size influenced by S sediment source from Panachaikon footwall
Panachaikon f.
Lakka f.
Decreasing maximum and average A-axis lengths away from S sediment source from Panachaikon footwall
37.8
12.0
5.9
4.0
24.2
8.3
8.2
5.5
37.7
12.1
40.0
14.5
16.2
7.3
19.5
7.4
19.8
8.6
2.9
1.8
20.5
6.8
25.5
8.9
15.6
7.5
21.0
7.8
14.0
7.0
26.5
8.8
10.0
5.1
12.2
6.7
14.0
7.4
12.0
7.3

Figure 5.4 (previous page) *Map of recorded maximum and average A-axis lengths of conglomerate clasts, separated by study site, across the study area. A-axis lengths are used here to represent the sizes of clasts present at each study site. Approximate location of study site LXX is shown. General trends are identified by dashed black lines.*

A weak decreasing trend in both maximum and average A-axis length is observed transitioning from west to east, away from the dominant northerly sediment input source (proximal to distal locations, respectively). Maximum A-axis lengths of 40.0 cm decrease to 16.0 to 25.0 cm lengths in central (medial) locations, before decreasing further to 12.0 to 20.5 cm in eastern (distal) sites. Average A-axis lengths follow similar decreasing trends. These data support the interpretation of a northerly sediment source that is deflected partly to the east by the uplifted Panachaikon footwall, with decreasing clast sizes representing the waning energy of depositional flows. Despite this, large clast sizes are still present in distal locations (e.g., two eastern study sites containing maximum clast A-axis lengths of 20.5 cm and 37.7 cm). This likely represents the spatio-temporal variability of flow strength.

Clast composition variations

The lithology of conglomerate clasts has been used in previous studies of continental deposits in rift settings to determine sediment sources, based on the knowledge of pre-rift basement lithologies and their spatial distribution around the sedimentary basin (Muravchik et al., 2014; Figueiredo et al., 2016). Depending on the lithologies carried by depositional flows, they can also be used as a rough proxy for transport distance, where higher density clasts are deposited in proximal areas, and lower density clasts are more likely to be carried further by the flow as it loses energy.

In this study, the NNW-SSE orientation of pre-rift fold-and-thrust belts leads to the deformed lithologies following that same structural trend (Skourlis & Doutsos, 2003). As a consequence, the pre-rift strata both to the south of the basin forming the Panachaikon footwall, and to the north forming the Pindos mountains of mainland Greece, are similar (Skourlis & Doutsos, 2003; Van Hinsbergen et al., 2005; Piper, 2006; Ford et al; 2016). This is clearly observed in the clast compositional data displayed in Figure 5.5; a mixture of coloured chert lithologies, limestone lithologies, and a prominent brown sandstone lithology, are present at all study locations with few significant discernible patterns. Two identifiable variations include: (i) the presence of increased proportions of sandstone clasts in the south and west of the study area (ten study sites with an average proportion of sandstone clasts of 36.8%, compared to an average of 21.4% across the other ten sites) likely representing an increased amount of sandstone basement forming the Panachaikon footwall compared to the northerly Pindos mountains; and (ii) steadily increasing proportions of chert clasts from west to east within the study area (13-15% total proportion in proximal locations, rising to 26-30% in distal locations).

Figure 5.5 (next page) *Map of conglomerate clast compositions, separated by study site, across the study area. Clast compositions comprise various coloured chert lithologies, limestone lithologies, and a sandstone lithology. The number of recorded clasts for each site is 100, unless otherwise stated (via an adjacent 'n = X' indicator). Approximate location of study site LXX is shown. General trends are identified by dashed black lines.*

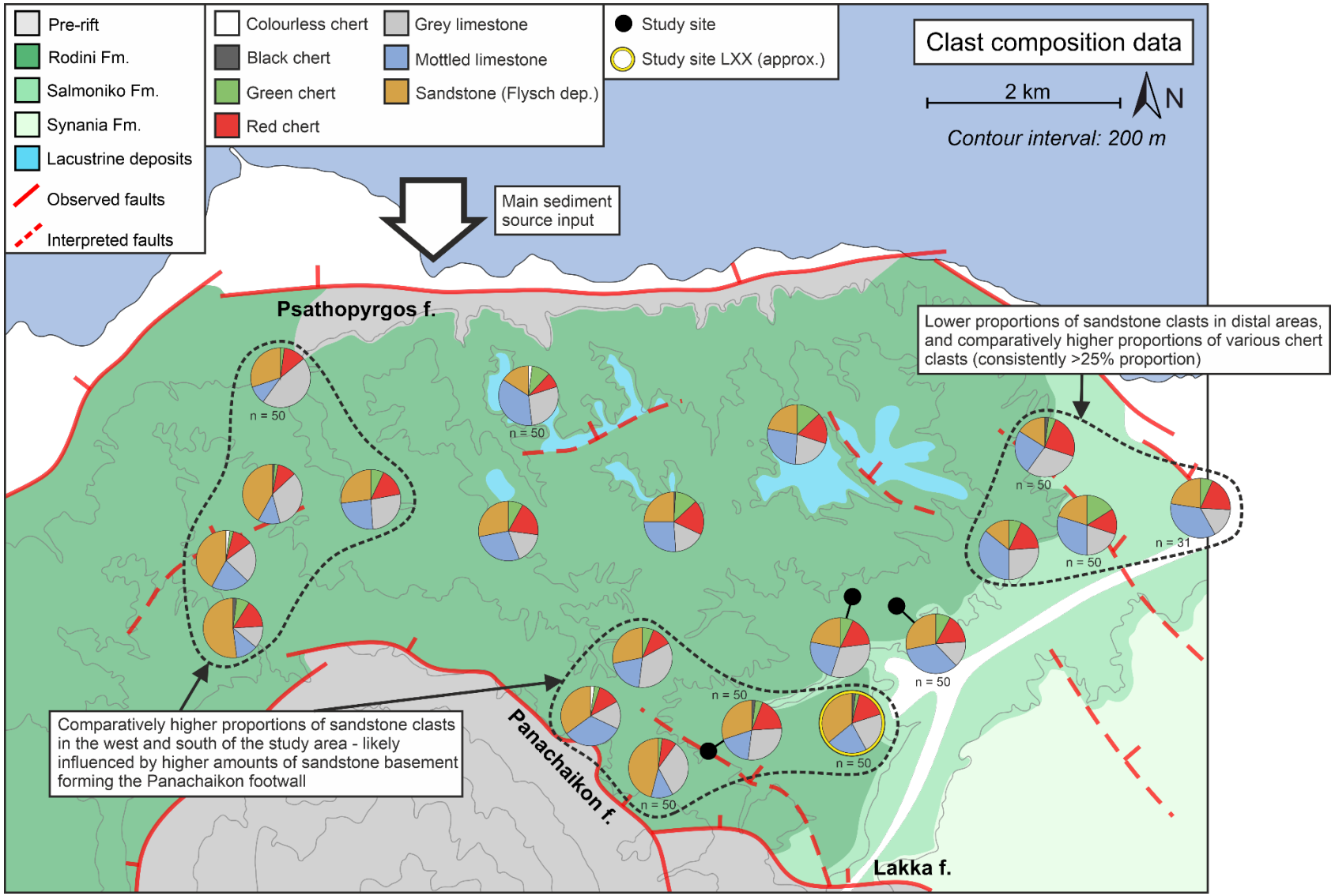
Pre-rift
Rodini Fm.
Salmoniko Fm.
Synania Fm.
Lacustrine deposits
Observed faults
Interpreted faults
Colourless chert
Black chert
Green chert
Red chert
Grey limestone
Mottled limestone
Sandstone (Flysch dep.)
Study site
Study site LXX (approx.)
Clast composition data
2 km
N
Contour interval: 200 m
Main sediment source input
Psathopyrgos f.
Lower proportions of sandstone clasts in distal areas, and comparatively higher proportions of various chert clasts (consistently >25% proportion)
Comparatively higher proportions of sandstone clasts in the west and south of the study area - likely influenced by higher amounts of sandstone basement forming the Panachaikon footwall
Panachaikon f.
Lakka f.
n = 50
n = 31

Clast roundness and shape variations

Roundness and shape variability of conglomerate clasts is interpreted to be a function of transport distance, whereby increasing transport distance corresponds to more rounded clasts, and a trend towards higher proportions of discoid and bladed clasts in fluvial systems. They may also be a function of lithology, as certain types of bedrock break apart into different shapes and variably angular pieces which are subsequently entrained in flows and deposited as clasts.

Figures 5.6 and 5.7 display the variability of clast roundness and shape across the study area. Similarly to the clast composition data, no prominent spatial patterns are discernible, with clasts at all sites being predominantly rounded to sub-rounded, and forming discoid or bladed shapes. The short transport distance from proposed sediment input location to the far east of the study area (approximately 6 km) is likely to be too short to develop observable differences in clast roundness and shape. Further, if the pre-existing drainage catchment to the north that sourced the sediments of the Rodini Fm. was a well-established fluvial system, it is likely that the effects of transport distance within the basin would be masked by the transport occurring within the drainage catchment.

Figure 5.6 (next page) *Map of conglomerate clast roundness, separated by study site, across the study area. Clasts are identified as rounded, sub-rounded, sub-angular, or angular, according to Figure 5.3. The number of recorded clasts for each site is 100, unless otherwise stated (via an adjacent 'n = X' indicator). Approximate location of study site LXX is shown. General trends are identified by dashed black lines.*

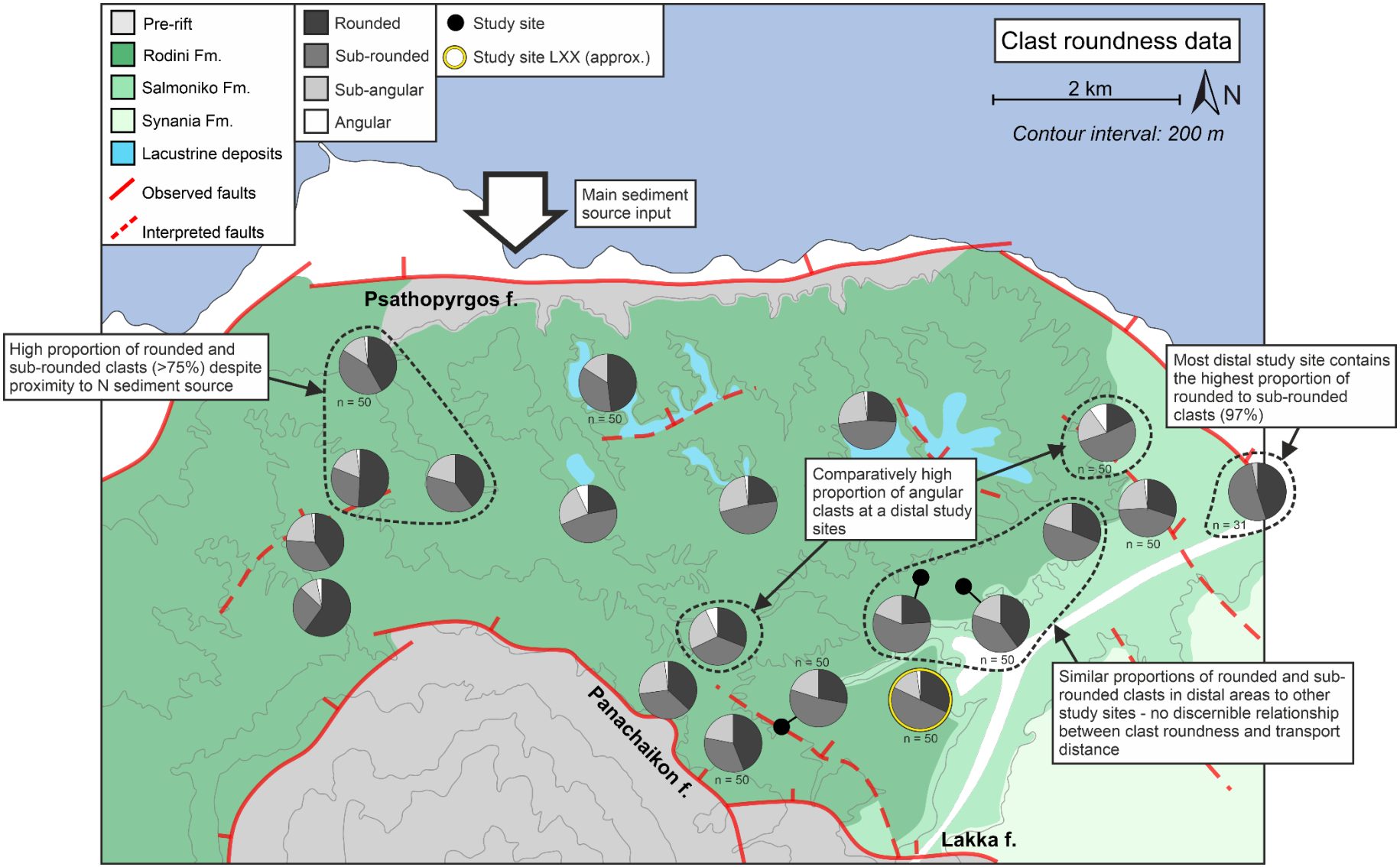
Pre-rift
Rodini Fm.
Salmoniko Fm.
Synania Fm.
Lacustrine deposits
Observed faults
Interpreted faults
Rounded
Sub-rounded
Sub-angular
Angular
Study site
Study site LXX (approx.)
Clast roundness data
2 km
N
Contour interval: 200 m
Main sediment source input
Psathopyrgos f.
High proportion of rounded and sub-rounded clasts (>75%) despite proximity to N sediment source
Comparatively high proportion of angular clasts at a distal study sites
Most distal study site contains the highest proportion of rounded to sub-rounded clasts (97%)
Similar proportions of rounded and sub-rounded clasts in distal areas to other study sites - no discernible relationship between clast roundness and transport distance
Panachaikon f.
Lakka f.
n = 50
n = 31

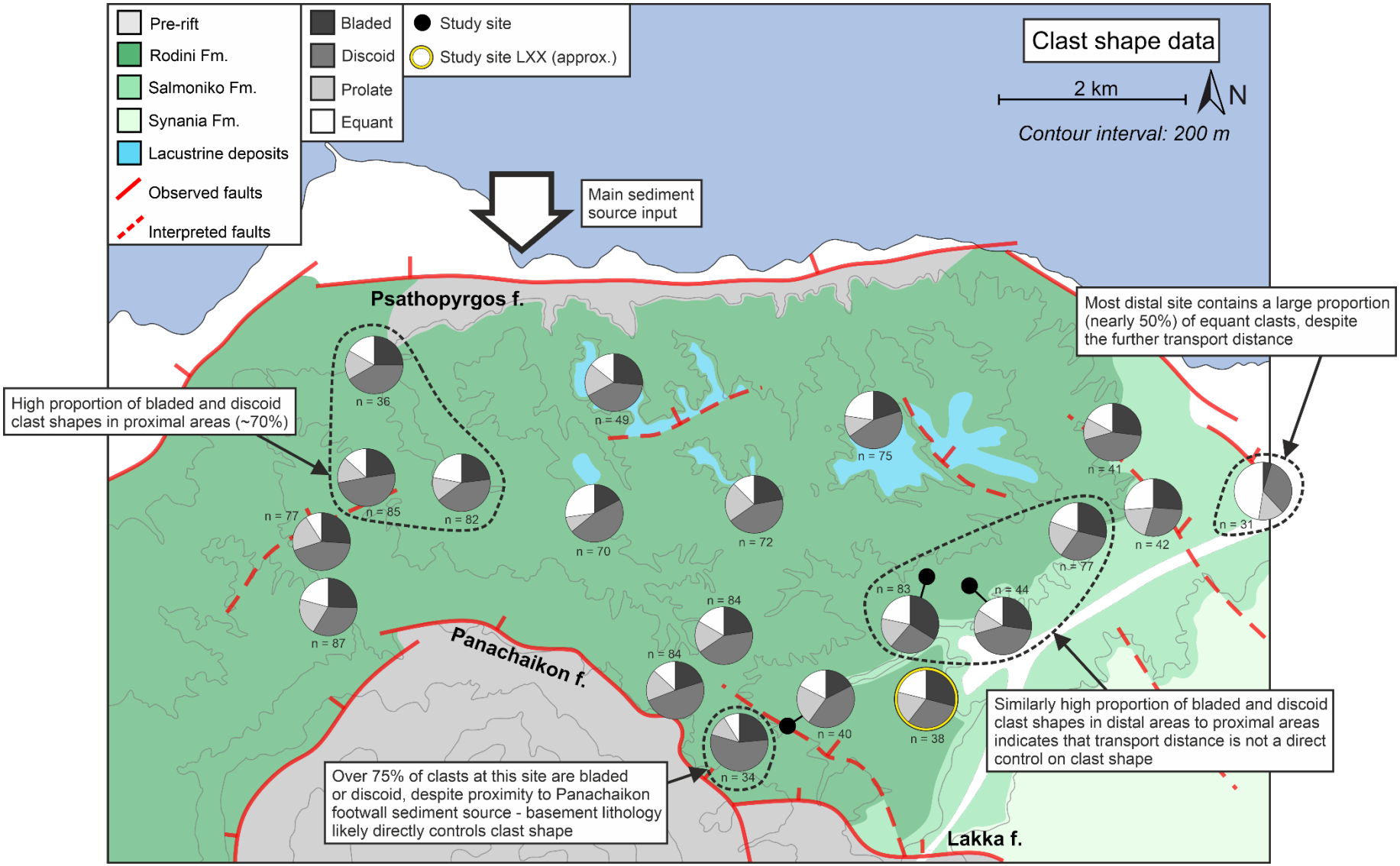
Pre-rift
Rodini Fm.
Salmoniko Fm.
Synania Fm.
Lacustrine deposits
Observed faults
Interpreted faults
Bladed
Discoid
Prolate
Equant
Study site
Study site LXX (approx.)
Clast shape data
2 km
N
Contour interval: 200 m
Main sediment source input
Psathopyrgos f.
Panachaikon f.
Lakka f.
High proportion of bladed and discoid clast shapes in proximal areas (~70%)
Most distal site contains a large proportion (nearly 50%) of equant clasts, despite the further transport distance
Similarly high proportion of bladed and discoid clast shapes in distal areas to proximal areas indicates that transport distance is not a direct control on clast shape
Over 75% of clasts at this site are bladed or discoid, despite proximity to Panachaikon footwall sediment source - basement lithology likely directly controls clast shape
n = 36
n = 49
n = 75
n = 41
n = 31
n = 85
n = 82
n = 77
n = 70
n = 72
n = 42
n = 77
n = 87
n = 84
n = 83
n = 44
n = 84
n = 40
n = 38
n = 34

Figure 5.7 (previous page) *Map of conglomerate clast shapes, separated by study site, across the study area. Clasts are identified as bladed, discoid, prolate, or equant, according to that clast's ratio of A-axis length : B-axis length : C-axis length (Zingg classification). The number of recorded clasts for each site is stated via an adjacent 'n = X' indicator. Approximate location of study site LXX is shown. General trends are identified by dashed black lines.*

5.4.2. Relationships between depositional flow process and clast orientations

Table 5.1 outlines the conglomeratic facies of the study area. Interpretations of their depositional setting and flow processes are outlined in Chapter 4 (Table 4.1). The eight conglomerate facies for which clast data were collected can be separated, based on their interpreted depositional flow processes, into two groups; facies deposited through non-cohesive debris flow processes (5 facies), and facies deposited through a mixture of flow processes, but predominantly hyperconcentrated- and stream-flow processes (3 facies). For each group, descriptions of clast orientations, and further detail on depositional flow processes derived from those clast orientations, are provided.

Non-cohesive debris flow dominated facies

The orientation data recorded for these 5 facies are displayed in Figure 5.8.

*Facies B-wtm (**B**oulder – **w**ell-sorted, **t**ightly packed, **m**assive)*

Observations: This facies only occurs in two study sites, located in the centre-west of the study area, and corresponding to a proximal to medial fan setting. The clasts are dominantly orientated with their C-axes perpendicular to the bedding plane, making their elongation sub-parallel to the bedding plane. One site displays prominent A-axis parallel imbrication (a(t)b(p), see section 5.3.2.), whereas the second site displays prominent B-axis parallel imbrication (a(t)b(i)) (Figure 5.8).

Interpretations: Containing the majority of the largest clasts seen across all sites, this facies represents the depositional expression of proximal debris flows (Somerville et al. 2020). Flows were potentially sourced from different areas of the larger northern catchment, as different parts of that catchment were likely preferentially eroded through time (cf. Nieuwenhuijzen & van Steijn, 1990; Bremer & Sass, 2012; Grelle et al., 2019). The matrix is dominated by gravel, as opposed to clay- to silt-grade sediment, resulting in non-cohesive flows (Johnson, 1970; Costa, 1984). The flows likely manifested as lobes resulting in incremental deposition of the facies, supported by low angle imbrication and sub-parallel clasts as indicated by short-axis orientation perpendicular to bedding surfaces (Major, 1997; Sohn et al., 1999). Observed a(t)b(p) clast orientations may arise as pebbles, cobbles and boulders become stacked and are pushed sideways at the front of lobe deposits (Major, 1998).

*Facies B-plm (**B**oulder – **p**oorly-sorted, **l**oosely packed, **m**assive)*

Observations: This facies is present at 7 locations, spread across the study area and corresponding to the medial to distal fan setting. In all sites bar one, the clasts of this facies are orientated with their C-axes dominantly perpendicular to the bedding plane, indicating clasts are near-flat lying. There is a strong mix between A-axes and B-axes being variably parallel to palaeoflow, regardless of location within the study area, however A-axes are typically more strongly aligned among all study sites (Figure 5.8).

Interpretations: The lack of clast sorting and grading in beds of this facies, in conjuncture with an increased proportion of silt- to sand-grade matrix, led to an interpretation of deposition by non-cohesive debris flows with high proportions of suspended sediment (Somerville et al., 2020). Typically found in the medial to distal fan setting both in the west and east of the study area, the debris flows were likely more powerful than those

that formed other facies and were deposited by frictional freezing of sediment (facies B-wtm) (e.g. Blair & McPherson, 1994; Blair & McPherson, 1998; Kim & Lowe, 2004). Two sets of data (one from site L7, and site L11) display A-axes clast orientations perpendicular to inferred palaeoflow (a(t)); measured intermediate axes in these data display weak alignment indicating the a(t) orientations are likely driven by the rotation and rolling of clasts transverse to flow direction at the head of a cohesionless debris flow (Major, 1998; Sohn et al., 1999) indicating flow had the potential to reach the medial to distal fan areas before either the cessation of sediment transport or the transition to more fluidal flow types (Bertran et al., 1997; Sohn et al., 1999).

*Facies B-pll (**B**oulder – **p**oorly-sorted, **l**oosely packed, **l**enses (sand))*

Observations: This facies is present at 2 locations, one in the south of the study area and one to the west. For the southern site, sediment is interpreted to be sourced from the uplifted footwall to the south; the western site is in a medial fan setting. All clasts are aligned near-flat to bedding planes, with C-axes perpendicular to those planes. A-axes and B-axes are both poorly aligned at both sites, with A-axes dominantly orientated parallel to palaeoflow at the southern site. In the western site, this facies does not display a dominant axis orientation relative to palaeoflow direction (Figure 5.8).

Interpretations: Similarities of these conglomerates to those of facies B-plm make this facies interpretable as the product of non-cohesive debris flows (Somerville et al., 2020); the presence of sand lenses might indicate a trailing hyperconcentrated flow, deposits of which were later eroded by subsequent flows leaving lens-shaped bodies of sand (Pierson & Scott, 1985; Pierson, 2005). Such sand lenses are considered as part of this facies due to their intimate genetic relation to the conglomerate, and therefore likely formed as part of the same flow event. The variability in orientations of A-axes and B-

axes at both sites is similar to that seen for facies B-plm, indicating a similar fabric organization by non-cohesive flow types; A-axes at the southern site are orientated parallel to palaeoflow, likely indicating their proximity to the source area (the uplifted footwall to the south) as a reduced transport distance inhibits a(t)b(i) orientations formed through bedload transport or the generation of a clast-rich lobe front. The presence of sand lenses within the conglomerate facies as opposed to distinctive, laterally extensive, well-developed massive sand beds (similar to those present at other medial to distal sites e.g. L3, L4, L5, L11) may represent a reduction in volume of sand-grade suspended sediment within depositional flows. This may be a function of both depositional units being sourced from comparatively smaller catchments formed in the uplifted footwall to the south, reducing the available sediment load and resulting in smaller hyperconcentrated flow deposits (Mack & Leeder, 1999; Mao et al., 2009).

*Facies C-rll (**C**obble – **r**elatively-sorted, **l**oosely packed, **l**enses (sand))*

Observations: This facies is present at 6 locations across the study area, corresponding to proximal (L2, L16, L10) and distal (L11, L12, LXX) fan settings. Clasts orientations are dominantly near-flat with respect to bedding planes (C-axes perpendicular to bedding), whereas both A-axes and B-axes appear preferentially orientated at all sites, particularly with respect to all previous examples (where B-axis preferential orientation is rare). Facies in the far south locations typically have clasts with A-axes parallel to palaeoflow direction, whereas facies in the central and eastern sites (proximal and distal locations, respectively) dominantly display clast B-axes orientated parallel to palaeoflow (Figure 5.8).

Interpretations: Similarities with facies B-pll and the lack of boulder clasts led to an interpretation of formation by the frictional freezing of higher energy non-cohesive

debris flows (Iverson, 1997; Sohn et al., 1999). In relatively more distal locations, observed a(t)b(i) clast orientations are indicative of the movement of clasts to the front of the debris flow, which then align parallel with the front of the evolving lobe, similar to the results of Nieuwenhuijzen & van Steijn (1990), Bertran et al. (1997), Major (1998) and Moscariello et al. (2002). In the two southern study sites (L10, L16) a(p) clast orientations to palaeoflow direction are indicative of rapid deposition in proximal areas close to their proposed source area of the southern uplifted footwall.

*Facies C-pth (**C**obble – **p**oorly-sorted, **t**ightly packed, **h**orizontally stratified)*

Observations: This facies is present at one location in the north-west of the study area, equivalent to the proximal fan setting. Clast orientations are near-flat with respect to bedding planes (C-axes perpendicular to bedding) with the inclination and alignment of A-axes occurring parallel to the inferred palaeoflow direction at the site. B-axes appear to be randomly orientated with a wide spread of inclinations (Figure 5.8).

Interpretations: Horizontal stratification of the beds leads to an interpretation of repeated laterally extensive flows and deposition through incremental sedimentation as those sediment-laden flows became unconfined on entry to the basin near the fan apex (Major, 1997; Clarke et al., 2010; Somerville et al., 2020). The orientation of clast A-axes parallel to palaeoflow direction is indicative of rapid sediment deposition following grain-grain interactions in non-cohesive flows (Eyles & Kocsis, 1988; Bertran et al., 1997). The orientation of C-axes perpendicular to stratification surfaces and the alignment of clasts sub-parallel to those surfaces likely indicates the incremental deposition of unconfined flow bodies (Major 1997; Manville & White, 2003).

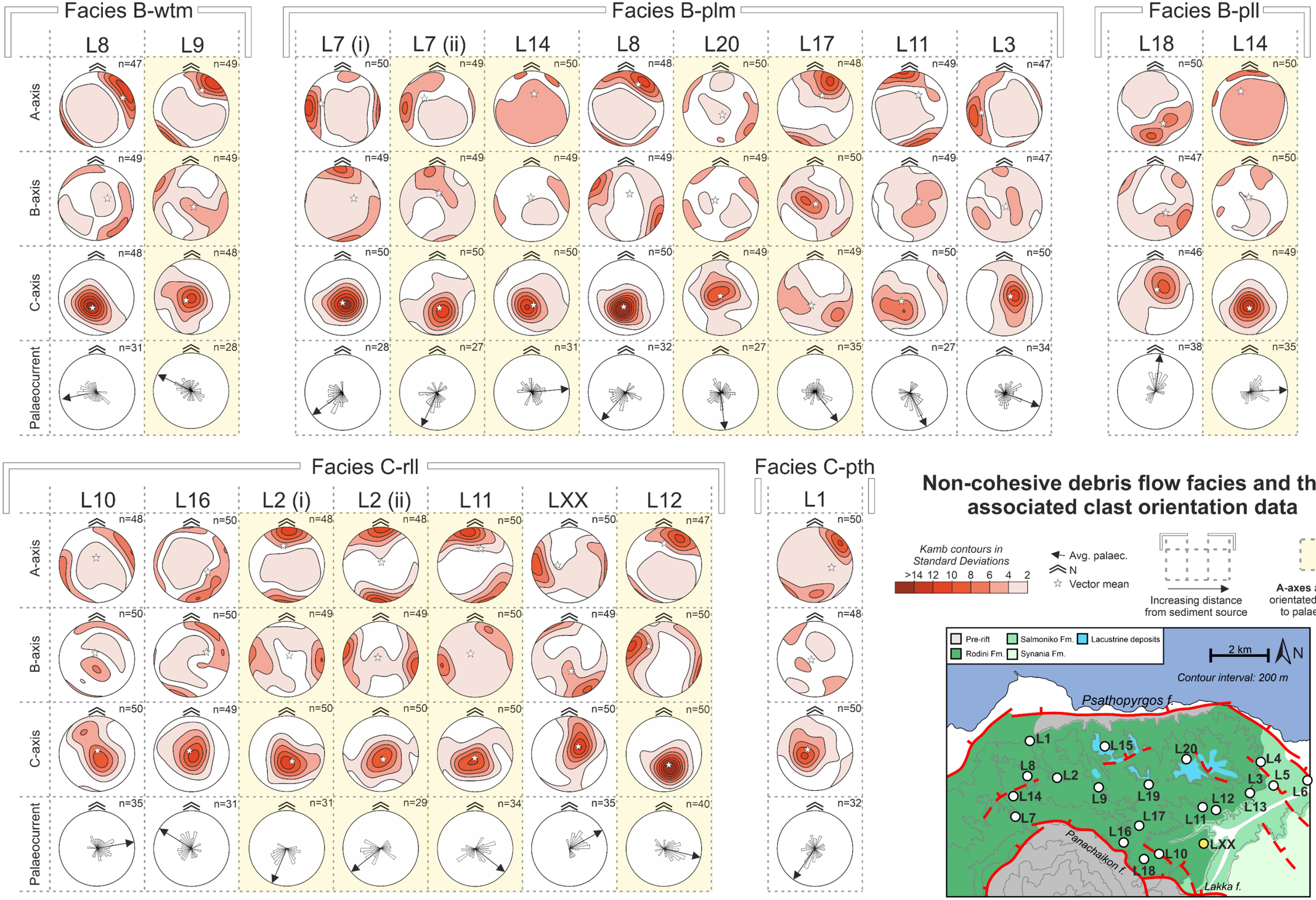
Facies B-wtm
L8
L9
Facies B-plm
L7 (i)
L7 (ii)
L14
L8
L20
L17
L11
L3
Facies B-pll
L18
L14
A-axis
B-axis
C-axis
Palaeocurrent
Facies C-rll
L10
L16
L2 (i)
L2 (ii)
L11
LXX
L12
Facies C-pth
L1
Non-cohesive debris flow facies and their associated clast orientation data
Kamb contours in Standard Deviations
>14 12 10 8 6 4 2
Avg. palaec.
N
Vector mean
Increasing distance from sediment source
A-axes are not orientated parallel to palaeoflow
Pre-rift
Salmoniko Fm.
Lacustrine deposits
Rodini Fm.
Synania Fm.
2 km
N
Contour interval: 200 m
Psathopyrgos f.
Panachaikon f.
Lakka f.
L1
L15
L20
L4
L8
L2
L3
L5
L6
L14
L9
L19
L12
L13
L7
L17
L11
L16
LXX
L10
L18

Figure 5.8 (previous page) *Contoured stereonets displaying clast axis orientation data, separated by host facies. The facies represented here are interpreted as being deposited by non-cohesive debris flow processes. Recorded datasets highlighted in yellow represent sets not displaying a(p)b(t) clast orientations. As these facies are interpreted as the product of non-cohesive debris flow processes, they are consequently interpreted to have been deposited rapidly with minimal tractional bedload rolling, which would typically manifest as a(p)b(t) clast orientations.*

Hyperconcentrated- and stream-flow dominated facies

The orientation data recorded for these 5 facies are displayed in Figure 5.9.

*Facies B-rlf (**B**oulder – **r**elatively-sorted, **l**oosely packed, **f**ines upward)*

Observations: This facies is present at 5 locations, dominantly in the centre of the study area, corresponding to a medial to distal fan setting. At all sites, the clasts are typically elongated parallel to the bedding planes, with C-axes perpendicular to bedding. The preferential orientation of A-axes with respect to palaeoflow varies across study sites: in two sites, A axes are dominantly oriented parallel to the palaeoflow direction, in one site they are dominantly perpendicular, whereas in two other sites clasts variably display A-axes or B-axes parallel to palaeoflow (Figure 5.9).

Interpretations: The normal grading of this facies type and its erosional contact and lenticular shape are consistent with an interpretation of high energy bedload stream deposits that waned through time and were recorded as a single facies unit (Somerville et al., 2020). A wide mix of clast-axis orientations suggests that more than a single mode of sediment transport may be recorded in this facies; the preferential orientation of A-axes indicates a large degree of grain-to-grain interaction in a reduced-matrix setting (Bertran et al., 1997). This is typical, in conjunction with resultant normal grading and

overlying sand-grade facies containing intermittent pebbles, of rapid sediment deposition from tripartite non-cohesive debris flows immediately succeeded by hyperconcentrated flows and streamflow conditions (Sohn et al., 1999, Benvenuti & Martini, 2002). The presence of some a(t)b(p) clast orientations may indicate bedload conditions and either the formation of streamflows on the fan surface (forming conglomerate facies similar to those in Mack & Leeder, 1999; Hemelsdaël et al., 2017) or combined debris-hyperconcentrated-stream – flows similar to those described in Sohn et al. (1999).

*Facies B-ple (**B**oulder – **p**oorly-sorted, **l**oosely packed, l**e**nses (stacked conglomerate))*

Observations: This facies is present at 2 locations in the far east of the study area, corresponding to a distal fan setting. Clast orientations are typically near-flat with respect to bedding planes (C-axes perpendicular to bedding) and have well-established alignments of clast A-axes parallel to the inferred palaeoflow direction at both sites (Figure 5.9).

Interpretations: The lower proportion of matrix in this facies, combined with each depositional unit being comprised of discontinuous lenses of moderately to well-sorted pebble to cobble grade clasts, led to an interpretation of deposition by variable strength waxing and waning stream flows in relatively distal fan locations (Somerville et al., 2020). Established a(p) clast orientations derived from these data are indicative of higher sediment concentrations within flows and the rapid deposition of non-tractional sediment (Nemec, 2009). This may represent deposition by hyperconcentrated flows, the higher energy of which explains the presence of boulder clasts at these distal locations (Hubert & Filipov, 1989; Blair & McPherson, 1998). The generally high roundness of the

clasts is further evidence for a distal fan location, relatively greater transport distance, and potential reworking of earlier fan deposits (Dec, 1992; Chamyal et al., 1997).

*Facies P-wtm (**P**ebble – **w**ell-sorted, **t**ightly packed, **m**assive)*

Observations: This facies is present at 3 locations in the study area, in the north, east, and south. These correspond to the proximal and distal fan settings, and to a sector fed by the uplifted southern footwall, respectively. Clasts are strongly orientated to near-flat with respect to bedding planes (C-axes perpendicular to those planes). A-axes are moderately preferentially orientated, and B-axes are poorly orientated. A-axes or B-axes are never orientated parallel to the palaeoflow direction (Figure 5.9).

Interpretations: The comparatively smaller, texturally mature clasts, in conjunction with a well-sorted fabric and typically 2D lenticular geometries, leads to an interpretation of deposition as the bedload of streamflows (Somerville et al., 2020). Channel geometries and interpretation of bedload deposition should be associated with clast B-axes aligning parallel to palaeoflow as clasts imbricate along the ab-plane and dip upstream (Yagishita, 1997). This is not the case for this facies, potentially indicating that (i) these deposits may have formed as a result of erosion and run-off on the fan surface of pebble-grade material (Larsen & Steel, 1978; de Haas et al., 2014) reorientating clasts and inhibiting the development of B-axis parallel imbrication, or (ii) these deposits originally formed from hyperconcentrated flows generated by dilution at the front of debris flows as they entered fan surface channels, depositing pebble-grade sediment by frictional freezing of the coarsest sediment load (Sohn et al., 1999; Benvenuti & Martini, 2002).

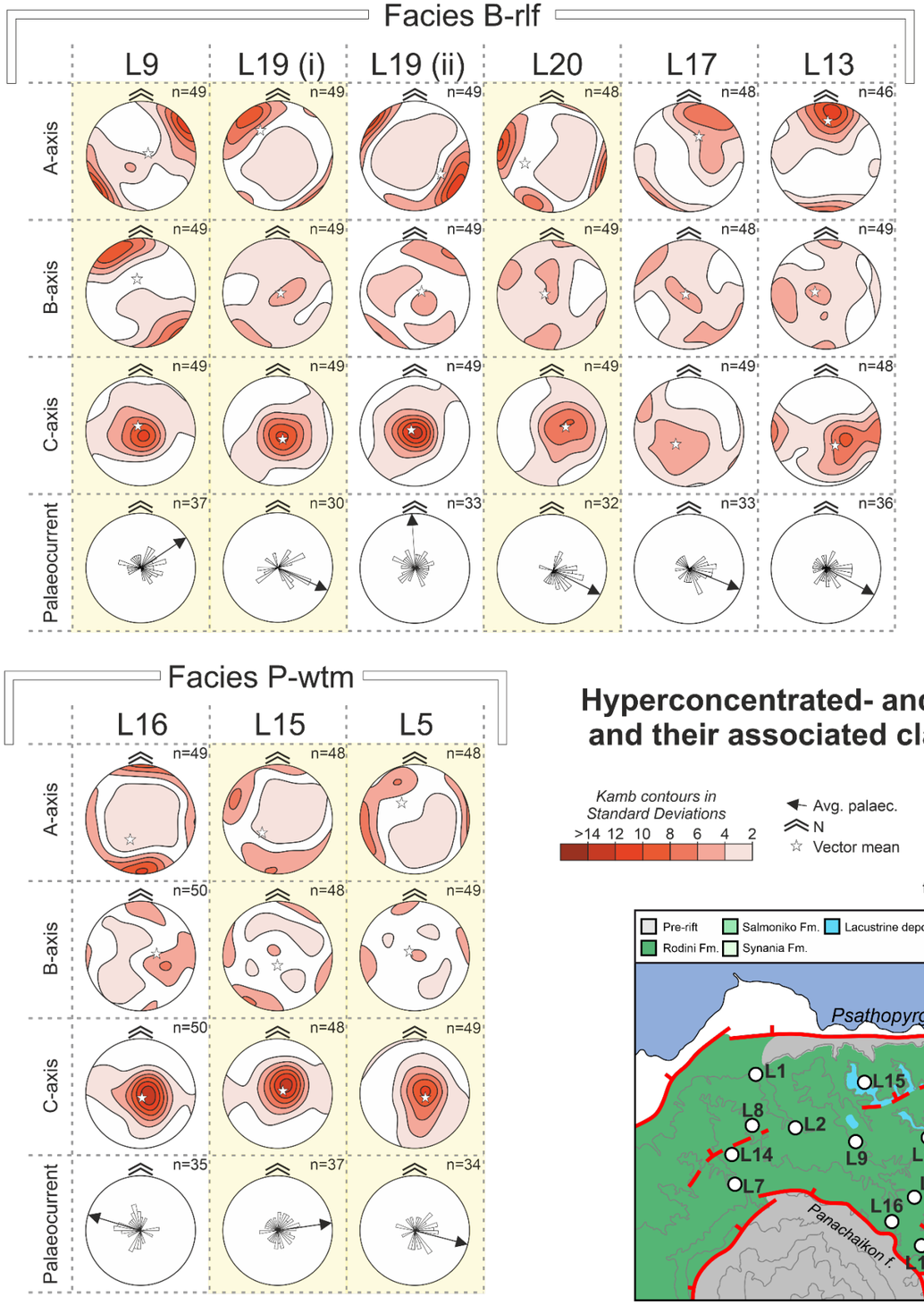

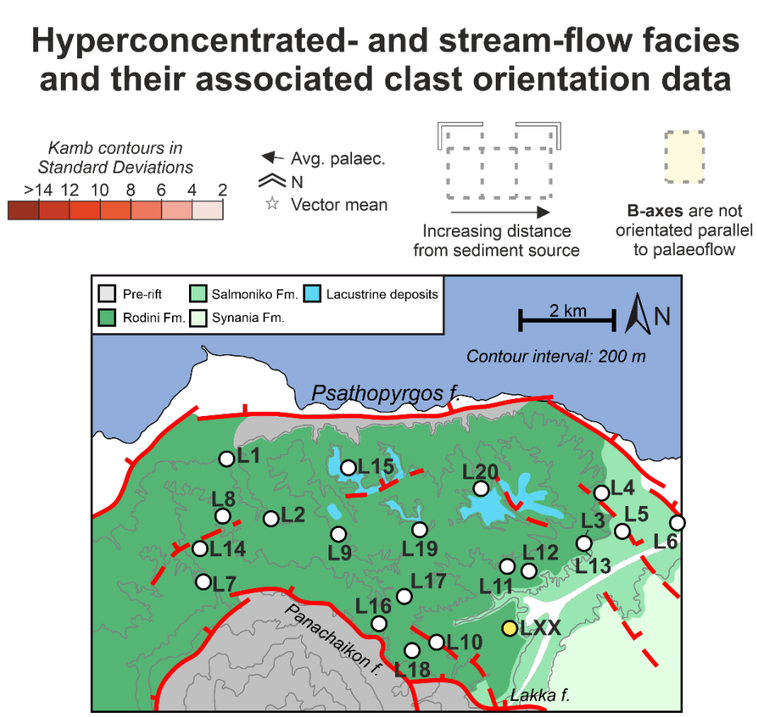

Figure 5.9 *Contoured stereonets displaying clast axis orientation data, separated by host facies. The facies represented here are interpreted as being deposited by a mixture of hyperconcentrated- and stream-flow processes. Recorded datasets highlighted in yellow represent sets not displaying a(t)b(i) clast orientations. As these facies are interpreted as the product of hyperconcentrated- and stream-flow processes, they are consequently interpreted to have been deposited via variable amounts of tractional bedload rolling, which would typically manifest as a(t)b(i) clast orientations.*

5.4.3. Relationships between stratigraphic interval and clast fabrics

Each study site from which data was collected was assigned to a stratigraphic interval, determined based on its elevation and the average strike and dip of the strata. The three intervals correspond to early, middle, and late phases of deposition of the Rodini Fm. (henceforth stratigraphic intervals 1, 2 and 3, respectively) (Chapter 4).

Stratigraphic interval 1

Observations: This stratigraphic interval is observed at 6 sites, located in the northwest and east of the study area (Figure 5.12A). Clast sizes are dominated by large pebbles and small cobbles (A-axes lengths of 6 to 12 cm) with some larger cobbles (up to 20 cm) and one measured oversized clast (37 cm) (Figure 5.12C). Clast shapes are typically discoid or equant (combined proportions of 80% to 92% of total measured clasts) (Figure 5.12D, E). Only 7 sub-angular to angular clasts were recognised across all measured clasts (total of 331) (Figure 5.12E). Clast compositions are dominated by limestones and sandstones, with more compositional variability between sites in the north-west than in the east (Figure 5.12E). Clast C-axes are orientated perpendicular to bedding planes at all sites; north-western sites are dominated by north-south (N-S) orientated A-axes, whereas eastern sites display a dominant east-west (E-W) A-axes orientation (Figure 5.12F).

Interpretations: The onset of accommodation generation is well documented to be associated with the influx and deposition of coarse-grained sediment in rift settings (Gawthorpe et al., 1994; Gawthorpe & Leeder, 2000; Graham et al., 2001), typically leading to the formation of an initial conglomeratic syn-rift unit before the establishment of longer-lived depositional environments (Gawthorpe & Leeder, 2000). In this case, the strike of the newly formed basins was perpendicular to the orientation of drainage (E-W and N-S, respectively) (Somerville et al., 2020) leading to the establishment of an alluvial

environment and a conglomeratic unit. The orientation of A-axes changes from N-S alignment to E-W alignment from proximal to distal locations, in accord with proposed palaeoflow directions of southward and subsequently eastward flow, as drainage is diverted to the established depocentres to the east (Ford et al., 2016; Gawthorpe et al., 2018). Proximal areas experienced deposition of lobate units from non-cohesive debris flows, where the transition of confined to unconfined flows as they entered an open, shallow basin led to incremental deposition and spreading of the flow before the establishment of a dominant fan surface, similar to deposits modelled by Clevis et al. (2003) and observed by Ventra et al. (2013). Conglomerate deposition may have occurred in the east, away from the subsidence loci of the Panachaikon fault to the south, due to (i) the overfilled nature of the basin masking any slope development or (ii) the presence of the south-dipping Trizonia fault to the east generating an east-dipping gradient and attracting more fluidal flows (leading to B-ple facies deposition).

Stratigraphic interval 2

Observations: This stratigraphic interval comprises 7 sites, evenly spread across the study area from west to east (Figure 5.13A). Clast sizes are dominated by large pebbles and small cobbles (A-axes lengths of 5 to 11 cm) with some larger cobbles (up to 25 cm). Oversized clasts are present in a range of sizes up to 40 cm (Figure 5.13C). Clasts are dominantly discoid in shape, with all but one site (L11) recording >50% discoid clasts (Figure 5.13D, E). These clasts are increasingly rounded to the west (>50% rounded clasts, dropping to 24 to 40% to the east) with the majority of sub-angular to angular clasts in the centre of the study area (4 to 12% proportion) (Figure 5.13E). There is a high proportion of sandstone clasts in the western sites (L7, L8) of 38 to 66%, dropping to 16% proportion to the east (L13); other clast compositions are variable in proportion across the study area but with no obvious pattern discernible (Figure 5.13E). Clast C-axes

are orientated perpendicular to bedding planes at all sites. Clast A-axes are orientated in an array of directions, from E-W (southwest in the study area; L7) to NE-SW (west, centre and south in the study area; L8, L9, L10) to N-S (east in the study area; L11, L12, L13) (Figure 5.13F).

Interpretations: The establishment of major faulting likely coincided with increased rates of accommodation generation (Gawthorpe & Leeder, 2000) and an increase in the gradient of the hangingwall dipslope. This led to the formation of an established alluvial fan (Somerville et al., 2020). Repeated non-cohesive debris flows (indicated by the prevalence of facies B-wtm, B-plm and C-rll, Figure 5.13B) into the basin had longer runout distances than the lobes of interval 1, due to the presence of proximal deposits introducing local topography and an increased depositional gradient toward the south and east as fault activity continued. Clast a(t) orientations to the east in sites L11, L12 and L13 could correspond to the deposition of debris-flow fronts, where clasts became orientated parallel to the closest edge of their transporting flow, which at the flow front would be perpendicular to inferred palaeoflow direction to the east (Major, 1998). The increased frequency of boulder-grade clasts in comparison to the earliest syn-rift deposits can be attributed to the increase in gradient of the hangingwall dipslope as unfilled accommodation was progressively generated, and the subsequent progradation of proximal (close to the fan-apex) facies into this part of the basin (Mack et al., 2008).

Stratigraphic interval 3

Observations: This stratigraphic interval was observed at 7 sites, one in the west of the study area and the others spread evenly along a north-south transect through the centre of the study area (Figure 5.14A). Clast sizes are dominated by large pebbles and small cobbles (4 to 10 cm A-axes lengths) with some larger cobbles (up to 20 cm) and rare small

boulders (>27 cm) (Figure 5.14C). Clasts are dominantly discoid throughout, with higher proportions of discoid clasts in the centre and north of the study area (52 to 68% proportion; L15, L17, L19, L20) (Figure 5.14D, E). Clast roundness is higher in the west and south (34 to 48% rounded clasts; L14, L16, L18) than the centre of the area (20 to 28% rounded clasts; L17, L19, L20) (Figure 5.14E). Sandstone clasts are increasingly common in the west and south of the study area (32-46% proportion; L14, L16, L18) and less common in the centre and north (16 to 30% proportion; L15, L17, L19, L20). The proportions of different limestone clasts vary across the sites in this interval (Figure 5.14E). Clast C-axes are orientated perpendicular to bedding planes at all sites bar one (L17). A-axes are well orientated at sites in the centre of the study area (L16, L17, L19, L20) and fluctuate from N-S alignment (L16, L17) to NW-SE alignment (L19, L20) (Figure 5.14F).

Interpretations: During this interval the alluvial-fan environment is well established, indicated by a high proportion of potentially channelised facies (B-rlf, P-wtm) formed during the final stage of sedimentation before the rupturing of the Psathopyrgos fault (Somerville et al., 2020). Despite channelisation, the alignment of A-axes parallel to palaeoflow directions (southward in the centre of the study area, changing to eastward flow in the east of the study area), in conjunction with normal grading, indicates continued sediment deposition via the deposition of coarser clasts at the frictional base of a hyperconcentrated flow (Pierson 2005; Calhoun & Clague, 2018). The evidence of clasts 'rolling' at the base of the flow, which would typically generate a(t)b(i) orientations (Yagishita, 1997), is absent. As flows entered the basin, the presence of incipient channels on the alluvial fan surface may have led to flow dilution of non-cohesive debris flows (as described by Pierson & Scott, 1985; Pierson, 2005) causing an increased frequency of hyperconcentrated flows, shown by the dominance of B-rlf facies in the medial fan

setting. It may be that repeated hyperconcentrated flow events exploited the same channels and redeposited the sediment of previous flows further downstream (Larsen & Steel, 1978; de Haas et al., 2014).

Strat. interval 1

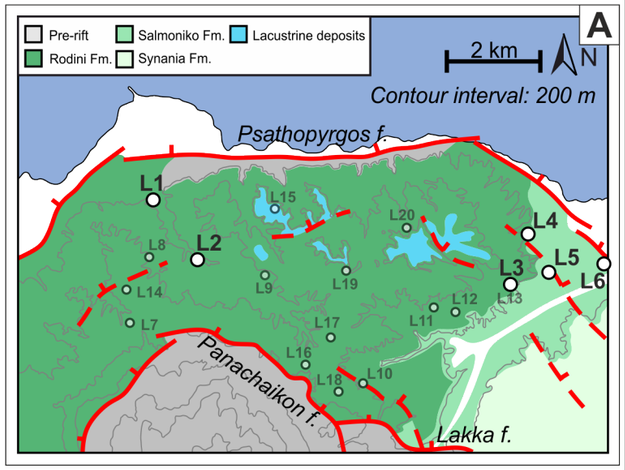

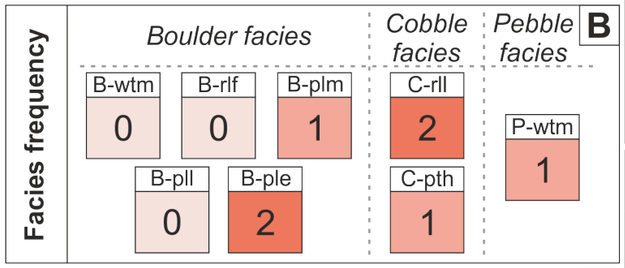

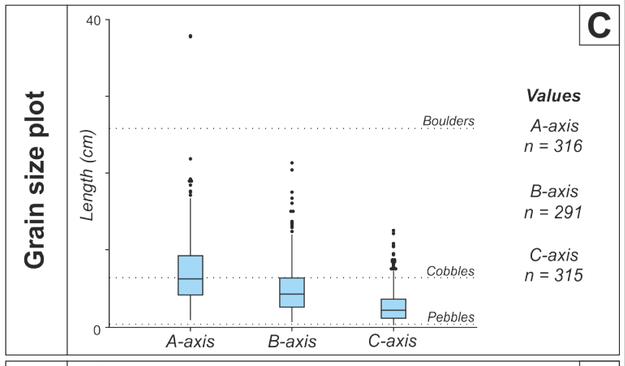

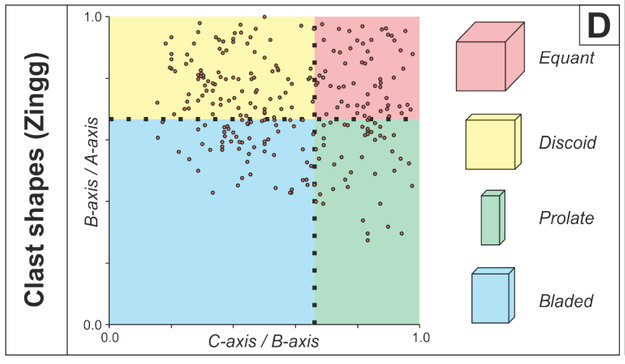

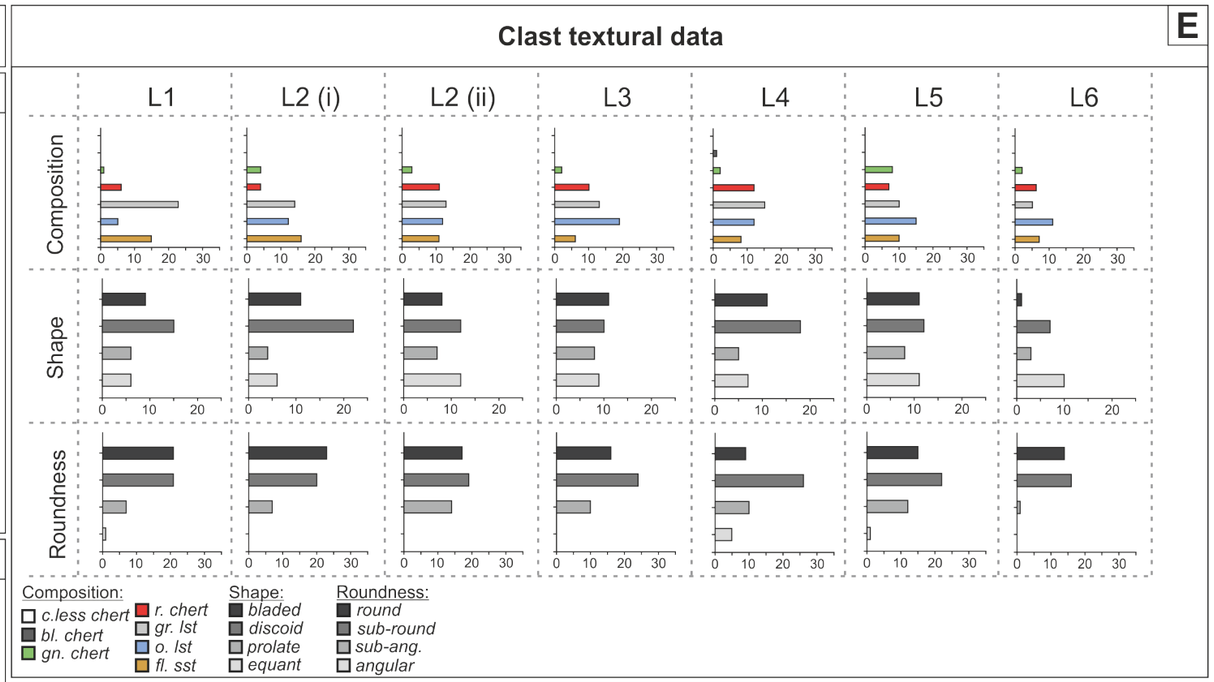

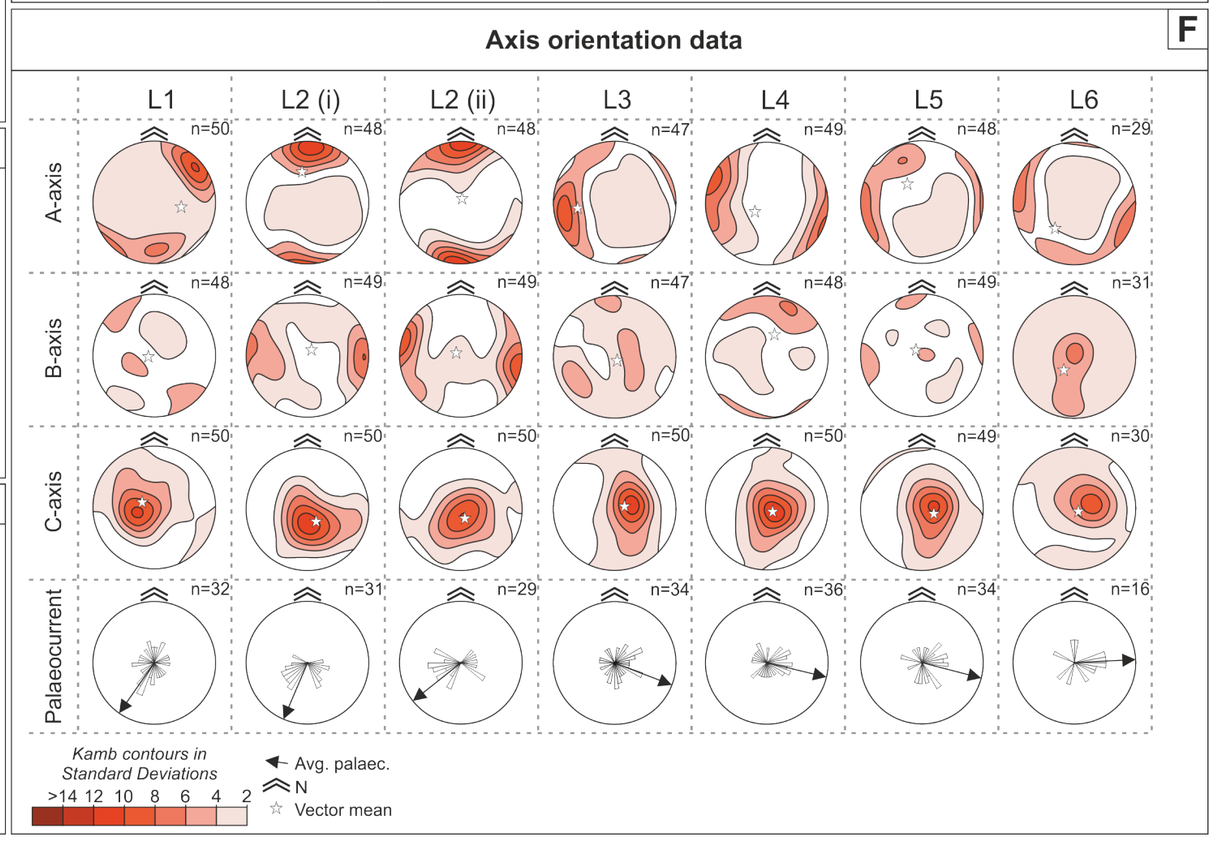

Figure 5.10 *Clast measurement data for proposed stratigraphic interval 1. See text for details of subsections A-F.*

Strat. interval 2

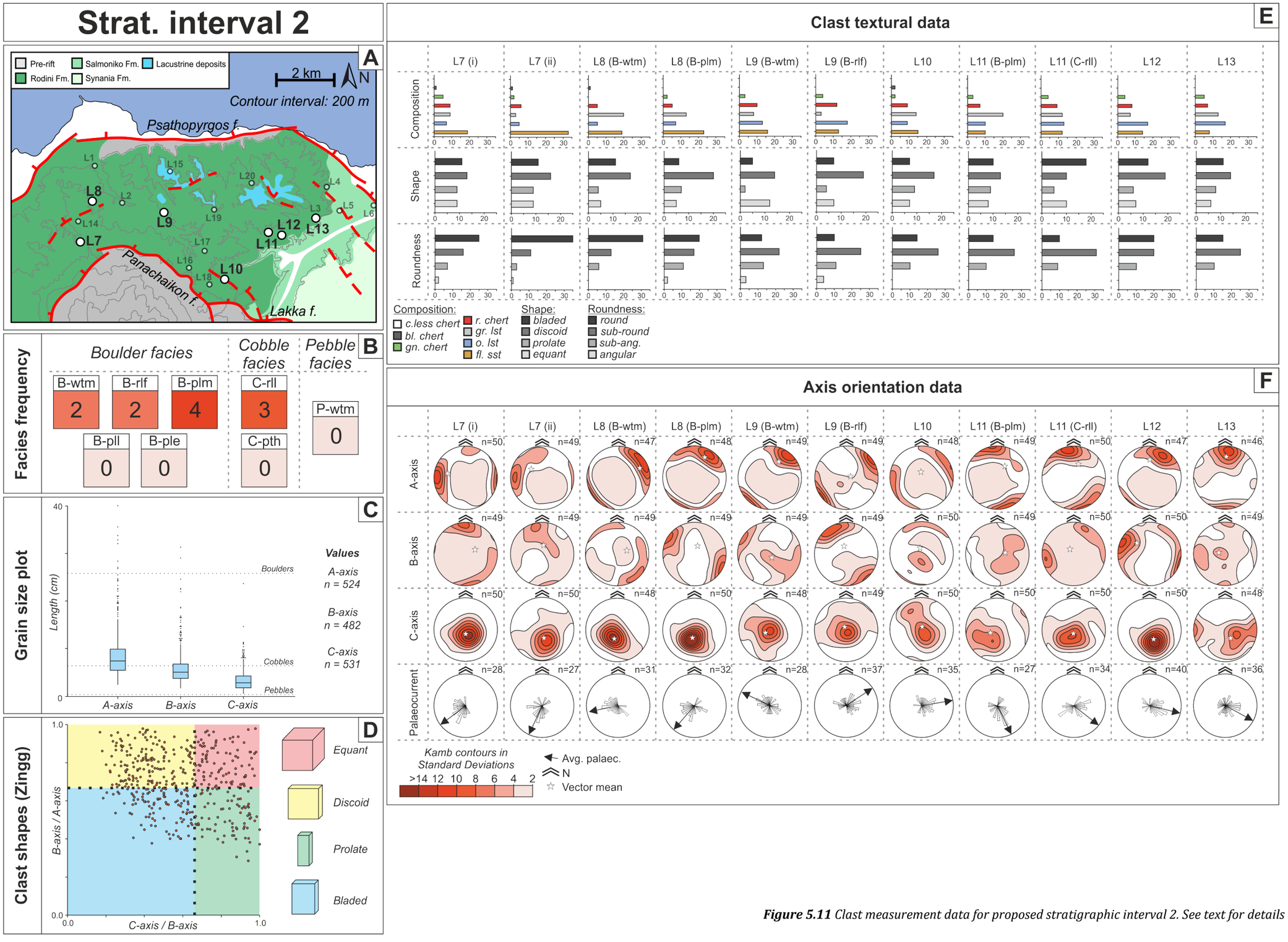

Figure 5.11 *Clast measurement data for proposed stratigraphic interval 2. See text for details of subsections A-F.*

Strat. interval 3

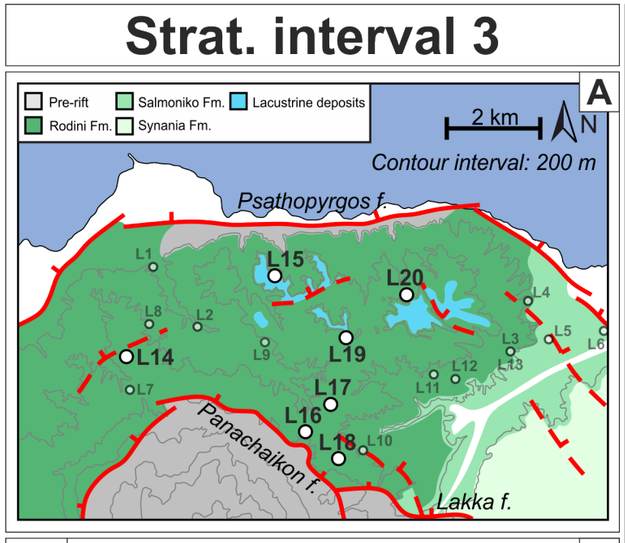

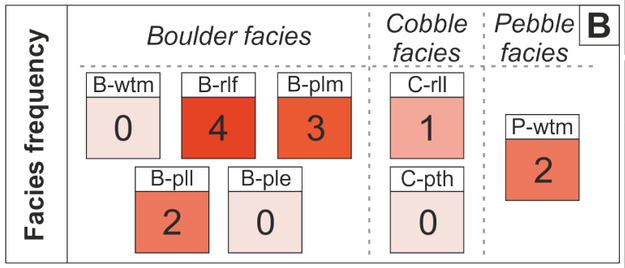

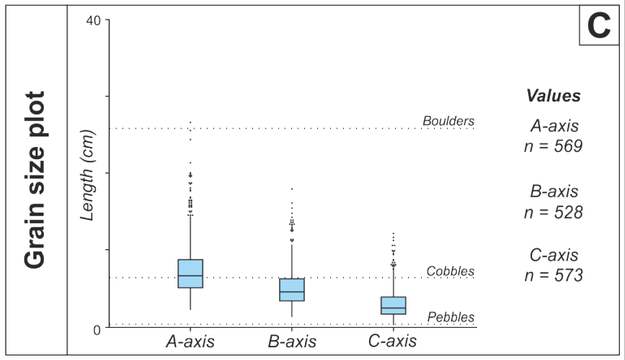

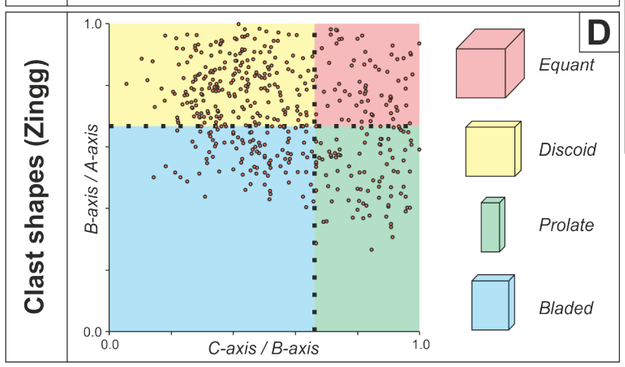

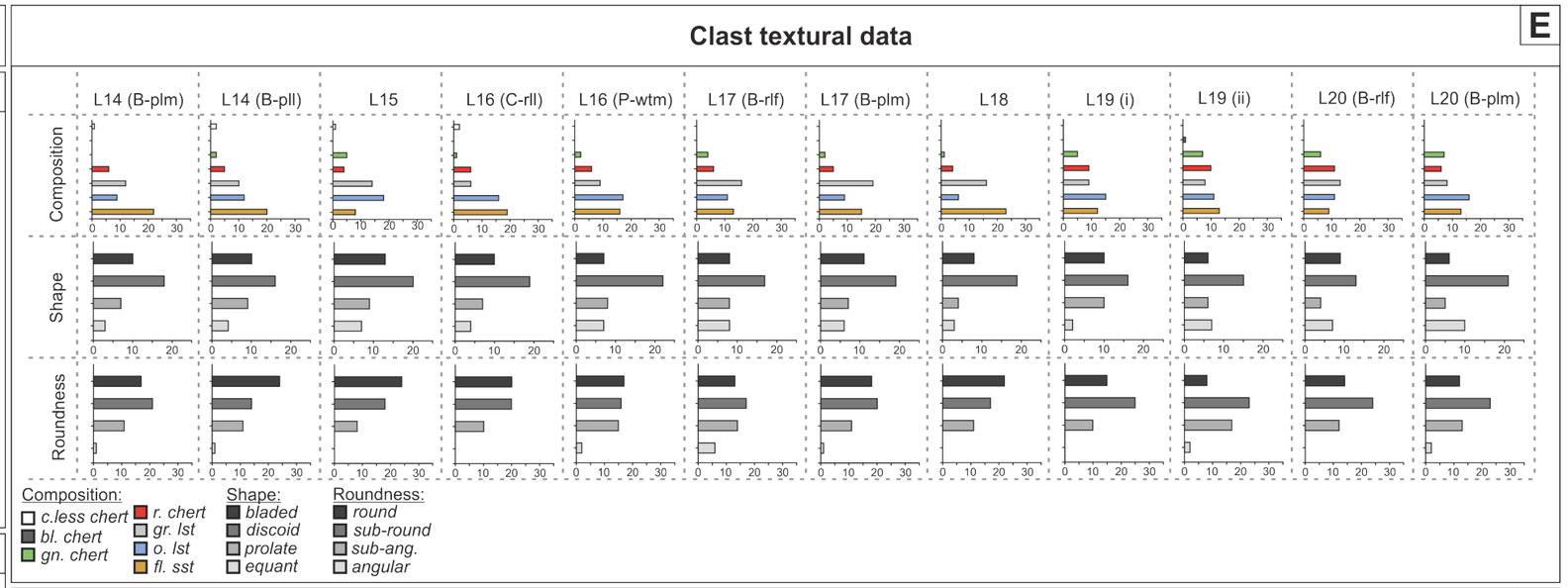

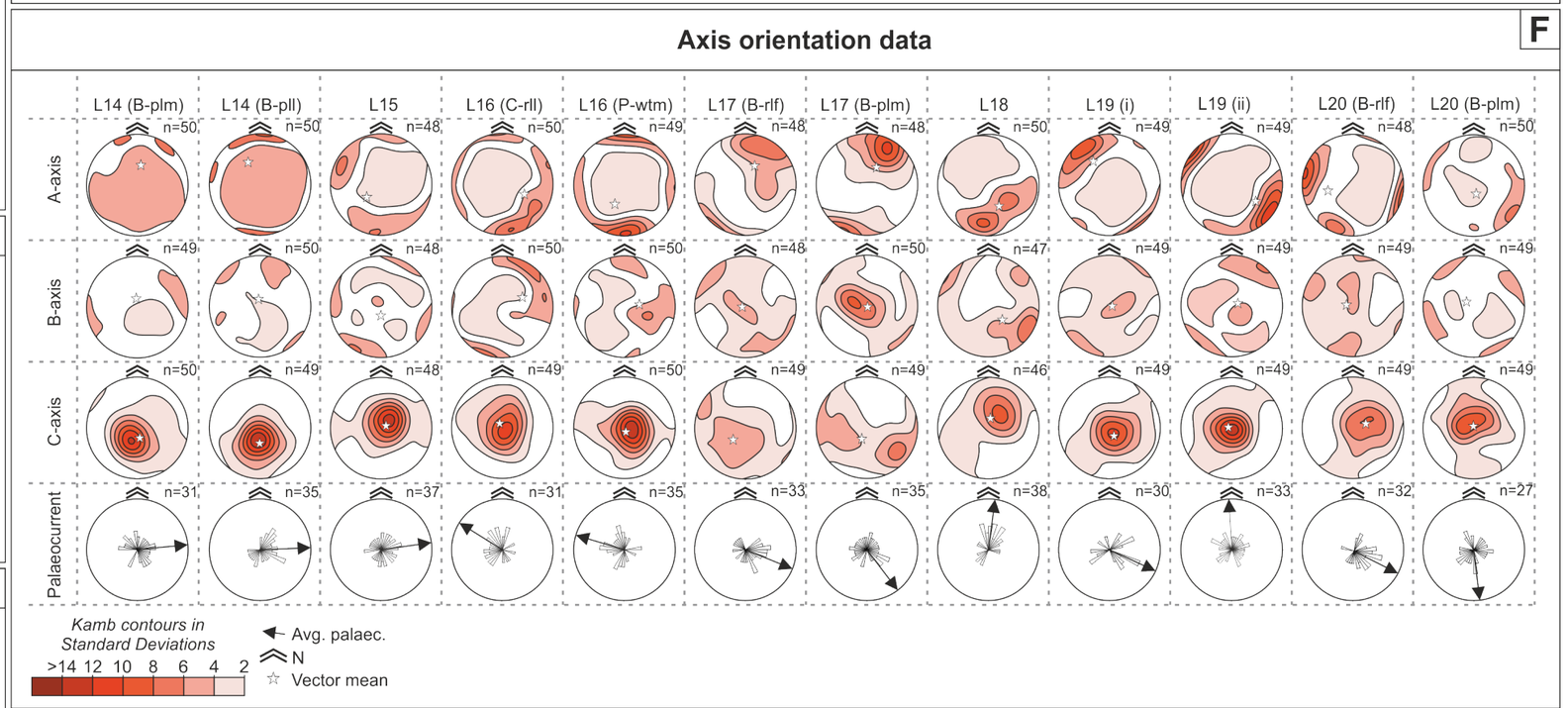

Figure 5.12 *Clast measurement data for proposed stratigraphic interval 3. See text for details of subsections A-F.*

5.4.4. Relationships between location and clast fabrics

Following the interpretation of a prograding hangingwall dipslope-sourced alluvial fan for the palaeoenvironment resulting in the deposition of the Rodini Fm. (Chapter 4), each study site can be assigned an approximate spatial position based on its distance from its sediment source. This corresponds to proximal fan, medial fan, distal fan, and footwall slope-sourced fan locations.

Proximal locations

Observations: These 5 sites are focussed on the north and north-west of the study area (Figure 5.15A). The majority of observed clasts are large pebble to cobble in size (6 to 12 cm length A-axes), with a number of clasts reaching boulder size (up to 27 cm A-axes lengths) and frequent oversized (>30 cm A-axes) clasts (Figure 5.15C). Clast shapes are dominantly discoid, with 62% to 88% of those clasts being sub-rounded to rounded in texture (Figure 5.15D, E). The proportion of sandstone clasts is comparatively high at these sites compared to other locations (16 to 46%) (Figure 5.15E). The orientations of C-axes are perpendicular to bedding planes at all sites, and A-axes are aligned in a northerly direction, fluctuating between NE-SW orientated in the western sites, to NW-SE orientated in the eastern sites. Clast B-axes are comparatively weakly aligned, but the strongest alignment displays E-W orientation in the western sites (Figure 5.15F).

Interpretations: A wide range of grain sizes, represented by a mix of boulder, cobble and pebble grade facies (Figure 5.15B), in conjunction with orientation of clast A-axes radially away from the northerly sediment source and parallel to the inferred palaeoflow, is indicative of initial radial sediment deposition away from the feeder valley (e.g. modelled alluvial fans by Clarke et al., 2010). The heavily sediment-laden flows would rapidly lose energy upon entering the newly formed accommodation leading to rapid deposition close

to the fan apex (similar to Ezquerro et al., 2020). Proximal sites also contain the highest proportion of coarse boulder clasts compared to the locations treated below, further supporting a northern sediment source as large boulders would be less likely to be transported further down the fan (Blair & McPherson, 1994; Blair & McPherson, 1998; Ezquerro et al., 2020).

Medial locations

Observations: These 7 sites are spread through the western and central parts of the study area (Figure 5.16A). The majority of observed clasts are large pebble to cobble in size (5 to 12 cm length A-axes) with some larger cobbles (up to 20 cm) and rare oversized large cobbles and small boulders (24 to 25 cm length A-axes) (Figure 5.16C). Clast shapes are dominantly discoid, and 60% to 80% of those clasts are sub-rounded to rounded in texture (Figure 5.16D, E). Clast compositions are dominated by sandstone and limestone clasts with small amounts of variation in their proportions, and a persistent 10 to 24% proportion of red chert clasts at each site (Figure 5.16E). A-axes are well-aligned at each site, with orientation switching from dipping NE in the 4 westernmost and southern sites (L14, L9, L17, L10) to dipping SE/NW in the central and eastern sites (L19, L20, L11). B-axes are weakly aligned at all sites except L9 and L17, where they are orientated to the NW/SE and perpendicular to the bedding plane, respectively. C-axes are dominantly orientated perpendicular to the bedding planes at all sites (Figure 5.16F).

Interpretations: Further down-fan, the proportion of increasingly channelised facies increases drastically (5 samples of B-rlf facies, Figure 5.16B). This may indicate the presence of incipient channels increasing the run-out distance of mass flows on the fan surface, due to an increased surface gradient and flow dilution (e.g. Pierson & Scott, 1985) and causing an increase in the presence of hyperconcentrated flows (Blair & McPherson,

1998). These flows would require higher energy in order to reach this part of the fan, and continued prevalence of a(p) clast orientations represents the high sediment concentration of flows and their rapid sediment emplacement (Bertran et al., 1997; Major, 1998). At two sites (L9, L17), observations of a(t)b(i) clast orientations in facies B-rlf may indicate a change in flow rheology: a transition from the deposition of clasts transported as suspended sediment with significant shear stress between particles, to those deposited as part of a tractional carpet within the flow (Sohn et al., 1999). Reduced depositional energy in these locations compared to proximal areas are represented by clast sizes being dominantly small cobble grade, with rare boulders and frequent medium cobbles (Jo et al., 1997).

Distal locations

Observations: The 7 sites interpreted in distal locations are located along the eastern edge of the study area (Figure 5.17A). The majority of observed clasts are small pebbles and small cobbles (4 to 8 cm A-axes lengths) with some medium cobbles (up to 17 cm) and rare large cobbles (>20 cm). One oversized 37 cm clast is present (Figure 5.17C). Similarly to other areas, clasts are dominantly rounded to sub-rounded and form discoid and bladed shapes (Figure 5.17D, E). Clast compositions are dominantly limestone rocks (48% to 64% proportion) with relatively lower proportions of sandstone clasts compared to other locations (12 to 30%) (Figure 5.17E). Clast C-axes are dominantly orientated perpendicular to bedding planes at all sites. In the northern half of the distal location sites (L3, L4, L5, L6), and for site L10 near the uplifted southern footwall, clast A-axes are orientated strongly in an E-W direction. The grouping of sites L11, L12 and L13 display clast A-axes orientations aligned in a N-S direction (Figure 5.17F).

Interpretations: At these locations, the successions contain a higher proportion of cobble grade facies, with boulder facies still present in northern sites (Figure 5.17B). Persistent A-axis parallel imbrication at nearly all sites continues to represent high sediment yield flows with suspended clasts during the earliest rift phase (sites L4, L5, L6, see section 5.4.3. stratigraphic interval 1). Some deposits could be indicative of the resedimentation of older up-fan deposits (similar to those described by Larsen & Steel, 1978; de Haas et al., 2014) resulting in stacked lenses of well sorted clasts with low matrix content (facies B-ple), which could explain the presence of rare oversized boulder clasts and large cobbles (Mack et al., 2008). Clast a(t)b(i) orientations are seen at two sites (L12, L11) which are interpreted here as representing lobe front deposits of debris flows as described in section 5.4.3.

Footwall slope-sourced locations

Observations: These 6 sites are located in the south and south-west of the study area (Figure 5.18A). The majority of observed clasts are small pebble to medium cobble in size (6 to 12 cm A-axes lengths) with some larger cobbles (<20 cm length) and rare small boulder clasts (25 cm length A-axis) (Figure 5.18C). Clast shapes are dominantly discoid and bladed, and 66% to 92% of those clasts are sub-rounded to rounded in texture (Figure 5.18D, E). Clast compositions are dominated by sandstone lithology (18 to 66% proportion) with an increasing portion of limestone clasts away from the uplifted footwall in the south (see sites L14 and L17) (Figure 5.18E). Clast C-axes are consistently orientated perpendicular to bedding planes at all sites except L17, which displays weak alignment both perpendicular to the bedding plane and to the SE. Clast A-axes vary between displaying well-aligned orientations, and a larger spread of orientations. All but one site displays a N-S to NE-SW orientation of A-axes; L7, the westernmost site, displays

a strong E-W alignment instead. B-axes orientations have a large spread at all measured sites (Figure 5.18F).

Interpretations: Deposits are formed by a range of facies from boulder grade to pebble grade, with the majority of those facies containing higher matrix proportions (B-plm) or sand lenses (B-pll and C-rll) than other facies (Figure 5.18B). This indicates that sediment of all grades is being deposited, representing limited flow transport distance, likely as a result of slope failure within small, isolated catchments in the uplifted footwall (similar to those described in Densmore et al., 2007; Alves & Cupkovic, 2018). In conjunction with palaeoflow directions orientated away from the uplifted Panachaikon footwall, this indicates a footwall crest source for these deposits. Two footwall crest sourced fans likely formed, one at the western edge of the Panachaikon fault (feeding site L7) and one at the juxtaposition of the Panachaikon and Lakka faults (feeding sites L16, L18). Site L7 displays B-axis parallel imbrication within facies interpreted as debris flow deposits (B-plm) indicating the rotation and orientation of clasts parallel to a lobe confined lobe front, similar to the fabrics observed to the east at sites L11 and L12 (Major, 1998). Sites L16 and L18 display A-axis parallel imbrication, formed from rapid deposition of sediment from non-cohesive debris flows with a reduced run-out distance (Bertran et al., 1997; Crosta & Frattini, 2004; Ventra & Clarke, 2018).

Proximal location

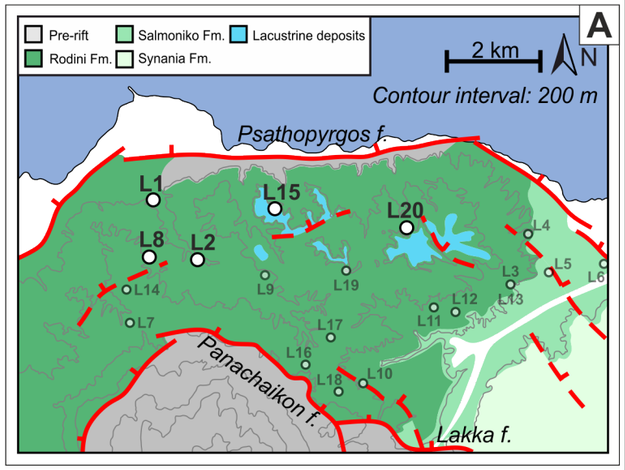

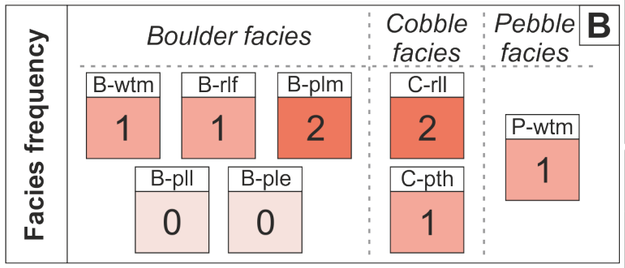

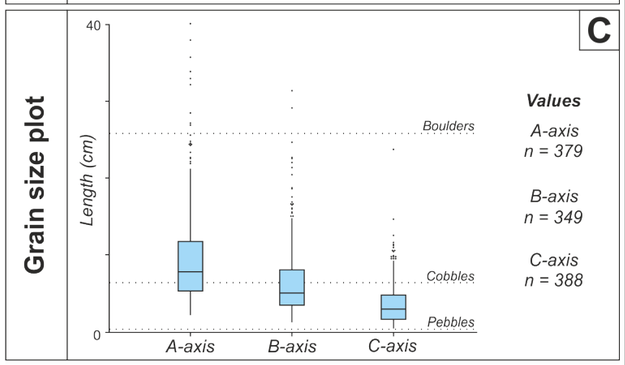

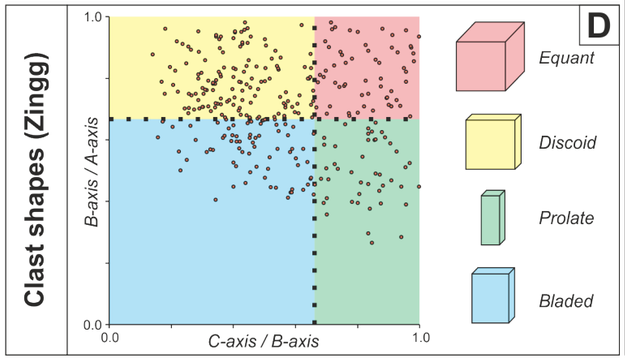

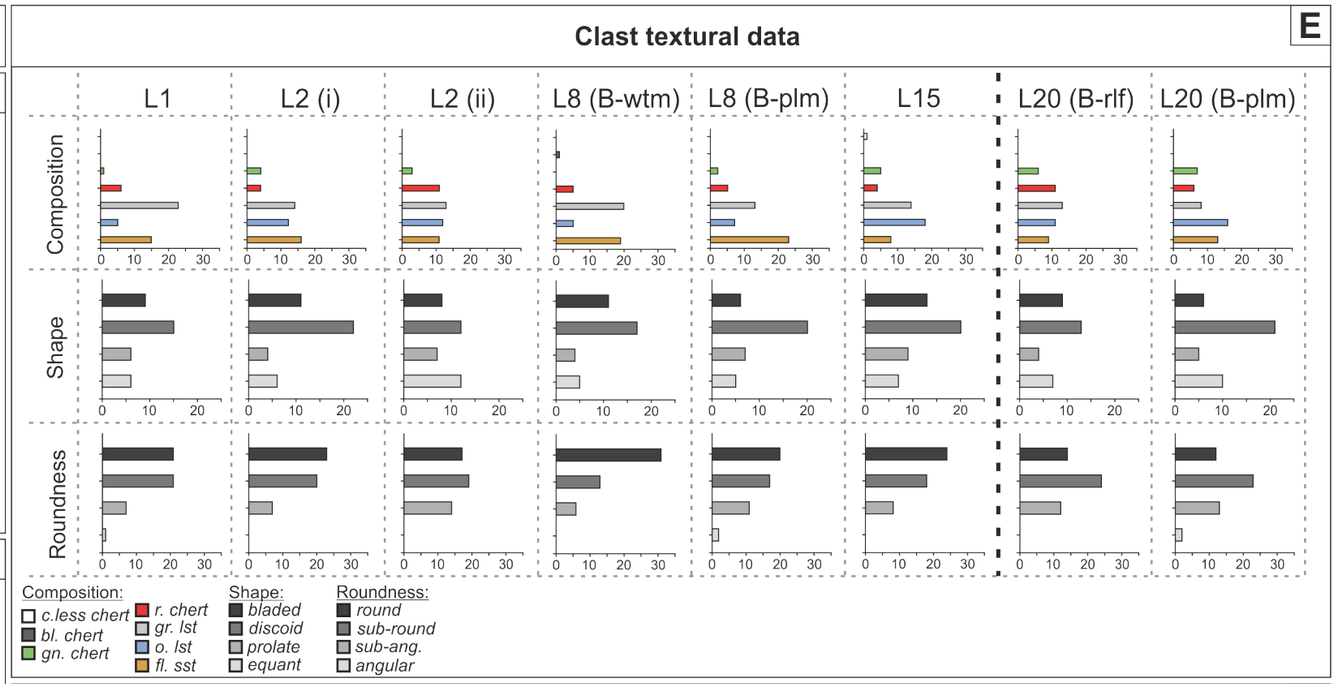

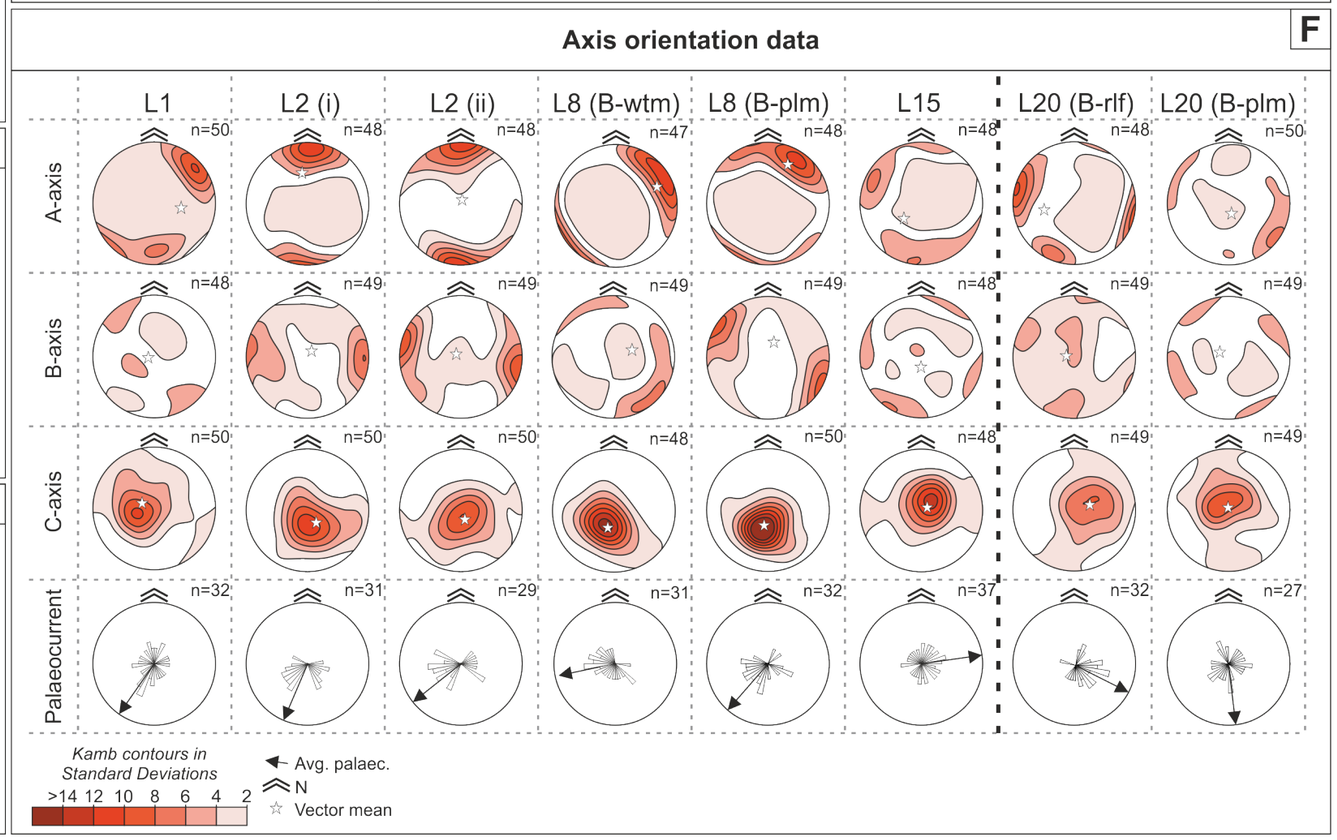

Figure 5.13 *Clast measurement data for proximal fan areas. See text for details of subsections A-F.*

Medial location

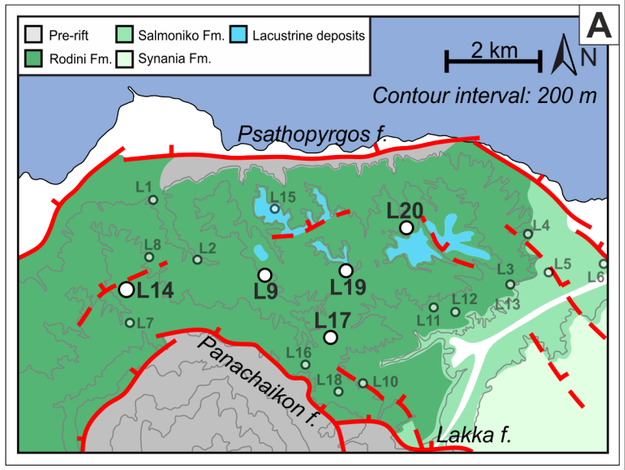

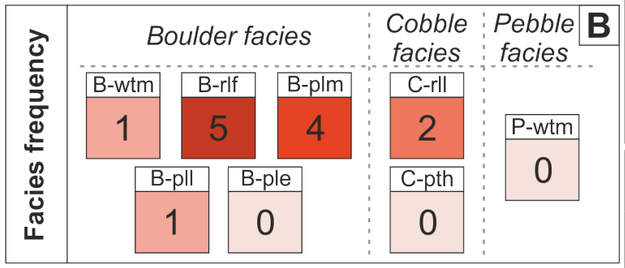

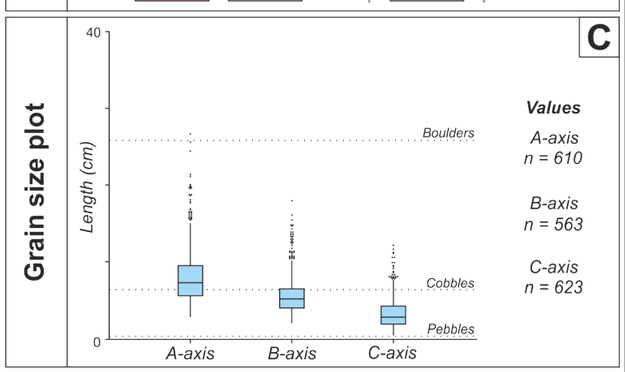

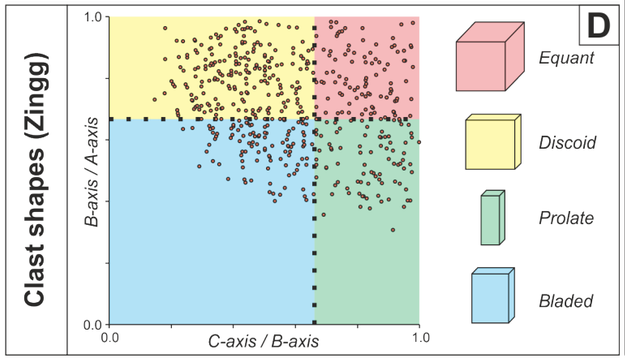

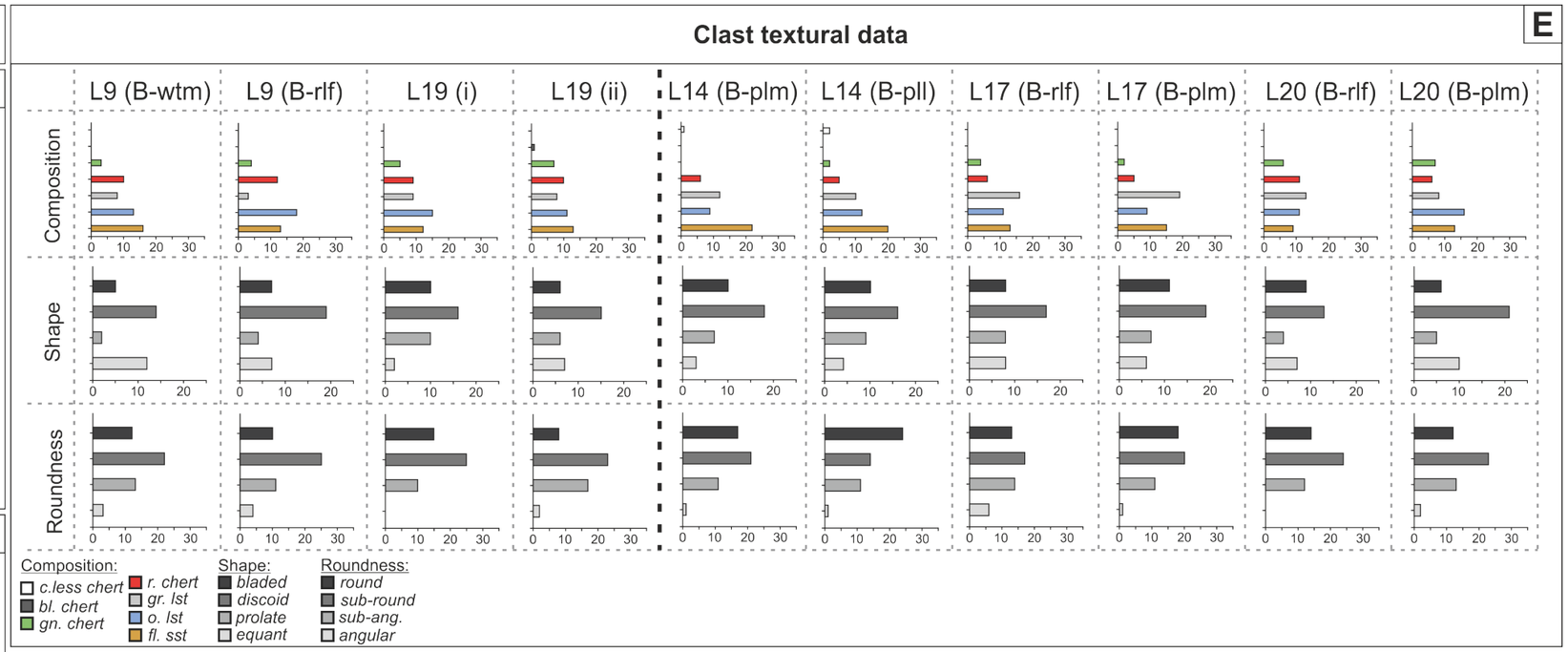

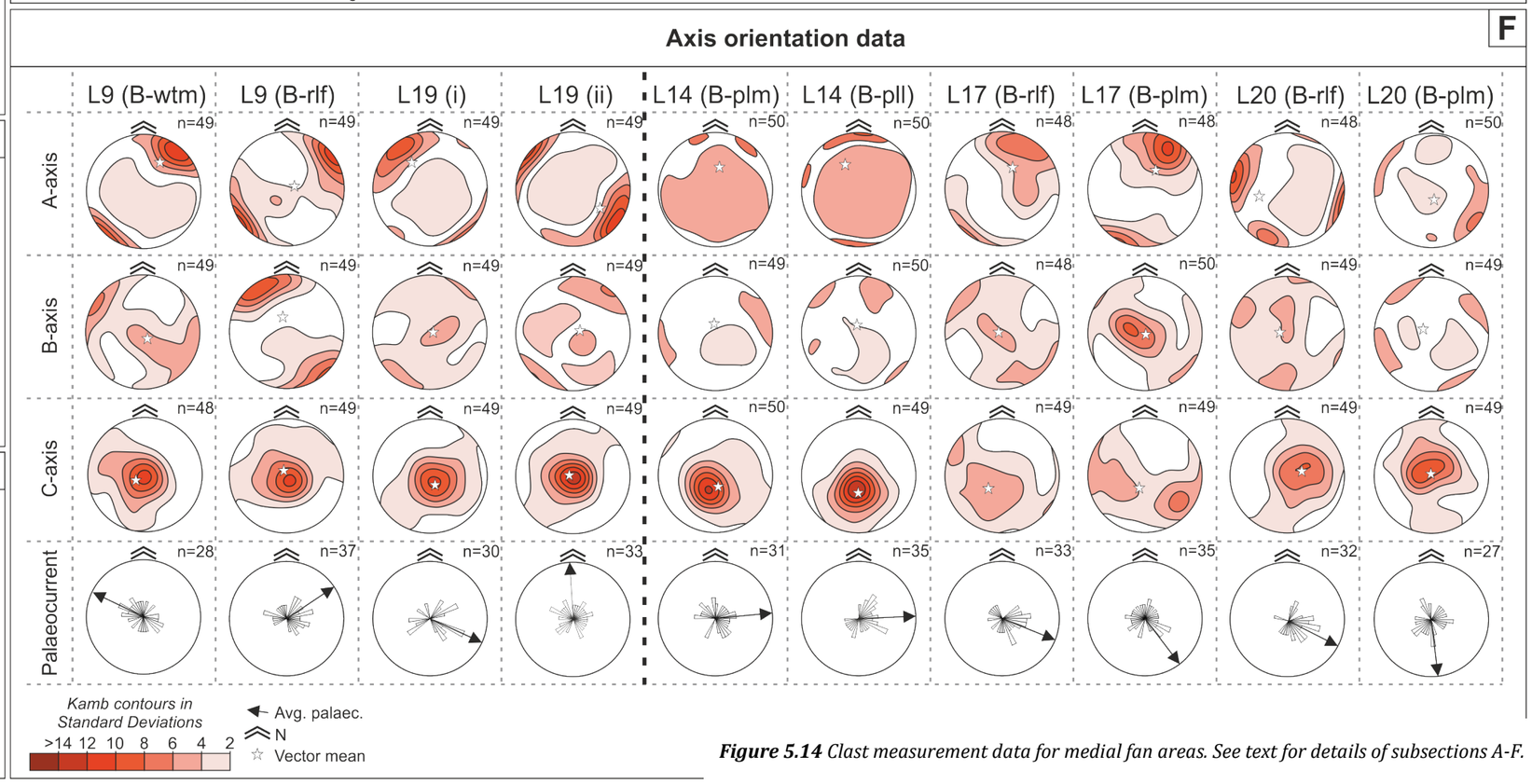

Figure 5.14 *Clast measurement data for medial fan areas. See text for details of subsections A-F.*

Distal location

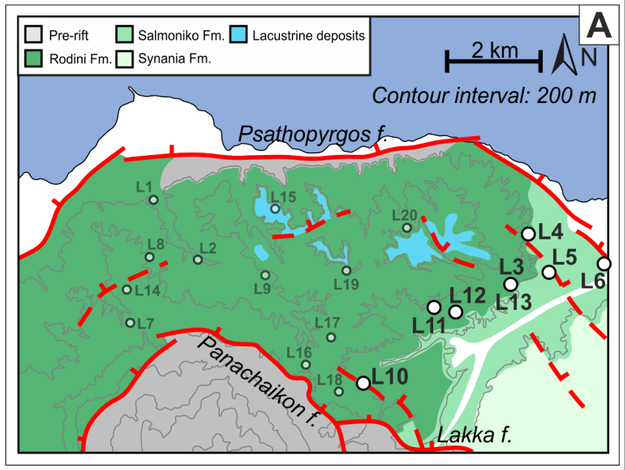

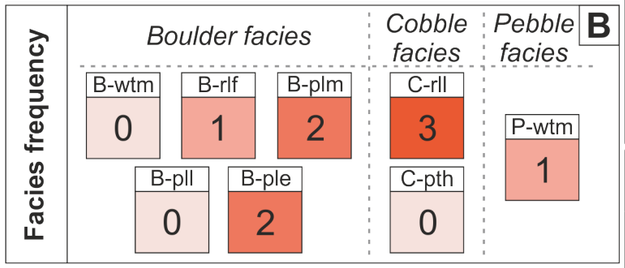

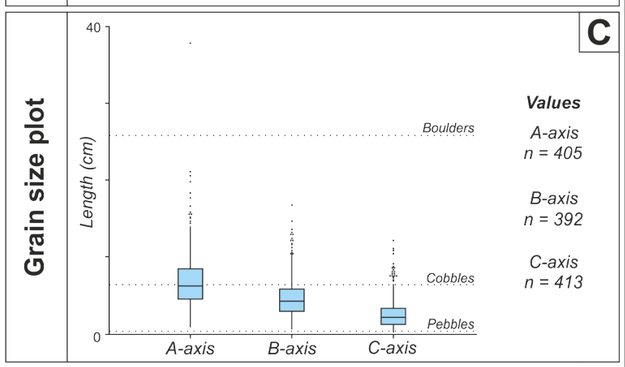

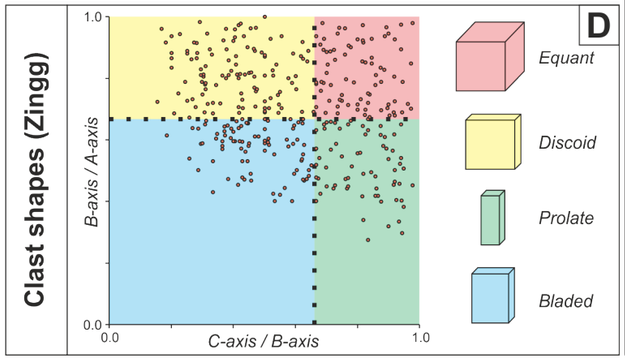

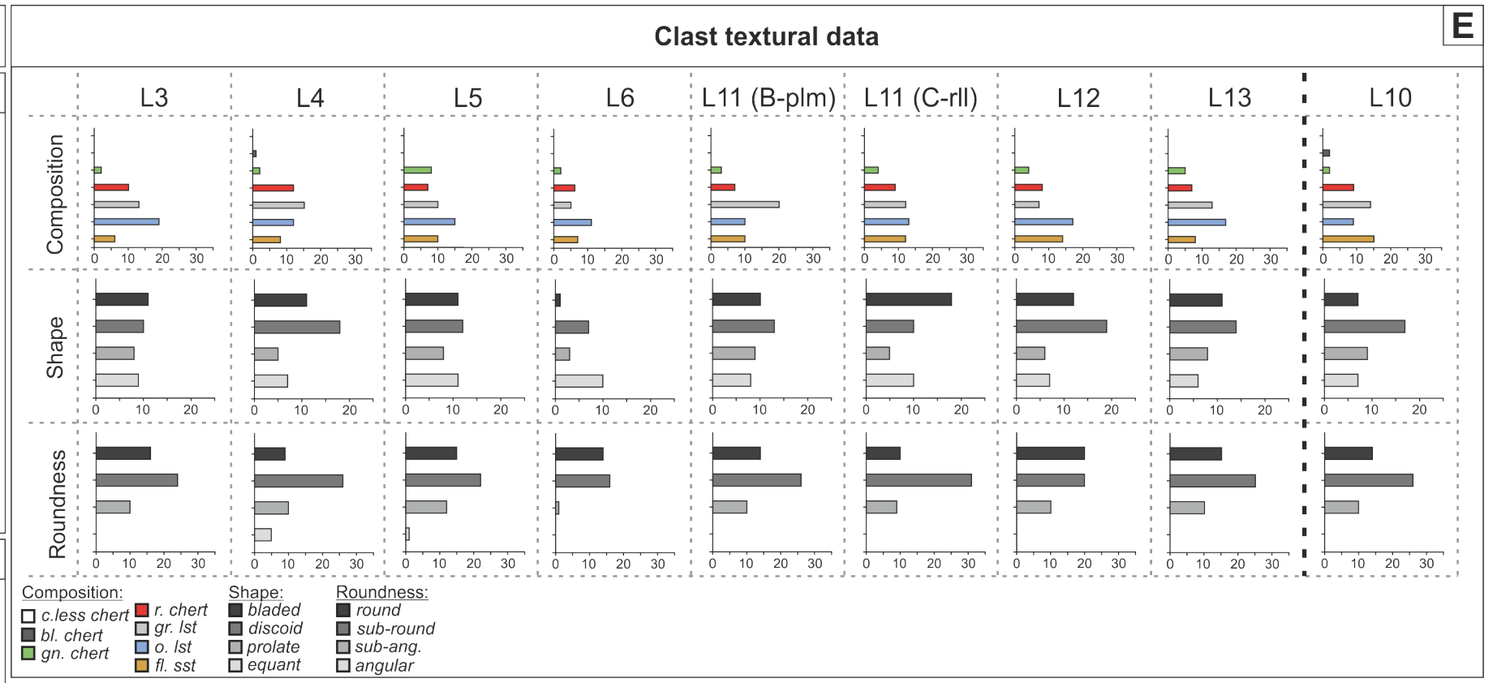

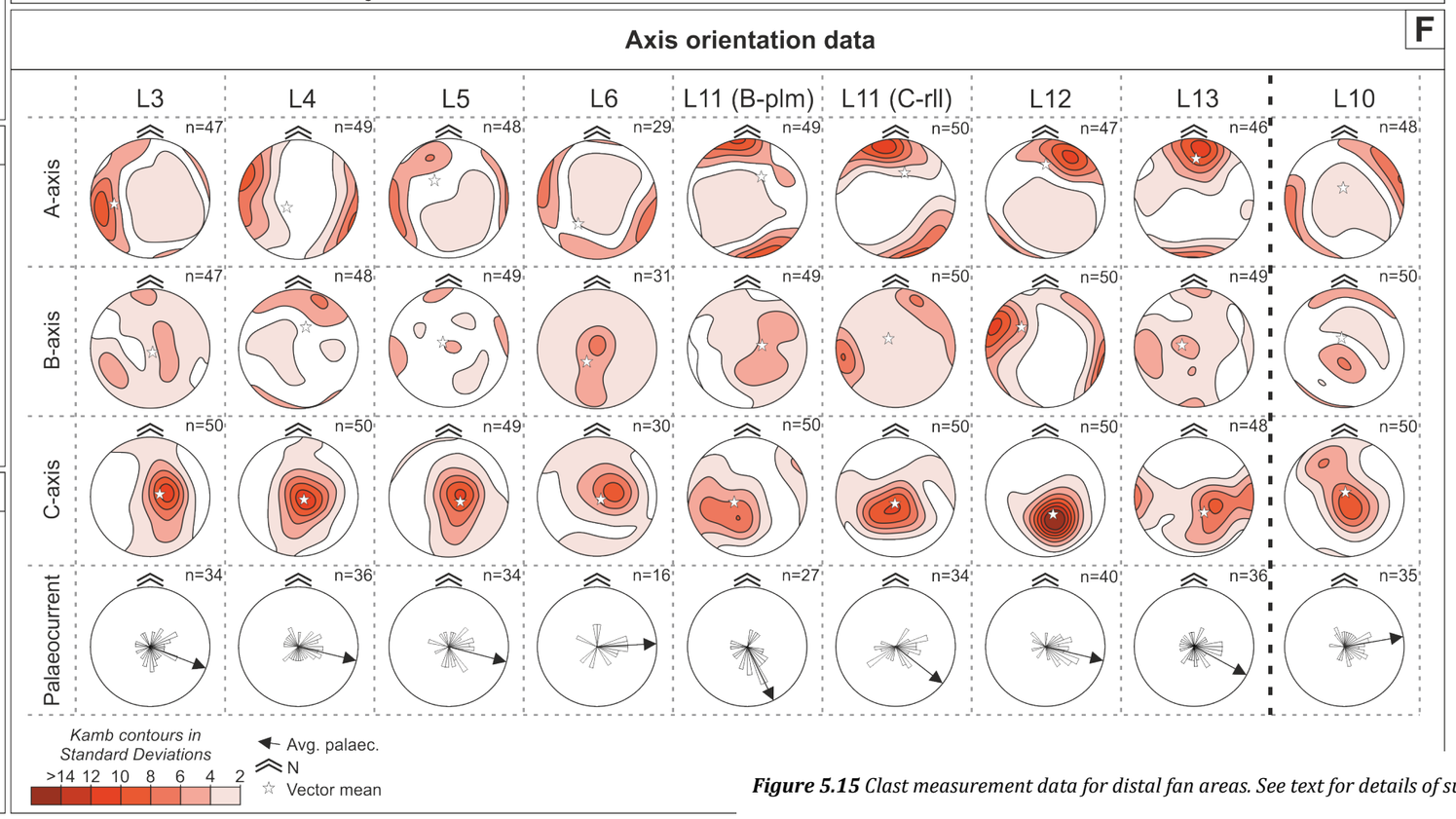

Figure 5.15 *Clast measurement data for distal fan areas. See text for details of subsections A-F.*

Footwall-source

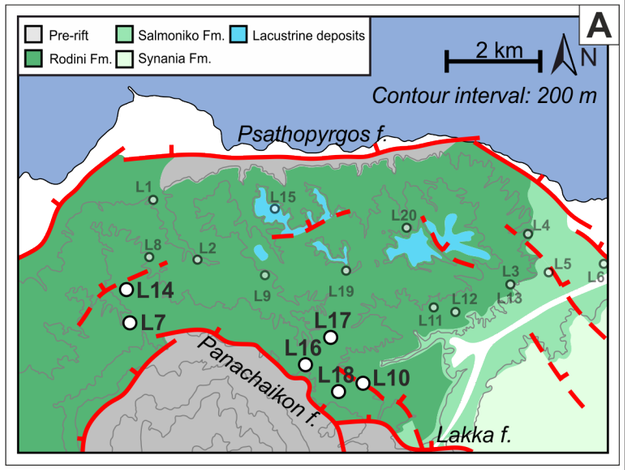

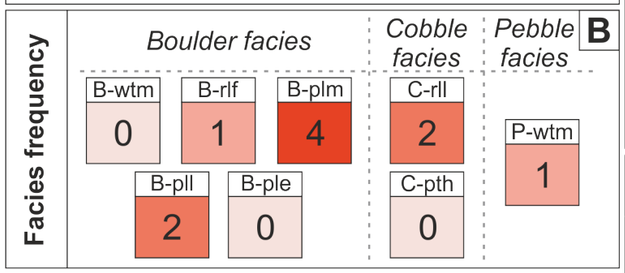

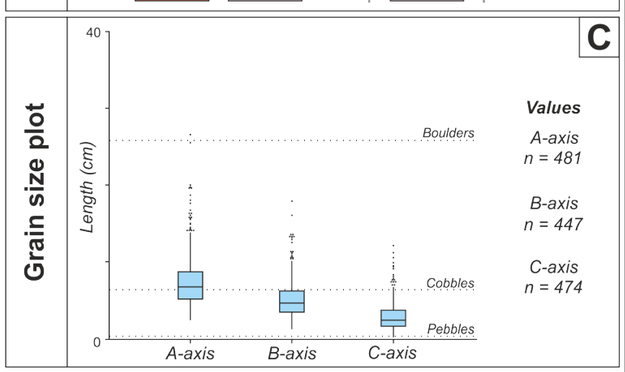

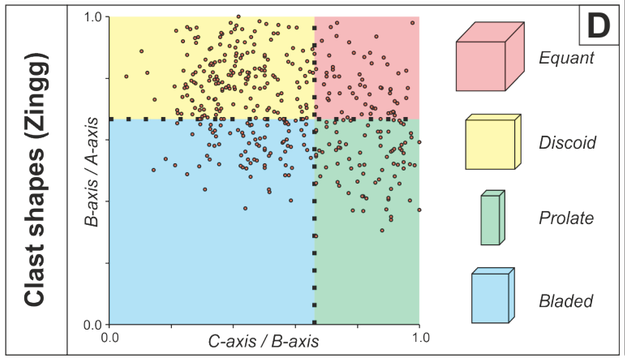

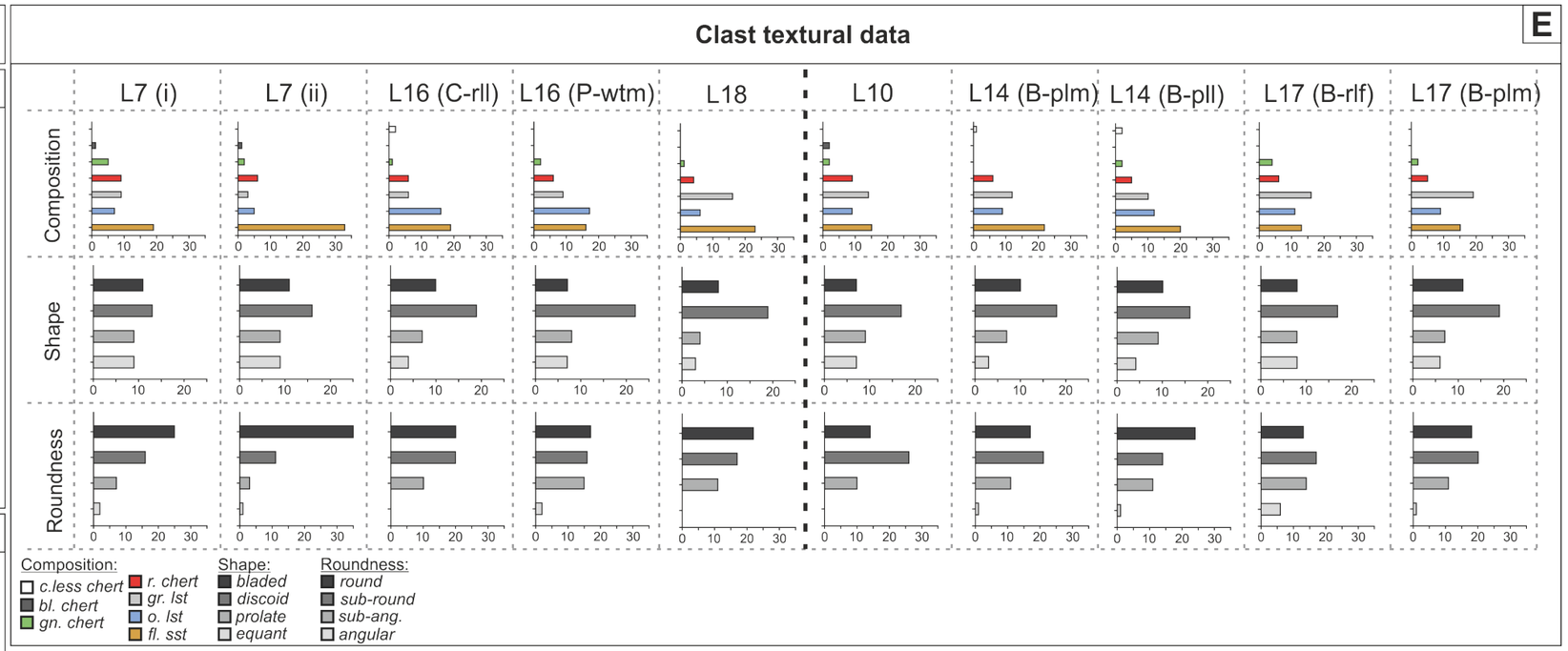

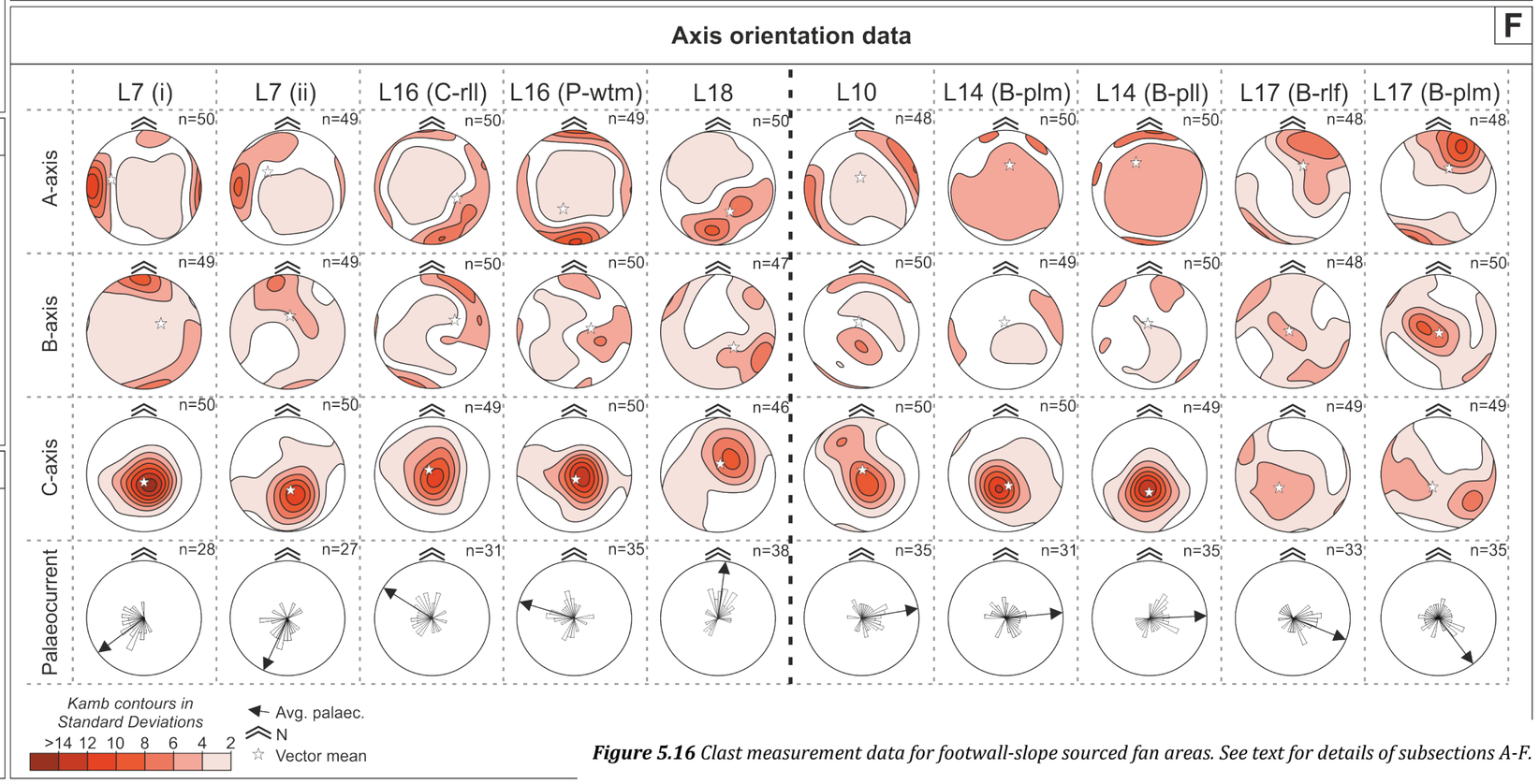

Figure 5.16 *Clast measurement data for footwall-slope sourced fan areas. See text for details of subsections A-F.*

5.5. Discussion

5.5.1. Detailed palaeogeographic reconstructions

It is important to consider both the preserved facies and the orientations of its clasts, in order to determine the part of the original flow that has been preserved (Major, 1998). Debris flow and hyperconcentrated flow deposits form a range of types of landforms including levees, channels, and lobes. Based on the distribution of the preserved expression of these geomorphic features, it ought to be possible to predict the likely development of the depositional fan surface through space and time.

Initial deposition into the extensional basin (stratigraphic interval 1, Figure 5.19) is dominated by horizontally stratified conglomerates formed through the dispersion of sediment-laden lobes as they enter the new accommodation (similar to modelled studies e.g. Clarke et al., 2010) in proximal locations. Slow rates of accommodation generation prevented the establishment of a high gradient south-dipping hangingwall dipslope increasing the dispersive nature of flows as they entered the basin and rapidly depositing sediment, enabling subsequent fan propagation (Clarke et al., 2015). This inhibited the development of specific lobe-front clast fabrics including a(p) orientations to flow edges (a(t) orientations to inferred palaeoflow) (Major, 1998). In the eastern, distal locations (sites L3, L4, L5, L6) clasts align in a(p) fashion to inferred eastern palaeoflow, with facies (B-plm, B-ple, C-rll, P-wtm) indicating a mix of depositional flows including debris flows (B-plm, C-rll), and possible hyperconcentrated flows (B-ple, P-wtm). Rapid deposition preserved clast a(p) alignments, and flows were directed here by a combination of (i) the overfilled nature of the basin reducing the fan surface gradient and allowing flows to be immediately drawn towards the east and ancient Lake Corinth, and (ii) the onset of the Trizonia fault to the east (Beckers et al., 2015; Gawthorpe et al., 2018) directing flows towards its potentially underfilled basin.

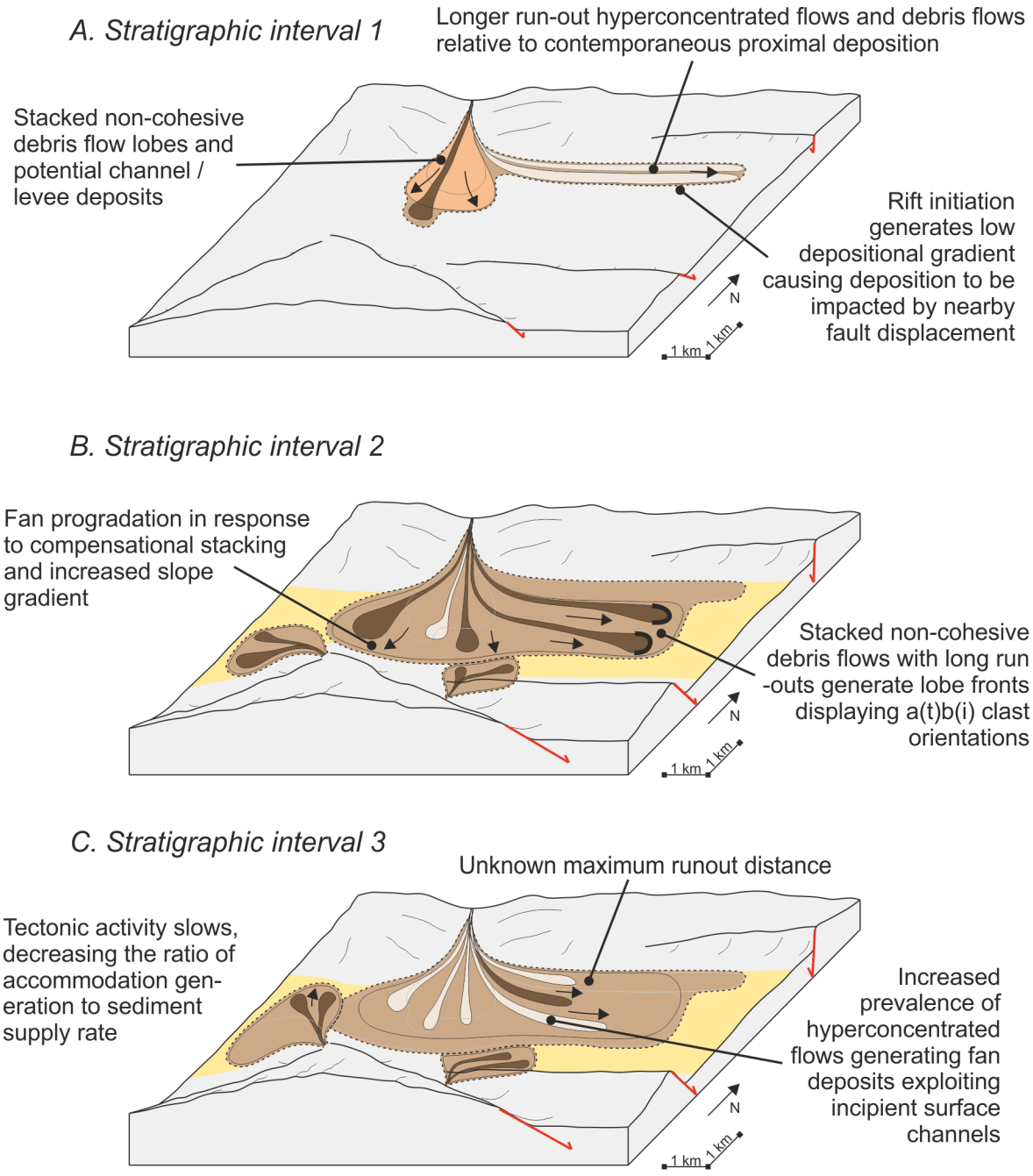
A. Stratigraphic interval 1
Longer run-out hyperconcentrated flows and debris flows relative to contemporaneous proximal deposition
Stacked non-cohesive debris flow lobes and potential channel / levee deposits
Rift initiation generates low depositional gradient causing deposition to be impacted by nearby fault displacement
N
1 km
1 km
B. Stratigraphic interval 2
Fan progradation in response to compensational stacking and increased slope gradient
Stacked non-cohesive debris flows with long run -outs generate lobe fronts displaying a(t)b(i) clast orientations
N
1 km
1 km
C. Stratigraphic interval 3
Unknown maximum runout distance
Tectonic activity slows, decreasing the ratio of accommodation gen- eration to sediment supply rate
Increased prevalence of hyperconcentrated flows generating fan deposits exploiting incipient surface channels
N
1 km
1 km
Legend
DF deposits
HCF deposits
Fan deposition
Silt/sand deposits
Pre-rift
Fan conglomerate extent
Active fan deposition
Outline of relic fan toes
Fault
Sediment pathways

Figure 5.17 *Proposed detailed palaeogeographic evolution of the study area through stratigraphic intervals 1-3 (A, B and C respectively). See text for details. (A) Stratigraphic interval 1 occurs directly after surface fault rupture and early subsidence. A new depocentre forms in the obliquely-cut Mornos catchment and initial deposition is dominated by lobate coarse sediment flows before the formation of a classical fan shape. Some flows are pulled to the east by the overall W-E dip of the Corinth Rift (Gawthorpe et al., 2018) and other depocentres. (B) Stratigraphic interval 2 comprises ongoing, more rapid subsidence and high sediment supply rates leading to repeated non-cohesive debris flows and the establishment of incipient surface channels as the fan aggrades and progrades. (C) Stratigraphic interval 3 is represented by the preservation of repeated debris flow and hyperconcentrated flow facies as fan aggradation and progradation slows.*

Key evidence for these interpretations are: (i) proximal horizontal stratification of poorly sorted cobble conglomerates containing flat lying clasts, indicating incremental mass flow deposition; (ii) a lack of a(t)b(i) clast orientations in the same deposits indicating increased dispersive pressures acting on flows; (iii) early-stage conglomerate deposition in eastern distal locations displaying a(p)a(i) fabrics forming facies derived from a variety of flow processes; and (iv) palaeocurrent analyses.

Further deposition into the basin (stratigraphic interval 2, Figure 5.19) is dominated by facies interpreted as debris flow deposits (B-wtm, B-plm, C-rll) with intermittent hyperconcentrated flow deposits (B-rlf). These flows extended into the basin as ongoing accommodation generation and previous proximal deposition to the north and north-east (sites L3, L4, L5, L6) increased the hangingwall dipslope gradient. The study sites representing stratigraphic interval 2 are in medial to distal areas, and all display preferred a(p)a(i) clast fabrics except for three distal sites; L11, L12, and L13. These sites contain dominantly debris flow facies (L11: B-plm and C-rll, L12: C-rll) and one observed hyperconcentrated flow facies (L13: B-rlf). These three sites display a(t)b(i) fabrics, interpreted here as representing the frontal deposits of debris flow and

hyperconcentrated flow lobes as clasts cluster and orientate parallel to the flow front (Major, 1998) and extended clast rolling as bedload in the tractional carpet of a hyperconcentrated flow (L13).

Debris flows (facies B-plm, B-pll, C-rll) continued to operate into the final depositional stage (stratigraphic interval 3, Figure 5.19) however the prevalence of hyperconcentrated flow deposits (indicated by normal grading of structureless boulder to pebble conglomerates overlain by pebbly sand facies, facies B-rlf) increases. The majority of these sites are located in medial areas, and record channelised hyperconcentrated flow deposits and intermittent unconfined, laterally extensive debris flow deposits. Hyperconcentrated flows may have exploited local debris flow-related depositional features (such as juvenile levees) causing confinement, and leading to flow dilution and an increased runout distance (Pierson & Scott, 1985; Pierson, 2005). As such these hyperconcentrated flow deposits are likely the downstream expression of upstream debris flows as they deposit their coarse grain fraction, allowing trailing dilute flows to overtake them indicated by overall fining upward sequences as opposed to the coarsening upward sequences of preceding dilute flows (Sohn et al., 1999).

5.5.2. Deposition through time of multiple stacked flow bodies

Sohn et al. (1999) studied the development of hyperconcentrated and debris flow deposits in a rift setting of South Korea and developed a depositional model after that of Pierson & Scott (1985) and Pierson (2005), detailing a hybrid flow comprised of a non-cohesive debris flow, a trailing hyperconcentrated flow, and a terminal streamflow. The original models of Pierson and Scott detailed the opposite; a streamflow would precede a consequent hyperconcentrated and then debris flow as the fluid volume entrained sediment. As the clay content of a flow increases, its cohesion increases, increasing the

likelihood of the flow being spatially variable between these flow states. In this example, the coarser silt- to sand-grade matrix decreases cohesion, inducing transitional hybrid flows that will vary temporally and spatially dependent on their sediment concentrations (Sohn et al., 1999). Figure 12 of Sohn et al. (1999) displays the predicted deposits from these flows; importantly, while both models display a transition downstream of relatively coarse to fine-grained sediment as you reach more distal areas from the flow entry point to the basin, the model of Sohn et al. shows that coarse grained debris flow units will reach distal fan locations at the start of depositional events. In this study, repeated fining-up facies associations are seen at sites on the proposed medial and distal fan, namely at sites L11, L13, L19, L20. This would indicate deposition via the model proposed by Sohn et al. (1999), supported by coarse grained debris flow deposition located in distal fan areas (such as by sites L4, L6, L13).

It may be that combinations of these different flow models may occur at different times during rifting, related to the rates of subsidence and fault slip. As subsidence increases relative to sediment supply (this study; stratigraphic interval 2), alluvial fans preferentially aggrade. New incipient channels form from flow events led by preceding debris flows (the proposed model of Sohn et al., 1999), which generate levees and lobe fronts of coarse-grained material (similar to confined aggradation described by Ventra et al., 2013) that can reach distal fan locations when flow magnitude allows (Figure 5.19). These channels are repeatedly filled and reformed, and their preserved deposits are interspersed with laterally extensive conglomerate sediments deposited by unchannelised flows. As subsidence slows (stratigraphic interval 3), fan aggradation rates are reduced and the fan preferentially progrades across the basin floor. Any incipient channels on the fan surface are exploited by flow events leading to preceding stream and hyperconcentrated flows, as sediment is deposited close to the fan apex

reducing the sediment concentration of the flow (Pierson & Scott, 1985). This leads to a prevalence of distal finer-grained deposits and proximal conglomeratic units. As a result, sediment stacking patterns displayed between stratigraphic interval 2 and stratigraphic interval 3 in Figure 5.20 display alternating sections of debris flow and hyperconcentrated flow deposits. The interbedded nature of these facies will be further enhanced by variable flow strengths, altering the sediment concentration of those flows and leading to intermittent beds of debris flow deposits within dominantly hyperconcentrated flow sections, and vice versa. The presence and activity of faulting will further affect the the spatio-temporal variability of flow sediment concentrations, consequently increasing the variability in preserved facies character.

Figure 5.18 (next page) *Strike and dip sections of inferred alluvial fan shape and predicted facies distributions through stratigraphic intervals 1-3 (A, B and C respectively).*

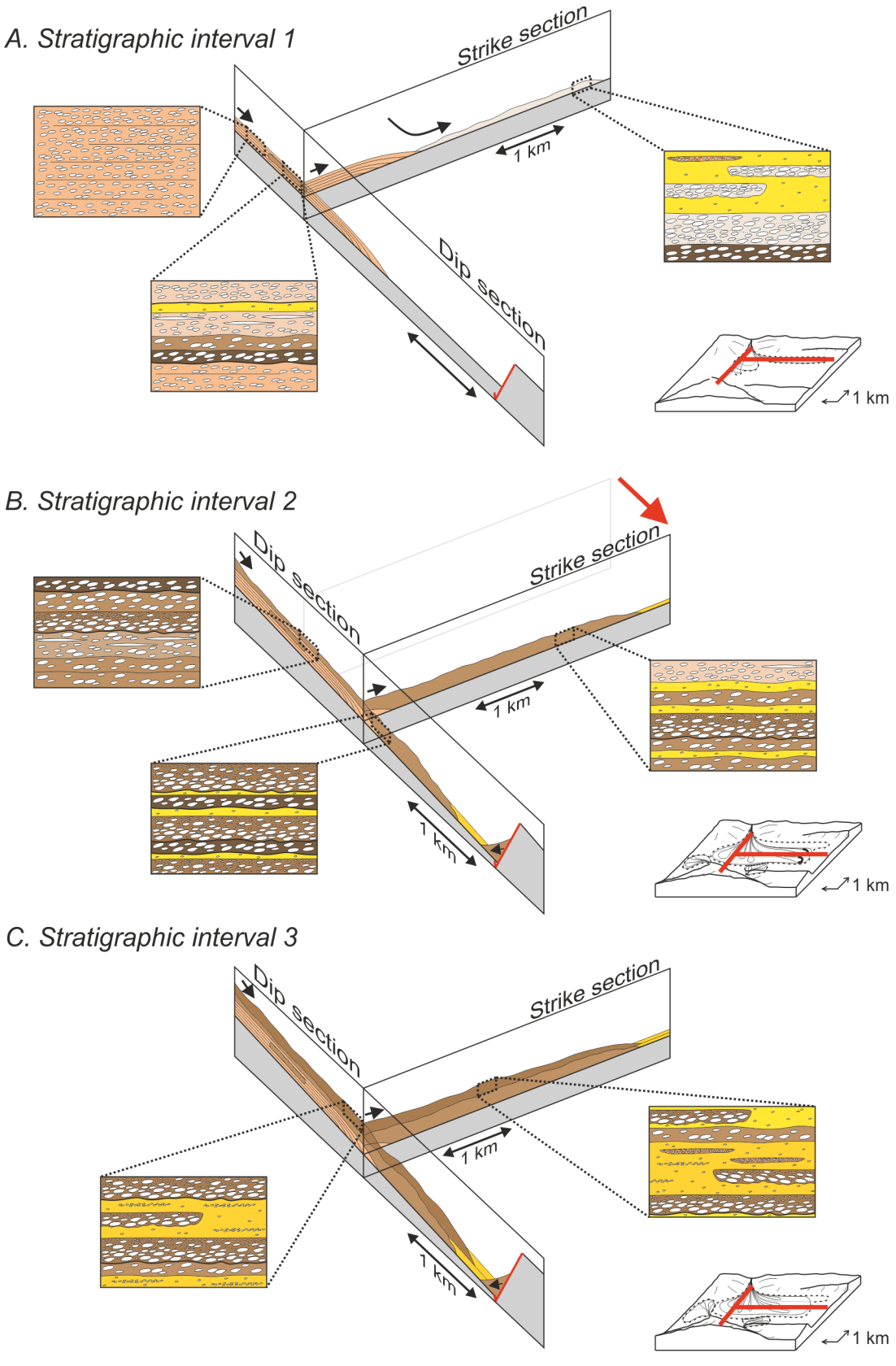
A. Stratigraphic interval 1
Strike section
1 km
Dip section
1 km
B. Stratigraphic interval 2
Dip section
Strike section
1 km
1 km
1 km
C. Stratigraphic interval 3
Dip section
Strike section
1 km
1 km
1 km
Legend
B-wtm
B-rlf
B-ple
C-rll
B-plm
B-pll
C-pth
P-wtm
S-l
S-s
Fault
Cross-section
Sediment pathways
Cross-section movement

5.5.3. In-depth clast axes orientations

The orientations of clasts have been shown by many previous studies of recent debris and stream flow deposits, and the modelling of alluvial fan systems, to be a result of their formative flow type (e.g. debris flow, streamflow - Allen, 1982; Mills, 1984; Bertran et al., 1997; Major 1997; Major 1998; Benvenuti & Martini, 2002) and their location within that flow, for example, levee (edge of a flow) and channel (centre of a flow) deposits for debris flow units (Major, 1998; Kim & Lowe, 2004). The importance of long axis orientations in determining the shear stress conditions, and functionally the flow conditions, has long been discussed (Myrow et al, 2004), and modelling of cohesionless debris flows by Major (1997, 1998) determined that typically the orientations of clast long and short axes (A-axes and C-axes) would display strong preferential orientation in most debris flows.

Typically, the short axes of clasts are orientated near-perpendicular to the depositional plane, with their long axes orientated sub-parallel to that plane. This process is enhanced on a slope where gravitational processes will rotate clasts to orientate with long axes sub-parallel to that slope (Mills, 1983; Bertran et al., 1997; Major, 1998); despite the slope gradient being unknown, it would have been present at the time of deposition. This may have occurred either due to (i) reduced clast-clast interaction within the flow preferentially 'flattening' the clasts due to gravitational processes (Sohn et al., 1999; Myrow et al., 2004) or (ii) post-depositional water-flow processes rolling and pushing clasts into flat-lying positions (Moscariello, 2002). Reduced clast-clast interaction within the flow can be caused by the position within the flow (where clasts are preferentially moved to the edges of non-cohesive flows, see Bertran et al., 1997; Major, 1997; Major, 1998), the presence of suspended clay particles acting as a buffer between clasts (Iverson, 1997) and an overall reduced density of suspended gravel or coarser clasts. In this study, in view of the high clast content of each facies (typically greater than 75% by volume)

and a lack of clay matrix (silt and sand grade material being the most common) it is likely that the dominance of flat-lying clasts is a function of their original position in the flow, with the majority of deposits forming from the main bodies of flows, as opposed to the flow edges where the clast long-axis might orientate vertically. Supposed reduced clast-clast interaction lowers the frequency of imbricated clasts being formed from the same flow; instead, deposition likely occurred incrementally, with clasts at the base of subsequent flows being arrested by the inclinations of the clasts deposited before them and coming to rest at a similar angle. This results in apparent imbrication and explains the presence of imbricated clasts despite the majority being sub-parallel to the depositional plane.

Clast long axes display strong preferential orientation across the study area, a common feature in flows with high sediment concentrations (Bertran et al., 1997). Importantly, A-axes are equally preferentially orientated in proximal areas and distal areas. The flows entering the depocentre over the hangingwall dipslope from the north were long-lived enough to develop the observed well-aligned conglomerate fabric (Somerville et al., 2020). Major (1998) showed that clast long axes will typically orientate parallel to flow direction (a(p)) within the flow body, and parallel to the edges of the flow (the lateral edges and front of the depositional lobes); this allows for possible inferences to be made on the prevalence of different depositional bodies in space and time (see section 5.5.1.).

The intermediate axes of clasts typically have a wide spread of orientations through all facies and across the study area and through the stratigraphy, with no one facies displaying a preferred tendency to B-axis alignment. This indicates that different depositional processes and different flow components may give rise to similar facies when observed in the field; for example, Facies B-plm (Figure 5.6) and C-rll (Figure 5.9).

B-axis orientation and imbrication arise as a result of reduced sediment-water ratios (streamflow conditions) and is defined by Pierson (2005) as indicative of flow longevity and bedload transport in hyperconcentrated flows. Facies C-rll displays the most prominent B-axis alignment, likely formed as a function of flow longevity, supported by a lack of coarser boulder grade clasts. Stratigraphic interval 2 also displays good B-axis alignment, potentially related to a higher frequency of depositional flows with lower sediment to water ratios.

The data displayed in this study shows that with detailed study of clast morphometrics formed via debris flows and hyperconcentrated flows, they are more variable in-situ than studied physical models of their behaviour, and interpretations of isolated deposits, would suggest (e.g. Potter & Pettijohn, 1977; Major, 1997; 1998; Bertran et al., 1997). This means that the identification of the flow processes that formed specific clast fabrics is difficult in preserved sediments. The data presented here indicate multiple discrepancies in these previously defined behaviours including: (i) no clear correlation between the distance travelled by a clast and its tendency toward presenting a(t)b(i) (ab-plane imbrication) orientations in interpreted hyperconcentrated and stream flow deposits (as inferred by Rust, 1972; Pfüger & Seilacher, 1991; Benvenuti & Martini, 2002); (ii) the dominance of flat-lying clasts in potential debris flow deposits (identified by their poorly sorted nature and lack of grading) as opposed to well-inclined clasts (as inferred and concluded by Carling, 1987; Brenna et al., 2020); and (iii) beds of similar facies containing clasts of differing A- and B-axis orientations when considered relative to palaeoflow direction, with no discernible correlations to their location on the fan or identifiable sedimentological features indicating different flow rheologies. The variability and complexity of repeated sediment-laden flows over uneven fan surfaces is represented in the variability of their resultant deposits; it is likely that small differences

in sediment concentrations, flow magnitudes, and surface permeability, in conjunction with post-depositional reworking, would have a pronounced effect on the final orientation and density of clasts.

5.6. Conclusions

Detailed measurements of conglomerate facies and their clast sizes, shapes and orientations have been used to unravel the evolution of depositional flow types on an early synrift alluvial fan in the Corinth Rift, Greece. Fan palaeogeographies have been derived for three time periods through the life cycle of the fan before the cessation of major sediment input, and flow distributions on the proximal, medial and distal fan areas have been considered.

1. Immediate mass flow deposition is recorded as incrementally aggraded non-cohesive debris flow lobes, where a rapid transition from a confined river valley to unconfined dipslope surface rapidly reduced available sediment transport energy and led to incremental sedimentation from a number of expansive debris flows. This manifested as flat lying, horizontally stratified cobble-pebble clasts suspended in a sand-grade matrix proximal to the dominant sediment input point. Flows that entered the basin with a reduced suspended sediment load, and subsequently reduced viscosities, were redirected to the east by subtle topographic gradients influenced by a nearby S-dipping fault and its immediate hangingwall, leading to hyperconcentrated flow deposition in distal areas.

2. Increased tectonic subsidence gave rise to an increased dipslope gradient, which in conjunction with previous lobe deposition gave rise to the formation of an alluvial fan structure. Fan aggradation and progradation occurred, as a result of high sediment supply and increased subsidence, leading to the formation of incipient channels likely formed

from the levees of repeated non-cohesive debris flows and their trailing, more dilute hyperconcentrated flows.

3. A subsequent decrease in the subsidence rate may have reduced the rate of fan aggradation, leading to the exploitation of incipient fan surface channels by flows as opposed to their infilling and avulsion. Reduced sediment carrying capacity of flows as accommodation became increasingly filled led to the majority of these flows having a reduced viscosity and trending toward hyperconcentrated and stream flow deposition in the medial and distal fan areas.

4. The interpretation of depositional flow processes derived from clast morphometrics forming alluvial fan stratigraphy are more variable in-situ than physical models of flow events, and interpretations of isolated alluvial deposits (e.g. Potter & Pettijohn, 1977; Major, 1997; 1998; Bertran et al., 1997). Consequently, linking specific morphometric data to specific formative flow processes is tenuous.

The sedimentary section studied here shows that the tectonic evolution of a catchment cut by a rift system at a high angle to pre-existing drainage directly controls the manner, distribution, and preservation potential of different subaerial fluvio-alluvial flow types through a newly formed basin. Importantly, despite the magnitude of data collected, trends and differences between the clast morphometrics of different facies are difficult to associate with any one depositional process. Nevertheless, there are clear depositional flow responses and consequently textural responses to the evolving basin dynamics.

6. Discussion

This chapter discusses the outcomes of the previous three chapters in terms of their ability to answer the three Research Questions outlined in Chapter 1. This enables those chapters to be placed into the context of other prior studies reported in the wider literature which assess the development of alluvial fan systems in continental rift settings. The significance of this study of drainage re-routing in response to rifting, alluvial fan stratigraphic stacking patterns, and alluvial fan facies response to different rift settings, is considered.

6.1. Research Question 1

What are the impacts of pre-existing and newly formed drainage catchments on the presence of underfilled and overfilled rift basin conditions, and consequent alluvial syn-rift sedimentation?

6.1.1. The different responses of drainage pathways to rift initiation

Many rift basins have endorheic sedimentary systems developed within them such that there is no appreciable transport of sediment to external locations. Such basins are largely reliant on the provision of sediment into the basin via runoff from the surrounding hinterlands forming internal drainage pathways that are commonly oriented transverse to the trend of the rift axis (Gawthorpe et al., 1994; Gawthorpe & Leeder, 2000; Cowie et al., 2006). These drainage pathways have commonly been portrayed as the dominant source of sediment in many classic models developed to account for rift depositional environments (e.g., Gawthorpe et al., 1994). Herein, such drainage routes are called 'rift-formed drainage pathways'. In their much-cited study, Gawthorpe and Leeder (2000) invoke two major rift-formed drainage pathways: (i) transverse input from the footwall

slope, and (ii) transverse input from the hangingwall dipslope (both discussed in detail in Section 6.2.).

The impact of antecedent drainage (i.e. pre-existing drainage routes) on sediment supply to rift basins has been previously considered by multiple authors (Dart et al., 1994; Ford et al., 2013), and is included in the aforementioned summary tectono-stratigraphic models of Gawthorpe and Leeder (2000). Antecedent drainage has been of particular focus in numerous studies since the turn of the millennium (e.g. Jackson et al., 2002; Santos et al., 2014; Hemelsdaël et al., 2017; Henstra et al., 2017; Cullen et al., 2020); these catchments are typically further reaching, drain larger areas and lead to the delivery of greater volumes of sediment into receiving basins than their fault-related, uplift-sourced counterparts. Gawthorpe and Leeder (2000) specify five resultant scenarios related to pre-existing drainage systems impacted by continental rifting: (i) the incision of the drainage system into uplifting footwalls; (ii) system diversion around fault tips, (iii) diversion of drainage through a segment boundary (or relay ramp zone); (iv) reversed drainage due to uplifted footwalls; (v) the adoption of an antecedent drainage system as an axial rift system, parallel to fault segments. Results from Chapters 3 and 4, and wider considerations on the interactions of sediment transport routes with rift initiation and evolution, has resulted in the recognition of different scenarios describing pre-existing and rift-formed drainage pathways within half-graben structural morphologies (Figure 6.1A).

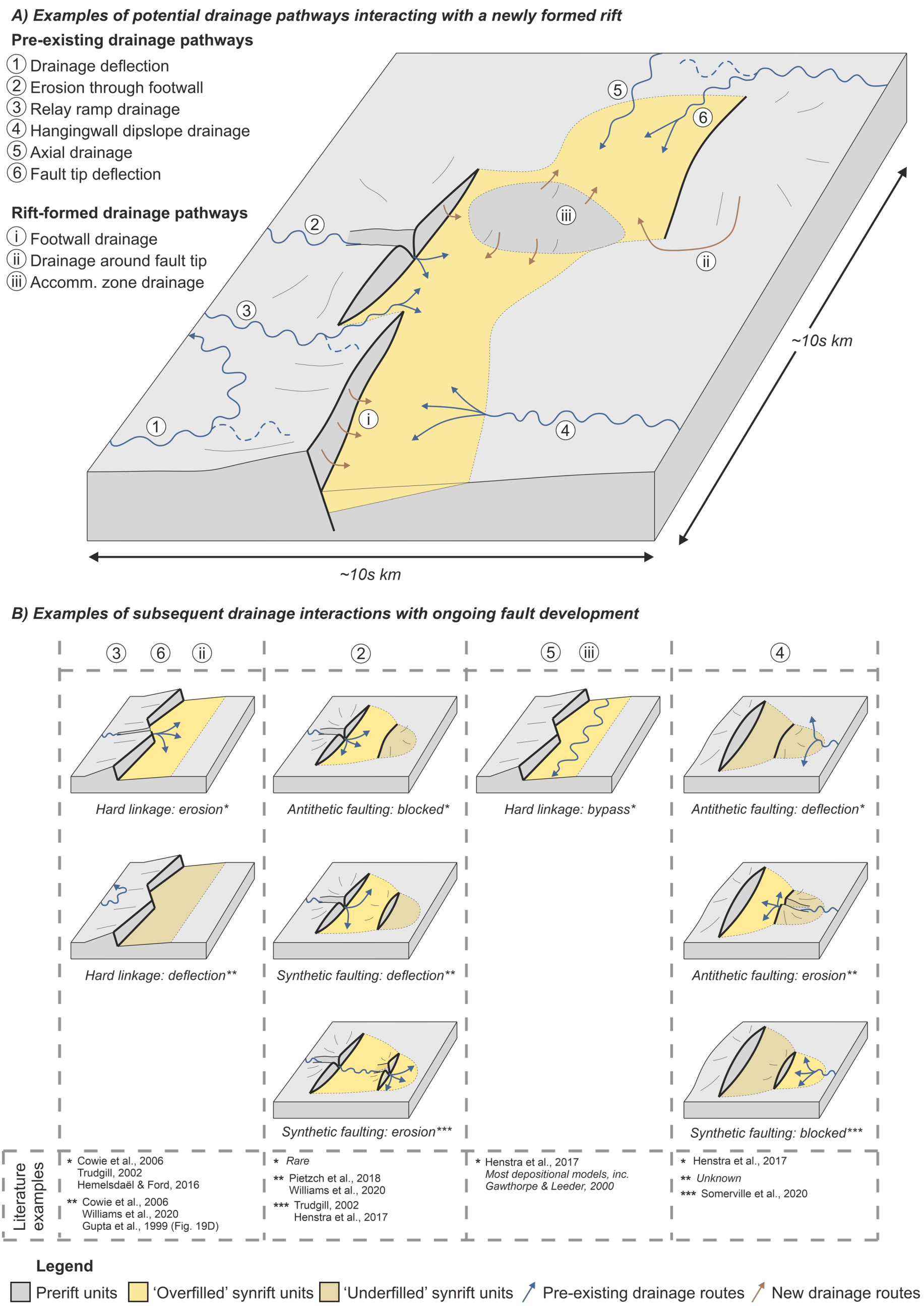

Figure 6.1 *Models displaying A) the interactions of pre-existing drainage pathways and rift-formed drainage pathways with newly formed rift depocentres, and B) their subsequent interactions with antithetic, and synthetic faulting, and relay ramp breaching.*

As surface rupture initiates as a result of extension, a major basin bounding fault is formed. Its orientation with respect to the pre-existing drainage routes, and its dip-direction, will initially govern which scenario will occur in consequence. As such, the drainage scenarios outlined in Figure 6.1A can be described in terms of their orientation to the rift system and the dip-direction of the major fault; four main scenarios are possible when the rift forms perpendicular or near-perpendicular to pre-existing drainage direction. Drainage deflection (scenario 1, Figure 6.1A) occurs in cases where the strike of footwall uplift occurs perpendicular to the main pre-existing drainage flow direction. The fault will develop so that the footwall is located on the upstream side of the pre-existing drainage route, and the hangingwall is located on the downstream side, The potential of the fluvial system to erode through the uplifting footwall may be inhibited, because of the uplift rate itself and the limited erodibility of the bedrock lithology of the footwall. As a result, the system is deflected away from the rift by the newly formed topography.

Cowie et al (2006) use numerical modelling and modern examples of pre-existing fluvial systems cross-cutting normal faults to detail the effect of stream length scales (L_f), and whether the fluvial system is close to being transport limited or under-supplied with transported sediment ($Qs \approx Qc$ and $Qs < Qc$ respectively; where Qs is the volume of transported sediment, and Qc is the transport capacity of a river), on its likelihood of eroding through an uplifting footwall (scenario 2, Figure 6.1A). When Lf is large, it is increasingly affected by tectonic back-tilting of the uplifting footwall and is more likely to be deflected by the uplifting footwall. When Lf is small, a larger proportion of the catchment area will be located in the uplifting footwall, and upstream knickpoint incision in response to faulting occurs rapidly. leading to an increased likelihood of the channel gradient being maintained and the fluvial system crossing the footwall (Cowie et al.,

2006). In this situation, sediment will be delivered directly into the adjacent hangingwall, and potentially directly into the zone of maximum generated available accommodation.

When multiple en-echelon normal faults form, with similar dip-directions to the direction of flow, the drainage system may exploit relay ramp zones (scenario 3, Figure 6.1A). These are commonly cited as a dominant routeway for the delivery of sediment into rift basins (Gupta et al., 1999; Trudgill, 2002; Henstra et al., 2017). This scenario may also occur when the rift faults form parallel to the pre-existing drainage direction, and the formation of topographic lows in the hangingwall of the new faults will divert rift-adjacent drainage down through into the hangingwall via relay ramps (Hopkins & Dawers, 2018).

When faulting occurs perpendicular to the flow direction of a pre-existing drainage system, with an upstream-located hangingwall and downstream-located footwall, sediment will be delivered over the hangingwall dipslope (scenario 4, Figure 6.1A). This scenario is the focus of Chapter 4. The introduction of accommodation to the system and formation of the hangingwall dipslope promotes more widespread sediment deposition. The pre-existing drainage pathway is now obstructed by the uplifting footwall and can form a depositional fan body which may or may not be deflected by the uplifting footwall to form an axial fluvial system (e.g. Santos et al., 2014).

Commonly, axial fluvial systems develop in rift basins in cases where drainage systems become routed parallel to the newly formed faults (scenario 5, Figure 6.1A). A prominent feature of the landmark Gawthorpe & Leeder (2000) models, this type of system development has been interpreted commonly as an outcome of many studies since (e.g. Mack et al., 2006; Nielsen et al., 2007; Alçiçek, 2007). Fordham et al. (2010) used observations of the Basin and Range province to argue that inherited axial systems are

not as common as has previously been suggested in dryland systems, as a consequence of limited drainage integration in a low moisture environment. The study of Chapter 4 supports the general assessment and extends it to rift settings under various other climatic regimes. The inherited hangingwall dipslope-derived sediment transport pathway inhibits axial system formation due to the high rates of sediment accumulation filling the available accommodation, and a lack of a previously established rift-parallel drainage system.

Finally, in many scenarios the rift strike will be orientated at an oblique angle to drainage flow direction. When this occurs, it is increasingly likely that fault tip deflection of the drainage system (scenario 6, Figure 6.1A) may occur, whereby stream drainage is deflected around the fault tip and into the new basin. This scenario is similar to the exploitation of relay zones and is applied here to describe scenarios where the new basin is isolated, and its basin bounding faults do not overlap with other major faults of the rift system.

Competing with the external sediment sources outlined above is the sediment delivery that arises as a result of rift formation. As the faults propagate and displace, new topography is formed generating rift-formed drainage pathways; the most prominent of these drainage pathways are fault slope catchments that form abutting the main basin bounding fault (scenario i, Figure 6.1A). These sources of sediment are interpreted as the dominant suppliers of sediment to a continental rift basin in many examples from the ancient rock record (e.g. Gawthorpe et al., 1994; Rohais et al., 2007; Hemeldaël et al., 2017). Typically, catchments form on the footwall slope with small width-to-length ratios, feeding fans that are more likely to form a bajada (or fan apron) as they compete for lateral space on the basin floor (Gawthorpe & Leeder, 2000). In Chapter 4,

palaeocurrent indicators indicative of palaeoflow away from the uplifted footwall are used to interpret the development of juvenile alluvial fan bodies, which actively compete for the available unfilled accommodation with the dominant hangingwall dipslope-derived system.

New catchments form a drainage divide at their highest points. On the opposing side of the new hinterland, catchments will form that can feed drainage systems that move sediment around the fault tip and into a hangingwall depocentre (scenario ii, Figure 6.1A). These systems may typically feed larger pre-existing drainage systems that transfer sediment away from the rift basins; they are reliant on a pre-rift topography to provide a regional gradient back down towards the rift basin in order to act as a sediment source for that basin. Where this scenario occurs on intrabasinal uplifted footwalls (tilt-block crests), these drainage systems will supply sediment over the hangingwall dipslope of an adjacent basin (as observed in the examples considered in Chapter 3).

Where the edges of faults that have opposing dips overlap, accommodation zones (specifically overlapping convergent transfer zones; see Morley et al., 1990, Figure 1) form basinal highs as the surface warps under the differential stress between the two faults. If the sedimentary basins on one or both sides are underfilled, these highs can source small amounts of sediment into adjacent depocentres (scenario iii, Figure 6.1A). Muravchik et al (2014) outline one scenario from the Argentinian Neuquén basin, whereby the development of a hangingwall topographic high sourced an alluvial fan that formed elongated along the strike of the fault. However, as the topographicic difference between the accommodation zone and the basin floor is typically small relative to the difference in topography across bounding faults (between areas of footwall uplift and the subsiding hangingwall), these sources are unlikely to feed major depositional systems.

The scenarios described here occur as a result of fault initiation, where a new basin forms with initial surface rupture. Further extension, potentially accommodated on new faults that propagate through the basin as intrabasinal structures, will affect the distribution of sediments into those different sub-basins in a variety of ways. The response of sediment transport pathways to intrabasinal faulting will be assessed in the following section.

6.1.2. Responses of sediment transport pathways to syn-sedimentary rift development

The responses of pre-existing drainage pathways to rift formation, and the formation of new drainage pathways detailed in section 6.1.1. have been discussed in part through previously developed models of syn-rift sedimentation (e.g. Gawthorpe et al., 1994; Ravnås & Steel 1998; Gawthorpe & Leeder, 2000). These discussions have been used as a starting point for numerous research hypotheses that have been tested in recent studies of tectonostratigraphy, both in field-based and subsurface-based investigations (e.g. Henstra et al., 2017). Numerous prior studies have considered the impact of syn-sedimentary basin development – notably the impact of synthetic faulting – on the distribution of fluvial and alluvial sediments within evolving rift basins (e.g. Cohen et al., 1995; Trudgill, 2002; Leleu et al., 2016; Hemelsdaël et al., 2017; Ezquerro et al., 2020). Ongoing syn-sedimentary structural development of a rift basin can be considered in its simplest form as occurring in one or several of the following of four different ways: (i) continued displacement of established faults, (ii) antithetic faulting, (iii) synthetic faulting, and (iv) the hard linkage of adjacent faults (causing relay ramp breaching) (Gawthorpe & Leeder, 2000; Cowie et al., 2000; Childs et al., 2017). How each of these continued rifting scenarios interact with the drainage routing systems outlined in section 6.1.1. (and in Figure 6.1A) controls the distribution of relatively 'overfilled' and 'underfilled' basin conditions (concepts described in Chapter 2) present within a rift and

its sub-basins. As a consequence, the stacking patterns of alluvial units will vary drastically between each scenario (a concept explored in Chapter 4).

Of the four possible expressions of rift evolution listed above, continued displacement of established faults may convert a drainage pathway that was able to erode through the uplifted footwall (scenario 3, Figure 6.1A) to a deflected pathway (scenario 1, Figure 6.1A). This requires a temporally variable subsidence rate, whereby the rate of fault displacement is initially slow but accelerates as the rift develops, leading to higher rates of footwall uplift. In this study, consideration is given to the three further faulting situations of antithetic faulting, synthetic faulting and the hard linkage of faults.

How these scenarios affect the pre-existing and rift-formed drainage routes is shown in Figure 6.1B, with literature examples provided as appropriate. Importantly, there are no drainage pathways that have been shown to be affected by all three further faulting scenarios; typically, a drainage pathway is affected by either hard linkage, or by a combination of both antithetic and synthetic faulting. In simple scenarios where one of antithetic or synthetic faults develop within the basin, that basin will become separated into smaller depocentres. Where rift-transverse drainage systems are the main sediment sources into the rift (such as the example in Chapter 4), one sub-basin will become overfilled, whereas the other will be underfilled. The rate of displacement of the new intrabasinal fault, the incisional response of the fluvial system to the new uplift, and the erodibility of the uplifting bedrock located within the fluvial channel (see Cowie et al., 2006, for review; e.g. Eqn. 1, p236, describing fluvial incision rate) will control which sub-basin becomes overfilled, and which becomes underfilled. Subsequent antithetic or synthetic faulting can be considered as further additions of the simple scenarios outlined in Figure 6.1B, leading to complex rift basins with multiple split depocentres.

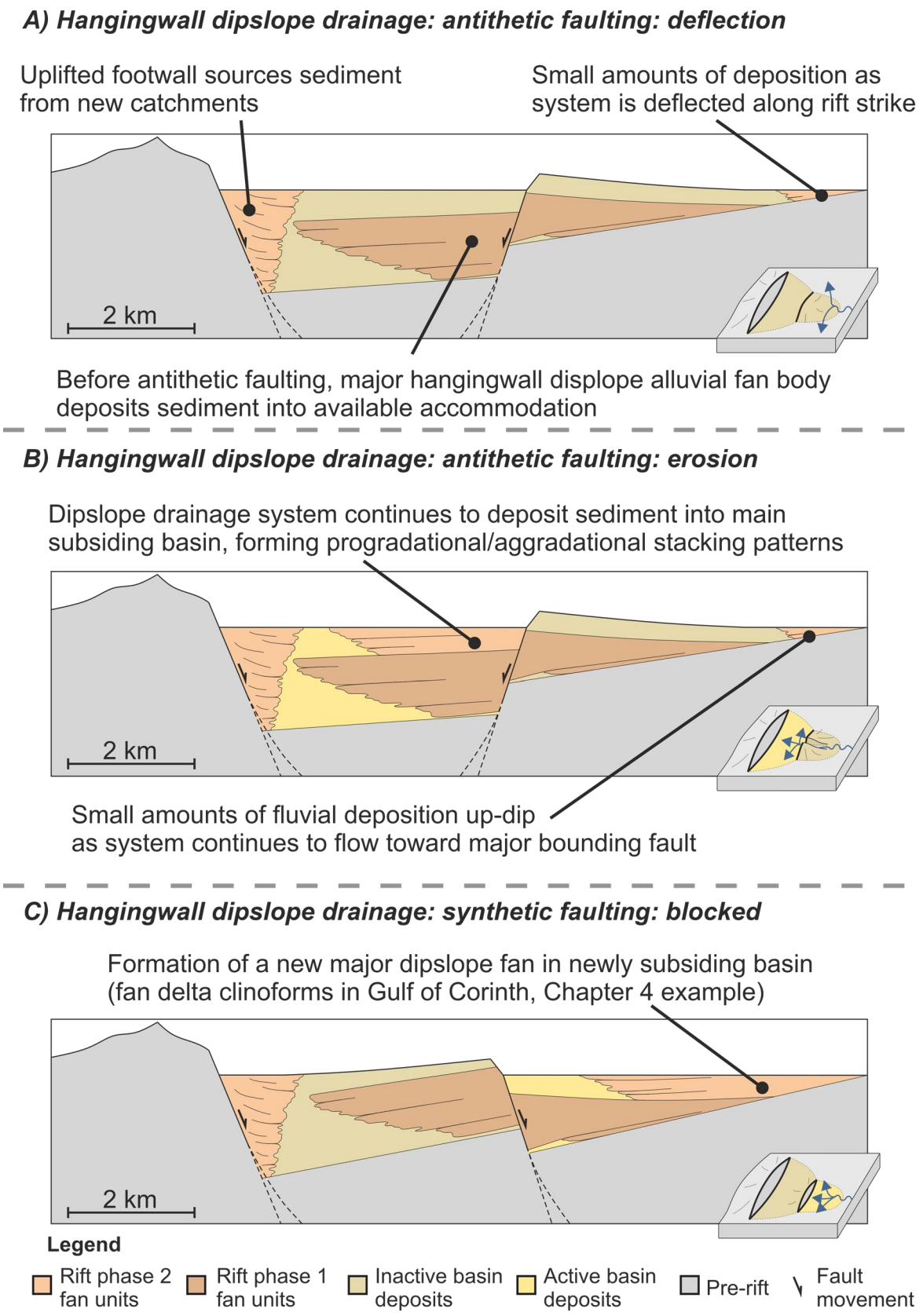

Figure 6.2 *Example cross sections of the predicted alluvial fan stacking patterns resulting from pre-existing drainage over the hangingwall dipslope.*

If intrabasinal faulting forms in an orientation oblique to the trend of the main basin-bounding fault (caused by a rotation in the extensional stress field), or forms offset to the basin bounding fault (i.e. the maximum displacement of the intrabasinal fault being located closer to the fault tip of the basin bounding fault), sediment supply pathways will be affected differently to the scenarios outlined in Figure 6.1B. For example, in a scenario where the major sediment source is over the hangingwall dipslope, an obliquely striking intrabasinal fault may preferentially divert sediment to one side of the rift. Similarly, if the intrabasinal fault formed parallel to the main basin bounding fault but laterally offset to it, sediment will be drawn towards the newly formed areas of maximum subsidence. Oblique or offset intrabasinal faulting scenarios are not considered in detail in this study, as many different situations may arise depending on the degree of intrabasinal fault offset or strike angle Importantly, oblique or offset intrabasinal faulting is unlikely to result in full diversion of sediment delivery at a similar magnitude to the examples considered in Figure 6.1B.

Chapter 4 considers the development of a transverse pre-existing drainage system feeding sediment over the hangingwall dipslope of a half-graben. Using observations from synrift field exposures in the Gulf of Corinth, Greece, the impact of intrabasinal synthetic faulting on the presence of overfilled and underfilled basin conditions in this scenario are considered. The sudden cessation of sediment supply to the area of maximum subsidence in the hangingwall is expressed in the accumulated succession as a sharp transition from continental alluvial fan facies (dominated by conglomerate and pebbly sandstone) to relatively fine-grained lacustrine facies. Subsequently, the alluvial fan system ceased progradation as a result of the loss of sediment supply, and was partly submerged by a lacustrine environment. The drainage feeding the alluvial system

subsequently formed a fan delta which built into the lake margin on the hangingwall dipslope.

Depending on the size of the newly formed basin, and the ratio of the rate of accommodation generation to the rate of sediment supply, that new basin will either become overfilled or underfilled. In the scenario outlined in Chapter 4, the rapid supply of sediment over the hangingwall dipslope and rapid formation of a large alluvial fan body resulted in overfilled basin conditions which inhibited the development of transverse footwall-slope-sourced systems and axial systems. The juvenile form (in the case of footwall-slope fans) or lack of development (in the case of a pronounced axial system) of other depositional environments present within the rift basin resulted in a period of underfilled conditions following intrabasinal faulting (see Figure 6.1B, 'Synthetic faulting: blocked' scenario, and Chapter 4, Figure 4.10).

The different scenarios for sediment supply into continental rift basins outlined in Figure 6.1 can be referred to when considering the potential stacking patterns of alluvial fan sediments that comprise the fills of rift basins. Based on observations from Chapter 4, as described above, and considerations from Chapter 3 and the wider literature, Figure 6.2 presents a series of different possible scenarios for the stacking patterns of alluvial fan bodies within rift basins where the dominant sediment input is from a pre-existing drainage system over the hangingwall dipslope. The presence and extent of alluvial fan deposits and the potential of those systems to prograde, aggrade, or retrograde, can be predicted for different ratios of rates of accommodation generation to rates of sediment supply in the newly formed sub-basins, depending on their size. In subsurface data, the relative timing of intrabasinal faulting can be discerned from cross-cutting relationships between normal faults and synrift basin fill, and by sedimentological relationships (e.g.

growth strata). By considering the orientation of pre-existing drainage pathways to both the initial rift fault and the subsequent intrabasinal fault, improved predictions of the sedimentary stacking patterns formed by alluvial fans in that rift basin can be determined using the scenarios shown in Figure 6.1A (e.g. Figure 6.2).

These interactions are possible scenarios that might be expected to arise rapidly following the initial development of new intrabasinal faults or the breaching of relay zones. As further extension continues, displacement may be accommodated on the newly formed intrabasinal faults rather than the original rift-bounding fault (Gawthorpe & Leeder, 2000). This causes the uplift and rotation of tilt-block crests within the basin and will form new rift-formed drainage pathways with time (Figure 6.1A, scenario ii) as the tilt-block crests are elevated above the basin floor. The newly developed catchments will deliver sediment into the two adjacent basins over the newly formed hangingwall dipslope and footwall slope.

6.2. Research Question 2

How does evolving rift fault development control the scale, stacking patterns, and sedimentary facies of alluvial fans in rift basins?

6.2.1. The influence of developing tilt-block crests on synrift sediment delivery

When considering evolving continental environments in rift systems, the review paper of Gawthorpe and Leeder (2000) is commonly cited as a guide to aid interpretation of the likely distribution of sedimentary environments across a basin floor during different stages of development of the rift system (e.g. adapted models in Coleman et al., 2017; Muravchik et al., 2018; Chen et al., 2020). Importantly, the Gawthorpe and Leeder models aid in the summary of general concepts and relationships. In this way, they help improve

understanding. However, these models lack specific important details: (i) they tend not to account for certain fault evolution scenarios (e.g. the presence of antithetic faulting and its effect on sedimentation); (ii) they do not provide specific information on the interactions of geographically different sediment sources into the basin (e.g. competing drainage catchments); (iii) they do not consider different depositional flow processes and sediment supply rates within those systems that act as sediment sources; and (iv) they do not predict detailed arrangements of resultant facies types and distributions thereof based on the factors outlined in (ii) and (iii).

Many studies have focussed on sediment entryways into a basin that are themselves sourced from outside the rift system via pre-rift drainage pathways (e.g. Santos et al., 2014; Hemelsdaël et al., 2017; Cullen et al., 2020), or transverse systems formed from a footwall slope (e.g. McArthur et al., 2012; Chen et al., 2020). The development of new source-to-sink sediment systems on uplifted intrabasinal tilt-block crests formed over both the hangingwall dipslope and footwall slope remain relatively understudied and poorly understood (though see Muravchik et al., 2018, for one such example). This is despite intra-basin block uplift being a common feature identified from multiple subsurface studies, including those of parts of the North Sea (such as the Inner Moray Firth; Underhill, 1991) and the North West Shelf, offshore Australia (e.g. Barrett et al., 2020). As discussed in Chapter 3, the scale of the rift system exerts control on the proportion of the adjacent basin floor area that is occupied by the newly generated transverse systems, and therefore directly controls their subsequent stacking patterns and arrangements of sedimentary facies preserved in the subsurface basin fill.

Figure 6.3A shows examples of rift systems of different sizes and how their constituent depositional environments compete for space on the basin floor. For relatively small-

scale basins, those that form with faulted blocks reaching up to 20 km in width (outlined in Chapter 3), a higher proportion of the basin floor area will be made up of alluvial fan environments formed from the uplifted tilt-block crests. For larger-scale blocks greater than 20 km in width (outlined in Chapter 3), the proportion of the basin floor occupied by alluvial fan systems will be less than that of small-scale systems. This is a function of the relationship between catchment area and fan surface area described below (see Chapter 3, Figure 3.12). The competition for unfilled but available accommodation on the basin floor between alluvial fan and axial fluvial environments is well documented; for example, Leeder & Mack (2001) document the preserved sedimentary expression of alluvial fan 'toe-cutting' by the axial fluvial system of the Rio Grande Rift, New Mexico.

In smaller scale rift settings, the axial and transverse sedimentary systems can be in direct competition rapidly following the moment of initial tilt-block crest erosion, as alluvial fans can rapidly reach length scales of many kilometres (Ventra & Clarke, 2018). On the hangingwall dipslope side of the tilt-block crest, newly formed alluvial fan environments may have a larger surface area relative to those present on the footwall slope side (e.g. in dryland environments, Fordham et al., 2010) as a consequence of the shallower depositional gradient on the hangingwall dipslope side, and a larger source area potentially feeding larger fans (Viseras et al., 2003).

Figure 6.3 (next page) *Schematic models depicting A) the predicted plan view distributions of alluvial fan environments in rift basins of different scales, and B) their cross-sectional stacking patterns of both footwall-slope sourced and hangingwall-dipslope sourced fans.*

Smaller-scale rift systems

Larger-scale rift systems

A) Tilt-block models

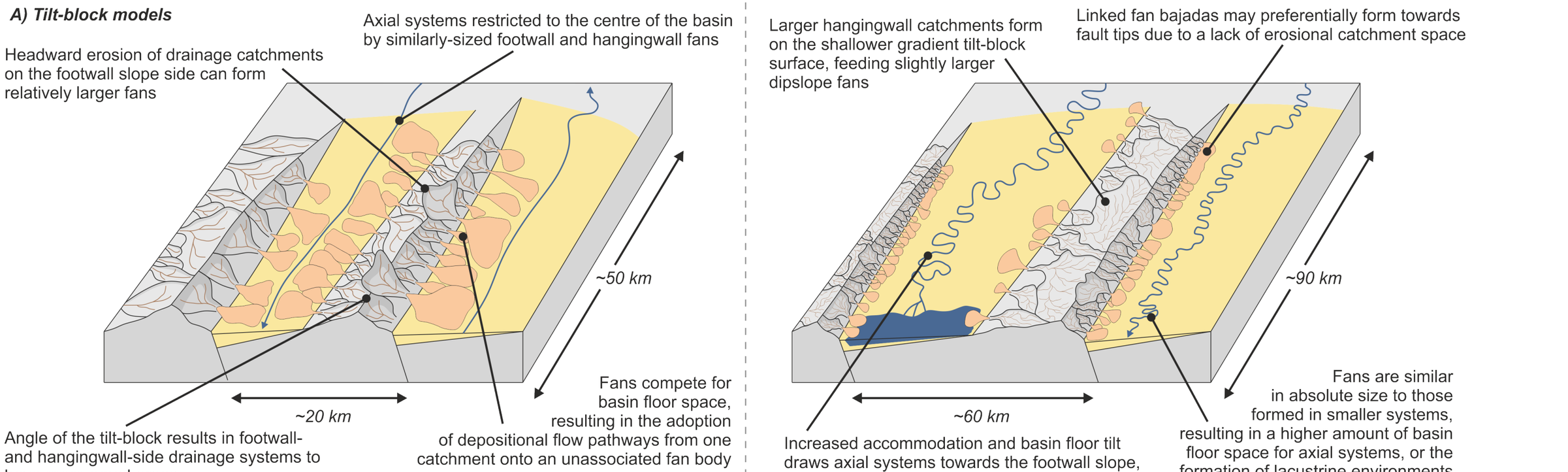

B) Predicted stacking patterns of alluvial units

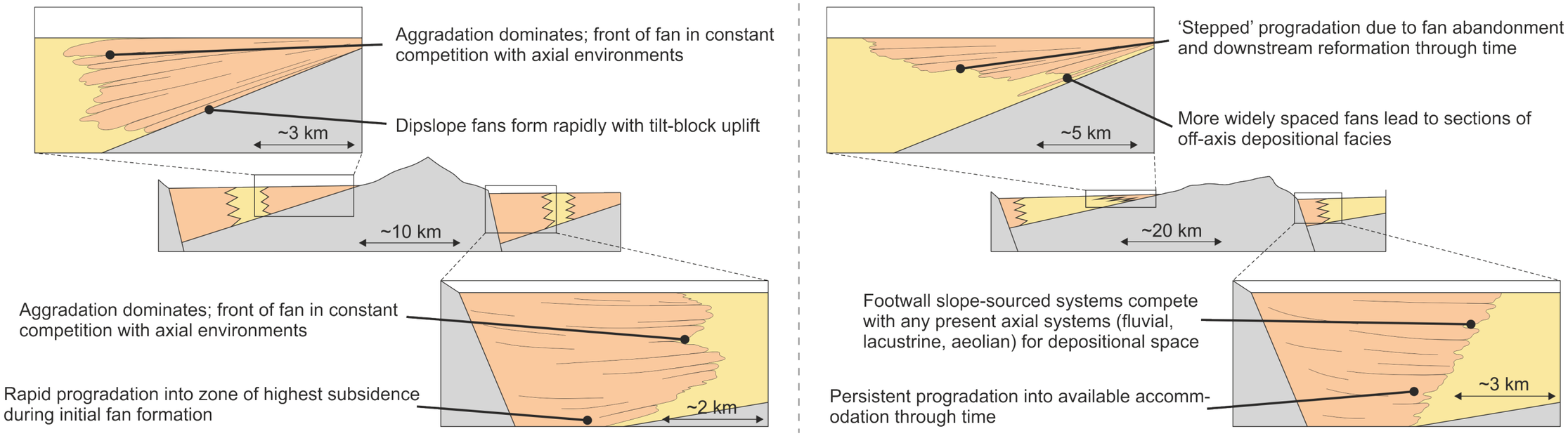

The tilt-block crests of small-scale rift systems provide a smaller erodible area for catchment formation when compared to tilt-block crests formed in large scale systems. It is shown in Chapter 3 (section 3.6.) and in previous studies (Allen & Hovius, 1998; Allen & Densmore, 2000) that a power-law relationship exists between catchment area and associated fan area. Consequently, despite the significantly reduced sizes of the catchments formed on smaller tilt-block crests, the effect on fan size will be comparatively reduced (see Chapter 3, Figure 3.12A), allowing fans sourced from both sides of a tilt-block crest to cover a higher proportion of the basin floor compared to large-scale rifts. Key differences to larger scale systems include: (i) a more centralized drainage divide on the tilt-block crest between the footwall slope and hangingwall dipslope sides; (ii) increased competition of transverse alluvial fans with axial systems (if present) for available unfilled accommodation within the basin; and (iii) an increased tendency of smaller sediment flow pathways to be adopted as part of larger 'host' fans, as a result of reduced basin floor space.

For larger systems – those where faulted blocks are greater than 20 km in width – Chapter 3 documents the development of comparatively larger catchments on the hangingwall dipslope side of tilt-block crests than on the footwall slope side. This occurs because the hinge of the tilt-block, and the extension that affects it, is located a significantly further distance away from the tilt-block crest drainage divide than in smaller systems. This provides a more extensive source area for hangingwall dipslope fans with a shallower gradient, compared to fans on the footwall slope side. In the example of the East African Rift (see Chapter 3, section 3.3.), one abnormally large southward-draining catchment dominates the hangingwall dipslope setting, containing evidence of developed channel systems, and forming a major drainage divide to smaller hangingwall dipslope catchments down-slope towards the basin (see Chapter 3, Figures 3.3 and 3.4). This may

have arisen as a consequence of part of a pre-existing drainage system being uplifted by the tilt-block crest (which is then exploited by the modern-day catchment and alluvial fan system), else as a result of the headward erosion of the catchment. The position of the drainage divide between hangingwall dipslope and footwall slope catchments varies with scale, with smaller systems developing a more centralised divide. This is both a function of the overall stretching factor of different systems, where increased stretching factors lead to increased tilting and a more centralised divide, and of the headward erosion of footwall slope catchments. The examples in this study show that footwall slope catchments can develop at similar sizes regardless of overall system scale (e.g., 18.81 km^2 average for the Hammar range; 15.32 km^2 average for the Toiyabe and Toquima ranges). This results in the headward erosion of those catchments, and the shifting of the drainage divide to a more central position, having a larger impact in smaller scale systems (where any drainage divide movement is amplified) than larger scale systems.

As fault displacement (and subsequently tilt-block crest uplift) continues, so catchments continue to erode and may integrate adjacent catchments through headward erosion. This is dependent on the relationship between accommodation formation and sediment supply rate (Geurts et al., 2018), as an increase in available accommodation will lower base level and will drive increased catchment erosion and sediment supply rates (Densmore et al., 2007). This is a particularly important process for the hangingwall dipslope side of the crest as opposed to the footwall slope side for two key reasons: (i) the larger source area increases the likelihood of local variations in bedrock lithology and climate, affecting potential erosion rates; and (ii) along-strike subsidence variations, which alter the amount of accommodation available for fan development, are amplified as the overall available accommodation on the hangingwall dipslope side of a half-graben is less than that of the footwall slope side. Specifically, where rates of accommodation

generation and rates of sediment supply are high, the catchments that feed fans directly into that depocentre are increasingly likely to dominate and integrate surrounding catchments (for example at the centre of basin bounding faults; e.g. Eliet & Gawthorpe, 1995). Further key differences between large-scale systems compared to small-scale systems include: (i) the formation of larger dipslope catchments as a result of the increased variation in erosional area to the footwall slope side of a tilt block; (ii) more widely spaced active dipslope fans as a result of their comparatively larger catchments; and (iii) little evidence of competition with axial systems for space on the basin floor.

A key similarity of both of these systems is the occurrence of headward erosion of catchments formed on the footwall slope side, penetrating the major drainage divide formed on the tilt-block crest (see examples from all three study areas in Chapter 3). This generates larger catchment and fan systems that develop next to comparatively smaller systems, as shown by the models of Gawthorpe & Leeder (2000) (see Chapter 2, Figure 2.6). This is particularly true for the Baikal rift and Basin and Range examples outlined in Chapter 3, sections 3.3. and 3.4. Cowie et al. (2006) modelled numerically evolving drainage catchments of an actively uplifting footwall and detail the headward erosion of hangingwall dipslope catchments towards major block-bounding faults. This is the opposite of what is observed in the Baikal Rift and Basin and Range examples. In these two studied examples, local climatic and bedrock lithology variations may allow footwall slope catchments to exploit these weaknesses and preferentially undergo headward erosion, leading to the observed differences with the numerical models of Cowie et al. (2006).

6.2.2. Variations in alluvial sediment stacking patterns and depositional flow processes on either side of a tilt-block crest

Based on analysis of catchment and alluvial fan morphometric data reported in Chapter 3, and further observations of fan surface processes from modern day imagery, inferences can be made on the different potential stacking patterns of alluvial deposits in variably sized rift systems through space and time. Figure 6.3B displays example cross-sections through relatively small- and large-scale systems. It depicts the similarities and differences in stacking patterns between them, and between alluvial fan sedimentary successions deposited on the footwall slope and hangingwall dipslope sides of tilt-blocks. In small-scale systems (tilt-blocks of <20 km width), the lack of basin floor space, and the formation of similarly sized fan bodies from both sides of the tilt-block crest, result in fan aggradational and incisional cycles (a process described extensively by Ventra & Nichols, 2014) as progradation and lateral expansion are inhibited by other basin environments. Along-strike, local variations in subsidence rates, bedrock lithology and climate controls the presence of larger 'host' fans (described in section 6.2.1.) and will affect the relative proportions of alluvial units present in that area of the basin.

In large-scale systems, the amount of available accommodation is typically higher than for small-scale systems, and there is an increased amount of basin floor space for depositional environments to develop. On the footwall slope side of tilt-block crests, an apron (or bajada) of fan bodies will form as newly formed catchments are closely spaced. This leads to a belt of basin-margin alluvial fan deposits forming adjacent to the fault plane, similar to those seen on both sides of the basin in smaller systems (observable from modern fan examples, Basin and Range province, Chapter 3). Such belts will exhibit either a progradational stacking pattern in a basinward direction in cases where the rate of sediment supply is high, else an aggradational stacking pattern in cases where the rate

of sediment supply is comparatively low (Eliet & Gawthorpe, 1995). If progradation of the depositional environment occurs, the footwall-slope sourced systems will push any axial system progressively away from the bounding fault (Gawthorpe & Leeder, 2000; similar to Pechlivanidou et al., 2018; Cullen et al., 2020).

On the hangingwall dipslope side of a tilt-block crest, catchments are comparatively large and sediment input points are widely spaced, allowing the formation of fan bodies with a single point source that may have limited interactions with one another (see Chapter 3, East African Rift and Baikal Rift examples). The amount of available vertical accommodation is severely restricted in comparison to the footwall slope side of tilt-blocks that shed sediment directly next to the bounding fault; as a result, fan bodies prograde rapidly into available space with little aggradation occurring (e.g. Viseras et al., 2003). On the hangingwall dipslope side of the Hammar Ridge (East African Rift example; Chapter 3, section 3.3.), relic fan bodies are visible that have been bypassed by through-fan trenching to form alluvial fans further into the basin. This leads to the 'stepped progradation' of fan units outlined in Figure 6.3 and is a function of the increased basin floor area in larger systems; in smaller scale systems, 'stepped progradation' would not have the opportunity to occur due to fan bodies formed from the footwall crest presenting a barrier to progradation. The process may be triggered by a combination of different factors, including: (i) where a fan fills the accommodation directly adjacent to the hinge point of the tilt-block crest or at the front of a previous fan body, leading to bypass; (ii) lacustrine systems in the basin undergo base-level fall, or axial fluvial systems avulse away from the hinge and no longer inhibit transverse sediment transport; (iii) larger catchments on the dipslope side of the tilt block in larger-scale systems form higher magnitude flow events (Allen et al., 2013; Ventra & Clarke, 2018), transporting sediment further into the basin. In these settings, there is high along-strike variability in alluvial

fan stacking patterns through time; fans may change location along-strike according to their catchment dynamics (including catchment integration), and established fans will eventually be bypassed forming new fans further into the basin.As a result of the larger catchments present on the hangingwall dipslope side of tilt-block crests, when compared to their footwall slope counterparts, it is increasingly likely that flow rheology will vary spatially as a flow travels downstream. Pierson and Scott (1985) give a detailed example of a volcaniclastic flow transitioning from initial streamflow, to a sediment-laden debris flow, due to erosive processes in the steepest parts of its source catchment. As the flow moves downstream, sediment concentration subsequently decreases again and the event transitions to a hyperconcentrated flow. Similar processes are likely to occur in the large hangingwall dipslope catchments of both the Hammar and Barguzin Ranges; depending on the amount of lateral sediment input from hillslope collapse near the mouth of the catchment, this will alter the sediment concentration of the flow as it reaches the fan surface and impact the occurrence of depositional streamflows, hyperconcentrated flows, and debris flows that form the fan stratigraphy.

From observations derived from satellite imagery and catchment morphometrics recorded in Chapter 3, it is possible to begin to predict what kinds of depositional flows and depositional features form the stacking patterns described above, and how they are influenced by the outlined interactions between progradational and aggradational processes. Although it is important to recognise that surface observations do not directly indicate what will be preserved in the subsurface, observations on depositional flow types and flow pathways can be used to infer the styles of deposition likely to occur (cf. Weissman et al., 2010; 2015). This is applied in a framework of the external and internal factors that would govern the active depositional surface of the fan body (e.g. de Haas et al., 2014).

Figure 6.4 displays different observations of surface features from the tilt block crests studied in Chapter 3, inferred from smaller scale (Basin and Range province) and larger scale (East African Rift, Baikal Rift) systems. As discussed in Chapter 3, the rheological flow types that occur on the fan surfaces are a function of the dynamics and morphometrics of the catchments that feed them (Welsh & Davies, 2011). For small-scale systems, the catchments either side of a tilt-block crest are of similar size and are more likely to erode similar lithologies, increasing the likelihood of similar flows occurring on both the hangingwall displope and footwall slope sides. In particular, values of the Melton's Ratio (described in Chapter 3, section 3.2.4.) for catchments in the studied Basin and Range system show an increased likelihood of deposition by higher viscosity flows over both the hangingwall dipslope and footwall slope sides of the tilt-block crest. This is supported by observations from linked fan and catchment systems of similar sizes from different tectonic settings (e.g. Sorriso-Valvo et al., 1998; de Scally et al., 2010; Welsh & Davies, 2011). The prevalence of higher viscosity flow deposition is also predicted to occur in the footwall slope catchments of large-scale system tilt-block crests (see Chapter 3, Figures 3.5 and 3.8). As system scale varies, the larger sizes of hangingwall displope catchments increases the likelihood of occurrence of comparatively lower sediment concentration flows (e.g. hyperconcentrated flows or streamflows) (see Chapter 3, Figure 3.5 and 3.8). These comparatively larger catchments may have a higher potential to contain a higher variation of bedrock lithologies, which would impact the depositional

processes occurring on the fan surface. This is explored further in Chapter 6.3.

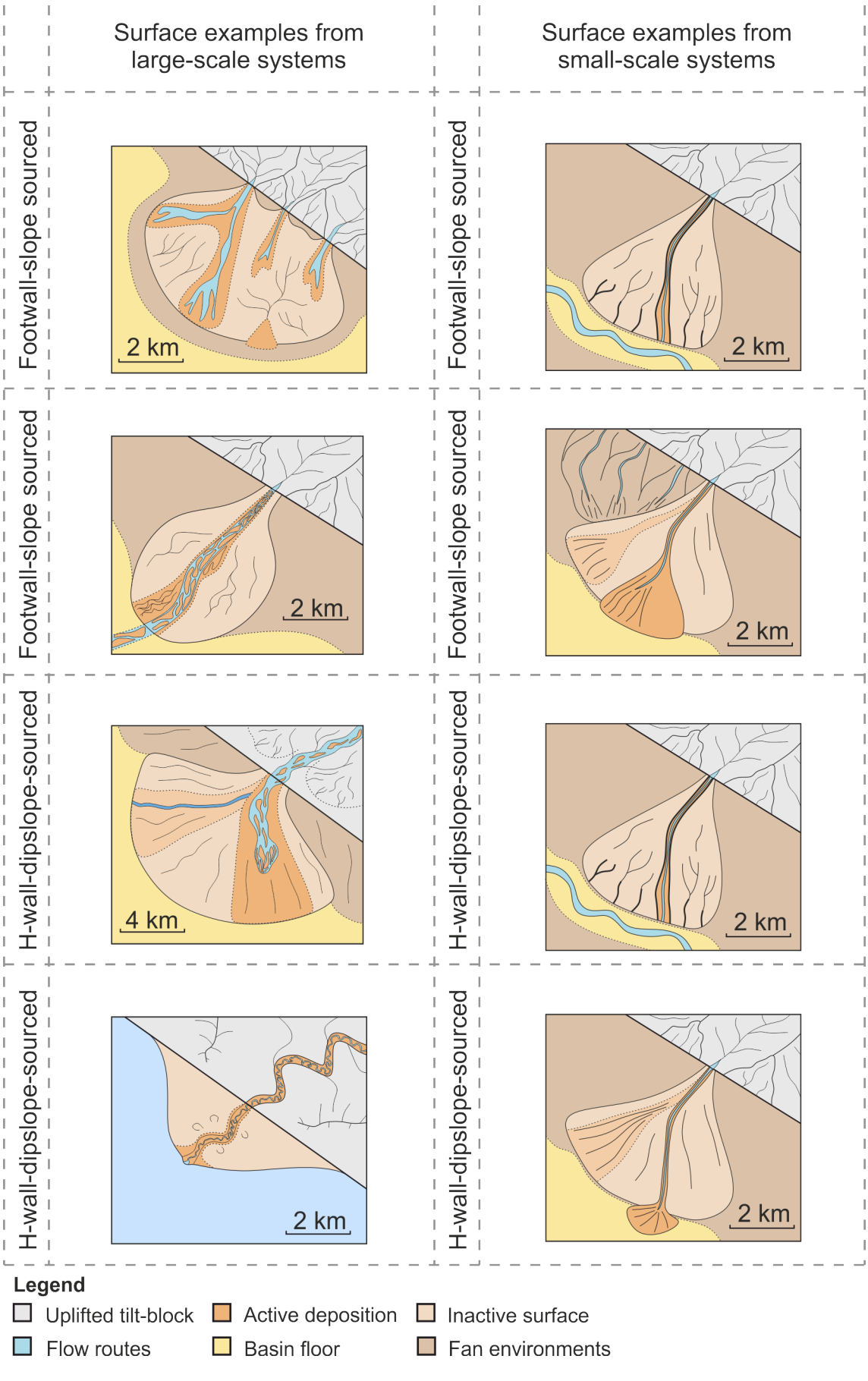

Figure 6.4 (previous page) *Example observations of surface flow features from the East African Rift, Baikal Rift and Basin and Range tilt-block examples. In large-scale systems, there is a larger amount of variation in the type and size of depositional feature visible on the fan surface between fans sourced from the footwall crest and those sourced over the hangingwall dipslope. Conversely, in small-scale systems, there are more observable similarities in the type and size of depositional feature visible on the fan surface between fans sourced from the footwall crest and over the hangingwall dipslope. The variability of features is a function of the depositional flow processes that lead to their formation; therefore, the similarities observed in small-scale systems supports the interpretation that the formative flow processes of footwall crest and hangingwall dipslope fans would be more similar than that of large-scale systems.*

The observations outlined here provide an understanding of the development of alluvial fan systems in response to ongoing rift formation that can applied to the prediction of alluvial fan units in subsurface data sets (Prosser, 1993). Alluvial fan units are typically difficult to identify on seismic sections (in particular, in data with low vertical resolution) due to the frequently similar sediment calibre to adjacent fluvial facies on the basin floor. Throughout much of the literature, the interpretation of alluvial fan units is underrepresented when compared to fluvial and lacustrine continental environments. Where well or core data of the basin fill are available, alluvial fan facies can be better identified (typically based on the presence of basin margin conglomerates, such as Heward, 1989; Ojakangas & Dickas, 2002), but predicting their extent and subsequently creating more accurate palaeogeographic models from this information is difficult.

Figure 6.5 outlines different possible scenarios for the prediction of subsurface stratigraphy in continental rift systems. Depending on the amount known about the rift setting, including its scale, basement lithologies, and climate at the time of formation, different predictions can be made for the extent and stacking patterns of basin margin alluvial fan units therein. Figure 6.5A shows a representative example of alluvial stacking patterns in large scale (> 20 km fault block width) rift systems displaying the stepped

progradation of hangingwall dipslope fan environments into the basin through time. In more humid settings, where lacustrine systems dominate the majority of the basin floor, prograding stacking patterns may be inhibited (dependent on sediment supply rates) leading to retrogradational stacking patterns on the hangingwall dipslope due to backstepping fan delta formation (Figure 6.5B). In small-scale (< 20 km fault block width) rift systems, progradational and retrogradation stacking patterns are inhibited by a lack of depositional space on the basin floor (Figure 6.5C).

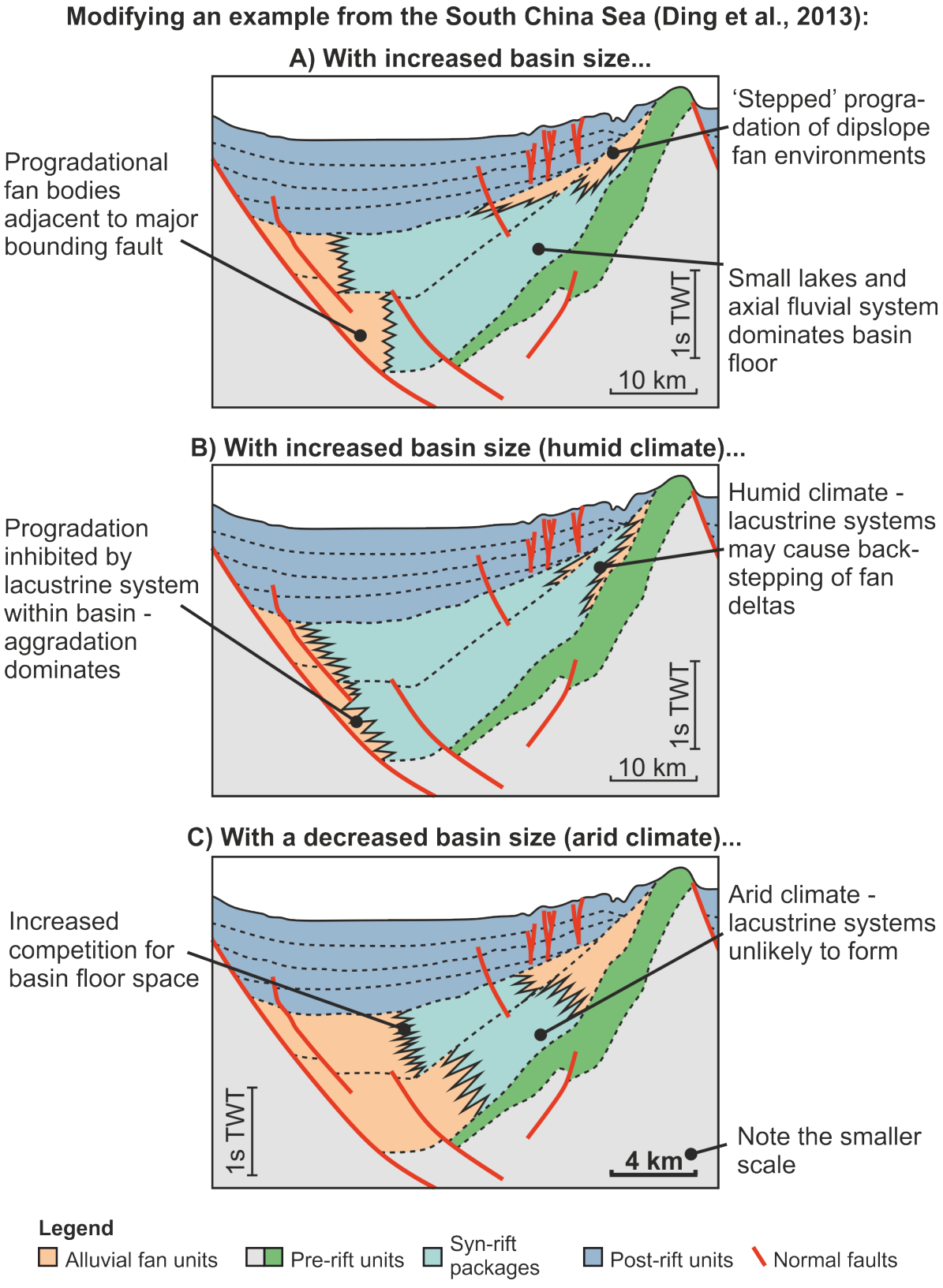

Figure 6.5 *Example interpreted seismic sections using the observations and interpretations derived from the study of modern-day systems. Data in this study can be used to better predict the extent of alluvial fan facies at the basin margin, and how they develop and change location through time, for different examples of system scale and climatic setting.*

6.3. Research Question 3

How can alluvial fan facies and their constituent components be used to determine depositional flow types, and their variable temporal and spatial positions, within rift basins?

6.3.1. Extrinsic and intrinsic controls on alluvial fan development

As discussed in section 6.2., there is an increased likelihood of the alluvial fan facies deposited over the hangingwall dipslope to be formed from lower viscosity flows such as hyperconcentrated flows or streamflows. Recent studies have suggested this is true based on evidence from the rock record (Mack et al., 2002; Muravchik et al., 2014) and that this is a function of the larger catchments that can feed longer flow pathways over the dipslope (section 6.1.). For pre-existing drainage routes over the dipslope, such as the Mornos catchment described in Chapter 4, it would be expected that the catchments feeding that system would be larger than their rift-formed counterparts. As established fluvial systems, pre-existing drainage catchments would logically continue into the basin and form fluvial fans.

Chapter 4 outlines that a large proportion of preserved depositional facies of the Rodini Formation (western Gulf of Corinth), which were formed from an alluvial fan environment potentially sourced by the modern-day Mornos catchment, are interpreted as non-cohesive debris flow facies. These sedimentary units would have been deposited by flows with high suspended sediment concentrations (Iverson, 1997; Sohn et al., 1999) and do not represent the predicted streamflow deposition outlined above. Interpretations of architectural elements comprising the conglomeratic Rodini Fm., analysed in Chapter 4, allows for estimations of the proportions of the succession that are comprised of those elements. As discussed in Chapter 4, each of the conglomeratic

architectural elements is interpreted to have formed from either non-cohesive debris flows (elements AE1, AE3 and AE4; Chapter 4, section 4.4.2.), or hyperconcentrated flows (elements AE5 and AE6, and likely the element AE2; Chapter 4, section 4.4.2.). Debris flow-related architectural elements comprise 39.45% of the measured succession by vertical thickness, whereas 23.38 – 58.38% of the vertical succession is represented by hyperconcentrated flow-related architectural elements. It is important to indicate here that the proposed architectural element AE2 from Chapter 4 is reinterpreted as potentially representing hyperconcentrated flow deposition based on data outlined in Chapter 5. It is clear that a large proportion of the preserved succession comprises debris flow-related deposits. Possible explanations for the observed high proportion of debris flow deposits are related to both extrinsic and intrinsic controls on the linked catchment and fan system that formed the sedimentary package.

Climate has been regarded as a major extrinsic control that acts to influence the type and magnitude of depositional flows into sedimentary systems (DeCelles et al., 1991; Allen et al., 2013). Studies on the links between climate and alluvial fan sedimentation are well-documented in terms of climatic cyclicity (Ventra et al., 2018) and the response of depositional environment locations, stacking patterns and constituent facies and their components to climatic forcing (e.g. D'Arcy et al., 2017; Meek et al., 2020). The case study outlined in Chapter 4 provides an example to test whether high-resolution climatic cyclicity is recorded in the sedimentary successions of overfilled rift basins.

Deposition of the studied Rodini Fm. occurred from 2.2-1.8 Ma to 0.42-0.4 Ma (Palyvos et al., 2007; Gawthorpe et al., 2018), during the Pleistocene, and straddled a climatic transitional period. From 2.2 Ma through to approximately 1.2-0.7 Ma, climatic cyclicity was controlled by 41 kyr obliquity orbital cycles; through the end of the deposition of the

Rodini Fm., climatic cyclicity switched to 100 kyr glacial-interglacial cycles (Suc & Popescu, 2005). As a consequence, the climate of the Mediterranean during the Pleistocene was highly variable, with periods of cold, warm, wet and dry conditions (Head & Gibbard, 2005).

Debris flows and hyperconcentrated flows occur with different frequencies when the climate is more arid or humid, with debris flows occurring more frequently under arid conditions when fluvial flow pathways within the catchment are poorly established or ephemeral, and slope instabilities can lead to localised failure (Iverson, 1997; Schlunegger et al., 2009). The interbedded nature of facies outlined in Chapter 4 (and Chapter 5, Figure 5.20), indicating the alternation of hyperconcentrated and debris flow conditions, may mirror the repeated climatic cyclicity from wetter to drier conditions in the palaeo-Mornos catchment. The presence of thin palaeosols and rare calcrete nodules observed in distal parts of the proposed fan are further evidence for this cyclicity. Grey, carbonate-poor palaeosols may develop on a quiescent fan surface during more humid conditions with a poorly drained state (Mack, 1992). By contrast, calcrete nodules and palaeosols are indicative of well-drained conditions (Retallack, 2001; Alonso-Zarza, 2003). The observations made here are similar to other Mediterranean areas at the time of deposition during the Pliocene (e.g. alluvial fan deposits in Spain, Wagner et al., 2012). It is possible that the destructive nature of the flow processes forming the conglomeratic units (for example, hyperconcentrated flow turbulence or the high shear stress at the base of non-cohesive debris flows) removed any evidence to indicate the former presence of palaeosol and calcrete nodules further up-fan within the basin.

The preservation of different alluvial facies, architectural, and depositional elements may also be influenced by ongoing tectonism. Previous studies have indicated that climatic

cyclicity exerts a larger control on facies relationships and depositional stacking patterns, whereas tectonism exerts a larger control on longer-scale fan depositional cycles and sediment supply rates (e.g. Leleu et al., 2005; Quigley et al., 2007). In the case of the Rodini Fm., the influence of ongoing tectonism on facies formation is masked due to the overall consistency in the composition of the conglomerate clasts across different facies (see Chapter 5). Sediment provenance studies are typically used to identify likely sediment sources arising as a consequence of ongoing tectonism (see section 6.3.2.) and these varying sources of sediment can be recorded in varying clast compositions in resultant deposits, in some cases. Nevertheless, Chapter 5 (sections 5.5. and 5.6.) assesses the potential tectonic signals recorded in conglomerate clast morphometrics and concludes that tectonic forcing impacted the distribution of conglomeratic deposits across the basin.

Using the observations from Chapters 4 and 5, Figure 6.6A presents the predicted three-dimensional stacking patterns of conglomeratic alluvial fan sediments formed over a hangingwall dipslope. Initial deposition from unconfined flows, arising as sediment flow pathways enter a newly formed basin, is observed from physical models of alluvial fan deposition. Clarke et al. (2010) describe sheet-like flows forming a prototype fan body and preceding the development of depositional lobes on the fan surface. This is an initial response to a sudden change in slope gradient and cessation of catchment-related confinement, causing the lateral expansion of the flow onto the new depositional surface (provided any inherited topography has been infilled). Ventra & Nichols (2014) interpret similar sheet-like deposits to represent a dominance of extrinsic controls on fan deposition rather than intrinsic factors. In the case of the Rodini Fm., high amounts of sediment input, and limited basin subsidence due to the system being located on the hangingwall dipslope, leads to rapid progradation of the alluvial fan into the basin (similar to Eliet & Gawthorpe, 1995; Viseras et al., 2003).

A) Example 3D block model of an alluvial fan formed from pre-existing drainage over a hangingwall dipslope

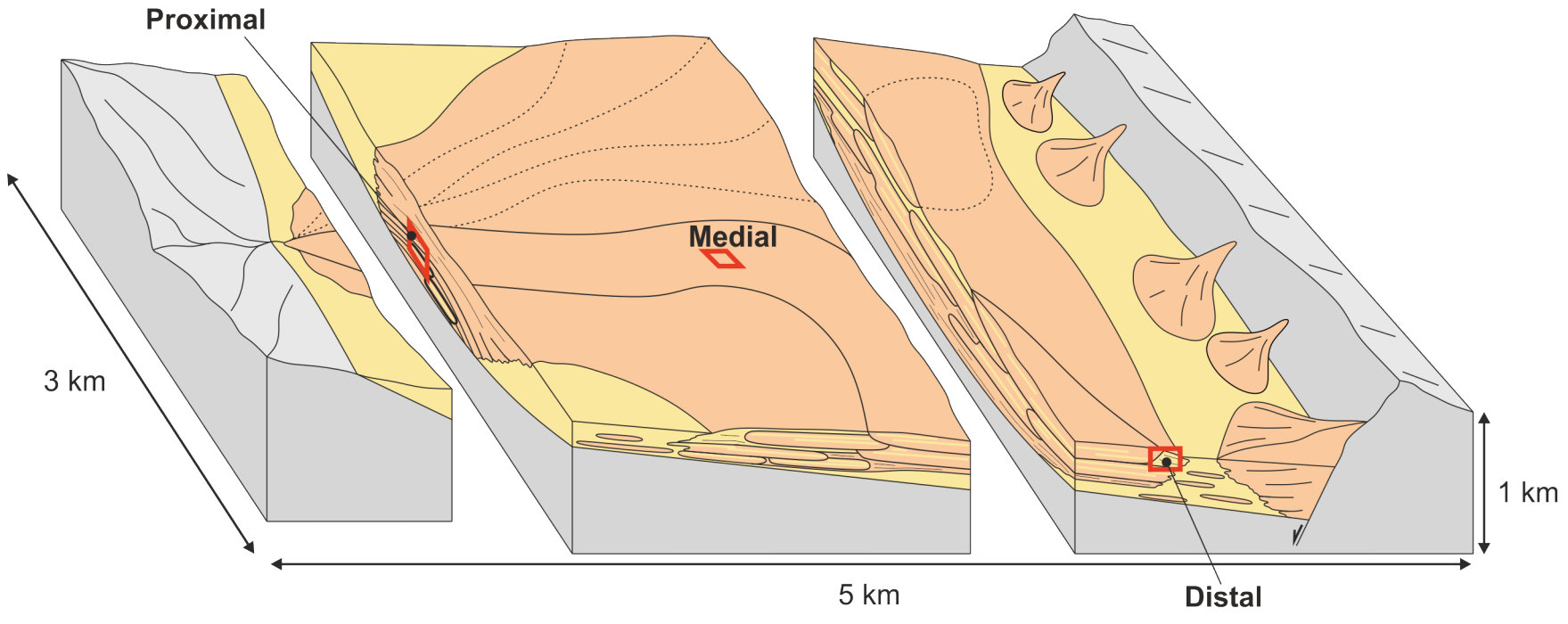

B) Predicted 3D stratigraphic architectures present on the proximal, median and distal fan (locations in part A)

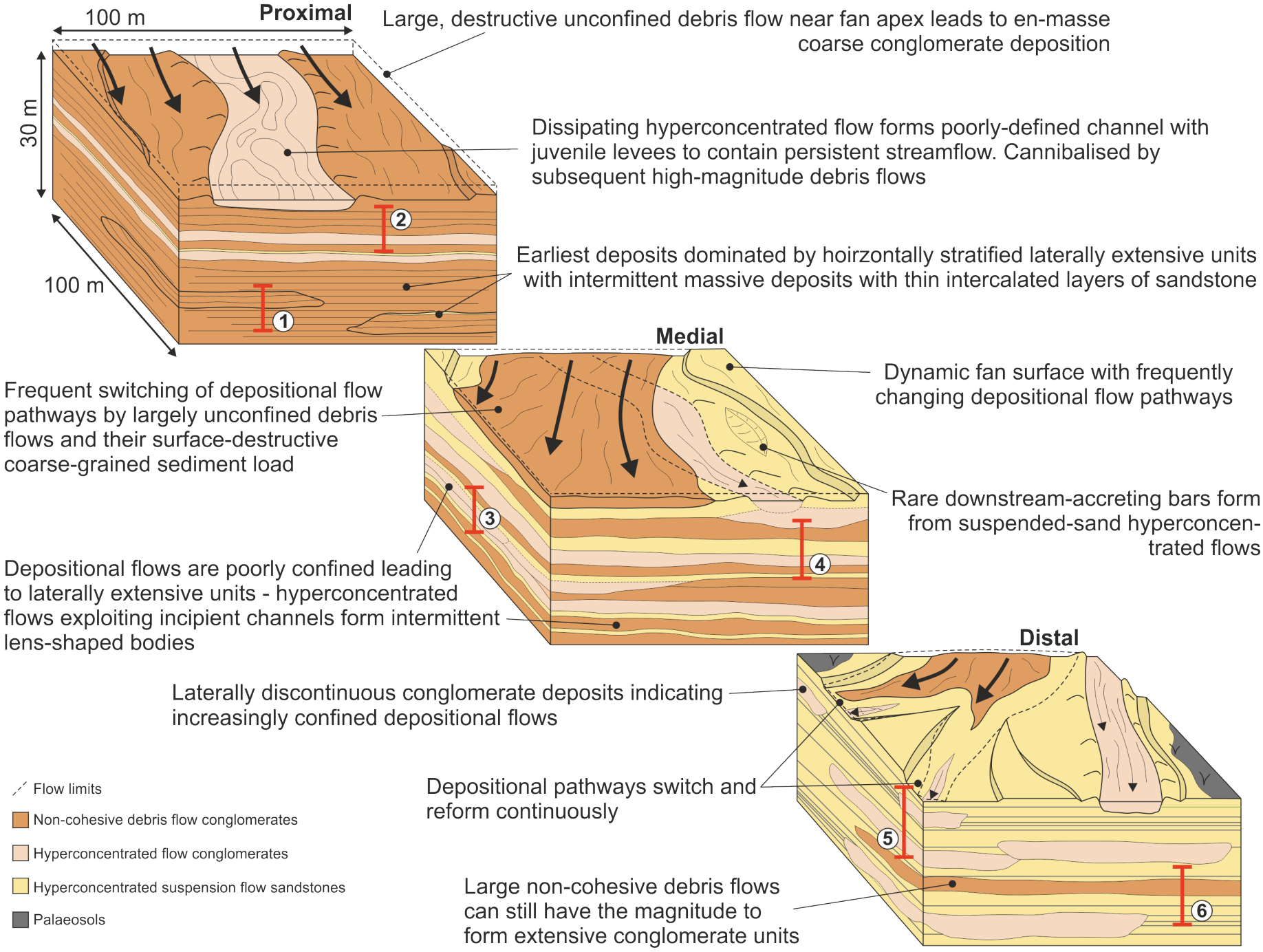

C) Example sedimentary facies logs (locations in part B)

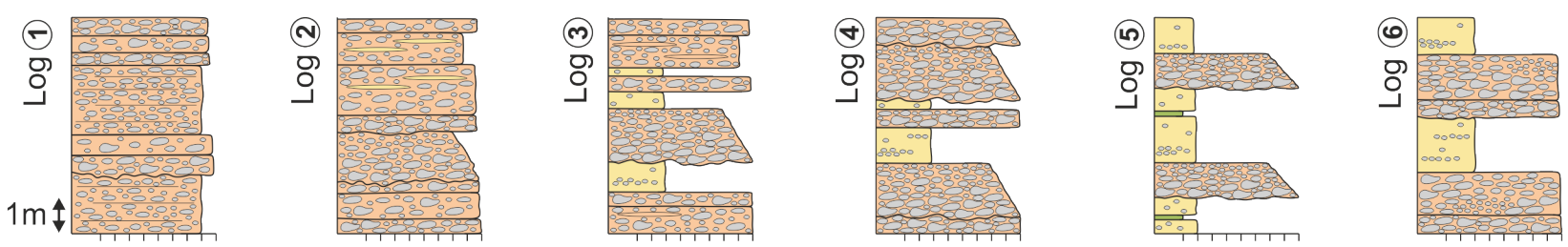

Figure 6.6. *A) Example 3D model of an alluvial fan developed in a half-graben, sourced from pre-existing drainage over the hangingwall dipslope. B) Example 3D block models of the sedimentary stacking patterns of different depositional facies and architectural elements forming the alluvial fan deposits. C) Example sedimentary logs showing the distribution of conglomeratic and sand facies within the basin.*

As outlined in section 6.2, the scale of the rift system being studied is an important consideration when predicting the extent of alluvial fan units in synrift sediments. In the Gulf of Corinth example, the delivery of large volumes of sediment to the basin from a pre-existing drainage catchment provides the hangingwall dipslope system with an immediate 'headstart' on the deposition of sediment into the basin, compared to footwall-slope sourced systems. The formation of footwall slope-derived sediment systems will be inhibited. The formation of an axial fluvial system will likely rely on the diversion of the hangingwall dipslope system along the rift axis (Chapter 4 example; e.g. Santos et al., 2014). In a modern-day example, the Okavango Delta, the case is even more severe; as the dipslope drainage system feeds sediment into the basin, there is no rift axis flow route available as the system has formed within an isolated rift basin. Consequently, the large amount of sediment provided over the hangingwall dipslope rapidly fills the available accommodation, inhibiting the development of fan bodies from the uplifted footwall as the hangingwall dipslope-sourced delta deposits sediment directly adjacent to the basin bounding fault (McCarthy et al., 2002).

6.3.2. Predicted facies variations of a hangingwall dipslope alluvial fan

From the observations of conglomerate and sandstone facies in Chapters 4 and 5, predictions of typical facies distributions and constituent architectural elements of externally sourced alluvial fans in rift settings can be deduced from proximal to distal locations;

Proximal facies and elements: Figure 6.6B; Proximal, Figure 6.6C; example logs 1, 2.

The succession in proximal areas is dominated (95%+) by coarse grain cobble- to boulder-grade conglomerates. Horizontally stratified clast-supported conglomerates with flat-lying clasts indicate incremental aggradation by repeated unchannelised non-

cohesive debris flows. These are interspersed with other non-cohesive debris flow deposits represented by variably coarse, ungraded and massive, clast-supported units with variable fine- to coarse grade sand matrix proportions (5-20% by volume). During episodes of higher rates of water supply and lower sediment supply, normally graded hyperconcentrated flow deposits with erosive bases are interbedded with the non-cohesive debris flow deposits described above. Further non-cohesive debris flow deposits containing lenses of massive sand also form, whereby their sandstone lenses are the expression of the settling of suspended sediment from a succeeding hyperconcentrated flow.

Constituent elements are dominated by laterally extensive (10^2 m scale) massive conglomerate beds representing the non-cohesive debris flow deposits. These are interspersed with rare laterally extensive (10^2 m scale) normally graded hyperconcentrated flow conglomerates, overlain by m-scale thickness laterally extensive hyperconcentrated flow sandstones with sharp boundaries at their base and top. Flows forming the deposits are unconfined, indicated by their laterally extensive nature and lack of identifiable depositional features (e.g. levees or barforms). Debris-flow deposits may have erosive bases, representing the destruction and reworking of likely hyperconcentrated flow and streamflow deposits that follow the higher magnitude storm events that form large debris flows. A limited fraction of clay content in suspension in the flow, and the variability and non-uniformity of temporal and spatial velocities of the unconfined flows, prevents the development of rigid cohesive bodies within the flow.

Medial facies and elements: Figure 6.6B; Medial, Figure 6.6C; example logs 3, 4.

At medial locations, there are a mix of sandstone and cobble- to boulder-grade conglomerate facies. The conglomerate facies present are the same as those in proximal

locations, however there is a higher proportion of normally graded hyperconcentrated flow facies as flows dilute downstream and become weakly channelised. These are typically juxtaposed against massive sandstone facies both up- and down-section, which contain pebble clasts and pebble lenses indicating deposition by the settling from suspension of high sediment yield hyperconcentrated flows. Massive non-cohesive debris flow facies occur both immediately down-section from conglomeratic hyperconcentrated flow beds, and interbedded with the massive sandstone facies.

Laterally-extensive non-cohesive debris flow deposits, similar to those in proximal areas, are juxtaposed against hyperconcentrated flow deposits both up- and down-section in medial areas. The frequent switching of depositional flow pathways, and increased space on the fan surface compared to proximal areas, allows for the preservation of finer grained units deposited from unconfined flow suspension. Elongate lens-shaped bodies (tens of metres wide) of conglomerate sediments that are normally graded are interpreted as weakly channelised hyperconcentrated flow deposits. Flows are initially unconfined, with trailing, more dilute flows becoming increasingly channelised. Off-axis flow events lead to the deposition of sandstones formed from hyperconcentrated flows, as they overrun their coarse-grained fraction and vary spatially and temporally in their carrying capacity, leading to the settling from suspension of sand and silt. The fan surface in medial areas is likely to be incredibly dynamic, with frequent lobe switching and frequent sediment reworking.

Distal facies and elements: Figure 6.6B; Distal, Figure 6.6C; example logs 5, 6.

In distal areas, the rock record is dominated by massive, ungraded, fine- to medium-grade sandstone facies containing intermittent pebble to gravel clasts and lenses of well-sorted pebble to granule clasts. The lack of sedimentary structures, grading, and presence of

intermittent pebble clasts represents the deposition of suspended sediment in hyperconcentrated flows. These are likely the downstream expression of upstream conglomeratic facies, whereby an increasingly fluidal part of the flow carrying sand and pebbles in suspension overruns its coarse-grained bedload fraction. Intermittent normally graded cobble- to boulder-grade conglomerate beds represent larger hyperconcentrated flows with enough magnitude to deliver coarse sediment to the distal fan. Rare non-cohesive debris flows may reach these locations forming ungraded, massive conglomeratic facies. Periods of quiescence are marked by palaeosol horizons.

Rare, laterally extensive (tens of metres) non-cohesive debris flow deposits represent the largest magnitude events delivering coarse cobble- to boulder-grade clasts to distal areas. The sedimentary succession is dominated by stacked massive sandstones formed from the rapid settling of suspended sand in hyperconcentrated flows. Frequent pebble clasts and decimetre-thick pebble lenses within the stacked sandstones indicate the variability in sediment carrying capacity of the depositional flows, and consequently their variable velocities across the fan surface. Laterally discontinuous conglomeratic hyperconcentrated flow deposits with erosive bases are preserved as lens shapes indicating increased amounts of confinement on distal reaches of the fan, potentially through the formation of poorly defined juvenile levees. Palaeosols form on quiescent fan surfaces away from active deposition, however the distal reaches of active lobes continue to be similarly dynamic systems to medial fan areas with frequent switching of flow pathways and a lack of established channel formation.

Whereas the simple case scenarios outlined in section 6.1. can help guide predictions of the presence of over- and underfilled basin sedimentary basin conditions, observations in the rock record of individual facies and architectural elements provide key insights

into the complexities of alluvial fan deposits and their response to generated rift topography. Figure 6.6C, Log 6, displays early synrift conglomerate deposition in a distal location, away from the dominant basin bounding fault and the locus of maximum subsidence; these deposits are likely formed by depositional flows which are drawn away from the main locus of subsidence by along-strike antithetic faulting during the early synrift (see Chapter 5, section 5.5.1.). Although not affecting the overall development of overfilled or underfilled basin conditions, the diverted flows have a pronounced effect on the expected facies within the basins themselves, indicating that subtle topographic variations must be considered when predicting alluvial fan facies distributions when sourced over a hangingwall displope.

Studies of sediment compositions are useful in many tectonic settings to determine sediment provenance, where the bedrock lithologies of local hinterlands are known (Steel & Thompson, 1983; Wandres et al., 2004). Their application to rift settings, however, remains ambiguous. Past studies have successfully used sediment composition in continental rifts: (i) to identify different sediment sources, such as from a local uplifted footwall or more far reaching areas feeding axial sediment systems (e.g. de Almeida et al., 2009); (ii) where a change in the lithological composition of catchment bedrock as a result of erosion alters the sediment supply source lithology (e.g. Figueiredo et al., 2016); or (iii) where local erodible bedrock is highly varied across short spatial distances (e.g. Muravchik et al., 2014). Where pre-existing drainage sources sediment over the hangingwall dipslope, there is a chance that the catchment area might erode a hinterland of a similar lithological composition to that that would be eroded by newly formed catchments on the uplifted footwall. Figures 5.4 to 5.18 (Chapter 5) clearly show the similarities in conglomerate clast compositions of different facies and locations of the Rodini Fm., and no trends based on clast composition can be discerned. Consequently, the

importance of palaeocurrent indicators from the facies observations become the primary driver of interpretations between depositional units sourced from different hinterlands.

6.4. Summary

This chapter assesses the results of this thesis in the context of the Research Questions outlined in Chapter 1. A multitude of different scenarios predicting the response of both pre-existing and rift-formed fluvial and alluvial systems to rift initiation and subsequent fault development are presented. The importance of system scale on sedimentary stacking patterns and facies distributions following the development of intrabasinal tilt-block crests is analysed. Finally, a model of alluvial fan deposition over a hangingwall dipslope from a rift-external sediment source is constructed, and its development in the context of the extrinsic and intrinsic controls that govern its formation are analysed.

7. Conclusions and future work

This chapter summarises the novel findings that have arisen as an outcome of this research; it discusses the extent to which the overarching aim of the research has been accomplished and it examines how the individual objectives have been met through consideration of and reflection on the original research questions set out in Chapter 1. This chapter then proposes a series of recommendations for future research that could be undertaken to further advance the concepts discussed in this thesis. This future research would enhance understanding of controls on alluvial fan development in continental rift systems.

7.1. Summary

Chapter 2

This chapter provided a detailed overview of the concepts underpinning this research, including the initiation and evolution of continental rift systems, how they interact with and generate source-to-sink systems, how sedimentary processes give rise to the generation of alluvial fan depositional systems, and how a range of external controls, including tectonics and climate, modulate those formative processes to leave a signature of their impact in the preserved sedimentary record.

This chapter also outlined the significant concepts within the literature that are applied and discussed as part of this research. Such concepts include: (i) the response of externally-sourced sediment transport pathways to ongoing rift evolution, with particular focus given to intrabasinal faulting as opposed to more frequently studied relay ramp systems; (ii) the distribution and magnitudes of source-to-sink systems formed on intrabasinal tilt-block crests and the similarities and differences in their formative processes, and how this affects consequent alluvial fan deposition into adjacent

basins; and (iii) whether detailed sedimentological analyses of facies and their constituent components can be used to recognise and distinguish the preserved sedimentary signatures of both extrinsic and intrinsic controls that govern alluvial and fluvial sedimentation in rift settings.

Chapter 3

Catchment and fan morphometric data were collected from the footwall slope and hangingwall dipslope sides of intrabasinal tilt-block crests from three modern-day active rift systems (East African Rift, Baikal Rift, Basin and Range province). This allowed for comparisons between similar depositional environments between different rift settings, and comparisons between footwall slope-sourced and hangingwall dipslope-sourced features.

The principal findings are as follows:

(i) Catchment area and fan surface area are linked in a power law relationship (Φ) similar to that described by previous studies. This relationship displays stronger positive correlation for footwall slope catchment-fan systems (r^2 = 0.75) than for hangingwall dipslope systems (r^2 = 0.25).

(ii) Despite having the potential to form much larger catchments due to the gentler slope of the hangingwall dipslope side of a tilt-block crest, fan surface area remains comparable to fans sourced over the footwall slope. The ratio of fan area to catchment area varies from 0.6 to 0.2 for footwall slope features, and 1.0 to 0.03 for hangingwall dipslope features.

(iii) Smaller-scale half-graben tilt block systems consequently contain alluvial fan bodies that dominate a larger proportion of the basin floor.

(iv) At these smaller catchment sizes, measurements of the Melton's Ratio and observations of fan surface processes indicate that sedimentary flows with higher viscosity have a stronger influence on fan formation, whereas lower viscosity flows are more likely to occur on the hangingwall dipslope features of larger scale rift settings.

Chapter 4

This chapter presents a field-based study of a synrift conglomeratic succession (Rodini Fm.) located on the southern coast of the Gulf of Corinth, Greece. Individual lithofacies are recorded in vertical profiles (15 total lithofacies), and their stacking patterns and geometric shapes in 2D and 3D lead to the identification seven parent architectural elements.

The system is interpreted as representing a prograding alluvial fan. Palaeocurrent information determined from clast imbrication represents a radial pattern of sediment dispersal (1,001 measurements from 20 localities) towards the southwest, south, and southeast. These observations support the interpretation of a rift-external, hangingwall dipslope sediment source from the north. The sediment source is likely to have been the be the modern-day Mornos river and catchment, based on the location of the present Mornos delta, the relatively young age of the studied formations (<2.2 Ma) and the size of the catchment itself.

The evolution of the sedimentary system was governed by ongoing tectonism, as the initial uplifting basin-bounding footwall to the south (formed between 2.2 and 1.8 Ma) formed a barrier to sediment transport and formed the alluvial fan system, which was deflected to the west and east to major along-strike rift depocentres. The formation of a large intrabasinal synthetic fault (initiated between 0.42 and 0.4 Ka) generated a second

barrier to transport and resulted in the transition of the basin from an overfilled state to an underfilled state.

The main findings are as follows:

(i) Intrabasinal faulting exerts a marked effect on the preserved sedimentary expression of a rift system. In this scenario, the initiation of the intrabasinal synthetic Psathopyrgos fault acted as a barrier to major sediment transport pathways and caused a rapid transition from overfilled basin conditions (subject to coarse-grained sedimentation) to underfilled basin conditions (subject to fine-grained sedimentation).

(ii) Three depositional models are outlined for antecedent drainage cut obliquely by rift systems (erosion through an uplifted footwall; diversion away from an uplifted footwall; deposition over a hangingwall dipslope). Intrabasinal faulting allows for the development of each scenario within the same basin segment as it evolves through time.

(iii) The provision of large amounts of sediment over the hangingwall dipslope, as a result of the strike of the rift system being perpendicular to the pre-existing drainage flow direction, inhibited the formation of a major axial system commonly interpreted within rift systems (e.g. Gawthorpe & Leeder, 2000) and further supports Fordham et al. (2010) interpretation that the presence of axial systems are likely overrepresented by many studies.

Chapter 5

This chapter presents a detailed study of the morphometrics of alluvially sourced conglomerate clasts from the Rodini Fm., Gulf of Corinth, Greece. The stratigraphic information outlined in Chapter 4 provides the framework for a detail facies analysis and

textural study, whereby the clasts of subtly different conglomerate facies were studied in detail to discern whether extrinsic or intrinsic signals controlling alluvial fan formation can be identified from small-scale features.

In total, 13 different characteristics were measured from 1,531 conglomerate clasts from eight different lithofacies. Data collected included qualitative measurements of clast composition (sandstone, limestone, chert), roundness (angular, sub-angular, sub-rounded, rounded) and shape (discoid, bladed, equant, prolate). Quantitative measurements of long, intermediate and short axis lengths of clasts, and the dip amounts and dip directions (azimuths) of those axes, were recorded. Finally, where clasts were imbricated, the nature of the imbrication and was interpreted to infer palaeoflow direction. All directional measurements were corrected for bedding dip and strike to generate comparable datasets.

The collected data allowed for the improved interpretation of some facies based on key concepts of clast imbrication such as (i) a(i)b(t) imbrication is indicative of rapid deposition of coarse sediment in high magnitude flows, and (ii) clasts will preferentially orientate with long axes parallel to the edge of the flow body.

The main findings are as follows:

(i) A distinct lack of consistency in clast orientations with relation to palaeoflow for many facies, indicating the variability of preserved coarse-grained sediment. Application of established principles of clast orientations in establishing flow processes should be used with caution.

(ii) When combined with interpretations of the host facies, clast information does allow for more detailed palaeogeographic interpretations to be derived; when

considered in the wider context of basin evolution this can help unravel the basin history.

(iii) Provenance studies in rift basins should be applied with caution, as source areas for different sediment inputs into a basin may be derived from similar pre-rift lithologies (this is particularly true for non-volcanic settings).

(iv) It is difficult to discern the impacts of extrinsic controls solely from studies of clast morphometrics, and consequently a multi-scale approach is the best option for determining their relative impacts on alluvial fan sedimentation in rift sub-basins.

Chapter 6

Research Question 1: *What are the impacts of pre-existing and newly formed drainage catchments on the presence of underfilled and overfilled rift basin conditions, and consequent alluvial syn-rift sedimentation?*

This research question is considered in terms of sediment source-to-sink relationships both inherited by the newly formed rift, and generated by the introduction of new topographical highs and lows as rifting occurs. Six responses of pre-existing sediment transport routes, and three responses of rift-formed sediment transport routes, are outlined. For each scenario, its subsequent response to ongoing fault evolution (manifesting as either the hard linkage of strike-adjacent faults, intrabasinal synthetic faulting, or intrabasinal antithetic faulting) is described. Finally, the sedimentary response of each system is detailed in terms of the presence of underfilled or overfilled sub-basins, with a specific example relating to Chapter 4 (hangingwall dipslope drainage) considered.

Research Question 2: *How does evolving rift fault development control the scale, stacking patterns, and sedimentary facies of alluvial fans in rift basins?*

This Research Question develops the concepts outlined in Chapter 3, and the response of sediment transport pathways formed on either side of a tilt-block crest formed within a rift basin. The relative influence of scale, tectonics, and climate are considered in terms of depositional processes forming their linked alluvial fan systems, and predictions on the presence of progradational, aggradational, and laterally variable alluvial fan sequences are outlined. Specifically, small-scale systems are compared directly to large-scale systems; small-scale systems will have a larger proportion of their basin floor inundated by alluvial fan environments, and depositional processes occurring on fan surfaces either side of a tilt-block crest will be increasingly similar as basin size decreases. The considered examples are then placed in an example framework, showing how stacking patterns of the stratigraphy formed from alluvial fan environments varies depending on external conditions.

Research Question 3: *How can alluvial fan facies and their constituent components be used to determine depositional flow types, and their variable temporal and spatial positions, within rift basins?*

This Research Question combines information from all three main data chapters regarding the depositional flow processes that lead to alluvial fan formation in rift settings. An example from the Gulf of Corinth is presented in detail, with descriptions of the observed facies and architectural elements from proximal to distal areas. These are considered in terms of the extrinsic and intrinsic controls that govern their formation, with climatic variations thought to control the variability in conglomeratic lithofacies and their parent architectural elements. These are then considered as part of the wider rift

system, and linked back to larger hierarchical scales discussed in Research Questions 1 and 2. Importantly, the influence of a variable warm temperate climate on deposition is outlined, impacting the frequency of hyperconcentrated flow and debris flow occurrence on the fan surface. As a pre-existing drainage system was adopted by the newly formed basin, the development of an axial fluvial system was inhibited by high sediment supply rates, indicating the need to understand pre-rift drainage pathways before the interpretation of the presence of an axial system in other rift systems around the globe.

7.2. Future research areas

7.2.1. Comparisons of rift strike and drainage direction, and resulting sediment transport pathways

As outlined in Chapter 6, there are six possible responses of pre-existing drainage systems to rift initiation. These have been interpreted from individual subsurface and field-based examples, but the direct relationship between the orientation of the drainage system compared to the orientation and offset of the initiating rift system has not been identified.

Observations can be made from modern-day rift settings, specifically the East African Rift, where pre-existing drainage directions are known or can be accurately estimated. The bearing of that direction can then be directly compared to a bearing of initial rift strike, and the distance between maximum fault throw and the dominant drainage pathway can be measured. These data could be recorded alongside the known system response to that faulting based on surface observations. On this basis, a database could be developed that can be used to predict the angle and offset of pre-existing drainage systems based on interpretations of synrift stratigraphic data and knowledge of rift fault development.

These observations could be supplemented with physical modelling and numerical modelling data (e.g. Cowie et al., 2006; Connell et al., 2012) allowing for data-driven predictions of antecedent system response to rifting.

7.2.2. Physical modelling of alluvial fan system response to intrabasinal faulting

Physical modelling has been used extensively to test the sedimentological and depositional process response of alluvial fan systems to intrinsic (e.g. Connell et al., 2012) and extrinsic (e.g. Van Dijk et al., 2012) controls. Connell et al. (2012) focussed on the interactions between an axial fluvial system and transverse fan systems formed over the hangingwall dipslope and footwall slope of a half-graben, based on variations in sediment flux between each of the three systems. This could be expanded drastically in order to observe the resultant stratigraphy in scenarios where: (i) axial systems are removed entirely, with variable sediment flux from footwall slope-sourced and hangingwall dipslope-sourced systems representing the dominance of different pre-existing drainage systems as sediment suppliers into rift basins; (ii) subsequent downstream boundary conditions are introduced, combining methodologies with Van Dijk et al. (2012) to observe the impact of intrabasinal faulting at different scales of fault displacement and contemporaneous or diachronous fault activity; or (iii) altering the direction at which hangingwall dipslope-derived sediment enters the basin, and its sedimentological response to the same tests outlined in (i) and (ii).

7.2.3. The potential of alluvial fan deposits in rift settings to be exploited for carbon sequestration

As discussed in Chapter 1, rift basin fill comprises economically important stratigraphic successions containing water, hydrocarbon and geothermal resources. They are also important for future carbon sequestration (the storage of CO_2 in subsurface reservoirs, preventing its emission into the atmosphere, or storage within saline aquifers) whereby

reservoirs from which previous resources have been extracted can be repurposed to store carbon emissions. Alluvial fan deposits have typically been overlooked for their fluvial, lacustrine, aeolian and marine counterparts for resource exploitation; their tendency to be comprised of coarser-grained material and contain a higher variety of clastic facies inhibits their potential as highly porous and permeable reservoirs. As shown in Chapters 4 and 6, however, they can be entirely reliant on the rift-external system that sources their deposition; if intrabasinal faulting occurs and acts as a barrier to the sedimentary system, the sub-basin quickly transitions from an overfilled to an underfilled state and may be overlain by a sealing lithology arising from, for example, a lacustrine or marine incursion. This would enhance the potential for these stratigraphic successions to be used for carbon sequestration.

References

Abdul Aziz, H., Sanz-Rubio, E., Calvo, J.P., Hilgen, F.J. & Krijgsman, W. (2003) Palaeoenvironmental reconstruction of a middle Miocene alluvial fan to cyclic shallow lacustrine depositional system in the Calatayud Basin (NE Spain). Sedimentology, 50, 211–236.

Alçiçek, H., Varol, B. & Özkul, M. (2007) Sedimentary facies, depositional environments and palaeogeographic evolution of the Neogene Denizli Basin, SW Anatolia, Turkey. Sedimentary Geology, 202, 596-637.

Alçiçek, M.C. (2007) Tectonic development of an orogen-top rift recorded by its terrestrial sedimentation pattern: The Neogene Eşen Basin of southwestern Anatolia, Turkey. Sedimentary Geology, 200(1-2), 117-140.

Alexander, J. & Leeder, M.R. (1987) Active tectonic control on alluvial architecture. In: Ethridge, F.G., Flores, R.M. & Harvey, M.D. (eds.) Recent Developments in Fluvial Sedimentology. SEPM Special Publication, 39, 243-252.

Allen, J.R.L. (1982) Orientation of Particles During Sedimentation: Shape-Fabrics. In: Sedimentary Structures – Their Character and Physical Basis, Volume I. Developments in Sedimentology, 30, Elsevier, Amsterdam, 179-235.

Allen, J.R.L. (1982) Sedimentary structures: their character and physical basis. Developments in Sedimentology, 30. Elsevier: Amsterdam.

Allen, J.R.L. (1996) Some recent advances in the physics of sedimentation. Proceedings of the Geologists' Association, 80(1), 1-42.

Allen, P.A. (2008a) From landscapes into geological history. Nature, 451, 274-276.

Allen, P.A. (2008b) Time scales of tectonic landscapes and their sediment routing systems. In: Gallagher, K., Jones, S.J. & Wainwright, J. (eds.) Landscape Evolution: Denudation, Climate and Tectonics Over Different Time and Space Scales. Geological Society, London, Special Publications, 296(1), 7-28.

Allen, P.A. & Allen, J.R. (2013) Basin Analysis: Principles and application to petroleum play assessment, Third Edition. John Wiley & Sons, Ltd., 619pp.

Allen, P.A., Armitage, J.J., Carter, A., Duller, R.A., Michael, N.A., Sinclair, H.D., Whitchurch, A.L & Whittaker, A.C. (2013) The Qs problem: Sediment volumetric balance of proximal foreland basin systems. Sedimentology, 60, 102-130.

Allen, P.A., & Densmore, A.L (2000) Sediment flux from an uplifting footwall block. Basin Research, 12, 367-380.

Allen, P.A. & Hovius, N. (1998) Sediment supply from landslide-dominated catchments: implications for basin-margin fans. Basin Research, 10(1), 19-35.

Alonso-Zarza, A.M. (2003) Palaeoenvironmental significance of palustrine carbonates and calcretes in the geological record. Earth-Science Reviews, 60, 261-298.

Alvarez-Zarikian, C.A., Soter, S. & Katsonopoulou, D. (2008) Recurrent Submergence and Uplift in the Area of Ancient Helike, Gulf of Corinth, Greece: Microfaunal and Archaeological Evidence. Journal of Coastal Research, 24, 110–125.

Alves, T.M. & Cupkovic, T. (2018) Footwall degradation styles and associated sedimentary facies distribution in SE Crete: Insights into tilt-block extensional basins on continental margins. Sedimentary Geology, 367, 1-19.

Amorosi, A., Farina, M., Severi, P., Preti, D., Caporale, L. & Di Dio, G. (1996) Genetically related alluvial deposits across active fault zones: an example of alluvial fan-terrace correlation from the upper Quaternary of the southern Po Basin, Italy. Sedimentary Geology, 102, 275-295.

Anders, M.H., Spiegelman, M., Rodgers, D.W. & Hagstrum, J.T. (1993) The growth of fault-bounded tilt blocks. Tectonics, 12(6), 1451-1459.

Anderson, R.E., Zoback, M.L. & Thompson, G.A. (1983) Implications of selected subsurface data on the structural form and evolution of some basins in the northern Basin and Range province, Nevada and Utah. Geological Society of America Bulletin, 94, 1055-1072.

Armstrong, R.L. & Ward, P. (1991) Evolving geographic patterns of Cenozoic magmatism in the North American Cordillera: The temporal and spatial association of magmatism and metamorphic core complexes. Journal of Geophysical Research: Solid Earth, 96(B8), 13201-13224.

Asrat, A., Bates, R., Berger, G., Beyene, Y., Brandt, S., DeGusta, D., Duller, G.,Ebinger, C., Endale, T., Hart, W.K., Hildebrand, E., Katoh, S., Kidane, T., Lamb, H.,Leng, M., Lezine, A.-M., Marshall, M., Morgan, L., Pearce, N., Prave, T., Renne, P.,Schäbitz, F., Strecker, M., Suwa, G., Tadesse, K., Tadesse, T., Trauth, M., Umer, M.,Vogelsang, R., White, T., Wolde Gabriel, G., & Zeleke, A. (2009) The Chew Bahir Drilling Project: A Plio-Pleistocene Climate Record from the Southern Ethiopian Rift, a Crucible of Human Evolution. Proposal for the ICDP-HSPDP (HominінSites and Palaeolakes Drilling Project), pp. 1-8

Babaie, H.A. (1987) Paleogeographic and tectonic implications of the Golconda allochthon, southern Toiyabe Range, Nevada. Geological Society of America Bulletin, 99, 231-243.

Backert, N., Ford, M. & Malartre, F. (2010) Architecture and sedimentology of the Kerinitis Gilbert-type fan delta, Corinth Rift, Greece. Sedimentology, 57, 543–586.

Bahadori, A. & Holt, W.E. (2019) Geodynamic evolution of southwestern North America since the Late Eocene. Nature Communications, 10, 5213.

Bahrami, S. (2013) Tectonic controls on the morphometry of alluvial fans around the Danehkhoshk anticline, Zagros, Iran. Geomorphology, 180-181, 217-230.

Barrett, B.J., Collier, R.E.Ll., Hodgson, D.M., Gawthorpe, R.L., Dorrell, R.M. & Cullen, T.M. (2019) Quantifying faulting and base level controls on syn-rift sedimentation using stratigraphic architectures of coeval, adjacent Early-Middle Pleistocene fan deltas in Lake Corinth, Greece. Basin Research, 31(6), 1040-1065.

Barrett, B.J., Hodgson, D.M., Jackson, C.A.-L., Lloyd, C., Casagrande, J. & Collier, R.E.Ll. (2020) Quantitative analysis of a footwall-scarp degradation complex and syn-rift stratigraphic architecture, Exmouth Plateau, NW Shelf, offshore Australia. Basin Research, online access view.

Bastow, I.D., Nyblade, A.A., Stuart, G.W., Rooney, T.O. & Benoit, M.H. (2008) Upper mantle seismic structure beneath the Ethiopian hot spot: Rifting at the edge of the African low-velocity anomaly. Geochemistry, Geophysics, Geosystems, 9(12), Q12022.

Beck, H.E., Zimmermann, N.E., McVicar, T.R., Vergopolan, N., Berg, A. & Wood, E.F. (2018) Present and future Köppen-Geiger climate classification maps at 1-km resolution. Scientific Data, 5:180214.

Beckers, A., Hubert-Ferrari, A., Beck, C., Bodeux, S., Tripsanas, E., Sakellariou, D. & De Batist, M. (2015) Active faulting at the western tip of the Gulf of Corinth, Greece, from high-resolution seismic data. Marine Geology, 360, 55-69.

Bell, R.E., McNeill, L.C., Bull, J.M., Henstock, T.J., Collier, R.E.L. & Leeder, M.R. (2009) Fault architecture, basin structure and evolution of the Gulf of Corinth rift, central Greece. Basin Research, 21, 824–855.

Bell, R.E., McNeill, L.C., Henstock, T.J. & Bull, J.M. (2011) Comparing extension on multiple time and depth scales in the Corinth Rift, Central Greece. Geophysical Journal International, 186(2), 463-470.

Benda, L. & Dunne, T. (1997) Stochastic forcing of sediment routing and storage in channel networks. Water Resources Research, 33(12), 2865-2880.

Bentham, P., Collier, R.E., Gawthorpe, R.L., Leeder, M.R. & Stark, C. (1991) Tectono-sedimentary development of an extensional basin: the Neogene Megara Basin, Greece. Journal of the Geological Society, 148, 923–934.

Benvenuti, M. & Martini, I.P. (2002) Analysis of terrestrial hyperconcentrated flows and their deposits. In: Martini, I.P., Baker, V.R. (eds.) Flood and Megaflood Processes and Deposits: Recent and Ancient Examples, International Association of Sedimentologists Special Publication, 32, 167-193.

Bertran, P., Hétu, B., Texier, J.- P. & Van Steijn, H. (1997) Fabric characteristics of subaerial slope deposits. Sedimentology, 44, 1-16.

Best, M.G., Christiansen, E.H., de Silva, S. & Lipman, P.W. (2016) Slab-rollback ignimbrite flareups in the southern Great Basin and other Cenozoic American arcs: A distinct style of arc volcanism. Geosphere, 12(4), 1097-1135.

Best, M.G., Christiansen, E.H., & Gromme, S. (2013) Introduction: The 36-18 Ma southern Great Basin, USA, ignimbrite province and flareup: Swarms of subduction-related supervolcanoes. Geosphere, 9(2), 260-274.

Beuhler, H.A., Weissmann, G.S., Scuderi, L.A. & Hartley, A.J. (2011) Spatial and Temporal Evolution of an Avulsion on the Taquari River Distributive Fluvial System from Satellite Image Analysis. Journal of Sedimentary Research, 81(8), 630-640.

Beverage, J.P. & Culbertson, J.K. (1964) Hyperconcentrations of Suspended Sediment. Journal of the Hydraulics Division, 90(6), 117-128.

Blackwelder, E. (1928) Mudflow as a Geologic Agent in Semiarid Mountains. Geological Society of America Bulletin, 39(2), 465-484.

Blair, T.C. (1987) Tectonic and hydrologic controls on cyclic alluvial fan, fluvial, and lacustrine rift-basin sedimentation, Jurassic-Lowermost Cretaceous Todos Santos Formation, Chiapas, Mexico. Journal of Sedimentary Research, 57(5), 845-862.

Blair, T.C. (1999a) Sedimentary processes and facies of the waterlaid Anvil Spring Canyon alluvial fan, Death Valley, California. Sedimentology, 46(5), 913-940.

Blair, T.C. (1999b) Sedimentology of the debris-flow-dominated Warm Spring Canyon alluvial fan, Death Valley, California. Sedimentology, 46(5), 941-965.

Blair, T.C. (1999c) Cause of dominance by sheetflood vs. debris-flow processes on two adjoining alluvial fans, Death Valley, California. Sedimentology, 46, 1015-1028.

Blair, T.C. & McPherson, J.G. (1994) Alluvial fans and their natural distinction from rivers based on morphology, hydraulic processes, sedimentary processes, and facies assemblages. Journal of Sedimentary Research, 64(3a), 450-489.

Blair, T.C. & McPherson, J.G. (1998) Recent debris-flow processes and resultant form and facies of the Dolomite alluvial fan, Owens Valley, California. Journal of Sedimentary Research, 68(5), 800-818.

Bonini, M., Corti, G., Innocenti, F., Manetti, P., Mazzarini, F., Adebe T. & Pecskay, Z. (2005) Evolution of the Main Ethiopian Rift in the frame of the Afar and Kenya rifts propagation. Tectonics, 24(1), TC1007.

Bosworth, W., Huchon, P. & McClay, K. (2005) The Red Sea and Gulf of Aden basins. Journal of African Earth Sciences, 43(1), 334-378.

Boulton, S.J. & Stokes, M. (2018) Which DEM is best for analysing fluvial landscape development in mountainous terrains? Geomorphology, 310, 168-187.

Bowman, D. (1978) Determination of intersection points within a telescopic alluvial fan complex. Earth Surface Processes, 3(3), 265-276.

Braathen, A., Baelum, K., Maher, H. & Buckley, S.J. (2011) Growth of extensional faults and folds during deposition of an evaporite-dominated half-graben basin; the Carboniferous Billefjorden Trough, Svalbard. Norsk Geologisk Tidsskrift, 91(3), 137-161.

Bremer, M. & Sass, O. (2012) Combining airborne and terrestrial laser scanning for quantifying erosion and deposition by a debris flow event. Geomorphology, 138(1), 49-60.

Brenna, A., Surian, N., Ghinassi, M. & Marchi, L. (2020) Sediment-water flows in mountain streams: Recognition and classification based on field evidence. Geomorphology, 371, 107413.

Bridge, J.S. (2006) Fluvial Facies Models: Recent Developments. In: Posamentier, H.W. & Walker, R.G. (eds.) Facies Models Revisited. SEPM Special Publication, 84, 85-170.

Brooke, S.A.S., Whittaker, A.C., Armitage, J.J., D'Arcy, M. & Watkins, S.E. (2018) Quantifying Sediment Transport Dynamics on Alluvial Fans from Spatial and Temporal Changes in Grain Size, Death Valley, California. Journal of Geophysical Research: Earth Surface, 123(8), 2039-2067.

Brunello, A.J., Molotov, V.C., Dugherkuu, B., Goldman, C., Khagamanova, E., Strijhova, T. & Sigman, R. (2006) Lake Baikal. Experience and Lessons Learned. Brief. Tahoe-Baikal Institute, South Lake Tahoe.

Buck, R.W., Martinez, F., Steckler, M.S. & Cochran, J.R. (1988) Thermal consequences of lithospheric extension: Pure and simple. Tectonics, 7(2), 213-234.

Buck, R.W. (1991) Modes of Continental Lithospheric Extension. Journal of Geophysical Research, 96(B12), 20161-20178.

Bull, W.B. (1997) Discontinuous ephemeral streams. Geomorphology, 19(3-4), 227-276.

Buslov, M.M. (2012) Geodynamic nature of the Baikal Rift Zone and its sedimentary filling in the Cretaceous-Cenozoic: the effect of the far-range impact of the Mongolo-Okhotsk and Indo-Eurasian collisions. Russian Geology and Geophysics, 53, 955-962.

Butter, J.C., Buck, R.W. & Zehnder, C.M. (1988) Convective partial melting: 1. A model for the formation of thick basaltic sequences during the initiation of spreading. Journal of Geophysical Research, 93(B2), 1031-1048.

Cain, S.A. & Mountney, N.P. (2009) Spatial and temporal evolution of a terminal fluvial fan system: the Permian Organ Rock Formation, South-east Utah, USA. Sedimentology, 56(6), 1774-1800.

Calhoun, N.C. & Clague, J.J. (2018) Distinguishing between debris flows and hyperconcentrated flows: an example from the eastern Swiss Alps. Earth Surface Processes and Landforms, 43, 1280-1294.

Camilleri, P.A. (2013) Geologic map and structure of the west-central part of the Grant Range, Nye County, Nevada. Geological Society of America Digital Map and Chart Series, 14, 25pp.

Carling, P.A. (1987) Hydrodynamic interpretation of a boulder berm and associate debris-torrent deposits. Geomorphology, 1(1), 53-67.

Chakraborty, T. & Ghosh, P. (2010) The geomorphology and sedimentology of the Tista megafan, Darjeeling Himalaya: Implications for megafan building processes. Geomorphology, 115, 252–266.

Chamyal, L.S., Khadkikar, A.S., Malik, J.N. & Mauraya, D.M. (1997) Sedimentology of the Narmada alluvial fan, western India. Sedimentary Geology, 107, 263-279.

Chandler, D.M. & Hubbard, B. (2008) Quantifying sample bias in clast fabric measurements. Sedimentology, 55(4), 925-938.

Chang, S.-J. & Van der Lee, S. (2011) Mantle plumes and associated flow beneath Arabia and East Africa. Earth and Planetary Science Letters, 302(3-4), 448-454.

Chen, H., Wood, L.J. & Gawthorpe, R.L. (2020) Sediment dispersal and redistributive processes in axial and transverse deep-time source-to-sink systems of marine rift basins: Dampier Sub-basin, Northwest Shelf, Australia. Basin Research, early access view.

Chen, L.-q., Guo, F.-s. & Tang, C. (2016) Evolution of the Late Cretaceous Yongfeng-Chongren Basin in Jiangxi Province, southeast China: insights from sedimentary facies analysis and pebble counting. Journal of Mountain Science, 13, 342-352.

Chernet, T., Hart, W.K., Aronson, J.L. & Walter, R.C. (1998) New age constraints on the timing of volcanism and tectonism in the northern Main Ethiopian Rift-southern Afar transition zone (Ethiopia). Journal of Volcanology and Geothermal Research, 80(3-4), 267-280.

Childs, C., Holdsworth, R.E., Jackson, C.A.-L., Manzocchi, T., Walsh, J.J. & Yielding, G. (2017) Introduction to the geometry and growth of normal faults. In: Childs, C., Holdsworth, R.E., Jackson, C.A.-L., Manzocchi, T., Walsh, J.J. & Yielding, G. (eds.) The Geometry and Growth of Normal Faults. Geological Society, London, Special Publications, 439, 1-9.

Christenson, G.E. & Purcell, C. (1985) Correlation and age of Quaternary alluvial-fan sequences, Basin and Range province, southwestern United States. In: Weide, D.L. (eds.) Soils and Quaternary Geology of the Southwestern United States, Geological Society of America, Special Paper, 203, 115-122.

Chorowicz, J. (2005) The East African rift system. Journal of African Earth Sciences, 43, 379-410.

Chun, S.S. & Chough, S.K. (1995) The Cretaceous Uhangri Formation, SW Korea: lacustrine margin facies. Sedimentology, 42(2), 293-322.

Church, M. & Jakob, M. (2020) What Is a Debris Flood? Water Resources Research, 56(8), e2020WR027144.

Clarke, L.E., Quine, T.A. & Nicholas, A. (2010) An experimental investigation of autogenic behaviour during alluvial fan evolution. Geomorphology, 115(3-4), 278-285.

Clarke, L.E. (2015) Experimental alluvial fans: Advances in understanding of fan dynamics and processes. Geomorphology, 244, 135-145.

Clevis, Q., de Boer, P. & Wachter, M. (2003) Numerical modelling of drainage basin evolution and three-dimensional alluvial fan stratigraphy. Sedimentary Geology, 163, 85-110.

Cochran, J.R. (1983) Effects of finite rifting times on the development of sedimentary basins. Earth and Planetary Science Letters, 66(C), 289-302.

Cohen, H.A., Dart, C.J., Akyüz, H.S. & Barka, A. (1995) Syn-rift sedimentation and structural development of the Gediz and Büyük Menderes graben, western Turkey. Journal of the Geological Society, 152(4), 629-638.

Coleman, A.J., Jackson, C.A.-L. & Duffy, O.B. (2017) Balancing sub- and supra-salt strain in salt-influenced rifts: Implications for extension estimates. Journal of Structural Geology, 102, 208-225.

Colgan, J.P., Dumitru, T.A., McWilliams, M. & Miller, E.L. (2006) Timing of Cenozoic volcanism and Basin and Range extension in northwestern Nevada: New constraints from the northern Pine Forest Range. Geological Society of America Bulletin, 118(1-2), 126-139.

Collier, R.E.L. & Dart, C.J. (1991) Neogene to Quaternary rifting, sedimentation and uplift in the Corinth Basin,Greece. Journal of the Geological Society, 148, 1049–1065.

Collier, R.E.L. & Gawthorpe, R.L. (1995) Neotectonics, drainage and sedimentation in central Greece: insights into coastal reservoir geometries in syn-rift sequences. Geological Society, London, Special Publications, 80, 165–181.

Collinson, J.D. & Mountney, N.P. (2019) Sedimentary Structures, Dunedin Academic Press, Edinburgh, 352pp.

Colombera, L. & Bersezio, R. (2011) Impact of the magnitude and frequency of debris-flow events on the evolution of an alpine alluvial fan during the last two centuries: Responses to natural and anthropogenic controls. Earth Surface Processes and Landforms, 36, 1632–1646.

Connell, S.D., Kim, W., Paola, C. & Smith, G.A. (2012) Fluvial Morphology and Sediment-Flux Steering of Axial-Transverse Boundaries In An Experimental Basin. Journal of Sedimentary Research, 82(5), 310-325.

Coronel, M.D., Isla, M.F., Veiga, G.D., Mountney, N.P. & Colombera, L. (2020) Anatomy and facies distribution of terminal lobes in ephemeral fluvial successions: Jurassic Tordillo Formation, Neuquén Basin, Argentina. Sedimentology, 67(5), 2596-2624.

Corti, G. (2009) Continental rift evolution: From rift initiation to incipient break-up in the Main Ethiopian Rift, East Africa. Earth-Science Reviews, 96(1-2), 1-53.

Corti, G., Bonini, M., Conticelli, S., Innocenti, F., Manetti, P. & Sokoutis, D. (2003) Analogue modelling of continental extension: a review focused on the relations between patterns of deformation and the presence of magma. Earth-Science Reviews, 63(3-4), 169-247.

Corti, G., Cioni, R., Franceschini, Z., Sani, F., Scaillet, S., Molin, P., Isola, I., Mazzarini, F., Brune, S., Keir, D., Erbello, A., Muluneh, A., Illsley-Kemp, F. & Glerum, A. (2019) Aborted propagation of the Ethiopian rift caused by linkage with the Kenyan rift. Nature Communications, 10, 1309.

Costa, J.E. (1984) Physical geomorphology of debris flows. In: Costa J.E, & Fleischer, P.J. (eds.), Developments and Applications of Geomorphology. Springer-Verlag, New York, 268-317.

Costa, J.E. (1988) Rheologic, geomorphic, and sedimentologic differentiation of water floods, hyperconcentrated flows, and debris flows. In: V.R. Baker, R.C. Kochel and P.C. Patton, (eds.), Flood geomorphology, 113-122. John Wiley & Sons, Inc., Chichester.

Courtillot, V., Jaupart, C., Manighetti, I., Tapponnier, P. & Besse, J. (1999) On causal links between flood basalts and continental breakup. Earth and Planetary Science Letters, 166(3-4), 177-195.

Cowie, P.A., Attal, M., Tucker, G.E., Whittaker, A.C., Naylor, M., Ganas, A. & Roberts, G.P. (2006) Investigating the surface process response to fault interaction and linkage using a numerical modelling approach. Basin Research, 18(3), 231-266.

Cowie, P.A., Gupta, S. & Dawers, N.H. (2000) Implications of fault array evolution for synrift depocentre development: insights from a numerical growth model. Basin Research, 12, 241-261.

Croci, A., Della Porta, G. & Capezzuoli, E. (2016) Depositional architecture of a mixed travertine-terrigenous system in a fault-controlled continental extensional basin (Messinian, Southern Tuscany, Central Italy). Sedimentary Geology, 332, 13–39.

Cronin, S.J., Lecointre, J.A., Palmer, A.S. & Neall, V.E. (2000) Transformation, internal stratification, and depositional processes within a channelised, multi-peaked lahar flow. New Zealand Journal of Geology and Geophysics, 43, 117–128.

Crosta, G.B. & Frattini, P. (2004) Controls on modern alluvial fan processes in the Central Alps, Northern Italy. Earth Surface Processes and Landforms, 29, 267-293.

Cullen, T.M., Collier, R.E.Ll., Gawthorpe, R.L., Hodgson, D.M. & Barrett, B.J. (2020) Axial and transverse deep-water sediment supply to syn-rift fault terraces: Insights from the West Xylokastro Fault Block, Gulf of Corinth, Greece. Basin Research, online access view.

D'Arcy, M., Whittaker, A.C. & Roda-Boluda, D.C. (2017) Measuring alluvial fan sensitivity to past climate changes using a self-similarity approach to grain-size fining, Death Valley, California. Sedimentology, 64(2), 388-424.

Dade, W.B. & Verdeyen, M.E. (2007) Tectonic and climatic controls of alluvial-fan size and source-catchment relief. Journal of the Geological Society, 164(2), 353-358.

Dart, C.J., Collier, R.E.Ll., Gawthorpe, R.L., Keller, J.V.A. & Nichols, G. (1994) Sequence stratigraphy of (?)Pliocene-Quaternary synrift, Gilbert-type fan deltas, northern Peloponnesos, Greece. Marine and Petroleum Geology, 11(5), 545-560.

Davidson, S.K., Leleu, S. & North, C. (2011) From river to rock record: the preservation of fluvial sediments and their subsequent interpretation. In: Stephanie, K., Davidson, S.K., Leleu S., & North, C. (eds.), From River to Rock Record. SEPM Special Publication, 97, 3-8.

Davidson, A. & Rex, D.C. (1980) Age of volcanism and rifting in southwestern Ethiopia. Nature, 283, 657-658.

Davies, N.S. & Gibling, M.R. (2010) Cambrian to Devonian evolution of alluvial systems: The sedimentological impact of the earliest land plants. Earth-Science Reviews, 98, 171–200.

Dawers, N.H., Anders, M.H. & Scholz, C.H. (1993) Growth of normal faults: Displacement-length scaling. Geology, 21(12), 1107-1110.

DeCelles, P.G., Gray, M.B., Ridgway, K.D., Cole, R.B., Pivnik, D.A., Pequera, N. & Srivastava, P. (1991) Controls on synorogenic alluvial-fan architecture, Beartooth Conglomerate (Palaeocene), Wyoming and Montana. Sedimentology, 38, 567-590.

DeCelles, P.G. (2004) Late Jurassic to Eocene evolution of the Cordilleran thrust belt and foreland basin system, western U.S.A. American Journal of Science, 304(2), 105-168.

de Almeida, R.P., Janikian, L., Fragoso-Cesar, A.R.S. & Marconato, A. (2009) Evolution of a rift basin dominated by subaerial deposits: The Guaritas Rift, Early Cambrian, Southern Brazil. Sedimentary Geology, 217, 30-51.

de Haas, T., Braat, L., Leuven, J.R.F.W., Lokhorst, I.R. & Kleinhans, M.G. (2015) Effects of debris flow composition on runout, depositional mechanisms, and deposit morphology in laboratory experiments. Journal of Geophysical Research: Earth Surface, 120(9), 1949-1972.

de Haas, T. & Densmore, A.L. (2019) Debris-flow volume quantile prediction from catchment morphometry. Geology, 47, 791-794.

de Haas, T., Kruijt, A. & Densmore, A.L. (2018) Effect of debris-flow magnitude-frequent distribution on avulsions and fan development. Earth Surface Processes and Landforms, 43(13), 2779-2793.

de Haas, T., van den Berg, W., Braat, L. & Kleinhans, M.G. (2016) Autogenic avulsion, channelization and backfilling dynamics of debris-flow fans. Sedimentology, 63(6), 1596-1619.

de Haas, T., Ventra, D., Carbonneau, P.E. & Kleinhans, M.G. (2014) Debris-flow dominance of alluvial fans masked by runoff reworking and weathering. Geomorphology, 217, 165-181.

de Heinzelin, J. (eds.) (1983) The Omo Group. Koninklijk Museum voor Midden-Afrika, Tervuren, Geologische Wetenschappen, pp85.

de Scally, F.A. & Owens, I.F. (2004) Morphometric controls and geomorphic responses on fans in the Southern Alps, New Zealand. Earth Surface Processes and Landforms, 29(3), 311-322.

de Scally, F.A., Owens, I.F. & Louis, J. (2010) Controls on fan depositional processes in the schist ranges of the Southern Alps, New Zealand, and implications for debris flow hazard assessment. Geomorphology, 122, 99-116.

Dec, T. (1992) Textural characteristics and interpretation of second-cycle, debris-flow-dominated alluvial fans (Devonian of Northern Scotland). Sedimentary Geology, 77(3-4), 269-296.

Degnan, P.J. & Robertson, A.H.F. (1998) Mesozoic-early Tertiary passive margin evolution of the Pindos ocean (NW Peloponnese, Greece). Sedimentary Geology, 117, 33–70.

Delcaillau, B., Amrhar, M., Namous, M., Laville, E., Pedoja, K. & Dugué O. (2011) Transpressional tectonics in the Marrakech High Atlas: Insight by the geomorphic evolution of drainage basins. Geomorphology, 134, 344-362.

Delorme, P., Devauchelle, O., Barrier, L. & Métivier, F. (2018) Growth and shape of a laboratory alluvial fan. Physical Review, 98, 012907.

Denny, C.S. (1965) Alluvial Fans in the Death Valley Region, California and Nevada. United States Geological Survey, Professional Paper, 466.

Densmore, A.L., Dawers, N.H., Gupta, S., Allen, P.A. & Gilpin, R. (2003) Landscape evolution at extensional relay zones. Journal of Geophysical Research, 108(B5), 2273.

Densmore, A.L., Allen, P.A. & Simpson, G. (2007) Development and response of a coupled catchment fan system under changing tectonic and climatic forcing. Journal of Geophysical Research, 112, F01002.

Densmore, A.L., Gupta, S., Allen, P.A. & Dawers, N.H. (2007) Transient landscapes at fault tips. Journal of Geophysical Research, 112(F3), F03S08.

Dickinson, W.R. (2002) The Basin and Range Province as a Composite Extensional Domain. International Geology Review, 44(1), 1-38.

Dickinson, W.R. (2006) Geotectonic evolution of the Great Basin. Geosphere, 2(7), 353-168.

Ding, W., Franke, D., Li, J. & Steuer, S. (2013) Seismic straigraphy and tectonic structure from a composite multi-channel seismic profile across the entire Dangerous Grounds, South China Sea. Tectonophysics, 582, 162-176.

Doutsos, T., Kontopoulos, N. & Poulimenos, G. (1988) The Corinth-Patras rift as the initial stage of continental fragmentations behind an active island arc (Greece). Basin Research, 1(3), 177-190.

Doutsos, T., Pe-Piper, G., Boronkay, K. & Koukouvelas, I. (1993) Kinematics of the central Hellenides. Tectonics, 12(4), 936-953.

Doutsos, T. & Piper, D.J.W. (1990) Listric faulting, sedimentation, and morphological evolution of the Quaternary eastern Corinth rift, Greece: First stages of continental rifting. Bulletin of the Geological Society of America, 102, 812–829.

Dunkelman, T.J., Rosendahl, B.R. & Karson, J.A. (1989) Structure and stratigraphy of the Turkana rift from seismic reflection data. Journal of African Earth Sciences (and the Middle East), 8(2-4), 489-510.

Ebinger, C.J. (1989) Tectonic development of the western branch of the East African rift system. Geological Society of America Bulletin, 101(7), 885-903.

Ebinger, C.J. (2005) Continental break-up: The East African perspective. Astronomy & Geophysics, 46(2), 2.16-2.21.

Ebinger, C.J., Yemane, T., Harding, D.J., Tesfaye, S., Kelley, S. & Rex, D.C. (2000) Rift deflection, migration, and propagation: Linkage of the Ethiopian and Eastern rifts, Africa. Bulletin of the Geological Society of America, 112, 163-176.

El-Naqa, A., Hammouri, N., Ibrahim, K. & El-Taj, M. (2009) Integrated Approach for Groundwater Exploration in Wadi Araba Using Remote Sensing and GIS. Jordan Journal of Civil Engineering, 3, 229-243.

Eliet, P.P. & Gawthorpe, R.L. (1995) Drainage development and sediment supply within rifts, examples from the Sperchios basin, central Greece. Journal of the Geological Society, 152(5), 883-893.

Epov, M.I., Nevedrova, N.N. & Sanchaa, A.M. (2007) A geoelectrical model of the Barguzin basin in the Baikal Rift Zone. Russian Geology and Geophysics, 48, 626-641.

Erratt, D., Thomas, G.M. & Wall, G.R.T. (1999) The evolution of the Central North Sea Rift. Geological Society, London, Petroleum Geology Conference series, 5, 63-82.

Espinoza, M., Montecino, D., Oliveros, V., Astudillo, N., Vásquez, P., Reyes, R., Celis, C., González, R., Contreras, J., Creixell, C. & Martínez, A. (2019) The synrift phase of the early Domeyko Basin (Triassic, northern Chile): Sedimentary, volcanic and tectonic interplay in the evolution of an ancient subduction-related rift basin. Basin Research, 31(1), 4-32.

Esu, D. & Girotti, O. (2015) The late Early Pleistocene non-marine molluscan fauna from the Synania Formation (Achaia, Greece), with description of nine new species (Mollusca: Gastropoda). Archiv Für Molluskunkunde: International Journal of Malacology, 144, 65-81.

Eyles, N. & Kocsis, S. (1988) Sedimentology and clast fabric of subaerial debris flow facies in a glacially-influenced alluvial fan. Sedimentary Geology, 59, 15-28.

Ezquerro, L., Luzón, A., Simon, J.L. & Liesa, C.L. (2020) Alluvial sedimentation and tectono-stratigraphic evolution in a narrow extensional zigzag basin margin (northern Teruel Basin, Spain). Journal of Palaeogeography, 8(1), 29.

Faccenna, C., Becker, T.W., Auer, L., Billi, A., Boschi, L., Brun, J.-P., Capitanio, F.A., Funiciello, F., Horvàth, F., Jolivet, L., Piromallo, C., Royden, L., Rosetti, F. & Serpelloni, E. (2014) Mantle dynamics in the Mediterranean. Reviews of Geophysics, 52(3), 283-332.

Faulds, J.E. & Varga, R.J. (1998) The role of accommodation zones and transfer zones in the regional segmentation of extended terranes. In: Faulds, J.E. & Stewart, J.H. (eds.) Accommodation Zones and Transfer Zones: The Regional Segmentation of the Basin and Range Province: Boulder, Colorado. Geological Society of America Special Paper 323.

Fernández, J., Bluck, B.J. & Viseras, C. (1993) The effects of fluctuating base level on the structure of alluvial fan and associated fan delta deposits: an example from the Tertiary of the Betic Cordillera, Spain. Sedimentology, 40(5), 879-893.

Fidolini, F., Ghinassi, M., Aldinucci, M., Billi, P., Boaga, J., Deiana, R. & Brivio, L. (2013) Fault-sourced alluvial fans and their interaction with axial fluvial drainage: An example from the Plio-Pleistocene Upper Valdarno Basin (Truscany, Italy). Sedimentary Geology, 289, 19-39.

Figueiredo, F.T., de Almeida, R.P., Freitas, B.T., Marconato, A., Carrera, S.C. & Turra, B.B. (2016) Tectonic activation, source area stratigraphy and provenance changes in a rift basin: the Early Cretaceous Tucano Basin (NE Brazil). Basin Research, 28, 433-445.

Flotté, N., Sorel, D., Müller, C. & Tensi, J. (2005) Along strike changes in the structural evolution over a brittle detachment fault: Example of the Pleistocene Corinth-Patras rift (Greece). Tectonophysics, 403, 77–94.

Foerster, V., Junginger, A., Langkamp, O., Gebru, T., Asrat, A., Umer, M., Lamb, H.F., Wennrich, V., Rethemeyer, J., Nowaczyk, N., Trauth, M.H. & Schaebitz, F. (2012) Climatic change recorded in the sediments of the Chew Bahir basin, southern Ethiopia, during the last 45,000 years. Quaternary International, 274, 25-37.

Fontana, A., Mozzi, P. & Marchetti, M. (2014) Alluvial fans and megafans along the southern side of the Alps. Sedimentary Geology, 301, 150-171.

Ford, M., Hemelsdaël, R., Mancini, M. & Palyvos, N. (2016) Rift migration and lateral propagation: evolution of normal faults and sediment-routing systems of the western Corinth Rift (Greece). In: Childs, C., Holdsworth, R.E., Jackson, C.A.-L., Manzocchi, T., Walsh, J.J. & Yielding, G. (eds.) The Geometry and Growth of Normal Faults. Geological Society, London, Special Publications, 439, 131-168.

Ford, M., Rohais, S., Williams, E.A., Bourlange, S., Jousselin, D., Backert, N. & Malarte, F. (2013) Tectono-sedimentary evolution of the western Corinth rift (Central Greece). Basin Research, 25(1), 3-25.

Fordham, A.M., North, C.P., Hartley, A.J., Archer, S.G. & Warwick, G.L. (2010) Dominance of lateral over axial sedimentary fill in dryland rift basins. Petroleum Geoscience, 16, 299-304.

Forte, A.M., Moucha, R., Simmons, N.A., Grand, S.P. & Mitovica, J.X. (2010) Deep-mantle contributions to the surface dynamics of the North American continent. Tectonophysics, 481(1-4), 3-15.

Fossen, H. & Rotevatn, A. (2016) Fault linkage and relay structures in extensional settings – A review. Earth-Science Reviews, 154, 14-28.

Franke, D., Hornung, J. & Hinderer, M. (2015) A combined study of radar facies, lithofacies and three-dimensional architecture of an alpine alluvial fan (Illgraben fan, Switzerland). Sedimentology, 62, 57–86.

Friedmann, S.J. & Burbank, D.W. (1995) Rift basins and supradetachment basins: intracontinental extensional end-members. Basin Research, 7, 109-127.

Frostick, L.E. & Reid, I. (1987) Tectonic control of desert sediments in rift basins ancient and modern. In: Frostick, L.E. & Reid, I. (eds.) Desert Sediments: Ancient and Modern. Geological Society Special Publication, 35, 53-68.

Frostick, L.E. & Reid, I. (1989) Climatic versus tectonic controls of fan sequences: lessons from the Dead Sea, Israel. Journal of the Geological Society, London, 146, 527-538.

Frostick, L.E. & Reid, I. (1989) Is structure the main control of river drainage and sedimentation in rifts? Journal of African Earth Sciences, 8(2-4), 165-182.

Gawthorpe, R.L. & Colella, A. (1990) Tectonic controls on coarse-grained delta depositional systems in rift basins. In: Colella, A. & Prior, D.B. (eds.) Coarse-Grained Deltas. International Association of Sedimentologists, Special Publications, 10, 113-127.

Gawthorpe, R.L., Fraser, A.J. & Collier, R.E.Ll. (1994) Sequence stratigraphy in active extensional basins: implications for the interpretation of ancient basin-fills. Marine and Petroleum Geology, 11(6), 642-658.

Gawthorpe, R.L. & Leeder, M.R. (2000) Tectono-sedimentary evolution of active extensional basins. Basin Research, 12(3-4), 195-218.

Gawthorpe, R.L., Leeder, M.R., Kranis, H., Skourtsos, E., Andrews, J.E., Henstra, G.A., Mack, G.H., Muravchik, M, Turner, J.A. & Stamatakis, M. (2018) Tectono-sedimentary evolution of the Plio-Pleistocene Corinth rift, Greece. Basin Research, 30(3), 448-479.

Gawthorpe, R.L., Jackson, C.A.-L., Young, M.J., Sharp, I.R., Moustafa, A.R. & Leppard, C.W. (2003) Normal fault growth, displacement localisation and the evolution of normal fault populations: the Hammam Faraun fault block, Suez rift, Egypt. Journal of Structural Geology, 25(6), 883-895.

Geurts, A.H., Cowie, P.A., Duclaux, G., Gawthorpe, R.L., Huismans, R.S., Pedersen, V.K. & Wedmore, L.N.J. (2018) Drainage integration and sediment dispersal in active continental rifts: A numerical modelling study of the central Italian Apennines. Basin Research, 30(5), 965-989.

Giaconia, F., Booth-Rea, G., Martínez-Martínez, J.M., Azañón, J.M., Pérez-Peña, J.V., Pérez-Romero, J. & Villegas, I. (2012) Geomorphic evidence of active tectonics in the Sierra Alhamilla (eastern Betics, SE Spain). Geomorphology, 145-146, 90-106.

Gloppen, T.G. & Steel, R.J. (1981) The deposits, internal structure and geometry in six alluvial fan-fan delta bodies (Devonian-Norway)-A study in the significance of bedding sequence in conglomerates. Society for Sedimentary Geology Special Publication, 31, 49–69.

Gluyas, J.G., Adams, C.A., Busby, J.P., Craig, J., Hirst, C., Manning, D.A.C., McCay, A., Narayan, N.S., Robinson, H.L., Watson, S., Westaway, R. & Younger, P.L. (2018) Keeping warm: a review of deep geothermal potential of the UK. Proceedings of the Institution of Mechanical Engineers, Part A: Journal of Power and Energy. 232, 115-126.

Govers, R. & Wortel, M.J.R. (2005) Lithosphere tearing at STEP faults: response to edges of subduction zones. Earth and Planetary Science Letters, 236(1-2), 505-523.

Graham, S.A., Hendrix, M.S., Johnson, C.L., Badamgarav, D., Badarch, G., Amory, J., Porter, M., Barsbold, R., Webb, L.E. & Hacker, B.R. (2001) Sedimentary record and tectonic implications of Mesozoic rifting in southeast Mongolia. Geological Society of America Bulletin, 113(12), 1560-1579.

Grelle, G., Rossi, A., Revellino, P., Guerriero, L., Guadagno, F.M. & Sappa, G. (2019) Assessment of Debris-Flow Erosion and Deposit Areas by Morphometric Analysis and a GIS-Based Simplified Procedure: A Case Study of Paupisi in the Southern Apennines. Sustainability, 11(8), 2382.

Gumbricht, T., McCarthy, T.S. & Merry, C.L. (2001) The topography of the Okavango Delta, Botswana, and its tectonic and sedimentological implications. South African Journal of Geology, 104, 243-264.

Gupta, S., Underhill, J.R., Sharp, I.R. & Gawthorpe, R.L. (1999) Role of fault interactions in controlling synrift sediment dispersal patterns: Miocene, Abu Alaqa Group, Suez Rift, Sinai, Egypt. Basin Research, 11(2), 167-189.

Guzzetti, F., Marchetti, M. & Reichenbach, P. (1997) Large alluvial fans in the north-central Po Plain (Northern Italy). Geomorphology, 18, 119-136.

Hamilton, W. (1987) Crustal extension in the Basin and Range Province, southwestern United States. In: Coward, M.P., Dewey, J.F. & Hancock, P.L. (eds.) Continental Extensional Tectonics. Geological Society, London, Special Publications, 28, 155-176.

Hampton, M.A. (1979) Buoyancy in Debris Flows. Journal of Sedimentary Petrology, 49(3), 753-758.

Hampton, B.A. & Horton, B.K. (2007) Sheetflow fluvial processes in a rapidly subsiding basin, Altiplano plateau, Bolivia. Sedimentology, 54(5), 1121-1148.

Hansen, S.E., Nyblade, A.A. & Benoit, M.H. (2012) Mantle structure beneath Africa and Arabia from adaptively parameterized P-wave tomography: Implications for the origin of Cenozoic Afro-Arabian tectonism. Earth and Planetary Science Letters, 319-320, 23-34.

Hansen, S.E. & Nyblade, A.A. (2013) The deep seismic structure of the Ethiopia/Afar hotspot and the African superplume. Geophysical Journal International, 194(1), 118-124.

Harries, R., Kirstein, L.A., Whittaker, A., Attal., M. & Main, I. (2019) Impact of recycling and lateral sediment input on grain size fining trends – implications for reconstructing tectonic and climatic forcings in ancient sedimentary basins. Basin Research, 31(5), 866-891.

Harrison, P.W. (1957) A Clay-Till Fabric: Its Character and Origin. The Journal of Geology, 65(3), 275-308.

Hartley, A.J., Weissmann, G.S., Nichols, G.J. & Warwick, G.L. (2010) Large Distributive Fluvial Systems: Characteristics, Distribution, and Controls on Development. Journal of Sedimentary Research, 80(2), 167-183.

Harvey, A.M. (2002) The role of base-level change in the dissection of alluvial fans: case studies from southeast Spain and Nevada. Geomorphology, 45, 67-87.

Harvey, A.M., Mather, A.E. & Stokes, M. (2005) Alluvial Fans: Geomorphology, Sedimentology, Dynamics. Geological Society, London, Special Publications, 251.

Head, M.J. & Gibbard, P.L. (2005) Early-Middle Pleistocene transitions: an overview and recommendation for defining the boundary. In: Head, M.J. & Gibbard, P.L. (eds.) Early-Middle Pleistocene Transitions: The Land-Ocean Evidence. Journal of the Geological Society, London, Special Publications, 247, 1-18.

Heki, K., Miyazaki, S., Takahashi, H., Kasahara, M., Kimata, F., Miura, S., Vasilenko, N.F., Ivashchenko, A. & An, K.-D. (1999) The Amurian Plate motion and current plate kinematics in eastern Asia. Journal of Geophysical Research, 104(B12), 29147-29155.

Helsen, M.M., Koop, P.J.M. & van Steijn, H. (2002) Magnitude-frequency relationship for debris flows on the fan of the Chalance torrent, Valgaudemar (French Alps). Earth Surface Processes and Landforms, 27(12), 1299-1307.

Hemelsdaël, R. & Ford, M. (2016) Relay zone evolution: a history of repeated fault propagation and linkage, central Corinth Rift, Greece. Basin Research, 28, 34-56.

Hemelsdaël, R., Ford, M., Malartre, F. & Gawthorpe, R.L. (2017) Interaction of an antecedent fluvial system with early normal fault growth: Implications for syn-rift stratigraphy, western Corinth rift (Greece). Sedimentology, 64(7), 1957-1997.

Henstra, G.A., Gawthorpe, R.L., Helland-Hansen, W., Ravnås, R. & Rotevatn, A. (2017) Depositional systems in multiphase rifts: seismic case study from the Lofoten margin, Norway. Basin Research, 29(4), 447-469.

Heward, A.P. (1989) Early Ordovician alluvial fan deposits of the Marmul oil field, South Oman. Journal of the Geological Society, London, 146, 557-565.

Higgs, B. (1988) Syn-sedimentary structural controls on basin deformation in the Gulf of Corinth, Greece. Basin Research, 1(3), 155-165.

Hinderer, M. (2012) From gullies to mountain belts: A review of sediment budgets at various scales. Sedimentary Geology, 280, 21-59.

Holmes, A. (1965) Principles of physical geology. London, England, Thomas Nelson and Sons Ltd., 1288p.

Hopkins, M.C. & Dawers, N.H. (2018) The role of fault length, overlap and spacing in controlling extensional relay ramp fluvial system geometry. Basin Research, 30, 20-34.

Hooke, R.L.B. (1972) Geomorphic Evidence for Late-Wisconsin and Holocene Tectonic Deformation, Death Valley, California. Geological Society of America Bulletin, 83(7), 2073-2098.

Howell, F.C., Haesaerts, P. & de Heinzelin, J. (1987) Depositional environments, archeological occurrences and hominids from Members E and F of the Shungura Formation (Omo basin, Ethiopia). Journal of Human Evolution, 16, 665-700.

Hubbard, B.P. & Glasser, N.F. (2005) Field Techniques in Glaciology and Glacial Geomorphology. Oxford, England, John Wiley & Sons, 412p.

Hubert, J.F. & Filipov, A.J. (1989) Debris-flow deposits in alluvial fans on the west flank of the White Mountains, Owens Valley, California, U.S.A. Sedimentary Geology, 61, 177-205.

Humphreys, E.D. (1995) Post-Laramide removal of the Farallon slab, western United States. Geology, 23(11), 987-990.

Hungr, O., Evans, S.G., Bovis, M.J. & Hutchinson, J.N. (2001) A Review of the Classification of Landslides of the Flow Type. Environmental and Engineering Geoscience, 8(3), 221-238.

Hwang, I.G., Chough, S.K., Hong, S.W. & Choe, M.Y. (1995) Controls and evolution of fan delta systems in the Miocene Pohang Basin, SE Korea. Sedimentary Geology, 98, 147–179.

Ingersoll, R.V., Cavazza, W., Baldridge, W.S. & Shafiqullah, M. (1990) Cenozoic sedimentation and paleotectonics of north-central New Mexico: Implications for the initiation and evolution of the Rio Grande rift. Geological Society of America Bulletin, 102(9), 1280-1296.

Ivanov, A.V., Demonterova, E.I., He, H., Perepelov, A.B., Travin, A.V. & Lebedev, V.A. (2015) Volcanism in the Baikal rift: 40 years of active-versus-passive model discussion. Earth-Science Reviews, 148, 18-43.

Iverson, R.M. (1997) The Physics of Debris Flows. Reviews of Geophysics, 35(3), 245-296.

Jackson, C.A.L., Gawthorpe, R.L., Leppard, C.W. & Sharp, I.R. (2006) Rift-initiation development of normal fault blocks: insights from the Hamman Faraun fault block, Suez Rift, Egypt. Journal of the Geological Society, London, 163, 165-183.

Jackson, C.A.-L., Gawthorpe, R.L. & Sharp, I.R. (2002) Growth and linkage of the East Tanka fault zone, Suez rift: structural style and syn-rift stratigraphic response. Journal of the Geological Society, 159, 175-187.

Jackson, C.A.-L. & Rotevatn, A. (2013) 3D seismic analysis of the structure and evolution of a salt-influenced normal fault zone: a test of competing fault growth models. Journal of Structural Geology, 54, 215-234.

Jackson, L.E., Kostaschuk, R.A. & MacDonald, G.M. (1987) Identification of debris flow hazard on alluvial fans in the Canadian Rocky Mountains. Reviews in Engineering Geology, 7, 115-124.

Jakob, M. & Friele, P. (2010) Frequency and magnitude of debris flows on Cheekye River, British Columbia. Geomorphology, 114(3), 382-395.

Jeffery, G.B. (1922) The motion of ellipsoidal particles immersed in a viscous fluid. Proceedings of the Royal Society, London, A, 102, 161-179.

Jerram, D.A. & Higgins, M.D. (2007) 3D Analysis of Rock Textures: Quantifying Igneous Microstructures. Elements, 3(4), 239-245.

Jo, H.R. & Chough, S.K. (2001) Architectural analysis of fluvial sequences in the Northwestern part of Kyongsang Basin (Early Cretaceous), SE Korea. Sedimentary Geology, 144, 307–334.

Jo, H.R., Rhee, C.W. & Chough, S.K. (1997) Distinctive characteristics of a streamflow-dominated alluvial fan deposit: Sanghori area, Kyongsang Basin (Early Cretaceous), southeastern Korea. Sedimentary Geology, 110(1-2), 51-79.

Johannessen, P.N., Nielsen, L.H., Nielsen, L., Møller, I., Pejrup, M. & Andersen, T.J. (2010) Architecture of an Upper Jurassic barrier island sandstone reservoir, Danish Central Graben: implications of a Holocene-Recent analogue from the Wadden Sea. In: Vining, B.A. & Pickering, S.C. (eds.) Petroleum Geology: From Mature Basins to New Frontiers. Geological Society, London, Petroleum Geology Conference series, 7, 145-155.

Johnson, A.M. (1970) Physical processes in Geology, W.H. Freeman, New York, 557pp.

Jolivet, M., De Boisgeollier, T., Petit, C., Fournier, M., Sankov, V.A., Ringenbach, J.-C., Byzov, L., Miroshnichenko, A.I., Kovalenko, S.N. & Anisimova, S.V. (2009) How old is the Baikal Rift Zone? Insight from apatite fission track thermochronology. Tectonics, 28, TC3008.

Jolivet, M., Bourquin, S., Heilbronn, G., Robin, C., Barrier, L., Dabard, M-P., Jia, Y., De Pelsmarker, E., & Fu, B. (2017) The Upper Jurassic-Lower Cretaceous alluvial-fan deposits of the Kalaza Formation (Central Asia): tectonic pulse or increased aridity? In: Brunet, M.-F., McCann, T. & Sobel, E.R. (eds.) Geological Evolution of Central Asian Basins and the Western Tien Shan Range. Geological Society Special Publication, 427, 491-521.

Jolivet, L., Faccenna, C., Huet, B., Labrousse, L., Le Pourheit, L., Lacombe, O., Lecomte, E., Burov, E., Denéle, Y., Brun, J.-P., Philippon, M., Paul, A., Salaün, G., Karabulut, H., Piromallo, C., Monilé, P., Gueydan, F., Okay, A.I., Oberhänsli, R., Pourteau, A., Augier, R., Gadenne, L. & Driussi, O. (2013) Aegean tectonics: Strain localisation, slab tearing and trench retreat. In: Papanikolaou, D., Roberts, G. & Royden, L. (eds.) The Aegean: a natural laboratory for tectonics – Neotectonics. Tectonophysics, 597-598, 1-33.

Kain, C.L., Rigby, E.H. & Mazengarb, C. (2018) A combined morphometric, sedimentary, GIS and modelling analysis of flooding and debris flow hazard on a composite alluvial fan, Caveside, Tasmania. Sedimentary Geology, 364, 286-301.

Karátson, D., Sztanó, O. & Telbisz, T. (2002) Preferred Clast Orientation in Volcaniclastic Mass-Flow Deposits: Application of a New Photo-Statistical Method. Journal of Sedimentary Research, 72(6), 823-835.

Karpeta, W. P. (1993) Sedimentology and gravel bar morphology in an Archaean braided river sequence: the Witpan Conglomerate Member (Witwatersrand Supergroup) in the Welkom Goldfield, South Africa. Geological Society, London, Special Publications, 75, 369–388.

Keen, C.E. (1985) The dynamics of rifting: deformation of the lithosphere by active and passive driving forces. Geophysical Journal International, 80(1), 95-120.

Kim, B.C. & Lowe, D.R. (2004) Depositional processes of the gravelly debris flow deposits, South Dolomite alluvial fan, Owens Valley, California. Geosciences Journal, 8(2), 153-170.

Kim, S.B. (1995) Alluvial fans and their natural distinction from rivers based on morphology, hydraulic processes, sedimentary processes, and facies assemblages: discussion and reply. Journal of Sedimentary Research, 65(4a), 706-711.

Khadkikar, A. S. (1999) Trough cross-bedded conglomerate facies. Sedimentary Geology, 128, 39–49.

Kohlbeck, F., Mojica, J. & Sceidegger, A.E. (1994) Clast orientations of the 1985 lahars of the Nevado del Ruiz, Colombia and implications for depositional processes. Sedimentary Geology, 88(3-4), 175-183.

Kolomiets, V.L. & Budaev, R.Ts. (2015) Barguzin rift valley: Sedimentogenesis and paleogeography (Baikalian area, Russia). Quaternary International, 355, 57-64.

Köykkä, J. (2011) Precambrian alluvial fan and braidplain sedimentation patterns: Example from the Mesoproterozoic Rjukan Rift Basin, southern Norway. Sedimentary Geology, 234, 89–108.

Krivonogov, S.K. & Safonova, I.Y. (2017) Basin structures and sediment accumulation in the Baikal Rift Zone: Implications for Cenozoic intracontinental processes in the Central Asian Orogenic Belt. Gondwana Research, 47, 267-290.

Kumar Singh, A., Parkash, B., Mohindra, R., Thomas, J.V. & Singhvi, A.K. (2001) Quaternary alluvial fan sedimentation in the Dehradun Valley Piggyback Basin, NW Himalaya: tectonic and palaeoclimatic implications. Basin Research, 13, 449-471.

Kusznir, N.J., Marsden, G. & Egan, S.S. (1991) A flexural-cantilever simple-shear/pure-shear model of continental lithosphere extension: applications to the Jeanne d'Arc Basin, Grand Banks and Viking Graben, North Sea. Geological Society, London, Special Publications, 56(1), 41-60.

Kusznir, N.J., Roberts, A.M. & Morley, C.K. (1995) Forward and reverse modelling of rift basin formation. In: Lambiase, J.J. (eds.) Hydrocarbon Habitat in Rift Basins, Geological Society, London, Special Publications, 80(1), 33-56.

Lambiase, J.J. & Bosworth, W. (1995) Structural controls on sedimentation in continental rifts. In: Lambiase, J.J. (eds.) Hydrocarbon Habitat in Rift Basins, Geological Society, London, Special Publications, 80(1), 117-144.

Larsen, P.H. (1988) Relay structures in a Lower Permian basement-involved extensional system, east Greenland. Journal of Structural Geology, 10, 3-8.

Larsen, V. & Steel, R.J. (1978) The sedimentary history of a debris-flow dominated, Devonian alluvial fan – a study of textural inversion. Sedimentology, 25(1), 37-59.

Le Pichon, X. & Angelier, J. (1979) The Hellenic arc and trench system: A key to the neotectonics evolution of the eastern Mediterranean area. Tectonophysics, 60(1-2), 1-42.

Leeder, M.R. (2011) Tectonic sedimentology: sediment systems deciphering global to local tectonics. Sedimentology, 58, 2-56.

Leeder, M.R. & Alexander, J. (1987) The origin and tectonic significance of asymmetrical meander-belts. Sedimentology, 34(2), 217-226.

Leeder, M.R. & Gawthorpe, R.L. (1987) Sedimentary models for extensional tilt-block/half-graben basins. In: Coward, M.P., Dewey, J.F. & Hancock, P.L. (eds.) Continental Extensional Tectonics. Geological Society, London, Special Publications, 28(1), 139-152.

Leeder, M.R. & Jackson, J.A. (1993) The interaction between normal faulting and drainage in active extensional basins, with examples from the western United States and central Greece. Basin Research, 5, 79-102.

Leeder, M.R. & Mack, G.H. (2001) Lateral erosion ('toe-cutting') of alluvial fans by axial rivers: implications for basin analysis and architecture. Journal of the Geological Society, 158(6), 885-893.

Leeder, M.R., Mark, D.F., Gawthorpe, R.L., Kranis, H., Loveless, S., Pedentchouk, N., Skourtsos, E., Turner, J., Andrews, J.E. & Stamatakis, M. (2012) A "Great Deepening": Chronology of rift climax, Corinth rift, Greece. Geology, 40, 999–1002.

Leeder, M.R., Seger, M.J. & Stark, C.P. (1991) Sedimentation and tectonic geomorphology adjacent to major active and inactive normal faults, southern Greece. Journal of the Geological Society, London, 148, 331-343.

Leleu, S., Ghienne, J.-F. & Manatschal, G. (2005) Upper Cretaceous-Palaeocene basin-margin alluvial fans documenting interaction between tectonic and environmental processes. In: Harvey, A.M., Mather, A.E. & Stokes, M. (eds.) Alluvial Fans: Geomorphology, Sedimentology, Dynamics. Geological Society, London, Special Publications, 251, 217-239.

Leleu, S., Hartley, A.J., van Oosterhout, C., Kennan, L., Ruckwied, K. & Gerdes, K. (2016) Structural, stratigraphic and sedimentological characterisation of a wide rift system: The Triassic rift system of the Central Atlantic Domain. Earth-Science Reviews, 158, 89-124.

Lewis, M.M., Jackson, C.A-L. & Gawthorpe, R.L. (2017) Tectono-sedimentary development of early syn-rift deposits: the Abura Graben, Suez Rift, Egypt. Basin Research, 29, 327–351.

Lindsay, J.F. (1968) The development of clast fabric in mudflows. Journal of Sedimentary Research, 38(4), 1242-1253.

Lindsey, D.A., Langer, W.H. & Knepper JR., D.H. (2005) Stratigraphy, lithology, and sedimentary features of Quaternary alluvial deposits of the South Platte River and some of its tributaries east of the Front Range, Colorado. U.S. Geological Survey Professional Paper 1705.

Logatchev, N.A. & Florensov, N.A. (1978) The Baikal system of rift valleys. Tectonophysics, 45(1), 1-13.

Logatchev, N.A. & Zorin, Y.A. (1987) Evidence and causes of the two-stage development of the Baikal rift. In: Ramberg, I.B., Milanovsky, E.E. & Qvale, G. (eds.) Continental Rifts – Principal and Regional Characteristics. Tectonophysics, 143(1-3), 225-234.

Long, S.P. (2018) Geometry and magnitude of extension in the Basin and Range Province (39°N), Utah, Nevada, and California, USA: Constraints from a province-scale cross section. Geological Society of America Bulletin, 131(1/2), 99-119.

Lowe, D. R. (1979) Sediment gravity flows: their classification and some problems of application to natural flows and deposits. SEPM Special Publication, 27, 75–82.

Macgregor, D. (2015) History of the development of the East African Rift System: A series of interpreted maps through time. Journal of African Earth Sciences, 101, 232-252.

Mack, G.H. (1992) Paleosols as an indicator of climatic change at the Early-Late Cretaceous boundary, southwestern New Mexico. Journal of Sedimentary Petrology, 62(3), 483-494.

Mack, G.H., James, W.C. & Monger, H.C. (1993) Classification of paleosols. Geological Society of America Bulletin, 105, 129–136.

Mack, G.H. & Leeder, M.R. (1999) Climatic and tectonic controls on alluvial-fan and axial-fluvial sedimentation in the Plio-Pleistocene Palomas half graben, southern Rio Grande Rift. Journal of Sedimentary Research, 69(3), 635-652.

Mack, G.H., Leeder, M.R. & Carothers-Durr, M. (2008) Modern flood deposition, erosion, and fan-channel avulsion on the semiarid Red Canyon and Palomas Canyon alluvial fans in the southern Rio Grande Rift, New Mexico, U.S.A. Journal of Sedimentary Research, 78, 432-442.

Mack, G.H., Leeder, M.R. & Salyards, S.L. (2002) Temporal and Spatial Variability of Alluvial-Fan and Axial-Fluvial Sedimentation in the Plio-Pleistocene Palomas Half Graben, Southern Rio Grande Rift, New Mexico, U.S.A. In: Renaut, R.W. & Ashley, G.M. (eds.) Sedimentation in Continental Rifts. SEPM Special Publication, 73, 165-177.

Mack, G.H., Love, D.W. & Seager, W.R. (1997) Spillover models for axial rivers in regions of continental extension: the Rio Mimbres and Rio Grande in the southern Rio Grande rift, USA. Sedimentology, 44, 637-652.

Mack, G.H. & Seager, W.R. (1990) Tectonic control on facies distribution of the Camp Rice and Palomas Formations (Pliocene-Pleistocene) in the southern Rio Grande rift. Bulletin of the Geological Society of America, 102, 45–53.

Mack, G.H., Seager, W.R., Leeder, M.R., Perez-Arlucea, M. & Salyards, S.L. (2006) Pliocene and Quaternary history of the Rio Grande, the axial river of the southern Rio Grande rift, New Mexico, USA. Earth-Science Reviews, 79(1-2), 141-162.

Maizels, J. (1993) Lithofacies variations within sandur deposits: the role of runoff regime, flow dynamics and sediment supply characteristics. Sedimentary Geology, 85, 299–325.

Major, J.J. (1997) Depositional Processes in Large-Scale Debris-Flow Experiments. The Journal of Geology, 105(3), 345-366.

Major, J.J. (1998) Pebble orientation on large, experimental debris-flow deposits. Sedimentary Geology, 117, 151-164.

Mammo, T. (2012) Analysis of gravity field to reconstruct the structure of Omo basin in SW Ethiopia and implications for hydrocarbon potential. Marine and Petroleum Geology, 29, 104-114.

Mann, P. (1997) Model for the formation of large, transtensional basins in zones of tectonic escape. Geology, 25(3), 211-214.

Mann, P., Gahagan, L. & Gordon, M.B. (2001) Tectonic Setting of the World's Giant Oil and Gas Fields. In: Halbouty, M.T. (eds.) Giant Oil and Gas Fields of the Decade 1990-1999. AAPG Memoir, 78.

Manville, V. & White, J.D.L. (2003) Incipient granular mass flows at the base of sediment-laden floods, and the roles of flow competence and flow capacity in the deposition of stratified bouldery sands. Sedimentary Geology, 155(1-2), 157-173.

Mao, L., Cavalli, M., Comiti, F., Marchi, L., Lenzi, M.A. & Arattano, M. (2009) Sediment transfer processes in two Alpine catchments of contrasted morphological settings. Journal of Hydrology, 364(1-2), 88-98.

Mark, D.M. (1973) Analysis of Axial Orientation Data, Including Till Fabrics. Geological Society of America Bulletin, 84(4), 1369-1374.

Maroukian, H., Gaki-Papanastassiou, K., Karymbalis, E., Vouvalidis, K., Pavlopoulos, K., Papanastassiou, D. & Albanakis, K. (2008) Morphometric control on drainage network evolution in the Perachora Peninsula, Greece. Geomorphology, 102, 81-92.

Martini, I.P. & Sagri, M. (1993) Tectono-sedimentary characteristics of Late Miocene-Quaternary extensional basins of the Northern Apennines, Italy. Earth-Science Reviews, 34, 197-233.

Martins-Neto, M. (2000) Tectonics and sedimentation in a paleo/Mesoproterozoic rift-sag basin (Espinhaço basin, southeastern Brazil). Precambrian Research, 103(3), 147-173.

Martins-Neto, M. & Catuneanu, O. (2010) Rift sequence stratigraphy. Marine and Petroleum Geology, 27(1), 247-253.

Mats, V.D. (1993) The structure and development of the Baikal rift depression. Earth-Science Reviews, 34, 81-118.

Mats, V.D. (2012) The sedimentary fill of the Baikal Basin: Implications for rifting age and geodynamics. Russian Geology and Geophysics, 53, 936-954.

Mats, V.D. & Perepelova, T.I. (2011) A new perspective on evolution of the Baikal Rift. Geoscience Frontiers, 2(3), 349-365.

McArthur, A.D., Hartley, A.J. & Jolley, D.W. (2012) Stratigraphic development of an Upper Jurassic deep marine syn-rift succession, Inner Moray Firth Basin, Scotland. Basin Research, 24, 1-25.

McCarthy, T.S. (2013) The Okavango Delta and its place in the geomorphological evolution of Southern Africa. South African Journal of Geology, 116(1), 1-54.

McCarthy, T.S. & Cadle, A.B. (1995) Alluvial fans and their natural distinction from rivers based on morphology, hydraulic processes, sedimentary processes, and facies assemblages – discussion. Journal of Sedimentary Research, 65(3a), 581-586.

McCarthy, T.S., Smith, N.D., Ellery, W.N. & Gumbricht, T. (2002) The Okavango Delta – Semiarid Alluvial-fan Sedimentation Related to Incipient Rifting. In: Renaut, R.W. & Ashley, G.M. (eds.) Sedimentation in Continental Rifts. SEPM Special Publication, 73, 179-193.

McClay, K.R. & White, M.J. (1995) Analogue modelling of orthogonal and oblique rifting. Marine and Petroleum Geology, 12(2), 137-151.

McClusky, S., Balassanian, S., Barka, A., Demir, C., Ergintav, S., Georgiev, I., Gurkan, O., Hamburger, M., Hurst, K., Kahle, H., Kastens, K., Kekelidze, G., King, R., Kotzev, V., Lenk, O., Mahmoud, S., Mishin, A., Nadariya, M., Ouzounis, A., Paradissis, D., Peter, Y., Prilepin, M., Reilinger, R., Sanli, I., Seeger, H., Tealeb, A., Toksöz, M.N. & Veis, G. (2000) Globla Positioning System constraints on plate kinematics and dynamics in the eastern Mediterranean and Caucasus. Journal of Geophysical Research: Solid Earth, 105(B3), 5696-5719.

McGee, W.J. (1897) Sheetflood Erosion. Geological Society of America Bulletin, 8(1), 87-112.

McHone, J.G. (2000) Non-plume magmatism and rifting during the opening of the central Atlantic Ocean. Tectonophysics, 316(3-4), 287-296.

McKee, E.H. (1968) Geologic Quadrangle Map, Spencer Hot Springs Quadrangle, Nevada, MAP GQ-770. Nevada Bureau of Mines and Geology.

McKee, E.H. (1976) Geologic Quadrangle Map, Austin Quadrangle, Nevada, MAP GQ-1307. Nevada Bureau of Mines and Geology.

McKenzie, D. (1978) Some remarks on the development of sedimentary basins. Earth and Planetary Science Letters, 40(1), 25-32.

McKenzie, D. & Bickle, M.J. (1988) The Volume and Composition of Melt Generated by Extension of the Lithosphere. Journal of Petrology, 29(3), 625-679.

McLeod, A.E., Dawers, N.H. & Underhill, J.R. (2000) The propagation and linkage of normal faults:: insights from the Strathspey-Brent-Statfjord fault array, northern North Sea. Basin Research, 12(3-4), 263-284.

McPherson, J.G., Shanmugam, G. & Moiola, R.J. (1987) Fan-deltas and braid deltas: Varieties of coarse-grained deltas. Geological Society of America Bulletin, 99, 331-340.

McQuarrie, N. & Wernicke, B.P. (2005) An animated tectonic reconstruction of southwestern North America since 36 Ma. Geosphere, 1(3), 147-172.

Meek, S.R., Carrapa, B. & DeCelles, P.G. (2020) Recognizing Allogenic Controls on the Stratigraphic Architecture of Ancient Alluvial Fans in the Western US. Frontiers in Earth Science, 8, online access view.

Melton, M.A. (1957) An analysis of the relations among elements of climate, surface properties and geomorphology. Off. Nav. Res., Geogr. Branch, Proj. NR. 389-042, Tech. Rep. 11, Columbia University. 88pp.

Miall, A.D. (1978) Fluvial Sedimentology. Canadian Society of Petroleum Geologists, Memoir 5, 859pp.

Miall, A.D. (1985) Architectural-element analysis: A new method of facies analysis applied to fluvial deposits. Earth-Science Reviews, 22(4), 261-308.

Miall, A.D. (1996) The Geology of Fluvial Deposits: Sedimentary Facies, Basin Analysis, and Petroleum Geology. Springer-Verlag, New York, 582pp.

Miao, X., Lu, H., Li, Z. & Cao, G. (2008) Paleocurrent and fabric analyses of the imbricated fluvial gravel deposits in Huangshi Valley, the northeastern Tibetan Plateau, China. Geomorphology, 99(1-4), 433-442.

Millar, S.W.S. (2006) Process dominating macro-fabric generation in periglacial colluvium. Catena, 67, 79-87.

Miller, K.L., Reitz, M.D. & Jerolmack, D.J. (2014) Generalized sorting profile of alluvial fans. Geophysical Research Letters, 41(20), 7191-7199.

Mills, H.H. (1983) Clast-fabric strength in hillslope colluvium as a function of slope angle. Geografiska Annaler, 65A(3-4), 255-262.

Mills, H.H. (1984) Clast orientation in Mount St. Helens debris-flow deposits, North Fork Toutle River, Washington. Journal of Sedimentary Research, 54(2), 626-634.

Mirabella, F., Bucci, F., Santangelo, M., Cardinali, M., Caielli, G., De France, R., Guzzetti, F. & Barchi, M.R. (2018) Alluvial fan shifts and stream captures driven by extensional tectonics in central Italy. Journal of the Geological Society, 175, 788-805.

Montelli, R., Nolet, G., Dahlen, F.A. & Masters, G. (2006) A catalogue of deep mantle plumes: New results from finite-frequency tomography. Geochemistry, Geophysics, Geosystems, 7(11), Q11007.

Moore, T.C., Klitgord, K.D., Golmshtok, A.J. & Weber, E. (1997) Sedimentation and subsidence patterns in the central and north basins of Lake Baikal from seismic stratigraphy. Bulletin of the Geological Society of America, 109(6), 746-766.

Morley, C.K. (1990) Developments in the structural geology of rifts over the last decade and their impact on hydrocarbon exploration. In: Lambiase, J.J. (eds.) Hydrocarbon Habitat in Rift Basins. Geological Society, London, Special Publications, 80, 1-32.

Morley, C.K., Nelson, R.A., Patton, T.L. & Munn, S.G. (1990) Transfer Zones in the East African Rift System and Their Relevance to Hydrocarbon Exploration in Rifts. American Association of Petroleum Geologists Bulletin, 74(8), 1234-1253.

Morley, C.K. (2002) Evolution of large normal faults: Evidence from seismic reflection data. AAPG Bulletin, 86(6), 961-978.

Morley, C.K., Haranya, C., Phoosongsee, W., Pongwapee, S., Kornsawan, A. & Wonganan, N. (2004) Activation of rift oblique and rift parallel pre-existing fabrics during extension and their effect on deformation style: examples from the rifts of Thailand. Journal of Structural Geology, 26(10), 1803-1829.

Moscariello, A. (2018) Alluvial fans and fluvial fans at the margins of continental sedimentary basins: geomorphic and sedimentological distinction for geo-energy exploration and development. In: Ventra, D. & Clarke, L.E. (eds.) Geology and Geomorphology of Alluvial and Fluvial Fans: Terrestrial and Planetary Perspectives. Geological Society, London, Special Publications, 440, 215-243.

Moscariello, A., Marachi, L., Maraga, F. & Mortara, G. (2002) Alluvial Fans in the Italian Alps: Sedimentary Facies and Processes. In: Martini, I.P., Baker, V.R., & Garzón, G. (eds.) Flood and Megaflood Processes and Deposits: Recent and Ancient Examples. International Association of Sedimentologists, Special Publication, 32, 141-166.

Moucha, R., Forte, A.M., Rowley, D.B., Mitrovica, J.X., Simmons, N.A. & Grand, S.P. (2008) Mantle convection and the recent evolution of the Colorado Plateau and the Rio Grande Rift valley. Geology, 36(6), 439-442.

Muravchik, M., Bilmes, A., D'Elia, L. & Franzese, J.R. (2014) Alluvial fan deposition along a rift depocentre border from the Neuquén Basin, Argentina. Sedimentary Geology, 301, 70-89.

Muravchik, M., Gawthorpe, R.L., Sharp, I.R., Rarity, F. & Hodgetts, D. (2018) Sedimentary environment evolution in a marine hangingwall dipslope settings. El Qaa Fault Block, Suez Rift, Egypt. Basin Research, 30(S1), 452-478.

Murcia, H.F., Hurtado, B.O., Cortés, G.P., Macías, J.L. & Cepeda, H. (2008) The ~ 2500 yr B.P. Chicoral non-cohesive debris flow from Cerro Machín Volcano, Colombia. Journal of Volcanology and Geothermal Research, 171, 201–214.

Myrow, P.M., Tice, L., Archuleta, B., Clark, B., Taylor, J.F. & Ripperdan, R.L. (2004) Flat-pebble conglomerate: its multiple origins and relationship to metre-scale depositional cycles. Sedimentology, 51(5), 973-996.

Nelson, C.H., Karabanov, E.B., Colman, S.M. & Escutia, C. (1999) Tectonic and sediment supply control of deep rift lake turbidite systems: Lake Baikal, Russia. Geology, 27, 163-166.

Nemec, W. (2009) What is a hyperconcentrated flow? Lecture abstract, annual meeting the IAS, Alghero, Spain. 20-23, Sept 2009.

Nemec, W. & Steel, R.J. (1984) Alluvial and coastal conglomerates: their significant features and some comments on gravelly flow deposits. In: Koster, E.H. & Steel, R.J. (eds.) Sedimentology of Gravels and Conglomerates. Memoirs of the Canadian Society of Petroleum Geologists, 10, 1-31.

Nichols, G.J. & Fisher, J.A. (2007) Processes, facies and architecture of fluvial distributary system deposits. Sedimentary Geology, 195, 75–90.

Nichols, G. & Uttamo, W. (2005) Sedimentation in a humid, interior, extensional basin: the Cenozoic Li Basin, northern Thailand. Journal of the Geological Society, London, 162, 333-347.

Nielsen, L.H., Petersen, H.I., Thai, N.D., Duc, N.A., Fyhn, M.B.W., Boldreel, L.O., Tuan, H.A., Lindström, S. & Hien, L.V. (2007) A Middle-Upper Miocene fluvial-lacustrine rift sequence in the Song Ba Rift, Vietnam: an analogue to oil-prone, small-scale continental rift basins. Petroleum Geoscience, 13(2), 145-168.

Nieuwenhuijzen, M.E., van Steijn, H. (1990) Alpine Debris Flows and Their Sedimentary Properties. A Case Study from the French Alps. Permafrost and Periglacial Processes, 1, 111-128.

Nixon, C.W., McNeill, L.C., Bull, J.M., Bell, R.E., Gawthorpe, R.L., Henstock, T.J., Christodoulou, D., Ford, M., Taylor, B., Sakellariou, D., Ferentinos, G., Papatheodorou, G., Leeder, M.R., Collier, R.E.L., Goodliffe, A.M., Sachpazi, M. & Kranis, H. (2016) Rapid spatiotemporal variations in rift structure during development of the Corinth Rift, central Greece. Tectonics, 35, 1225–1248.

North, C.P. & Warwick, G.L. (2007) Fluvial Fans: Myths, Misconceptions, and the End of the Terminal-Fan Model. Journal of Sedimentary Research, 77(9), 693-701.

North, C.P. & Davidson, S.K. (2012) Unconfined alluvial flow processes: Recognition and interpretation of their deposits, and the significance for palaeogeographic reconstruction. Earth-Science Reviews, 111(1-2), 199-223.

Ohmori, H. (1993) Changes in the hypsometric curve through mountain building resulting from concurrent tectonics and denudation. Geomorphology, 8, 263-277.

Ojakangas, R.W. & Dickas, A.B. (2002) The 1.1-Ga Midcontinent Rift System, central North America: sedimentology of two deep boreholes, Lake Superior region. Sedimentary Geology, 147, 13-36.

Oldow, J.S. & Bartel, R.L. (1987) Early to Middle(?) Jurassic extensional tectonism in the western Great Basin: Growth faulting and synorogenic deposition of the Dunlap Formation. Geology, 15, 740-743.

Ori, G.G. (1989) Geologic history of the extensional basin of the Gulf of Corinth (?Miocene-Pleistocene), Greece. Geology, 17, 918–921.

Osborn, G. (1989) Glacial Deposits and Tephra in the Toiyabe Range, Nevada, U.S.A. Arctic and Alpine Research, 21(3), 256-267.

Osipov, E.Yu., Grachev, M.A., Mats, V.D., Khlystov, O.M. & Breitenbach, S. (2003) Mountain glaciers of the Pleistocene Glacial Maximum in the northwestern Barguzin Range (Northern Baikal Ragion): Paleoglacial reconstruction. Russian Geology and Geophysics, 44(7), 652-663.

Palyvos, N., Sorel, D., Lemeille, F., Mancini, M., Pantosti, D., Julia, R., Triantaphyllou, M. & De Martini, P.-M. (2007) Review and new data on uplift rates at the W termination of the Corinth Rift and the NE Rion graben area (Achaia, NW Peloponnesos). Bulletin of the Geological Society of Greece, 40, 412-424.

Palyvos, N., Mancini, M., Sorel, D., Lemeille, F., Pantosti, D., Julia, R., Triantaphyllou, M. & de Martini, P.-M. (2010). Geomorphological, stratigraphic and geochronological evidence of fast Pleistocene coastal uplift in the westernmost part of the Corinth Gulf Rift (Greece). Geological Journal, 45, 78–104.

Park, Y. & Nyblade, A.A. (2006) P-wave tomography reveals a westward dipping low velocity zone beneath the Kenya Rift. Geophysical Research Letters, 33(7), L07311.

Patranabis-Deb, S. & Chaudhuri, A.K. (2007) A retreating fan-delta system in the Neoproterozoic Chattisgarh rift basin, central India: Major controls on its evolution. AAPG Bulletin, 91(6), 785-808.

Pechlivanidou, S., Cowie, P.A., Hannisdal, B., Whittaker, A.C., Gawthorpe, R.L., Pennos, C. & Riiser, O.S. (2018) Source-to-sink analysis in an active extensional setting: Holocene erosion and deposition in the Sperchios rift, central Greece. Basin Research, 30(3), 522-543.

Pérez-Peña, J.V., Azañón, J.M. & Azor, A. (2009) CalHypso: An ArcGIS extension to calculate hypsometric curves and their statistical moments. Applications to drainage basin analysis in SE Spain. Computers & Geosciences, 35, 1214-1223.

Petit, C. & Déverchère, J. (2006) Structure and evolution of the Baikal rift: A synthesis. Geochemistry, Geophysics, Geosystems, 7(11), Q11016.

Pfüger, F. & Seilacher, A. (1991) Flash flood conglomerates. In: Einsele, G., Ricken, W., Seilacher, A. (eds.) Cycles and Events in Stratigraphy. Springer, Berlin, Germany, 383-391.

Pierson, T.C. (2005) Hyperconcentrated flow – transitional process between water flow and debris flow. In: Jakob, M. & Hungr, O. (eds.) Debris-flow Hazards and Related Phenomena. Springer Praxis Books. Springer, Berlin, Heidelberg. 159-202.

Pierson, T.C. & Costa, J.E. (1987) A rheologic classification of subaerial sediment-water flows. In: Costa, J.E. & Wieczorek, G.F. (eds.) Debris Flows/Avalanches: Process, Recognition, and Mitigation, Geological Society of America, 7, 1-12.

Pierson, T.C. & Scott, K.M. (1985) Downstream Dilution of a Lahar: Transition From Debris Flow to Hyperconcentrated Streamflow. Water Resources Research, 21(10), 1511-1524.

Pietzsch, R., Oliveira, D.M., Tedeschi, L.R., Queiroz Neto, J.V., Figueiredo, M.F., Vazquez, J.C. & Schiffer de Souza, R. (2018) Palaeohydrology of the Lower Cretaceous pre-salt lacustrine system, from rift to post-rift phase, Santos Basin, Brazil. Palaeogeography, Palaeoclimatology, Palaeoecology, 507, 60-80.

Pigott, J.D., Kang, M.-H. & Han, H.-C. (2013) First order seismic attributes for clastic seismic facies interpretation: Examples from the East China Sea. Journal of Asian Earth Sciences, 66, 34-54.

Piper, D.J.W. (2006) Sedimentology and tectonic setting of the Pindos Flysch of the Peloponnese, Greece. In: Robertson, A.H.F. & Mountrakis, D. (eds.) Tectonic Development of the Eastern Mediterranean Region. Geological Society, London, Special Publications, 260, 493-505.

Piper, D.J.W., Kontopoulos, N., Anagnostou, C., Chronis, G. & Panagos, A.G. (1990) Modern Fan Deltas in the Western Gulf of Corinth, Greece. Geo-Marine Letters, 10(1), 5-12.

Platt, N.H. & Keller, B. (1992) Distal alluvial deposits in a foreland basin setting—the Lower Freshwater Miocene, Switzerland: sedimentology, architecture and palaeosols. Sedimentology, 39, 545–565.

Plyusnin, A.M., Chernyavskii, M.K. & Posokhov, V.F. (2008) Formation Conditions of Thermal Springs in the Barguzin-Baikal Area: Evidence from Trace Element and Isotopic Composition. Geochemistry International, 46, 996-1004.

Popov, A.M. (1990) A deep geophysical study in the Baikal region. Pure and Applied Geophysics, 134(4), 575-587.

Potter, P.E. & Pettijohn, F.J. (1977) Paleocurrents and Basin Analysis. 2nd Eds. Springer-Verlag Berlin Heidelberg, Berlin, 460pp.

Powers, M.C. (1953) A new roundness scale for sedimentary particles. Journal of Sedimentary Research, 23(2), 117-119.

Proffet, J.M. (1977) Cenozoic geology of the Yerington district, Nevada, and implications for the nature and origin of Basin and Range faulting. Geological Society of America Bulletin, 88, 247-266.

Prosser, S. (1993) Rift-related linked depositional systems and their seismic expression. In: Williams, G.D. & Dobb, A. (eds.) Tectonics and Seismic Sequence Stratigraphy. Geological Society, London, Special Publications, 71(1), 35-66.

Puy-Alquiza, M.J., Miranda-Avilés, R., García-Barragán, J.C., Loza-Aguirre, I., Li, Y. & Zanor, G.A., (2017) Facies analysis, stratigraphic architecture and depositional environments of the Guanajuato conglomerate in the Sierra de Guanajuato, Mexico. Boletin de La Sociedad Geologica Mexicana, 69, 385–408.

Quigley, M.C., Sandiford, M. & Cupper, M.L. (2007) Distinguishing tectonic from climatic controls on range-front sedimentation. Basin Research, 19(4), 491-505.

Rapp, A. (1960a) Recent Development of Mountain Slopes in Kärkevagge and Surroundings, Northern Scandinavia. Geografiska Annaler, 42(2-3), 65-200.

Rasskazov, S.V. (1994) Magmatism related to the East Siberia rift system and the geodynamics. Bulletin des Centres de Recherches Exploration – Production Elf-Aquitaine, 18, 437-452.

Rasskazov, S.V., Luhr, J.F., Bowring, S.A., Ivanov, A.V., Brandt, I.S., Brandt, S.B., Demonterova, E.I., Boven, A.A., Kunk, M., Housh, T. & Duncan, M.A. (2003b) Late Cenozoic volcanism in the Baikal rift system: evidence for formation of the Baikal and Khubsugul basins due to thermal impacts on the lithosphere and collision-derived tectonics. Berliner Paläobiol. Abhand., 4, 33-48.

Rattey, R.P. & Hayward, A.B. (1993) Sequence stratigraphy of a failed rift systems: the Middle Jurassic to Early Cretaceous basin evolution of the Central and Northern North Sea. Geological Society, London, Petroleum Geology Conference series, 4, 215-249.

Ravnås, R. & Steel, R.J. (1998) Architecture of Marine Rift-Basin Successions. AAPG Bulletin, 82(1), 110-146.

Reading, H.G. (1996) Sedimentary Environments: Processes, Facies and Stratigraphy, 3rd. Blackwell Scientific, Oxford.

Reading, H.G. (2006) Sedimentary Environments: Processes, Facies and Stratigraphy. Blackwell Publishing Inc., Oxford. 688pp.

Reitz, M.D. & Jerolmack, D.J. (2012) Experimental alluvial fan evolution: Channel dynamics, slope controls, and shoreline growth. Journal of Geophysical Research, 117(F2), F02021.

Ren, J., Tamaki, K., Li, S. & Junxia, Z. (2002) Late Mesozoic and Cenozoic rifting and its dynamic setting in Eastern China and adjacent areas. Tectonophysics, 344(3-4), 175-205.

Reston, T.J. (2009) The structure, evolution and symmetry of the magma-poor rifted margins of the North and Central Atlantic: A synthesis. Tectonophysics, 468(1-4), 6-27.

Retallack, G.J. (2001) Soils of the Past. An introduction to Paleopedology. 2nd Ed. Blackwell Science, Oxford, 404pp.

Rickenmann, D. (1991) Hyperconcentrated Flow and Sediment Transport at Steep Slopes. Journal of Hydraulic Engineering, 117(11), 1419-1439.

Ritsema, J., van Heijst, H.J. & Woodhouse, J.H. (1999) Complex Shear Wave Velocity Structure Imaged Beneath Africa and Iceland. Science, 286(5446), 1925-1928.

Ritsema, J., Deuss, A., van Heijst, H.J. & Woodhouse, J.H. (2011) S40RTS: a degree-40 shear-velocity model for the mantle from new Rayleigh wave dispersion, teleseismic traveltime and normal-mode splitting function measurements. Geophysical Journal International, 184(3), 1223-1236.

Ritter, J.B., Miller, J.R., Enzel, Y. & Wells, S.G. (1995) Reconciling the roles of tectonism and climate in Quaternary alluvial fan evolution. Geology, 23(3), 245-248.

Rohais, S., Eschard, R., Ford, M., Guillocheau, F. & Moretti, I. (2007a) Stratigraphic architecture of the Plio-Pleistocene infill of the Corinth Rift: Implications for its structural evolution. Tectonophysics, 440(1-4), 5-28.

Rohais, S., Eschard, R. & Guillocheau, F. (2008) Depositional model and stratigraphic architecture of rift climax Gilbert-type fan deltas (Gulf of Corinth, Greece). Sedimentary Geology, 210, 132–145.

Rohais, S., Joannin, S., Colin, J.P., Suc, J.P., Guillocheau, F. & Eschard, R. (2007b) Age and environmental evolution of the syn-rift fill of the southern coast of the Gulf of Corinth (Akrata-Derveni region, Greece). Bull. Soc. Géol. Fr., 178, 231-243.

Rohais, S., Moretti, I. (2017) Structural and Stratigraphic Architecture of the Corinth Rift (Greece): An Integrated Onshore to Offshore Basin-Scale Synthesis. In: Roure, F., Amin, A.A., Khomsi, S. & Al Garni, M.A.M. (eds.), Lithosphere Dynamics and Sedimentary Basins of the Arabian Plate and Surrounding Areas. Frontiers in Earth Sciences. 89-120.

Royden, L.H. & Papanikolaou, D.J. (2011) Slab segmentation and late Cenozoic disruption of the Hellenic arc. Geochemistry, Geophysics, Geosystems, 12(3), Q03010.

Rust, B.R. (1972) Pebble orientation in fluvial sediments. Journal of Sedimentary Research, 42(2), 384-388.

Sachpazi, M., Laigle, M., Charalampakis, M., Diaz, J., Kissling, E., Gesret, A., Becel, A., Flueh, E., Miles, P. & Hirn, A. (2015) Segmented Hellenic slab rollback driving Aegean deformation and seismicity. Geophysical Research Letters, 43(2), 651-658.

Santillan, J.R. & Makinano-Santillan, M. (2016) Vertical accuracy assessment of 30-m resolution ALOS, ASTER and SRTM global DEMs over northeastern Mindanao, Philippines. The International Archives of the Photogrammetry, Remote Sensing and Spatial Information Sciences – ISPRS Archives, 41, 149-156.

Santos, M.G.M., Almeida, R.P., Godinho, L.P.S., Marconato, A. & Mountney, N.P. (2014) Distinct styles of fluvial deposition in a Cambrian rift basin. Sedimentology, 61, 881-914.

Schlische, R.W. (1992) Structural and stratigraphic development of the Newark extensional basin, eastern North America; Evidence for the growth of the basin and its bounding structures. Geological Society of America Bulletin, 104(10), 1246-1263.

Schlische, R.W. (1995) Geometry and origin of fault-related folds in extensional settings. American Association of Petroleum Geologists Bulletin, 79, 1661-1678.

Schlische, R.W. & Anders, M.H. (1996) Stratigraphic effects and tectonic implications of the growth of normal faults and extensional basins. In: Beratan, K.K. (eds.) Reconstructing the structural history of Basin and Range extension using sedimentology and stratigraphy. Geological Society of America Special Paper, 303, 183-203.

Schlunegger, F., Badoux, A., McArdell, B.W., Gwerder, C., Schnydrig, D., Rieke-Zapp, D. & Molnar, P. (2009) Limits of sediment transfer in an alpine debris-flow catchment, Illgraben, Switzerland. Quaternary Science Reviews, 28, 1097-1105.

Scholz, C.A., Rosendahl, B.R. & Scott, D.L. (1990) Development of coarse-grained facies in lacustrine rift basins: Examples from East Africa. Geology, 18(2), 140-144.

Schumm, S.A. (1956) Evolution of drainage systems and slopes in Badlands at Perth Amboy, New Jersey. Bulletin of the Geological Society of America, 67, 597-646.

Scott, K.M., Vallance, J.W. & Pringle, P.T. (1995) Sedimentology, Behavior, and Hazards of Debris Flows at Mount Rainier, Washington. USGS Professional Paper, 1547, 56pp.

Segele, Z.T. & Lamb, P.J. (2005) Characterization and variability of Kiremt rainy season over Ethiopia. Meteorology and Atmospheric Physics, 89, 153-180.

Seger, M. & Alexander, J. (2009) Distribution of Plio-Pleistocene and Modern Coarse-Grained Deltas South of the Gulf of Corinth, Greece. Tectonic Controls and Signatures in Sedimentary Successions, 20, 37-48.

Sengör, A.M.C. & Burke, K. (1978) Relative timing of rifting and volcanism on Earth and its tectonic implications. Geophysical Research Letters, 5(6), 419-421.

Shukla, U.K. (2009) Sedimentation model of gravel-dominated alluvial piedmont fan, Ganga Plain, India. International Journal of Earth Sciences, 98, 443–459.

Shultz, A.W. (1984) Subaerial debris-flow deposition in the Upper Palaeozoic Cutler Formation, Western Colorado. Journal of Sedimentary Petrology, 54(3), 759-772.

Shuster, D. L., Ehlers, T.A., Rusmore, M. E. & Farley, K. A. (2005) Rapid Glacial Erosion at 1.8 Ma Revealed by the 4He/3He Thermochronometry. Science, 310(5754), 1668-1670.

Simmons, N.A., Forte, A.M. & Grand, S.P. (2007) Thermochemical structure and dynamics of the African superplume. Geophysical Research Letters, 34(2), L02301.

Simmons, N.A., Forte, A.M. & Grand, S.P. (2009) Joint seismic, geodynamic and mineral physical constraints on three-dimensional mantle heterogeneity: Implications for the relative importance of thermal versus compositional heterogeneity. Geophysical Journal International, 177(3), 1284-1304.

Sinclair, I.K., Shannon, P.M., Williams, B.P.J., Harker, S.D. & Mooren, J.G. (1994) Tectonic control on sedimentary evolution of three North Atlantic borderland Mesozoic basins1. Basin Research, 6, 193–217.

Skourlis, K. & Doutsos, T. (2003) The Pindos Fold-and-thrust belt (Greece): inversion kinematics of a passive continental margin. International Journal of Earth Sciences, 92(6), 891-903.

Smyrak-Sikora, A., Johannessen, E.P., Olaussen, S., Sandal, G. & Braathen, A. (2019) Sedimentary architecture during Carboniferous rift initiation – the arid Billefjorden Trough, Svalbard. Journal of the Geological Society, 176(2), 225-252.

Sohn, Y.K., Rhee, C.W. & Kim, B.C. (1999) Debris Flow and Hyperconcentrated Flood-Flow Deposits in an Alluvial Fan, Northwestern Part of the Cretaceous Yongdong Basin, Central Kora. The Journal of Geology, 107(1), 111-132.

Somerville, D.J.P., Mountney, N.P., Colombera, L. & Collier, R.E.Ll. (2020) Impact of a pre-existing transverse drainage system on active rift stratigraphy: An example from the Corinth Rift, Greece. Basin Research, 32(4), 764-788.

Sorel, D. (2000) A Pleistocene and still-active detachment fault and the origin of the Corinth-Patras rift, Greece. Geology, 28(1), 83-85.

Sorriso-Valvo, M., Antronico, L., & Le Pera, E. (1998) Controls on modern fan morphology in Calabria, Southern Italy. Geomorphology, 24, 169-187.

Stab, M., Bellahsen, N., Pik, R., Quidelleur, X., Ayalew, D. & Leroy, S. (2016) Modes of rifting in magma-rich settings: Tectono-magmatic evolution of Central Afar. Tectonics, 35(1), 2-38.

Stanistreet, I.G. & McCarthy, T.S. (1993) The Okavango Fan and the classification of subaerial fan systems. Sedimentary Geology, 85(1-4), 115-133.

Steel, R.J. & Thompson, D.B. (1983) Structures and textures in Triassic braided stream conglomerates ('Bunter' Pebble Beds) in the Sherwood Sandstone Group, North Staffordshire, England. Sedimentology, 30, 341-367.

Stewart, J.H. (1980) Regional tilt patterns of late Cenozoic basin-range fault blocks, western United States. Geological Society of America Bulletin, 91, 460-464.

Stock, J.D., Schmidt, K.M. & Miller, D.M. (2008) Controls on alluvial fan long-profiles. Geological Society of America Bulletin, 120(5-6), 619-640.

Strahler, A.N. (1952) Hypsometric (area-altitude) analysis of erosional topography. Bulletin of the Geological Society of America, 63, 1117-1142.

Strecker, U., Steidtmann, J.R. & Smithson, S.B. (1999) A Conceptual Tectonostratigraphic Model for Seismic Facies Migrations in a Fluvio-Lacustrine Extensional Basin. AAPG Bulletin, 83(1), 43-61.

Suc, J.-P. & Popescu, S.-M. (2005) Pollen records and climatic cycles in the North Mediterranean region since 2.7 Ma. In: Head, M.J. & Gibbard, P.L. (eds.) Early-Middle Pleistocene Transitions: The Land-Ocean Evidence. Journal of the Geological Society, London, Special Publications, 247, 147-158.

Sultan, M., Yousef, A.F., Metwally, S.E., Becker, R., Milewski, A., Sauck, W., Sturchio, N.C., Mohamed, A.M.M., Wagdy, A., El Alfy, Z., Soliman, F., Rashed, N., Becker, D., Sagintayev, Z., Ahmed, N. & Welton, B. (2011) Red Sea rifting controls on aquifer distribution: Constraints from geochemical, geophysical, and remote sensing data. GSA Bulletin, 123, 911-924.

Suresh, N., Bagati, T.N., Kumar, R. & Thakur, V.C. (2007) Evolution of quaternary alluvial fans and terraces in the intramontane Pinjaur Dun, Sub-Himalaya, NW India: Interaction between tectonics and climate change. Sedimentology, 54, 809–833.

Suzuki, K. & Ui, T. (1982) Grain orientation and depositional ramps as flow direction indicators of a large-scale pyroclastic flow deposit in Japan. Geology, 10(8), 429-432.

Tadono, T., Nagai, H., Ishida, H., Oda, F., Naito, S., Minakawa, K. & Iwamoto, H. (2016) Generation of the 30 m-mesh global digital surface model by ALOS PRISM. The International Archives of the Photogrammetry, Remote Sensing and Spatial Information Sciences – ISPRS Archives. 41, 157-162.

Takaku, J., Tadono, T. & Tsutsui, K. (2014) Generation of high resolution global DSM from ALOS PRISM. International Archives of the Photogrammetry, Remote Sensing and Spatial Information Sciences – ISPRS Archives. 40 (4), 243-248.

Talling, P.J. (2013) Hybrid submarine flows comprising turbidity current and cohesive debris flow: Deposits, theoretical and experimental analyses, and generalized models. Geosphere, 9(3), 460-488.

Teixeira, B.M.N., Astini, R.A., Gomez, F.J., Morales, N. & Pimentel, M.M. (2018). Source-to-sink analysis of continental rift sedimentation: Triassic Cuyo basin, Precordillera Argentina. Sedimentary Geology, 376, 164–184.

Thybo, H., & Nielsen, C.A. (2009) Magma-compensated crustal thinning in continental rift zones. Nature, 457, 873-876.

Tiercelin, J.J. (1990) Rift-basin sedimentation: responses to climate, tectonism and volcanism. Examples of the East African Rift. Journal of African Earth Sciences, 10, 283-305.

Todd, S.P. (1989) Stream-driven, high-density gravelly traction carpets: possible deposits in the Trabeg Conglomerate Formation, SW Ireland and some theoretical considerations of their origin. Sedimentology, 36, 513–530.

Törnqvist, R., Jarsjö, J., Pietroń, J., Bring, A., Rogberg, P., Asokan, S.M. & Destouni, G. (2014) Evolution of the hydro-climate system in the Lake Baikal basin. Journal of Hydrology, 519, 1953-1962.

Trudgill, B.D. (2002) Structural controls on drainage development in the Canyonlands grabens of southeast Utah. AAPG Bulletin, 86(6), 1095-1112.

Trudgill, B. & Cartwright, J. (1994) Relay-ramp forms and normal fault linkages, Canyonlands Nation Park, Utah. Geological Society of America Bulletin, 106, 1143-1157.

Tucholke, B.E., Sawyer, D.S. & Sibuet, J.-C. (2007) Breakup of the Newfoundland-Iberia rift. In: Karner, G.D., Manatschal, G. & Pinheiro, L.M. (eds.) Imaging, Mapping and Modelling Continental Lithosphere Extension and Breakup. Geological Society, London, Special Publications, 282, 9-46.

Tugend, J., Gillardf, M., Manatschal, G., Nirrengarten, M., Harkin, C., Epin, M.-E., Sauter, D., Autin, J., Kusznir, N. & McDermott, K. (2018) Reappraisal of the magma-rich versus magma-poor rifted margin archetypes. Geological Society, London, Special Publications, 476, 23-47.

Turner, S.A. (2010) Sedimentary record of Late Neoproterozoic rifting in the NW Tarim Basin, China. Precambrian Research, 181, 85–96.

Underhill, J.R. (1989) Late Cenozoic deformation of the Hellenic foreland, Western Greece. Bull. Geol. Soc. Am., 101, 613–634.

Underhill, J.R. (1991) Implications of Mesozoic-Recent basin development in the western Inner Moray Firth, UK. Marine and Petroleum Geology, 8, 359-369.

van Dijk, M., Kleinhans, M.G., Postma, G. & Kraal, E. (2012) Contrasting morphodynamics in alluvial fans and fan deltas: effect of the downstream boundary. Sedimentology, 59(7), 2125-2145.

van Hinsbergen, D.J.J., Zachariase, W.J., Wortel, W.J.R. & Meulenkamp, J.E. (2005) Underthrusting and exhumation: A comparison between the External Hellenides and the "hot" Cycladic and "cold" South Aegean core complexes (Greece). Tectonics, 24(2), TC2011.

Vassilakis, E., Royden, L.H. & Papanikolaou, D.J. (2011) Kinematic links between subduction along the Hellenic trench and extension in the Gulf of Corinth, Greece: A multidisciplinary analysis. Earth and Planetary Science Letters, 3030(1-2), 108-120.

Ventra, D. & Clarke, L.E. (2018) Geology and geomorphology of alluvial and fluvial fans: current progress and research perspectives. In: Ventra, D. & Clarke, L.E. (eds.) Geology and Geomorphology of Alluvial and Fluvial Fans: Terrestrial and Planetary Perspectives. Geological Society, London, Special Publications, 440, 1-21.

Ventra, D., Díaz, G.C. & de Boer, P.L. (2013) Colluvial sedimentation in a hyperarid setting (Atacama Desert, northern Chile): Geomorphic controls and stratigraphic facies variability. Sedimentology, 60, 1257-1290.

Ventra, D. & Nichols, G.J. (2014) Autogenic dynamics of alluvial fans in endorheic basins: Outcrop examples and stratigraphic significance. Sedimentology, 61(3), 767-791.

Viseras, C., Calvache, M.L., Soria, J.M. & Fernández, J. (2003) Differential features of alluvial fans controlled by tectonic or eustatic accommodation space. Examples from the Betic Cordillera, Spain. Geomorphology, 50(1-3), 181-202.

Volker, H.X., Wasklewicz, T.A. & Ellis, M.A. (2007) A topographic fingerprint to distinguish alluvial fan formative processes. Geomorphology, 88, 34-45.

Wagner, S., Günster, N. & Skowronek, A. (2012) Genesis and climatic interpretation of paleosols and calcretes in a plio-pleistocene alluvial fan of the costa blanca (SE Spain). Quaternary International, 265, 170-178.

Walker, R.G. (1979) Facies Models. Geological Association of Canada, Toronto.

Walsh, J.J. & Watterson, J. (1988) Analysis of the relationship between displacements and dimensions of faults. Journal of Structural Geology, 10(3), 239-247.

Walsh, J.J., Nicol, A. & Childs, C. (2002) An alternative model for the growth of faults. Journal of Structural Geology, 24(11), 1669-1675.

Wandres, A.M., Bradshaw, J.D., Weaver, S., Maas, R., Ireland, T. & Eby, N. (2004) Provenance analysis using conglomerate clast lithologies: a case study from the Pahau terrane of New Zealand. Sedimentary Geology, 167, 57-89.

Waresback, D.B. & Turbeville, B.N. (1990) Evolution of a Plio-Pleistocene volcanogenic-alluvial fan: The Puye Formation, Jemez Mountains, New Mexico. Bulletin of the Geological Society of America, 102(3), 298-314.

Watterson, J. (1986) Fault Dimensions, Displacements and Growth. Pure and Applied Geophysics PAGEOPH, 124(1-2), 365-373.

Watts, A.B. & Burov, E.B. (2003) Lithospheric strength and its relationship to the elastic and seismogenic layer thickness. Earth and Planetary Science Letters, 213(1-2), 113-131.

Weissmann, G.S., Hartley, A.J., Nichols, G.J., Scuderi, L.A., Olson, M., Buehler, H. & Banteah, R. (2010) Fluvial form in modern continental sedimentary basins: Distributive fluvial systems. Geology, 38(1), 39-42.

Weissmann, G.S., Hartley, A.J., Scuderi, L.A., Nichols, G.J., Owen, A., Wright, S., Felicia, A.L., Holland, F. & Anaya, F.M.L. (2015) Fluvial geomorphic elements in modern sedimentary basins and their potential preservation in the rock record: A review. Geomorphology, 250, 187-219.

Wells, N.A. (1984) Sheet debris flow and Sheetflood conglomerates in Cretaceous cool-maritime alluvial fans, South Orkney Islands, Antarctica. Sedimentology of Gravels and Conglomerates, 10, 133-145.

Wells, M.L. & Hoisch, T.D. (2008) The role of mantle delamination in widespread Late Cretaceous extension and magmatism in the Corilleran orogen, western United States. Geological Society of America Bulletin, 120(5-6), 515-530.

Welsh, A.J. (2008) Delineating debris-flow hazards on alluvial fans in the Coromandel and Kaimai regions, New Zealand using GIS. MSc Thesis, University of Canterbury, New Zealand, 169pp + App.

Welsh, A.J. & Davies, T. (2011) Identification of alluvial fans susceptible to debris-flow hazards. Landslides, 8, 183-194.

Went, D.J. (2005) Pre-vegetation alluvial fan facies and processes: An example from the Cambro-Ordovician Rozel Conglomerate Formation, Jersey, Channel Islands. Sedimentology, 52, 693–713.

Wernicke, B. & Burchfiel, B.C. (1982) Modes of extensional tectonics. Journal of Structural Geology, 4(2), 105-115.

Wernicke, B. (1985) Uniform-sense normal simple shear of the continental lithosphere. Canadian Journal of Earth Sciences, 22(1), 108-125.

Whipple, K.X., Parker, G., Paola, C. & Mohrig, D. (1998) Channel Dynamics, Sediment Transport, and the Slope of Alluvial Fans: Experimental Study. The Journal of Geology, 106(6), 677-694.

Whipple, K.X. & Trayler, C.R. (1996) Tectonic control of fan size: the importance of spatially variable subsidence rates. Basin Research, 8, 351-366.

White, R. & McKenzie, D. (1989) Magmatism at rift zones: The generation of volcanic continental margins and flood basalts. Journal of Geophysical Research, 94(B6), 7685-7729.

Whittaker, A.C., Attal, M. & Allen, P.A. (2010) Characterising the origin, nature and fate of sediment exported from catchments perturbed by active tectonics. Basin Research, 22(6), 809-828.

Whittaker, A.C., Cowie, P.A., Attal, M., Tucker, G.E. & Roberts, G.P. (2007) Contrasting transient and steady-state rivers crossing active normal faults: new field observations from the Central Apennines, Italy. Basin Research, 19, 529-556.

Wilford, D.J., Sakals, M.E., Innes, J.L., Sidle, R.C. & Bergerud, W.A. (2004) Recognition of debris flow, debris flood and flood hazard through watershed morphometrics. Landslides, 1, 61-66.

Williams, R.M., Underhill, J.R. & Jamieson, R.J. (2020) The role of relay ramp evolution in governing sediment dispersal and petroleum prospectivity of syn-rift stratigraphic plays in the Northern North Sea. Petroleum Geoscience, 26, 232-246.

Withjack, M.O., Schlische, R.W., Malinconico, M.L. & Olsen, P.E (2013) Rift-basin development: Lessons from the Triassic-Jurassic Newark basin of eastern North America. In: Mohriak, W.U., Danforth, A., Post, P.J., Brown, D.E., Tari, G.C., Nemcok, M. & Sinha, S.T. (eds.) Conjugate Divergent Margins. Geological Society Special Publication, 369, 301-321.

Withjack, M.A., Schlische, R.W. & Olsen, P.E. (2002) Rift-Basin Structure and its Influence on Sedimentary Systems. In: Renaut, R.W. & Ashley, G.M. (eds.) Sedimentation in Continental Rifts. SEPM Special Publication, 73, 57-81.

WMO (1981) Climatic Atlas of Asia. UNESCO, Geneva, 28 pp.

Woldegabriel, G., Aronson, J.L. & Walter, R.C. (1990) Geology, geochronology, and rift basin development in the central sector of the Main Ethiopia Rift. Geological Society of America Bulletin, 102(4), 439-458.

Wolfenden, E., Ebinger, C.J., Yirgu, G., Deino, A. & Ayalew, D. (2004) Evolution of the northern Main Ethiopian rift: birth of a triple junction. Earth and Planetary Science Letters, 224(1-2), 213-228.

Wortel, M.J.R. & Spakman, W. (2000) Subduction and Slab Detachment in the Mediterranean-Carpathian Region. Science, 290(5498), 1910-1917.

Wu, J.E., McClay, K., Whitehouse, P. & Dooley, T. (2009) 4D analogue modelling of transtensional pull-apart basins. Marine and Petroleum Geology, 26(8), 1608-1623.

Yagishita, K. (1997) Paleocurrent and fabric analyses of fluvial conglomerates of the Paleogene Noda Group, northeast Japan. Sedimentary Geology, 109, 53-71.

Yan, N., Colombera, L. & Mountney, N.P. (2020) Three-dimensional forward stratigraphic modelling of the sedimentary architecture of meandering-river successions in evolving half-graben rift basins. Basin Research, 32, 68-90.

Yin, A. (2000) Mode of Cenozoic east-west extension in Tibet suggesting a common origin of rifts in Asia during the Indo-Asian collision. Journal of Geophysical Research, 105, 21,745-21,579.

Young, M.J., Gawthorpe, R.L. & Sharp, I.R. (2000) Sedimentology and sequence stratigraphy of a transfer zone coarse-grained delta, Miocene Suez Rift, Egypt. Sedimentology, 47(6), 1081-1104.

Zelilidis, A. (2000) Drainage evolution in a rifted basin, Corinth graben, Greece. Geomorphology, 35, 69-85.

Zhao, D., Lei, J., Inoue, T., Yamada, A. & Gao, S.S. (2006) Deep structure and origin of the Baikal rift zone. Earth and Planetary Science Letters, 243(3-4), 681-691.

Ziegler, P.A. & Cloetingh, S. (2004) Dynamic processes controlling evolution of rifted basins. Earth-Science Reviews, 64(1-2), 1-50.

Zonenshain, L.P. & Savostin, L.A. (1981) Geodynamics of the Baikal rift zone and plate tectonics of Asia. Tectonophysics, 76(1-2), 1-45.

Zorin, Yu.A., Turutanov, E.Kh., Mordvinova, V.V., Kozhevnikov, V.M., Yanovskaya, T.B. & Treussov, A.V. (2003) The Baikal rift zone: the effect of mantle plumes on older structure. Tectonophysics, 371(1-4), 153-173.

Appendices

Received: 13 March 2019 | Revised: 21 June 2019 | Accepted: 27 July 2019

DOI: 10.1111/bre.12396

ORIGINAL ARTICLE

Basin Research | IAS EAGE | WILEY

Impact of a pre-existing transverse drainage system on active rift stratigraphy: An example from the Corinth Rift, Greece

David J. P. Somerville[1] | **Nigel P. Mountney**[1] | **Luca Colombera**[1] | **Richard E. Ll. Collier**[2]

[1]Fluvial & Eolian Research Group, University of Leeds, School of Earth and Environment, Leeds, Northern Ireland

[2]Basin Structure Group, University of Leeds, School of Earth and Environment, Leeds, Northern Ireland

Correspondence
David J. P. Somerville, Somerville, Fluvial & Eolian Research Group, University of Leeds, School of Earth and Environment, Leeds, Northern Ireland.
Email: d.j.p.eeds@leeds.ac.uk

Funding information
Areva; BHP Billiton; Chevron; ConocoPhillips; Saudi Aramco; Shell; University of Leeds; Hopkins

Abstract

Models to explain alluvial system development in rift settings commonly depict fans that are sourced directly from catchments formed in newly uplifted footwalls, which leads to the development of steep-sided talus-cone fans in the actively subsiding basin depocentre. The impact of basin evolution on antecedent drainage networks orientated close to perpendicular to a rift axis, and flowing over the developing hangingwall dip slope, remains relatively poorly understood. The aim of this study is to better understand the responses to rift margin uplift and subsequent intrabasinal fault development in determining sedimentation patterns in alluvial deposits of a major antecedent drainage system. Field-acquired data from a coarse-grained alluvial syn-rift succession in the western Gulf of Corinth, Greece (sedimentological logging and mapping) has allowed analysis of the spatial distribution of facies associations, stratigraphic architectural elements and patterns of palaeoflow. During the earliest rifting phase, newly uplifted footwalls redirected a previously established fluvial system with predominantly southward drainage. Footwall uplift on the southern basin margin at an initially relatively slow rate led to the development of an overfilled basin, within which an alluvial fan prograded to the south-west, south and south-east over a hangingwall dip slope. Deposition of the alluvial system sourced from the north coincided with the establishment of small-scale alluvial fans sourced from the newly uplifted footwall in the south. Deposits of non-cohesive debris flows close to the proposed hangingwall fan apex pass gradationally downstream into predominantly bedload conglomerate deposits indicative of sedimentation via hyperconcentrated flows laden with sand- and silt-grade sediment. Subsequent normal faulting in the hangingwall resulted in the establishment of further barriers to stream drainage, blocking flow routes to the south. This culminated in the termination of sediment supply to the basin depocentre from the north, and the onset of underfilled basin conditions as signified by an associated lacustrine transgression. The evolution of the fluvial system described in this study records transitions between three possible end-member types of interaction between active rifting and antecedent drainage systems: (a) erosion through an uplifted footwall, (b) drainage diversion away from an

uplifted footwall and (c) deposition over the hangingwall dip slope. The orientation of antecedent drainage pathways at a high angle to the trend of a developing rift axis, replete with intrabasinal faulting, exerts a primary control on the timing and location of development of overfilled and underfilled basin states in evolving depocentres.

KEYWORDS
alluvial fan, antecedent river, conglomerate, Gulf of Corinth, rift basin

1 | INTRODUCTION

The onset of extensional faulting and associated rift-basin subsidence commonly trigger the accumulation of conglomerate and sandstone bodies, many of alluvial origin (Graham et al., 2001; Martins-Neto & Catuneanu, 2010; Zaghloul et al., 2010; Hemelsdaël, Ford, Malartre, & Gawthorpe, 2017; Teixeira, Astini, Gomez, Morales, & Pimentel, 2018). In the continental realm, conglomerate bodies that form the initial fill of evolving rift basins typically record sedimentation from alluvial fans, and commonly transition up-section into fluvio-lacustrine deposits (cf. Sinclair, Shannon, Williams, Harker, & Mooren, 1994; Graham et al., 2001; Zaghloul et al., 2010; Turner, 2010). Newly uplifted footwalls are prone to denudation by erosional processes and source these earliest syn-rift deposits (Mack & Leeder, 1999). This denudation is most notable where the impact of antecedent drainage is relatively subdued, and either rifting does not crosscut major drainage networks or fluvial systems are diverted away from the rift zone, for example by growing rift shoulders (Gawthorpe & Leeder, 2000). Where extensional regimes evolve at a high angle relative to pre-existing drainage networks, coarse-grained sedimentary deposits typically accumulate downstream of the point where drainage networks are sourced over, or deflected around, the newly uplifted footwall (cf. Gupta, Underhill, Sharp, & Gawthorpe, 1999; Hemelsdaël et al., 2017; Hopkins & Dawers, 2018). Although newly developed normal faults are known to act as buffers to drainage over the hangingwall dip slope (Gawthorpe & Leeder, 2000; Leeder & Jackson, 1993), limited research has been undertaken to date to compare subsequent deposition on the hangingwall dip slope to their footwall-sourced counterparts.

The Corinth rift, Greece (Figure 1), provides a location to study the impact of antecedent drainage on deposition over the hangingwall dip slope during the onset of rifting. Alluvial-fan deposits dominated by coarse grained, clast- to matrix-supported conglomeratic bodies are exposed in cliff faces—notably along valley sides—as part of an uplifted footwall block on the northern coast of the Peloponnese (Ford et al., 2013; Ford et al., 2016; Gawthorpe et al., 2017). Exposures of sedimentary successions juxtaposed against normal faults allows for the detailed examination of sedimentary processes in a single fault block during the early syn-rift, and the impact of intra-basinal faulting on the prevalence of 'overfilled' and 'underfilled' depositional conditions (Gawthorpe & Leeder, 2000).

Highlights

- High-resolution dataset of the sedimentology of an early syn-rift conglomerate succession.
- Facies and architectural element interpretation indicate large alluvial fan formation over the hangingwall dip slope.
- Orientation of drainage compared to rift axis controls basin sedimentation, with three potential phases of interaction explored.
- Intra-basinal faulting controls transitions between 'overfilled' and 'underfilled' depositional conditions.
- Applications to facies distributions and environment prediction in rift basin settings.

The aim of this study is to establish a depositional model to account for the generation of the early syn-rift conglomerate units deposited from antecedent drainage flowing over a hangingwall dip slope, and to describe the sedimentological variations that occur across the newly formed depocentre. Specific objectives of this research are as follows: (a) to map lithofacies variations of an alluvial fan sourced over the hangingwall dip slope of an evolving rift basin through space and time; (b) to determine the processes by which sediment was transported and deposited by an alluvial fan present in the rift basin; (c) to show how the alluvial-fan system responded to fault block rotation and local uplifted footwall blocks and (d) to propose palaeogeographic models that describe the depositional processes occurring in the basin from rift initiation to the present day.

These analyses are novel, significant and of broad appeal because they allow for the sedimentological history of a developing rift basin to be reconstructed in detail. The outcome of this study demonstrates the following key insights: (a) the benefits of underpinning tectonostratigraphic analyses with

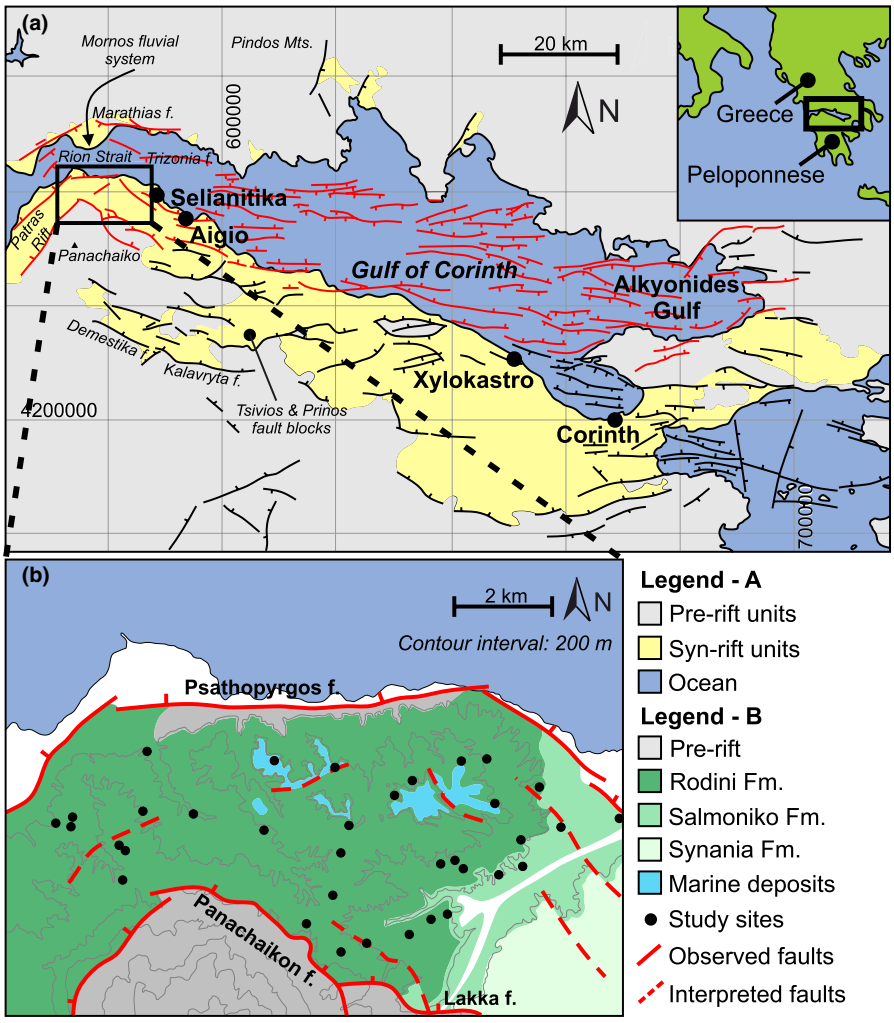

FIGURE 1 Map of the study area and the Gulf of Corinth rift, adapted from Gawthorpe et al. (2017). (a) Map of the entire Corinth Rift detailing distributions of syn-rift sediments and pre-rift basement. Active faults and inactive faults are represented in red and black colours respectively. Fault mapping is defined from Rohais et al. (2007), Ford et al. (2013), Ford, Hemelsdaël, Mancini, and Palyvos (2016), Gawthorpe et al., (2017). (b) Detailed map of the study area for this paper showing the mapped extent of the Rodini, Salmoniko and Synania Fms., and study sites used in this research

detailed sedimentological observations; (b) the importance of antecedent drainage direction in the prediction of the distributions of alluvial facies and architectures in a single extensionally faulted block and (c) the influence of subsequent intra-basinal faulting in the switching between high sediment supply to accommodation ratios, and low sediment supply to accommodation ratios (i.e. 'overfilled' and 'underfilled' scenarios).

2 | GEOLOGICAL SETTING

2.1 | The Gulf of Corinth

The Gulf of Corinth is an area of active extension between the Peloponnese and mainland Greece. It formed as a result of extension associated with the subduction of the African tectonic plate underneath the Aegean Sea plate (forming the Hellenic Arc) to the west and south of the gulf (Bell et al., 2009; Doutsos, Kontopoulos, & Poulimenos, 1988). Prior to the onset of extension, a NNW-*SSE* trending fold-and-thrust belt, the Pindos thrust sheet, formed during the Late Eocene (Skourlis & Doutsos, 2003). This feature now forms the pre-rift basement, and the associated tectonic evolution originally separated the pre-existing drainage into a series of north-south orientated catchments that drained predominantly towards the north (Seger & Alexander 1993; Zelilidis, 2000). Each catchment eroded the same Pindos thrust sheet, which is composed of Mesozoic carbonates and sandy clastic turbidites deposited on a passive margin and orogenic wedge (Degnan & Robertson, 1998). Rifting commenced in the Pliocene (Ford et al., 2016; Nixon et al., 2016) with the principal trend of the developing rift striking east-west, at high angle to the direction of antecedent drainage (Figure 1; Collier & Gawthorpe, 1995). Rifting has continued to the present day and covers an area of approximately 105 × 30 km (Figure 1). Current extension rates vary from 10 to 16 mm/year (Nixon et al., 2016), with higher rates in the west of the rift (Ford et al., 2016). Initial rifting led to the development of northward-dipping extensional faults on the northern coast of the Peloponnese. Extension has progressively migrated to the north, with more recent faulting in the last 400 kyr (Gawthorpe et al., 2017) having occurred in the hangingwalls of older structures to form the morphology of the present-day Gulf (Ford et al., 2013; Ori, 1989). As a result, Plio-Pleistocene

syn-rift successions up to 3 km thick, and of mixed continental and marine origin, are now exposed onshore as uplifted footwalls (Gawthorpe et al., 2017). Offshore in the present-day Gulf, sedimentary successions up to 2.5 km thick have accumulated as the Late Pleistocene and Holocene fill of rift basins. Both sets of successions record sedimentation in a variety of environmental settings, including continental, shallow-marine and deep-marine environments (Nixon et al., 2016). Due to the relatively short extensional history of the rift and the lack of subsequent overprinting by other structural regimes, this area is especially well suited to the study of both onshore and offshore syn-rift sedimentation in settings adjacent to active extensional faults (Bell et al., 2009).

Syn-rift sedimentation occurred in two distinct phases: the first from the Pliocene to the Middle Pleistocene (400 ka), and the second from the Middle Pleistocene to the Present (Esu & Gerotti, 2015). This study focuses on the nature of sedimentation in the latter part of the first phase, during which depocentres hosted deep-water lacustrine systems with water depths of 300–600 m, indicated by deltaic foreset stratal packages that are several hundred metres thick (Gawthorpe et al., 2017) in the east (from the Alkonyides Gulf extending to the town of Selianitika; Figure 1). These deltaic deposits pass into continental environments to the west (west of Selianitika) (Ford et al., 2013; Ford et al., 2016; Gawthorpe et al., 2017). The sedimentology of these palaeoenvironmental settings provides a record of both axially derived deposits that fed into Lake Corinth to the east (Ford et al., 2016; Gawthorpe et al., 2017), and transverse drainage systems that resulted in deposition of sediment over relic uplifted footwalls (Collier & Dart, 1991).

As extension progressively migrated northward, the oldest stratigraphic intervals recording syn-rift sedimentation were progressively uplifted into the footwalls of younger faults, thereby resulting in the exhumation and exposure of older sedimentary successions of deep-water, deltaic and alluvial origin—from east to west, respectively (Dart, Collier, Gawthorpe, Keller, & Nichols, 1994; Ford et al., 2016). Large, Gilbert-type deltaic deposits are present across exposed cliff sections from Xylokastro to Aigio (Figure 1; Collier & Dart, 1991; Dart et al., 1994). These fan deltas were sourced from feeder valleys that cut down through uplifting footwalls, or which exploited topographic lows between fault tips (Leeder & Jackson, 1993). Presently, over 1,000 m of continental syn-rift deposits are exposed in a series of cliff faces up to 600-m high and hills in the footwall of the Psathopyrgos fault, directly west of Aigio (Figure 1) (Bell et al., 2009).

2.2 | The Profitis Elias Group

The early-rift deposits between Aigio and the Patras Rift are dominantly represented by the older Profitis Elias Gp. and the younger Galada Gp., both of which are well preserved in the Panachaikon fault block, a 7–8 km-wide unit between the Rion Strait and the Panachaiko mountain, where these two groups attain a combined thickness of 1.4 km (Palyvos et al., 2007; Ford et al., 2016). The Profitis Elias Gp. contains three formations of similar age: the Rodini Formation (west), the Salmoniko Formation and the Synania Formation (east), which are interpreted by Ford et al. (2016) to represent alluvial fan, braided stream and lacustrine environments, respectively. These formations record a progressive fining in mean sediment calibre from west to east (Palyvos et al., 2010, 2007). The main focus of this study is the Rodini Fm., deposited furthest to the west on the northern tip of the Peloponnese.

Together, the three formations represent the major proportion of the Profitis Elias massif and attain a preserved (post-uplift) thickness of up to 600 m (Esu & Gerotti, 2015), with original depositional thickness estimated at over 1,000 m (Ford et al., 2016). Multiple wadis expose the formations, where erosion over the last 400 kyr has left a reduced thickness (ca. 10 m) of sandy siltstone of the Synania Fm. at the highest points of the massif, overlying large cliff faces that are 50–120 m high and which expose sections of the underlying Rodini Fm.

The Rodini Formation has not been the focus of prior detailed study; the majority of prior research efforts in the Gulf of Corinth region have focussed on the eastern parts of the rift (see Collier & Dart, 1991; Collier & Gawthorpe, 1995; Rohais et al., 2007). Previous studies of the Rodini Fm. are based on limited and fundamental observations of lithology over the area (see Doutsos et al., 1988; Esu & Gerotti, 2015; Ford et al., 2016), where the Rodini Fm. is present in the form of reddish to grey conglomerates dominated by cobbles and boulders. These deposits have previously been interpreted as the depositional record of an alluvial or fluvial system sourced from the north (Doutsos et al., 1988; Gawthorpe et al., 2017). However, this general interpretation needs to be refined through the development of a detailed palaeoenvironmental reconstruction based on analysis of lithofacies, sedimentary architectures, and on analysis of the spatial and temporal distribution of palaeocurrent data. These interpretations are the focus of this study, which is based on a detailed field-acquired data set.

3 | DATA AND METHODS

3.1 | Lithological mapping

Mapping was undertaken to document lithological variations across the study area, based on the three main rock types present: conglomerate, sandstone and siltstone. In addition to regional mapping, 37 sites were selected for detailed study; for these sites proportions of lithologies were recorded as percentages. Two hundred dip and strike readings (from 20 of the 37 sites), ranging from 04 to 40° dip angle, were separated into three groups of equal size based on their relative

elevations and their magnitudes. This allowed the relative chronostratigraphic positions of the different sites to be determined; in conjunction with lithological data, a tectonostratigraphic framework was then established (see Section 3.3. for detail).

For conglomerate lithologies, the percentage volume of both matrix and clasts was recorded to map subtle variations in lithofacies across the study area. The matrix of conglomerate lithofacies is defined as grains from clay to medium-sand size (similar to the procedures implemented by Kim & Lowe, 2004; Puy-Alquiza et al., 2017; Sohn, Rhee, & Kim, 1999; Steel & Thompson, 1983, in their studies of alluvial deposits). The maximum grain size of the matrix, and minimum clast size of the overall deposit, define a bimodality in grain size.

3.2 | Vertical profiles

Twenty of the 37 locations were chosen for detailed sedimentological analysis based on the description of vertical profiles at the decimetre scale (Figure 2). Special attention was dedicated to detailing clast fabric and texture variations in conglomeratic bodies by tabulating individual clast features. Lithofacies were tabulated recording their thicknesses and key sedimentological features (e.g. grading, sedimentary structures, clast-to-matrix proportions). Profiles were placed in their approximate chronostratigraphic positions through extrapolation by combining observations of tectonic dip and topographic data (see below). There is no biostratigraphic control within the Rodini Fm., and there is no clear opportunity to establish an event stratigraphy, for example via radiometric dating. In total, 20 vertical profiles with a cumulative thickness of 250 m were recorded in detail.

These data were supplemented by an additional six large-scale log profiles recorded to capture larger-scale stratigraphic variations in lithology, through 533 m of the approximately 600-m-thick formation. These vertical profiles enabled the construction of a tectonostratigraphic framework for the area by combining them with data used for lithological mapping and structural data, as outlined above.

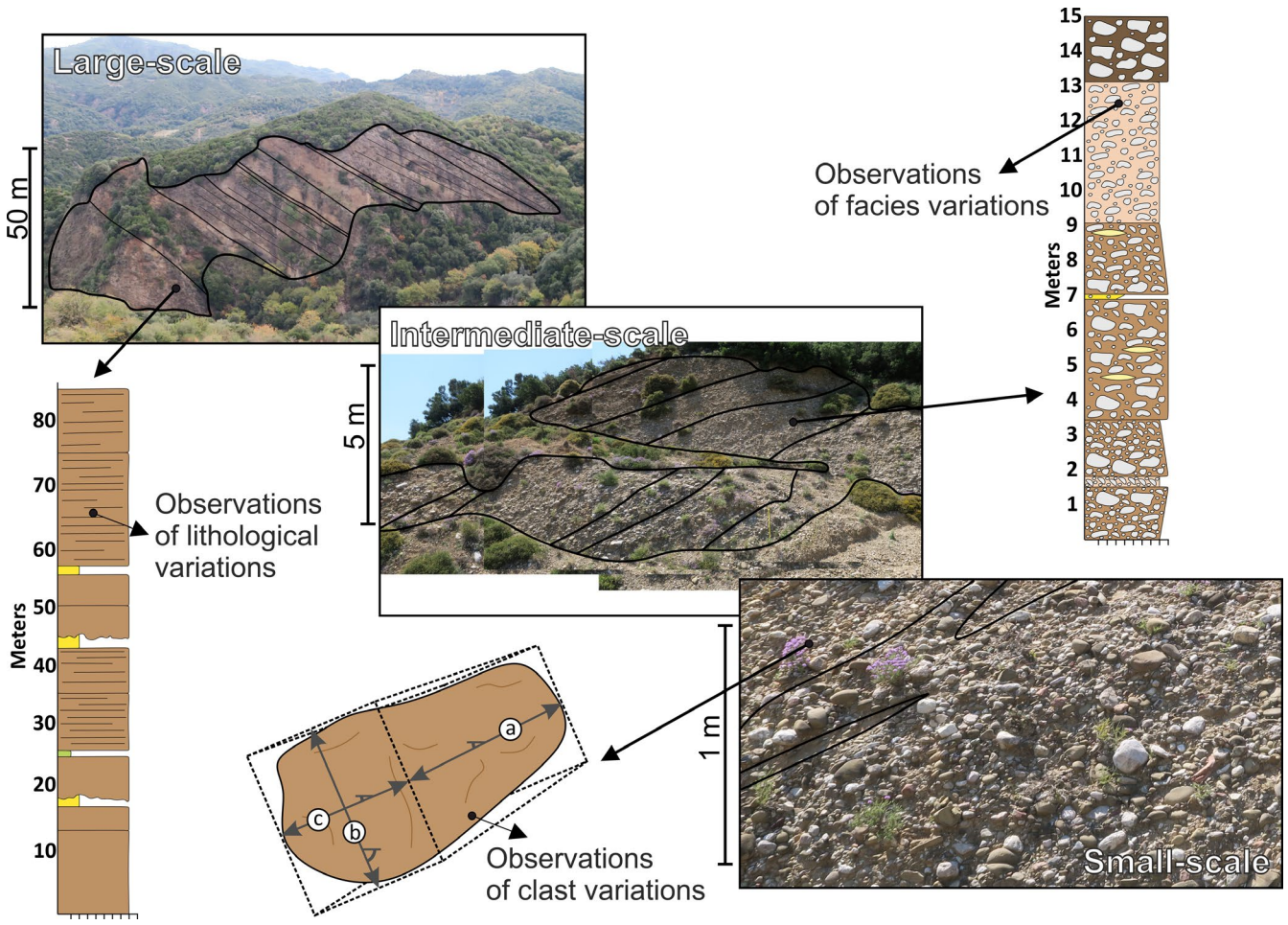

FIGURE 2 Images detailing data collection methods at three different scales (tens of metres, metres and centimetre scale). Integration of datasets in this study allows for the underpinning of larger-scale regional variations by higher-resolution facies and individual clast analyses (where 'a', 'b' and 'c' represent clast long, intermediate and short axes respectively)

3.3 | Tectonostratigraphy definitions

Establishment of the chronostratigraphy of the studied succession is problematic due to a lack of biostratigraphic control or of datable ash deposits similar to those found in syn-rift sediments to the east (Gawthorpe et al., 2017). To develop a well-defined tectonostratigraphy for the study area, bedding dip and strike data and topographic elevation were combined to determine the relative ages of deposits at different localities across the study area, as a function of varying amounts of rift-induced differential tilting (Figure 3). Depositional gradients are likely to have been low, given the absence of high-angle inclined foresets. Small-scale intra-basinal faulting is also assumed to have minimal effect, with the few observed post-depositional faults experiencing throws of <5 m. This approach has allowed a tentative chronology of the deposits and has enabled establishment of a tectonostratigraphy with which to support interpretations of depositional environment, and of the influence of active faulting on palaeogeography.

The initiation of sediment accumulation is considered to have commenced in response to the onset of movement on the Panachaikon fault at 2.2–1.8 Ma (Figure 4) (Gawthorpe et al., 2017). For this study, the rate of sediment supply is assumed constant, as the climatic and tectonic conditions of the inferred catchments for sediment delivery were persistent throughout the episode of sediment accumulation (Skourlis & Doutsos, 2003), leading to the definitions of timings outlined in this study. This is necessary in order to assign the sedimentary logs intervals recorded into their likely time episodes.

3.4 | Clast fabric and texture description

At each of the 20 sites where vertical profiles were recorded, conglomeratic facies were subject to detailed clast-fabric and texture analysis. At each site, up to two facies were chosen for clast measurements, and a square grid of 1 m^2 in area was placed on the outcrop surface. The 50 largest clasts within that square were characterized with respect to three qualitative attributes (composition, shape and roundness) and 10 quantitative features (length, plunge and azimuth of three axes, from which palaeocurrent direction was inferred based on identification of types of clast imbrication). These features were later corrected for bedding strike and dip. This approach was taken to randomize the clasts chosen for measurement, to obtain data in a systematic fashion, and to collect data for future studies on clast metrics. In total, 1,531 clasts were measured for these features from 10 conglomerate facies types; in addition, 1,001 palaeocurrent indicators were derived from patterns of clast imbrication. In this paper, focus is given to clast axis orientation data, composition data, and palaeocurrent data for the purpose of determining flow

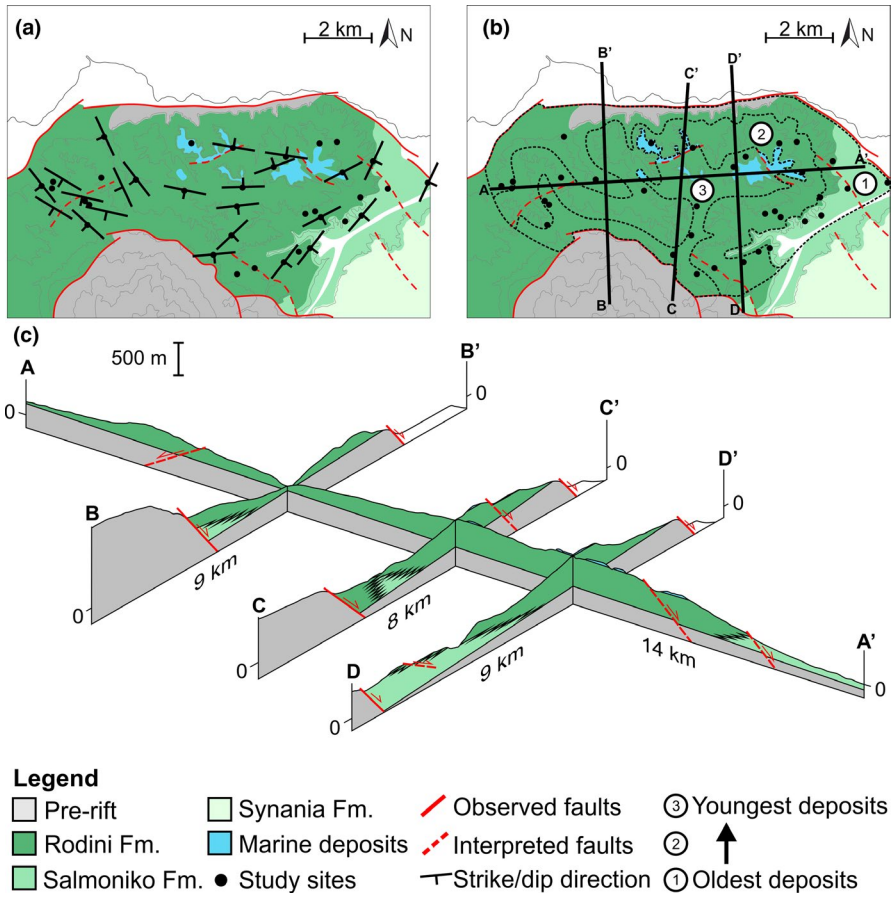

FIGURE 3 (a) Study area map displaying regional variations in stratigraphic dip and dip direction. Note the approximate radial pattern of dips away from the north of the study area. (b) Approximate areas of time slices through the study area between relatively older, middle-aged and younger stratigraphy. Lines of section A-A', B-B', C-C' and D-D' are located. (c) Fence diagram of structural cross sections through study area

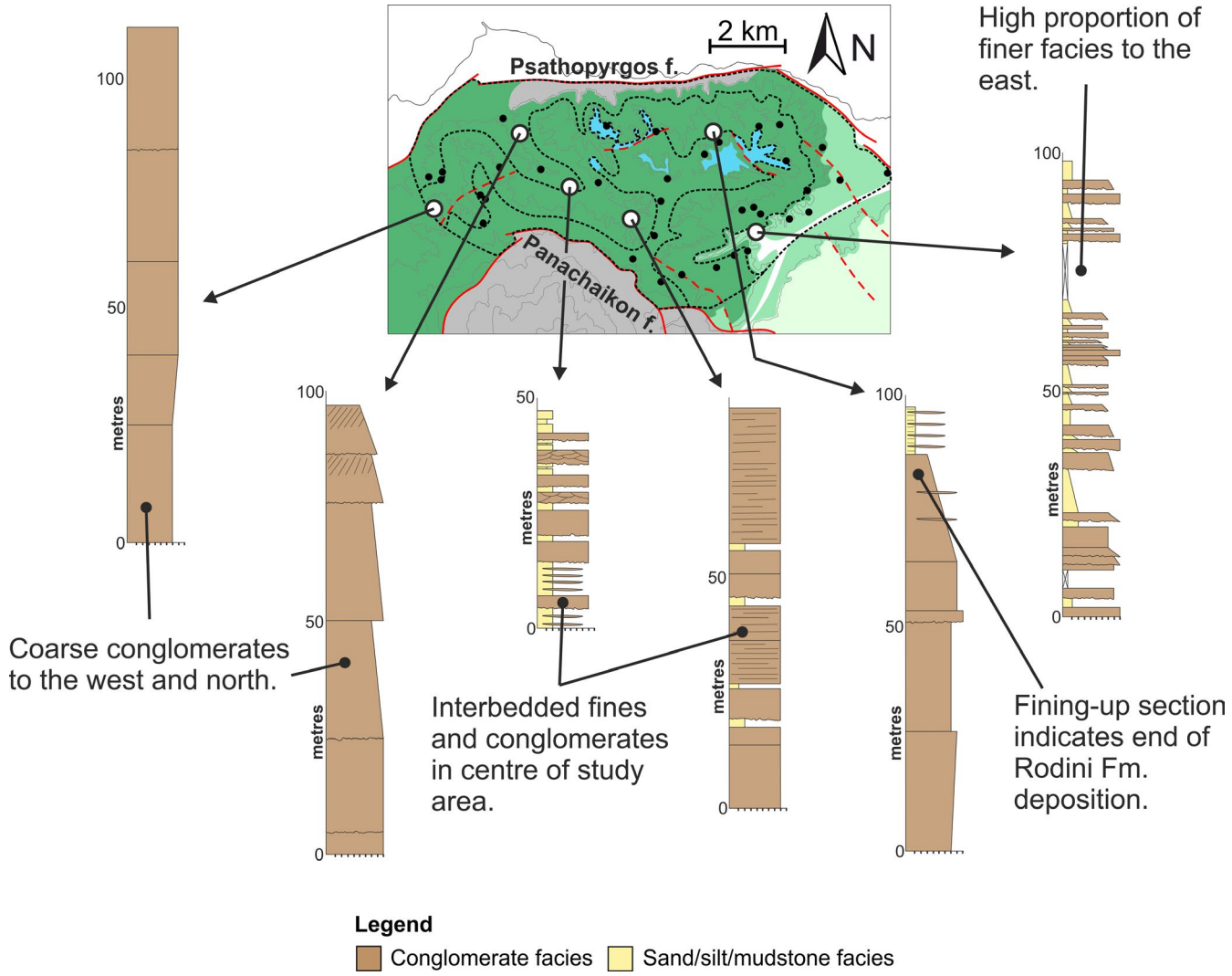

FIGURE 4 Regional logs detailing lithological variations over the study area. Note the increase in conglomeratic facies both up-section (towards the end of the deposition of the Rodini Fm.) and towards the west and north [Colour figure can be viewed at wileyonlinelibrary.com]

processes, sediment input sources and sediment flow directions over the basin. From clast composition alone, the detailed province cannot be determined given the presence of similar lithologies in the basement rocks on both sides of the basin. However, where information on clast composition is combined with clast-fabric analysis, an indication of palaeotransport direction (as indicated by clast imbrication) can be used to deduce the likely provenance for the basin-filling conglomerates.

4 | RESULTS

4.1 | Lithofacies

Fifteen distinct lithofacies types are identified within the Rodini Fm: 10 types of conglomerate and 5 types of sandstone and siltstone (Table 1; Figure 5). In the conglomerate facies, clast composition is dominated by a mixture of well-sorted sandstone, well-cemented limestone, and metamorphosed sandstones and limestones. All clasts were apparently sourced from basement units (dominated by metamorphosed carbonates and flysch deposits; Skourlis & Doutsos, 2003) that formed the Pindos Mountains to the north, or were uplifted in nearby footwalls. The distribution of lithofacies and architectural elements through the formation is represented by 20 vertical profiles (Figure 6a and c) taken from across the study area (Figure 1).

4.2 | Architectural elements

Architectural elements are defined here as discrete packages of sediment with a measurable lateral and vertical extent (and associated 3D geometry), deposited as a result of a specific depositional process and its associated processes (e.g. a braided fluvial channel deposit and its associated overbank sediments) (Figure 7). Their comprising facies, in conjuncture with the elements themselves, form a specific set of arrangements (facies associations) leading to the interpreted

TABLE 1 Descriptions and interpretations of studied lithofacies. Facies codes are based on the following pattern; (largest grain size; B, C, P, G, S, F) – (sorting; w – well, r – moderate, p – poor)(clast packing; t – tight, l – loose)(structures; m – massive, f – fining up, l – sand lenses, c – cement, e – conglom. lenses, h – horizontal stratification)

Code	Lithofacies	Description	Interpretation
B-wtm	Well-sorted boulder conglomerate	Clearly bedded, clast-supported (90–100%), with granule matrix. Tightly packed with sub-rounded to sub-angular clasts up to 50 cm in diameter. Form massive beds with erosional bases	Conglomeratic debris-flow deposits proximal to the sediment source at the apex of an alluvial fan. More consistent, high- energy flows represented by tight packing of boulders and their large sizes (Puy-Alquiza et al., 2017; Teixeira et al., 2018)
B-rlf	Moderately sorted normally graded boulder conglomerate	Clearly bedded, clast-supported (80%–100%), with medium-coarse sand matrix. Loosely packed with rounded-sub-rounded clasts up to 30 cm in diameter. Normally grade to granule-pebble clasts and have erosive bases	Bedload stream deposits in the upper-fan to mid-fan transition, close to fan apex, with discrete units formed by stream avulsions Fining-upward grain-size trend and imbrication indicate turbulent nature of flow. (Moscariello, Marchi, Maraga, & Mortara, 2002; Reitz & Jerolmack, 2012)
B-plm	Poorly sorted boulder conglomerate	Clearly bedded, clast-supported (80%–90%), with medium sand-granule matrix. Loosely packed with sub-rounded to sub-angular clasts up to 50 cm in diameter. Form massive beds, may have erosive bases	Non-cohesive debris flow deposits in the mid-fan represented by an increased matrix proportion and lack of sorting, indicating single event deposits. Further supported by erosive bases to units. (Colombera & Bersezio, 2011; Murcia, Hurtado, Cortés, Macías, & Cepeda, 2008)
B-pll	Poorly sorted boulder conglomerate with sand lenses	Crudely bedded, clast-supported (70%–90%) with medium-coarse sand matrix. Loosely packed with rounded to sub-angular clasts up to 30 cm in diameter. Beds contain medium sand lenses	Non-cohesive debris flow deposits close to the fan toe. Higher matrix proportions and sand lenses represent a decrease in energy, either in distal locations or as trails behind transported clasts. (Kim et al., 2009; Shukla, 2009)
B-plc	Poorly sorted boulder conglomerate with strong cement	Crudely bedded, clast-supported (70%–90%) with well-cemented medium sand-granule matrix. Loosely packed with sub-rounded to sub-angular clasts up to 30 cm in diameter. Form massive beds	Cemented debris flow deposits, predicted to have experienced dissolution of carbonate clasts and subsequent reprecipitation, common in other areas of the Gulf of Corinth. (Backert et al., 2010; Gawthorpe et al., 2017)
B-ple	Poorly sorted, polymodal boulder conglomerate	Crudely bedded, clast-supported (90%) with medium sand-granule matrix. Loosely packed with rounded to sub-angular clasts up to 30 cm in diameter. Contains coarser and finer discontinuous lenses in each unit	Streamflow deposits represented by highly variable flows leading to the interbedding of finer and coarser clast-supported, clean conglomerate lenses, forming low-relief bars. (Karpeta, 1993; Kim et al., 2009)
C-rll	Moderately sorted cobble conglomerate	Clearly bedded, clast-supported (80%–90%) with medium-coarse sand matrix. Loosely packed with rounded-sub-angular clasts up to 15 cm in diameter. Form massive beds. Some discontinuous sand lenses	Debris-flow deposits close to the fan toes, finer grain sizes represent lower energy compared to B-pll. Sand lenses represent poorly developed flood dune bar deposits. (Chakraborty & Ghosh, 2010; Lindsey et al., 2005)
C-pth	Poorly sorted, horizontally stratified cobble conglomerate	Crudely bedded, clast-supported (80%–90%) with medium-coarse sand matrix. Tightly packed with rounded to sub-angular clasts up to 15 cm in diameter. Beds are horizontally stratified	Cobble bedload sheet deposits in the upper-fan to mid-fan transition as a result of turbulent flash flood flows, creating horizontal stratification. (Moscariello et al., 2002; Teixeira et al., 2018)
P-wtm	Well-sorted pebble conglomerate	Clearly bedded, clast-supported (90%–100%) with medium sand matrix. Tightly packed with sub-rounded clasts up to 5 cm in diameter. Form massive beds of texturally mature clasts	Relatively low-energy streamflow bedload deposits. Flow is consistent leading to clean, well-sorted fine-grained conglomerates. Deposited away from large fan toe, or more proximally on a smaller alluvial fan. (Steel & Thompson, 1983; Ford et al., 2016)
G-wtm	Well-sorted granule conglomerate	Clearly bedded, clast-supported (90%–100%) with medium sand matrix. Tightly packed with sub-rounded clasts up to 1 cm in diameter. Form massive beds of texturally mature clasts	Relatively very low-energy streamflow bedload deposits. Flows wash away silt and clay particulates, leading to clean, very well-sorted fine-grained conglomerates. (Steel & Thompson, 1983; Ford et al., 2016)

(Continues)

TABLE 1 (Continued)

Code	Lithofacies	Description	Interpretation
S-l	Massive silty sandstone with granule-cobble lenses	Crudely bedded, poorly sorted silt to coarse grade sand. Intermittent well-sorted granule to cobble grade lenses throughout	Rapid finer-grained sediment dumping from suspension in flows, with periods of high energy allowing upper plane-bed conglomerate deposition. (Franke, Hornung, & Hinderer, 2015; Lindsey et al., 2005)
S-s	Massive silty sandstone with intermittent clasts	Crudely bedded, poorly sorted silt to coarse grade sand. Single clasts present randomly throughout massive beds, up to 2 cm in diameter	Deposited in the most distal portions of a hyperconcentrated flow, where energy can only sustain rare small clasts. Rapid deposition from suspension. (Franke et al., 2015; Wells, 1984)
S-h	Silty sandstone with horizontal laminations	Crudely bedded, poorly sorted silt to coarse grade sand. Horizontally laminated picking out fine-grained sections, laminations typically 3–5 mm apart and increase in frequency up-section	Waning debris flows or streamflow deposit laminated sands and silts away from main channel flow locations. (Allen, 1982; Colombera & Bersezio, 2011)
S-sh	Massive silty sandstone with shell fragments	Crudely bedded, poorly sorted silt to coarse grade sand. Contain shell fragments up to 0.5–1 cm diameter that are present randomly or in thin < 15 cm laterally discontinuous lenses	Low-moderate energy shallow lacustrine deposits where fragile shells are broken up by small amounts of current and wave action. (Alvarez-Zarikian, Soter, & Katsonopoulou, 2008; Ford et al., 2016)
F	Fine-grained mudstone	Clearly bedded, well-sorted clay-mud grade unit. Light to dark grey, brown and cream colours present. Highly fissile with no structure, form laterally continuous beds up to 10 cm thick	Overbank palaeosol development representing areas away from the influence of floods and channel processes. (Franke et al., 2015; Lindsey et al., 2005)

natural progression of depositional environments described in sections 4.3. and 4.4.

4.2.1 | AE1: Coarse non-cohesive debris flow elements

Description

This element type comprises 25.7% of the measured succession. Sedimentary units of this type range from 3 to 10 m thick and are dominated by beds that are laterally extensive over tens of metres, themselves each from 0.5 to 5 m thick. Compared with other associations, beds exhibit lateral variations in thickness up to 0.5 m. The base of each element of AE1 is strongly erosional with 10–20 cm persistent relief. Basal erosion surfaces of these elements are overlain by a coarse boulder conglomerate bed (B-wtm, B-plm). Up-section, stacked beds of finer conglomerates (typically cobble to boulder grade) dominate. All beds are massive with no discernible internal stratification (B-wtm, B-plm, B-ple, C-rll). Beds contain a higher proportion of matrix (15%–20%) than other architectural elements. Thin beds of finer facies (S-s) may be present within the element, and are laterally extensive with a maximum thickness of 0.2 m. AE1 units may be stacked vertically, resulting in amalgamated conglomerate packages, or may occur as isolated elements separated by other types of architectural elements (AE3, AE4, AE5).

Interpretation

Structureless, matrix- to clast-supported conglomerates are most commonly the result of rapid deposition by non-cohesive debris flows that typically wane over time to deposit relatively more well-sorted and fining-up conglomerate beds up-section from hyperconcentrated flows (Calhoun & Clague, 2018; Costa, 1988; Nemec & Steel, 1984; Sohn et al., 1999; Went, 2005). Poorly sorted units with isolated boulders and a wide range of clast sizes are interpreted as the rapid freezing of coarse clasts within flows, with stacked sets and erosional bases to each bed. This indicates that flow events were frequent and initially erosive (Miall, 1996), and representative of more turbulent flow types (Blair & McPherson, 1994; Jo, Rhee, & Chough, 1997). These types of elements and their constituent lithofacies are typical of proximal alluvial-fan environments, notably in locations close to their feeder valley (Gloppen & Steel, 1981).

4.2.2 | AE2: Coarse, poorly channelized streamflow units and associated waning-flood elements

Description

This element type comprises 35.0% of the measured succession. These associations are 2–17 m thick and are dominated by conglomerates and silty sandstones arranged into two or more beds, each of which is 0.2–3 m thick. Conglomerate beds are lenticular over distances of 5–10 m where outcrop extent permits characterization, with finer-grained facies being more laterally extensive. Coarse-grained conglomerates with erosional bases (B-wtm, B-rlf) are overlain by normally graded conglomerates, either forming a single bed (B-rlf) or fining-upward bedsets with multiple beds (B-rlf, C-rll, P-wtm,

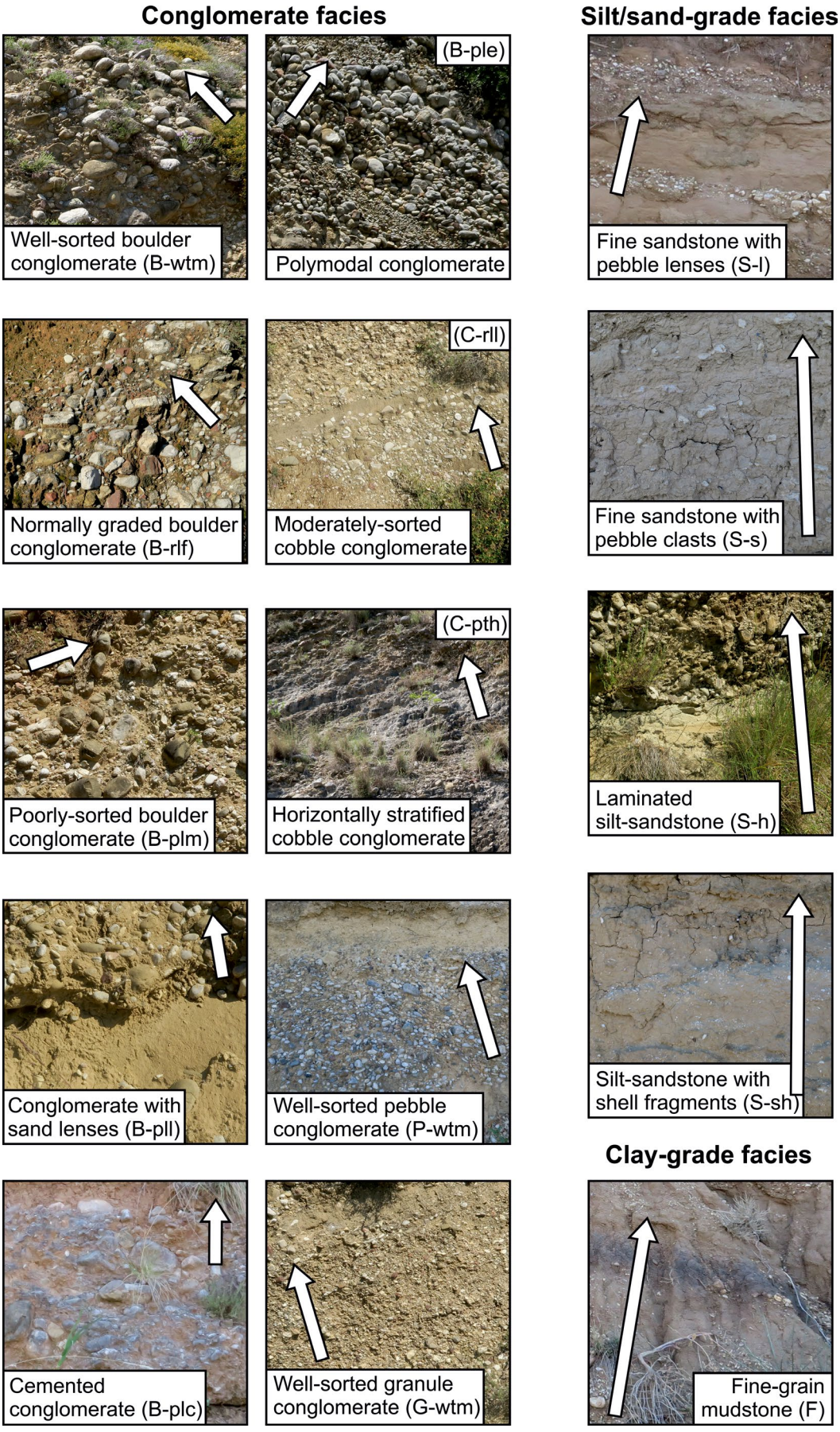

FIGURE 5 Outcrop images of each of the 15 facies detailed in Table 1. Arrows represent 1 m scale and indicate younging direction

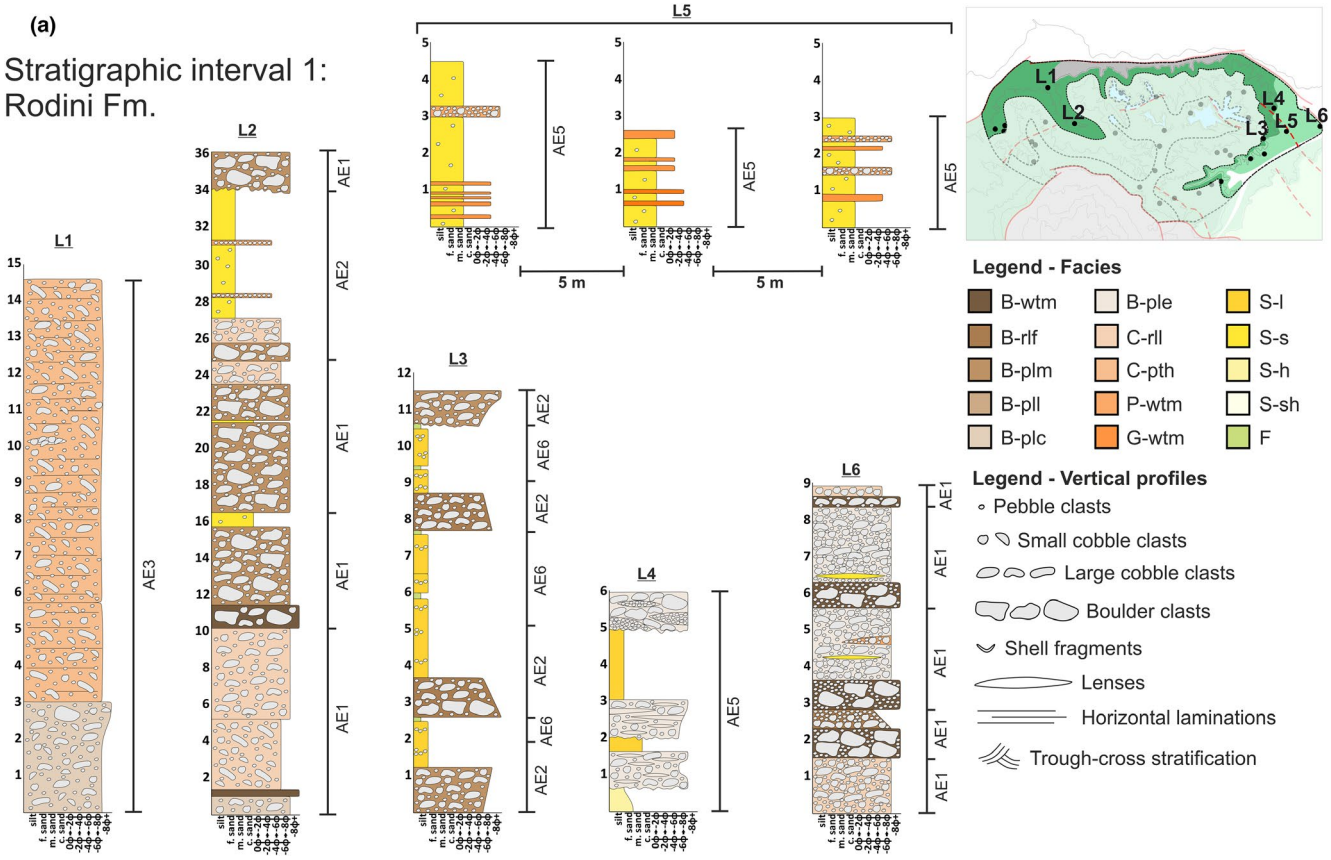

FIGURE 6 (a) Sedimentary logs of the Rodini Fm. and Salmoniko Fm. deposited during rift initiation (vertical scale in metres). Initial sheet-like mass flows (AE3 in L1) close to the fan apex transition downstream into persistent non-cohesive debris flows and intermittent sand-laden hyperconcentrated flows (AE1 and AE2 in L2). Further to the east, finer-grained facies dominate in distal locations (L3, L4, L5) with intermittent active lobe deposition represented by coarse debris-flow conglomerates (L6). See Figure 3 for inset map definition. (b) Sedimentary logs of the Rodini Fm. deposited after rift initiation (vertical scale in metres). Coarse conglomerates close to the fan apex (L7, L8, L9) extend further into the basin than during rift initiation. These transitions laterally into finer-grained facies on inactive lobes (L10) and recently active lobes (L11, L12, L13). Pedogenic development in L12 combined with frequent conglomerate horizons (formed under upper flow regime) indicates frequent lobe switching. See Figure 3 for inset map definition. (c) Sedimentary logs of the Rodini Fm. during its final phase of deposition before lacustrine transgression (vertical scale in metres). Coarse debris-flow conglomerates sourced from the north dominate deposition across the study area (L14, L19, L20) with smaller fans sourced from the uplifted footwall in the south developed (L16, L18, L19). L15 represents the lacustrine transgression and prolonged activity on the Psathopyrgos fault. See Figure 3 for inset map definition

G-wtm), which may be sharply overlain up-section by silt- and sand-grade facies (S-l, S-s, S-h). Conglomerates are compositionally and texturally mature, with a high (90–100%) clast proportion by volume. Fine-grained units are dominantly massive. AE2 typically occur as stacked sets of unknown maximum thickness (due to outcrop limitations), but observed to be over 50 m, or interbedded with elements AE5 and AE1.

Interpretation

Moderately to well-sorted conglomerate units of texturally and compositionally mature clasts that fine upward are typical of bedload transport processes (Miall, 1996); deposits are subsequently represented up-section by sand and silt deposits representing the waning of floods (Maizels, 1993; Sohn et al., 1999). Decimetre- to metre-scale infilled scours show these events to be highly erosive and often rapid in nature (Collinson, Mountney, & Thompson, 2006; Jo & Chough, 2001) where each element is taken as a single, or stacked set, of depositional events. In places, fine-grained facies show horizontal lamination picked out by subtle grain-size variations from silt to fine sand, here speculatively interpreted as the expression of waning deposits during flood events (Gloppen & Steel, 1981; Sohn et al., 1999). The lozenge shape of the conglomerate beds in cross section, in conjunction with their stacking style, indicates elements of weak channelization (Collinson et al., 2006; Khadkikar, 1999) of coarse-grained bedload conglomerates (Miall, 1996). AE2 is interpreted as occurring on the medial section of an alluvial fan, and likely as a downstream expression of AE1.

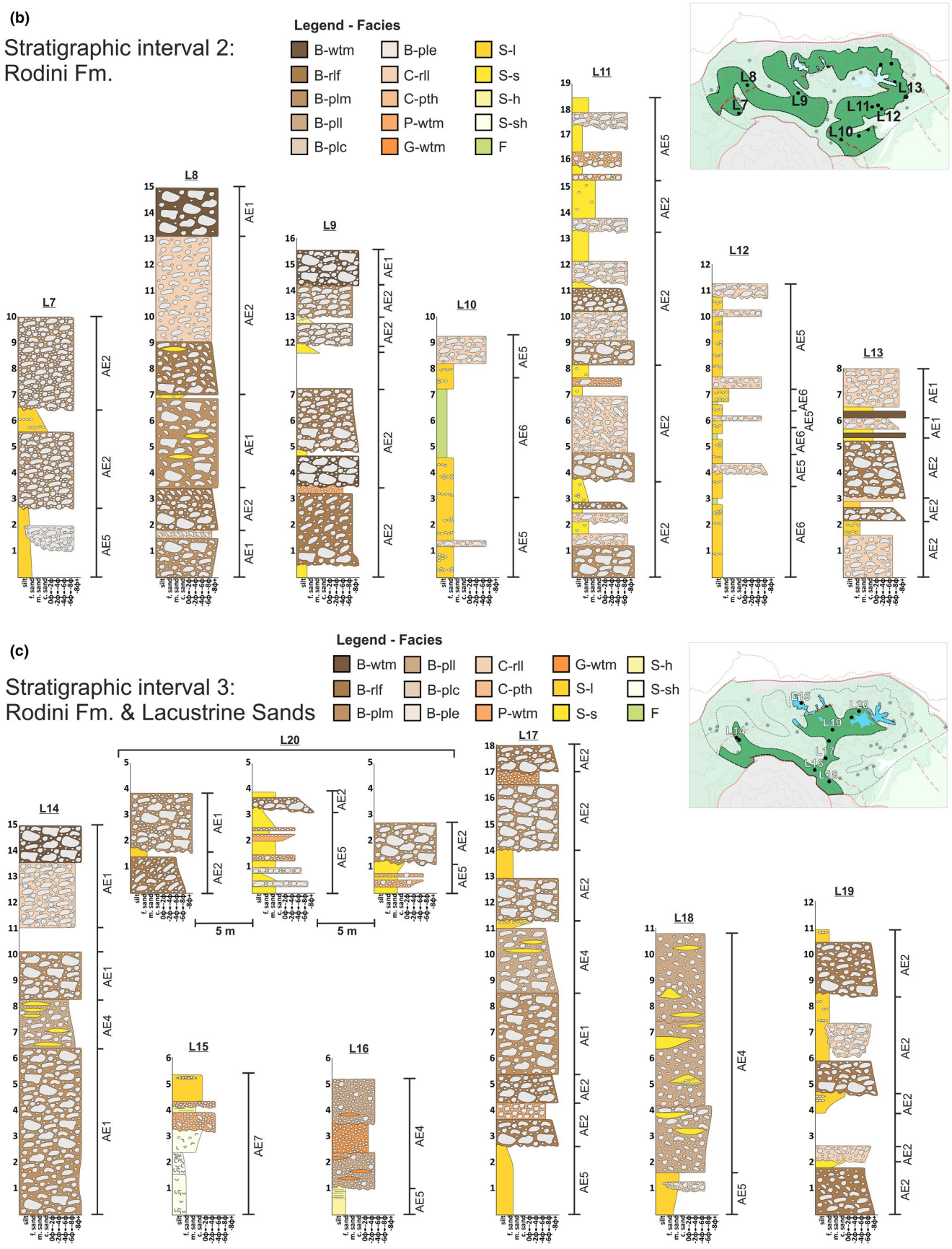

FIGURE 6 (Continued)

4.2.3 | AE3: Coarse, unchannelized flow elements

Description

This element type comprises 6.14% of the measured succession. These elements are at least 10–15 m thick and are composed of one sheet-like coset of conglomerate, divided internally into 0.5-m-thick horizontal beds delineated by traceable surfaces (marked by a change in matrix grain size from fine sand to silt grade, and a reduction in clast frequency to 50% 10 cm either side of the surface) and clast orientation variations between beds. The elements are laterally extensive across outcrops and cliff sections at a minimum of 20 m, and have flat, sharp bases. Cobbles dominate and reach up to 15 cm in diameter, with a medium-sand-grade matrix (C-pth) forming up to 20% of the beds. Within horizontally stratified sets, clast long axes are typically flat-lying, parallel to stratification. Although AE3 elements are not common over the study area, where present they are bounded by AE1 elements at their base and top.

Interpretation

Repeated non-channelized flows lead to multiple stacked horizons of cobble-grade conglomerates being deposited (Gloppen & Steel, 1981; Mack & Leeder, 1999) where lateral continuity of units, a lack of grading, and lack of erosional bases, indicate a highly viscous rheology (Kim & Lowe, 2004; Todd, 1989). Deposition occurred in a relatively proximal setting within the fluvial system, likely close to a primary feeder valley of the alluvial fan, as indicated by the large cobble clast sizes that dominate throughout (North & Davidson, 2012). A high sediment load led to a traction carpet of clasts being deposited (Todd, 1989) and preferentially orientated with long axes parallel to bedding surfaces. A lack of fine-grained deposits in AE3 indicates that repeated events were of high magnitude and possibly of high frequency, allowing for consistent coarse-grained deposition with no time for the settling of sediment from suspension (Hwang, Chough, Hong, & Choe, 1995; Wells, 1984).

4.2.4 | AE4: Medial fan debris-flow elements

Description

This element type comprises 7.61% of the measured succession. These elements are typically 1.5–9 m thick, but may be thicker locally. They are formed by 1.5–4 m thick conglomerate beds which are laterally extensive across outcrops (ca. 50 m). The thickness of each bed varies laterally by up to 50 cm, but does not pinch out. Each bed has an erosional base to underlying deposits of poorly sorted boulder conglomerates containing sand lenses (B-pll) or moderately sorted cobble conglomerate (C-rll), which together form the element. Repeated sandy-silt lenses are common throughout elements. Conglomerates are clast supported, varying from pebble to boulder grade (up to 30 cm in diameter) and have a fine silty-sand matrix making up 5%–20% of the lithology. Beds in the element are massive; however, silty-sand lenses within B-pll and C-rll beds locally demonstrate trough cross-stratification on the decimetre scale with sets up to 20 cm thick. AE4 elements are typically deposited in association with AE1 and AE5 elements; larger AE4 elements are deposited subsequent to AE5 elements with a transitional boundary over several metres as the proportion of B-pll and C-rll facies increases. In some cases, smaller examples of AE4 elements occur nested within successions otherwise dominated by AE1 elements.

Interpretation

Ungraded conglomerates of poorly to moderately sorted clasts are commonly formed by cohesive debris flows (Lowe, 1979; Suresh, 2007) as sediment undergoes frictional freezing, subduing settling processes (Cronin, Lecointre, Palmer, & Neall, 2000). Sandstone formation displays rare weakly developed sets of trough cross-stratification possibly representative of juvenile unit bar development (as stratification does not extend through entire sand units where present) or 3D dune development (Gloppen & Steel, 1981; Reading, 1996) during the later stages of flows. These units are largely reworked and partially eroded by further mass-flow events (Lindsey, Langer, & Knepper, 2005) leading to limited preservation.

4.2.5 | AE5: Fan-toe sandstones settled from suspension (with upper plane-bed conglomerate lenses) elements

Description

This element type comprises 17.2% of the measured succession. These elements are 1 to 6 m thick and laterally persistent between outcrops. Internally, they are composed of sets of sandstones that are 0.2–2 m thick and conglomerate units that are 0.1–1 m thick. Fine-grained facies extend laterally for up to tens of metres (S-l, S-s), whereas conglomerate facies (B-ple, C-rll, P-wtm, G-wtm) are 2–5 m in width. Boundaries between sets (and the elements themselves) are sharp but not erosional. Fine-grained units are moderately sorted, whereas conglomerate facies are well sorted with little to no matrix (typically $< 5\%$) and contain texturally and compositionally mature (well-rounded) clasts; 98% of clasts are < 5 cm in diameter (but up to 15 cm at certain locations). All beds are internally massive. Rare in-situ calcrete nodules are found close to the tops of some sandstone beds, and are typically 2 cm in diameter. These elements are interbedded with AE2, AE5, AE7 and rarely AE1 units, and are common across the study area.

Interpretation

Massive, structureless sands and silts are most commonly deposited from rapid suspension during waning

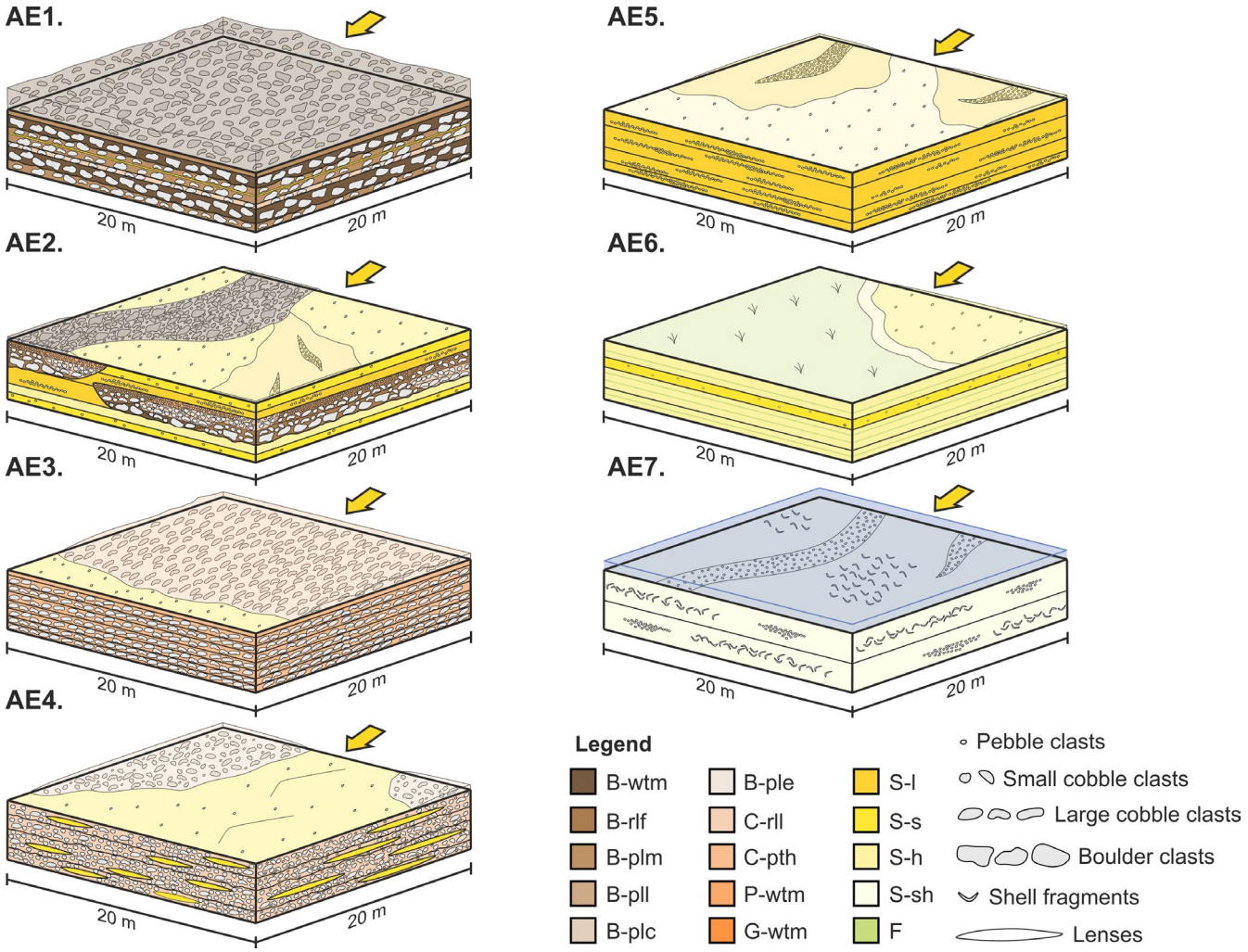

FIGURE 7 3D architectural element models displaying vertical and lateral nature of individual elements, and interpretations of their depositional processes. Yellow arrows indicate dominant sediment transport direction

hyperconcentrated flows (Köykkä, 2011; Lewis, Jackson, & Gawthorpe, 2017; Nichols & Fisher, 2007) commonly observed on the distal sections of an alluvial fan. Pebble-grade conglomerate lenses within the units represent higher-energy upper plane-bed deposition (Jo & Chough, 2001) forming channelized pebble streams (Croci, Della Porta, & Capezzuoli, 2016). The maturity of the clasts, both texturally and compositionally, are representative of their increased distance from the sediment input source (Miall, 1996). Rare calcrete nodules in AE5 units are indicative of an arid or semi-arid climatic setting (Alonso-Zarza, 2003; Retallack, 2001), and a prolonged period of stability allowing calcrete formation in a silt-prone substrate (Alonso-Zarza, 2003).

4.2.6 | AE6: Fan-toe overbank elements

Description

This element type comprises 6.18% of the measured succession. These elements are 0.5–5 m thick and laterally persistent between outcrops. They are composed internally of silty sandstone (S-s, S-h) and predominantly clayey lithologies (F) that are 0.2 to 2 m and 0.05 to 0.1 m thick respectively. Silty sandstones (S-s, S-h) are laterally extensive by tens of metres; however, clayey units vary in thickness from 5 cm to 10 cm within the same bed. Bed boundaries are sharp, and the two lithologies alternate through the element. Silty sandstone beds are moderately sorted ranging up to medium sand; a marked colour change and sharp increase in clay proportions denotes change to finer lithology. Beds are dominantly massive, though with some millimetre-thick horizontal laminations at the top of some silty sandstone beds. These elements occur in larger packages tens of metres thick, in association with AE5 and AE2 elements.

Interpretation

Similar to AE5, sand and siltstone units represent deposition from suspension of waning flows (Köykkä, 2011; Lewis et al., 2017; Nichols & Fisher, 2007). Thin clay horizons represent the end-of-flow deposition (both from tractional and

suspension processes), and the development of palaeosols identified by their lateral continuity and a lack of further structure (Mack, James, & Monger, 1993; Platt & Keller, 1992). Where AE6 and AE2 elements are found together, potential active channels are interpreted to have been abandoned through time and subsequently subject to low sedimentation rates, as active deposition occurs elsewhere on the fan (Davies & Gibling, 2010).

4.2.7 | AE7: Shallow-lacustrine elements

Description

This element type comprises 2.21% of the measured succession. These elements attain thicknesses of 4–10 m and are laterally extensive for up to 20 m. Elements are composed internally of 0.5–1 m beds of silty sandstone and conglomerate lithologies. Finer-grained units (S-sh) are laterally extensive over tens of metres, whereas conglomerates (P-wtm, G-wtm) typically pinch out laterally over 2–10 m. Silty sandstone beds contain small shell fragments such as *Melanopsis synaniae* and *Goniochilus achaiae,* freshwater gastropods (Esu & Gerotti, 2015); shell fossils are less than 2 cm in length and occur as shell beds intermittently within the element or single dispersed shells amongst the finer-grained lithofacies. Conglomerate facies are characterized by 1–5 cm diameter, well-rounded clasts and contain no matrix. Beds are mostly massive, but some contain shell horizons within beds and horizontal laminations. These elements do not appear to be preferentially associated with other architectural elements.

Interpretation

These elements are similar in origin to deposits of AE6; however, the presence of laterally persistent laminae deposited during steady suspension fallout conditions and the occurrence of freshwater shell fragments (outlined in Esu & Gerotti, 2015) testifies to the development of potential shallow lacustrine conditions (Abdul Aziz et al., 2003; Ford et al., 2016), associated with the inundation of the depocentre by Lake Corinth to the east and, later, the opening of the Rion Strait to the west (Gawthorpe et al., 2017).

4.3 | Chronostratigraphy

As a result of the Rodini Fm. being dominated by rapidly deposited conglomeratic units, absolute dating within the sediments is difficult due to a lack of potential data sources (Gawthorpe et al., 2017). Movement on major bounding faults to the south of the depocentre initiated at approximately 2.2–1.8 Ma (Gawthorpe et al., 2017) and this activity likely generated the initial accommodation to allow for the onset of accumulation of the conglomerates of the Rodini Fm. Corals and shells found in the overlying Synania Fm. siltstones provide a biostratigraphic age of approximately 420–400 ka (biozone MNN20) (Palyvos et al., 2010; Esu & Gerotti, 2015) that delimits the end of the episode of accumulation of the Rodini conglomerates. Thus, the total time available for accumulation of the Rodini Fm. is 1.8–1.4 Myr and the proposed relative time periods in this study would each represent one third of that value (approximately 600–470 Kyr each, assuming constant accumulation rates). Thirds were chosen in order to show a clear chronostratigraphic progression of sedimentological features, while retaining as much accuracy as possible in the relative geological ages of each study site.

Bedding dips reflect both tectonic and sedimentological factors: (a) original rotation of the palaeotopography as activity on the main bounding fault to the south occurred, forming shallower dips up-section, (b) post-depositional fault block rotation as extension became accommodated by new north-dipping faults to the north, increasing the dips of beds towards the south and (c) deposition predominantly occurred in an alluvial-fan setting, which results in a general decrease in depositional dip angles away from the fan-apex feeder valley. Dip angles vary between 6 and 40 degrees across the study area, with maximum dips recorded in the west and south (corresponding with lower elevations and earlier stratigraphy that has been subject to greater fault-induced post-depositional rotation), and minimum dips recorded to the east and in the centre of the study area (corresponding with higher elevations and later stratigraphy, with less fault-induced post-depositional rotation).

The integration of structural and topographic data allow for the definition of three relative time slices through the Rodini Fm. into which the study sites can be grouped (based on their locations within the study area). Sedimentological variations through both time and space can subsequently be defined and used to create an overall tectonostratigraphy in both dip and strike orientations (Figure 8). A relative increase in the proportion of conglomerate deposits towards the margins of the depocentre through time, in conjunction with an increase in AE1 and AE2 architectural elements across the study area, indicates that the fan system prograded across the basin.

4.4 | Definition of tectonostratigraphy and the use of clast-fabric analysis

The prevalence of dominantly debris flow and flood-sourced architectural elements across the study area, as outlined in Figure 6a and c, is consistent with the development of an alluvial fan. This is further supported by the facies themselves, with the fabric of many structureless, coarse conglomeratic units indicative of alluvial-fan flow processes (Table 1). The lack of well-developed sandy mesoforms of fluvial origin is notable.

Sedimentological data derived from vertical profiles, when placed within the outlined relative time frame, allow for tectonostratigraphic definition as outlined in Figure 8. Clast orientations

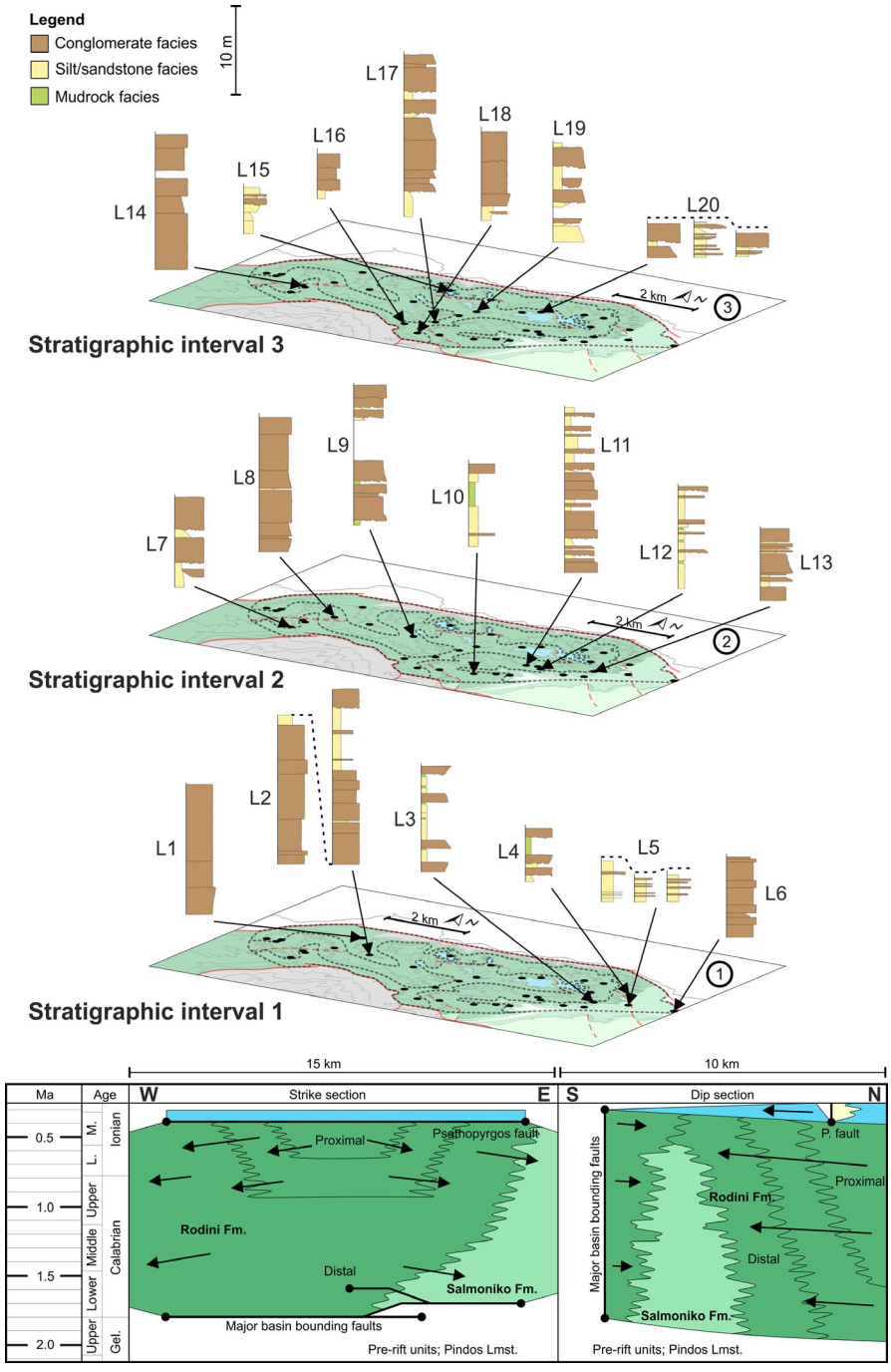

FIGURE 8 Diagram displaying lithological variations across the study area through time. The tectonostratigraphic record shows the progradational nature of the hangingwall-sourced fan and of smaller, footwall-sourced fans through times before lacustrine transgression. Relative timings are detailed in Palyvos et al. (2007)

with respect to palaeoflow directions indicate flow processes: long axes parallel to palaeoflow suggest deposition by debris flows, whereas intermediate axes parallel to palaeoflow suggest deposition by streamflow (Major, 1998). On this basis, debris-flow deposition in an alluvial-fan environment apparently prevailed in the north of the study area and extended into the depocentre towards the south and east as extension progressed. Streamflow processes (AE2) are predominantly recorded in the east and south, and their prevalence lessens through time as the alluvial fan prograded and subdued their depositional environment.

The nature of the hangingwall dip slope alluvial fan was progradational to the west into the Patras Rift, to the south towards smaller-scale alluvial fans sourced from the uplifted footwall of the depocentre, and advancing towards lacustrine-dominated depocentres to the east (represented by Synania Fm. deposits) (Figure 9). The progradation is represented by the advancement of facies belts away from the feeder valley with time, interpretable from the overall coarsening up of facies in distal locations. Footwall-derived alluvial fans, indicated by larger clast sizes and increased clast angularity, in conjuncture with northward palaeoflow directions, were smaller. As the basin cuts the pre-rift drainage at high angle, the northward-dipping fault develops small drainage catchments as footwall uplift occurs to feed into the basin

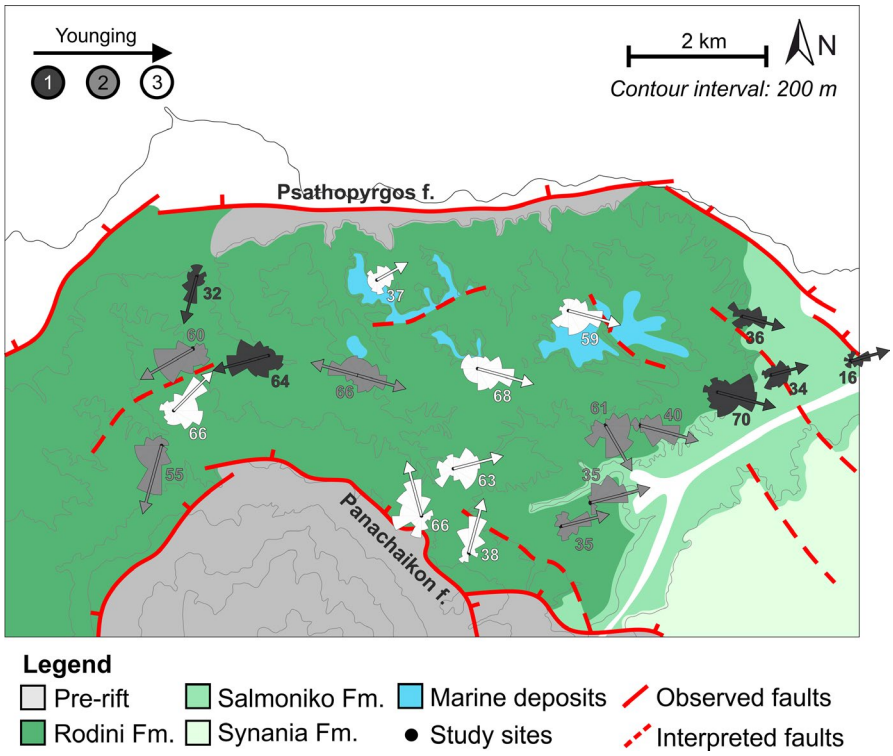

FIGURE 9 Palaeocurrent map showing directions of palaeoflow across the study area through time. Persistent flow to the west and east (with a southerly influence) indicate diversion of the alluvial system into axial depocentres in the rift. Small-scale fans sourced over the uplifted footwall are indicated by northerly dominated flow during late-phase deposition

dominated by south-flowing drainage over the hanging-wall. Due to increased erosion of syn-rift units close to the Panachaikon footwall scarp, it is difficult to recognize the development of these smaller fans through time; it is likely that these alluvial fans increased in size due to continued denudation of the associated uplifted footwall (cf. Densmore, Allen, & Simpson, 2007; Mirabella et al., 2018; Pechlivanidou et al., 2018).

The sand and silt deposits of the Synania Fm., which overlies the Rodini Fm., are interpreted to represent a lacustrine incursion caused by the northward migration of faulting and accommodation generation (Ford et al., 2016). Observations of shells and shell horizons within the unit (Palyvos et al., 2007; Esu & Gerotti, 2015), and extensive deposits interpreted as shallow-lacustrine deposition (see AE7) support this. The major sediment source from the north was eventually cut off by the formation of new normal faults, causing key sediment routeways from the north to be blocked, thereby shutting down the depositional system before the basin began to uplift over the last 400 Kyr.

5 | DISCUSSION

5.1 | The impact of rifting on fluvial drainage

The architectural elements detailed in this study represent different parts of the gradual transition (from proximal to distal locations) down-system of a large alluvial fan; massive debris flows lead into normally graded bedload conglomerates that decrease in frequency away from major sediment source points, counterbalanced by an increase in fine-grained facies. Towards the east, fine-grained units containing shell fragments represent the lateral facies transition to lacustrine-dominated systems.

Placing the detailed sedimentological vertical profiles in the context of relative time slices allows for the creation of palaeogeographic models detailing the evolution of the depocentre (Figure 10). To the north of the present-day Gulf of Corinth, the River Mornos catchment drains the structurally quiescent Pindos Mountains (Piper, Kontopoulos, Anagnostou, Chronis, & Panagos, 1990) and forms an 8 × 4 km southward-prograding modern delta. This system is likely to be the ancestral fluvial system described in this study (the catchment of which has been inherited in the present day), and acted as the principal sediment source that fed the alluvial fan represented by the Rodini Fm. The fluvial system is interpreted to have flowed south-west, following the alignment of east to west propagating fold-and-thrust structures with a south-west to north-east strike. These were formed during the Early Oligocene to Late Eocene (Skourlis & Doutsos, 2003; Underhill, 1989), and were also exploited by other antecedent drainage systems in the Gulf (Gawthorpe, Fraser, & Collier, 1994). As the fold-and-thrust structures form topographic highs between catchments, subtle variation in topographic dips between structures allow for the switching of dominant drainage direction from north to south across the elevated highs (Gawthorpe et al., 2017).

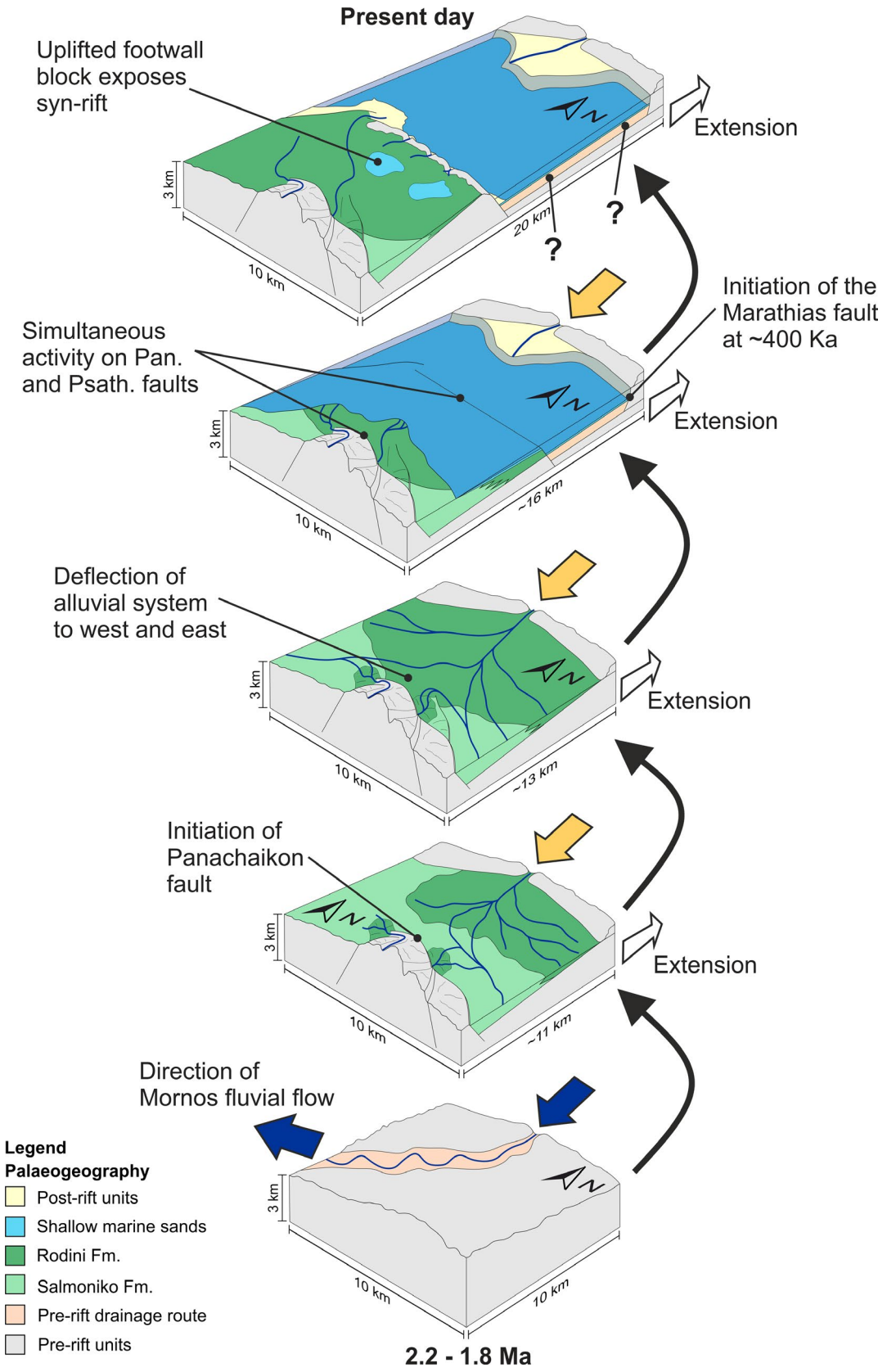

FIGURE 10 Palaeoenvironmental reconstruction of the Panachaikon-Psathopyrgos fault block through time, from 2 Ma—present day. Faulting initially cut through the pre-rift Hellenide thrust-and-fold belt, with uplifted footwalls blocking fluvial flow to the southwest and forming an alluvial fan and associated axial fluvial systems (Rodini Fm. and Salmoniko Fm.). Initiation of the Psathopyrgos fault cut off sediment supply from the north, causing a lacustrine transgression and the backstepping of a major delta up the hangingwall dip slope

Rifting propagated through the catchment at high angle, with the major northward-dipping master fault uplifting pre-rift basement to the south of the study area and forming a barrier to flow. As the hangingwall subsided, accommodation was created and an alluvial fan began to build out into the depocentre as flows spread radially to fill the available accommodation and attain an equilibrium profile. This process is interpreted to have continued until a new master fault developed in the north and acted to uplift the depocentre, and as a new footwall created a barrier to sediment pathways, sediment supply ceased and caused the exposure and erosion of the Rodini Fm. to the present day.

This interpretation represents one of three possible end-member scenarios whereby a rift system cuts a large-scale drainage catchment, examples of which are found across the Gulf of Corinth. The three evolutionary scenarios are explained below.

1. Drainage incision keeps pace with footwall uplift; flow is orientated in the same direction as the dip of major normal faults. Erosion down into the bedrock lithology forms valleys in the footwall and eroded sediment is deposited directly into the newly formed depocentre (see Backert, Ford, & Malartre, 2010; Bentham, Collier, Gawthorpe, Leeder, & Stark, 1991; Hemelsdaël et al., 2017; Leeder et al., 2012).
2. Drainage is diverted away from the uplifting footwall; flow is orientated in the same direction as the dip of major normal faults, however, a combination of low erosive power and bedrock resistance to erosion (Allen & Densmore, 2000) results in the diversion or complete reversal of drainage away from uplifted sections (see Rohais et al., 2007; Gawthorpe et al., 2017). Small catchments form on the uplifted footwall close to the fault face, forming relatively small, high-gradient fans and fan deltas along the length of the fault (Gawthorpe et al., 1994).
3. Drainage flows over the hangingwall dip slope; flow is orientated in opposite direction to dip of major normal faults. This causes wider, lower-gradient fans and deltas. Sediment yield is influenced by antecedent catchment parameters (in conjunction with a dominant tectonic uplift control), such as bedrock lithology and climate, which are not influenced by the evolving rift system (described in detail in this study; see further examples in Mack & Seager, 1990; Martini & Sagri, 1993). Experimental work by Clarke, Quine, and Nicholas (2010) studying alluvial fan development with a downstream boundary condition (such as a fluvial system preventing progradation, or structural barrier) found that initial deposition from sheet-like (i.e. non-confined) flows developed to channelized flows with time and advancement of the fan. In this study, the Panachaikon fault provides a boundary condition, and early deposits of the Rodini Fm. representing possible sheet-like flows (see Figure 6a, log L1) transitioning up-section into proposed channelized flow sediments (see Figure 6a, log L3) indicating a subduing of autogenic fan cycles of deposition (van Dijk, 2012).

These end-members have been explored previously (Gawthorpe & Colella, 1990; Gawthorpe et al., 1994); however, few studies focus on intrabasinal faulting acting as barriers to hangingwall dip slope routes of sediment transport. Although scenario (3) is described in detail in this study (and can be supported by the pattern of local sedimentation within the depocentre), Figure 10 shows that conditions allowing for scenarios (1) and (2) to occur were present between the initiation of extension and the present day if considering this sub-basin in a regional context. The Trizonia fault to the north-east, located under the present-day Gulf and likely active at the same time as the Panachaikon fault (Ford et al., 2016) may have provided a barrier to the Mornos drainage and diverted the system over the hangingwall dip slope of the Panachaikon fault—scenario (2). Following deposition of the Rodini conglomerates, initiation of the Marathias (see Figure 1) and Psathopyrgos faults at approximately 400 ka (Palyvos et al., 2010) has led to a marked increase in extension rates in the modern Western Gulf (Ford et al., 2016; Gawthorpe et al., 2017). This has developed more pronounced graben conditions with a northern basin-bounding fault (the Marathias fault, see Figure 10) (Beckers et al., 2015) of which the uplifted footwall is eroded sufficiently by the Mornos fluvial system to allow the formation of a modern fan-delta depositing directly into the hangingwall—representing scenario (1). A significant novel outcome of this study is that the succession records evidence that all three scenarios can be present during the life cycle of a single fault block depending on the presence and activity of intrabasinal faulting.

The results of this study demonstrate the effect of a downstream boundary condition (in this case, an uplifted footwall) on alluvial-fan deposition. Numerical modelling studies (e.g. Clarke, 2015; Clarke et al., 2010; Van Dijk, Kleinhans, Postma, & Kraal, 2012) commonly focus on the autogenic development of fan systems and surface depositional processes. Results from this study can be incorporated into future models to provide more realistic structural settings for alluvial-fan development, which will aid in the study of alluvial system response to fault development and basin subsidence for a variety of scenarios (e.g. analysis of the effect of differing rift and drainage orientations). Comparing results from such modelling efforts to real-world studies of ancient outcropping successions (this study), and similar modern analogues (e.g. the Okavango delta—a large alluvial fan oriented perpendicular to the trend of active rifting) will markedly increase our understanding of sedimentary system response to active faulting at a variety of scales.

5.2 | The Rodini Fm. in the wider context of the Gulf of Corinth

Across the uplifted footwall exposures of the northern Peloponnesos, multiple different syn-rift depositional environments are represented. In the east near Corinth, sediments are dominated by fan deltas and deep-marine deposits of the ancient Lake Corinth, within the depocentre of the now uplifted footwall (Doutsos & Piper, 1990); these deposits transition up-section into shallow-marine sands related to the transition from the lake to the modern day Gulf (Rohais, Eschard, Ford, Guillocheau, & Moretti, 2007; Ford et al., 2016). Further to the west towards the study area, the influence of continental sedimentation becomes apparent in the hangingwalls of the Kalavryta and Demestika Faults (Hemelsdaël et al., 2017) and in the study area of this paper, where conglomeratic deposition represents alluvial-fan and possible braided stream environments. Gawthorpe et al. (2017) show that the uplifted sections exposed today can be separated into two distinct rift phases; the first where extension is localized around Corinth and extends as far west as Aigio (5.0–3.6 Ma to 2.2–1.8 Ma), and the second where extension has begun in the study area on the Lakka and Panachaikon faults (allowing the deposition of the Rodini Fm.), north of Corinth (2.2–1.8 Ma to present). Within this second phase, the initiation of the Psathopyrgos fault on the present-day coastline uplifts the Rodini Fm. and causes the opening of the Rion Strait. This period has been narrowed down to approximately 400 ka by dating of overlying shell fauna in the Synania Fm. (Palyvos et al., 2007; Esu & Gerotti, 2015) which was deposited during a period of simultaneous activity on both the major Panachaikon Fault and Psathopyrgos Fault (Figure 10).

In the outlined first rifting phase, similar deposits to those found of the Rodini Fm. are found in the hangingwalls of the Kalavryta and Demestika Faults. Hemelsdaël et al. (2017) outlined the tectonosedimentary evolution of these deposits and found multiple similar facies and facies associations to those outlined in this paper; similar units of coarse boulder conglomerates deposited close to a dominant sediment input source, transitioned distally to finer-grained sands and siltstones. The drainage system leading to the deposition of the facies described by Hemelsdaël et al. (2017) differs from the one described herein in two key ways; (a) although orientated at high angle to fault strike, antecedent drainage and flow is over the footwall and keeps pace with the uplifting bedrock, depositing sediment directly into the newly formed depocentres, and (b) the drainage system as a result cuts across multiple fault blocks, where older normal faults to the north are buried by syn-rift sediments. It is inferred that similarly high sediment supply through one dominant sediment input source prevailed. This, in combination with both drainage catchments eroding similar bedrock (due to the inherited palaeotopography around Kalavryta being dominated by the same Pindos Units forming the bedrock lithologies of the Mordos catchment (Degnan & Robertson, 1998)), leads to strikingly similar deposits in these two depocentres at different times. In the Prinos and Tsivios fault blocks, coarse basal conglomerates of interpreted alluvial origin, fill in the palaeotopography, in a very similar manner to the one documented herein for the Rodini Fm.

To the west of the Panachaikon fault hangingwall, the Patras rift extends towards the south-west, having initiated on an extensive low-angle listric fault which underpins extension in the Gulf of Corinth (Sorel, 2000). The rifts are linked by two transfer fault zones trending towards the north-east, on the western end of the Panachaikon fault (Flotté, Sorel, Müller, & Tensi, 2005). Imbricated cobbles within the Rodini Fm. indicate that part of the river drainage was directed into the Patras rift axially, as the uplifted footwall of the Panachaikon fault acted as a buffer to flow. The sediment supply likely outpaced the formation of an accommodation zone between the differently orientated rift segments (Morley, Nelson, Patton, & Munn, 1990) allowing for the continued progradation and deposition of fluvio-alluvial deposits into the Patras rift (Doutsos et al., 1988). This is similar to other locations in the Gulf of Corinth where steep-sided Gilbert fan deltas would build into both the ancient Lake Corinth and the more recent Gulf (Rohais et al., 2007; Backert et al., 2010; Rohais, Eschard, & Guillocheau, 2008), across multiple hangingwall depocentres each with varying amounts of accommodation space.

Following deposition of coarse alluvial conglomerates in the study area, the initiation of the Psathopyrgos fault (Figure 1) formed a hangingwall depocentre north of the fault. Sediment supply into the hangingwall of the Panachaikon fault was subsequently shut off; hence during the period of simultaneous activity on the Panachaikon and Psathopyrgos faults, deposition of coarse-grained units was unable to cross over the faults to provide a linkage between depocentres. This is a direct result of drainage being orientated to flow over the hangingwall dip slope as opposed to the uplifted footwall. In both scenarios, younger faults are orientated in the same direction as their predecessors.

6 | CONCLUSIONS

1. The Rodini Fm. is characterized by a 600–800-m-thick succession of upward coarsening conglomerates (up to ca. 75 cm clast sizes) with subordinate finer-grained lithologies. The succession represents the accumulated deposits of a major prograding alluvial-fan system. In western locations, stacked elements of boulder-to-cobble grade conglomerates represent proximal debris-flow and hyperconcentrated-flow deposits. In central and southern locations, distal to sites of major sediment input,

conglomerates fine to pebble- and granule-grade, and the proportion of sand-grade and silt-grade facies increases significantly. Further to the east and up-section, a lacustrine influence is recorded by the occurrence of siltstone units containing a lacustrine shelly fauna.
2. Palaeocurrent data collected from 20 study sites (1,001 measurements total) indicate a dominant major sediment input source from the north of the study area flowing south over the hangingwall dip slope of the Panachaikon fault, a major basin-bounding fault. This alluvial system likely inherited the ancient course of the Mornos River and its catchment.
3. The uplifted footwall of the Panachaikon fault acted as a barrier to the Mornos catchment, and subsequently diverted drainage into adjacent depocentres to the east (ancient Lake Corinth) and west (Patras rift).
4. Palaeocurrent data indicating northerly flow, close to the uplifted footwall of the Panachaikon fault, indicate footwall-derived sediment deposition occurred in the basin on a small scale at both the fault tip of the Panachaikon fault to the west, and the point of hard linkage between the Panachaikon and Lakka faults. These areas were exploited by small drainage catchments eroding the uplifted footwall.
5. The initiation of the Psathopyrgos fault to the north at approximately 400 ka provided a barrier to flow over the Panachaikon fault hangingwall. Simultaneous extension on both of these faults induced an episode of rapid basin subsidence that resulted in an initially lacustrine transgression over the recently deposited conglomerates, prior to the opening of the Rion Strait shortly after 400 ka (Gawthorpe et al., 2017).
6. Original fluvial flow of the pre-rift Mornos river to the south-south-west was blocked and buttressed by the newly formed Panachaikon fault and associated uplifted footwall, leading to the formation of the described alluvial fan and the diversion of drainage to the west and east into newly formed rift depocentres. In the present day, the south-flowing Mornos river forms a large delta that progrades south into the Gulf of Corinth.
7. Results from this research record the sedimentological expression of rift-basin evolution that cross-cuts an antecedent drainage network at a high angle. Three depositional models for this exist: (i) erosion through an uplifted footwall; (ii) diversion away from an uplifted footwall; (iii) deposition over the hangingwall dip slope. While examples of each scenario can be found around the Gulf in the present day, here we show that intrabasinal faulting allows for the development of each scenario within the same basin segment as it evolves through time.

ACKNOWLEDGEMENTS

This research was funded by Aker BP, Anadarko, Areva (now Orano), BHP Billiton, Cairn India (Vedanta), Chevron, ConocoPhillips, Murphy Oil Corporation, Nexen-CNOOC, Saudi Aramco, Shell, Tullow Oil, Woodside and YPF, through their sponsorship of the Fluvial & Eolian Research Group at the University of Leeds. We are also grateful to our project partner Petrotechnical Data Systems (PDS) for support. We thank Ben Said, Rob Shuter and Dan Tek for their assistance with field data collection. We thank reviewers Michael Hopkins, Bárbara Teixeira and Gary Axen, and Editor Cynthia Ebinger for their valuable comments and suggestions, which have significantly improved the manuscript.

REFERENCES

Abdul Aziz, H., Sanz-Rubio, E., Calvo, J. P., Hilgen, F. J., & Krijgsman, W. (2003). Palaeoenvironmental reconstruction of a middle Miocene alluvial fan to cyclic shallow lacustrine depositional system in the Calatayud Basin (NE Spain). *Sedimentology*, *50*, 211–236. https://doi.org/10.1046/j.1365-3091.2003.00544.x

Allen, J. R. L. (1982). *Sedimentary Structures: Their Character and Physical Basis.* Developments in Sedimentology, 30. Amsterdam: Elsevier.

Allen, P. A., & Densmore, A. L. (2000). Sediment flux from an uplifting fault block. *Basin Research*, *12*, 367–380.

Alonso-Zarza, A. M. (2003). Palaeoenvironmental significance of palustrine carbonates and calcretes in the geological record. *Earth-Science Reviews*, *60*, 261–298. https://doi.org/10.1016/S0012-8252(02)00106-X

Alvarez-Zarikian, C. A., Soter, S., & Katsonopoulou, D. (2008). Recurrent submergence and uplift in the area of ancient Helike, gulf of corinth, Greece: Microfaunal and archaeological evidence. *Journal of Coastal Research*, *24*, 110–125. https://doi.org/10.2112/05-0454.1

Backert, N., Ford, M., & Malartre, F. (2010). Architecture and sedimentology of the Kerinitis Gilbert-type fan delta, Corinth Rift, Greece. *Sedimentology*, *57*, 543–586. https://doi.org/10.1111/j.1365-3091.2009.01105.x

Beckers, A., Hubert-Ferrari, A., Beck, C., Bodeux, S., Tripsanas, E., Sakellariou, D., & de Batist, M. (2015). Active faulting at the western tip of the Gulf of Corinth, Greece, from high-resolution seismic data. *Marine Geology*, *360*, 55–69. https://doi.org/10.1016/j.margeo.2014.12.003

Bell, R. E., McNeill, L. C., Bull, J. M., Henstock, T. J., Collier, R. E. L., & Leeder, M. R. (2009). Fault architecture, basin structure and evolution of the Gulf of Corinth rift, central Greece. *Basin Research*, *21*, 824–855. https://doi.org/10.1111/j.1365-2117.2009.00401.x

Bentham, P., Collier, R. E., Gawthorpe, R. L., Leeder, M. R., & Stark, C. (1991). Tectono-sedimentary development of an extensional basin: The Neogene Megara Basin, Greece. *Journal of the Geological Society*, *148*, 923–934. https://doi.org/10.1144/gsjgs.148.5.0923

Blair, T. C., & McPherson, J. G. (1994). Alluvial fans and their natural distinction from rivers based on morphology, hydraulic processes, sedimentary processes, and facies assemblages. *SEPM Journal of Sedimentary Research*, *64A*, 450–489.

Calhoun, N. C., & Clague, J. J. (2018). Distinguishing between debris flows and hyperconcentrated flows: An example from the eastern Swiss Alps. *Earth Surface Processes and Landforms*, *43*, 1280–1294. https://doi.org/10.1002/esp.4313

Chakraborty, T., & Ghosh, P. (2010). The geomorphology and sedimentology of the Tista megafan, Darjeeling Himalaya: Implications for megafan building processes. *Geomorphology*, *115*, 252–266. https://doi.org/10.1016/j.geomorph.2009.06.035

Clarke, L. E. (2015). Experimental alluvial fans: Advances in understanding of fan dynamics and processes. *Geomorphology*, *244*, 135–145. https://doi.org/10.1016/j.geomorph.2015.04.013

Clarke, L., Quine, T. A., & Nicholas, A. (2010). An experimental investigation of autogenic behaviour during alluvial fan evolution. *Geomorphology*, *115*, 278–285. https://doi.org/10.1016/j.geomorph.2009.06.033

Collier, R. E. L., & Dart, C. J. (1991). Neogene to quaternary rifting, sedimentation and uplift in the Corinth Basin, Greece. *Journal of the Geological Society*, *148*, 1049–1065. https://doi.org/10.1144/gsjgs.148.6.1049

Collier, R. E. L., & Gawthorpe, R. L. (1995). Neotectonics, drainage and sedimentation in central Greece: Insights into coastal reservoir geometries in syn-rift sequences. *Geological Society, London, Special Publications*, *80*, 165–181. https://doi.org/10.1144/GSL.SP.1995.080.01.08

Collinson, J., Mountney, N. P., & Thompson, D. (2006). *Sedimentary structures*, 3rd ed. Harpenden: Terra Publishing.

Colombera, L., & Bersezio, R. (2011). Impact of the magnitude and frequency of debris-flow events on the evolution of an alpine alluvial fan during the last two centuries: Responses to natural and anthropogenic controls. *Earth Surface Processes and Landforms*, *36*, 1632–1646. https://doi.org/10.1002/esp.2178

Costa, J. E. (1988). Rheologic, geomorphic, and sedimentologic differentiation of water floods, hyperconcentrated flows, and debris flows. In V. R. Baker, R. C. Kochel, & P. C. Patton (Eds.), *Flood geomorphology* (pp. 113–122). Chichester: John Wiley & Sons Inc.

Croci, A., Della Porta, G., & Capezzuoli, E. (2016). Depositional architecture of a mixed travertine-terrigenous system in a fault-controlled continental extensional basin (Messinian, Southern Tuscany, Central Italy). *Sedimentary Geology*, *332*, 13–39. https://doi.org/10.1016/j.sedgeo.2015.11.007

Cronin, S. J., Lecointre, J. A., Palmer, A. S., & Neall, V. E. (2000). Transformation, internal stratification, and depositional processes within a channelised, multi-peaked lahar flow. *New Zealand Journal of Geology and Geophysics*, *43*, 117–128. https://doi.org/10.1080/00288306.2000.9514874

Dart, C. J., Collier, R. E. L., Gawthorpe, R. L., Keller, J. V. A., & Nichols, G. (1994). Sequence stratigraphy of (?)Pliocene-Quaternary synrift, Gilbert-type fan deltas, northern Peloponnesos, Greece. *Marine and Petroleum Geology*, *11*, 545–560. https://doi.org/10.1016/0264-8172(94)90067-1

Davies, N. S., & Gibling, M. R. (2010). Cambrian to Devonian evolution of alluvial systems: The sedimentological impact of the earliest land plants. *Earth-Science Reviews*, *98*, 171–200. https://doi.org/10.1016/j.earscirev.2009.11.002

Degnan, P. J., & Robertson, A. H. F. (1998). Mesozoic-early Tertiary passive margin evolution of the Pindos ocean (NW Peloponnese, Greece). *Sedimentary Geology*, *117*, 33–70. https://doi.org/10.1016/S0037-0738(97)00113-9

Densmore, A. L., Allen, P. A., & Simpson, G. (2007). Development and response of a coupled catchment fan system under changing tectonic and climatic forcing. *Journal of Geophysical Research*, *112*, F01002. https://doi.org/10.1029/2006JF000474

Doutsos, T., Kontopoulos, N., & Poulimenos, G. (1988). The Corinth-Patras rift as the initial stage of continental fragmentation behind an active island arc (Greece). *Basin Research*, *1*, 177–190. https://doi.org/10.1111/j.1365-2117.1988.tb00014.x

Doutsos, T., & Piper, D. J. W. (1990). Listric faulting, sedimentation, and morphological evolution of the Quaternary eastern Corinth rift, Greece: First stages of continental rifting. *Bulletin of the Geological Society of America*, *102*, 812–829. https://doi.org/10.1130/0016-7606(1990)102<0812:LFSAME>2.3.CO;2

Esu, D., & Girotti, O. (2015). The late Early Pleistocene non-marine molluscan fauna from the Synania Formation (Achaia, Greece), with description of nine new species (Mollusca: Gastropoda). *Archiv Für Molluskenkunde: International Journal of Malacology*, *144*, 65–81. https://doi.org/10.1127/arch.moll/1869-0963/144/065-081

Flotté, N., Sorel, D., Müller, C., & Tensi, J. (2005). Along strike changes in the structural evolution over a brittle detachment fault: Example of the Pleistocene Corinth-Patras rift (Greece). *Tectonophysics*, *403*, 77–94. https://doi.org/10.1016/j.tecto.2005.03.015

Ford, M., Hemelsdaël, R., Mancini, M., & Palyvos, N. (2016) Rift migration and lateral propagation: evolution of normal faults and sediment-routing systems of the western Corinth rift (Greece). In: C. Childs, R. E. Holdsworth, C. A.-L. Jackson, T. Manzocchi, J. J. Walsh, & G. Yielding (Eds.), *The Geometry of Normal Faults*. Geological Society, London, Special Publications, (439) London.

Ford, M., Rohais, S., Williams, E. A., Bourlange, S., Jousselin, D., Backert, N., & Malarte, F. (2013). Tectono-sedimentary evolution of the western Corinth rift (Central Greece). *Basin Research*, *25*, 3–25. https://doi.org/10.1111/j.1365-2117.2012.00550.x

Franke, D., Hornung, J., & Hinderer, M. (2015). A combined study of radar facies, lithofacies and three-dimensional architecture of an alpine alluvial fan (Illgraben fan, Switzerland). *Sedimentology*, *62*, 57–86. https://doi.org/10.1111/sed.12139

Gawthorpe, R., & Colella, A. (1990) Tectonic controls on coarse-grained delta depositional systems in rift basins. In A. Colella & D. B. Prior (Eds.), *Coarse-grained Deltas* (113–127). Chichester, UK: John Wiley & Sons Inc.

Gawthorpe, R. L., Fraser, A. J., & Collier, R. E. L. (1994). Sequence stratigraphy in active extensional basins: Implications for the interpretation of ancient basin-fills. *Marine and Petroleum Geology*, *11*, 642–658. https://doi.org/10.1016/0264-8172(94)90021-3

Gawthorpe, R. L., & Leeder, M. R. (2000). Tectono-sedimentary evolution of active extensional basins. *Basin Research*, *12*, 195–218. https://doi.org/10.1046/j.1365-2117.2000.00121.x

Gawthorpe, R. L., Leeder, M. R., Kranis, H., Skourtsos, E., Andrews, J. E., Henstra, G. A., … Stamatakis, M. (2017). Tectono-sedimentary evolution of the Plio-Pleistocene Corinth rift, Greece. *Basin Research*, *30*, 448–479. https://doi.org/10.1111/bre.12260

Gloppen, T. G., & Steel, R. J. (1981). The deposits, internal structure and geometry in six alluvial fan-fan delta bodies (Devonian-Norway)-A study in the significance of bedding sequence in conglomerates. *Society for Sedimentary Geology Special Publication*, *31*, 49–69.

Graham, S. A., Hendrix, M. S., Johnson, C. L., Badamgarav, D., Badarch, G., Amory, J., … Hacker, B. R. (2001). Sedimentary record and tectonic implications of Mesozoic rifting in southeast Mongolia. *Bulletin of the Geological Society of America*, *113*, 1560–1579. https://doi.org/10.1130/0016-7606(2001)113<1560:SRATIO>2.0.CO;2

Gupta, S., Underhill, J. R., Sharp, I. R., & Gawthorpe, R. L. (1999). Role of fault interactions in controlling synrift sediment dispersal patterns: Miocene, Abu Alaqa Group, Suez Rift, Sinai. *Egypt. Basin Research*, *11*, 167–189. https://doi.org/10.1046/j.1365-2117.1999.00300.x

Hemelsdaël, R., Ford, M., Malartre, F., & Gawthorpe, R. L. (2017). Interaction of an antecedent fluvial system with early normal fault growth: Implications for syn-rift stratigraphy, western Corinth rift (Greece). *Sedimentology*, *64*, 1957–1997. https://doi.org/10.1111/sed.12381

Hopkins, M. C., & Dawers, N. H. (2018). The role of fault length, overlap and spacing in controlling extensional relay ramp fluvial system geometry. *Basin Research*, *30*, 20–34. https://doi.org/10.1111/bre.12240

Hwang, I. G., Chough, S. K., Hong, S. W., & Choe, M. Y. (1995). Controls and evolution of fan delta systems in the Miocene Pohang Basin, SE Korea. *Sedimentary Geology*, *98*, 147–179. https://doi.org/10.1016/0037-0738(95)00031-3

Jo, H. R., & Chough, S. K. (2001). Architectural analysis of fluvial sequences in the Northwestern part of Kyongsang Basin (Early Cretaceous), SE Korea. *Sedimentary Geology*, *144*, 307–334. https://doi.org/10.1016/S0037-0738(01)00123-3

Jo, H. R., Rhee, C. W., & Chough, S. K. (1997). Distinctive characteristics of a streamflow-dominated alluvial fan deposit: Sanghori area, Kyongsang Basin (Early Cretaceous), southeastern Korea. *Sedimentary Geology*, *110*, 51–79. https://doi.org/10.1016/S0037-0738(96)00083-8

Karpeta, W. P. (1993). Sedimentology and gravel bar morphology in an Archaean braided river sequence: The Witpan Conglomerate Member (Witwatersrand Supergroup) in the Welkom Goldfield, South Africa. *Geological Society, London, Special Publications*, *75*, 369–388. https://doi.org/10.1144/GSL.SP.1993.075.01.21

Khadkikar, A. S. (1999). Trough cross-bedded conglomerate facies. *Sedimentary Geology*, *128*, 39–49. https://doi.org/10.1016/S0037-0738(99)00060-3

Kim, S. B., Kim, Y.-G., Jo, H. R., Jeong, K. S., & Chough, S. K. (2009). Depositional facies, architecture and environments of the Sihwa Formation (Lower Cretaceous), mid-west Korea with special reference to dinosaur eggs. *Cretaceous Research*, *30*(1), 100–126.

Kim, B. C., & Lowe, D. R. (2004). Depositional processes of the gravelly debris flow deposits, South Dolomite alluvial fan, Owens Valley, California. *Geosciences Journal*, *8*, 153–171. https://doi.org/10.1007/BF02910191

Köykkä, J. (2011). Precambrian alluvial fan and braidplain sedimentation patterns: Example from the Mesoproterozoic Rjukan Rift Basin, southern Norway. *Sedimentary Geology*, *234*, 89–108. https://doi.org/10.1016/j.sedgeo.2010.12.004

Leeder, M. R., & Jackson, J. A. (1993). The interaction between normal faulting and drainage in active extensional basins, with examples from the western United States and central Greece. *Basin Research*, *5*, 79–102. https://doi.org/10.1111/j.1365-2117.1993.tb00059.x

Leeder, M. R., Mark, D. F., Gawthorpe, R. L., Kranis, H., Loveless, S., Pedentchouk, N., … Stamatakis, M. (2012). A "Great Deepening": Chronology of rift climax, Corinth rift, Greece. *Geology*, *40*, 999–1002. https://doi.org/10.1130/G33360.1

Lewis, M. M., Jackson, C.-L., & Gawthorpe, R. L. (2017). Tectono-sedimentary development of early syn-rift deposits: The Abura Graben, Suez Rift. *Egypt. Basin Research*, *29*, 327–351. https://doi.org/10.1111/bre.12151

Lindsey, D. A., Langer, W. H., & Knepper, D.H. Jr., (2005). Stratigraphy, lithology, and sedimentary features of Quaternary alluvial deposits of the South Platte River and some of its tributaries east of the Front Range. Colorado. U.S. Geological Survey Professional Paper. 1705.

Lowe, D. R. (1979). Sediment gravity flows: Their classification and some problems of application to natural flows and deposits. *SEPM Special Publication*, *27*, 75–82.

Mack, G. H., James, W. C., & Monger, H. C. (1993). Classification of paleosols. *Geological Society of America Bulletin*, *105*, 129–136. https://doi.org/10.1130/0016-7606(1993)105<0129:COP>2.3.CO;2

Mack, G. H., & Leeder, M. R. (1999). Climatic and tectonic controls on alluvial-fan and axial-fluvial sedimentation in the Plio-Pleistocene Palomas half graben, southern Rio Grande Rift. *Journal of Sedimentary Research*, *69*, 635–652. https://doi.org/10.2110/jsr.69.635

Mack, G. H., & Seager, W. R. (1990). Tectonic control on facies distribution of the Camp Rice and Palomas Formations (Pliocene-Pleistocene) in the southern Rio Grande rift. *Bulletin of the Geological Society of America*, *102*, 45–53. https://doi.org/10.1130/0016-7606(1990)102<0045:TCOFDO>2.3.CO;2

Maizels, J. (1993). Lithofacies variations within sandur deposits: The role of runoff regime, flow dynamics and sediment supply characteristics. *Sedimentary Geology*, *85*, 299–325. https://doi.org/10.1016/0037-0738(93)90090-R

Major, J. J. (1998). Pebble orientation on large, experimental debris-flow deposits. *Sedimentary Geology*, *117*, 151–164. https://doi.org/10.1016/S0037-0738(98)00014-1

Martini, I. P., & Sagri, M. (1993). Tectono-sedimentary characteristics of Late Miocene-Quaternary extensional basins of the Northern Apennines, Italy. *Earth Science Reviews*, *34*, 197–233. https://doi.org/10.1016/0012-8252(93)90034-5

Martins-Neto, M. A., & Catuneanu, O. (2010). Rift sequence stratigraphy. *Marine and Petroleum Geology*, *27*, 247–253. https://doi.org/10.1016/j.marpetgeo.2009.08.001

Miall, A. D. (1996). *The Geology of Fluvial Deposits, Sedimentary Facies, Basin Analysis, and Petroleum Geology* (p. 582). New York: Springer.

Mirabella, F., Bucci, F., Santangelo, M., Cardinali, M., Caielli, G., de Franco, R., … Barchi, M. R., (2018). In press. Alluvial fan shifts and stream captures driven by extensional tectonics in central Italy. *Journal of the Geological Society*, *175*, 788–805. https://doi.org/10.1144/jgs2017-138

Morley, C. K., Nelson, R. A., Patton, T. L., & Munn, S. G. (1990). Transfer Zones in the East African Rift System and Their Relavance to Hydrocarbon Exploration in Rifts. *American Association of Petroleum Geologists Bulletin*, *74*, 1234–1253.

Moscariello, A., Marchi, L., Maraga, F., & Mortara, G. (2002). Alluvial fans in the Italian Alps: Sedimentary facies and processes. *Flood and Megaflood Processes and Deposits: Recent and Ancient Examples*, *32*, 141–166.

Murcia, H. F., Hurtado, B. O., Cortés, G. P., Macías, J. L., & Cepeda, H. (2008). The ~ 2500 yr B.P. Chicoral non-cohesive debris flow from Cerro Machín Volcano, Colombia. *Journal of Volcanology and Geothermal Research*, *171*, 201–214. https://doi.org/10.1016/j.jvolgeores.2007.11.016

Nemec, W., & Steel, R. J. (1984). Alluvial and coastal conglomerates: Their significant features and some comments on gravelly mass-flow deposits. *Sedimentology of Gravels and Conglomerates*, *10*, 1–31.

Nichols, G. J., & Fisher, J. A. (2007). Processes, facies and architecture of fluvial distributary system deposits. *Sedimentary Geology*, *195*, 75–90. https://doi.org/10.1016/j.sedgeo.2006.07.004

Nixon, C. W., McNeill, L. C., Bull, J. M., Bell, R. E., Gawthorpe, R. L., Henstock, T. J., … Kranis, H. (2016). Rapid spatiotemporal variations

in rift structure during development of the Corinth Rift, central Greece. *Tectonics*, *35*, 1225–1248. https://doi.org/10.1002/2015TC004026

North, C. P., & Davidson, S. K. (2012). Unconfined alluvial flow processes: Recognition and interpretation of their deposits, and the significance for palaeogeographic reconstruction. *Earth-Science Reviews*, *111*, 199–223. https://doi.org/10.1016/j.earscirev.2011.11.008

Ori, G. G. (1989). Geologic history of the extensional basin of the Gulf of Corinth (?Miocene-Pleistocene), Greece. *Geology*, *17*, 918–921. https://doi.org/10.1130/0091-7613(1989)017<0918:GHOTEB>2.3.CO;2

Palyvos, N., Mancini, M., Sorel, D., Lemeille, F., Pantosti, D., Julia, R., … de Martini, P.-M. (2010). Geomorphological, stratigraphic and geochronological evidence of fast Pleistocene coastal uplift in the westernmost part of the Corinth Gulf Rift (Greece). *Geological Journal*, *45*, 78–104. https://doi.org/10.1002/gj.1171

Palyvos, N., Sorel, D., Lemeille, F., Mancini, M., Pantosti, D., Julia, R., … de Martini, P.-M. (2007). Review and new data on uplift rates at the W termination of the Corinth Rift and the NE Rion graben area (Achaia, NW Peloponnesos). *Bulletin of the Geological Society of Greece*, *40*, 412–424. https://doi.org/10.12681/bgsg.16631

Pechlivanidou, S., Cowie, P. A., Hannisdal, B., Whittaker, A. C., Gawthorpe, R. L., Pennos, C., & Riiser, O. S. (2018). Source-to-sink analysis in an active extensional setting: Holocene erosion and deposition in the Sperchios rift, central Greece. *Basin Research*, *30*, 522–543. https://doi.org/10.1111/bre.12263

Piper, D. J. W., Kontopoulos, N., Anagnostou, C., Chronis, G., & Panagos, A. G. (1990). Modern Fan Deltas in the Western Gulf of Corinth, Greece. *Geo-Marine Letters*, *10*, 5–12. https://doi.org/10.1007/BF02431016

Platt, N. H., & Keller, B. (1992). Distal alluvial deposits in a foreland basin setting—the Lower Freshwater Miocene, Switzerland: Sedimentology, architecture and palaeosols. *Sedimentology*, *39*, 545–565. https://doi.org/10.1111/j.1365-3091.1992.tb02136.x

Puy-Alquiza, M. J., Miranda-Avilés, R., García-Barragán, J. C., Loza-Aguirre, I., Li, Y., & Zanor, G. A. (2017). Facies analysis, stratigraphic architecture and depositional environments of the Guanajuato conglomerate in the Sierra de Guanajuato, Mexico. *Boletin De La Sociedad Geologica Mexicana*, *69*, 385–408. https://doi.org/10.18268/BSGM2017v69n2a5

Reading, H. G. (1996). *Sedimentary Environments: Processes, Facies and Stratigraphy, 3rd*. Oxford: Blackwell Scientific.

Reitz, M. D., & Jerolmack, D. J. (2012). Experimental alluvial fan evolution: Channel dynamics, slope controls, and shoreline growth. *Journal of Geophysical Research: Earth Surface*, *117*, 1–19. https://doi.org/10.1029/2011JF002261

Retallack, G. J. (2001). *Soils of the Past. An introduction to Paleopedology*, 2nd ed. (p. 404). Oxford: Blackwell Science.

Rohais, S., Eschard, R., Ford, M., Guillocheau, F., & Moretti, I. (2007). Stratigraphic architecture of the Plio-Pleistocene infill of the Corinth Rift: Implications for its structural evolution. *Tectonophysics*, *440*, 5–28. https://doi.org/10.1016/j.tecto.2006.11.006

Rohais, S., Eschard, R., & Guillocheau, F. (2008). Depositional model and stratigraphic architecture of rift climax Gilbert-type fan deltas (Gulf of Corinth, Greece). *Sedimentary Geology*, *210*, 132–145. https://doi.org/10.1016/j.sedgeo.2008.08.001

Seger, M., & Alexander, J. (1993). Distribution of Plio-Pleistocene and Modern Coarse-Grained Deltas South of the Gulf of Corinth, Greece. *Tectonic Controls and Signatures in Sedimentary Successions*, *20*, 37–48.

Shukla, U. K. (2009). Sedimentation model of gravel-dominated alluvial piedmont fan, Ganga Plain, India. *International Journal of Earth Sciences*, *98*, 443–459. https://doi.org/10.1007/s00531-007-0261-4

Sinclair, I. K., Shannon, P. M., Williams, B. P. J., Harker, S. D., & Mooren, J. G. (1994). Tectonic control on sedimentary evolution of three North Atlantic borderland Mesozoic basins1. *Basin Research*, *6*, 193–217. https://doi.org/10.1111/j.1365-2117.1994.tb00085.x

Skourlis, K., & Doutsos, T. (2003). The Pindos Fold-and-thrust belt (Greece): Inversion kinematics of a passive continental margin. *International Journal of Earth Sciences*, *92*, 891–903. https://doi.org/10.1007/s00531-003-0365-4

Sohn, Y. K., Rhee, C. W., & Kim, B. C. (1999). Debris Flow and Hyperconcentrated Flood-Flow Deposits in an Alluvial Fan, Northwestern Part of the Cretaceous Yongdong Basin, Central Korea. *The Journal of Geology*, *107*, 111–132. https://doi.org/10.1086/314334

Sorel, D. (2000). A Pleistocene and still-active detachment fault and the origin of the Corinth-Patras rift, Greece. *Geology*, *28*, 83–86. https://doi.org/10.1130/0091-7613(2000)28<83:APASDF>2.0.CO;2

Steel, R. J., & Thompson, D. B. (1983). Structures and textures in Triassic braided stream conglomerates ("Bunter" Pebble Beds) in the Sherwood Sandstone Group, North Staffordshire, England. *Sedimentology*, *30*, 341–367. https://doi.org/10.1111/j.1365-3091.1983.tb00677.x

Suresh, N., Bagati, T. N., Kumar, R., & Thakur, V. C. (2007). Evolution of quaternary alluvial fans and terraces in the intramontane Pinjaur Dun, Sub-Himalaya, NW India: Interaction between tectonics and climate change. *Sedimentology*, *54*, 809–833. https://doi.org/10.1111/j.1365-3091.2007.00861.x

Teixeira, B. M. N., Astini, R. A., Gomez, F. J., Morales, N., & Pimentel, M. M. (2018). Source-to-sink analysis of continental rift sedimentation: Triassic Cuyo basin, Precordillera Argentina. *Sedimentary Geology*, *376*, 164–184. https://doi.org/10.1016/j.sedgeo.2018.08.007

Todd, S. P. (1989). Stream-driven, high-density gravelly traction carpets: Possible deposits in the Trabeg Conglomerate Formation, SW Ireland and some theoretical considerations of their origin. *Sedimentology*, *36*, 513–530. https://doi.org/10.1111/j.1365-3091.1989.tb02083.x

Turner, S. A. (2010). Sedimentary record of Late Neoproterozoic rifting in the NW Tarim Basin, China. *Precambrian Research*, *181*, 85–96. https://doi.org/10.1016/j.precamres.2010.05.015

Underhill, J. R. (1989). Late Cenozoic deformation of the Hellenic foreland, Western Greece. *Bulletin of the Geological Society of America*, *101*, 613–634.

van Dijk, M., Kleinhans, M. G., Postma, G., & Kraal, E. (2012). Contrasting morphodynamics in alluvial fans and fan deltas: Effect of the downstream boundary. *Sedimentology*, *59*, 2125–2145. https://doi.org/10.1111/j.1365-3091.2012.01337.x

Wells, N. A. (1984). Sheet debris flow and Sheetflood conglomerates in Cretaceous cool-maritime alluvial fans, South Orkney Islands, Antarctica. *Sedimentology of Gravels and Conglomerates*, *10*, 133–145.

Went, D. J. (2005). Pre-vegetation alluvial fan facies and processes: An example from the Cambro-Ordovician Rozel Conglomerate Formation, Jersey, Channel Islands. *Sedimentology*, *52*, 693–713. https://doi.org/10.1111/j.1365-3091.2005.00716.x

Zelilidis, A. (2000). Drainage evolution in a rifted basin, Corinth graben, Greece. *Geomorphology*, *35*, 69–85. https://doi.org/10.1016/S0169-555X(00)00023-4

Zaghloul, M. N., Critelli, S., Perri, F., Mongelli, G., Perrone, V., Sonnino, M., … Ventimiglia, C. (2010). Depositional systems, composition and geochemistry of Triassic rifted-continental margin redbeds of the Internal Rif Chain. *Morocco. Sedimentology*, *57*(2), 312–350.

How to cite this article: Somerville DJP, Mountney NP, Colombera L, Collier REL. Impact of a pre-existing transverse drainage system on active rift stratigraphy: An example from the Corinth Rift, Greece. *Basin Res*. 2020;32:764–788. https://doi.org/10.1111/bre.12396

ID	form	fan_area	catchment_area	active_lobe_area	active_lobe_%	fan_slope	w_l_fan	w_l_catchment	meltons
fwall_1	iso	2.95	14.59	0.4	13.56	0.018	1.17	0.42	0.09
fwall_2	iso	13.31	45.87	1.68	12.62	0.014	1.80	0.45	0.05
fwall_3	baj	2.04	4.62	0.44	21.57	0.026	1.34	0.81	0.15
fwall_4	baj	4.97	10.83	0.87	17.51	0.024	0.87	1.50	0.11
fwall_5	iso	24.31	75.57	13.87	57.05	0.014	1.19	0.50	0.05
fwall_6	baj	5.91	6.59	2.47	41.79	0.021	0.65	1.15	0.17
fwall_7	baj	1.65	2.56	0.2	12.12	0.027	0.56	0.27	0.27
fwall_8	baj	38.62	74.42	14.79	38.30	0.020	0.58	1.70	0.06
fwall_9	baj	63.65	82.14	24.46	38.43	0.021	1.13	0.86	0.07
fwall_10	iso	35.48	109.26	15.12	42.62	0.029	1.74	0.99	0.11
fwall_11	iso	1.30	4.44	0.18	13.85	0.044	0.97	0.73	0.37
fwall_12	baj	4.50	10.22	2.22	49.33	0.042	1.40	0.92	0.36
fwall_13	baj	2.41	5.61	1.22	50.62	0.031	0.72	0.43	0.46
fwall_14	baj	1.48	4.37	1	67.57	0.035	0.72	0.64	0.44
fwall_15	iso	6.37	19.84	1.42	22.29	0.031	1.14	0.74	0.22
fwall_16	baj	2.91	6.40	0.6	20.62	0.043	0.95	0.63	0.40
fwall_17	baj	2.92	5.72	1.2	41.10	0.042	0.56	0.96	0.40
fwall_18	baj	2.72	2.95	0.54	19.85	0.040	0.43	0.71	0.55
fwall_19	baj	2.81	4.32	0.48	17.08	0.038	0.37	0.73	0.48
fwall_20	baj	3.43	3.54	0.54	15.74	0.039	0.34	0.49	0.55
fwall_21	baj	3.38	4.24	0.59	17.46	0.030	0.27	0.33	0.53
fwall_22	baj	7.48	10.00	3.39	45.32	0.035	0.56	0.66	0.39
fwall_23	baj	5.99	6.03	2.24	37.40	0.031	0.62	0.30	0.47
fwall_24	baj	8.52	14.56	3.65	42.84	0.034	0.82	0.47	0.36
fwall_25	iso	0.80	2.06	0.21	26.25	0.037	1.22	0.48	0.35
fwall_26	iso	14.26	30.84	5.17	36.26	0.024	1.62	0.44	0.28
fwall_27	iso	0.63	1.85	0.1	15.87	0.042	1.11	0.81	0.23
fwall_28	iso	0.54	1.41	0.1	18.52	0.034	1.16	0.42	0.36
fwall_29	baj	0.76	3.51	0.19	25.00	0.035	0.90	0.88	0.37
fwall_30	iso	4.74	18.40	1.54	32.49	0.042	1.00	0.68	0.34
fwall_31	baj	1.77	6.76	0.6	33.90	0.042	1.00	0.19	0.58
fwall_32	iso	5.78	28.11	1.57	27.16	0.032	1.59	0.43	0.29
fwall_33	iso	0.53	2.71	0.24	45.28	0.063	1.44	0.49	0.61
fwall_34	iso	3.35	10.62	1.45	43.28	0.049	1.48	0.77	0.39
fwall_35	iso	6.68	26.55	1.67	25.00	0.050	1.37	1.04	0.27
fwall_36	iso	6.48	22.37	2.22	34.26	0.047	1.46	0.50	0.32
fwall_37	iso	3.46	11.95	0.55	15.90	0.051	1.28	0.37	0.41
hwall_1	iso	20.63	37.49	8.88	43.04	0.008	0.63	0.50	0.02
hwall_2	baj	26.82	139.59	5.93	22.11	0.010	0.88	0.28	0.02
hwall_3	baj	10.36	24.61	3.26	31.47	0.012	0.47	0.20	0.04
hwall_4	iso	29.33	286.89	10.68	36.41	0.011	0.68	0.20	0.04
hwall_5	iso	17.26	222.17	7.72	44.73	0.011	0.44	0.45	0.03
hwall_6	iso	9.30	80.88	1.97	21.18	0.013	0.82	0.45	0.03
hwall_7	iso							0.32	0.04
hwall_8	iso	6.73	166.67	1.85	27.49	0.011	0.80	0.33	0.04
hwall_9	iso	4.16	89.41	1.89	45.43	0.013	0.56	0.41	0.04
hwall_10	iso	16.64	28.08	3.88	23.32	0.013	0.88	0.19	0.04
hwall_11	iso	13.52	213.33	5.73	42.38	0.014	0.81	0.34	0.04
hwall_12	iso	28.08	330.97	10.39	37.00	0.016	0.73	0.51	0.05
hwall_13	iso	6.88	42.42	1.83	26.60	0.016	0.82	0.59	0.06
hwall_14	iso	6.72	382.65	2.1	31.25	0.016	0.60	0.88	0.07
hwall_7		72.23	1760.87	14.8	20.49	0.009	1.29	0.32	0.04

	catchment_elevation_difference
fwall1	339
	367
	325
	370
	447
	435
	429
	548
	655
	1163
	789
	1138
	1083
	914
	958
	1003
	965
	937
	995
	1032
	1082
	1237
	1163
	1375
	501
	1540
	317
	428
	691
	1469
	1509
	1518
	1011
	1285
	1373
	1498
	1423
hwall1	121
	286
	179
	690
	478
	234
	1703
	512
	352
	219
	550
	872
	368
	1279

blue HWALL
green FWALL

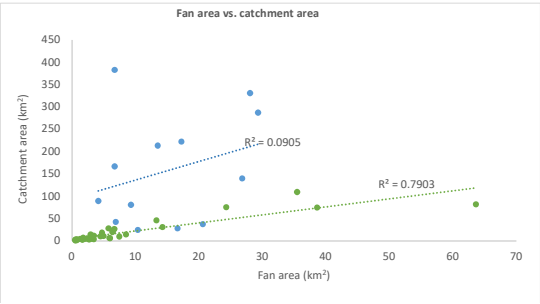

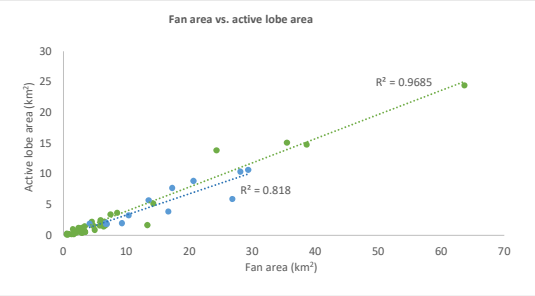

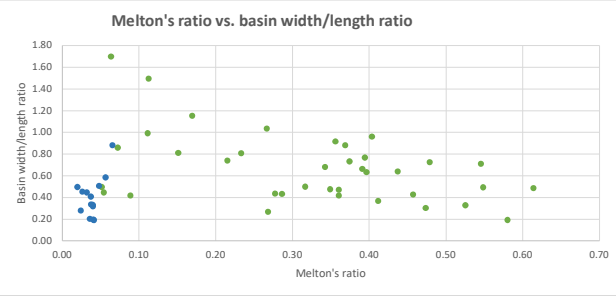

ID	form	fan_area	catchment_area	active_lobe_area	active_lobe_%	fan_slope	w_l_fan	shape_factor w_l_catchment	meltons	elevation_diff	catchment_width	catchment_length
fwall_1		8.99	33.91	1.01	11.23	0.065	1.48	0.89	0.32	1847	7824	8831
fwall_2		6.74	6.80	1.33	19.73	0.110	0.57	0.60	0.58	1517	2309	3848
fwall_3		5.99	16.63	1.41	23.54	0.077	1.04	0.59	0.44	1782	3707	6312
fwall_4		2.76	14.97	0.56	20.29	0.086	1.53	0.44	0.48	1846	3235	7408
fwall_5		8.92	31.25	1.12	12.56	0.059	1.16	0.75	0.30	1664	5573	7431
fwall_6		4.73	23.95	1.44	30.44	0.056	0.73	0.63	0.35	1710	4855	7698
fwall_7		3.68	21.39	0.91	24.73	0.067	0.31	0.51	0.38	1763	3664	7251
fwall_8		7.66	32.75	1.23	16.06	0.032	1.21	0.40	0.36	2034	4790	11939
fwall_9		18.02	25.27	3.59	19.92	0.028	1.08	0.58	0.39	1962	4837	8289
fwall_10		7.00	10.84	0.97	13.86	0.075	0.49	0.59	0.41	1362	3232	5470
fwall_11		38.74	150.24	6.30	16.26	0.018	1.64	0.57	0.16	2005	12456	21715
fwall_12		10.65	30.30	2.83	26.57	0.054	0.64	1.11	0.30	1629	7590	6833
fwall_13		8.30	20.89	0.46	5.54	0.050	0.93	0.57	0.30	1370	3982	6979
fwall_14		33.05	184.14	2.36	7.14	0.019	1.23	0.35	0.14	1950	9777	28034
fwall_15		49.43	66.44	4.63	9.37	0.044	0.87	0.55	0.23	1908	8096	14617
fwall_16		24.39	81.09	5.89	24.15	0.024	0.47	0.39	0.22	1963	6226	16025
fwall_17		50.45	236.52	8.83	17.50	0.021	1.24	0.29	0.13	1960	8862	30654
fwall_18		38.18	144.39	5.62	14.72	0.030	0.96	0.96	0.15	1805	15773	16353
fwall_19		14.83	29.82	2.55	17.19	0.063	0.69	0.48	0.29	1571	5092	10697
fwall_20		15.19	40.84	2.21	14.55	0.054	0.96	0.61	0.29	1835	6648	10842
fwall_21		71.70	607.36	14.77	20.60	0.013	0.80	0.53	0.08	1888	21613	41119
hwall_1		84.82	498.59	11.58	13.65	0.013	0.75	1.29	0.09	1975	31450	24463
hwall_2		15.19	997.35	9.02	59.38	0.007	0.68	0.45	0.07	2176	29158	65062
hwall_3		34.54	603.16	2.51	7.27	0.013	3.39	0.40	0.08	1974	22249	55006
hwall_4		36.09	781.66	3.83	10.61	0.009	2.05	0.70	0.07	1930	30232	43075
hwall_5		110.55	1855.56	18.93	17.12	0.004	1.14	0.49	0.05	2175	36985	76176

0.916416 correlation coefficient, footwall fan area to active lobe area
0.817002 correlation coefficient, hangingwall fan area to active lobe area

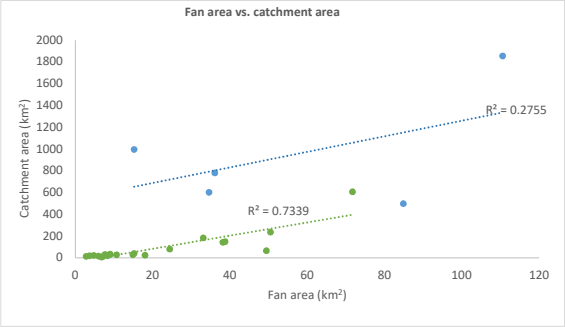

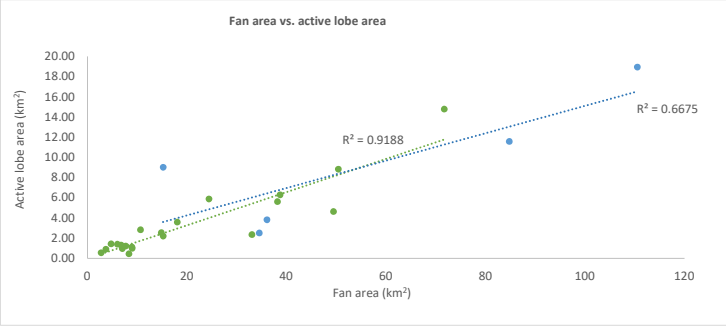

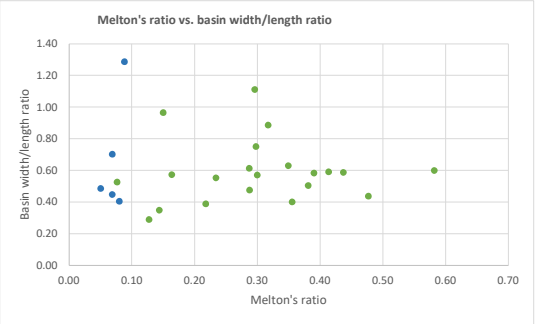

TOIYABE								shape_factor			**FAN**		**CATCHMENT**		**SLOPE**	
ID	form	fan area	catchment area	active lobe area	active lobe %	fan slope	w l fan	w l catchment	meltons	elevation diff	width	length	width	length	length	height
fwall 1		42.58	39.86	8.45	19.84	0.023	0.61	0.97	0.24	1510	7540	12461	7579	7851	12600	291
fwall 2		1.98	3.83	0.28	14.14	0.090	0.77	0.37	0.57	1124	1407	1827	1443	3953	1810	163
fwall 3		5.02	11.32	1.01	20.12	0.050	0.45	0.39	0.41	1376	1633	3644	2651	6821	4060	203
fwall 4		6.91	10.60	0.44	6.37	0.041	0.32	0.41	0.41	1333	1753	5440	2642	6451	5540	227
fwall 5		4.96	11.03	1.03	20.77	0.044	0.27	0.33	0.40	1315	1355	5029	2238	6825	5010	221
fwall 6		7.70	9.41	1.22	15.84	0.062	0.49	0.52	0.40	1229	2211	4489	2684	5197	4490	278
fwall 7		8.45	11.56	1.14	13.50	0.077	0.84	0.82	0.40	1361	2917	3461	3344	4079	3850	296
fwall 8		16.60	14.36	0.88	5.30	0.065	0.79	2.11	0.33	1245	3862	4889	6160	2922	5420	354
fwall 9		11.20	9.54	0.76	6.79	0.037	0.80	0.84	0.41	1258	3830	4779	3456	4103	5540	205
fwall 10		3.07	5.12	0.82	26.71	0.055	0.43	0.26	0.65	1462	1418	3319	1379	5392	3400	188
fwall 11		2.49	2.82	0.31	12.45	0.078	0.32	0.36	0.74	1246	1168	3673	1334	3712	3620	281
fwall 12		2.50	2.46	0.24	9.60	0.065	0.37	0.48	0.55	861	1327	3551	1208	2512	3630	236
fwall 13		12.29	19.57	1.09	8.87	0.045	0.51	0.56	0.31	1359	3202	6246	3639	6485	6250	279
fwall 14		51.69	71.78	8.61	16.66	0.020	0.86	0.45	0.19	1581	9677	11271	6698	14917	10700	210
fwall 15		5.95	11.04	0.45	7.56	0.078	0.96	0.80	0.45	1498	2723	2822	3588	4460	2970	232
fwall 16		3.53	4.05	0.43	12.18	0.077	0.46	0.43	0.67	1355	1593	3471	1564	3647	3500	269
fwall 17		4.60	5.35	0.70	15.22	0.084	0.46	0.60	0.58	1336	1700	3661	2368	3949	3740	314
fwall 18		4.22	4.98	0.56	13.27	0.083	0.40	0.41	0.60	1343	1444	3614	1610	3938	3530	293
fwall 19		3.63	4.63	0.47	12.95	0.086	0.42	0.53	0.59	1280	1512	3570	1916	3642	3380	292
fwall 20		14.27	9.34	2.79	19.55	0.035	1.06	0.49	0.41	1250	5761	5428	2538	5201	5570	197
fwall 21		6.32	6.52	0.49	7.75	0.051	0.42	0.43	0.51	1292	2036	4883	2159	5056	4900	248
fwall 22		1.73	3.15	0.37	21.39	0.076	0.17	0.46	0.59	1052	804	4766	1372	2987	4840	369
fwall 23		2.97	4.00	0.60	20.20	0.062	0.28	0.55	0.43	869	1547	5540	1777	3246	5730	357
fwall 24		79.61	48.15	11.31	14.21	0.013	0.92	0.56	0.20	1405	11330	12256	6977	12378	12300	160
hwall 1		14.91	36.62	1.87	12.54	0.028	0.72	0.95	0.19	1139	4619	6452	8007	8426	6360	179
hwall 2		18.52	49.10	3.18	17.17	0.028	1.43	0.96	0.18	1281	6966	4881	8837	9242	5850	162
hwall 3		16.86	24.00	2.09	12.40	0.029	0.53	0.33	0.27	1314	3627	6846	3349	10078	6920	198
hwall 4		23.80	23.31	2.17	9.12	0.043	1.21	0.80	0.24	1160	7047	5844	5318	6628	6650	286
hwall 5		7.84	12.66	3.18	40.56	0.052	0.56	1.23	0.30	1052	3727	6660	5174	4206	6640	342
hwall 6		10.16	6.52	1.56	15.35	0.046	0.86	1.04	0.38	969	3874	4526	3376	3246	4500	209
hwall 7		10.45	11.38	1.49	14.26	0.036	0.46	1.15	0.31	1041	2850	6223	4191	3645	5970	213
hwall 8		48.83	30.49	8.58	17.57	0.022	1.17	1.01	0.25	1401	9826	8388	7241	7152	9390	209

TOQUIMA								shape_factor			**FAN**		**CATCH**		**SLOPE**	
ID	form	fan area	catchment area	active lobe area	active lobe %	fan slope	w l fan	w l catchment	meltons	elevation diff	width	length	width	length	length	height
fwall 1		17.23	66.30	1.37	7.95	0.014	0.76	1.21	0.13	1089	5742	7533	10891	9027	7500	103
fwall 2		6.33	18.24	1.49	23.54	0.019	0.93	0.65	0.18	764	4451	4769	4666	7187	4720	90
fwall 3		7.56	4.28	2.20	29.10	0.026	0.89	0.54	0.24	494	3222	3626	1903	3546	3680	97
fwall 4		4.48	2.10	1.48	33.04	0.026	0.67	0.28	0.27	389	2398	3595	925	3327	3390	89
fwall 5		13.84	11.52	2.31	16.69	0.029	0.83	0.45	0.19	641	4283	5183	2748	6125	5580	160
fwall 6		21.68	30.70	5.54	25.55	0.030	0.60	0.71	0.24	1311	4286	7193	5692	8028	6660	201
fwall 7		12.94	18.41	4.37	33.77	0.017	0.55	1.02	0.12	528	3538	6449	5803	5688	5720	97
fwall 8		1.96	2.53	0.42	21.43	0.037	0.57	0.77	0.20	314	1317	2300	1642	2145	2550	95
fwall 9		1.61	3.60	0.36	22.36	0.047	0.87	0.38	0.21	402	1448	1661	1469	3875	1780	84
fwall 10		16.17	32.85	1.94	12.00	0.021	1.00	0.42	0.11	635	5311	5288	4516	10707	5420	112
fwall 11		9.95	22.11	0.43	4.32	0.021	0.78	0.38	0.19	903	3450	4400	3719	9877	4440	95
fwall 12		17.94	22.58	2.44	13.60	0.028	0.85	0.81	0.20	943	4844	5692	5285	6557	6300	177
fwall 13		8.97	5.06	0.80	8.92	0.054	0.60	0.57	0.38	853	2758	4567	2229	3926	4590	248
fwall 14		18.21	17.35	1.61	8.84	0.034	0.98	0.61	0.22	933	5630	5737	3665	5961	5770	199
hwall 1		11.53	8.47	1.86	16.13	0.054	0.24	0.36	0.43	1252	2135	8715	2043	5699	8340	449
hwall 2		13.80	19.75	2.69	19.49	0.049	0.31	0.65	0.30	1334	2897	9400	4100	6323	9460	459
hwall 3		8.97	7.66	1.52	16.95	0.039	0.37	0.52	0.33	909	2146	5795	2367	4577	6110	240
hwall 4		27.42	47.75	4.97	18.13	0.027	0.38	0.63	0.23	1621	3801	9991	6132	9660	9930	269
hwall 5		19.78	86.14	4.73	23.91	0.023	0.39	1.11	0.10	955	3062	7881	12276	11099	8600	202
hwall 6		15.93	17.98	5.23	32.83	0.051	0.55	0.67	0.14	577	3319	6066	3671	5456	6030	309
hwall 7		42.68	35.35	13.75	32.22	0.023	0.60	0.68	0.19	1146	7349	12233	6442	9483	12100	280
hwall 8		3.04	4.64	3.04	100.00	0.031	0.18	0.36	0.19	413	1198	6501	1454	4090	6220	195
hwall 9		10.41	10.37	10.41	100.00	0.026	0.22	0.29	0.31	987	2349	10764	2266	7892	10400	269
hwall 10		41.69	49.36	19.30	46.29	0.035	0.41	0.90	0.17	1215	4636	11386	6727	7506	11700	406

Toiyabe	Toquima	
0.974495	0.632231729	correlation coefficient, footwall fan area to active lobe area
0.894026	0.801005081	correlation coefficient, hangingwall fan area to active lobe area

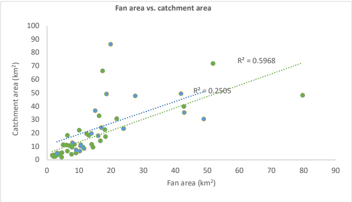

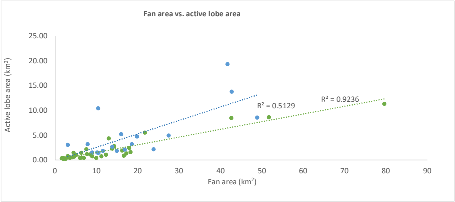

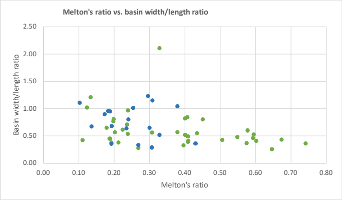

	FOOTWALL_ALL					HWALL_ALL				
	fan	catch	phi	log10catch		fan	catch	phi	log10catch	
	2.95	14.59	0.20	1.16		20.63	37.49	0.55	1.57	
	13.31	45.87	0.29	1.66		26.82	139.59	0.19	2.14	
	2.04	4.62	0.44	0.66		10.36	24.61	0.42	1.39	
	4.97	10.83	0.46	1.03		29.33	286.89	0.10	2.46	
	24.31	75.57	0.32	1.88		17.26	222.17	0.08	2.35	
	5.91	6.59	0.90	0.82		9.30	80.88	0.11	1.91	
	1.65	2.56	0.64	0.41		6.73	166.67	0.04	2.22	
	38.62	74.42	0.52	1.87		4.16	89.41	0.05	1.95	
	63.65	82.14	0.77	1.91		16.64	28.08	0.59	1.45	
	35.48	109.26	0.32	2.04		13.52	213.33	0.06	2.33	
	1.30	4.44	0.29	0.65		28.08	330.97	0.08	2.52	
	4.50	10.22	0.44	1.01		6.88	42.42	0.16	1.63	
	2.41	5.61	0.43	0.75		6.72	382.65	0.02	2.58	**EARS**
	1.48	4.37	0.34	0.64		84.82	498.59	0.17	2.70	
	6.37	19.84	0.32	1.30		15.19	997.35	0.02	3.00	
	2.91	6.40	0.45	0.81		34.54	603.16	0.06	2.78	
	2.92	5.72	0.51	0.76		36.09	781.66	0.05	2.89	
	2.72	2.95	0.92	0.47		110.55	1855.56	0.06	3.27	**BAIKAL**
	2.81	4.32	0.65	0.64		14.91	36.62	0.41	1.56	
	3.43	3.54	0.97	0.55		18.52	49.10	0.38	1.69	
	3.38	4.24	0.80	0.63		16.86	24.00	0.70	1.38	
	7.48	10.00	0.75	1.00		23.80	23.31	1.02	1.37	
	5.99	6.03	0.99	0.78		7.84	12.66	0.62	1.10	
	8.52	14.56	0.59	1.16		10.16	6.52	1.56	0.81	
	0.80	2.06	0.39	0.31		10.45	11.38	0.92	1.06	
	14.26	30.84	0.46	1.49		48.83	30.49	1.60	1.48	**TOIYABE**
	0.63	1.85	0.34	0.27		11.53	8.47	1.36	0.93	
	0.54	1.41	0.38	0.15		13.80	19.75	0.70	1.30	
	0.76	3.51	0.22	0.55		8.97	7.66	1.17	0.88	
	4.74	18.40	0.26	1.26		27.42	47.75	0.57	1.68	
	1.77	6.76	0.26	0.83		19.78	86.14	0.23	1.94	
	5.78	28.11	0.21	1.45		15.93	17.98	0.89	1.25	
	0.53	2.71	0.20	0.43		42.68	35.35	1.21	1.55	
	3.35	10.62	0.32	1.03		3.04	4.64	0.66	0.67	
	6.68	26.55	0.25	1.42		10.41	10.37	1.00	1.02	
	6.48	22.37	0.29	1.35		41.69	49.36	0.84	1.69	**TOQUIMA**
EARS	3.46	11.95	0.29	1.08						
	8.99	33.91	0.27	1.53						
	6.74	6.80	0.99	0.83						
	5.99	16.63	0.36	1.22						
	2.76	14.97	0.18	1.18			298.89			
	8.92	31.25	0.29	1.49			695.83			
	4.73	23.95	0.20	1.38			0.42954			
	3.68	21.39	0.17	1.33						
	7.66	32.75	0.23	1.52			429.40			
	18.02	25.27	0.71	1.40			1809.79			
	7.00	10.84	0.65	1.04			0.23727			
	38.74	150.24	0.26	2.18						
	10.65	30.30	0.35	1.48						
	8.30	20.89	0.40	1.32						
	33.05	184.14	0.18	2.27						
	49.43	66.44	0.74	1.82						
	24.39	81.09	0.30	1.91						
	50.45	236.52	0.21	2.37						
	38.18	144.39	0.26	2.16						
	14.83	29.82	0.50	1.47						
	15.19	40.84	0.37	1.61						
BAIKAL	71.70	607.36	0.12	2.78						
	42.58	39.86	1.07	1.60						
	1.98	3.83	0.52	0.58						
	5.02	11.32	0.44	1.05						
	6.91	10.60	0.65	1.03						
	4.96	11.03	0.45	1.04						
	7.70	9.41	0.82	0.97						
	8.45	11.56	0.73	1.06						
	16.60	14.36	1.16	1.16						
	11.20	9.54	1.17	0.98						
	3.07	5.12	0.60	0.71						
	2.49	2.82	0.88	0.45						
	2.50	2.46	1.02	0.39						
	12.29	19.57	0.63	1.29						
	51.69	71.78	0.72	1.86						
	5.95	11.04	0.54	1.04						
	3.53	4.05	0.87	0.61						
	4.60	5.35	0.86	0.73						
	4.22	4.98	0.85	0.70						
	3.63	4.63	0.78	0.67						
	14.27	9.34	1.53	0.97						
	6.32	6.52	0.97	0.81						
	1.73	3.15	0.55	0.50						
	2.97	4.00	0.74	0.60						
TOIYABE	79.61	48.15	1.65	1.68						
	17.23	66.30	0.26	1.82						
	6.33	18.24	0.35	1.26						
	7.56	4.28	1.77	0.63						
	4.48	2.10	2.13	0.32						
	13.84	11.52	1.20	1.06						
	21.68	30.70	0.71	1.49						
	12.94	18.41	0.70	1.27						
	1.96	2.53	0.77	0.40						
	1.61	3.60	0.45	0.56						
	16.17	32.85	0.49	1.52						
	9.95	22.11	0.45	1.34						
	17.94	22.58	0.79	1.35						
	8.97	5.06	1.77	0.70						
TOQUIMA	18.21	17.35	1.05	1.24						

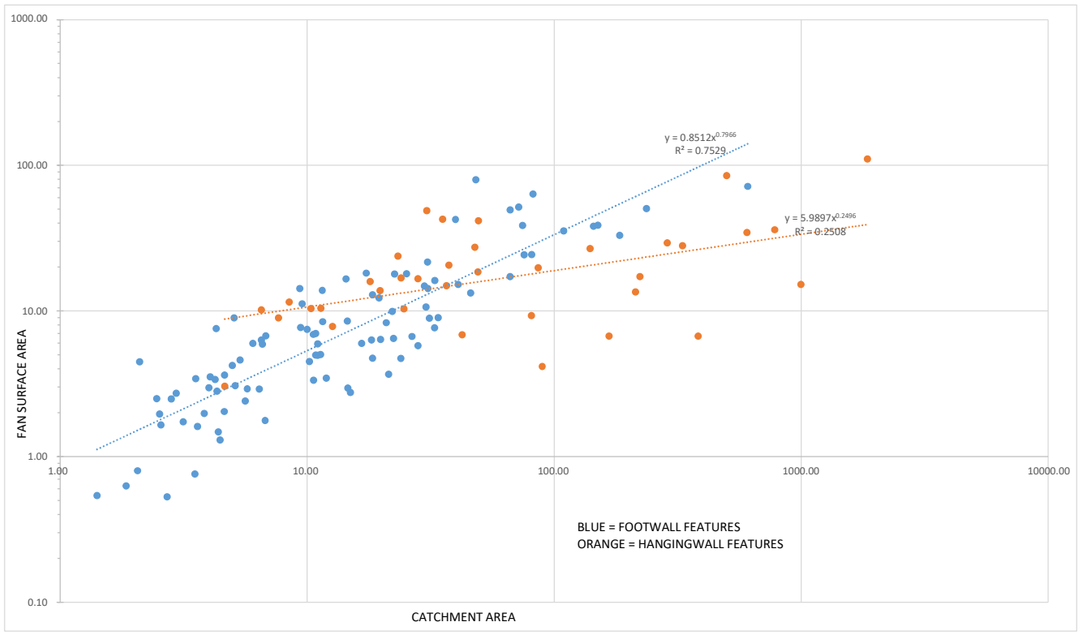

graphs below show phi vs log10 catchment area, according to Luca instructions

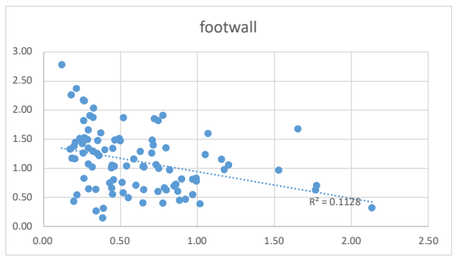

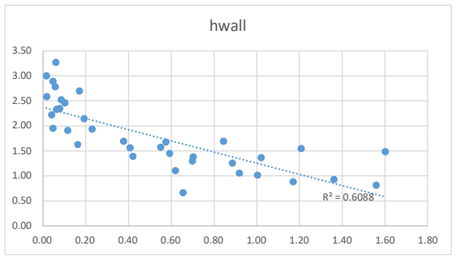

Sedimentary logs : Rodini Fm., Gulf of Corinth, Greece

The following pages contain blown-up images of the sedimentary log profiles taken from the Rodini Fm., Greece, shown in Chapter 4. Log locations are provided in the form of latitude and longitude values, and site locations (L1 -> L20) are also provided.

Vertical scale is in metres (m).

LOG L1
LAT: N38.31127
LONG: E21.85608

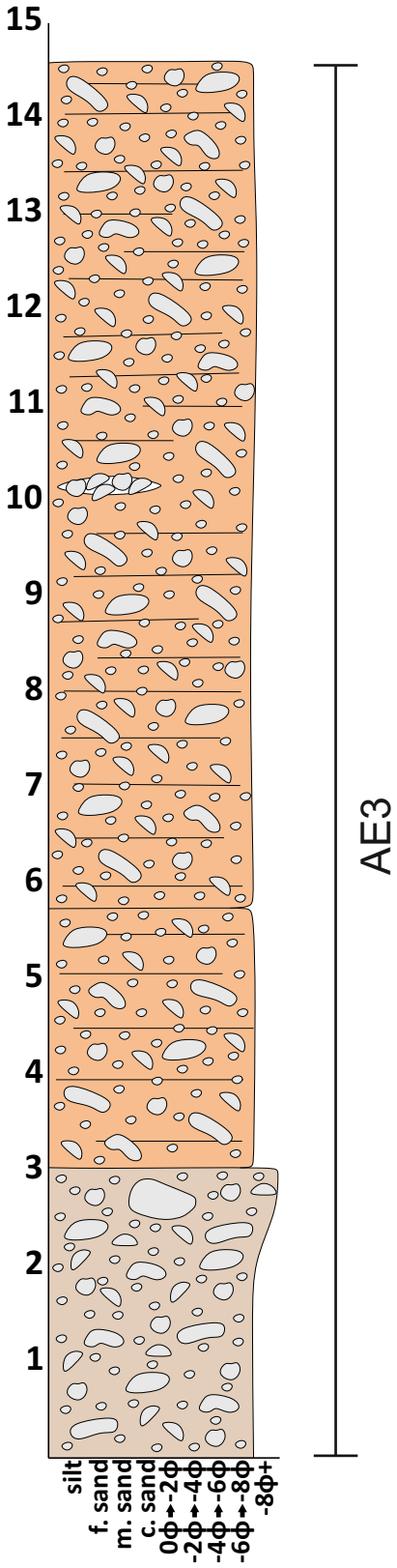

LOG L2
LAT: N38.29997
LONG: E21.86515

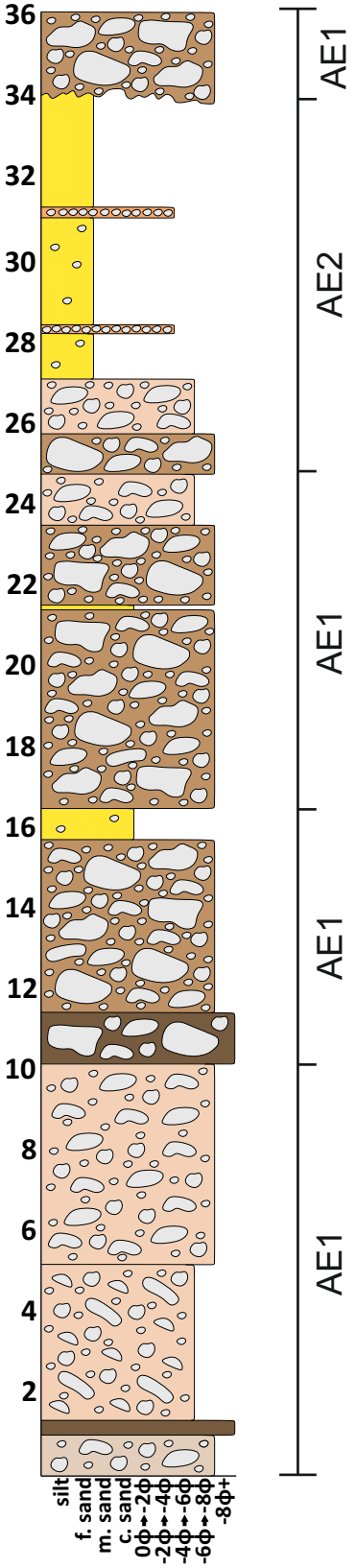

LOG L3
LAT: N38.28727
LONG: E21.96482

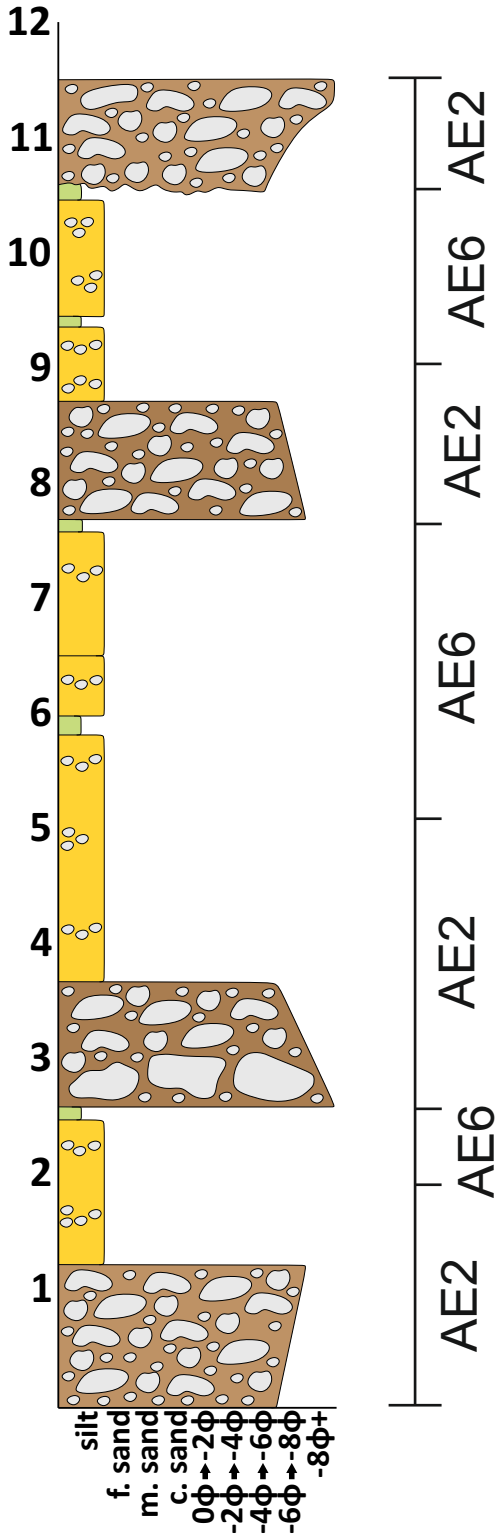

LOG L4
LAT: N38.30036
LONG: E21.97479

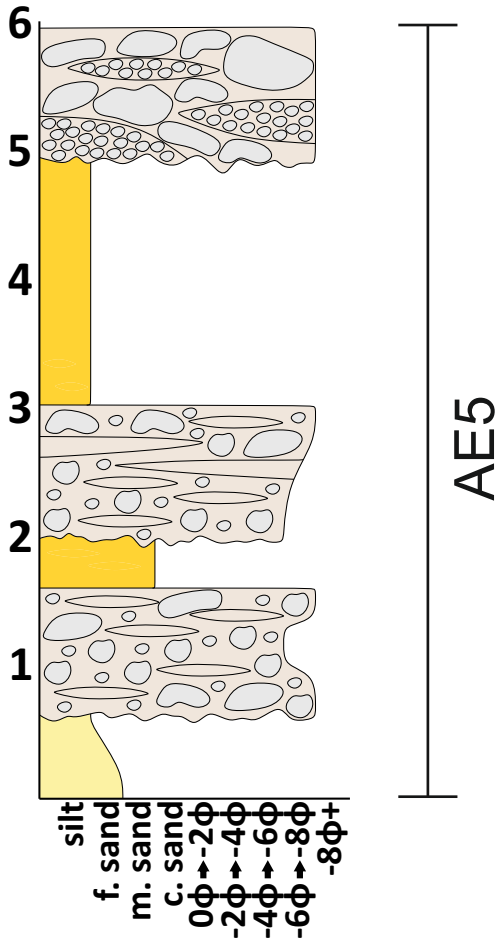

LOG L5
LAT: N38.29324
LONG: E21.98454

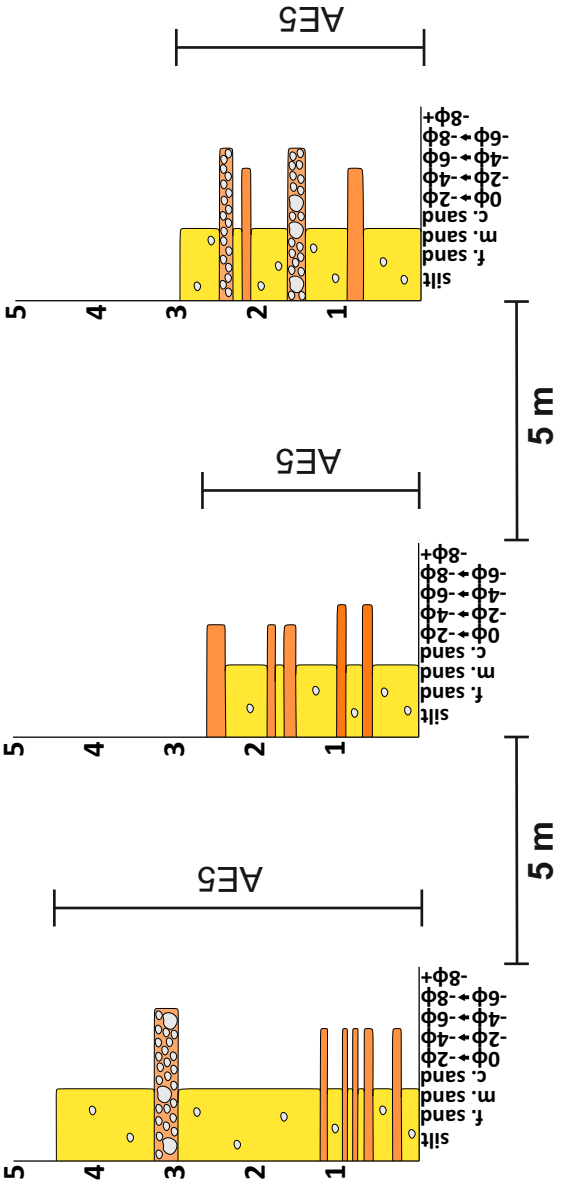

LOG L6
LAT: N38.29593
LONG: E21.99937

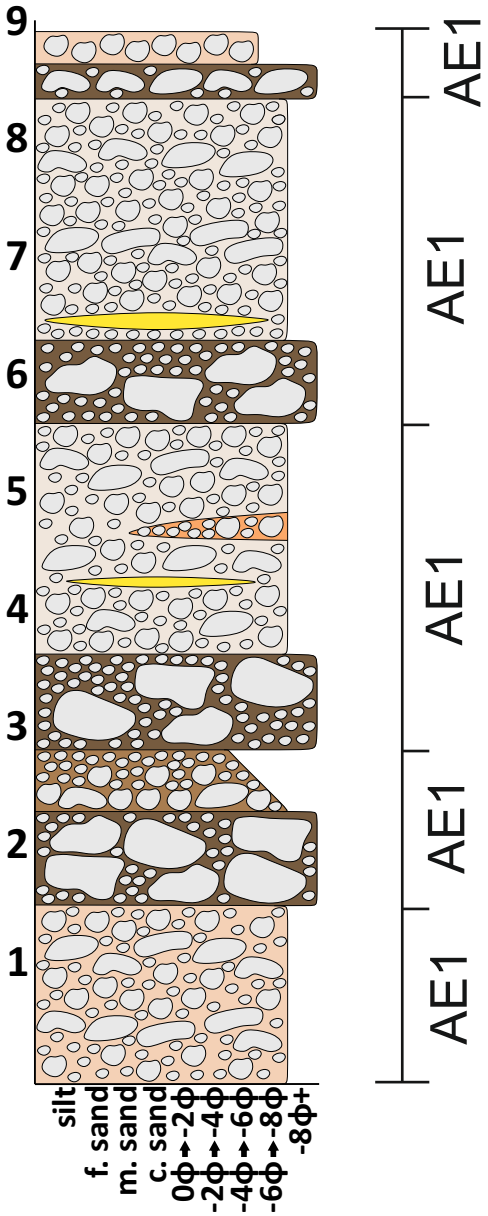

LOG L7
LAT: N38.27789
LONG: E21.85541

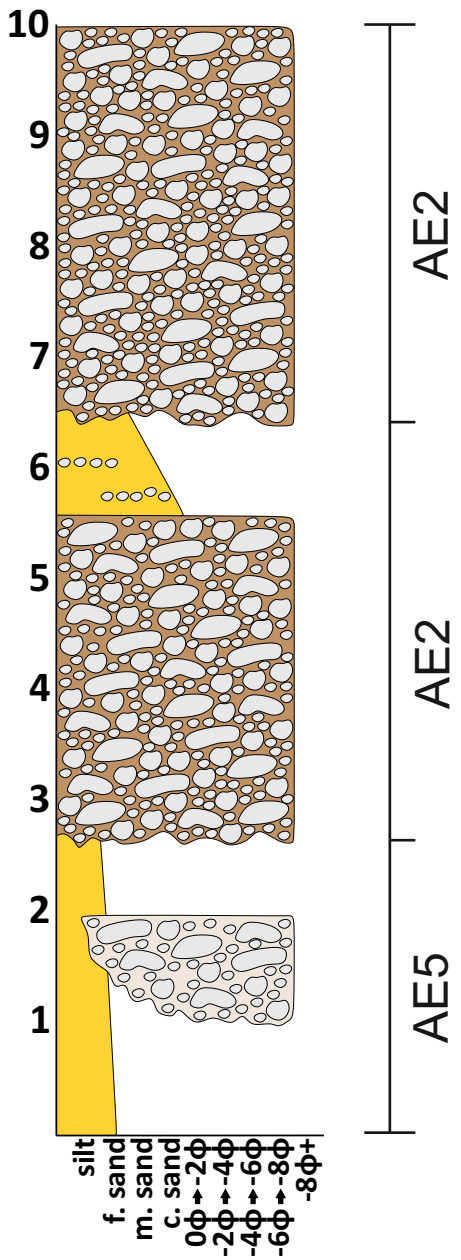

LOG L8
LAT: N38.29603
LONG: E21.85713

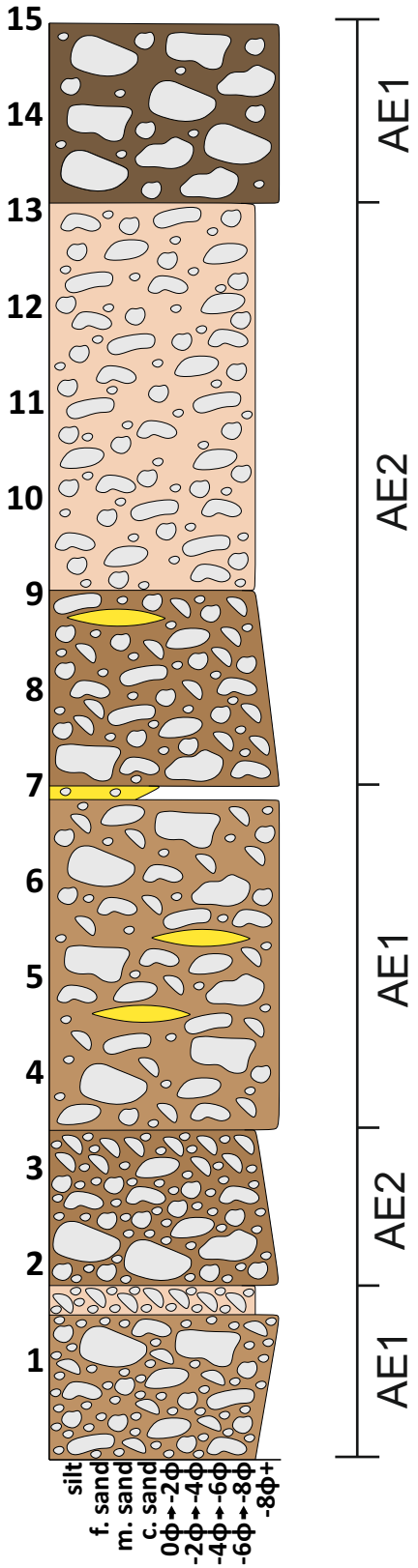

LOG L9
LAT: N38.28931
LONG: E21.89430

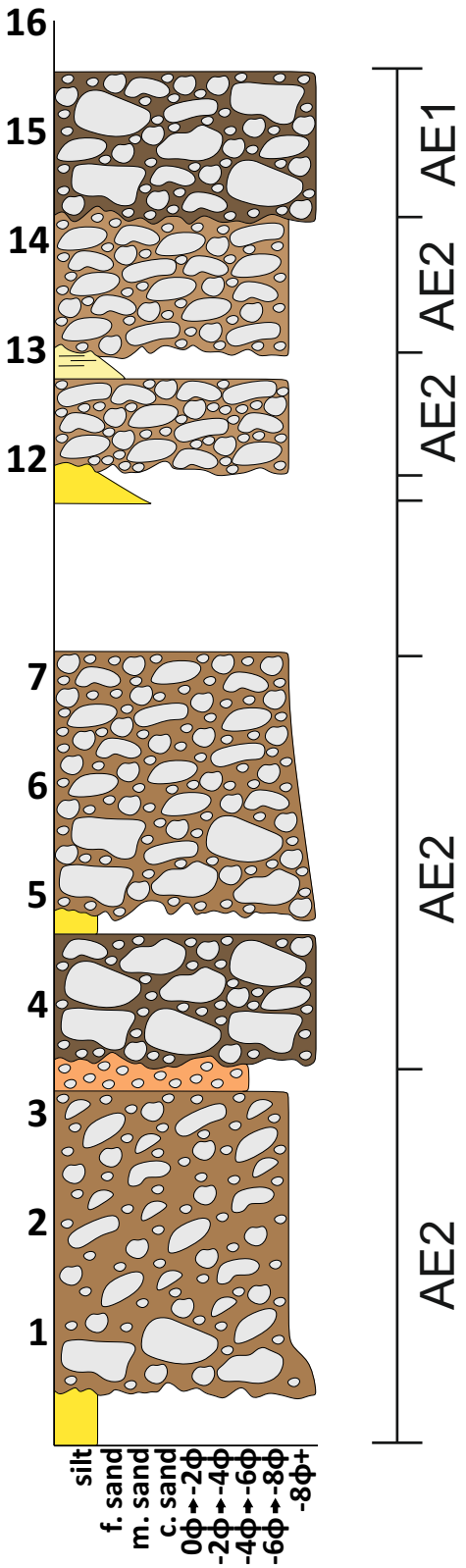

LOG L10
LAT: N38.26672
LONG: E21.93384

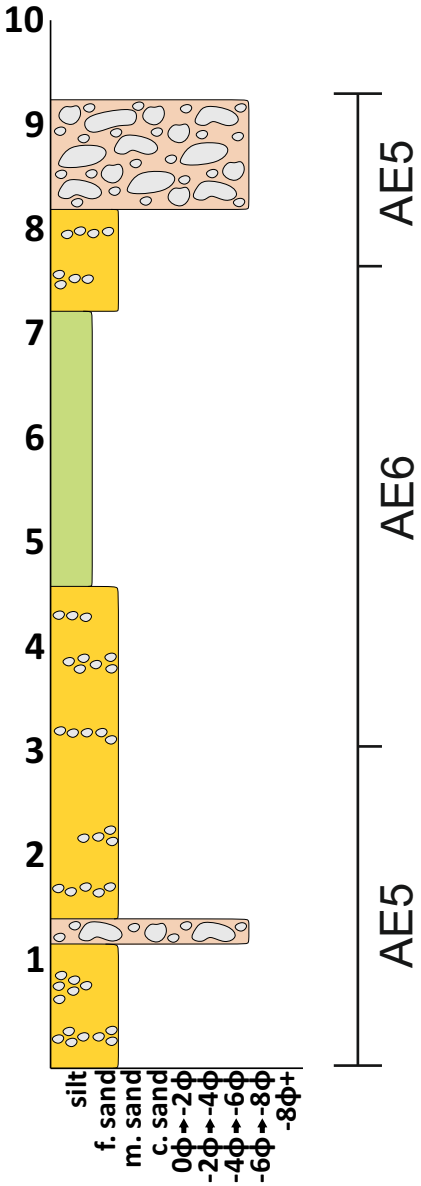

LOG L11
LAT: N38.28339
LONG: E21.94674

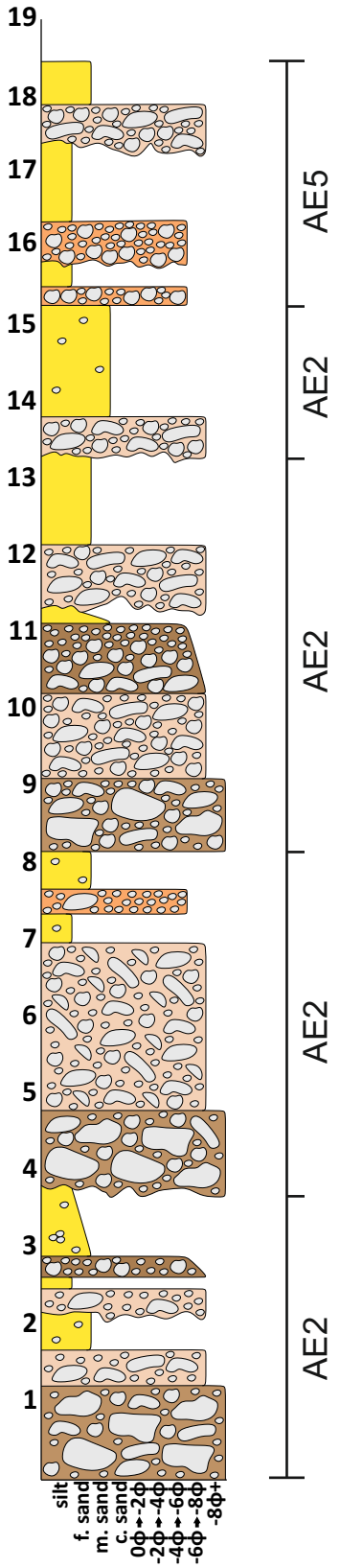

LOG L12
LAT: N38.28038
LONG: E21.95557

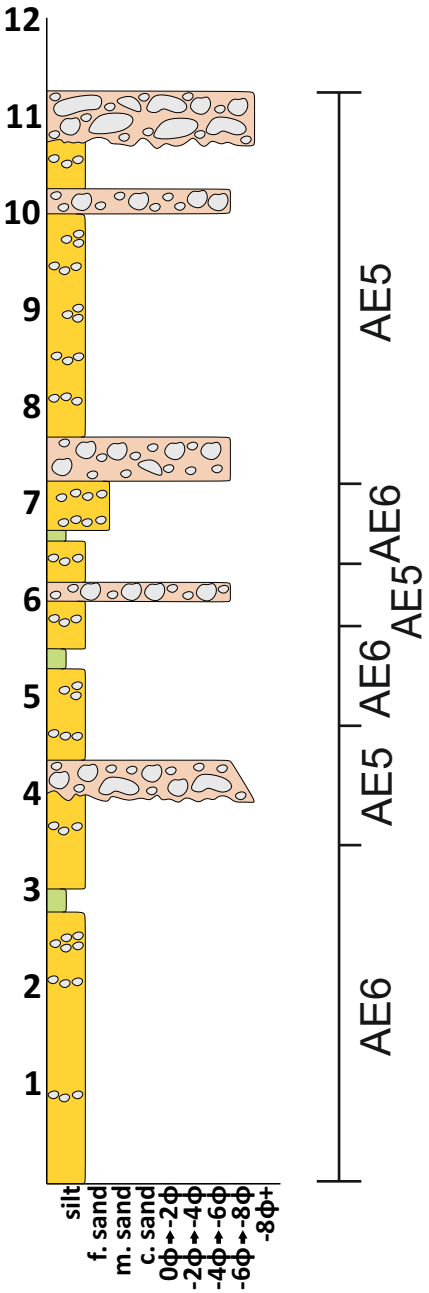

LOG L13
LAT: N38.28727
LONG: E21.96482

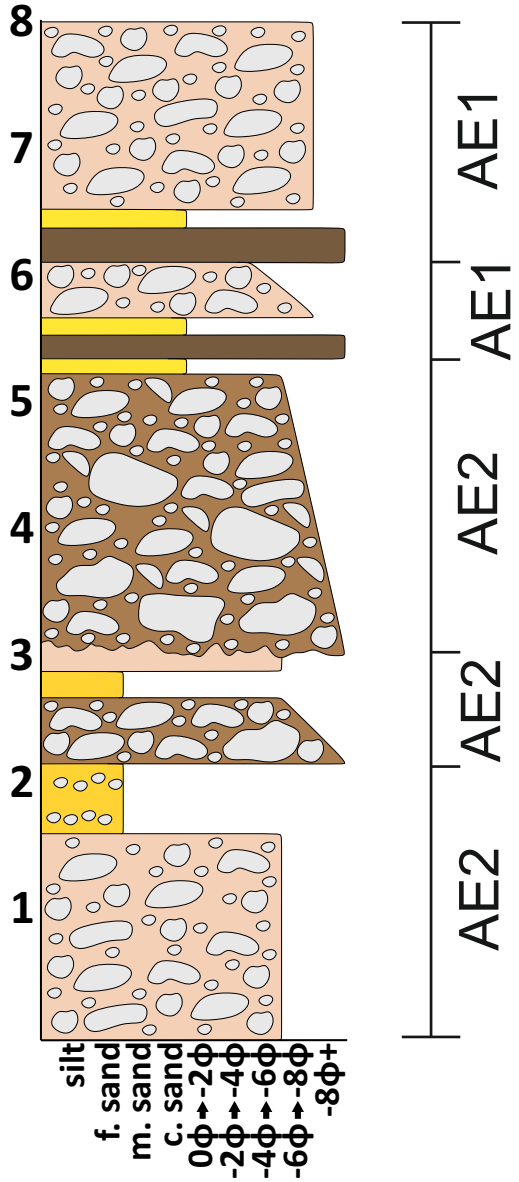

LOG L14
LAT: N38.28664
LONG: E21.85233

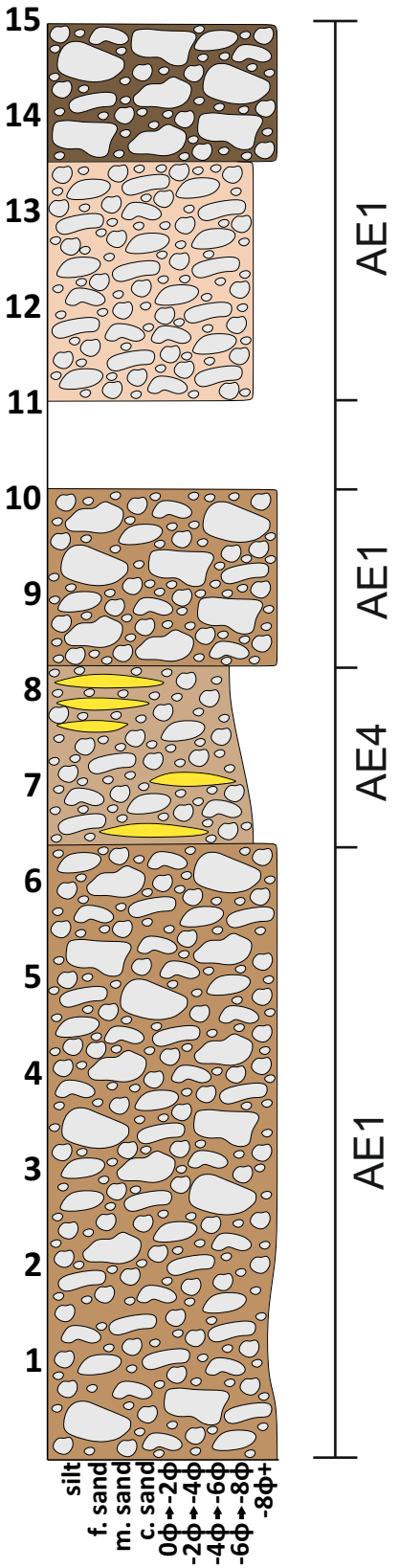

LOG L15
LAT: N38.30569
LONG: E21.89776

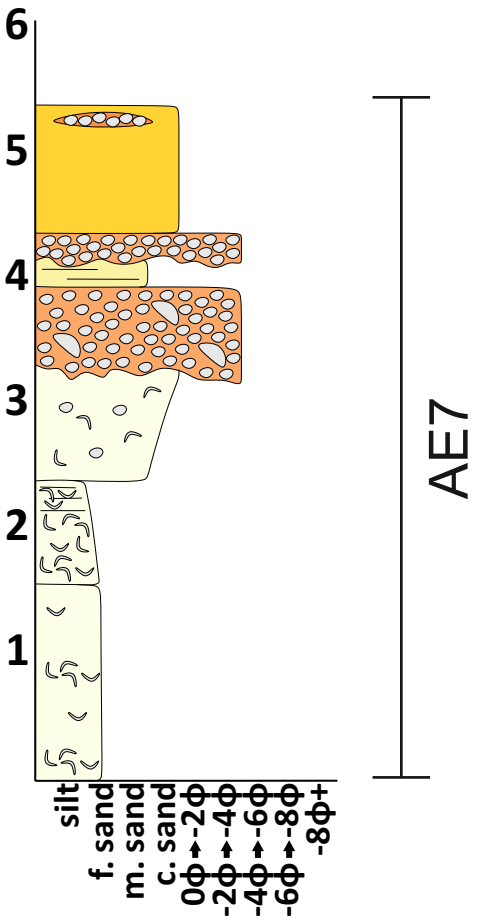

LOG L16
LAT: N38.26787
LONG: E21.90760

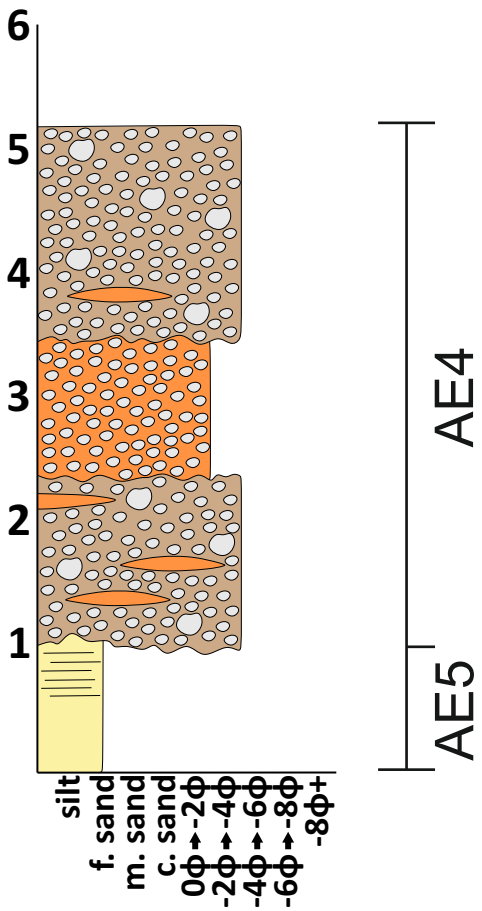

LOG L17
LAT: N38.28983
LONG: E21.91924

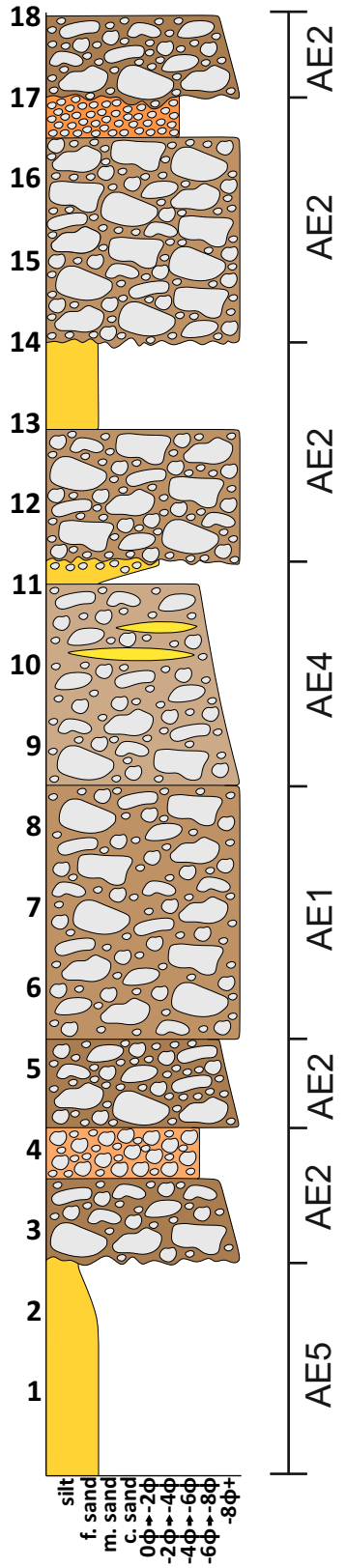

LOG L18
LAT: N38.26310
LONG: E21.91430

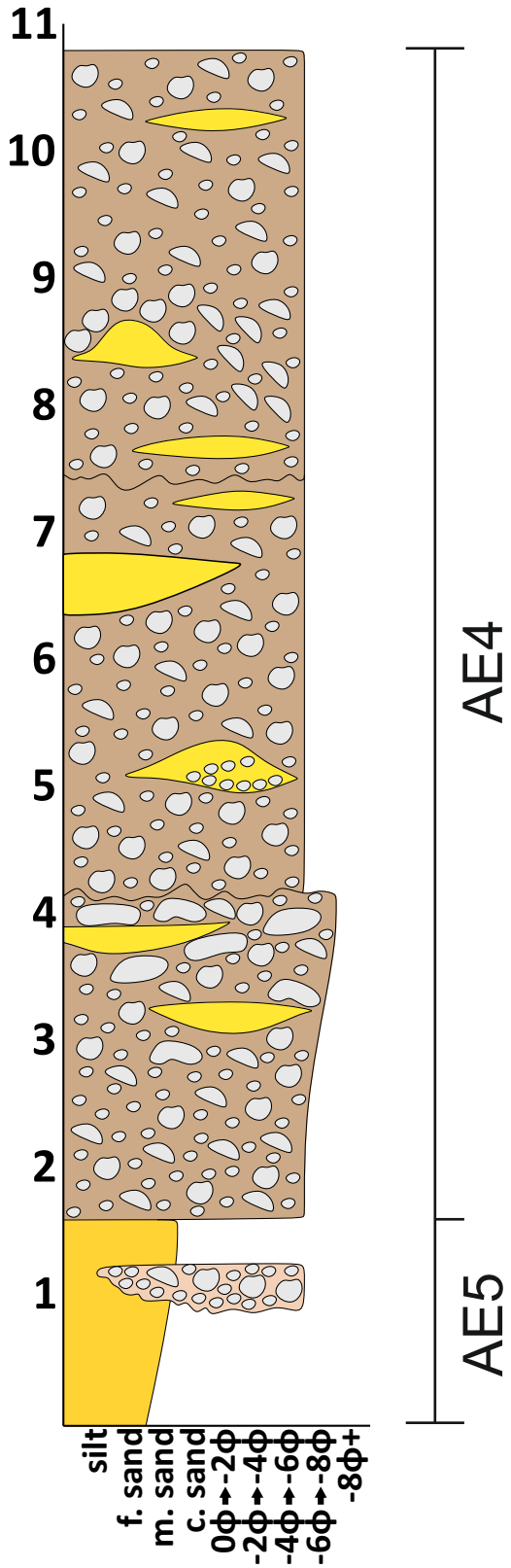

LOG L19
LAT: N38.27411
LONG: E21.91491

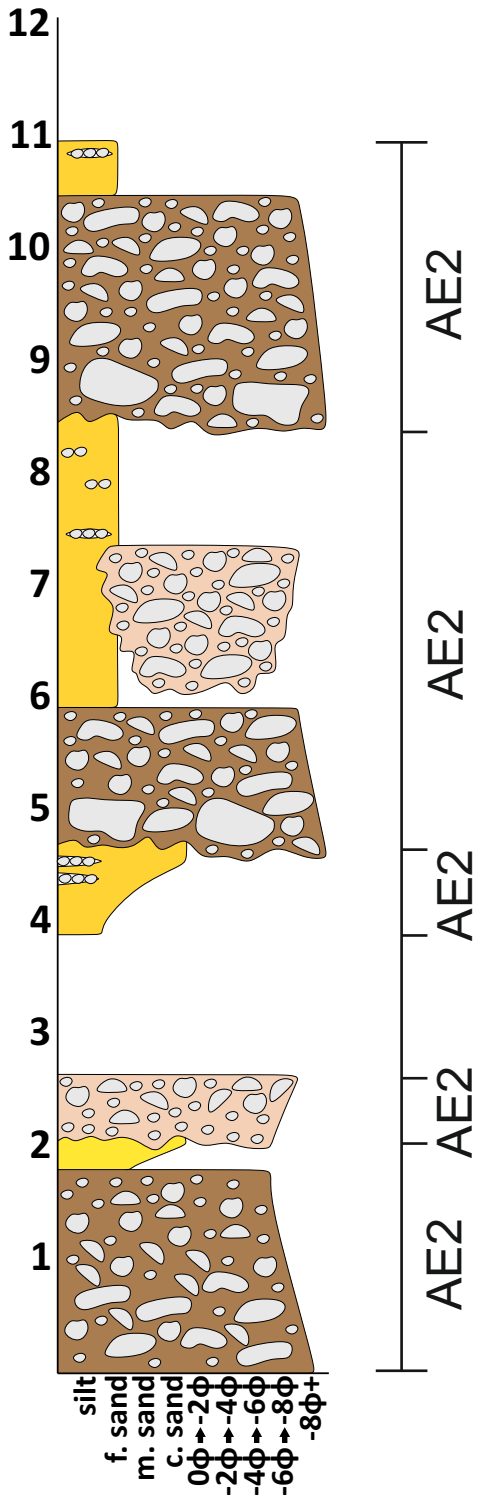

LOG L20
LAT: N38.30222
LONG: E21.93405

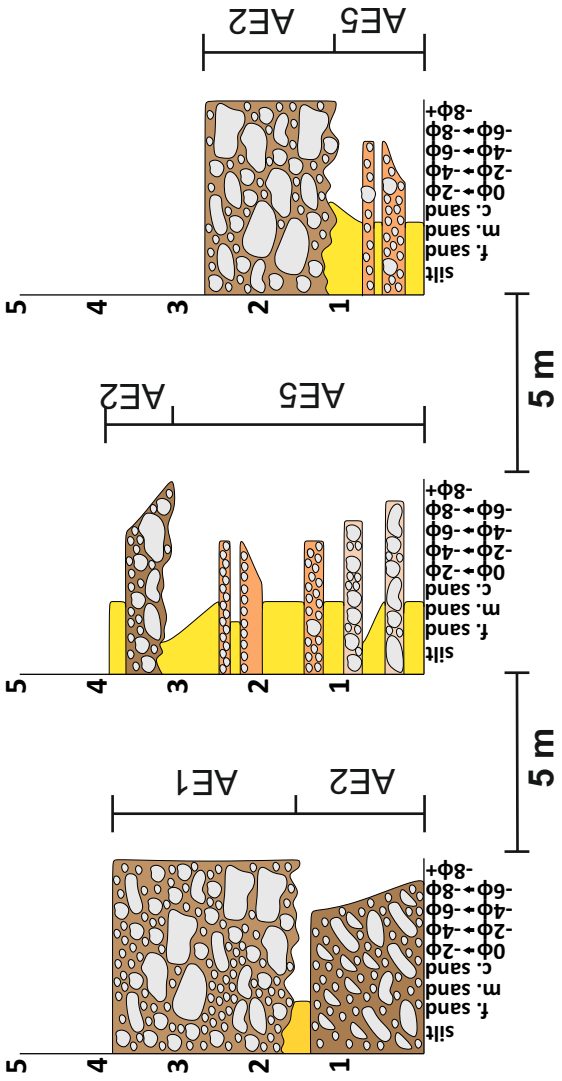

B-ple : M16, M1

B-pll : M4, M9

B-plm : M9, M13, M22, M30, M29, M32, M35

B-rlf : M26, M20, M30, M22, M32

B-wtm : M13, M26

C-pth : M14

C-rll : M19, M33, M35, M10, M12, M37

P-wtm : M19, M24, M34

B-ple : L4, L6

B-pll : L18, L14

B-plm : L14, L8, L17, L20, L7, L3, L11

B-rlf : L9, L19, L20, L17, L13

B-wtm : L8, L9

C-pth : L1

C-rll : L16, L12, L11, L10, XX, L2

P-wtm : L16, L15, L5

M1 = L6

M4 = L18

M9 = L14

M10 = L10

M12 = XX

M13 = L8

M14 = L1

M16 = L4

M19 = L16

M20 = L19

M22 = L17

M24 = L15

M26 = L9

M29 = L7

M30 = L20

M32 = L3+L13

M33 = L12

M34 = L5

M35 = L11

M37 = L2

site	strike	dips	direction	rotation?
M1	~	~		
M4	15.7	10.8	E	
M9	119.6	25.5	S	
M10	283.3	19.3	S	
M12	~	~		
M13	92	30.8	S	
M14	153.7	25.7	SW	
M16	28.4	11.4	E	
M19	30.3	17.7	E	
M20	60.7	11.3	S	
M22	20.7	27.9	NW	
M24	137.5	16.6	NE	
M26	316.2	10.9	SW	
M29	208.5	21.1	SE	
M30	96.1	21.3	N	
M32	352.8	19.8	NE	
M33	113.2	25.8	S	
M34(15)	5.4	7.1	E	
M35	260.2	35.9	S	
M37	105	28.4	S	

STRAT INTERVAL 3

site	dip	strike	
M4	10	15	S
M4	10	12	
M4	10	25	
M4	12	23	
M4	8	8	
M4	11	14	
M4	13	15	
M4	12	13	
M4	12	15	
M4	10	17	
	10.8	**15.7**	
site	**dip**	**strike**	
M19	18	32	S
M19	17	32	
M19	17	31	
M19	20	35	
M19	16	30	
M19	18	25	
M19	22	40	
M19	15	12	
M19	18	30	
M19	16	36	
	17.7		
site	**dip**	**strike**	
M9	26	120	S
M9	24	118	
M9	29	115	
M9	22	122	
M9	26	130	
M9	30	120	
M9	25	115	
M9	26	112	
M9	24	123	
M9	23	121	
	25.5		
site	**dip**	**strike**	
M24	16	131	N
M24	19	146	
M24	18	140	
M24	17	135	
M24	16	142	
M24	19	130	
M24	16	133	
M24	14	140	
M24	16	140	
M24	15	138	
	16.6		
site	**dip**	**strike**	
M22	25	-4	N
M22	32	44	
M22	33	6	
M22	23	-18	
M22	29	12	
M22	34	38	
M22	25	45	
M22	21	32	
M22	26	30	
M22	31	22	
	27.9		
site	**dip**	**strike**	
M20	12	56	S
M20	14	58	
M20	8	58	
M20	11	70	
M20	10	66	
M20	12	55	
M20	12	52	
M20	12	60	
M20	11	67	
M20	11	65	
	11.3		
site	**dip**	**strike**	
M30	22	99	N
M30	19	109	
M30	21	88	
M30	25	104	
M30	22	93	
M30	20	92	
M30	21	85	
M30	22	100	
M30	18	95	
M30	23	96	
	21.3		

STRAT INTERVAL 2

site	dip	strike	
M13	31	95	S
M13	30	80	
M13	35	90	
M13	33	92	
M13	32	93	
M13	30	80	
M13	29	102	
M13	25	103	
M13	30	92	
M13	33	93	
	30.8		
site	**dip**	**strike**	
M26	9	310	S
M26	12	305	
M26	9	326	
M26	10	340	
M26	10	312	
M26	15	320	
M26	8	318	
M26	18	315	
M26	8	307	
M26	10	309	
	10.9		
site	**dip**	**strike**	
M29	25	219	S
M29	19	198	
M29	20	205	
M29	21	203	
M29	19	203	
M29	23	212	
M29	18	208	
M29	22	209	
M29	22	215	
M29	22	213	
	21.1		
site	**dip**	**strike**	
M33	26	114	S
M33	25	118	
M33	26	105	
M33	28	111	
M33	31	121	
M33	22	118	
M33	25	116	
M33	26	109	
M33	24	110	
M33	25	110	
	25.8		
site	**dip**	**strike**	
m35	35	257	S
m35	38	264	
m35	40	260	
m35	35	259	
m35	39	262	
m35	34	270	
m35	36	255	
m35	37	258	
m35	32	260	
m35	33	257	
	35.9		
site	**dip**	**strike**	
M10	22	285	S
M10	18	282	
M10	18	285	
M10	20	280	
M10	16	284	
M10	18	286	
M10	22	287	
M10	21	280	
M10	21	279	
M10	17	285	
	19.3		
site	**dip**	**strike**	

STRAT INTERVAL 1

site	dip	strike	
M14	26	156	SW
M14	29	160	
M14	18	145	
M14	22	147	
M14	20	159	
M14	30	155	
M14	29	158	
M14	27	154	
M14	28	153	
M14	28	150	
	25.7		
site	**dip**	**strike**	
M16	12	73	E
M16	12	24	
M16	10	30	
M16	15	21	
M16	9	18	
M16	10	22	
M16	12	25	
M16	11	23	
M16	11	27	
M16	12	21	
	11.4		
site	**dip**	**strike**	
M32	26	342	N
M32	18	402	
M32	16	345	
M32	19	340	
M32	20	335	
M32			
M32			
M32			
M32			
M32			
	19.8		
site	**dip**	**strike**	
M15	5	4	E
M15	8	10	
M15	9	8	
M15	4	-1	
M15	6	9	
M15	11	5	
M15	8	6	
M15	7	4	
M15	5	3	
M15	8	6	
	7.1		
site	**dip**	**strike**	
M37	28	106	S
M37	26	100	
M37	25	102	
M37	30	105	
M37	29	109	
M37	28	110	
M37	31	104	
M37	30	103	
M37	28	112	
M37	29	99	
	28.4		
site	**dip**	**strike**	

locality	bed		facies	comp	round	shape	a_length	a_plunge	a_azimuth	b_length	b_plunge	b_azimuth	c_length	c_plunge	c_azimuth	palaeocurrent
M13		21	B-wtm	fl. sst	sr	equant		22	136	31.2	17	045	23.6	70	313	258
M13		21	B-wtm	gr. lst	r	prolate	35.5	09	160	16.8	08	075	10.9	84	322	280
M13		21	B-wtm	gr. lst	r	disc	32.0	22	131	24.5	11	042	9.7	76	300	258
M13		21	B-wtm	fl. sst	r	disc	19.5	08	238	12.7	66	326	7.2	34	149	200
M13		21	B-wtm	gr. lst	sr	equant	20.8	08	063	15.5	50	161	9.5	32	342	
M13		21	B-wtm	gr. lst	r	disc	24.7	22	147	21.9	18	058	6.3	58	288	273
M13		21	B-wtm	black b.	sr	disc	14.4	09	096	10.3	83	341	6.7	02	172	130
M13		21	B-wtm	gr. lst	r	disc	13.6	10	225		16	124	6.0	73	035	227
M13		21	B-wtm	red b.	sa	equant	11.5	11	095	8.0	08	190	6.8	69	358	
M13		21	B-wtm	fl. sst	r	disc	24.2	24	090		08	352	6.4	76	180	180
M13		21	B-wtm	fl. sst	sr	disc	40.0	07	062	16.5	12	331	9.5	80	224	244
M13		21	B-wtm	gr. lst	r	equant	23.2	03	077		19	172	14.5	84	334	
M13		21	B-wtm	red b.	sr	disc	27.0	05	067	22.5	12	145	11.3	86	243	289
M13		21	B-wtm	gr. lst	r	disc	16.7	38	144	14.5	05	053	8.0	62	322	328
M13		21	B-wtm	fl. sst	sr	disc	18.8	02	248	13.3	30	145	4.0	67	330	308
M13		21	B-wtm	fl. sst	r	disc	16.0	24	129	13.3	04	059	5.4	58	304	304
M13		21	B-wtm	red b.	sa	equant	11.4	60	102	10.5	05	198	7.3	28	288	
M13		21	B-wtm	o. lst	r	prolate	16.1	10	077	6.4	73	168	5.0	36	352	
M13		21	B-wtm	fl. sst	sr	equant	17.5	02	079	11.8	19	175	7.7	81	346	
M13		21	B-wtm	gr. lst	sa	disc	10.5	07	083	5.4	26	343	2.2	54	170	170
M13		21	B-wtm	o. lst	sa	disc	10.0	13	239		18	325	1.9	74	064	164
M13		21	B-wtm	red b.	sa	disc	24.4	06	206		48	307	7.6	40	116	143
M13		21	B-wtm	fl. sst	r	prolate	26.8	14	208	11.0	12	118	7.7	72	028	
M13		21	B-wtm	gr. lst	sr	prolate	24.1	04	121	16.5	24	221	9.0	65	333	
M13		21	B-wtm	fl. sst	r	disc	22.4	08	240		18	328	6.5	58	136	136
M13		21	B-wtm	o. lst	sr	disc	12.6	08	251	11.5	60	157	2.7	35	334	292
M13		21	B-wtm	o. lst	sr	disc	24.3	30	227	18.6	24	108	8.9	69	293	
M13		21	B-wtm	fl. sst	r	disc	19.9	11	208	13.5	41	108	7.6	54	289	289
M13		21	B-wtm	gr. lst	r	disc	22.0	03	210	14.2	50	153	3.7	64	138	138
M13		21	B-wtm	gr. lst	r	equant	15.3	29	188		49	309	7.4	51	086	
M13		21	B-wtm	fl. sst	r	equant	18.5	20	189	13.7	63	092		25	288	
M13		21	B-wtm	gr. lst	r	disc	33.7	17	250	22.4	23	196	11.1	79	357	237
M13		21	B-wtm	fl. sst	r	disc	18.6	60	074	8.8	13	237	6.0	29	263	263
M13		21	B-wtm	gr. lst	r	prolate	16.2	17	209	11.0	53	296	8.5	21	118	
M13		21	B-wtm	fl. sst	r	equant	9.1	38	155	8.8	29	076	6.4	50	330	
M13		21	B-wtm	fl. sst	r	disc	10.0	03	341	7.9	16	074	3.3	79	336	266
M13		21	B-wtm	gr. lst	r	disc	21.0	01	228	15.9	39	153	3.5	56	347	347
M13		21	B-wtm	gr. lst	r	equant	10.0	32	218		48	316	6.1	29	136	
M13		21	B-wtm	fl. sst	r	disc	12.3	19	224	7.9	48	147	1.6	51	311	319
M13		21	B-wtm	red b.	sa	prolate	6.0	01	200	1.7	19	095	1.6	64	289	
M13		21	B-wtm	gr. lst	r	disc	11.9	25	244		17	303	4.5	70	090	090
M13		21	B-wtm	gr. lst	sr	equant	32.8	24	049	29.0	35	227				
M13		21	B-wtm	fl. sst	r	disc	28.3	18	213	18.5	33	117	9.0	54	355	312
M13		21	B-wtm	gr. lst	r	disc	25.5	17	200	16.4	23	105	9.7	57	300	260
M13		21	B-wtm	fl. sst	r	disc	17.0	34	207		20	111	5.5	55	012	335
M13		21	B-wtm	gr. lst	r	disc	15.4	08	055	10.5	34	145	3.8	61	290	263
M13		21	B-wtm	fl. sst	sr	disc	22.6	12	096	12.1	30	125	3.0	75	306	274
M13		21	B-wtm	o. lst	sr	equant	14.2	18	102	12.5	22	165	8.1	81	201	
M13		21	B-wtm	fl. sst	r	disc	9.8	05	042	5.6	05	205	3.3	81	256	248
M13		21	B-wtm	gr. lst	r	equant	12.5	22	253	12.0	12	069	8.6	36	237	
M26		53	B-wtm	o. lst	sr	equant	9.6	10	030	8.7	15	297	8.0	71	131	
M26		53	B-wtm	fl. sst	r	disc	8.1	19	038		21	295	3.4	78	210	210
M26		53	B-wtm	gr. lst	sr	disc	6.2	27	027		04	276	2.0	68	188	
M26		53	B-wtm	o. lst	sa	disc	8.6	05	234	7.5	40	134	2.9	50	325	325
M26		53	B-wtm	o. lst	sr	equant	6.5	03	353	5.5	20	080	3.5	72	255	255
M26		53	B-wtm	gr. lst	sr	disc	9.3	42	183	5.2	10	092	2.5	53	000	355
M26		53	B-wtm	o. lst	sa	disc	6.5	47	002	4.5	02	262	2.5	38	180	180
M26		53	B-wtm	fl. sst	sr	disc	6.7	24	054	6.2	04	315	1.7	70	223	223
M26		53	B-wtm	o. lst	a	equant	8.3	06	217	6.5	38	117		60	306	
M26		53	B-wtm	green b.	sa	prolate	11.5	06	236	4.5	77	337		15	158	
M26		53	B-wtm	gr. lst	a	disc	10.5	19	222		12	112	3.8	72	020	328
M26		53	B-wtm	red b.	sr	equant	5.9	53	045	5.5	32	235		13	317	
M26		53	B-wtm	gr. lst	r	prolate		14	317	4.6	35	048	3.5	45	220	
M26		53	B-wtm	o. lst	sr	disc	9.5	06	225	6.5	33	120	3.0	60	313	313
M26		53	B-wtm	red b.	sa	disc	5.2	00			24	296	1.7	72	104	104
M26		53	B-wtm	fl. sst	sr	disc	7.2	14	034		06	297	3.1	69	202	178
M26		53	B-wtm	green b.	sa	disc	7.2	32	267	5.0	05	353	2.2	65	084	084
M26		53	B-wtm	gr. lst	sa	prolate		23	288	3.1	51	029	2.4	45	199	
M26		53	B-wtm	o. lst	sa	disc	4.5	18	316	3.9	08	222	1.7	76	048	048
M26		53	B-wtm	fl. sst	sr	disc	8.8	08	235		16	323	3.1	78	138	138
M26		53	B-wtm	fl. sst	r	equant	4.9	11	352	4.2	60	084	4.0	20	265	
M26		53	B-wtm	fl. sst	r	equant	7.5	03	157	5.5	82	041	5.1	08	252	
M26		53	B-wtm	red b.	sa	disc	4.7	02	201	3.3	50	112	1.2	38	292	292
M26		53	B-wtm	fl. sst	sr	disc	8.0	05	041	6.6	12	303	2.9	80	116	116
M26		53	B-wtm	red b.	sr	equant	7.4	11	203	5.3	74	292	4.1	20	104	
M26		53	B-wtm	gr. lst	sr	equant	10.3	12	342	5.5	23	254	5.2	64	091	
M26		53	B-wtm	green b.	sa	disc	7.2	00		5.0	56	313	2.4	48	130	130
M26		53	B-wtm	red b.	sa	equant	5.4	02	047	4.0	82	142	3.3	10	327	
M26		53	B-wtm	fl. sst	r	equant	5.4	57	078	4.0	18	174	3.5	30	275	275
M26		53	B-wtm	o. lst	r	equant	7.5	27	238	6.4	03	322	5.0	59	051	
M26		53	B-wtm	fl. sst	r	disc	15.4	54	012		05	274	7.3	36	191	191
M26		53	B-wtm	red b.	sa	disc	6.4	10	019	5.4	12	169	3.0	76	292	292
M26		53	B-wtm	fl. sst	sr	equant	4.7	04	274	4.0	53	002	3.3	28	188	
M26		53	B-wtm	fl. sst	sa	equant	8.0	02	035	5.5	85	288	4.7	06	116	
M26		53	B-wtm	gr. lst	sr	prolate	6.8	05	283	3.8	19	199	3.2	71	021	
M26		53	B-wtm	red b.	sa	disc	4.7	08	198	3.0	43	295	1.0	57	116	116
M26		53	B-wtm	fl. sst	r	equant	5.2	18	034	3.3	60	132		12	195	
M26		53	B-wtm	fl. sst	sr	disc	6.5	12	037		11	305	2.4	81	202	162
M26		53	B-wtm	red b.	sr	disc	6.4	04	204		40	112	2.0	48	284	284
M26		53	B-wtm	gr. lst	sr	equant	6.8	24	222		16	136	4.7	65	036	
M26		53	B-wtm	o. lst	sr	disc	6.9	21	228	4.0	20	334	2.1	65	092	092
M26		53	B-wtm	fl. sst	r	equant	5.2	12	306		90		3.5	00		
M26		53	B-wtm	o. lst	sr	prolate	7.7	25	197	4.8	14	299	3.0	73	018	018
M26		53	B-wtm	o. lst	sr	disc	4.8	65	172	4.4	09	080	2.1	20	271	271
M26		53	B-wtm	o. lst	r	disc	4.4	12	154	3.7	05	258	1.2	80	344	344
M26		53	B-wtm	red b.	sr	equant	5.0	06	239	3.8	03	149	3.0	83	052	
M26		53	B-wtm	fl. sst	r	equant	7.3	22	137	6.5	20	228	5.0	76	034	
M26		53	B-wtm	red b.	a	equant	5.5	36	038	4.0	40	148	3.7	31	295	295
M26		53	B-wtm	fl. sst	r	disc	6.0	12	036	3.8	60	130	0.9	35	306	306
M26		53	B-wtm	o. lst	sr	disc	4.2	03	056	3.5	72	148	0.8	33	339	339

ZINGG CLAST SHAPES

c/b ratio	b/a ratio
0.649	0.473
0.396	0.766
0.567	0.651
0.613	0.745
0.288	0.887
0.650	0.715
0.850	0.696
0.576	0.413
0.502	0.833
0.552	0.868
0.301	0.707
0.406	0.831
0.695	0.921
0.781	0.398
0.653	0.674
0.407	0.514
0.700	0.410
0.545	0.685
0.235	0.913
0.478	0.765
0.563	0.678
0.261	0.645
0.496	0.665
0.682	0.473
0.773	0.679
0.727	0.967
0.418	0.790
0.220	0.757
0.203	0.642
0.941	0.283
0.362	0.682
0.248	0.535
0.648	0.880
0.589	0.571
0.717	0.960
0.920	0.906
0.387	0.872
0.636	0.846
0.481	0.559
0.556	0.692
0.274	0.925
0.462	0.684
0.440	0.694
0.436	0.867
0.952	0.857
0.927	0.733
0.364	0.702
0.439	0.825
0.774	0.716
0.945	0.534
0.480	0.694
0.825	0.741
0.875	0.741
0.781	0.853
0.556	0.844
0.825	0.851
0.855	0.688
0.842	0.559
0.333	0.638
0.789	0.760
0.769	0.890
0.925	0.727
0.237	0.633
0.229	0.833

CLASS	NO.
bladed	11
disc	17
prolate	4
equant	5

CLASS	NO.
bladed	5
disc	14
prolate	2
equant	12

M13

chert	0	equant	13	r	31
black b.	1	prolate	6	sr	13
green b.	0	disc	31	sa	6
red b.	5			a	0
gr. lst	20				
o. lst	5				
fl. sst	19				
	31		50		50

M26

chert	0	equant	19	r	12
black b.	0	prolate	5	sr	22
green b.	3	disc	26	sa	13
red b.	10			a	3
gr. lst	8				
o. lst	13				
fl. sst	16				
	50		50		50

PALAEOC TOTALS

	M13
0-30	0
31-60	0
61-90	1
91-120	0
121-150	4
151-180	3
181-210	1
211-240	2
241-270	8
271-300	6
301-330	5
331-360	2
	32

PALAEOC TOTALS

	M26
0-30	1
31-60	1
61-90	1
91-120	4
121-150	2
151-180	3
181-210	2
211-240	1
241-270	1
271-300	6
301-330	4
331-360	3
	29

ZINGG CLAST SHAPES

locality	bed	facies	comp	round	shape	a_length	a_plunge	a_azimuth	b_length	b_plunge	b_azimuth	c_length	c_plunge	c_azimuth	palaeocurrent	c/b ratio	b/a ratio
M22	33	B-ff	fl. sst	sr	prolate	13.4	17	240	5.7	34	142	4.4	55	342		0.772	0.425
M22	33	B-ff	fl. sst	sr	disc	9.5	13	232	8.7	70	132	3.8	10	321	136	0.437	0.916
M22	33	B-ff	o. lst	r	equant	12.5	12	104	6.5	55	025	6.3	28	193		0.969	0.520
M22	33	B-ff	qr. lst	r	equant	8.4	60	148	7.3	29	342	6.0	22	252		0.822	0.869
M22	33	B-ff	fl. sst	r	equant	9.3	24	229	8.2	24	136	6.9	62	051		0.841	0.882
M22	33	B-ff	o. lst	sr	disc	12.6	38	016	6.5	25	284	3.7	34	152	104	0.569	0.516
M22	33	B-ff	qr. lst	sr	equant	8.5	70	048	6.5	07	149	5.9	27	248		0.908	0.765
M22	33	B-ff	qr. lst	sr	disc	11.3	17	057	6.5	28	325	3.8	67	223	149	0.585	0.575
M22	33	B-ff	gr. lst	sr	equant	7.2	32	016	4.8	51	175	4.2	30	086	086	0.875	0.667
M22	33	B-ff	fl. sst	r	disc	9.5	40	026		42	292	3.1	25	190	195		
M22	33	B-ff	fl. sst	sa	equant	10.3	39	077	8.4	74	163		17	340			
M22	33	B-ff	fl. sst	r	disc	5.7	45	114	4.4	11	021	1.3	34	293	334	0.295	0.772
M22	33	B-ff	fl. sst	sr	equant	9.2	21	217	6.5	59	118	5.5	24	312	098	0.846	0.707
M22	33	B-ff	fl. sst	r	prolate	11.6	08	204	5.3	81	300		22	118	118		
M22	33	B-ff	o. lst	sa	disc	5.1	36	262	4.5	31	020	2.0	34	130	075	0.444	0.882
M22	33	B-ff	red b.	sr	disc	3.3	18	267	2.7	65	357	1.2	14	178	155	0.444	0.818
M22	33	B-ff	o. lst	a	equant	6.6	02	035	5.3	42	125		33	306			
M22	33	B-ff	gr. lst	sr	disc	9.1	44	065	5.3	04	152	1.7	34	249	307	0.321	0.582
M22	33	B-ff	o. lst	sr	prolate	10.2	07	226	4.4	50	125		41	301			
M22	33	B-ff	qr. lst	sa	disc	6.9	16	040	4.0	37	316	2.3	54	140	094	0.575	0.580
M22	33	B-ff	fl. sst	sr	disc	10.7	08	051	7.5	15	334	2.7	68	186	154	0.360	0.701
M22	33	B-ff	qr. lst	sr	disc	8.9	06	104	7.6	87	006	3.1	03	188	188	0.408	0.854
M22	33	B-ff	qr. lst	sa	equant	8.7	02	074	6.0	35	164	4.5	45	355		0.750	0.690
M22	33	B-ff	o. lst	sr	disc	6.8	11	135	5.2	39	046	2.1	34	227	227	0.404	0.765
M22	33	B-ff	o. lst	sr	equant	7.5	00		4.3	34	321	3.2	60	139	051	0.744	0.573
M22	33	B-ff	qr. lst	sr	disc	9.4	37	350	7.5	02	074	3.3	50	143	089	0.440	0.798
M22	33	B-ff	o. lst	sr	disc	5.2	22	123	4.5	88	212	1.9	02	028	155	0.422	0.865
M22	33	B-ff	red b.	sa	disc	4.0	09	215	3.4	82	330		11	142	118		
M22	33	B-ff	qr. lst	r	disc	4.5	02	021	2.8	15	286	1.3	75	110	093	0.464	0.622
M22	33	B-ff	qreen b.	sa	prolate	5.3	05	162	2.2	00		1.8	86	354		0.818	0.415
M22	33	B-ff	qr. lst	r	disc	5.3	32	089	3.3	11	183	1.1	66	278	324	0.333	0.623
M22	33	B-ff	red b.	a	prolate	5.6	32	107	2.9	28	025	2.7	48	213		0.931	0.518
M22	33	B-ff	gr. lst	sa	disc	7.1	03	051		14	318	2.3	68	145	105		
M22	33	B-ff	fl. sst	r	equant	5.8	23	104	5.6	04	208	4.0	77	292		0.714	0.966
M22	33	B-ff	red b.	a	disc	4.3	63	271	3.6	10	180	1.8	33	086	086	0.500	0.837
M22	33	B-ff	red b.	sa	disc	4.7	35	234	3.2	43	071	1.1	08	318	318	0.344	0.681
M22	33	B-ff	fl. sst	r	disc	8.7	37	093	6.7	30	199	2.7	32	299	299	0.403	0.770
M22	33	B-ff	o. lst	sa	disc	5.2	10	055	3.8	43	331	2.3	34	165	154	0.605	0.731
M22	33	B-ff	qr. lst	sa	disc	5.7	22	007	3.5	10	106	2.2	78	278	266	0.629	0.614
M22	33	B-ff	fl. sst	r	equant	5.2	32	110	4.4	40	016	2.6	20	202		0.591	0.846
M22	33	B-ff	green b.	a	equant	4.6	10	014	2.4	54	102	2.2	32	278		0.917	0.522
M22	33	B-ff	o. lst	r	disc	4.9	15	026		20	285	2.0	38	110	083		
M22	33	B-ff	gr. lst	r	disc	6.0	20	352	4.5	10	082	2.5	59	173	173	0.556	0.750
M22	33	B-ff	o. lst	a	equant	6.3	04	029	4.3	35	123	3.5	52	303		0.814	0.683
M22	33	B-ff	fl. sst	sa	disc	6.3	29	000		39	263	2.1	26	162	108		
M22	33	B-ff	gr. lst	sa	equant	3.2	36	048	3.0	15	141	2.2	44	236		0.733	0.938
M22	33	B-ff	green b.	a	equant	3.6	35	037	2.0	47	306	1.9	26	120		0.950	0.556
M22	33	B-ff	qr. lst	sr	disc	5.3	40	015	3.0	27	286	1.5	48	190	122	0.500	0.566
M22	33	B-ff	red b.	sa	disc	3.4	50	266	2.8	06	188	1.4	45	077	077	0.500	0.824
M22	33	B-ff	green b.	sa	disc	2.8	49	258	2.2	10	164	0.8	52	070	054	0.364	0.786
M26	51	B-ff	red b.	sa	disc	15.0	02	052	9.3	81	314	4.7	10	134	152	0.505	0.620
M26	51	B-ff	green b.	sr	disc	19.5	28	083	14.7	18	355	6.5	62	239	282	0.442	0.754
M26	51	B-ff	fl. sst	r	disc	12.6	04	048	7.5	30	317	4.7	63	159	146	0.627	0.595
M26	51	B-ff	red b.	sa	disc	10.3	10	331	8.4	18	231	3.3	72	062	062	0.393	0.816
M26	51	B-ff	fl. sst	r	equant	12.2	69	183	10.0	08	076	7.2	20	333		0.720	0.820
M26	51	B-ff	o. lst	sr	disc	13.5	80	194	8.4	02	302	4.2	09	034	034	0.500	0.622
M26	51	B-ff	o. lst	sr	equant	7.0	03	181	6.0	83	089	5.7	06	273		0.950	0.857
M26	51	B-ff	o. lst	sr	disc		18	292	6.7	76	197	2.9	10	022	022		
M26	51	B-ff	red b.	sa	disc	7.8	65	275	5.0	23	095	2.5	14	350	350	0.500	0.641
M26	51	B-ff	o. lst	sa	equant	8.3	03	205	5.9	40	302	1.9	59	103	103	0.322	0.711
M26	51	B-ff	o. lst	sa	prolate	10.7	22	061	4.9	05	320	4.3	70	225		0.878	0.458
M26	51	B-ff	o. lst	sr	equant	8.2	06	244	5.0	85	153	4.5	04	320		0.900	0.610
M26	51	B-ff	qr. lst	r	disc	7.3	08	223	6.5	18	317	1.8	70	122	116	0.277	0.890
M26	51	B-ff	o. lst	r	disc	9.7	12	261		14	143	3.2	69	082	082		
M26	51	B-ff	red b.	sr	prolate	14.9	21	083	6.2	60	267	3.9	19	354		0.629	0.416
M26	51	B-ff	o. lst	sr	disc	10.2	10	194	5.5	56	098	3.5	37	283	283	0.636	0.539
M26	51	B-ff	red b.	a	equant	6.7	17	048	4.5	09	313	4.0	71	217		0.889	0.672
M26	51	B-ff	o. lst	sr	disc	7.6	33	138	6.0	30	229	1.2	54	340	340	0.200	0.789
M26	51	B-ff	fl. sst	r	equant	9.0	08	228	4.7	10	319		80	153			
M26	51	B-ff	o. lst	sr	equant	8.3	90		6.5	02	171	5.9	03	074		0.908	0.783
M26	51	B-ff	red b.	a	disc	6.5	47	285	4.3	05	176	1.8	51	092	092	0.419	0.662
M26	51	B-ff	o. lst	sr	disc	6.0	08	231	5.2	22	135	1.3	63	328	328	0.250	0.867
M26	51	B-ff	fl. sst	r	disc	5.0	24	230		05	130	1.3	60	032	032		
M26	51	B-ff	red b.	sa	equant	5.5	08	022	5.0	63	176	4.3	24	264		0.860	0.909
M26	51	B-ff	red b.	sr	disc	6.7	15	233	5.4	40	127	1.5	52	317	317	0.278	0.806
M26	51	B-ff	fl. sst	sr	disc	7.1	12	223		10	117	2.5	17	040	103		
M26	51	B-ff	o. lst	sr	prolate		23	162	3.2	47	062	2.7	34	244			
M26	51	B-ff	qreen b.	sa	disc	5.5	12	265	4.4	32	148	1.5	55	341	030	0.341	0.800
M26	51	B-ff	fl. sst	r	disc	6.6	45	086	5.1	10	348	3.0	55	243	243	0.588	0.773
M26	51	B-ff	fl. sst	sr	disc	8.0	04	236	6.0	45	137	3.6	39	335	335	0.600	0.750
M26	51	B-ff	o. lst	r	equant	5.2	02	060	4.0	28	157	3.2	73	337		0.800	0.769
M26	51	B-ff	o. lst	sa	disc	7.0	11	286		10	359	1.7	75	102	102		
M26	51	B-ff	red b.	sa	disc	5.5	09	248		16	342	0.8	73	090	078		
M26	51	B-ff	fl. sst	sr	disc	6.3	03	231		12	325	1.3	80	132	132		
M26	51	B-ff	qreen b.	a	equant	5.2	73	178	3.8	20	347	3.7	08	068		0.974	0.731
M26	51	B-ff	fl. sst	r	disc	6.6	13	243	5.4	10	334	2.2	82	071	071	0.407	0.818
M26	51	B-ff	o. lst	sr	disc	8.7	17	239		24	325	0.9	72	062	141		
M26	51	B-ff	red b.	a	prolate	5.5	05	278	2.1	62	016	1.7	22	205		0.810	0.382
M26	51	B-ff	fl. sst	sr	disc	4.4	65	070	3.3	12	193	1.0	32	278	278	0.303	0.750
M26	51	B-ff	gr. lst	sr	equant	7.9	27	223	3.9	22	123	3.8	64	024	024	0.974	0.494
M26	51	B-ff	red b.	sa	disc	5.4	08	086	3.7	22	328	1.9	80	169	169	0.514	0.685
M26	51	B-ff	fl. sst	r	disc	4.3	67	258	4.0	06	007	1.4	21	097	076	0.350	0.930
M26	51	B-ff	o. lst	sr	equant	5.3	23	270	4.4	06	171	2.8	58	076	076	0.636	0.830
M26	51	B-ff	fl. sst	sr	disc	8.0	36	071		27	159	3.5	65	269	269		
M26	51	B-ff	red b.	sa	disc	6.2	75	230		14	330	2.8	15	058	058		
M26	51	B-ff	fl. sst	sr	disc	4.5	40	297	3.7	10	028	1.3	55	118	118	0.351	0.822
M26	51	B-ff	o. lst	sr	disc	6.3	06	143	5.2	52	230	2.6	38	050	050	0.500	0.825
M26	51	B-ff	qr. lst	sr	disc	5.8	10	042	5.0	08	305	0.9	82	118	126	0.180	0.862
M26	51	B-ff	qreen b.	sr	disc	5.5	30	105	4.7	11	010	2.4	55	280	280	0.511	0.855
M26	51	B-ff	o. lst	sr	disc	4.1	18	231		05	131	1.2	75	024	024		
M20	65	B-ff	o. lst	sr	disc	19.8	30	324	13.8	55	085	4.0	57	173	173	0.290	0.697
M20	65	B-ff	o. lst	sr	equant	25.4	17	340	14.8	08	241	10.2	76	149	149	0.689	0.583
M20	65	B-ff	fl. sst	sr	disc	11.5	11	342	8.0	16	075	3.7	80	245	245	0.463	0.696
M20	65	B-ff	o. lst	sa	equant	15.6	05	321	10.0	72	060	8.3	25	149		0.830	0.641
M20	65	B-ff	qreen b.	sa	prolate	15.6	07	334	6.3	79	057	4.0	09	246		0.635	0.404
M20	65	B-ff	fl. sst	r	disc	11.7	33	344	9.1	22	258	5.0	53	113	113	0.549	0.778
M20	65	B-ff	red b.	sa	prolate	11.0	34	288	6.3	71	114	4.5	12	215		0.714	0.573
M20	65	B-ff	red b.	sr	equant		04	256	5.8	51	173	5.5	43	350			
M20	65	B-ff	o. lst	sr	disc	8.3	08	326	4.8	55	065	2.2	35	234	234	0.458	0.578
M20	65	B-ff	fl. sst	r	prolate	14.4	16	094	8.8	18	350	6.0	69	192		0.682	0.611
M20	65	B-ff	red b.	sa	prolate		08	229	4.0	28	342	3.1	72	160			
M20	65	B-ff	o. lst	sr	equant	7.9	23	069	7.6	32	170	6.2	60	335		0.816	0.962
M20	65	B-ff	fl. sst	r	disc	7.0	32	210	5.9	08	316	2.8	63	062	062	0.475	0.843
M20	65	B-ff	o. lst	sr	disc	8.7	22	233	5.6	18	312	1.8	62	072	072	0.321	0.644
M20	65	B-ff	qr. lst	sr	equant	6.8	07	113	4.7	53	202		35	035			
M20	65	B-ff	qr. lst	r	equant	9.0	17	313	6.0	73	225	5.6	22	050		0.933	0.667
M20	65	B-ff	qreen b.	sa	disc	5.9	05	009	5.5	65	285	1.8	28	110	110	0.327	0.932
M20	65	B-ff	o. lst	sr	disc	10.2	10	332	9.4	41	242	2.6	48	068	068	0.277	0.922
M20	65	B-ff	fl. sst	r	disc	11.4	30	309		06	215	4.3	59	144	144		
M20	65	B-ff	gr. lst	sr	disc	8.9	04	151	5.2	58	053	3.4	30	235	235	0.654	0.584
M20	65	B-ff	red b.	sa	equant	9.0	48	082	5.2	12	348	4.2	33	256		0.808	0.578
M20	65	B-ff	qreen b.	sa	disc	4.7	03	303	2.5	06	203	1.3	84	032	032	0.520	0.532
M20	65	B-ff	red b.	sr	disc	5.5	11	320	4.1	07	223	2.1	80	119	119	0.512	0.745
M20	65	B-ff	qr. lst	sr	prolate	7.2	26	036	4.8	32	134	3.2	51	312		0.667	0.667
M20	65	B-ff	fl. sst	r	disc	6.2	08	294		43	201	1.9	58	036	036		
M20	65	B-ff	fl. sst	sr	disc	6.0	18	178	4.0	47	068	2.1	40	267	267	0.525	0.667
M20	65	B-ff	qreen b.	sr	prolate	14.2	10	113	6.0	20	222	4.3	74	038		0.717	0.423
M20	65	B-ff	o. lst	r	disc	4.1	04	060	3.9	25	172	1.6	68	344	344	0.410	0.951
M20	65	B-ff	fl. sst	r	disc	14.4	23	078	12.5	36	337	2.8	38	222	137	0.224	0.868
M20	65	B-ff	o. lst	sr	equant	7.5	23	007	5.7	71	269		12	093			
M20	65	B-ff	red b.	sr	disc	11.7	04	140		26	046	3.3	72	236	236		
M20	65	B-ff	qr. lst	r	disc	10.5	20	278	7.0	38	004	2.4	61	184	126	0.343	0.667
M20	65	B-ff	o. lst	sr	disc		04	014	5.9	13	112	2.8	78	303	115		
M20	65	B-ff	qr. lst	sr	prolate	8.5	08	138		20	230	2.2	79	322			
M20	65	B-ff	red b.	sa	equant	4.6	05	285	3.9	15	181	2.5	77	093		0.641	0.848
M20	65	B-ff	qr. lst	sa	disc	4.7	12	143	3.2	35	048	1.5	64	313	263	0.469	0.681
M20	65	B-ff	fl. sst	r	disc	5.5	45	298	3.9	05	202	1.1	46	114	114	0.282	0.709
M20	65	B-ff	o. lst	sr	prolate	11.8	04	275	6.7	75	020	4.8	22	206		0.716	0.568
M20	65	B-ff	o. lst	r	disc	8.8	18	030	5.9	10	116	2.6	72	238	148	0.441	0.670
M20	65	B-ff	o. lst	sr	disc	9.7	23	041	8.8	08	154	2.6	75	258	137	0.295	0.907
M20	65	B-ff	qreen b.	sr	prolate	7.5	33	137	2.3	52	032	2.1	12	217		0.913	0.307
M20	65	B-ff	red b.	sa	disc	7.0	59	234	4.5	07	136	1.8	28	047	047	0.400	0.643
M20	65	B-ff	fl. sst	r	disc	4.7	10	216	3.7	60	314	1.1	30	124	115	0.297	0.787
M20	65	B-ff	fl. sst	r	equant	8.2	08	156		12	045	4.7	76	292			
M20	65	B-ff	o. lst	r	disc		10	217	5.2	25	328	2.0	70	156	156		
M20	65	B-ff	gr. lst	r	equant	8.5	02	154	5.5	63	242	5.3	32	074		0.964	0.647
M20	65	B-ff	qr. lst	sr	equant	6.1	06	167	5.8	85	076	4.3	07	164		0.741	0.951
M20	65	B-ff	fl. sst	sr	disc		18	286	5.1	12	190	2.3	68	061	061		
M20	65	B-ff	o. lst	sr	disc	9.3	26	208	5.6	30	112	1.9	65	306	300	0.339	0.602
M20	65	B-ff	red b.	sr	disc	6.6	12	130	6.0	08	231	3.1	77	069	069	0.517	0.909

CLASS	NO.
bladed	8
disc	17
prolate	8
equant	8

PALAEOC TOTALS

	M22
0-30	0
31-60	2
61-90	6
91-120	8
121-150	3
151-180	5
181-210	2
211-240	1
241-270	1
271-300	1
301-330	3
331-360	1
	33

CLASS	NO.
bladed	7
disc	19
prolate	4
equant	7

PALAEOC TOTALS

	M26
0-30	4
31-60	4
61-90	6
91-120	6
121-150	4
151-180	2
181-210	0
211-240	0
241-270	2
271-300	4
301-330	2
331-360	3
	37

CLASS	NO.
bladed	10
disc	16
prolate	10
equant	2

PALAEOC TOTALS

	M20i
0-30	0
31-60	3
61-90	5
91-120	6
121-150	6
151-180	2
181-210	0
211-240	3
241-270	3
271-300	1
301-330	0
331-360	1
	30

M22/L17

black b.	0	equant	16	r	13
green b.	4	prolate	5	sr	17
qr. lst	16	disc	29	sa	14
red b.	6			a	6
fl. sst	13				
o. lst	11				
	50		**50**		**50**

M26/L9

black b.	0	equant	12	r	10
green b.	4	prolate	4	sr	25
qr. lst	3	disc	34	sa	11
red b.	12			a	4
fl. sst	13				
o. lst	18				
	50		**50**		**50**

M20/L19

black b.	0	equant	12	r	15
green b.	5	prolate	9	sr	25
qr. lst	9	disc	29	sa	10
red b.	9			a	0
fl. sst	12				
o. lst	15				
	50		**50**		**50**

M20/L19

black b.	1	equant	12	r	8
green b.	7	prolate	8	sr	23
qr. lst	8	disc	30	sa	17
red b.	10			a	2
fl. sst	13				
o. lst	11				
	50		**50**		**50**

M30/L20

black b.	0	equant	10	r	14
green b.	6	prolate	8	sr	24
qr. lst	13	disc	32	sa	12
red b.	11			a	0
fl. sst	9				
o. lst	11				
	50		**50**		**50**

M32/L13

black b.	0	equant	14	r	15
green b.	5	prolate	6	sr	25
qr. lst	13	disc	30	sa	10
red b.	7			a	0
fl. sst	8				
o. lst	17				
	50		**50**		**50**

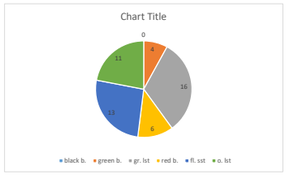

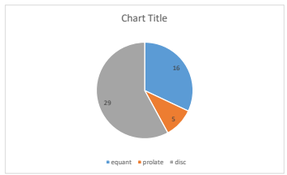

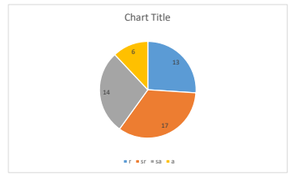

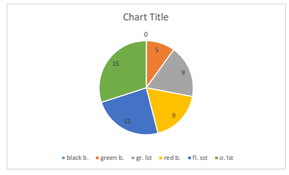

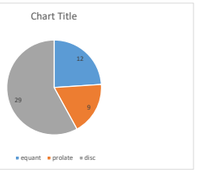

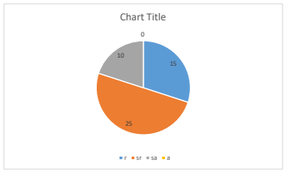

M20	68	B-rif	fl. sst	sr	prolate	15.5	15	131	5.5	82	128	3.8	23	042	043	0.691	0.355
M20	68	B-rif	gr. lst	sr	disc	10.4	10	142	5.7	12	231	3.3	58	322	322	0.579	0.548
M20	68	B-rif	red b.	sa	disc	10.5	42	088	8.7	10	177	2.7	43	275	239	0.310	0.829
M20	68	B-rif	gr. lst	sa	disc	16.4	06	003	8.5	23	098	5.4	57	263	134	0.635	0.518
M20	68	B-rif	green b.	sa	prolate	10.3	20	167	4.5	67	263	4.3	22	086		0.956	0.437
M20	68	B-rif	green b.	sa	disc	9.7	13	132	5.6	10	036	3.5	75	298	298	0.625	0.577
M20	68	B-rif	green b.	sa	prolate	19.4	21	202	7.8	77	115	7.5	12	299		0.962	0.402
M20	68	B-rif	black b.	sa	equant	10.0	22	098	9.3	37	208	8.5	36	029		0.914	0.930
M20	68	B-rif	o. lst	sr	disc	13.0	28	137		22	048	5.3	66	318	318		
M20	68	B-rif	fl. sst	sr	prolate	18.6	04	073	8.5	12	335	4.4	75	244		0.518	0.457
M20	68	B-rif	qr. lst	sa	equant	6.5	13	132	5.2	08	230	4.3	77	321		0.827	0.800
M20	68	B-rif	qr. lst	sr	disc	12.5	06	142	9.6	56	050	5.3	32	231	231	0.552	0.768
M20	68	B-rif	o. lst	sa	equant	10.2	22	136		08	045	6.6	79	312			
M20	68	B-rif	o. lst	sr	prolate	7.3	18	100		22	010	4.0	60	290			
M20	68	B-rif	red b.	a	disc	6.6	08	082		12	318	1.7	78	222	222		
M20	68	B-rif	red b.	sr	equant	6.5	15	093	4.3	15	194	3.5	80	016	044	0.814	0.662
M20	68	B-rif	fl. sst	r	disc	5.3	43	164	3.6	28	271	0.8	62	015	084	0.222	0.679
M20	68	B-rif	fl. sst	sr	prolate	10.2	04	306	5.1	70	108		22	036			
M20	68	B-rif	o. lst	sa	disc	8.3	30	108		17	019	2.9	62	294	294		
M20	68	B-rif	green b.	a	disc	4.3	20	145	3.9	03	060	1.9	80	334	334	0.487	0.907
M20	68	B-rif	fl. sst	sr	disc	12.9	05	117		43	018	3.9	48	204	118		
M20	68	B-rif	qr. lst	sr	disc	8.2	19	232	7.0	05	319	3.6	79	058	074	0.514	0.854
M20	68	B-rif	fl. sst	r	disc	8.3	07	185	6.0	09	085	2.6	81	359	359	0.433	0.723
M20	68	B-rif	fl. sst	r	equant	5.5	37	092	4.6	15	345	4.5	44	217		0.978	0.836
M20	68	B-rif	gr. lst	sa	equant	11.2	34	131	9.4	78	042		08	237			
M20	68	B-rif	red b.	sa	disc	7.2	24	353	6.0	54	091	3.1	40	208	208	0.517	0.833
M20	68	B-rif	o. lst	sr	prolate		17	212	6.6	10	116	4.5	69	018			
M20	68	B-rif	fl. sst	sr	disc	6.5	15	346	5.5	06	250	2.3	76	150	150	0.418	0.846
M20	68	B-rif	red b.	sr	prolate	5.5	03	252	2.7	60	153	2.3	27	350		0.852	0.491
M20	68	B-rif	o. lst	sa	equant	4.2	14	225	4.0	62	135	3.0	28	325		0.750	0.952
M20	68	B-rif	fl. sst	sr	equant	5.3	11	090	5.2	78	181	3.8	17	006	006	0.731	0.981
M20	68	B-rif	fl. sst	r	disc	6.4	34	178		30	075	1.4	35	333	333		
M20	68	B-rif	o. lst	sa	disc	7.3	11	312	4.5	30	050	3.0	64	152	152	0.667	0.616
M20	68	B-rif	o. lst	sr	disc	6.5	17	119		21	017	2.0	72	291	291		
M20	68	B-rif	gr. lst	sr	equant	6.4	25	190	3.9	13	357	3.4	77	022		0.872	0.609
M20	68	B-rif	red b.	sa	disc	4.2	03	140	3.7	12	236	1.5	80	054	054	0.405	0.881
M20	68	B-rif	o. lst	sr	disc	7.2	23	118		14	207	2.1	18	299	072		
M20	68	B-rif	red b.	sr	disc	4.8	58	052	3.6	05	158	1.6	32	244	244	0.444	0.750
M20	68	B-rif	fl. sst	r	disc	5.0	40	105		10	213	1.7	45	296	016		
M20	68	B-rif	red b.	sr	disc	5.0	42	101	3.5	18	004	1.7	35	275	275	0.486	0.700
M20	68	B-rif	green b.	sa	disc	3.5	16	205	2.9	12	101	0.8	75	034	034	0.276	0.829
M20	68	B-rif	o. lst	r	disc	4.2	11	128	3.5	59	249	1.0	33	064	064	0.286	0.833
M20	68	B-rif	red b.	sr	equant	8.0	08	284		10	190	4.7	84	094	094		
M20	68	B-rif	qr. lst	sr	disc	5.3	24	032	3.8	30	309	1.2	65	128		0.316	0.717
M20	68	B-rif	green b.	sa	disc	3.4	33	137	2.5	09	034	0.7	66	308	308	0.280	0.735
M20	68	B-rif	fl. sst	r	disc	7.8	16	134		27	222	2.3	78	226	226		
M20	68	B-rif	o. lst	r	disc	5.6	24	210	3.0	12	114	2.0	79	032	032	0.667	0.536
M20	68	B-rif	fl. sst	sr	disc	6.5	09	132		80	043	1.6	11	216	021		
M20	68	B-rif	red b.	sr	equant	8.2	16	094	6.4	78	201	5.3	16	352		0.828	0.780
M20	68	B-rif	green b.	sa	equant	4.5	10	120	4.0	86	028	3.8	02	222		0.950	0.889
M30	69	B-rif	o. lst	sr	prolate	13.3	03	280	5.0	79	016	4.2	16	176		0.840	0.376
M30	69	B-rif	fl. sst	sr	prolate	27.2	04	028	10.0	18	123	7.9	75	310		0.790	0.368
M30	69	B-rif	gr. lst	r	equant	7.6	03	261	5.6	72	170	5.0	22	358		0.893	0.737
M30	69	B-rif	red b.	sr	equant	5.8	74	026	4.6	10	268	3.8	21	183		0.826	0.793
M30	69	B-rif	qr. lst	sr	disc	8.5	24	275	6.0	03	180	3.4	53	088	088	0.567	0.706
M30	69	B-rif	o. lst	sa	disc	7.9	07	283		31	197	2.8	66	019	019		
M30	69	B-rif	fl. sst	r	disc	6.5	02	096	4.0	25	002	2.3	65	188	188	0.575	0.615
M30	69	B-rif	gr. lst	sr	disc	9.3	06	283	7.8	75	012	3.7	12	175	140	0.474	0.839
M30	69	B-rif	red b.	sr	disc	7.8	03	295	4.8	60	193	1.9	28	024	024	0.396	0.615
M30	69	B-rif	red b.	sr	prolate	9.2	01	280	4.2	28	182	3.5	70	005		0.833	0.457
M30	69	B-rif	qr. lst	sr	disc	8.6	03	264	5.3	52	012	2.4	38	192	149	0.453	0.616
M30	69	B-rif	o. lst	sr	prolate	9.8	49	286	5.5	12	187	3.2	12	080	080	0.582	0.561
M30	69	B-rif	fl. sst	r	disc	6.3	58	318	4.4	22	060	1.2	30	131	131	0.273	0.698
M30	69	B-rif	fl. sst	r	disc		13	301	11.2	55	206	5.3	38	108	108		
M30	69	B-rif	gr. lst	sr	equant	6.4	77	197	5.0	05	291	3.8	12	022		0.760	0.781
M30	69	B-rif	qr. lst	sr	equant	11.5	22	300	8.6	65	202	7.0	32	023	023	0.814	0.748
M30	69	B-rif	red b.	sr	disc	8.6	07	274	7.0	55	005	2.5	46	168	168	0.357	0.814
M30	69	B-rif	o. lst	sr	disc		10	191	8.2	18	290	3.1	69	089			
M30	69	B-rif	red b.	sr	disc	7.5	01	288	5.2	10	025	1.7	81	202	105	0.327	0.693
M30	69	B-rif	fl. sst	r	disc	5.2	86	016	5.0	14	283	0.9	05	202	202	0.180	0.962
M30	69	B-rif	o. lst	r	disc	5.6	35	315		06	052	1.2	55	156	130		
M30	69	B-rif	red b.	sa	disc	7.5	33	270		13	180	2.2	58	078	078		
M30	69	B-rif	green b.	sr	equant	4.2	50	240	4.0	18	145		31	006			
M30	69	B-rif	o. lst	sa	equant	5.8	43	340	4.4	42	158	4.0	22	064		0.909	0.759
M30	69	B-rif	red b.	sr	disc	5.4	24	276		10	170	1.9	58	082	082		
M30	69	B-rif	qr. lst	sa	disc	11.4	13	300		04	207	3.2	72	111			
M30	69	B-rif	o. lst	r	disc	5.0	02	274	3.9	25	001	0.8	70	180	151	0.205	0.780
M30	69	B-rif	green b.	sa	disc	5.7	05	250	4.9	40	351	2.2	30	164	164	0.449	0.860
M30	69	B-rif	red b.	sr	equant	5.4	15	066	4.6	25	323	4.0	55	153		0.870	0.852
M30	69	B-rif	fl. sst	r	disc		07	212	5.0	33	305	1.6	50	125	103		
M30	69	B-rif	fl. sst	sr	disc	5.0	13	311	2.8	15	041	1.2	70	212	212	0.429	0.560
M30	69	B-rif	o. lst	sr	disc	5.4	32	338	3.5	12	244	1.4	53	169	116	0.400	0.648
M30	69	B-rif	qr. lst	sr	prolate	7.3	05	258	3.2	72	350	2.0	20	174		0.625	0.438
M30	69	B-rif	green b.	sa	disc	8.3	04	288		20	018	2.6	65	212	140		
M30	69	B-rif	o. lst	r	disc		00		4.0	19	299	0.6	79	102	102		
M30	69	B-rif	red b.	sa	prolate	5.7	05	339	3.1	62	068	1.6	31	255		0.516	0.544
M30	69	B-rif	o. lst	sr	prolate	8.5	12	025	3.6	61	288	2.9	32	118		0.806	0.424
M30	69	B-rif	red b.	sa	prolate		05	023	2.3	41	285	0.8	38	103	103		
M30	69	B-rif	fl. sst	r	disc		13	023	5.3	07	297	1.1	78	195	195		
M30	69	B-rif	gr. lst	r	disc	4.3	13	015	3.4	28	096	1.7	60	287	287	0.500	0.791
M30	69	B-rif	green b.	sa	disc		20	017	3.2	33	272	0.9	61	097	097		
M30	69	B-rif	green b.	sa	disc	4.8	05	215	3.5	62	311	1.5	29	128	128	0.429	0.729
M30	69	B-rif	qr. lst	sr	disc	5.1	58	219	3.8	03	119	1.0	36	032	032	0.263	0.745
M30	69	B-rif	gr. lst	sr	equant	6.4	06	107		24	022	3.5	68	208			
M30	69	B-rif	red b.	sr	disc	6.4	42	278		02	185	1.9	48	088	088		
M30	69	B-rif	gr. lst	sr	disc	5.7	18	023	4.5	67	298	2.2	21	117		0.489	0.789
M30	69	B-rif	fl. sst	r	equant		10	034	5.8	78	130	5.0	14	210			
M30	69	B-rif	o. lst	r	disc	4.2	33	221	3.0	82	332	1.2	06	135	135	0.400	0.714
M30	69	B-rif	fl. sst	r	disc	5.7	05	006	3.2	27	264	1.0	65	091	091	0.313	0.561
M30	69	B-rif	green b.	sa	equant	4.0	33	343	3.6	65	176	3.5	20	080		0.972	0.900
M32	124	B-rif	qr. lst	sa	equant	26.6	24	353	12.5	20	245	8.2	58	072	072	0.656	0.470
M32	124	B-rif	gr. lst	sa	equant	13.0	17	018	9.5	81	274	7.7	12	094	094	0.811	0.731
M32	124	B-rif	gr. lst	sr	prolate	19.7	04	333	8.7	06	079	7.5	82	172		0.862	0.442
M32	124	B-rif	gr. lst	sr	disc	18.2	39	005	12.8	52	180	5.5	13	086	086	0.430	0.703
M32	124	B-rif	o. lst	sr	equant	13.3	30	006	7.7	64	196	6.8	12	098	064	0.883	0.579
M32	124	B-rif	fl. sst	r	disc	12.3	13	357	9.0	43	266	2.4	50	102	102	0.267	0.732
M32	124	B-rif	o. lst	r	equant	4.8	10	012	4.5	72	112	2.5	15	279		0.556	0.938
M32	124	B-rif	o. lst	r	disc		07	325	8.2	78	218	2.9	04	058	058		
M32	124	B-rif	gr. lst	sr	disc	10.0	48	352	6.6	29	212	2.7	14	096	096	0.409	0.660
M32	124	B-rif	fl. sst	sr	prolate	8.7	80	001	3.5	18	100	3.3	20	191		0.943	0.402
M32	124	B-rif	o. lst	sr	equant		17	271	7.4	06	003	4.3	75	104	026		
M32	124	B-rif	fl. sst	r	prolate	11.0	36	010	5.2	47	198	3.5	24	085		0.673	0.473
M32	124	B-rif	o. lst	sr	disc	8.2	05	006	3.9	59	276	3.0	32	092	092	0.769	0.476
M32	124	B-rif	o. lst	sr	equant	8.5	78	003	7.2	20	180	7.0	04	081		0.972	0.847
M32	124	B-rif	o. lst	r	prolate	13.5	45	342	4.9	30	175		16	272			
M32	124	B-rif	red b.	sa	disc		00		6.8	05	190	2.2	83	025	354		
M32	124	B-rif	fl. sst	r	equant	4.7	17	169	3.7	55	002	3.5	00			0.946	0.787
M32	124	B-rif	gr. lst	sr	equant	8.7	13	048	6.6	48	303	4.5	30	149	149	0.682	0.759
M32	124	B-rif	red b.	sa	disc	6.5	14	014	4.3	12	282	2.2	65	169	084	0.512	0.662
M32	124	B-rif	o. lst	r	disc	6.0	05	359	3.5	65	271	1.8	32	085	085	0.514	0.583
M32	124	B-rif	fl. sst	r	equant	9.6	57	344		08	353	3.6	22	161			
M32	124	B-rif	o. lst	r	disc	5.0	12	153	4.2	10	065	1.3	78	264	296	0.310	0.840
M32	124	B-rif	gr. lst	sr	disc	7.0	35	295	4.0	68	030	1.7	11	218	218	0.425	0.571
M32	124	B-rif	gr. lst	sa	equant	11.0	00		10.7	62	078		30	264			
M32	124	B-rif	green b.	sr	equant	6.3	20	352	3.5	42	242	2.8	35	077		0.800	0.556
M32	124	B-rif	o. lst	r	disc	3.0	08	276	2.7	11	004	1.2	44	178	178	0.444	0.900
M32	124	B-rif	green b.	sa	disc	4.7	37	007		08	264	1.6	46	182	182		
M32	124	B-rif	o. lst	sr	disc	8.4	45	334	5.0	11	225	2.0	59	142	142	0.400	0.595
M32	124	B-rif	gr. lst	r	disc	4.5	04	064	4.0	13	318	1.0	78	154	108	0.250	0.889
M32	124	B-rif	fl. sst	sr	prolate	6.7	07	174	2.7	70	076	2.5	27	272		0.926	0.403
M32	124	B-rif	o. lst	sr	equant	4.8	49	324	4.0	32	218	3.5	30	104		0.875	0.833
M32	124	B-rif	red b.	sr	disc	10.5	27	112	7.2	51	016	2.4	30	202	202	0.333	0.686
M32	124	B-rif	gr. lst	sr	disc	9.4	30	000	5.0	19	274	3.1	46	163		0.620	0.532
M32	124	B-rif	gr. lst	r	disc	3.7	07	272	3.2	20	014	0.9	70	204	022	0.281	0.865
M32	124	B-rif	red b.	sa	disc	10.3	12	004		20	094	3.0	80	190	310		
M32	124	B-rif	o. lst	sr	disc	4.5	20	018	3.5	49	215	1.2	32	094	094	0.343	0.778
M32	124	B-rif	qr. lst	sr	disc	4.4	08	340	2.7	31	079	0.5	64	272	272	0.185	0.614
M32	124	B-rif	red b.	sa	disc	2.5	36	095	2.4	07	348	0.4	48	257	257	0.167	0.960
M32	124	B-rif	o. lst	sr	prolate	9.4	38	110	6.0	30	018	2.5	25	215	215	0.417	0.638
M32	124	B-rif	o. lst	sr	disc	5.3	29	312	4.0	05	048	2.2	59	127	127	0.550	0.755
M32	124	B-rif	red b.	sa	equant	2.8	32	284	2.6	10	180	2.2	70	090		0.846	0.929
M32	124	B-rif	fl. sst	sr	disc		10	273	5.0	38	356	1.9	32	175	175		
M32	124	B-rif	o. lst	r	disc	5.0	25	345	2.9	04	243	1.3	68	106	106	0.448	0.580
M32	124	B-rif	gr. lst	r	equant	7.7	17	180	4.9	42	282	3.4	50	105	105	0.694	0.636
M32	124	B-rif	green b.	sr	disc	6.0	39	347	5.3	12	254	2.6	44	160	160	0.491	0.883
M32	124	B-rif	fl. sst	r	disc	6.4	30	016		08	110	1.7	54	197	136		
M32	124	B-rif	green b.	sr	disc	4.8	69	040	3.3	08	293	1.8	22	192	192	0.545	0.688
M32	124	B-rif	red b.	sr	disc	5.0	16	342		10	244	1.6	68	141	141		
M32	124	B-rif	green b.	sa	disc	6.3	12	183	4.0	57	285	2.0	25	087	087	0.500	0.635
M32	124	B-rif	o. lst	sr	disc	4.8	00		3.9	06	099	1.7	86	284	340	0.436	0.813

CLASS	NO.
bladed	6
disc	15
prolate	6
equant	7

PALAEOC TOTALS

	M20ii
0-30	3
31-60	5
61-90	4
91-120	2
121-150	2
151-180	1
181-210	1
211-240	4
241-270	1
271-300	4
301-330	3
331-360	3
	33

CLASS	NO.
bladed	9
disc	13
prolate	4
equant	7

PALAEOC TOTALS

	M30
0-30	3
31-60	1
61-90	5
91-120	8
121-150	7
151-180	3
181-210	3
211-240	1
241-270	0
271-300	1
301-330	0
331-360	0
	32

CLASS	NO.
bladed	11
disc	14
prolate	8
equant	6

PALAEOC TOTALS

	M32
0-30	2
31-60	1
61-90	6
91-120	8
121-150	5
151-180	3
181-210	3
211-240	2
241-270	1
271-300	2
301-330	1
331-360	2
	36

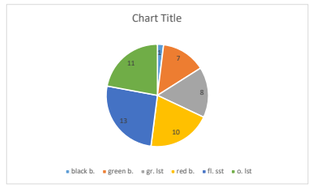

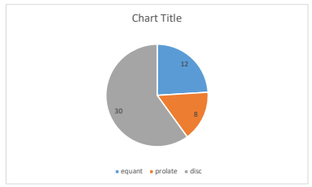

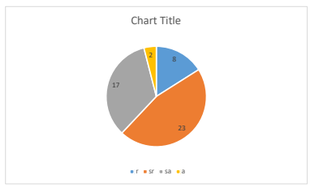

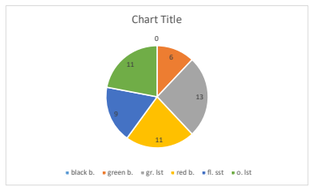

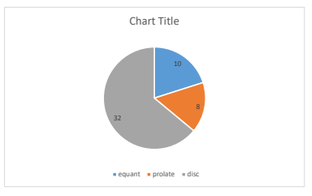

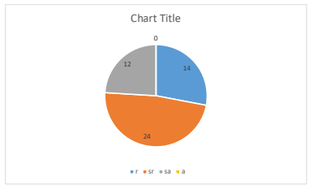

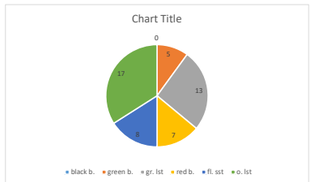

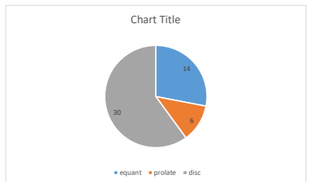

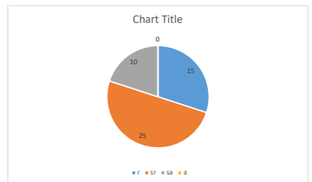

locality	bed	facies	comp	round	shape	a length	a plunge	a azimuth	b length	b plunge	b azimuth	c length	c plunge	c azimuth	palaeocurrent	ZINGG CLAST SHAPES c/b ratio	b/a ratio
M9	9	B-plm	qr. lst	sr	equant	25.5	08	156	13.3	86	064	9.8	03	230		0.737	0.522
M9	9	B-plm	o. lst	sr	equant	19.9	16	252	13.2	57	363	12.1	09	037		0.917	0.663
M9	9	B-plm	fl. sst	r	disc	16.7	30	149	13.5	58	245	5.3	27	053	053	0.393	0.808
M9	9	B-plm	red b.	sr	disc		19	225	13.1	01	333	5.3	61	069	069		
M9	9	B-plm	fl. sst	r	prolate	17.6	54	220	10.3	37	001	4.9	06	128	317	0.476	0.585
M9	9	B-plm	red b.	sa	equant	12.6	31	199	11.3	17	280	6.7	69	055	055	0.593	0.897
M9	9	B-plm	gr. lst	sr	equant	13.7	02	166		03	072	4.6	82	250			
M9	9	B-plm	fl. sst	r	prolate	19.7	41	195	17.9	36	004	6.4	09	111	316	0.358	0.909
M9	9	B-plm	qr. lst	sr	equant	11.5	18	227	7.7	39	115	4.9	51	328		0.636	0.670
M9	9	B-plm	o. lst	sa	equant		28	090	9.4	35	147	6.9	78	279			
M9	9	B-plm	fl. sst	sr	disc	13.6	21	196	10.5	69	297	2.2	31	099	099	0.210	0.772
M9	9	B-plm	qr. lst	sr	equant	9.7	01	030	6.3	01	036	4.0	90			0.635	0.649
M9	9	B-plm	fl. sst	sr	disc	9.3	08	159	7.4	15	266	2.5	77	083	083	0.338	0.796
M9	9	B-plm	qr. lst	sa	equant	7.2	45	116	5.8	49	269	4.3	13	018		0.741	0.806
M9	9	B-plm	fl. sst	sr	disc	7.9	34	314	5.3	16	054	2.5	38	155	155	0.472	0.671
M9	9	B-plm	gr. lst	sr	equant	11.6	35	325	7.2	40	250	7.0	77	110		0.972	0.621
M9	9	B-plm	fl. sst	sr	disc	8.4	03	208	5.3	55	296	2.2	37	123	123	0.415	0.631
M9	9	B-plm	fl. sst	r	equant	14.0	16	267	10.3	45	359	8.2	33	165	153	0.796	0.736
M9	9	B-plm	o. lst	sr	equant	7.7	24	209	6.4	13	121	3.0	69	350	355	0.469	0.831
M9	9	B-plm	fl. sst	sr	disc		13	238	8.3	28	314	2.6	67	135	135		
M9	9	B-plm	o. lst	sa	disc	7.8	08	053	7.0	04	143	2.3	72	238	274	0.329	0.897
M9	9	B-plm	fl. sst	sr	equant	8.7	55	294	4.5	10	208	3.7	33	112		0.822	0.517
M9	9	B-plm	qr. lst	r	disc	8.7	50	261	8.0	11	164	1.9	15	073	073	0.238	0.920
M9	9	B-plm	qr. lst	r	disc	7.2	20	336	6.1	28	248	2.0	56	090	104	0.328	0.847
M9	9	B-plm	fl. sst	r	equant		11	248	5.7	06	165	5.0	64	345			
M9	9	B-plm	o. lst	sa	equant	8.8	04	110	7.3	60	200	4.5	64	027		0.616	0.830
M9	9	B-plm	fl. sst	r	disc	6.6	28	326	6.0	02	245	2.8	58	133	142	0.467	0.909
M9	9	B-plm	chert	sa	equant	7.0	35	336	6.0	38	173		11	048			
M9	9	B-plm	o. lst	sa	disc	8.1	04	168		05	264	2.4	84	050	045		
M9	9	B-plm	fl. sst	r	disc	6.1	11	305		08	042	1.8	81	142	160		
M9	9	B-plm	red b.	sa	disc	7.0	09	129		18	204	2.2	60	294	283		
M9	9	B-plm	fl. sst	r	disc	5.6	18	148	3.4	30	043	1.7	64	308	290	0.500	0.607
M9	9	B-plm	fl. sst	sr	disc	5.6	19	142	4.1	35	029	1.4	33	202	202	0.341	0.732
M9	9	B-plm	o. lst	sr	disc	8.1	09	181		02	274	2.7	84	003	353		
M9	9	B-plm	fl. sst	r	disc	5.4	13	168	3.6	16	078	1.3	60	345	321	0.361	0.667
M9	9	B-plm	fl. sst	sr	disc	5.7	19	322	4.8			1.6	85	144	144	0.333	0.842
M9	9	B-plm	red b.	sa	equant	4.4	69	144	3.4	12	230	2.8	04	322		0.824	0.773
M9	9	B-plm	fl. sst	r	prolate	7.4	03	344	3	16	256	2.7	74	165		0.900	0.405
M9	9	B-plm	red b.	sa	equant	6.6	28	178	4	06	268	3.9	77	006		0.975	0.606
M9	9	B-plm	fl. sst	r	disc	6.3	08	288	4	34	190	1.3	64	012	034	0.325	0.635
M9	9	B-plm	qr. lst	sr	equant	6.9	38	209	4	17	293	3.5	45	028		0.875	0.580
M9	9	B-plm	fl. sst	r	disc	8.4	36	034	6.5	60	131	2.5	10	288	279	0.385	0.774
M9	9	B-plm	qr. lst	sr	equant	12.0	09	208	8	64	303	5.0	16	119		0.625	0.667
M9	9	B-plm	o. lst	sa	disc	7.9	04	238	5.1	18	322	2.6	80	138	138	0.510	0.646
M9	9	B-plm	fl. sst	r	prolate		07	216	6.3	05	310	4.1	80	034			
M9	9	B-plm	fl. sst	sr	disc	7.3	34	307	5	24	195	1.1	18	065	082	0.220	0.685
M9	9	B-plm	qr. lst	sr	equant	6.4	02	270	5.5	58	183	1.7	28	004	004	0.309	0.859
M9	9	B-plm	gr. lst	r	disc	6.8	10	151	5.3	42	236	1.3	31	074	074	0.245	0.779
M9	9	B-plm	red b.	a	equant		06	264	8.2	24	165	6.2	88	074			
M9	9	B-plm	o. lst	r	prolate	7.7	12	283	4.4	14	019	2.2	75	204	204	0.500	0.571
M13	17	B-plm	fl. sst	sr	equant	19.4	23	166	13.4	35	081	8.0	70	255		0.597	0.691
M13	17	B-plm	fl. sst	sr	disc	13.6	33	124	11.7	03	027	3.6	68	306	273	0.308	0.860
M13	17	B-plm	fl. sst	r	equant		12	275	10.7	58	010	10.4	24	169	196		
M13	17	B-plm	red b.	sa	equant	9.0	02	034		12	136	6.6	75	300			
M13	17	B-plm	fl. sst	r	disc	18.0	25	211	7.3	08	312	2.5	57	040	113	0.342	0.406
M13	17	B-plm	qr. lst	sr	equant	9.0	03	006	7.2	30	102	4.6	62	278	278	0.639	0.800
M13	17	B-plm	fl. sst	sr	equant	12.2	08	049		13	146	5.3	81	304	233		
M13	17	B-plm	gr. lst	sa	equant	7.3	36	229	6.4	12	321	4.8	64	143		0.750	0.877
M13	17	B-plm	o. lst	sr	disc	12.9	21	228	6.4	10	128	2.9	60	037	206	0.453	0.496
M13	17	B-plm	gr. lst	sa	equant	10.2	08	026	9.2	04	120	6.5	87	295		0.707	0.902
M13	17	B-plm	qr. lst	sa	disc		02	149	10.7	22	053	3.1	77	278	229		
M13	17	B-plm	fl. sst	r	disc	8.0	37	200	5.5	29	113	1.4	20	295	290	0.255	0.688
M13	17	B-plm	fl. sst	sr	equant	9.5	14	160	8.0	08	255	5.8	68	340		0.725	0.842
M13	17	B-plm	qr. lst	sa	disc	8.5	05	191	6.5	22	099	2.0	76	002	244	0.308	0.765
M13	17	B-plm	fl. sst	sr	equant	8.6	05	041	4.4	32	304	4.2	75	212		0.955	0.512
M13	17	B-plm	fl. sst	r	disc	10.0	18	205		12	112	3.6	82	020	261		
M13	17	B-plm	fl. sst	sr	disc	14.0	06	058	8.5	12	155	4.0	86	252	252	0.471	0.607
M13	17	B-plm	fl. sst	r	disc	12.2	23	174	7.4	13	092	2.7	67	356	238	0.365	0.607
M13	17	B-plm	red b.	sa	disc	8.3	24	125	7.5	04	032	1.9	75	304	276	0.253	0.904
M13	17	B-plm	fl. sst	r	equant	8.0	15	213	4.8	06	116	4.1	65	027		0.854	0.600
M13	17	B-plm	fl. sst	r	equant	9.3	12	058	4.2	04	159	3.7	85	259		0.881	0.452
M13	17	B-plm	gr. lst	sr	disc	7.5	18	167	5.3	29	075	1.8	38	258	244	0.340	0.707
M13	17	B-plm	o. lst	sa	equant	12.0	08	038		36	295	6.7	50	119			
M13	17	B-plm	fl. sst	r	equant	18.1	05	212		35	305	8.2	54	128	113		
M13	17	B-plm	fl. sst	sr	equant	12.7	01	015	9.0	02	291	6.4	83	110	110	0.711	0.709
M13	17	B-plm	red b.	a	disc	9.9	18	238	7.0	09	131	2.1	77	232	232	0.300	0.707
M13	17	B-plm	qr. lst	sa	prolate	7.4	02	150	4.0	25	258	2.4	83	004		0.600	0.541
M13	17	B-plm	green b.	sa	disc	4.6	01	135	3.1	28	247	1.4	88	334	254	0.452	0.674
M13	17	B-plm	o. lst	sr	equant	7.5	00		3.8	75	277	2.8	20	093	104	0.737	0.507
M13	17	B-plm	fl. sst	r	equant	8.9	17	225	6.8	62	120		18	325			
M13	17	B-plm	fl. sst	r	disc	8.0	08	142	5.8	33	240	2.2	48	056	246	0.379	0.725
M13	17	B-plm	gr. lst	r	disc	8.3	23	101	6.4	00		2.9	80	275	267	0.453	0.771
M13	17	B-plm	fl. sst	r	equant	9.6	24	185	5.4	15	097	5.0	70	280	271	0.926	0.563
M13	17	B-plm	green b.	sa	prolate	6.0	07	093	3.6	22	186	3.0	70	001		0.833	0.600
M13	17	B-plm	qr. lst	r	equant	6.3	01	218	5.4	28	306	5.3	55	136		0.981	0.857
M13	17	B-plm	fl. sst	sr	disc	6.7	11	259	3.0	29	193	1.2	64	007	058	0.400	0.448
M13	17	B-plm	o. lst	r	equant	7.4	26	115	6.2	72	217	3.9	29	359		0.629	0.838
M13	17	B-plm	red b.	sr	disc	6.4	09	203	4.5	18	091	1.3	70	292	207	0.289	0.703
M13	17	B-plm	qr. lst	r	equant	10.9	06	249	9.9	27	119	5.0	50	029		0.505	0.908
M13	17	B-plm	o. lst	sr	disc	9.7	30	180	6.5	23	090	3.1	52	357	227	0.477	0.670
M13	17	B-plm	fl. sst	r	disc	4.5	80	096	3.7	05	213	1.6	24	292		0.432	0.822
M13	17	B-plm	o. lst	r	prolate	5.8	20	133	2.6	25	216	2.6	84	257	191	1.000	0.448
M13	17	B-plm	fl. sst	r	equant		41	134	5.9	28	034	4.2	71	243			
M13	17	B-plm	fl. sst	r	disc	5.5	23	150	4.6	35	064	1.7	49	288	199	0.370	0.836
M13	17	B-plm	gr. lst	sr	equant	4.6	23	199	3.5	28	120	2.3	63	296	179	0.657	0.761
M13	17	B-plm	fl. sst	r	disc		00		4.5	01	259	2.0	83	273	192		
M13	17	B-plm	fl. sst	a	equant	18.3	01	047		04	299	8.5	89	326			
M13	17	B-plm	red b.	sa	disc	11.4	31	208	8.2	21	132	2.8	74	343	211	0.341	0.719
M13	17	B-plm	o. lst	sr	disc	4.4	26	151	3.1	21	223	1.3	58	028	028	0.419	0.705
M22	41	B-plm	fl. sst	r	disc	26.5	26	185	12.8	08	277	7.4	57	355	158	0.578	0.483
M22	41	B-plm	qr. lst	sr	equant	19.6	05	204	16.0	32	108	10.5	78	299		0.656	0.816
M22	41	B-plm	qr. lst	sr	disc	15.8	52	054	8.2	05	154	2.9	21	241	241	0.354	0.519
M22	41	B-plm	red b.	sr	disc	16.2	30	348	10.1	18	261	7.4	53	152	127	0.733	0.623
M22	41	B-plm	qr. lst	r	equant	13.9	10	273	9.5	70	174	8.0	04	359		0.842	0.683
M22	41	B-plm	fl. sst	r	equant	14.8	23	158	12.5	76	265	11.2	32	087		0.896	0.845
M22	41	B-plm	qr. lst	sa	prolate	16.2	12	252	7.5	63	346	6.0	14	157	086	0.800	0.463
M22	41	B-plm	fl. sst	sr	disc	15.5	33	058	11.3	02	157	3.0	33	252	252	0.265	0.729
M22	41	B-plm	gr. lst	sr	oblate	19.6	05	214	10.0	42	133	4.3	63	313	340	0.430	0.510
M22	41	B-plm	qr. lst	sa	equant	16.0	18	030		22	309	9.5	60	142	058		
M22	41	B-plm	gr. lst	sr	equant	18.0	24	039	13.2	68	134	9.3	08	317		0.705	0.733
M22	41	B-plm	o. lst	r	disc	18.6	15	044		30	305	7.3	73	133	133		
M22	41	B-plm	fl. sst	r	disc	11.4	14	195	9.7	52	090	3.3	32	281	281	0.340	0.851
M22	41	B-plm	o. lst	r	equant	11.0	52	113	6.5	43	296	6.5	26	203		1.000	0.591
M22	41	B-plm	qr. lst	r	disc	14.3	03	011	11.2	38	106	5.7	44	278	278	0.509	0.783
M22	41	B-plm	qr. lst	sr	disc	10.2	19	196	6.4	12	296	3.7	64	020	020	0.578	0.627
M22	41	B-plm	o. lst	sa	equant	8.8	28	133	7.0	03	242	3.8	62	317	298	0.543	0.795
M22	41	B-plm	fl. sst	sa	prolate		24	100	7.7	36	022	6.5	55	204			
M22	41	B-plm	fl. sst	r	disc	15.8	27	004	13.5	83	118	4.8	07	285	238	0.356	0.854
M22	41	B-plm	o. lst	sa	equant	11.2	06	036	6.6	50	127	6.3	31	112		0.955	0.589
M22	41	B-plm	qr. lst	sr	disc	8.3	03	346	7.9	10	254	3.7	77	093	075	0.468	0.952
M22	41	B-plm	qr. lst	sr	disc	7.9	42	058	5.5	28	320	2.8	31	156	118	0.509	0.696
M22	41	B-plm	o. lst	sr	equant	8.4	23	025	6.3	66	123	5.7	27	308	308	0.905	0.750
M22	41	B-plm	qr. lst	sr	disc	9.2	12	095	6.5	30	008	4.0	32	192	192	0.615	0.707
M22	41	B-plm	red b.	r	disc	7.7	10	215	6.4	49	130	3.1	32	318	012	0.484	0.831
M22	41	B-plm	red b.	sr	disc	9.2	21	055		17	334	4.1	52	230	151		
M22	41	B-plm	o. lst	r	disc	5.5	28	055	3.1	12	331	2.1	56	223	223	0.677	0.564
M22	41	B-plm	gr. lst	sa	disc	6.3	23	172	4.5	40	075	1.8	38	266	266	0.400	0.714
M22	41	B-plm	qr. lst	sa	disc	7.3	64	040	7.0	21	222	3.0	04	123	115	0.429	0.959
M22	41	B-plm	o. lst	sr	disc	7.3	13	058	4.0	48	156	1.7	45	336	352	0.425	0.548
M22	41	B-plm	qr. lst	sr	disc	6.4	09	196	4.9	83	300	1.9	08	120	112	0.388	0.766
M22	41	B-plm	red b.	sa	equant	6.2	01	218	3.5	85	315	3.2	05	140		0.914	0.565
M22	41	B-plm	o. lst	sr	disc	8.2	73	296	5.3	03	045	2.4	30	121	109	0.453	0.646
M22	41	B-plm	fl. sst	sr	disc	6.4	74	142	3.5	24	348	1.8	12	250	271	0.514	0.547
M22	41	B-plm	fl. sst	r	prolate	8.2	84	004	3.3	14	193	3.2	12	109		0.970	0.402
M22	41	B-plm	qr. lst	sr	equant	14.0	00		10.5	87	136		02	314			
M22	41	B-plm	o. lst	sa	disc	6.3	08	148	6.2	74	061	3.0	12	237	237	0.484	0.984
M22	41	B-plm	fl. sst	r	disc	5.4	51	038	2.9	21	296	1.6	52	205	138	0.552	0.537
M22	41	B-plm	green b.	sa	disc	4.2	43	000	3.3	16	275	2.0	53	170	140	0.606	0.786
M22	41	B-plm	fl. sst	r	equant	11.3	22	044	8.5	63	137		15	308			
M22	41	B-plm	fl. sst	r	equant	5.5	18	343	4.8	61	075	3.4	32	266		0.708	0.873
M22	41	B-plm	qr. lst	sr	disc	7.2	16	036	4.4	85	298	1.9	12	130	130	0.432	0.611
M22	41	B-plm	qr. lst	r	equant	9.4	23	352	8.4	35	088	5.5	20	273		0.655	0.894
M22	41	B-plm	fl. sst	sr	disc	8.3	24	054	5.5	12	136	3.1	71	224	195	0.564	0.663
M22	41	B-plm	green b.	a	equant	5.2	12	017	4.0	88	284	3.1	00			0.775	0.769
M22	41	B-plm	red b.	sa	disc	4.6	27	046	3.2	61	144	0.7	06	312	018	0.219	0.696
M22	41	B-plm	fl. sst	r	equant	5.5	00		5.3	89	296	3.2	02	116		0.604	0.964
M22	41	B-plm	qr. lst	sr	disc	6.3	43	350		38	266	1.8	28	160	110		
M22	41	B-plm	fl. sst	r	disc	8.5	05	041	6.2	27	144	0.9	75	273	327	0.145	0.729
M22	41	B-plm	fl. sst	r	disc	7.3	13	206	4.3	66	301	2.4	25	018	035	0.558	0.589

CLASS	NO.
bladed	10
disc	18
prolate	7
equant	3

PALAEOC TOTALS

	M9
0-30	1
31-60	4
61-90	5
91-120	2
121-150	5
151-180	3
181-210	2
211-240	0
241-270	0
271-300	4
301-330	3
331-360	2
	31

CLASS	NO.
bladed	6
disc	20
prolate	7
equant	5

PALAEOC TOTALS

	M13
0-30	1
31-60	1
61-90	0
91-120	4
121-150	1
151-180	1
181-210	6
211-240	6
241-270	7
271-300	5
301-330	0
331-360	0
	32

CLASS	NO.
bladed	11
disc	19
prolate	7
equant	6

PALAEOC TOTALS

	M22
0-30	3
31-60	2
61-90	2
91-120	5
121-150	5
151-180	2
181-210	2
211-240	3
241-270	3
271-300	4
301-330	2
331-360	2
	35

M9/L14

chert	1				
black b.	0	equant	21	r	17
green b.	0	prolate	5	sr	21
qr. lst	12	disc	24	sa	11
red b.	6			a	1
fl. sst	22				
o. lst	9				
	50		50		50

M13/L8

black b.	0	equant	23	r	20
green b.	2	prolate	3	sr	17
qr. lst	13	disc	24	sa	11
red b.	5			a	2
fl. sst	23				
o. lst	7				
	50		50		50

M22/L17

black b.	0	equant	16	r	18
green b.	2	prolate	3	sr	20
qr. lst	19	disc	30	sa	11
red b.	5	oblate	1	a	1
fl. sst	15				
o. lst	9				
	50		50		50

M30/L20

black b.	0	equant	16	r	12
green b.	7	prolate	8	sr	23
qr. lst	8	disc	26	sa	13
red b.	6			a	2
fl. sst	13				
o. lst	16				
	50		50		50

M29/L7(ii)

black b.	1	equant	17	r	25
green b.	5	prolate	8	sr	16
qr. lst	9	disc	25	sa	7
red b.	9			a	2
fl. sst	19				
o. lst	7				
	50		50		50

M29/L7(iii)

black b.	1	equant	17	r	35
green b.	2	prolate	7	sr	11
qr. lst	3	disc	26	sa	3
red b.	6			a	1
fl. sst	33				
o. lst	5				
	50		50		50

M32/L3

black b.	0	equant	19	r	16
green b.	2	prolate	5	sr	24
qr. lst	13	disc	26	sa	10
red b.	10			a	0
fl. sst	6				
o. lst	19				
	50		50		50

M35/L11

black b.	0	equant	25	r	14
green b.	3	prolate	8	sr	26
qr. lst	20	disc	17	sa	10
red b.	7			a	0
fl. sst	10				
o. lst	10				
	50		50		50

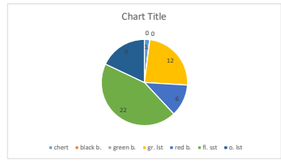

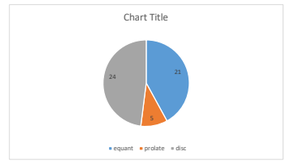

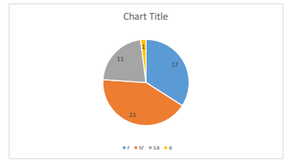

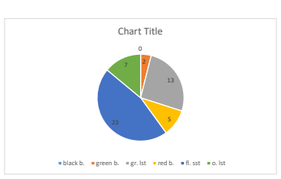

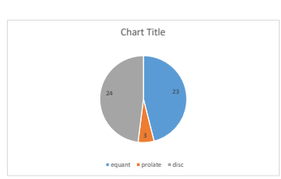

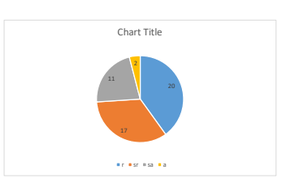

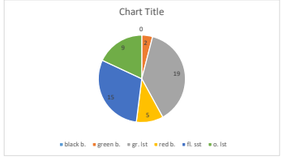

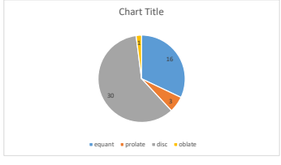

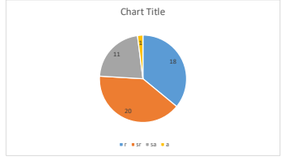

M30	71	B-plm	fl. sst	sr	prolate	24.2	36	352	12.3	34	100	8.6	12	263		0.699	0.508
M30	71	B-plm	o. lst	sa	equant	16.8	08	189	12.6	42	296	10.5	54	123		0.833	0.750
M30	71	B-plm	green b.	a	equant	11.4	22	312	11.2	10	230	8.0	68	126		0.714	0.982
M30	71	B-plm	o. lst	sr	disc	16.0	35	062	14.7	09	321	6.3	57	226	168	0.429	0.919
M30	71	B-plm	gr. lst	sr	equant	18.5	60	286	12.7	28	106	9.8	07	008		0.772	0.686
M30	71	B-plm	qr. lst	sr	disc	13.2	08	356	8.1	23	073	3.9	72	176	176	0.481	0.614
M30	71	B-plm	qr. lst	sa	disc	10.5	07	307		36	050	2.5	57	226	226		
M30	71	B-plm	o. lst	r	prolate	19.5	25	103	9.0	37	197	7.3	52	293		0.811	0.462
M30	71	B-plm	o. lst	sr	disc		25	211	14.1	90		9.7	00				
M30	71	B-plm	fl. sst	sr	equant	21.2	10	293		13	193	11.5	78	093	093		
M30	71	B-plm	o. lst	sr	disc	16.4	04	306	13.8	38	044	6.1	55	213	213	0.442	0.841
M30	71	B-plm	o. lst	sa	equant	14.4	28	323	9.0	36	069	7.9	35	170	170	0.878	0.625
M30	71	B-plm	fl. sst	sr	equant	9.6	37	052	6.5	42	251	6.3	13	350		0.969	0.677
M30	71	B-plm	red b.	sa	prolate		13	037	6.8	20	322	5.1	65	223			
M30	71	B-plm	green b.	sa	disc	7.5	34	110	6.0	28	007	3.1	46	273	178	0.517	0.800
M30	71	B-plm	gr. lst	sr	equant	5.7	28	071	4.5	05	326	4.3	64	241		0.956	0.789
M30	71	B-plm	green b.	sr	disc	6.9	35	246	4.8	77	349	2.0	03	162	162	0.417	0.696
M30	71	B-plm	qr. lst	r	disc	9.4	43	090	9.3	12	350	4.2	61	248		0.452	0.989
M30	71	B-plm	o. lst	sr	disc	11.0	07	136	8.0	28	054	4.6	61	234	234	0.575	0.727
M30	71	B-plm	fl. sst	sa	disc	17.7	25	262	15.3	42	009	8.0	50	117	117	0.523	0.864
M30	71	B-plm	fl. sst	sr	prolate	12.4	69	087	5.7	12	270	2.5	04	168		0.439	0.460
M30	71	B-plm	fl. sst	r	equant		12	181	8.6	41	082	4.9	19	273			
M30	71	B-plm	o. lst	sr	disc	9.5	03	082	8.9	54	184	3.2	31	350	350	0.360	0.937
M30	71	B-plm	o. lst	sa	equant	9.6	43	317	8.5	57	132	7.9	22	042		0.929	0.885
M30	71	B-plm	red b.	sa	equant	9.0	41	145	5.3	03	248	4.8	44	336	336	0.906	0.589
M30	71	B-plm	red b.	sa	prolate	8.0	33	225	3.9	09	326	3.4	66	055	055	0.872	0.488
M30	71	B-plm	green b.	sa	disc	5.6	01	317	5.5	50	056	2.4	52	227	227	0.436	0.982
M30	71	B-plm	fl. sst	sr	equant	5.0	11	356	4.5	10	263	4.1	76	101		0.911	0.900
M30	71	B-plm	green b.	sr	equant	7.6	14	125		04	220	5.4	78	313			
M30	71	B-plm	gr. lst	r	disc	6.7	11	112	4.6	16	223	2.8	72	038	038	0.609	0.687
M30	71	B-plm	fl. sst	r	disc	11.5	12	233	10.6	30	334	2.3	68	093	093	0.217	0.922
M30	71	B-plm	gr. lst	sr	equant	7.5	06	139	6.8	61	306	6.6	15	209		0.971	0.907
M30	71	B-plm	green b.	sa	disc	5.6	72	304	5.4	13	206	2.4	15	105	105	0.444	0.964
M30	71	B-plm	fl. sst	r	disc	6.0	22	236	4.5	31	322	0.8	42	122	122	0.178	0.750
M30	71	B-plm	o. lst	r	disc	5.5	16	086	4.3	10	174	1.9	64	335	335	0.442	0.782
M30	71	B-plm	red b.	sa	prolate	5.4	23	321	2.8	70	222	1.7	21	115		0.607	0.519
M30	71	B-plm	o. lst	r	disc	4.6	10	274	3.3	70	007	2.0	12	192	192	0.606	0.717
M30	71	B-plm	green b.	a	prolate	8.9	42	072	4.5	23	312	2.3	51	210		0.511	0.506
M30	71	B-plm	o. lst	sr	disc	4.6	72	103	4.2	24	006	1.8	20	278	278	0.429	0.913
M30	71	B-plm	red b.	sa	disc	4.8	05	141	4.6	08	053	2.0	73	235	235	0.435	0.958
M30	71	B-plm	fl. sst	r	equant	7.0	12	244	5.5	08	344	4.0	75	181		0.727	0.786
M30	71	B-plm	fl. sst	sr	disc	5.7	85	224	4.1	08	080	2.3	04	322	322	0.561	0.719
M30	71	B-plm	red b.	sr	disc	8.2	41	150	7.3	12	252	3.9	47	335	045	0.534	0.890
M30	71	B-plm	o. lst	r	equant	6.5	31	175	5.6	08	073	4.8	52	327		0.857	0.862
M30	71	B-plm	o. lst	sr	disc	3.4	08	285	3.2	10	194	1.1	79	095	075	0.344	0.941
M30	71	B-plm	gr. lst	sr	equant	4.7	11	356		12	266	2.7	75	180			
M30	71	B-plm	fl. sst	r	prolate	9.0	31	026	3.8	22	298	2.5	67	114		0.658	0.422
M30	71	B-plm	o. lst	sr	disc	6.6	09	277	3.9	73	178	1.8	19	008		0.462	0.591
M30	71	B-plm	fl. sst	r	disc		05	190	5.8	13	105	2.3	78	282	250		
M30	71	B-plm	o. lst	sr	disc	4.4	69	059	3.7	16	315	2.0	52	214	206	0.541	0.841
M29	101	B-plm	qr. lst	sr	prolate	14.4	12	106	7.3	18	010	4.3	72	210	242	0.589	0.507
M29	101	B-plm	red b.	sr	disc	10.3	09	239	10.0	01	320	4.1	79	068	257	0.410	0.971
M29	101	B-plm	o. lst	sr	disc	8.3	43	081	6.5	30	170	1.8	37	264		0.277	0.783
M29	101	B-plm	fl. sst	r	equant	9.2	20	246	5.2	06	136	4.9	72	052		0.942	0.565
M29	101	B-plm	qr. lst	sa	equant	7.7	10	010	7.2	35	108	6.2	63	220		0.861	0.935
M29	101	B-plm	fl. sst	r	disc	9.0	33	079		07	172	1.9	61	257	257		
M29	101	B-plm	fl. sst	r	equant	10.3	03	248	7.9	35	144	7.6	59	339		0.962	0.767
M29	101	B-plm	o. lst	sr	equant	12.2	08	281	6.3	12	184	6.2	73	356		0.984	0.516
M29	101	B-plm	red b.	sa	disc	6.4	11	079	5.0	09	173	2.2	75	260	260	0.440	0.781
M29	101	B-plm	fl. sst	r	equant	12.6	31	346		62	174	7.6	09	270			
M29	101	B-plm	red b.	sr	disc		30	163	7.5	45	076	3.7	29	274			
M29	101	B-plm	green b.	sa	equant	9.2	01	016	6.1	24	280	4.6	75	114	298	0.754	0.663
M29	101	B-plm	gr. lst	r	disc	7.2	01	110	5.5	02	359	2.0	87	186	186	0.364	0.764
M29	101	B-plm	o. lst	r	prolate	7.1	03	008	3.8	27	098	1.7	67	280		0.447	0.535
M29	101	B-plm	fl. sst	r	equant	7.3	58	008	6.1	30	146	4.4	12	260		0.721	0.836
M29	101	B-plm	fl. sst	r	disc	11.6	04	305	6.2	42	040	2.0	48	207	207	0.323	0.534
M29	101	B-plm	red b.	r	equant	6.7	62	350		26	252	3.7	28	158	158		
M29	101	B-plm	o. lst	sr	equant	6.4	14	006	4.3	06	278	3.3	72	177		0.767	0.672
M29	101	B-plm	fl. sst	r	equant	6.8	01	058	5.1	73	321	4.0	16	154		0.784	0.750
M29	101	B-plm	fl. sst	r	disc	6.3	29	111	3.2	32	002	1.6	60	256	204	0.500	0.508
M29	101	B-plm	qr. lst	r	equant	7.7	11	107	6.2	22	355	4.5	70	204		0.726	0.805
M29	101	B-plm	fl. sst	r	prolate	8.2	08	267	2.5	02	174	2.2	83	080		0.880	0.305
M29	101	B-plm	fl. sst	r	disc	8.5	13	268	4.3	09	358	1.9	73	090	202	0.442	0.506
M29	101	B-plm	gr. lst	sr	disc	10.1	10	315	5.2	04	046	2.2	79	176	176	0.423	0.515
M29	101	B-plm	o. lst	sr	disc	4.3	03	265	2.7	17	173	1.8	64	014	274	0.667	0.628
M29	101	B-plm	red b.	a	prolate	9.7	37	198	3.6	32	092	3.6	52	340		1.000	0.371
M29	101	B-plm	fl. sst	r	prolate	10.2	09	070	4.1	27	160	2.4	52	258		0.585	0.402
M29	101	B-plm	green b.	sa	equant	2.4	07	101	2.2	23	022	1.7	71	200		0.773	0.917
M29	101	B-plm	o. lst	sa	disc	7.0	10	090	5.3	12	354	1.6	78	186	186	0.302	0.757
M29	101	B-plm	green b.	sr	prolate	5.2	09	356	2.5	25	093	2.3	52	274		0.920	0.481
M29	101	B-plm	qr. lst	sr	disc		10	190	4.0	17	096	1.2	71	290	290		
M29	101	B-plm	fl. sst	r	disc	9.2	23	095		37	194	1.6	59	273	273		
M29	101	B-plm	qr. lst	r	disc	4.8	12	147	4.6	50	052	1.2	22	224		0.261	0.958
M29	101	B-plm	gr. lst	r	equant	7.4	02	281	6.5	28	021	4.3	63	206	206	0.662	0.878
M29	101	B-plm	fl. sst	sr	equant	9.8	02	083	5.5	03	352	5.0	88	256		0.909	0.561
M29	101	B-plm	red b.	sr	disc	5.8	06	082	4.4	04	357	1.6	85	210	210	0.364	0.759
M29	101	B-plm	fl. sst	r	disc	5.2	22	110	4.0	06	205	1.5	67	295	225	0.375	0.769
M29	101	B-plm	red b.	r	prolate	5.2	19	003	2.5	40	092	1.7	36	272	231	0.680	0.481
M29	101	B-plm	fl. sst	r	disc	5.7	03	325	4.0	40	048	1.1	60	244	244	0.275	0.702
M29	101	B-plm	black b.	r	equant	6.2	02	095	4.7	00		2.0	84	282	203	0.426	0.758
M29	101	B-plm	green b.	a	prolate	3.8	54	114	2.0	36	326	1.9	14	220		0.950	0.526
M29	101	B-plm	fl. sst	sr	disc	5.0	10	344	4.6	30	082	1.9	57	231	231	0.413	0.920
M29	101	B-plm	o. lst	sr	disc	8.5	18	091	6.2	27	005	2.1	71	195	233	0.339	0.729
M29	101	B-plm	green b.	sa	disc	2.9	15	044	1.8	04	318	0.7	79	195	195	0.389	0.621
M29	101	B-plm	red b.	sa	disc	3.2	03	043	2.1	40	148	1.2	60	353	353	0.571	0.656
M29	101	B-plm	fl. sst	r	disc		28	203	4.4	48	112	1.8	45	314	314		
M29	101	B-plm	red b.	sr	disc	4.4	19	104		04	205	1.7	71	304	304		
M29	101	B-plm	gr. lst	sr	equant	3.2	14	088	2.4	07	166	1.7	68	255		0.708	0.750
M29	101	B-plm	fl. sst	r	equant	7.3	05	226	5.0	39	132	4.5	60	323		0.900	0.685
M29	101	B-plm	fl. sst	r	disc	3.7	05	284	2.0	35	192	1.3	32	025	215	0.650	0.541
M29	103	B-plm	fl. sst	r	prolate	9.4	28	186	5.5	78	097	4.2	06	289		0.764	0.585
M29	103	B-plm	red b.	sa	disc	9.4	06	127	7.2	68	040	3.5	20	239		0.486	0.766
M29	103	B-plm	fl. sst	r	disc	8.2	08	278	5.3	17	184	1.9	73	020	200	0.358	0.646
M29	103	B-plm	o. lst	r	disc	11.0	22	052	7.5	10	148	2.0	68	227	227	0.267	0.682
M29	103	B-plm	fl. sst	r	equant	7.0	45	324	4.9	48	152	4.2	03	054		0.857	0.700
M29	103	B-plm	fl. sst	r	disc	7.8	43	075		04	168	2.1	36	260	260		
M29	103	B-plm	fl. sst	r	equant	10.0	23	025	8.2	28	114	5.3	52	231		0.646	0.820
M29	103	B-plm	fl. sst	r	equant	8.7	01	107	7.0	52	009	4.9	36	200		0.700	0.805
M29	103	B-plm	gr. lst	r	disc	10.7	02	075	6.2	32	335	2.1	58	154	154	0.339	0.579
M29	103	B-plm	fl. sst	r	prolate	11.2	08	285		38	195	4.0	46	025			
M29	103	B-plm	qr. lst	sr	equant	8.4	21	232	4.8	46	138	4.5	32	333	333	0.938	0.571
M29	103	B-plm	fl. sst	r	equant	8.5	00		7.0	40	160	6.7	50	352		0.957	0.824
M29	103	B-plm	fl. sst	r	disc	7.1	05	106	5.0	60	005	2.2	22	198	020	0.440	0.704
M29	103	B-plm	fl. sst	r	prolate	6.0	14	350	2.7	22	248	2.0	42	082		0.741	0.450
M29	103	B-plm	fl. sst	r	prolate	6.2	01	329	4.5	04	075	2.5	86	162		0.556	0.726
M29	103	B-plm	fl. sst	sr	equant	6.5	33	327	3.7	14	068	3.4	50	160		0.919	0.569
M29	103	B-plm	fl. sst	r	equant	5.2	31	164	4.0	70	074	3.5	10	340		0.875	0.769
M29	103	B-plm	green b.	sa	disc	8.7	02	078	7.0	15	339	3.3	73	166	166	0.471	0.805
M29	103	B-plm	fl. sst	r	disc	9.2	18	152	6.0	80	063	3.4	08	253	068	0.567	0.652
M29	103	B-plm	green b.	sa	equant	8.0	26	337		82	080	4.2	08	264			
M29	103	B-plm	red b.	sr	disc		18	138	9.5	52	036	3.8	44	224	224		
M29	103	B-plm	fl. sst	r	disc	8.2	13	293	5.6	05	027	1.3	77	151	195	0.232	0.683
M29	103	B-plm	fl. sst	r	disc	5.2	26	102	4.0	03	004	2.0	65	252	252	0.500	0.769
M29	103	B-plm	fl. sst	r	disc	8.2	38	339	4.8	35	090	1.7	28	202	218	0.354	0.585
M29	103	B-plm	red b.	sr	equant	13.3	03	091	8.4	28	348	5.2	62	184		0.619	0.632
M29	103	B-plm	fl. sst	r	disc	8.0	08	114	3.5	06	356	1.8	84	192	192	0.514	0.438
M29	103	B-plm	fl. sst	r	equant	4.8	45	218	3.0	12	311	2.6	50	042		0.867	0.625
M29	103	B-plm	red b.	a	equant	4.8	28	186	3.3	60	090	3.0	24	295		0.909	0.688
M29	103	B-plm	black b.	sr	equant	3.0	02	082	2.6	64	170	2.3	28	354		0.885	0.867
M29	103	B-plm	fl. sst	r	disc	4.7	20	354	4.6	04	084	1.8	69	176	176	0.391	0.979
M29	103	B-plm	o. lst	sr	disc	6.2	08	183	4.3	30	093	2.0	55	294	294	0.465	0.694
M29	103	B-plm	fl. sst	r	equant	8.5	02	088	6.5	67	352		36	176		0.000	0.765
M29	103	B-plm	fl. sst	r	disc	7.0	51	025	4.4	12	282	1.5	40	192	192	0.341	0.629
M29	103	B-plm	fl. sst	sr	disc	6.1	10	016	4.1	05	110	1.3	78	201	201	0.317	0.672
M29	103	B-plm	fl. sst	r	equant	3.4	22	064	2.7	06	154	2.2	70	238		0.815	0.794
M29	103	B-plm	red b.	sr	prolate	7.6	25	046	3.5	22	309	3.0	60	215		0.857	0.461
M29	103	B-plm	fl. sst	r	disc	6.2	03	250	3.0	07	347	1.7	67	184	184	0.567	0.484
M29	103	B-plm	fl. sst	r	disc	10.0	71	230		09	325	3.3	21	056	056		
M29	103	B-plm	fl. sst	r	prolate	8.5	05	265	3.2	37	353	1.4	60	178	178	0.438	0.376
M29	103	B-plm	o. lst	r	equant	6.0	13	226	3.5	48	322	3.3	43	155		0.943	0.583
M29	103	B-plm	qr. lst	sr	disc	10.3	83	284	7.5	11	178	5.3	12	083		0.707	0.728
M29	103	B-plm	fl. sst	r	prolate	15.6	19	308	10.0	31	217	7.0	46	052		0.700	0.641
M29	103	B-plm	o. lst	sr	disc	5.9	10	351	5.6	00		2.2	83	181	181	0.393	0.949
M29	103	B-plm	fl. sst	r	disc	13.6	03	212	10.0	30	311	3.2	68	130	130	0.320	0.735
M29	103	B-plm	fl. sst	r	disc	7.5	03	350	7.0	13	078	3.2	77	261	261	0.457	0.933
M29	103	B-plm	red b.	r	equant	6.5	10	108	4.2	40	358	3.5	51	196	196	0.833	0.646
M29	103	B-plm	o. lst	sr	disc	5.4	06	259	3.2	04	156	1.8	74	000	216	0.563	0.593
M29	103	B-plm	fl. sst	r	equant	5.2	08	330	4.3	31	053	3.1	62	240		0.721	0.827
M29	103	B-plm	fl. sst	r	disc	7.4	50	035	5.0	08	290	1.5	43	200	200	0.300	0.676
M29	103	B-plm	fl. sst	r	disc	5.7	28	091	3.8	20	170	1.4	63	264	264	0.368	0.667

CLASS	NO.
bladed	6
disc	21
prolate	5
equant	10

M30	
0-30	0
31-60	3
61-90	1
91-120	4
121-150	1
151-180	5
181-210	2
211-240	5
241-270	1
271-300	1
301-330	1
331-360	3
	27

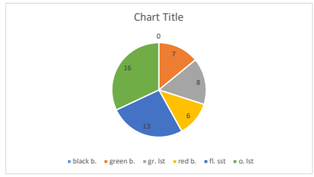

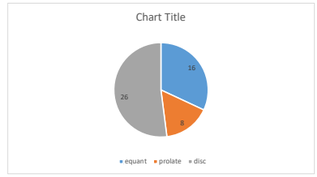

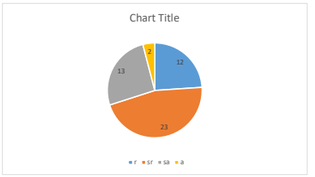

CLASS	NO.
bladed	11
disc	13
prolate	9
equant	9

M29ii	
0-30	0
31-60	0
61-90	0
91-120	0
121-150	0
151-180	2
181-210	9
211-240	5
241-270	5
271-300	4
301-330	2
331-360	1
	28

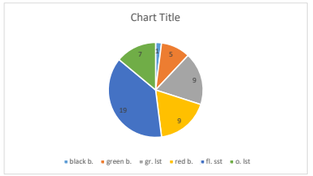

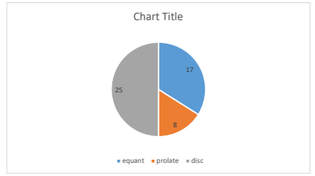

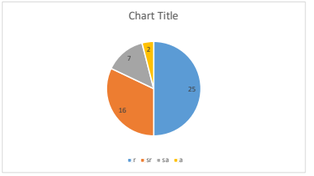

CLASS	NO.
bladed	11
disc	16
prolate	9
equant	9

M29iii	
0-30	1
31-60	1
61-90	1
91-120	0
121-150	1
151-180	4
181-210	9
211-240	4
241-270	4
271-300	1
301-330	0
331-360	1
	27

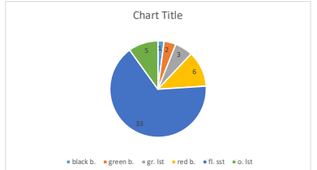

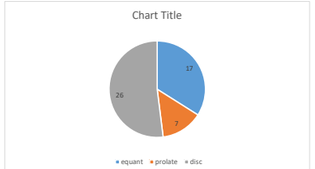

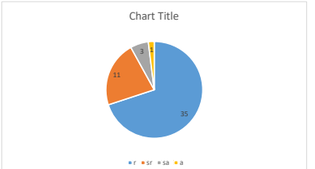

M32	104	B-plm	red b.	sr	equant	9.6	01	250	7.5	24	147	5.0	65	344	344	0.667	0.781
M32	104	B-plm	o. lst	sr	equant	11.7	13	148	7.7	04	258	5.5	80	347		0.714	0.658
M32	104	B-plm	fl. sst	sr	equant	10.2	21	028	6.3	62	118	5.2	20	284	284	0.825	0.618
M32	104	B-plm	gr. lst	sa	equant	9.3	03	235	6.0	77	342	4.9	08	149	149	0.817	0.645
M32	104	B-plm	o. lst	sa	equant	10.6	03	020	7.2	22	117	6.5	75	293		0.903	0.679
M32	104	B-plm	o. lst	sr	disc	5.8	27	182	3.3	22	103	1.2	72	004	062	0.364	0.569
M32	104	B-plm	o. lst	r	equant	6.0	65	028	3.7	23	290	3.4	28	194	194	0.919	0.617
M32	104	B-plm	red b.	sr	disc	6.5	08	249	4.2	10	348	1.6	72	168	168	0.381	0.646
M32	104	B-plm	qr. lst	sr	equant	7.3	02	108	5.2	12	210	4.0	80	042	042	0.769	0.712
M32	104	B-plm	o. lst	sr	disc	6.5	09	100	6.0	72	009	2.2	13	194	194	0.367	0.923
M32	104	B-plm	o. lst	sr	prolate	5.0	13	334	2.5	22	230	2.3	70	063	063	0.920	0.500
M32	104	B-plm	gr. lst	sr	disc	7.7	18	325	4.6	18	236	2.3	72	070	070	0.500	0.597
M32	104	B-plm	o. lst	sr	disc	4.2	10	094	2.8	16	356	1.2	68	189	130	0.429	0.667
M32	104	B-plm	fl. sst	r	disc	6.4	22	288	4.5	05	194	2.5	70	115	115	0.556	0.703
M32	104	B-plm	gr. lst	sr	disc		04	170	4.4	08	258	1.1	83	077	077		
M32	104	B-plm	red b.	sa	equant	5.0	12	059	3.4	56	164	2.8	38	352		0.824	0.680
M32	104	B-plm	o. lst	sr	prolate	6.3	03	150	3.4	01	058	3.2	88	334		0.941	0.540
M32	104	B-plm	o. lst	sa	prolate	6.3	08	312	2.0	12	225	1.8	79	129	104	0.900	0.317
M32	104	B-plm	o. lst	sr	disc	5.0	09	281		30	025	0.9	57	208	173		
M32	104	B-plm	gr. lst	r	disc	3.7	12	038	2.2	10	151	0.8	70	328	328	0.364	0.595
M32	104	B-plm	red b.	sr	equant	6.2	11	218	3.5	80	310	3.2	04	127		0.914	0.565
M32	104	B-plm	fl. sst	r	disc	4.4	07	046	2.8	10	320	0.8	78	236	112	0.286	0.636
M32	104	B-plm	o. lst	sr	disc		04	205	3.5	42	301	2.4	40	112	112		
M32	104	B-plm	o. lst	r	equant	4.2	06	166	3.0	70	242	2.4	14	065	065	0.800	0.714
M32	104	B-plm	gr. lst	r	disc		08	048	6.2	42	315	2.3	40	150	150		
M32	104	B-plm	o. lst	sr	disc	6.4	15	292	2.9	08	037	1.2	69	138	096	0.414	0.453
M32	104	B-plm	o. lst	r	disc	4.1	05	263		65	355	1.0	40	173	173		
M32	104	B-plm	green b.	sa	equant	2.7	62	194	2.5	60	100	2.0	02	008		0.800	0.926
M32	104	B-plm	o. lst	r	equant	6.0	03	078	4.0	88	170		01	355			
M32	104	B-plm	gr. lst	sr	disc	4.5	09	072	2.2	36	348	1.0	60	350	332	0.455	0.489
M32	104	B-plm	red b.	sr	equant	2.7	18	346	2.5	12	250	2.3	82	157		0.920	0.926
M32	104	B-plm	gr. lst	r	disc	3.5	02	090	2.4	42	184	0.5	48	016	016	0.208	0.686
M32	104	B-plm	fl. sst	r	disc	3.4	09	252	2.5	05	163	1.3	81	350	038	0.520	0.735
M32	104	B-plm	gr. lst	sa	equant	6.5	02	080	5.8	70	184	4.2	19	003		0.724	0.892
M32	104	B-plm	fl. sst	sr	disc	6.0	00			34	356	1.8	55	176	176		
M32	104	B-plm	gr. lst	r	equant	6.4	35	245	4.0	50	178		10	344			
M32	104	B-plm	o. lst	r	equant	4.4	17	068	3.2	53	158	2.4	40	337		0.750	0.727
M32	104	B-plm	red b.	sa	disc	5.2	03	277	3.6	66	005	1.8	16	015	037	0.500	0.692
M32	104	B-plm	o. lst	sr	disc	7.4	22	067		44	324	2.0	38	162	162		
M32	104	B-plm	gr. lst	r	prolate	4.4	00		2.1	42	171	0.9	54	006		0.429	0.477
M32	104	B-plm	red b.	sr	disc	5.0	09	332	3.9	35	068	1.2	52	243	243	0.308	0.780
M32	104	B-plm	green b.	sa	equant	3.4	22	249	2.0	72	150		04	344			
M32	104	B-plm	qr. lst	r	disc	5.3	02	170	4.3	32	075	1.3	63	274	274	0.302	0.811
M32	104	B-plm	fl. sst	r	disc		17	332	2.4	29	233	1.2	68	064	064		
M32	104	B-plm	o. lst	sr	disc	3.8	55	340	3.5	13	252	1.4	35	161	115	0.400	0.921
M32	104	B-plm	o. lst	r	prolate	3.9	03	252	2.2	18	152	1.1	72	343		0.500	0.564
M32	104	B-plm	red b.	sa	equant	5.0	47	075		14	344	3.0	36	246			
M32	104	B-plm	red b.	sa	equant	2.5	00		1.8	06	000	1.5	85	179		0.833	0.720
M32	104	B-plm	red b.	sr	disc	2.4	63	355	1.7	05	260	0.8	40	166	085	0.471	0.708
M32	104	B-plm	gr. lst	sr	disc	4.2	09	290	2.7	52	030	1.0	30	212	212	0.370	0.643
M35	180	B-plm	fl. sst	r	equant	12.5	52	104	8.2	08	010	5.0	55	294	294	0.610	0.656
M35	180	B-plm	fl. sst	r	prolate	12.2	44	180	5.5	62	010	4.0	06	275		0.727	0.451
M35	180	B-plm	gr. lst	sr	prolate	11.6	12	032	5.8	42	126	3.5	38	288	288	0.603	0.500
M35	180	B-plm	gr. lst	r	equant	10.5	04	330	7.2	60	076	5.3	33	258		0.736	0.686
M35	180	B-plm	red b.	sa	equant	7.4	55	044	5.9	24	220	4.5	10	312		0.763	0.797
M35	180	B-plm	gr. lst	sr	prolate	12.5	32	173	5.3	64	078	2.8	21	267	267	0.528	0.424
M35	180	B-plm	gr. lst	sa	equant	14.9	55	134	8.0	12	038	7.2	24	304		0.900	0.537
M35	180	B-plm	o. lst	sr	disc	21.0	20	130	12.8	22	039	6.0	70	228	228	0.469	0.610
M35	180	B-plm	qr. lst	r	equant		22	104	14.5	04	007	7.5	76	254	126		
M35	180	B-plm	fl. sst	sr	equant	7.8	12	048	6.8	00		4.2	83	240	130	0.618	0.872
M35	180	B-plm	gr. lst	sa	prolate	9.1	60	130	4.5	25	328	3.8	15	060		0.844	0.495
M35	180	B-plm	gr. lst	sr	equant	11.7	54	146	6.5	35	326		05	230			
M35	180	B-plm	o. lst	sr	equant	6.5	12	222	5.8	80	141	4.0	03	336		0.690	0.892
M35	180	B-plm	o. lst	sr	prolate	10.2	20	175	4.9	30	084	4.2	57	282		0.857	0.480
M35	180	B-plm	o. lst	sr	equant	7.4	28	183	4.5	25	015	4.0	26	265		0.889	0.608
M35	180	B-plm	gr. lst	sr	equant	9.8	17	150	8.7	60	050	6.2	18	232		0.713	0.888
M35	180	B-plm	fl. sst	sa	equant	13.1	32	175	8.5	52	284	8.0	10	034	034	0.941	0.649
M35	180	B-plm	red b.	sr	equant	10.2	03	136	8.8	12	044	5.5	79	236	122	0.625	0.863
M35	180	B-plm	fl. sst	r	disc		39	204	7.3	32	112	3.6	38	350	018		
M35	180	B-plm	gr. lst	r	disc	8.7	27	130	4.5	10	232	3.0	72	324	134	0.667	0.517
M35	180	B-plm	o. lst	sr	disc	9.7	32	052	8.5	38	148	2.8	35	280	194	0.329	0.876
M35	180	B-plm	qr. lst	r	equant	11.7	05	180	10.3	46	090	6.1	70	280	150	0.592	0.880
M35	180	B-plm	gr. lst	sr	equant	12.0	02	195	11.7	78	290	11.0	17	120		0.940	0.975
M35	180	B-plm	red b.	sa	equant	5.3	35	176	5.2	52	016		30	272			
M35	180	B-plm	red b.	sr	equant	6.3	32	175	5.0	18	086	3.3	61	274	158	0.660	0.794
M35	180	B-plm	qr. lst	sr	disc	8.0	22	254	7.7	26	164	3.5	71	346	159	0.455	0.963
M35	180	B-plm	o. lst	sr	disc		06	258	5.8	24	154	1.9	55	348	155		
M35	180	B-plm	gr. lst	sa	disc	8.2	30	154		05	060	3.0	65	322	147		
M35	180	B-plm	o. lst	sr	equant	5.7	34	045	5.0	22	139	3.8	47	238		0.760	0.877
M35	180	B-plm	qr. lst	r	equant	8.9	40	185	6.8	34	029	4.1	32	280		0.603	0.764
M35	180	B-plm	green b.	sa	equant	5.4	23	027	2.5	20	300	2.3	66	197		0.920	0.463
M35	180	B-plm	o. lst	r	equant	8.7	26	144	5.0	80	243		07	070	172		
M35	180	B-plm	fl. sst	sr	disc	7.4	02	085	7.2	20	174	3.0	72	012	198	0.417	0.973
M35	180	B-plm	green b.	sa	prolate	4.5	07	060	2.6	12	318	1.5	83	227		0.577	0.578
M35	180	B-plm	gr. lst	r	equant	6.4	42	162	5.2	08	070		38	316			
M35	180	B-plm	o. lst	sr	disc	9.2	42	146	6.5	08	050	1.8	52	324	156	0.277	0.707
M35	180	B-plm	fl. sst	r	equant	13.5	60	116	12.0	12	024	7.7	18	299		0.642	0.889
M35	180	B-plm	gr. lst	sr	equant	7.9	00		6.4	50	074	5.5	48	268		0.859	0.810
M35	180	B-plm	qr. lst	sr	prolate	10.5	24	079	4.0	80	334	3.8	02	132		0.950	0.381
M35	180	B-plm	red b.	sr	disc		09	082	5.7	58	170	2.0	32	001	172		
M35	180	B-plm	gr. lst	sr	disc	5.0	25	172	4.2	20	266	1.3	67	104	154	0.310	0.840
M35	180	B-plm	red b.	sr	disc	6.2	35	179		06	275	3.0	54	012	175		
M35	180	B-plm	fl. sst	r	prolate	9.5	10	190	4.0	70	099	2.2	09	290		0.550	0.421
M35	180	B-plm	gr. lst	sr	equant	9.2	52	142	4.8	19	334	4.5	14	226		0.938	0.522
M35	180	B-plm	green b.	sa	equant	6.5	30	129	6.0	48	020	4.9	10	234		0.817	0.923
M35	180	B-plm	fl. sst	r	disc	6.8	07	175	5.5	88	272	2.0	03	085	115	0.364	0.809
M35	180	B-plm	red b.	sa	disc	5.0	35	126	4.8	12	038	1.8	58	306	235	0.375	0.960
M35	180	B-plm	o. lst	sr	disc	9.4	01	002	6.0	78	264	1.6	15	100	100	0.267	0.638
M35	180	B-plm	fl. sst	r	disc	8.2	08	044	5.0	68	314	2.4	16	143	143	0.480	0.610
M35	180	B-plm	qr. lst	sr	disc	7.7	58	245	4.9	15	010	2.9	45	090	042	0.592	0.636

CLASS	NO.
bladed	11
disc	10
prolate	8
equant	9

M32	
0-30	1
31-60	3
61-90	7
91-120	6
121-150	3
151-180	5
181-210	2
211-240	1
241-270	1
271-300	2
301-330	1
331-360	2
	34

CLASS	NO.
bladed	10
disc	13
prolate	9
equant	8

M35	
0-30	1
31-60	2
61-90	0
91-120	2
121-150	7
151-180	8
181-210	2
211-240	2
241-270	1
271-300	2
301-330	0
331-360	0
	27

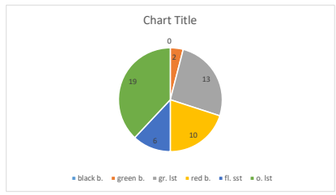

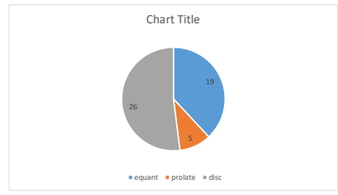

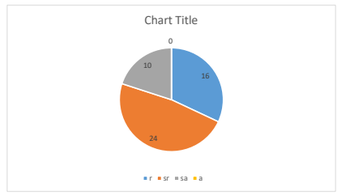

ZINGG CLAST SHAPES

locality	bed	facies	comp	round	shape	a_length	a_plunge	a_azimuth	b_length	b_plunge	b_azimuth	c_length	c_plunge	c_azimuth	palaeocurrent	c/b ratio	b/a ratio
M4	3	B-pll	fl. sst	r	disc	8.0	22	137	7.0	28	223	3.5	66	040	018	0.500	0.875
M4	3	B-pll	fl. sst	sr	disc	11.0	24	192	9.0	30	202	2.5	63	027	006	0.278	0.818
M4	3	B-pll	fl. sst	r	disc	14.0	31	092	7.0	54	182	1.0	55	008	356	0.143	0.500
M4	3	B-pll	fl. sst	sr	equant	7.0	58	142	5.0	02	038						
M4	3	B-pll	fl. sst	r	equant	9.0	34	187	8.0	22	116	5.0	47	009	004	0.625	0.889
M4	3	B-pll	fl. sst	sr	equant	8.5	55	130	8.2	23	033	2.3	22	272	246	0.280	0.965
M4	3	B-pll	gr. lst	r	disc	13.3	64	214		08	302	6.2	14	035	031		
M4	3	B-pll	fl. sst	r	equant	7.6	20	261	7.0	23	182	4.8	36	007	004	0.686	0.921
M4	3	B-pll	gr. lst	sr	equant	13.7	74	142		09	312	5.6	15	033	033		
M4	3	B-pll	gr. lst	r	equant	8.7	60	146	7.2	21	039						
M4	3	B-pll	gr. lst	sr	disc	11.5	69	289	7.1	32	023	1.9	18	135	104	0.268	0.617
M4	3	B-pll	gr. lst	r	prolate	8.6	17	055	4.8	63	165	3.3	07	329		0.688	0.558
M4	3	B-pll	o. lst	sr	equant	8.7	46	149	5.0	05	254	3.7	36	343	017	0.740	0.575
M4	3	B-pll	fl. sst	r	equant	7.9	20	221	7.3	33	133	3.8	71	022	015	0.521	0.924
M4	3	B-pll	gr. lst	sa	equant	6.9	18	108	5.7	13	181	2.8	61	056	012	0.491	0.826
M4	3	B-pll	fl. sst	sr	disc	7.4	04	219		13	136	3.4	82	028			
M4	3	B-pll	gr. lst	sa	equant	6.7	17	028		12	119	3.5	53	212	224		
M4	3	B-pll	gr. lst	sr	disc	6.9	30	135	5.4	04	221	1.9	37	306	306	0.352	0.783
M4	3	B-pll	red b.	sa	equant	7.3	33	090	5.2	78	358	3.3	05	189	205	0.635	0.712
M4	3	B-pll	fl. sst	r	disc	7.9	35	226		13	149	2.7	47	037	037		
M4	3	B-pll	gr. lst	sa	equant	6.7	76	122		18	304	3.5	28	020	030		
M4	3	B-pll	red b.	sa	disc	6.8	39	212	5.4	33	125	2.4	41	052	052	0.444	0.794
M4	3	B-pll	fl. sst	r	equant	5.4	21	034	4.4	02	154	4.1	35	229	229	0.932	0.815
M4	3	B-pll	gr. lst	r	equant	7.1	24	193	5.6	28	114		31	295			
M4	3	B-pll	gr. lst	r	equant	6.5	65	068				4.6	23	218	218		
M4	3	B-pll	fl. sst	r	disc	5.6	04	154	4.5	58	224	2.4	11	062	062	0.533	0.804
M4	3	B-pll	gr. lst	sa	equant	8.5	33	185	5.1	17	267	2.4	67	011	349	0.471	0.600
M4	3	B-pll	o. lst	sr	prolate	8.1	35	193	4.1	51	050	3.2	20	246	349	0.780	0.506
M4	3	B-pll	o. lst	sa	disc	6.8	43	105	4.5	19	052	2.7	85	215	296	0.600	0.662
M4	3	B-pll	fl. sst	r	disc	6.0	17	229	4.9	32	123	0.6	75	336	052	0.122	0.817
M4	3	B-pll	fl. sst	r	equant	5.9	50	185		29	100	3.2	71	044	013		
M4	3	B-pll	gr. lst	sr	disc	8.3	87	119	7.5	43	214	2.9	31	356		0.387	0.904
M4	3	B-pll	fl. sst	sr	disc	6.1	28	196	5.2	12	290	3.0	58	078	030	0.577	0.852
M4	3	B-pll	fl. sst	r	disc	7.6	69	157		27	349	4.2	06	267			
M4	3	B-pll	red b.	sa	equant	3.6	60	119	2.9	31	055	1.0	32	254		0.345	0.806
M4	3	B-pll	o. lst	sa	equant	5.6	30	076	4.0	72	149	3.3	11	245		0.825	0.714
M4	3	B-pll	gr. lst	sr	disc	6.5	41	090	4.5	49	174	1.6	14	352	352	0.356	0.692
M4	3	B-pll	fl. sst	r	disc	4.3	18	183	3.2	42	109	0.8	36	274	208	0.250	0.744
M4	3	B-pll	gr. lst	sr	disc	4.4	20	201	3.9	31	111	0.4	46	322	341	0.103	0.886
M4	3	B-pll	o. lst	r	prolate	10.0	16	069	5.7	51	162		52	351	351		
M4	3	B-pll	fl. sst	sr	disc	8.2	12	242		17	120	1.1	70	341	027		
M4	3	B-pll	o. lst	sr	prolate	8.9	24	126	3.9	29	066	1.2	77	095	346	0.308	0.438
M4	3	B-pll	fl. sst	r	prolate	4.1	20	116	2.2	37	030	1.7	16	220		0.773	0.537
M4	3	B-pll	fl. sst	r	prolate	8.9	23	167	4.6	21	241	2.3	46	044	040	0.500	0.517
M4	3	B-pll	fl. sst	r	disc	5.0	20	268	2.9	14	154	1.4	46	349	349	0.483	0.580
M4	3	B-pll	fl. sst	sr	disc	6.9	32	006	4.8	40	268	1.4	67	095	095	0.292	0.696
M4	3	B-pll	fl. sst	sr	disc	5.3	17	193	3.6	20	111	1.1	53	102	015	0.306	0.679
M4	3	B-pll	gr. lst	r	prolate	6.4	27	198	3.3	35		0.7	66	295	009	0.212	0.516
M4	3	B-pll	red b.	sa	equant	4.5	52	134	3.2	09	230						
M4	3	B-pll	green b.	sa	equant	2.4	03	088	2.4	72	180						
M9	10	B-pll	red b.	sa	equant	8.3	31	197	5.1	03	292	4.2	69	278	013	0.824	0.614
M9	10	B-pll	fl. sst	r	equant	12.1	19	176	9.3	15	077	5.7	81	046		0.613	0.769
M9	10	B-pll	o. lst	sa	equant	28.9	24	096	15.0	60	359	10.5	31	200		0.700	0.519
M9	10	B-pll	gr. lst	sr	equant	11.5	10	135	4.7	31	038	3.9	51	217		0.830	0.409
M9	10	B-pll	fl. sst	sr	equant	28.4	03	072	15.6	07	146	11.1	85	331		0.712	0.549
M9	10	B-pll	o. lst	r	equant	11.8	19	180	10.6	21	272	4.3	73	081	081	0.406	0.898
M9	10	B-pll	fl. sst	r	equant	8.3	02	112	8.1	77	206	4.1	14	037	037	0.506	0.976
M9	10	B-pll	o. lst	sa	equant	9.3	21	290		20	200	3.5	70	090	049		
M9	10	B-pll	chert	a	equant	11.5	20	177	5.4	69	273	4.7	75	002		0.870	0.470
M9	10	B-pll	gr. lst	r	disc	6.7	24	205	5.3	29	329	1.7	60	112	112	0.321	0.791
M9	10	B-pll	gr. lst	sr	prolate	11.5	23	267	5.3	58	183	3.9	15	006		0.736	0.461
M9	10	B-pll	fl. sst	r	equant	9.0	05	326		02	074	5.9	84	161	161		
M9	10	B-pll	fl. sst	r	disc	27.1	04	292	14.2	20	028	6.2	68	214	214	0.437	0.524
M9	10	B-pll	red b.	sr	equant	8.9	06	155		14	058	6.1	76	238	238		
M9	10	B-pll	fl. sst	r	disc	12.0	17	311	8.0	03	212	4.5	71	116	110	0.563	0.667
M9	10	B-pll	fl. sst	sr	equant	27.3	10	328	13.9	31	050	7.4	54	148	193	0.532	0.509
M9	10	B-pll	o. lst	sa	disc	7.4	02	287	4.8	08	204	2.2	86	033	058	0.458	0.649
M9	10	B-pll	o. lst	sa	disc	6.0	30	192	4.0	32	286	2.2	66	028	028	0.550	0.667
M9	10	B-pll	fl. sst	r	equant	7.2	32	278		09	354	4.6	55	182			
M9	10	B-pll	o. lst	sa	equant	11.3	18	275	11.0	09	190	6.0	60	094		0.545	0.973
M9	10	B-pll	fl. sst	r	equant	7.8	59	307	6.9	40	029	3.2	35	091	091	0.464	0.885
M9	10	B-pll	fl. sst	r	disc	8.4	29	185	6.0	23	320	2.1	83	139	031	0.350	0.714
M9	10	B-pll	gr. lst	r	disc	8.3	04	336	6.6	31	241	2.3	61	103	103	0.348	0.795
M9	10	B-pll	red b.	sa	disc	6.6	23	196	3.7	31	100	2.1	48	276	020	0.568	0.561
M9	10	B-pll	red b.	sr	equant	5.9	31	108	5.2	84	209	4.1	15	049		0.788	0.881
M9	10	B-pll	fl. sst	r	disc	5.9	12	272	5.7	01	132	3.3	87		041	0.579	0.966
M9	10	B-pll	gr. lst	sr	disc	6.6	83	260	4.4	18	141	1.3	54	005	077	0.295	0.667
M9	10	B-pll	gr. lst	sr	disc	12.9	17	348		04	106	3.8	75	217	192		
M9	10	B-pll	fl. sst	r	equant	6.8	28	298	4.7	03	198	4.3	79	109	109	0.915	0.691
M9	10	B-pll	red b.	sr	equant	6.6	18	310	4.0	29	189	3.5	70	039	117	0.875	0.606
M9	10	B-pll	fl. sst	sr	disc	7.4	16	260	3.8	06	355	1.1	73	159	145	0.289	0.514
M9	10	B-pll	fl. sst	r	disc	6.2	44	252	4.4	20	020	1.3	40	175	118	0.295	0.710
M9	10	B-pll	gr. lst	r	equant	7.6	37	238	4.7	16	148		55	062			
M9	10	B-pll	gr. lst	sr	disc	6.3	65	045	5.4	08	312	2.0	28	229	229	0.370	0.857
M9	10	B-pll	o. lst	sa	disc	6.9	11	144		19	232	2.1	72	037	037		
M9	10	B-pll	o. lst	sa	disc	5.3	15	164		40	251	1.8	62	353	037		
M9	10	B-pll	o. lst	r	disc	10.0	12	168	6.1	22	251	2.1	80	054	054	0.344	0.610
M9	10	B-pll	green b.	sa	equant	5.2	18	147	3.9	10	227	2.9	86	033		0.744	0.750
M9	10	B-pll	fl. sst	r	equant	7.1	11	195	4.7	82	080	4.4	12	270		0.936	0.662
M9	10	B-pll	o. lst	r	disc	7.0	17	172		31	074	2.2	62	243	243		
M9	10	B-pll	fl. sst	r	disc	6.4	05	212	5.6	57	310	1.4	38	130	130	0.250	0.875
M9	10	B-pll	green b.	sa	disc	5.1	25	198	4.2	44	284	1.0	37	100	084	0.238	0.824
M9	10	B-pll	o. lst	sr	prolate	5.3	15	222	3.1	07	127	2.2	84	041		0.710	0.585
M9	10	B-pll	gr. lst	sr	disc	5.2	40	222	4.0	04	314	1.0	52	048	048	0.250	0.769
M9	10	B-pll	fl. sst	r	equant	8.1	23	242		31	006	5.4	39	165			
M9	10	B-pll	fl. sst	r	disc	8.3	32	237	5.8	18	140	2.0	69	060	060	0.345	0.699
M9	10	B-pll	o. lst	sr	equant		63	008	7.3	40	265	6.5	24	180			
M9	10	B-pll	gr. lst	r	equant	5.7	01	292	4.0	30	188	3.4	37	006	006	0.850	0.702
M9	10	B-pll	fl. sst	r	disc	7.9	38	182	4.2	16	100	2.0	42	262	262	0.476	0.532
M9	10	B-pll	fl. sst	r	disc	6.2	12	198	4.5	58	285	1.2	32	110	110	0.267	0.726

CLASS	NO.
bladed	8
disc	19
prolate	4
equant	3

PALAEOC TOTALS

	M4
0-30	13
31-60	6
61-90	1
91-120	2
121-150	0
151-180	0
181-210	2
211-240	3
241-270	1
271-300	1
301-330	1
331-360	8
	38

CLASS	NO.
bladed	10
disc	16
prolate	9
equant	4

	M9
0-30	4
31-60	10
61-90	3
91-120	8
121-150	2
151-180	1
181-210	2
211-240	3
241-270	2
271-300	0
301-330	0
331-360	0
	35

M4/L18

black b.	0	equant	21	r	22
green b.	1	prolate	7	sr	17
gr. lst	16	disc	22	sa	11
red b.	4			a	0
fl. sst	23				
o. lst	6				
	50		**50**		**50**

M9/L14

black b.	0	equant	24	r	24
green b.	2	prolate	2	sr	14
gr. lst	10	disc	24	sa	11
red b.	5			a	1
fl. sst	20				
o. lst	12				
chert	1		**50**		**50**
	50				

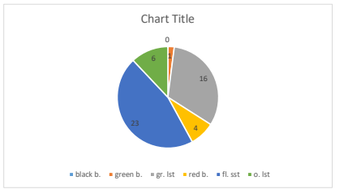

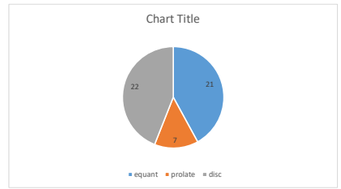

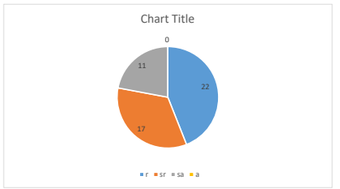

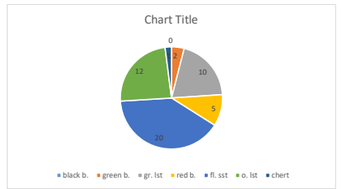

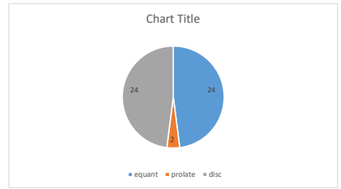

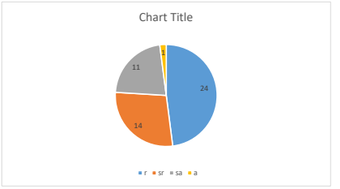

ZINGG CLAST SHAPES

locality	bed	facies	comp	round	shape	a_length	a_plunge	a_azimuth	b_length	b_plunge	b_azimuth	c_length	c_plunge	c_azimuth	palaeocurrent	c/b ratio	b/a ratio
M16	45	B-ple	red b.	a	equant	8.2	04	034	5.7	37	130	5.0	44	308		0.877	0.695
M16	45	B-ple	red b.	a	equant	7.6	16	247	6.5	37	139	5.3	48	331		0.815	0.855
M16	45	B-ple	gr. lst	sr	equant	7.7	33	299	5.3	52	119	5.0	08	019		0.943	0.688
M16	45	B-ple	red b.	sa	equant	4.9	18	144	4.8	22	065	3.3	61	320	085	0.688	0.980
M16	45	B-ple	o. lst	r	disc	5.6	17	317	5.5	08	212	1.6	70	126	095	0.291	0.982
M16	45	B-ple	gr. lst	sr	disc	5.8	14	118	3.2	39	026	1.7	64	220	220	0.531	0.552
M16	45	B-ple	o. lst	sr	prolate	6.5	14	150	2.2	13	252	1.8	81	341		0.818	0.338
M16	45	B-ple	gr. lst	sr	disc	7.9	20	302	6.8	08	042	1.8	72	126	126	0.265	0.861
M16	45	B-ple	gr. lst	r	disc	6.7	07	258	5.0	00		1.5	87	072	072	0.300	0.746
M16	45	B-ple	o. lst	sr	disc	7.2	02	080	5.9	07	353	2.7	84	174	119	0.458	0.819
M16	45	B-ple	gr. lst	sr	disc	6.3	36	129	3.4	24	030	2.3	33	276	276	0.676	0.540
M16	45	B-ple	red b.	sa	disc	5.5	67	002	4.2	12	104	2.0	38	179	179	0.476	0.764
M16	45	B-ple	gr. lst	r	equant		00		4.7	02	332	3.1	86	157			
M16	45	B-ple	o. lst	r	disc	6.8	20	096	4.1	04	186	2.1	77	280	280	0.512	0.603
M16	45	B-ple	red b.	sa	equant	4.7	28	106	4.6	79	289		12	190			
M16	45	B-ple	black b.	a	disc	3.4	01	231	2.0	01	139	1.0	88	333	114	0.500	0.588
M16	45	B-ple	fl. sst	sr	disc	5.9	07	128	3.5	35	228	1.5	59	049	049	0.429	0.593
M16	45	B-ple	qr. lst	sr	disc	5.2	34	250	4.5	08	327	0.9	44	075	075	0.200	0.865
M16	45	B-ple	red b.	sa	equant	5.6	36	205	5.2	18	082	2.7	45	004		0.519	0.929
M16	45	B-ple	red b.	a	disc	6.5	10	242	4.2	04	139	2.5	73	330	330	0.595	0.646
M16	45	B-ple	red b.	sa	disc	7.0	07	063	4.3	33	161	1.6	54	330	330	0.372	0.614
M16	45	B-ple	o. lst	r	equant	6.5	07	292	5.2	40	198	3.0	51	030	062	0.577	0.800
M16	45	B-ple	o. lst	sr	disc	5.2	13	102		27	003	1.9	64	208	208		
M16	45	B-ple	gr. lst	r	disc	7.0	18	115	5.3	38	016	2.5	33	206	183	0.472	0.757
M16	45	B-ple	fl. sst	sr	disc	5.0	68	196	4.4	30	107	1.1	13	020	049	0.250	0.880
M16	45	B-ple	o. lst	sr	disc	6.5	10	176	3.5	23	240	0.9	66	069	069	0.257	0.538
M16	45	B-ple	fl. sst	r	disc	4.0	10	158	2.6	33	256	0.8	63	068	068	0.308	0.650
M16	45	B-ple	o. lst	sr	equant	4.6	32	250	3.1	08	152	2.6	42	058		0.839	0.674
M16	45	B-ple	qr. lst	sr	disc	5.2	11	119		02	022	0.6	83	284	103		
M16	45	B-ple	fl. sst	sr	disc	4.1	18	286	3.4	57	028	1.0	48	194	194	0.294	0.829
M16	45	B-ple	fl. sst	sr	prolate	5.9	03	259	2.5	75	164	1.7	12	343		0.680	0.424
M16	45	B-ple	fl. sst	sr	disc	5.0	04	289	3.6	28	024	1.2	73	199	100	0.333	0.720
M16	45	B-ple	o. lst	sr	equant	6.2	20	219	4.0	42	307	3.5	35	143		0.875	0.645
M16	45	B-ple	gr. lst	sr	disc	5.2	15	305		06	032	2.0	69	125	123		
M16	45	B-ple	red b.	a	disc	6.5	02	145		11	238	1.8	83	328	325		
M16	45	B-ple	red b.	sr	disc	3.6	38	094	3.2	19	351	1.5	30	252	218	0.469	0.889
M16	45	B-ple	gr. lst	sa	disc	7.2	52	049	4.7	13	303	2.1	30	220	220	0.447	0.653
M16	45	B-ple	green b.	sa	equant	2.8	20	050	2.7	18	136	2.0	61	238		0.741	0.964
M16	45	B-ple	o. lst	sr	disc	2.8	04	283		01	013	0.7	82	118	118		
M16	45	B-ple	qr. lst	sr	disc	4.1	07	115	3.3	46	030	1.0	53	194	165	0.303	0.805
M16	45	B-ple	o. lst	r	disc	3.5	12	056	2.4	62	321	0.8	24	148	148	0.333	0.686
M16	45	B-ple	green b.	sa	disc	4.3	04	125	2.7	32	051	1.0	67	306	306	0.370	0.628
M16	45	B-ple	gr. lst	sa	equant	4.8	53	012	3.4	06	106	2.5	43	202		0.735	0.708
M16	45	B-ple	red b.	sr	prolate		36	220	3.5	79	120	2.1	08	304			
M16	45	B-ple	fl. sst	sr	prolate	7.0	11	081	3.3	27	178	2.1	66	001	001	0.636	0.471
M16	45	B-ple	fl. sst	sr	disc	3.0	40	256	2.5	18	353	0.5	49	094	094	0.200	0.833
M16	45	B-ple	o. lst	sr	disc	4.6	22	289	4.0	02	012	2.0	74	098	098	0.500	0.870
M16	45	B-ple	gr. lst	r	disc	3.3	32	140	2.4	12	046	0.6	58	313	313	0.250	0.727
M16	45	B-ple	red b.	sr	disc	4.5	24	103				1.1	69	288	358		
M16	45	B-ple	gr. lst	sa	prolate	6.1	18	071	1.8	75	168	1.7	18	344		0.944	0.295
M1	-	B-ple	gr. lst	sr	equant	16.5	25	000	11.6	46	265	10.4	28	084		0.897	0.703
M1	-	B-ple	o. lst	sr	prolate	37.7	08	114	16.6	74	013	12.0	12	196		0.723	0.440
M1	-	B-ple	fl. sst	r	disc	15.1	10	299	13.5	62	190	5.1	35	018	018	0.378	0.894
M1	-	B-ple	fl. sst	r	disc	15.7	04	290		45	190	3.5	48	009	009		
M1	-	B-ple	fl. sst	r	equant	15.5	11	275		22	180	8.6	68	082	082		
M1	-	B-ple	qr. lst	sr	equant	10.8	13	259	8.7	56	158	8.0	38	335		0.920	0.806
M1	-	B-ple	o. lst	r	equant	11.8	05	112	10.1	87	025		02	207			
M1	-	B-ple	red b.	sr	equant	10.7	03	272	10.4	75	012	8.5	16	170		0.817	0.972
M1	-	B-ple	fl. sst	r	equant	13.8	34	096	8.8	14	208		58	295	295		
M1	-	B-ple	green b.	sr	equant	12.7	32	102	12.0	23	196	10.8	57	298		0.900	0.945
M1	-	B-ple	o. lst	r	equant	15.5	15	112	10.3	82	019		13	196	196		
M1	-	B-ple	red b.	sr	prolate	8.9	13	212	4.2	82	120	3.2	08	306		0.762	0.472
M1	-	B-ple	o. lst	sr	disc		06	197	12.3	13	302	4.5	79	116	116		
M1	-	B-ple	green b.	sr	disc	8.7	05	144	8.5	25	246	3.6	60	065	065	0.424	0.977
M1	-	B-ple	o. lst	r	disc		20	199	13.1	30	288	4.2	60	076	076		
M1	-	B-ple	red b.	r	disc	9.4	02	317	6.6	40	069	3.3	52	226	226	0.500	0.702
M1	-	B-ple	o. lst	sr	prolate	10.2	17	256	4.6	18	357	4.5	68	094	094	0.978	0.451
M1	-	B-ple	o. lst	r	disc	7.7	50	285	6.5	03	191	3.5	37	104	104	0.538	0.844
M1	-	B-ple	fl. sst	r	disc		00		6.8	11	250	2.3	78	081			
M1	-	B-ple	fl. sst	r	disc	13.0	22	193	10.2	32	282	6.0	50	084	084	0.588	0.785
M1	-	B-ple	o. lst	sr	prolate	17.6	34	263		06	160	7.5	60	073			
M1	-	B-ple	gr. lst	sr	equant	10.7	17	180	7.5	18	088	7.3	66	269		0.973	0.701
M1	-	B-ple	red b.	r	disc	5.7	27	232	5.5	72	325	2.6	09	148	148	0.473	0.965
M1	-	B-ple	fl. sst	r	equant	5.4	00		4.6	23	175	3.8	72	355	355	0.826	0.852
M1	-	B-ple	o. lst	r	disc		04	354	6.5	32	262	1.8	60	090	090		
M1	-	B-ple	gr. lst	sr	equant	7.4	17	038	5.3	10	307	5.1	70	118		0.962	0.716
M1	-	B-ple	o. lst	sr	equant	8.4	13	270	6.6	65	006	5.2	02	188		0.788	0.786
M1	-	B-ple	gr. lst	sa	prolate	8.9	17	136	4.6	17	132	3.0	65	024		0.652	0.517
M1	-	B-ple	red b.	sr	equant	12.3	18	195	9.7	85	102	8.5	03	294		0.876	0.789
M1	-	B-ple	red b.	sr	disc	7.7	12	356	6.2	64	254	2.9	33	071	071	0.468	0.805
M1	-	B-ple	o. lst	sr	equant	8.7	07	127	8.4	45	210	7.5	35			0.893	0.966

CLASS	NO.
bladed	11
disc	18
prolate	5
equant	7

PALAEOC TOTALS

	M16
0-30	1
31-60	2
61-90	6
91-120	8
121-150	3
151-180	2
181-210	3
211-240	3
241-270	0
271-300	2
301-330	5
331-360	1
	36

M16/L4

black b.	1	equant	12	r	9
green b.	2	prolate	5	sr	26
gr. lst	15	disc	33	sa	10
red b.	12			a	5
fl. sst	8				
o. lst	12				
	50		**50**		**50**

M1/L6

black b.	0	equant	14	r	14
green b.	2	prolate	5	sr	16
gr. lst	5	disc	12	sa	1
red b.	6			a	0
fl. sst	7				
o. lst	11				
	31		**31**		**31**

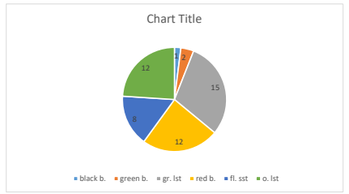

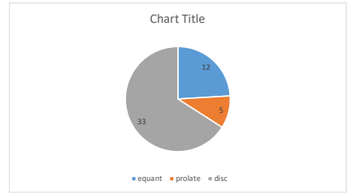

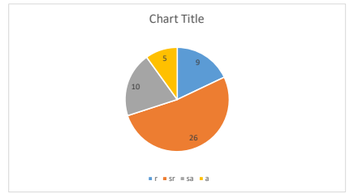

CLASS	NO.
bladed	1
disc	7
prolate	3
equant	10

	M1
0-30	2
31-60	0
61-90	6
91-120	3
121-150	1
151-180	0
181-210	1
211-240	1
241-270	0
271-300	1
301-330	0
331-360	1
	16

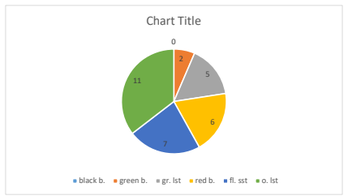

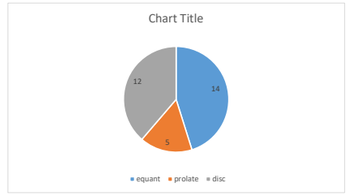

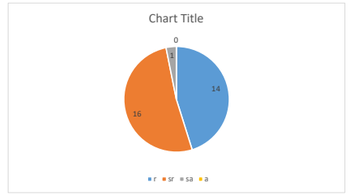

																ZINGG CLAST SHAPES	
locality	bed	facies	comp	round	shape	a length	a plunge	a azimuth	b length	b plunge	b azimuth	c length	c plunge	c azimuth	palaeocurrent	c/b ratio	b/a ratio
M19	6	C-rll	gr. lst	r	equant	8.2	22	190		18	095	4.5	73	016			
M19	6	C-rll	fl. sst	sr	disc	8.2	40	129	4.4	11	028	0.8	42	299	308	0.182	0.537
M19	6	C-rll	red b.	sa	equant	8.0	22	174	5.2	47	092	3.0	14	288		0.577	0.650
M19	6	C-rll	o. lst	sa	equant	6.4	34	181	4.7	44	093	4.5	28	008		0.957	0.734
M19	6	C-rll	chert	sr	equant	5.0	02	186	3.9	74	273	2.7	18	357		0.692	0.780
M19	6	C-rll	fl. sst	sr	equant	6.4	26	183	4.0	58	094	3.5	52	006	016	0.875	0.625
M19	6	C-rll	gr. lst	sr	equant	7.1	39	155	4.9	30	065	2.6	48	312		0.531	0.690
M19	6	C-rll	fl. sst	r	disc	4.8	26	139	4.2	18	208	1.8	64	018	343	0.429	0.875
M19	6	C-rll	fl. sst	sr	equant	6.0	35	177	3.1	84	274	2.5	52	359	359	0.806	0.517
M19	6	C-rll	gr. lst	sa	equant	6.4	09	236	3.1	73	130						
M19	6	C-rll	fl. sst	r	disc	5.6	29	192		04	288	2.5	44	012	012		
M19	6	C-rll	fl. sst	r	prolate	6.5	17	237	2.2	32	148	2.0	60	061	331	0.909	0.338
M19	6	C-rll	red b.	sa	equant	5.0	56	129	4.3	13	034	2.2	32	295		0.512	0.860
M19	6	C-rll	o. lst	r	disc	5.8	02	093	3.5	79	288	1.7	04	104	104	0.486	0.603
M19	6	C-rll	fl. sst	r	equant	4.3	70	116	3.3	08	206	2.9	01	028		0.879	0.767
M19	6	C-rll	o. lst	sa	disc	5.0	14	120	4.4	25	042	1.8	58	236	225	0.409	0.880
M19	6	C-rll	fl. sst	r	prolate	6.3	22	014	3.3	10	028	1.5	65	191		0.455	0.524
M19	6	C-rll	fl. sst	r	equant	5.2	05	183	3.4	17	286	3.2	75	014	064	0.941	0.654
M19	6	C-rll	o. lst	sa	equant	5.7	06	303	4.6	23	054	2.9	66	222	222	0.630	0.807
M19	6	C-rll	fl. sst	r	disc	5.6	15	152	3.0	35	068	1.4	61	241	143	0.467	0.536
M19	6	C-rll	fl. sst	sr	equant	6.2	12	009	4.4	84	117	2.1	04	301		0.477	0.710
M19	6	C-rll	fl. sst	sr	disc	6.7	19	090	4.6	10	026	2.5	45	350	013	0.543	0.687
M19	6	C-rll	o. lst	r	disc	4.0	19	123	3.5	03	182	1.3	61	342		0.371	0.875
M19	6	C-rll	o. lst	sr	equant		24	334	3.9	43	061	2.4	49	249	249		
M19	6	C-rll	fl. sst	sr	disc	5.1	20	046	4.3	27	128	1.4	56	300	211	0.326	0.843
M19	6	C-rll	fl. sst	r	disc	3.7	24	055	3.5	19	343	1.9	70	254		0.543	0.946
M19	6	C-rll	o. lst	sr	disc	4.9	25	027	4.0	18	303	1.6	61	138	210	0.400	0.816
M19	6	C-rll	o. lst	sr	equant	3.9	09	117	2.8	14	038	2.6	83			0.929	0.718
M19	6	C-rll	chert	sr	equant	3.6	56	117	3.4	12	209	1.8	52	299	299	0.529	0.944
M19	6	C-rll	green b.	sa	equant	3.8	56	131	3.6	34	199	1.3	90	111	323	0.361	0.947
M19	6	C-rll	red b.	r	disc	4.6	26	094	3.7	05	335	0.2	73	286	244	0.054	0.804
M19	6	C-rll	o. lst	r	equant	7.1	03	064	4.6	56	151	1.5	20	329		0.326	0.648
M19	6	C-rll	red b.	sr	equant	4.6	19	071	2.6	08	354	1.9	55	177		0.731	0.565
M19	6	C-rll	fl. sst	r	equant	4.7	26	067	3.9	19	183	2.6	89	153		0.667	0.830
M19	6	C-rll	o. lst	r	prolate	4.7	40	128	3.3	16	190	2.1	73	267	306	0.636	0.702
M19	6	C-rll	fl. sst	r	disc	4.9	18	166	2.8	27	072		42	261	258		
M19	6	C-rll	o. lst	sa	disc	4.9	02	199	3.2	22	111	0.7	68	289	308	0.219	0.653
M19	6	C-rll	o. lst	sr	disc	5.7	29	167		16	082	1.7	68	018	348		
M19	6	C-rll	o. lst	sr	prolate	5.0	18	058	2.2	84	144	2.0	16	337		0.909	0.440
M19	6	C-rll	gr. lst	sr	disc	4.2	10	048	1.2	09	132	0.8	78	312	267	0.667	0.286
M19	6	C-rll	o. lst	sr	disc	4.4	04	067	2.4	22	318	1.6	44	152	152	0.667	0.545
M19	6	C-rll	gr. lst	sr	disc	3.5	58	100	3.3	04	015	1.2	08	276	276	0.364	0.943
M19	6	C-rll	fl. sst	r	disc	3.0	26	108	2.8	18	044	1.0	64	208	172	0.357	0.933
M19	6	C-rll	red b.	sa	equant	6.6	01	173	4.0	56	077		24	253			
M19	6	C-rll	red b.	sr	disc	7.7	28	170		22	092	1.4	85	352	348		
M19	6	C-rll	fl. sst	r	disc	5.5	23	198		06	107	1.6	48	005	005		
M19	6	C-rll	o. lst	sr	disc	4.5	17	169	2.8	18	085	1.2	78	343	324	0.429	0.622
M19	6	C-rll	o. lst	sa	disc	5.6	53	114	4.2	12	223		18	322	322		
M19	6	C-rll	gr. lst	r	disc	4.6	15	098	3.4	05	009	0.8	80	282	263	0.235	0.739
M19	6	C-rll	fl. sst	r	prolate	6.0	37	074	2.2	04	171	1.8	81	266		0.818	0.367
M33	135	C-rll	red b.	sa	equant	8.7	22	186	7.7	41	076	5.4	46	272	272	0.701	0.885
M33	135	C-rll	fl. sst	r	equant	14.0	15	026	7.0	57	299	4.5	28	116	116	0.643	0.500
M33	135	C-rll	gr. lst	sr	equant	8.6	22	052	6.0	23	316	4.8	66	252	252	0.800	0.698
M33	135	C-rll	o. lst	sr	disc	8.0	11	222	5.8	47	320	2.9	68	144	144	0.500	0.725
M33	135	C-rll	gr. lst	r	disc	7.4	03	329	7.0	24	236	2.2	69	064	064	0.314	0.946
M33	135	C-rll	gr. lst	sr	prolate	7.0	25	247	4.1	42	327	3.0	40	160	160	0.732	0.586
M33	135	C-rll	o. lst	r	prolate	7.6	32	342	4.5	05	226	2.3	60	118	118	0.511	0.592
M33	135	C-rll	fl. sst	r	disc		24	281	4.5	09	198	1.8	70	105	105		
M33	135	C-rll	o. lst	sr	equant	10.5	10	290	7.5	06	192	4.1	81	097	097	0.547	0.714
M33	135	C-rll	red b.	sr	disc	3.7	00		2.9	32	283	0.9	64	116	116	0.310	0.784
M33	135	C-rll	red b.	sa	disc	3.9	04	356	2.8	06	262	1.0	87	085	085	0.357	0.718
M33	135	C-rll	green b.	sr	equant	4.8	88	142	4.5	04	315	4.0	09	053		0.889	0.938
M33	135	C-rll	o. lst	r	disc	8.0	17	246	5.5	48	346	2.3	48	144	144	0.418	0.688
M33	135	C-rll	fl. sst	r	disc	5.7	33	317		02	226	2.0	67	119	119		
M33	135	C-rll	fl. sst	r	disc	7.9	02	143	4.7	30	240	1.9	63	065	065	0.404	0.595
M33	135	C-rll	o. lst	sr	prolate	8.5	11	183	3.4	30	279	2.0	64	095	095	0.588	0.400
M33	135	C-rll	o. lst	sr	equant	5.3	19	022	2.4	82	219	2.2	10	310	310	0.917	0.453
M33	135	C-rll	green b.	sa	disc	4.5	58	028	4.2	22	120	1.7	35	216	216	0.405	0.933
M33	135	C-rll	fl. sst	r	disc	5.2	06	217	4.1	30	315	1.0	63	120	120	0.244	0.788
M33	135	C-rll	o. lst	sr	disc	13.8	05	331	11.2	31	232	4.6	57	073	073	0.411	0.812
M33	135	C-rll	gr. lst	sa	prolate	13.4	15	195	6.0	15	283	4.2	55	096	096	0.700	0.448
M33	135	C-rll	o. lst	r	disc	7.0	07	265	6.6	07	170	1.5	60	007	007	0.227	0.943
M33	135	C-rll	fl. sst	r	prolate	5.5	02	248	3.8	02	078	2.5	06	176		0.658	0.691
M33	135	C-rll	red b.	sa	equant	3.2	28	244	2.7	28	344	1.9	45	110	110	0.704	0.844
M33	135	C-rll	o. lst	sr	equant	6.6	18	036	4.8	18	307	3.4	54	148	148	0.708	0.727
M33	135	C-rll	o. lst	sr	prolate	9.0	03	344	3.0	03	241	2.8	60	072		0.933	0.333
M33	135	C-rll	o. lst	sr	equant	5.5	01	174	3.3	01	271	2.0	32	078	078	0.606	0.600
M33	135	C-rll	fl. sst	r	disc	9.6	06	198		06	095	3.1	44	293	293		
M33	135	C-rll	gr. lst	sr	disc	13.5	42	226		42	141	4.9	52	044	044		
M33	135	C-rll	red b.	sa	disc	3.6	35	296	2.7	35	208	0.6	66	110	110	0.222	0.750
M33	135	C-rll	o. lst	sr	disc	5.3	06	222	3.2	06	120	1.1	45	310	310	0.344	0.604
M33	135	C-rll	o. lst	sr	disc	5.5	04	026	4.2	04	295	1.3	62	120	120	0.310	0.764
M33	135	C-rll	gr. lst	r	disc	5.8	28	235	3.4	28	330	1.0	62	052	052	0.294	0.586
M33	135	C-rll	fl. sst	r	disc	6.8	25	178	4.5	25	264	1.4	30	075	075	0.311	0.662
M33	135	C-rll	red b.	sa	equant	3.4	02	012	2.5	02	281		04	110			
M33	135	C-rll	green b.	sa	equant	6.2	05	295	5.0	05	209	3.0	32	037		0.600	0.806
M33	135	C-rll	fl. sst	r	equant	7.4	03	037	4.2	03	292	3.0	87	122		0.714	0.568
M33	135	C-rll	fl. sst	r	disc	5.8	60	345	3.9	60	244	1.0	32	054	054	0.256	0.672
M33	135	C-rll	red b.	sa	prolate	8.4	10	035	3.5	10	307	3.0	80	214		0.857	0.417
M33	135	C-rll	o. lst	sr	disc	8.5	00		7.3	00	312	2.8	77	134	134	0.384	0.859
M33	135	C-rll	red b.	r	disc	6.4	19	212		19	314	2.7	65	132	132		
M33	135	C-rll	fl. sst	sr	disc	5.3	12	204	3.8	12	301	1.2	70	125	125	0.316	0.717
M33	135	C-rll	o. lst	sr	disc	3.5	27	204	3.2	27	294	0.9	55	116	116	0.281	0.914
M33	135	C-rll	fl. sst	r	disc	4.8	02	215	3.5	02	295	1.5	68	124	124	0.429	0.729
M33	135	C-rll	fl. sst	r	prolate	5.8	18	295	2.8	18	210	1.8	75	112		0.643	0.483
M33	135	C-rll	green b.	sa	equant	5.5	20	093	5.0	20	190	3.4	62	282		0.680	0.909
M33	135	C-rll	o. lst	sr	equant	9.6	10	220	7.0	10	321	5.2	49	134		0.743	0.729
M33	135	C-rll	o. lst	sr	disc	4.8	00		3.2	00	282	1.6	49	100	100	0.500	0.667
M33	135	C-rll	gr. lst	r	prolate	7.5	20	184	3.5	20	279	2.2	58	078	078	0.629	0.467
M33	135	C-rll	fl. sst	r	disc	5.8	03	032	3.2	03	299	2.0	81	122	122	0.625	0.552
M35	188	C-rll	fl. sst	r	disc	8.4	17	100	5.2	23	184	1.8	62	000	176	0.346	0.619
M35	188	C-rll	o. lst	sr	disc	7.3	09	169		06	276	2.0	81	024	192		
M35	188	C-rll	gr. lst	sa	equant	6.4	28	180	5.5	13	084	4.0	60	355		0.727	0.859
M35	188	C-rll	gr. lst	sa	equant	6.4	09	115	5.3	84	221	4.7	06	038	084	0.887	0.828
M35	188	C-rll	gr. lst	sa	disc	4.8	30	159	3.3	15	052	2.3	70	333	152	0.697	0.688
M35	188	C-rll	gr. lst	sr	prolate	14.3	12	154	5.7	84	344	5.0	06	072		0.877	0.399
M35	188	C-rll	gr. lst	r	disc	6.4	40	179		09	264	2.0	48	357	082		
M35	188	C-rll	fl. sst	sr	disc	7.6	18	188	4.6	87	275	1.8	02	100	100	0.391	0.605
M35	188	C-rll	red b.	sa	equant	5.2	64	013	5.0	25	203	3.8	07	298		0.760	0.962
M35	188	C-rll	green b.	sr	disc	7.5	03	008	3.5	65	275	1.6	32	105	105	0.457	0.467
M35	188	C-rll	fl. sst	sr	equant	4.9	08	214	4.5	10	193	2.8	78	303		0.622	0.918
M35	188	C-rll	fl. sst	r	prolate	4.9	25	098	2.3	05	195	1.0	60	284		0.435	0.469
M35	188	C-rll	fl. sst	sa	equant	3.3	30	138	2.3	62	336	1.9	05	065	078	0.826	0.697
M35	188	C-rll	green b.	sr	disc	5.0	34	136		15	041	1.4	51	293	239		
M35	188	C-rll	red b.	r	disc	3.2	28	161	3.0	05	255	1.3	62	348	216	0.433	0.938
M35	188	C-rll	gr. lst	r	disc	5.1	38	081	2.7	12	172	0.9	49	266	266	0.333	0.529
M35	188	C-rll	o. lst	sr	disc	4.6	54	082	2.7	20	321	1.6	22	223	038	0.593	0.587
M35	188	C-rll	gr. lst	sa	disc	8.4	12	032	5.0	83	294	2.1	12	125	125	0.420	0.595
M35	188	C-rll	o. lst	sr	disc	6.2	35	168		15	261	2.1	54	007	074		
M35	188	C-rll	gr. lst	sr	disc	4.4	13	130	2.8	25	235	1.1	63	055	075	0.393	0.636
M35	188	C-rll	o. lst	sr	prolate	7.2	45	127	3.0	06	024	2.6	45	300		0.867	0.417
M35	188	C-rll	fl. sst	sr	disc	6.9	36	170	4.5	10	084	2.8	55	347	288	0.622	0.652
M35	188	C-rll	red b.	sr	disc	5.2	30	167	2.3	33	268	1.3	43	012	093	0.565	0.442
M35	188	C-rll	red b.	sa	equant	9.8	48	101	5.6	15	192	5.0	45	276		0.893	0.571
M35	188	C-rll	fl. sst	sr	disc	5.2	23	155	3.4	12	050	1.5	57	336	233	0.441	0.654
M35	188	C-rll	fl. sst	sr	disc	4.5	24	170		20	266	1.4	52	014	104		
M35	188	C-rll	o. lst	sr	disc	4.4	04	354	3.3	42	266	1.4	53	095	095	0.424	0.750
M35	188	C-rll	gr. lst	sr	equant	5.2	62	124	4.1	17	212	2.8	15	312		0.683	0.788
M35	188	C-rll	gr. lst	sr	disc	4.8	07	103	4.3	20	202	2.0	62	014	145	0.465	0.896
M35	188	C-rll	red b.	sr	equant	5.3	60	112	4.8	25	292	3.7	08	023		0.771	0.906
M35	188	C-rll	o. lst	sr	equant	5.9	12	170	4.4	43	070	3.3	47	266	266	0.750	0.746
M35	188	C-rll	green b.	sr	prolate	7.5	22	118	3.0	20	216	1.6	66	328		0.533	0.400
M35	188	C-rll	red b.	sr	prolate	7.2	34	103	3.4	25	202	1.3	55	285		0.382	0.472
M35	188	C-rll	fl. sst	sr	disc	7.3	70	176	4.7	14	271	2.0	16	007	032	0.426	0.644
M35	188	C-rll	fl. sst	r	disc	9.0	58	180	6.2	37	073	1.9	16	276	233	0.306	0.689
M35	188	C-rll	red b.	sr	disc	6.8	35	071	6.0	17	158	1.7	56	262	235	0.283	0.882
M35	188	C-rll	red b.	sr	equant	7.2	33	356	6.8	43	172	5.0	05	074	074	0.735	0.944
M35	188	C-rll	o. lst	sa	equant	7.4	05	208	5.8	28	106	4.0	64	294		0.690	0.784
M35	188	C-rll	fl. sst	r	disc	9.6	14	180	4.7	02	280	2.8	73	016	159	0.596	0.490
M35	188	C-rll	fl. sst	r	disc	10.3	10	170		17	270	3.0	76	097	112		
M35	188	C-rll	o. lst	sr	disc	8.5	09	180	6.7	09	282	2.0	75	094	146	0.299	0.788
M35	188	C-rll	o. lst	sr	disc	6.8	34	153	3.0	51	251	2.3	36	350	070	0.767	0.441
M35	188	C-rll	o. lst	sa	disc	14.6	12	163		18	260	3.1	70	078	149		
M35	188	C-rll	red b.	sr	equant	4.2	08	039	3.3	19	134	2.2	80	246		0.667	0.786
M35	188	C-rll	gr. lst	sr	disc	6.6	09	176	3.5	18	095	1.5	77	265	236	0.429	0.530
M35	188	C-rll	green b.	sr	prolate	5.4	31	115	2.9	08	027	1.8	57	274		0.621	0.537
M35	188	C-rll	gr. lst	sr	disc	5.8	46	130	4.9	07	043	2.0	46	301	251	0.408	0.845
M35	188	C-rll	o. lst	sr	prolate	4.4	48	206	2.1	45	321	1.4	05	045		0.667	0.477
M35	188	C-rll	o. lst	r	equant	3.2	12	223	3.0	45	128	2.0	42	312		0.667	0.938
M35	188	C-rll	o. lst	r	equant	5.5	30	218	3.5	05	124	2.6	70	064	064	0.743	0.636

CLASS	**NO.**
bladed	10
disc	19
prolate	7
equant	4

PALAEOC TOTALS

	M19
0-30	4
31-60	0
61-90	1
91-120	1
121-150	1
151-180	2
181-210	1
211-240	3
241-270	5
271-300	2
301-330	6
331-360	5
	31

CLASS	**NO.**
bladed	12
disc	19
prolate	6
equant	7

	M33
0-30	1
31-60	3
61-90	7
91-120	14
121-150	8
151-180	1
181-210	0
211-240	1
241-270	1
271-300	2
301-330	2
331-360	0
	40

CLASS	**NO.**
bladed	18
disc	10
prolate	5
equant	10

	M35
0-30	0
31-60	2
61-90	8
91-120	6
121-150	4
151-180	3
181-210	1
211-240	6
241-270	3
271-300	1
301-330	0
331-360	0
	34

M19/L16

chert	2				
black b.	0	equant	21	r	20
green b.	1	prolate	5	sr	20
gr. lst	6	disc	24	sa	10
red b.	6			a	0
fl. sst	19				
o. lst	16				
	50		**50**		**50**

M33/L12

black b.	0	equant	14	r	20
green b.	4	prolate	9	sr	20
gr. lst	7	disc	27	sa	10
red b.	8			a	0
fl. sst	14				
o. lst	17				
	50		**50**		**50**

M35/L11

black b.	0	equant	14	r	10
green b.	4	prolate	7	sr	31
gr. lst	12	disc	29	sa	9
red b.	9	oblate	0	a	0
fl. sst	12				
o. lst	13				
	50		**50**		**50**

M10/L10

black b.	1	equant	16	r	14
green b.	2	prolate	6	sr	26
gr. lst	14	disc	28	sa	10
red b.	9			a	0
fl. sst	15				
o. lst	9				
	50		**50**		**50**

M12/XX

black b.	1	equant	16	r	16
green b.	1	prolate	3	sr	25
gr. lst	11	disc	31	sa	8
red b.	8			a	1
fl. sst	18				
o. lst	11				
	50		**50**		**50**

M37/L2

black b.	0	equant	12	r	23
green b.	4	prolate	4	sr	20
gr. lst	14	disc	34	sa	7
red b.	4			a	0
fl. sst	16				
o. lst	12				
	50		**50**		**50**

M37/L2

black b.	0	equant	16	r	17
green b.	3	prolate	4	sr	19
gr. lst	13	disc	30	sa	14
red b.	11			a	0
fl. sst	11				
o. lst	12				
	50		**50**		**50**

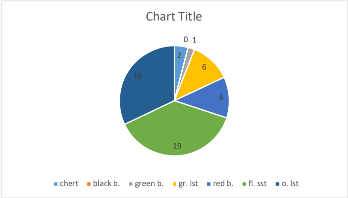

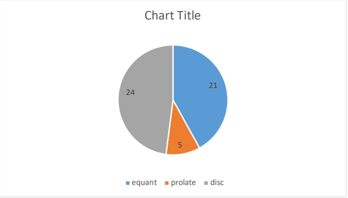

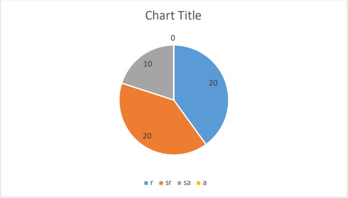

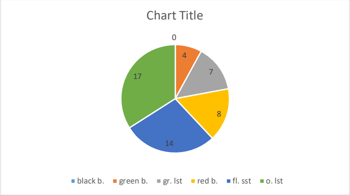

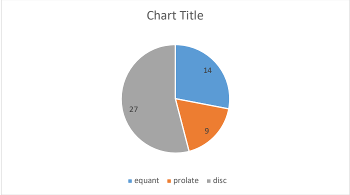

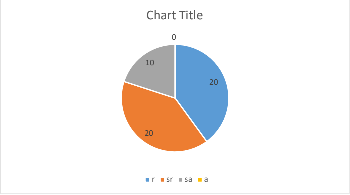

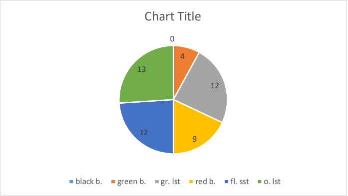

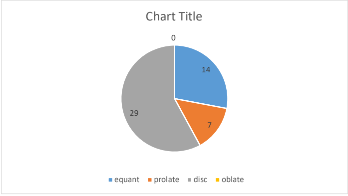

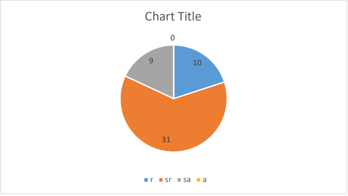

M10		211	C-rll	o. lst	sr	equant	9.5	83	109	9.3	04	293	9.1	08	026		0.978	0.979
M10		211	C-rll	qr. lst	sa	equant	12.2	25	212	6.8	58	111	5.5	15	002		0.809	0.557
M10		211	C-rll	o. lst	sa	equant	6.9	02	080	5.0	85	352	4.6	06	172	172	0.920	0.725
M10		211	C-rll	fl. sst	r	prolate	6.8	15	238	3.1	10	144	2.9	78	045	118	0.935	0.456
M10		211	C-rll	o. lst	sa	prolate	6.5	03	349	2.7	25	250	2.2	67	078	078	0.815	0.415
M10		211	C-rll	qr. lst	sr	disc	9.4	33	278		10	174	1.8	54	080	080		
M10		211	C-rll	qr. lst	sr	disc	6.8	08	114	5.6	16	212	2.2	70	024	024	0.393	0.824
M10		211	C-rll	qr. lst	sr	equant	10.9	06	042	8.8	84	138		12	315			
M10		211	C-rll	red b.	sa	equant	7.7	48	236	3.9	12	324	3.7	36	052	052	0.949	0.506
M10		211	C-rll	red b.	sr	equant	6.8	60	044	4.5	10	222	3.5	18	310		0.778	0.662
M10		211	C-rll	o. lst	sr	disc	10.4	08	284	5.3	75	027	3.7	16	209	209	0.698	0.510
M10		211	C-rll	red b.	sa	disc		05	017	7.0	42	284	3.8	38	110	110		
M10		211	C-rll	fl. sst	r	equant	7.5	24	340	5.6	72	170	4.7	04	282		0.839	0.747
M10		211	C-rll	red b.	sr	disc	3.8	68	145	3.4	10	242	1.1	22	336	336	0.324	0.895
M10		211	C-rll	fl. sst	r	disc	4.7	29	325	3.3	32	222	1.7	48	072	072	0.515	0.702
M10		211	C-rll	o. lst	sr	disc	6.2	15	192	5.4	21	285	2.2	64	105	105	0.407	0.871
M10		211	C-rll	fl. sst	r	disc	4.9	34	148	4.0	18	242	1.8	60	355	090	0.450	0.816
M10		211	C-rll	qr. lst	sa	equant	9.5	02	231	6.0	64	135	4.0	28	329		0.667	0.632
M10		211	C-rll	o. lst	sr	disc	8.7	01	251		10	346	2.5	76	164	164		
M10		211	C-rll	gr. lst	r	equant	10.0	00		7.7	65	338	3.6	30	005	005	0.468	0.770
M10		211	C-rll	fl. sst	sr	disc		04	150	8.2	70	258	2.0	30	076	076		
M10		211	C-rll	black b.	sr	disc	4.2	01	068	2.9	28	332	1.8	63	154	154	0.621	0.690
M10		211	C-rll	fl. sst	r	disc	5.1	18	290	3.6	08	204	2.4	69	124	124	0.667	0.706
M10		211	C-rll	fl. sst	r	disc	7.6	15	265		12	172	1.7	74	067	067		
M10		211	C-rll	o. lst	sr	equant	4.9	26	295	4.0	04	198	2.8	60	030	030	0.700	0.816
M10		211	C-rll	qr. lst	sr	disc	7.0	08	277	4.2	66	011	2.4	32	196	196	0.571	0.600
M10		211	C-rll	qr. lst	sr	disc	7.4	03	265	6.0	33	168	2.3	65	355	355	0.383	0.811
M10		211	C-rll	o. lst	sa	equant	5.5	15	264	4.7	52	142	3.0	35	324		0.638	0.855
M10		211	C-rll	red b.	sr	disc	4.6	28	240	4.0	52	061	2.0	03	164	164	0.500	0.870
M10		211	C-rll	gr. lst	sr	disc	6.1	33	259	4.0	04	159	2.8	75	068	068	0.700	0.656
M10		211	C-rll	fl. sst	r	disc	6.9	09	246	4.5	08	135	2.0	84	065	065	0.444	0.652
M10		211	C-rll	qr. lst	sa	equant	7.2	37	069	5.4	39	193		20	346			
M10		211	C-rll	fl. sst	sr	disc	6.0	28	296	3.5	11	216	2.2	58	128	128	0.629	0.583
M10		211	C-rll	fl. sst	sr	equant	8.7	02	243	6.0	79	131	5.5	12	334	334	0.917	0.690
M10		211	C-rll	gr. lst	r	disc	5.2	05	053	4.2	66	318	2.1	38	145	115	0.500	0.808
M10		211	C-rll	red b.	sr	prolate	4.5	46	159	2.2	04	067	1.8	55	338		0.818	0.489
M10		211	C-rll	qr. lst	sr	disc	4.8	31	206	4.2	04	118	2.1	62	010	045	0.500	0.875
M10		211	C-rll	fl. sst	sr	disc	7.0	06	090	5.7	15	180	2.4	82	002	083	0.421	0.814
M10		211	C-rll	green b.	sr	prolate	3.4	03	044	2.0	70	142	0.9	17	333		0.450	0.588
M10		211	C-rll	fl. sst	r	disc	4.8	12	286	3.2	08	193	1.6	77	107	107	0.500	0.667
M10		211	C-rll	red b.	sr	disc	6.8	32	143	5.5	11	056	2.9	56	323	323	0.527	0.809
M10		211	C-rll	fl. sst	r	equant	7.2	00		4.9	88	157		05	358			
M10		211	C-rll	qr. lst	sr	disc	4.9	04	208	4.7	15	115	1.9	82	301	018	0.404	0.959
M10		211	C-rll	qr. lst	sr	prolate		07	179	3.1	54	272	2.0	40	095			
M10		211	C-rll	red b.	sa	equant	4.6	24	212	3.9	50	117	3.3	15	315		0.846	0.848
M10		211	C-rll	green b.	sa	prolate	8.4	22	026	5.5	69	282	4.0	20	199		0.727	0.655
M10		211	C-rll	fl. sst	r	disc	5.7	08	210	3.2	08	324	1.4	78	145	145	0.438	0.561
M10		211	C-rll	o. lst	sr	equant	5.6	54	170	3.8	10	094	3.5	33	008		0.921	0.679
M10		211	C-rll	fl. sst	r	disc	4.7	24	186	3.5	40	286	1.9	58	027	064	0.543	0.745
M10		211	C-rll	red b.	sr	disc		07	168	3.6	19	080	1.5	62	272	272		
M12	-		C-rll	fl. sst	sr	equant	9.8	08	113	9.5	42	216	6.7	54	031	031	0.705	0.969
M12	-		C-rll	qr. lst	sa	equant	10.6	06	298	7.0	85	043	5.7	04	224		0.814	0.660
M12	-		C-rll	gr. lst	r	disc	8.4	32	236		01	330	3.5	67	054	054		
M12	-		C-rll	o. lst	sr	disc	11.4	22	295	8.0	75	198	2.3	14	023	023	0.288	0.702
M12	-		C-rll	fl. sst	sr	disc		61	185	8.0	20	294	4.0	32	016	016		
M12	-		C-rll	o. lst	sr	disc	9.6	15	052	5.3	20	001	2.4	66	176	176	0.453	0.552
M12	-		C-rll	qr. lst	sr	disc	10.4	12	298	5.5	51	197	3.5	42	035	035	0.636	0.529
M12	-		C-rll	o. lst	sr	disc	9.0	33	240	6.4	11	142	3.9	57	045	045	0.609	0.711
M12	-		C-rll	gr. lst	sa	equant	10.3	37	357	10.0	13	089	7.5	59	183		0.750	0.971
M12	-		C-rll	fl. sst	sr	disc	4.4	27	236	3.2	08	325	1.8	64	072	072	0.563	0.727
M12	-		C-rll	fl. sst	r	disc	7.5	05	078	4.0	04	180	2.0	85	272	088	0.500	0.533
M12	-		C-rll	qr. lst	sr	disc	5.4	08	299	4.7	25	203	2.2	66	040	040	0.468	0.870
M12	-		C-rll	red b.	sa	equant	6.4	32	276	4.8	69	090		18	176			
M12	-		C-rll	fl. sst	r	disc	6.2	30	038	4.3	23	137	1.6	68	075	075	0.372	0.694
M12	-		C-rll	o. lst	sr	disc	5.5	22	264	5.2	34	158	1.6	51	077	077	0.308	0.945
M12	-		C-rll	red b.	a	equant	5.2	26	061	3.7	64	256	3.0	12	339		0.811	0.712
M12	-		C-rll	o. lst	sr	disc	7.7	12	071	5.8	30	339	2.7	66	175		0.466	0.753
M12	-		C-rll	fl. sst	r	prolate	11.8	40	169	6.7	35	255	5.4	42	074		0.806	0.568
M12	-		C-rll	fl. sst	r	disc	5.0	12	088		08	359	1.3	74	266	142		
M12	-		C-rll	gr. lst	sr	equant	9.5	56	190	6.0	02	293	5.2	42	020		0.867	0.632
M12	-		C-rll	qr. lst	sa	disc	6.9	10	116	3.8	72	206	2.8	25	029	029	0.737	0.551
M12	-		C-rll	fl. sst	r	prolate	7.7	18	153	5.0	38	247	2.5	22	074	074	0.500	0.649
M12	-		C-rll	fl. sst	sr	disc	9.8	08	267		00		3.4	80	086	086		
M12	-		C-rll	o. lst	sr	equant	7.0	53	082	6.3	04	175	5.2	35	260		0.825	0.900
M12	-		C-rll	fl. sst	sr	disc	7.9	22	260	5.6	08	157	3.2	67	065	065	0.571	0.709
M12	-		C-rll	red b.	sr	equant	5.0	26	327	4.4	09	070	2.5	65	160	160	0.568	0.880
M12	-		C-rll	o. lst	r	equant	6.5	38	228	4.7	29	124	4.1	25	030	030	0.872	0.723
M12	-		C-rll	fl. sst	sr	disc	10.1	28	222	6.3	09	107	3.4	63	038	038	0.540	0.624
M12	-		C-rll	fl. sst	sr	disc	12.0	29	039		06	141	3.4	60	057	057		
M12	-		C-rll	red b.	sa	equant	5.7	58	076	5.0	29	270		05	358			
M12	-		C-rll	o. lst	r	disc	5.0	28	270	3.2	08	182	2.0	72	088	088	0.625	0.640
M12	-		C-rll	red b.	sr	disc	5.5	07	146	3.3	37	042	2.0	38	061	061	0.606	0.600
M12	-		C-rll	o. lst	sr	disc	5.4	08	276	3.3	65	188	1.8	22	014	014	0.545	0.611
M12	-		C-rll	fl. sst	r	equant	6.0	73	078		16	162	4.0	12	075			
M12	-		C-rll	gr. lst	sa	disc	6.6	34	267	3.4	26	166	1.9	49	083	083	0.559	0.515
M12	-		C-rll	fl. sst	sr	disc	5.3	37	044	2.5	02	140	1.4	52	045	045	0.560	0.472
M12	-		C-rll	fl. sst	r	equant	5.6	12	278	4.5	50	165	3.4	35	010		0.756	0.804
M12	-		C-rll	qr. lst	sr	equant	10.6	88	165	6.2	05	266	5.5	03	359		0.887	0.585
M12	-		C-rll	fl. sst	r	disc		36	156	5.4	19	260	2.6	72	087	087		
M12	-		C-rll	red b.	sa	disc	6.8	35	235	5.6	13	120	3.0	48	036	036	0.536	0.824
M12	-		C-rll	qr. lst	r	equant	6.7	55	352	5.6	08	240	5.0	38	149		0.893	0.836
M12	-		C-rll	red b.	sr	disc	4.1	81	236		08	145	1.3	09	051	051		
M12	-		C-rll	qr. lst	sr	equant	7.0	04	273	4.8	85	020	3.2	02	196		0.667	0.686
M12	-		C-rll	black b.	sr	equant	9.4	19	246	7.8	71	000	6.5	27	158	158	0.833	0.830
M12	-		C-rll	green b.	sa	disc	3.3	08	280	1.8	57	178	0.9	30	015	015	0.500	0.545
M12	-		C-rll	o. lst	sr	disc	5.1	20	258		12	352	1.8	69	090	090		
M12	-		C-rll	fl. sst	r	disc	6.2	03	250	4.2	18	134	2.3	74	340	340	0.548	0.677
M12	-		C-rll	fl. sst	r	disc	8.5	06	278	5.5	44	180	4.0	55	035	035	0.727	0.647
M12	-		C-rll	o. lst	r	disc	6.3	22	054		15	154	2.4	70	064	064		
M12	-		C-rll	red b.	r	prolate	3.4	06	114	2.1	41	022	1.7	57	219		0.810	0.618
M37		214	C-rll	fl. sst	r	disc	10.5	02	195	8.4	19	288	2.4	77	104	172	0.286	0.800
M37		214	C-rll	fl. sst	r	equant	11.7	19	348	9.7	61	179		15	080			
M37		214	C-rll	gr. lst	sr	disc	10.8	12	199	6.8	10	090	3.7	79	348	202	0.544	0.630
M37		214	C-rll	fl. sst	r	disc	10.0	14	180	8.5	10	285	2.1	73	026	242	0.247	0.850
M37		214	C-rll	qr. lst	sr	disc	9.6	25	135	7.0	10	040	2.7	58	298	252	0.386	0.729
M37		214	C-rll	green b.	sr	equant	4.5	00		3.2	63	289	3.0	18	108		0.938	0.711
M37		214	C-rll	fl. sst	r	disc	9.8	13	275	6.5	10	003	3.2	76	104	152	0.492	0.663
M37		214	C-rll	gr. lst	r	disc	7.0	08	002	6.5	03	266	2.3	81	173	234	0.354	0.929
M37		214	C-rll	o. lst	sr	prolate	12.2	62	214	5.5	33	308		20	097			
M37		214	C-rll	o. lst	sr	disc	8.6	28	188	6.5	03	270	3.7	62	004	202	0.569	0.756
M37		214	C-rll	o. lst	sr	disc		12	292	6.4	14	021	1.4	72	215	215		
M37		214	C-rll	qr. lst	sr	disc	7.5	07	298	4.3	30	034	1.8	49	218	218	0.419	0.573
M37		214	C-rll	o. lst	r	disc	5.4	42	161	4.0	11	078	2.2	35	350	292	0.550	0.741
M37		214	C-rll	fl. sst	r	disc	6.3	08	179	5.2	32	284	1.1	65	104	144	0.212	0.825
M37		214	C-rll	qreen b.	sa	disc	4.3	10	185	3.5	18	288	1.0	66	106	106	0.286	0.814
M37		214	C-rll	qr. lst	sa	prolate	11.9	08	188	6.2	48	270	4.5	45	106		0.726	0.521
M37		214	C-rll	fl. sst	r	equant	8.3	20	177	5.2	58	275	4.4	23	085		0.846	0.627
M37		214	C-rll	fl. sst	r	disc	7.1	55	202		28	098	2.6	33	357	269		
M37		214	C-rll	o. lst	sr	disc	6.1	08	259	4.4	35	160	2.0	42	339	152	0.455	0.721
M37		214	C-rll	fl. sst	r	equant	8.5	20	173	6.7	00		4.5	71	350		0.672	0.788
M37		214	C-rll	o. lst	sr	disc	11.7	04	170		02	079	2.8	83	348	212		
M37		214	C-rll	red b.	sr	equant	5.8	17	270	3.6	27	007	3.0	60	121		0.833	0.621
M37		214	C-rll	fl. sst	r	disc	10.3	17	002		04	103	3.9	75	204	232		
M37		214	C-rll	fl. sst	r	disc	9.6	22	191	7.0	06	298	2.0	72	034	124	0.286	0.729
M37		214	C-rll	qr. lst	r	disc	6.5	05	209	3.7	46	299	1.2	54	116	154	0.324	0.569
M37		214	C-rll	qr. lst	r	disc	6.1	32	204	4.3	07	324	1.1	55	061	085	0.256	0.705
M37		214	C-rll	qr. lst	sr	equant	4.8	18	185	4.0	53	288	3.8	45	100		0.950	0.833
M37		214	C-rll	fl. sst	r	disc	13.5	20	168	8.2	06	060	3.7	65	320	254	0.451	0.607
M37		214	C-rll	o. lst	sr	disc	6.3	02	352	4.8	04	256	1.6	87	092	231	0.333	0.762
M37		214	C-rll	o. lst	sr	disc	8.7	13	198	6.9	08	299	2.2	80	044	228	0.319	0.793
M37		214	C-rll	fl. sst	r	equant	11.0	64	303	8.5	07	196	6.3	20	103		0.741	0.773
M37		214	C-rll	red b.	sr	disc	4.2	07	146	4.0	34	236	1.7	52	066	146	0.425	0.952
M37		214	C-rll	o. lst	sa	equant	5.5	04	265	5.3	52	166	3.5	37	350		0.660	0.964
M37		214	C-rll	fl. sst	r	disc	3.3	13	123	2.7	24	228	0.8	67	046	245	0.296	0.818
M37		214	C-rll	o. lst	r	equant	4.0	29	328	3.3	18	229	2.3	58	069		0.697	0.825
M37		214	C-rll	qr. lst	sr	disc	8.4	10	248	5.0	02	146	2.1	83	048	222	0.420	0.595
M37		214	C-rll	fl. sst	r	disc	5.3	03	028	3.5	28	289	0.6	74	126	139	0.171	0.660
M37		214	C-rll	gr. lst	sr	disc	4.2	53	206	3.2	05	123	1.0	48	022		0.313	0.762
M37		214	C-rll	red b.	sr	disc	4.4	28	160	4.2	10	260	1.2	64	015	203	0.286	0.955
M37		214	C-rll	green b.	sa	prolate	5.2	40	301	3.0	67	128	1.4	16	223		0.467	0.577
M37		214	C-rll	fl. sst	r	disc	5.3	00		3.5	08	074	1.6	80	261	220	0.457	0.660
M37		214	C-rll	o. lst	sr	disc	6.0	42	207	4.7	28	102	1.6	48	354	241	0.340	0.783
M37		214	C-rll	gr. lst	r	prolate	5.5	09	222	2.5	36	320	1.6	50	145		0.640	0.455
M37		214	C-rll	o. lst	sr	disc	6.3	30	004		25	100	2.5	38	212			
M37		214	C-rll	gr. lst	sr	disc	7.2	28	176	4.0	09	090	1.8	61	342	212	0.450	0.556
M37		214	C-rll	fl. sst	r	equant	3.2	08	000	2.4	77	190	2.0	05	075		0.833	0.750
M37		214	C-rll	gr. lst	sa	equant	7.4	52	194	4.5	45	016	4.0	02	276		0.889	0.608
M37		214	C-rll	gr. lst	r	disc	4.2	35	254	3.3	05	170	1.1	47	079	105	0.333	0.786
M37		214	C-rll	green b.	sa	disc	5.0	23	212	3.4	64	302	1.5	10	128		0.441	0.680
M37		214	C-rll	red b.	sa	equant	2.4	08	151	1.7	54	241	1.0	36	064		0.588	0.708

CLASS	NO.
bladed	7
disc	17
prolate	9
equant	7

M10	
0-30	4
31-60	2
61-90	10
91-120	5
121-150	3
151-180	4
181-210	2
211-240	0
241-270	0
271-300	1
301-330	1
331-360	3
	35

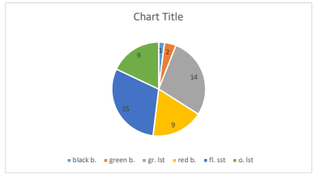

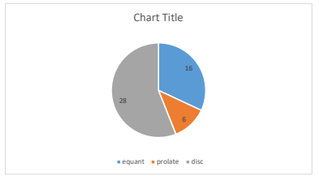

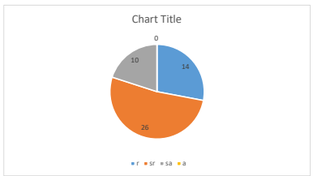

CLASS	NO.
bladed	11
disc	12
prolate	7
equant	8

M12	
0-30	6
31-60	11
61-90	13
91-120	0
121-150	1
151-180	3
181-210	0
211-240	0
241-270	0
271-300	0
301-330	0
331-360	1
	35

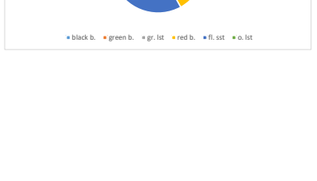

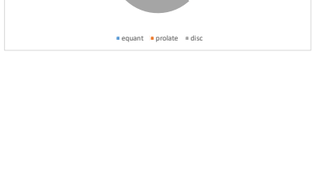

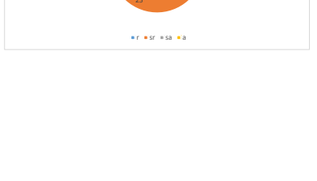

CLASS	NO.
bladed	11
disc	22
prolate	4
equant	6

M37i	
0-30	0
31-60	0
61-90	1
91-120	2
121-150	4
151-180	4
181-210	3
211-240	10
241-270	6
271-300	1
301-330	0
331-360	0
	31

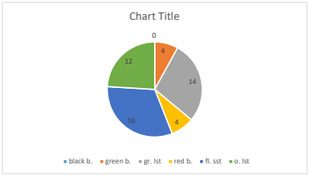

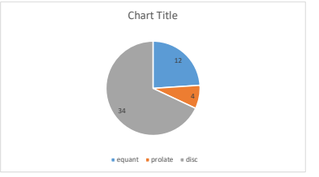

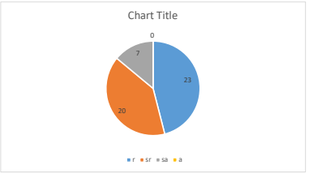

M37	222	C-rll	o. lst	sa	equant	15.4	22	192	15.0	54	288	9.3	38	088		0.620	0.974
M37	222	C-rll	gr. lst	sr	disc	13.8	07	340		04	241	5.9	83	153	153		
M37	222	C-rll	gr. lst	sr	disc	12.0	38	202	8.1	06	303	4.3	50	043	125	0.531	0.675
M37	222	C-rll	gr. lst	sr	equant	11.8	24	186	6.2	60	010	6.0	05	265		0.968	0.525
M37	222	C-rll	red b.	sr	disc	15.5	24	168	6.8	73	065	4.0	20	267	267	0.588	0.439
M37	222	C-rll	fl. sst	r	equant	11.0	09	335	7.8	46	226	6.4	42	065		0.821	0.709
M37	222	C-rll	gr. lst	sr	disc	8.4	43	202	6.2	04	298	2.5	49	033	125	0.403	0.738
M37	222	C-rll	red b.	sa	disc	8.9	32	177	5.2	03	078	3.6	68	342	258	0.692	0.584
M37	222	C-rll	green b.	sa	equant	7.0	10	005	5.0	42	270	4.5	59	103		0.900	0.714
M37	222	C-rll	fl. sst	sr	disc	12.0	11	192		08	095	3.6	76	006	232		
M37	222	C-rll	red b.	sa	equant	8.5	26	151	8.0	18	242	7.3	75	066		0.913	0.941
M37	222	C-rll	fl. sst	r	disc	13.5	50	233	7.6	04	141	1.7	45	048	086	0.224	0.563
M37	222	C-rll	o. lst	sr	disc	8.7	08	356	7.0	09	092	2.8	77	277	277	0.400	0.805
M37	222	C-rll	o. lst	sr	disc	10.6	19	180		08	281	3.3	74	020	195		
M37	222	C-rll	gr. lst	r	disc	8.3	32	181	6.7	05	295	2.4	52	035	108	0.358	0.807
M37	222	C-rll	gr. lst	sa	disc	10.7	29	010	6.5	02	127	4.5	52	215	215	0.692	0.607
M37	222	C-rll	green b.	sr	disc		05	104	7.6	66	357	3.0	38	198	198		
M37	222	C-rll	o. lst	sr	equant	7.4	52	345	5.6	14	244		31	110			
M37	222	C-rll	fl. sst	r	equant	10.1	30	190	9.0	07	096	7.5	68	000		0.833	0.891
M37	222	C-rll	red b.	sr	equant	9.4	49	198	9.0	13	306	8.6	26	124		0.956	0.957
M37	222	C-rll	o. lst	sr	disc	6.1	05	198		21	102	1.5	68	295	295		
M37	222	C-rll	fl. sst	r	prolate	7.3	29	143	5.0	12	234	3.5	64	332		0.700	0.685
M37	222	C-rll	gr. lst	sr	disc	5.3	48	189	3.9	10	284	1.4	48	020	206	0.359	0.736
M37	222	C-rll	fl. sst	r	prolate	16.2	22	186	4.8	20	296	4.0	51	097		0.833	0.296
M37	222	C-rll	o. lst	sr	disc	5.7	02	342	2.8	58	083	2.4	45	258	258	0.857	0.491
M37	222	C-rll	o. lst	sr	equant	7.2	04	252	5.8	31	348	4.0	62	114		0.690	0.806
M37	222	C-rll	gr. lst	sa	disc	4.2	38	166	3.5	68	352	1.9	07	256	256	0.543	0.833
M37	222	C-rll	gr. lst	sr	disc	6.7	38	190		28	082	1.8	33	348	292		
M37	222	C-rll	fl. sst	r	disc	4.0	34	182		00		1.2	52	014	290		
M37	222	C-rll	red b.	sa	disc	4.4	19	188	3.2	14	096	2.1	55	344	267	0.656	0.727
M37	222	C-rll	fl. sst	r	disc	5.5	50	193	3.6	06	288	1.6	29	019	045	0.444	0.655
M37	222	C-rll	red b.	sa	prolate	8.3	12	178	3.4	53	268		40	098			
M37	222	C-rll	qr. lst	r	equant	5.4	57	033	4.6	55	264	3.5	08	148		0.761	0.852
M37	222	C-rll	red b.	sa	equant	3.0	04	065	2.4	37	152	2.1	34	322		0.875	0.800
M37	222	C-rll	gr. lst	r	equant	5.3	00		4.7	24	288	3.5	75	024		0.745	0.887
M37	222	C-rll	green b.	sa	equant	2.6	76	334	2.5	11	180	2.2	05	250		0.880	0.962
M37	222	C-rll	red b.	sr	prolate	2.4	22	092	2.0	74	350	1.3	08	186		0.650	0.833
M37	222	C-rll	o. lst	sa	disc	5.4	14	129	3.6	20	222	1.8	76	046	234	0.500	0.667
M37	222	C-rll	red b.	sa	equant	3.2	53	253	2.1	35	025	1.8	18	125		0.857	0.656
M37	222	C-rll	gr. lst	r	equant	4.7	02	313	3.0	73	123	2.5	21	046		0.833	0.638
M37	222	C-rll	o. lst	sr	disc	4.5	16	136	3.0	35	218	1.6	59	037	120	0.533	0.667
M37	222	C-rll	o. lst	sr	disc	4.7	09	146	4.4	37	239	2.0	54	064	064	0.455	0.936
M37	222	C-rll	red b.	r	disc	3.6	09	123	2.2	57	228	0.9	32	056		0.409	0.611
M37	222	C-rll	o. lst	r	disc	4.0	06	178	2.6	32	078	1.4	52	269	269	0.538	0.650
M37	222	C-rll	fl. sst	r	disc	6.6	03	108	4.5	18	011	1.9	70	208	208	0.422	0.682
M37	222	C-rll	gr. lst	r	disc	4.5	02	180	3.7	10	276	1.3	82	098	234	0.351	0.822
M37	222	C-rll	fl. sst	r	disc	5.0	30	011		12	103	2.1	55	204	244		
M37	222	C-rll	o. lst	sa	disc	5.6	03	163	3.2	16	078	2.0	72	262	262	0.625	0.571
M37	222	C-rll	fl. sst	r	disc	6.3	00			18	087	2.0	74	269	200		
M37	222	C-rll	red b.	sa	equant	5.8	40	181	4.0	12	282	3.2	48	025		0.800	0.690

CLASS	NO.
bladed	8
disc	12
prolate	7
equant	12

	M37ii
0-30	0
31-60	1
61-90	2
91-120	2
121-150	2
151-180	1
181-210	5
211-240	4
241-270	8
271-300	4
301-330	0
331-360	0
	29

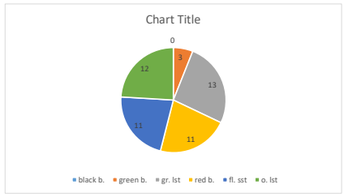

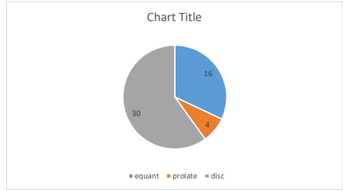

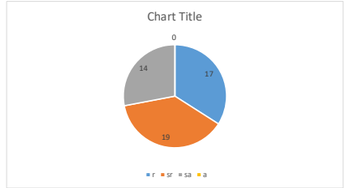

ZINGG CLAST SHAPES

locality	bed	facies	comp	round	shape	a_length	a_plunge	a_azimuth	b_length	b_plunge	b_azimuth	c_length	c_plunge	c_azimuth	palaeocurrent	c/b ratio	b/a ratio
M14	-	C-pth	fl. sst	r	equant	22.8	09	238	21.3	73	325		15	130			
M14	-	C-pth	gr. lst	r	prolate	18.9	07	019	10.3	35	123	8.4	78	216	228	0.816	0.545
M14	-	C-pth	gr. lst	r	disc	15.0	15	232		05	141	5.1	75	059	216		
M14	-	C-pth	red b.	sr	equant	15.2	62	142		65	240	8.4	05	046			
M14	-	C-pth	gr. lst	r	disc	14.3	02	105	13.6	07	016	5.5	85	217	217	0.404	0.951
M14	-	C-pth	gr. lst	r	disc	17.5	14	233		30	325	5.1	65	159	183		
M14	-	C-pth	fl. sst	sr	equant	16.7	05	108	16.0	80	196	12.4	16	022	022	0.775	0.958
M14	-	C-pth	gr. lst	r	disc	10.5	12	211	9.3	10	124	3.4	78	305	208	0.366	0.886
M14	-	C-pth	gr. lst	sr	equant	15.5	26	133	12.0	18	221	10.5	30	328		0.875	0.774
M14	-	C-pth	gr. lst	sr	disc	14.3	02	053	13.4	50	155	4.6	64	325	262	0.343	0.937
M14	-	C-pth	red b.	sa	disc	8.7	40	219		23	132	1.9	35	036	238		
M14	-	C-pth	fl. sst	r	equant	10.5	09	236	9.0	44	149		23	344			
M14	-	C-pth	o. lst	sr	prolate	10.7	36	215	4.6	52	033	2.7	04	138	210	0.587	0.430
M14	-	C-pth	gr. lst	sr	equant	15.9	27	136	12.8	04	333	8.3	60	070		0.648	0.805
M14	-	C-pth	o. lst	sr	prolate	12.2	04	236	4.8	24	326	4.2	62	144	168	0.875	0.393
M14	-	C-pth	gr. lst	r	disc	7.4	34	179	5.3	25	275	1.9	50	068	068	0.358	0.716
M14	-	C-pth	fl. sst	r	disc	9.2	49	109	7.0	05	199	3.0	33	284	133	0.429	0.761
M14	-	C-pth	fl. sst	r	equant	6.5	35	170	4.8	04	261	4.3	60	352		0.896	0.738
M14	-	C-pth	o. lst	sr	disc	6.4	42	346		75	007	3.1	03	098	098		
M14	-	C-pth	gr. lst	sr	equant	11.0	62	216		36	315	6.7	18	049			
M14	-	C-pth	gr. lst	sa	disc	18.9	35	203	8.4	08	304	4.5	38	032	327	0.536	0.444
M14	-	C-pth	red b.	sr	disc	4.7	02	072	3.3	06	159	0.8	89	338	221	0.242	0.702
M14	-	C-pth	gr. lst	sr	equant	9.3	37	229	5.6	02	140	4.8	64	048	206	0.857	0.602
M14	-	C-pth	fl. sst	sr	disc	10.4	67	252		05	345	4.0	31	080	071		
M14	-	C-pth	o. lst	r	disc	8.6	38	341	5.7	16	086		40	332	268		
M14	-	C-pth	green b.	a	prolate	5.6	03	007	2.4	74	108	1.4	23	284		0.583	0.429
M14	-	C-pth	gr. lst	r	equant	6.9	11	065	5.6	71	329	3.8	12	165		0.679	0.812
M14	-	C-pth	o. lst	sa	disc	6.9	13	201	6.2	32	106	2.2	58	302	348	0.355	0.899
M14	-	C-pth	gr. lst	r	disc	4.3	09	116	3.6	05	040	0.7	83	297	273	0.194	0.837
M14	-	C-pth	fl. sst	sr	equant	5.8	02	217	4.5	00		3.4	88	326		0.756	0.776
M14	-	C-pth	fl. sst	r	equant	18.4	05	237	15.0	70	140		12	326			
M14	-	C-pth	gr. lst	r	equant	10.5	01	236	8.4	10	334	5.4	80	070	202	0.643	0.800
M14	-	C-pth	fl. sst	sr	equant	11.0	06	069	9.7	34	338	9.5	72	244		0.979	0.882
M14	-	C-pth	gr. lst	sr	prolate	13.7	23	231	6.8	35	144	5.3	37	337		0.779	0.496
M14	-	C-pth	fl. sst	r	disc	8.2	04	201	6.8	81	298	3.7	02	182	144	0.544	0.829
M14	-	C-pth	gr. lst	sr	disc	15.3	05	036		69	295	5.2	18	122	194		
M14	-	C-pth	red b.	sr	prolate	10.7	25	156	4.2	30	257	2.9	60	016		0.690	0.393
M14	-	C-pth	gr. lst	sa	disc	9.2	16	250		40	336	3.5	65	068	203		
M14	-	C-pth	fl. sst	r	prolate	14.3	27	132	6.5	62	228	4.3	26	043		0.662	0.455
M14	-	C-pth	red b.	sa	disc	9.0	56	170	7.2	29	255	3.3	31	357	152	0.458	0.800
M14	-	C-pth	red b.	sr	disc	17.1	07	217	10.2	03	120	4.0	83	301	027	0.392	0.596
M14	-	C-pth	gr. lst	r	equant	19.1	28	236	17.5	00		7.8	69	317	184	0.446	0.916
M14	-	C-pth	gr. lst	r	prolate	9.4	30	174	6.0	39	080	2.3	21	290	290	0.383	0.638
M14	-	C-pth	fl. sst	r	disc	7.4	27	149	4.5	32	266	0.7	60	077	351	0.156	0.608
M14	-	C-pth	gr. lst	r	prolate	8.9	04	221	4.7	69	114	3.0	19	294		0.638	0.528
M14	-	C-pth	fl. sst	sa	prolate	6.6	30	163	4.1	11	252	2.7	77	097	002	0.659	0.621
M14	-	C-pth	gr. lst	sa	disc	6.8	03	283	5.1	25	188	1.3	79	036	209	0.255	0.750
M14	-	C-pth	gr. lst	sr	equant	8.3	18	270	5.4	06	182	4.1	63	166		0.759	0.651
M14	-	C-pth	fl. sst	sr	disc	19.0	39	166		45	294	6.3	26	090			
M14	-	C-pth	fl. sst	sr	disc	21.8	31	161	20.3	10	056	8.1	59	340	340	0.399	0.931

CLASS	NO.
bladed	9
disc	15
prolate	6
equant	6

PALAEOC TOTALS

	M14
0-30	3
31-60	0
61-90	2
91-120	1
121-150	2
151-180	2
181-210	9
211-240	5
241-270	2
271-300	2
301-330	1
331-360	3
	32

M14/L1

chert	0				
black b.	0	equant	16	r	21
green b.	1	prolate	10	sr	21
gr. lst	23	disc	24	sa	7
red b.	6			a	1
fl. sst	15				
o. lst	5				
	50		**50**		**50**

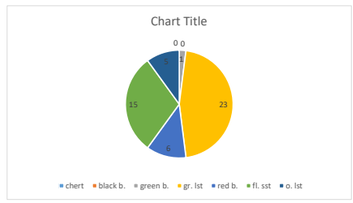

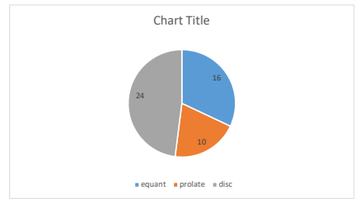

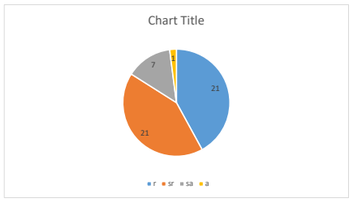

																ZINGG CLAST SHAPES	
locality	bed	facies	comp	round	shape	a length	a plunge	a azimuth	b length	b plunge	b azimuth	c length	c plunge	c azimuth	palaeocurrent	c/b ratio	b/a ratio
M19	7	P-wtm	o. lst	sa	equant	6.2	44	183	5.0	40	100	4.4	45	018		0.880	0.806
M19	7	P-wtm	o. lst	sa	equant	6.0	16	183	4.7	75	098	3.0	70	012		0.638	0.783
M19	7	P-wtm	gr. lst	sr	equant	5.9	03	036	3.0	30	137	2.7	83	235	305	0.900	0.508
M19	7	P-wtm	o. lst	sr	equant	5.5	05	162	3.9	77	276	2.9	85	003	087	0.744	0.709
M19	7	P-wtm	gr. lst	sr	equant	6.0	11	266	3.9	46	010	3.7	33	168	190	0.949	0.650
M19	7	P-wtm	fl. sst	r	prolate	6.3	02	076	2.8	08	346	2.5	82	164		0.893	0.444
M19	7	P-wtm	fl. sst	sr	prolate	6.3	15	194	2.2	16	301	2.0	68	099		0.909	0.349
M19	7	P-wtm	gr. lst	sr	prolate	6.2	12	122	3.0	29	022	2.2	82	288	200	0.733	0.484
M19	7	P-wtm	fl. sst	r	disc	4.7	33	097	4.3	11	008	1.2	75	280	280	0.279	0.915
M19	7	P-wtm	o. lst	sa	equant	5.3	31	183		22	288	2.8	72	029	029		
M19	7	P-wtm	fl. sst	r	disc	4.2	38	176	3.3	16	099	0.9	68	008	354	0.273	0.786
M19	7	P-wtm	fl. sst	r	prolate	4.9	17	120	2.7	42	028	1.8	37	203	203	0.667	0.551
M19	7	P-wtm	red b.	sa	disc	4.3	03	085	4.0	10	356	1.1	82	190	190	0.275	0.930
M19	7	P-wtm	fl. sst	r	prolate		20	096	2.2	32	193	1.5	68	288	355		
M19	7	P-wtm	gr. lst	sa	disc	4.5	13	129	3.3	11	041	1.5	69	215	276	0.455	0.733
M19	7	P-wtm	red b.	sa	equant	5.1	09	201	4.7	63	108		20	286			
M19	7	P-wtm	gr. lst	sr	disc	6.4	26	177	3.5	58	098	1.1	27	200	200	0.314	0.547
M19	7	P-wtm	o. lst	sr	disc	4.3	17	178	3.3	03	090	0.8	64	347	347	0.242	0.767
M19	7	P-wtm	o. lst	sa	equant	5.0	09	194	4.9	82	284	3.6	07	103		0.735	0.980
M19	7	P-wtm	gr. lst	r	disc	4.8	04	198	3.8	66	100	1.0	18	280	280	0.263	0.792
M19	7	P-wtm	gr. lst	sr	disc	3.6	03	069	2.4	31	177	0.7	60	332	241	0.292	0.667
M19	7	P-wtm	fl. sst	r	disc	3.7	29	086	3.1	31	167	0.9	44	270	270	0.290	0.838
M19	7	P-wtm	o. lst	sa	disc	3.4	36	183	2.8	04	063	1.2	77	332	332	0.429	0.824
M19	7	P-wtm	o. lst	sr	equant	6.2	18	309	6.0	79	230	4.2	47	061		0.700	0.968
M19	7	P-wtm	green b.	a	equant	3.8	27	180	1.4	84	270	1.1	23	095		0.786	0.368
M19	7	P-wtm	o. lst	sr	prolate	4.5	19	198	2.5	79	110	1.3	25	292	339	0.520	0.556
M19	7	P-wtm	o. lst	r	disc	3.6	34	171	2.9	20	067	1.3	68	346	346	0.448	0.806
M19	7	P-wtm	gr. lst	r	equant	4.2	33	083	3.2	30	014	2.9	71	170		0.906	0.762
M19	7	P-wtm	red b.	sa	equant	5.8	11	359	5.0	52	084		29	259			
M19	7	P-wtm	fl. sst	r	disc	3.2	31	083	2.6	10	346	0.7	62	156	270	0.269	0.813
M19	7	P-wtm	o. lst	sr	disc	5.6	11	302	4.7	31	056	1.9	55	186	186	0.404	0.839
M19	7	P-wtm	o. lst	sr	equant	3.2	10	217	2.6	06	344	2.1	64	104		0.808	0.813
M19	7	P-wtm	fl. sst	r	disc	2.4	12	099	2.4	15	180	1.0	58	007	007	0.417	1.000
M19	7	P-wtm	o. lst	sa	disc	2.8	44	155	2.3	18	078	0.7	89	330	320	0.304	0.821
M19	7	P-wtm	o. lst	sr	disc	4.1	29	163	2.0	25	094	0.5	65	010	313	0.250	0.488
M19	7	P-wtm	fl. sst	r	disc	3.3	05	172	2.3	58	085	0.7	46	266	266	0.304	0.697
M19	7	P-wtm	fl. sst	r	equant	3.5	08	170	1.9	25	076	1.7	56	261	261	0.895	0.543
M19	7	P-wtm	o. lst	sa	disc	3.0	09	051	2.8	54	136	0.8	20	312	282	0.286	0.933
M19	7	P-wtm	o. lst	r	disc	4.4	88	288	4.2	02	020	0.9	04	111	111	0.214	0.955
M19	7	P-wtm	fl. sst	r	disc	3.3	06	041	2.7	24	126	0.9	60	305	305	0.333	0.818
M19	7	P-wtm	fl. sst	sr	disc	4.6	06	053	3.7	15	166	1.2	74	342	342	0.324	0.804
M19	7	P-wtm	fl. sst	sr	disc	5.3	12	182		10	098	1.2	83	015			
M19	7	P-wtm	red b.	sa	equant	3.2	00		2.0	12	290	1.8	81	113		0.900	0.625
M19	7	P-wtm	green b.	a	equant	2.7	14	022	2.1	74	129	1.7	03	293		0.810	0.778
M19	7	P-wtm	gr. lst	sr	disc	2.9	17	101	2.8	12	005	0.7	73	180	180	0.250	0.966
M19	7	P-wtm	red b.	sa	disc	4.6	03	257	2.2	43	164	1.0	60	347	347	0.455	0.478
M19	7	P-wtm	o. lst	sa	disc	4.1	04	012	3.2	50	274	1.1	38	089	089	0.344	0.780
M19	7	P-wtm	fl. sst	r	equant	3.2	19	353		20	278	2.3	67	170	161		
M19	7	P-wtm	fl. sst	r	equant	3.2	02	045	2.8	39	132	1.6	59	299		0.571	0.875
M19	7	P-wtm	red b.	sa	disc	4.2	10	156	2.7	37	051	0.8	74	271	271	0.293	0.650
M24	28	P-wtm	o. lst	r	prolate	5.9	01	318	2.3	82	228	2.2	05	040		0.957	0.390
M24	28	P-wtm	o. lst	sr	disc	4.4	13	203	3.3	84	297	1.0	08	105	105	0.303	0.750
M24	28	P-wtm	red b.	sa	equant	5.3	04	019	2.3	07	288	2.0	80	116		0.870	0.434
M24	28	P-wtm	gr. lst	sr	prolate	6.0	28	217	2.9	68	302	2.6	26	128		0.897	0.483
M24	28	P-wtm	gr. lst	sr	equant	3.7	07	228	3.2	08	130	2.5	83	040	078	0.781	0.865
M24	28	P-wtm	green b.	sr	equant	4.4	65	266	4.0	02	158	3.3	18	263		0.825	0.909
M24	28	P-wtm	gr. lst	sr	prolate	5.6	15	166	2.5	60	267	1.3	22	085	085	0.520	0.446
M24	28	P-wtm	fl. sst	r	disc	4.3	24	136	3.2	02	038	1.5	52	299	299	0.469	0.744
M24	28	P-wtm	o. lst	r	disc	4.7	23	166	4.2	10	263	1.1	73	008	008	0.262	0.894
M24	28	P-wtm	fl. sst	r	prolate	5.6	17	196	2.0	81	085	1.4	02	267	280	0.700	0.357
M24	28	P-wtm	o. lst	r	disc	4.0	05	035	2.7	19	127	1.3	68	286	348	0.481	0.675
M24	28	P-wtm	fl. sst	r	disc	3.8	10	224	3.0	12	310	0.5	78	082	057	0.167	0.789
M24	28	P-wtm	o. lst	sr	equant	3.2	45	265	3.0	15	087	3.0	04	343		1.000	0.938
M24	28	P-wtm	gr. lst	r	disc	3.7	32	176	2.2	03	270	0.9	65	001	001	0.409	0.595
M24	28	P-wtm	gr. lst	sr	disc	5.2	89	164	3.5	08	255	1.3	00		160	0.371	0.673
M24	28	P-wtm	o. lst	r	disc	4.4	18	172	3.5	16	273	1.2	73	020	020	0.343	0.795
M24	28	P-wtm	o. lst	sr	prolate	4.9	25	312	1.3	09	047	1.1	70	162	114	0.846	0.265
M24	28	P-wtm	o. lst	r	disc	4.4	10	079	4.2	00		1.7	72	265	265	0.405	0.955
M24	28	P-wtm	green b.	sa	prolate	4.7	19	103	2.2	52	004	2.0	25	198		0.909	0.468
M24	28	P-wtm	gr. lst	r	disc	3.8	27	022	2.2	13	112	1.6	51	210	228	0.727	0.579
M24	28	P-wtm	o. lst	r	disc	3.2	00		2.3	05	216	0.8	87	058	058	0.348	0.719
M24	28	P-wtm	o. lst	sr	disc	3.8	21	358	2.0	20	102	0.8	72	180	180	0.400	0.526
M24	28	P-wtm	gr. lst	sr	disc	4.2	07	277	3.0	05	357	1.7	87	090	139	0.567	0.714
M24	28	P-wtm	red b.	sa	equant	3.1	03	334	2.2	16	047	2.0	73	256		0.909	0.710
M24	28	P-wtm	red b.	sa	disc	3.3	22	301	2.6	75	203	1.1	11	038	038	0.423	0.788
M24	28	P-wtm	fl. sst	r	disc	3.5	05	292	2.3	27	185	0.8	67	020	020	0.348	0.657
M24	28	P-wtm	green b.	sa	disc	3.6	34	311	2.4	15	200	0.9	69	078	078	0.375	0.667
M24	28	P-wtm	o. lst	sr	prolate	3.8	22	009	1.5	59	132	1.2	33	214	214	0.800	0.395
M24	28	P-wtm	o. lst	sr	prolate	4.2	10	282	2.4	05	183	1.3	82	117	117	0.542	0.571
M24	28	P-wtm	fl. sst	sr	disc	3.0	16	322	1.8	55	231	0.5	35	070	070	0.278	0.600
M24	28	P-wtm	o. lst	r	disc	2.1	11	000	1.9	06	086	0.8	69	310	310	0.421	0.905
M24	28	P-wtm	fl. sst	r	disc	2.6	02	091	2.0	25	356	0.6	74	160	160	0.300	0.769
M24	28	P-wtm	o. lst	r	equant	3.7	22	012	2.7	21	119	2.5	89	157		0.926	0.730
M24	28	P-wtm	gr. lst	r	oblate	3.7	00		1.9	58	121	0.9	39	321	321	0.474	0.514
M24	28	P-wtm	green b.	sa	equant	2.1	18	271	2.0	07	014	1.6	77	320		0.800	0.952
M24	28	P-wtm	gr. lst	r	prolate	4.2	01	300	2.0	36	217	1.3	60	036	138	0.650	0.476
M24	28	P-wtm	green b.	sa	disc	3.0	09	305	2.5	28	189	1.0	78	040	307	0.400	0.833
M24	28	P-wtm	gr. lst	r	disc	3.7	17	270	2.1	90		0.7	00		173	0.333	0.568
M24	28	P-wtm	gr. lst	r	disc	3.4	17	120	2.4	21	040	1.6	67	186	186	0.667	0.706
M24	28	P-wtm	red b.	sr	disc	3.3	14	227	2.9	11	135	0.4	83	322	032	0.138	0.879
M24	28	P-wtm	fl. sst	r	equant	2.8	13	142	2.3	22	040	2.2	59	236		0.957	0.821
M24	28	P-wtm	o. lst	r	equant		30	073	3.5	04	030	3.2	56	267			
M24	28	P-wtm	chert	sa	disc	2.8	20	169	2.6	71	215	1.3	18	048	048	0.500	0.929
M24	28	P-wtm	gr. lst	sr	prolate	4.2	07	223	2.0	13	332	1.0	59	147		0.500	0.476
M24	28	P-wtm	gr. lst	r	prolate	3.6	19	289	1.7	16	030	1.2	70	187		0.706	0.472
M24	28	P-wtm	o. lst	sr	disc	5.9	62	108	3.5	16	005	0.8	12	264	264	0.229	0.593
M24	28	P-wtm	o. lst	r	disc	3.1	07	003	2.2	51	278	0.7	37	102	102	0.318	0.710
M24	28	P-wtm	fl. sst	sr	disc	2.4	04	183	1.8	62	288	0.5	21	094	085	0.278	0.750
M24	28	P-wtm	o. lst	sr	disc	4.4	09	140	2.7	30	026	1.0	47	250	209	0.370	0.614
M24	28	P-wtm	gr. lst	r	disc	2.3	34	019	1.8	28	109	0.6	57	196	196	0.333	0.783
M34	158	P-wtm	red b.	sa	disc	1.8	07	305	1.3	25	213	0.2	72	050	050	0.154	0.722
M34	158	P-wtm	fl. sst	r	equant	2.0	11	073	1.3	62	330	1.0	23	162	162	0.769	0.650
M34	158	P-wtm	o. lst	sa	equant	2.1	21	108	1.2	52	208	0.8	25	013	013	0.667	0.571
M34	158	P-wtm	o. lst	sr	equant	2.1	17	035	1.5	28	210	1.2	62	044	044	0.800	0.714
M34	158	P-wtm	o. lst	sr	disc	1.7	34	285	0.9	12	210	0.4	45	042	042	0.444	0.529
M34	158	P-wtm	red b.	a	equant	1.5	08	095	1.3	15	190	1.1	81	004		0.846	0.867
M34	158	P-wtm	gr. lst	sr	disc	2.4	09	282	1.5	39	190	0.6	60	020	020	0.400	0.625
M34	158	P-wtm	gr. lst	sr	equant		03	233	1.5	32	137	1.2	68	338			
M34	158	P-wtm	green b.	r	equant	1.0	46	340	0.9	32	262	0.7	45	350		0.778	0.900
M34	158	P-wtm	o. lst	sr	disc	2.8	10	239	1.2	58	144	0.4	49	328	328	0.333	0.429
M34	158	P-wtm	o. lst	sr	equant	1.9	30	326	1.7	18	055	1.6	42	180		0.941	0.895
M34	158	P-wtm	green b.	sa	equant	2.4	90		2.2	14	054	1.8	00			0.818	0.917
M34	158	P-wtm	o. lst	sr	prolate	1.9	32	034	1.2	84	315	1.0	08	140	140	0.833	0.632
M34	158	P-wtm	gr. lst	sa	equant	1.3	22	330	0.8	31	075	0.7	54	247	247	0.875	0.615
M34	158	P-wtm	fl. sst	r	prolate	1.5	24	212	0.6	05	132	0.4	76	322		0.667	0.400
M34	158	P-wtm	gr. lst	sr	disc	2.3	08	276	1.9	35	016	1.0	48	188	188	0.526	0.826
M34	158	P-wtm	green b.	sr	equant	1.4	19	316	1.3	21	050	1.1	62	190		0.846	0.929
M34	158	P-wtm	o. lst	sa	disc		11	158	1.5	04	259	0.8	81	082	082		
M34	158	P-wtm	fl. sst	r	disc	1.6	28	359	1.5	18	266	0.3	72	094	094	0.200	0.938
M34	158	P-wtm	gr. lst	sr	equant	2.0	16	031	1.3	70	286	0.9	02	110	110	0.692	0.650
M34	158	P-wtm	gr. lst	r	equant	2.0	10	260		05	260	1.5	81	352			
M34	158	P-wtm	fl. sst	r	equant	1.0	01	350	1.0	28	350	0.5	60	075	075	0.500	1.000
M34	158	P-wtm	gr. lst	sr	prolate	2.2	03	235	0.6	25	235	0.5	65	148	148	0.833	0.273
M34	158	P-wtm	green b.	sa	disc	1.2	11	128	1.1	85	128	0.2	16	042	042	0.182	0.917
M34	158	P-wtm	red b.	sr	equant	1.8	50	010	1.2	10	010	0.7	41	185		0.583	0.667
M34	158	P-wtm	gr. lst	r	disc	1.5	39	258	1.2	00	258	0.5	55	093	093	0.417	0.800
M34	158	P-wtm	o. lst	sr	disc	2.6	13	090		03	090	1.1	75	280	280		
M34	158	P-wtm	gr. lst	sr	disc	1.4	12	239	0.7	70	239	0.2	14	168	168	0.286	0.500
M34	158	P-wtm	gr. lst	r	disc	1.7	06	062	1.0	46	062	0.3	62	151	151	0.300	0.588
M34	158	P-wtm	fl. sst	r	equant	1.4	62	260	1.3	14	260	0.9	22	080	080	0.692	0.929
M34	158	P-wtm	green b.	sr	disc	2.1	05	099	1.7	25	099	0.5	58	190	190	0.294	0.810
M34	158	P-wtm	o. lst	sa	equant	1.4	34	290	1.0	18	290	0.9	22	106	106	0.900	0.714
M34	158	P-wtm	fl. sst	r	equant	0.8	43	166	0.6	06	166	0.5	51	344	344	0.833	0.750
M34	158	P-wtm	o. lst	sr	disc	1.0	11	196	0.8	04	196	0.3	74	090	090	0.375	0.800
M34	158	P-wtm	green b.	sa	equant	0.9	68	299	0.7	52	299	0.6	04	132		0.857	0.778
M34	158	P-wtm	o. lst	sr	disc	2.0	04	106		07	106	0.3	82	286	286		
M34	158	P-wtm	red b.	sa	disc	1.8	03	120		19	120	0.2	74	057	057		
M34	158	P-wtm	fl. sst	r	disc	2.9	04	227	2.0	35	227	1.0	50	144	144	0.500	0.690
M34	158	P-wtm	o. lst	sr	prolate	2.2	00		1.2	64		0.9	22	108	108	0.750	0.545
M34	158	P-wtm	green b.	sa	equant	2.8	10	262	1.4	90	262		04	002			
M34	158	P-wtm	red b.	sa	prolate	1.7	08	095	0.8	69	095	0.5	22	190		0.625	0.471
M34	158	P-wtm	o. lst	r	disc	2.4	22	345	1.6	07	345	1.0	78	075	075	0.625	0.667
M34	158	P-wtm	green b.	sr	equant	1.8	32	348	1.2	30	348	1.0	61	274		0.833	0.667
M34	158	P-wtm	fl. sst	sr	disc	1.2	35	325	1.1	05	325	0.3	52	148	148	0.273	0.917
M34	158	P-wtm	red b.	sa	disc	1.9	08	078	1.1	20	078	0.4	71	182	182	0.364	0.579
M34	158	P-wtm	o. lst	r	disc	1.7	75	026	1.5	08	026	0.3	21	199	199	0.200	0.882
M34	158	P-wtm	fl. sst	r	prolate	2.9	14	328	1.3	24	328	1.0	62	062		0.769	0.448
M34	158	P-wtm	red b.	sr	disc	1.7	18	324	1.2	12	324	0.5	76	070	070	0.417	0.706
M34	158	P-wtm	o. lst	sr	disc	1.8	10	052	1.4	76	052	1.0	10	155		0.714	0.778
M34	158	P-wtm	fl. sst	r	equant		03	351	1.1	0	351	0.8	88	182			

M19/L16

chert	0				
black b.	0	equant	18	r	17
green b.	2	prolate	6	sr	16
gr. lst	9	disc	26	sa	15
red b.	6			a	2
fl. sst	16				
o. lst	17				
	50		**50**		**50**

M24/L15

black b.	0	equant	9	r	24
green b.	5	prolate	11	sr	18
gr. lst	14	disc	29	sa	8
red b.	4	oblate	1	a	0
fl. sst	8				
o. lst	18				
chert	1		**50**		**50**
	50				

M34/L5

black b.	0	equant	21	r	15
green b.	8	prolate	6	sr	22
gr. lst	10	disc	23	sa	12
red b.	7	oblate	0	a	1
fl. sst	10				
o. lst	15				
	50		**50**		**50**

PALAEOC TOTALS

	M19
0-30	2
31-60	0
61-90	2
91-120	1
121-150	0
151-180	2
181-210	6
211-240	0
241-270	5
271-300	5
301-330	4
331-360	8
	35

CLASS	**NO.**
bladed	7
disc	22
prolate	8
equant	7

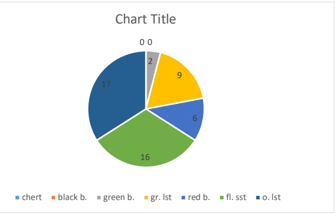

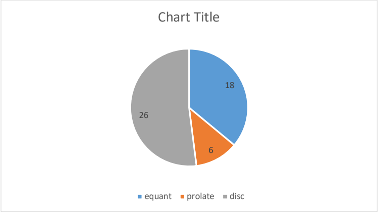

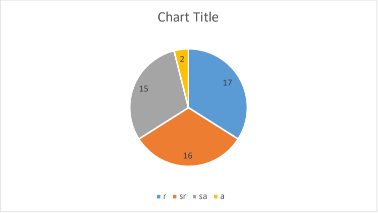

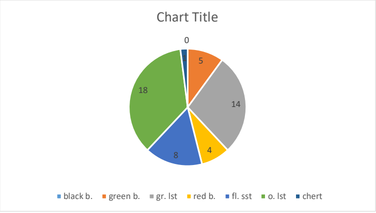

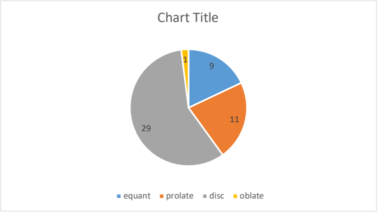

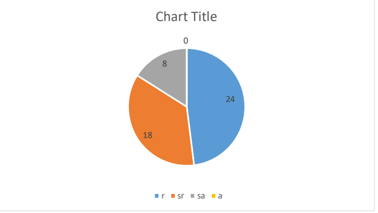

	M24
0-30	4
31-60	5
61-90	5
91-120	4
121-150	2
151-180	4
181-210	3
211-240	2
241-270	2
271-300	2
301-330	3
331-360	1
	37

CLASS	**NO.**
bladed	13
disc	20
prolate	9
equant	7

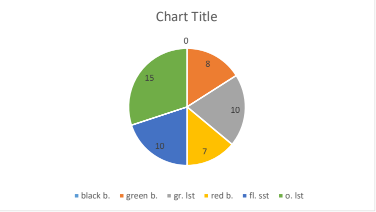

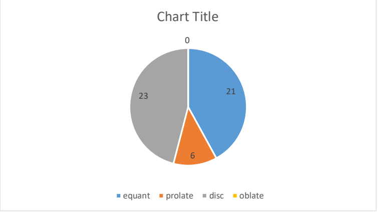

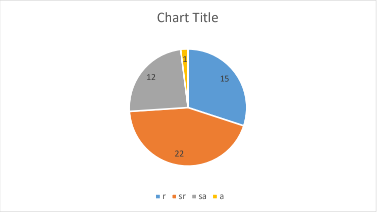

	M34
0-30	2
31-60	5
61-90	6
91-120	5
121-150	4
151-180	3
181-210	4
211-240	0
241-270	1
271-300	2
301-330	1
331-360	1
	34

CLASS	**NO.**
bladed	11
disc	12
prolate	8
equant	11

Conglomerate facies figure panels of clast data

The following pages contain panel figures of all of the previous facies data shown in table format. These figures are similar to figures displayed in Chapter 5.

Facies B-wtm

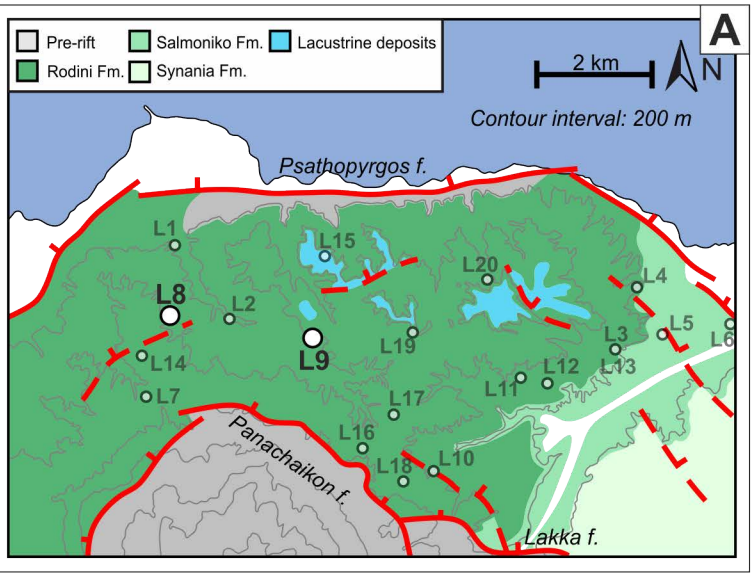

Facies images

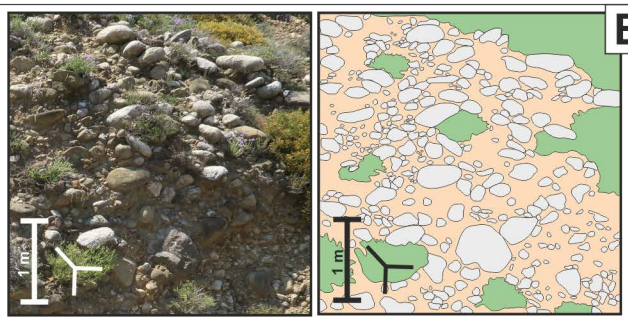

Grain size plot

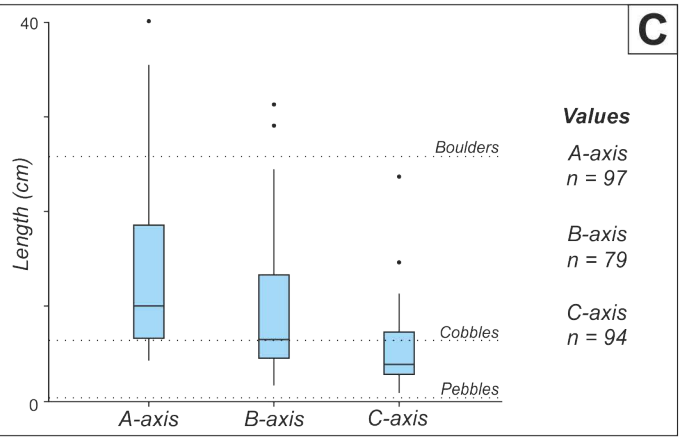

Clast shapes (Zingg)

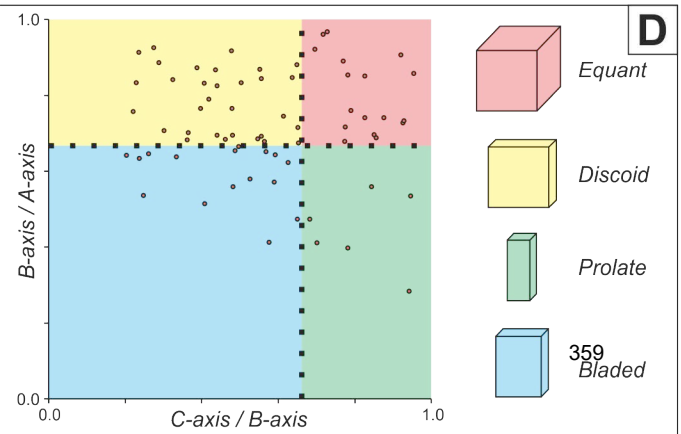

Clast textural data

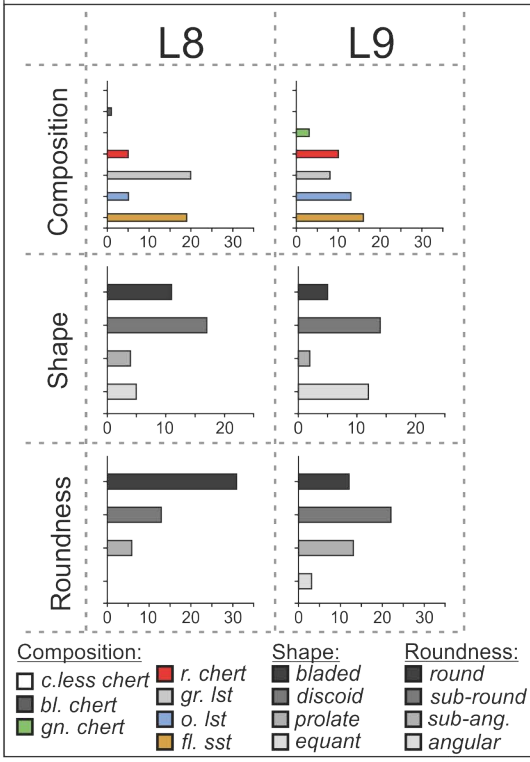

Axis orientation data

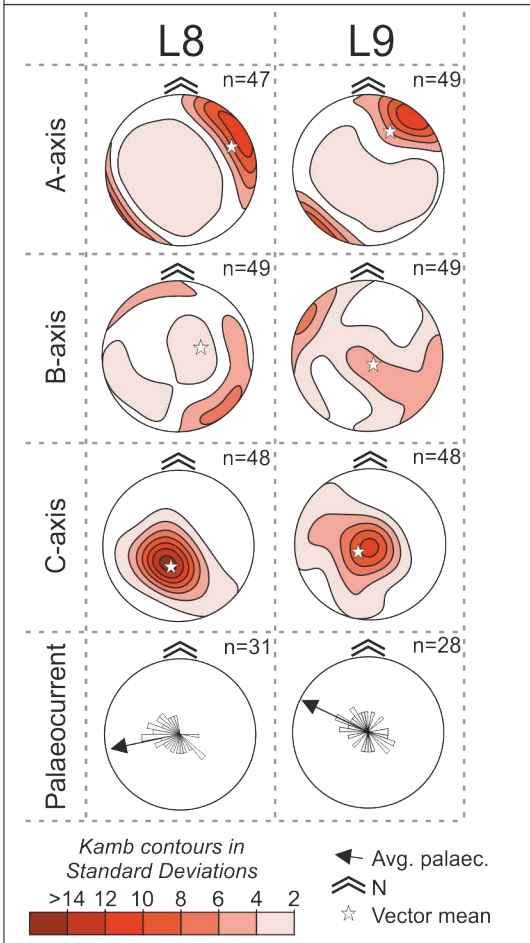

Facies B-rlf

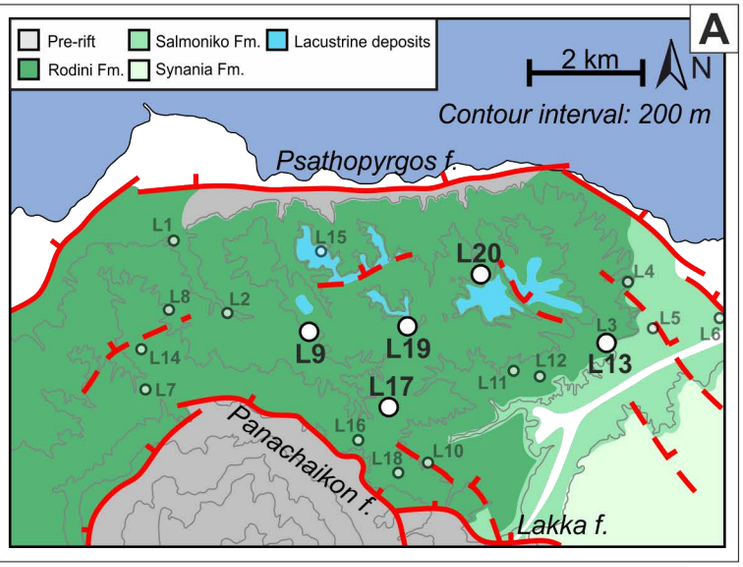

Facies images

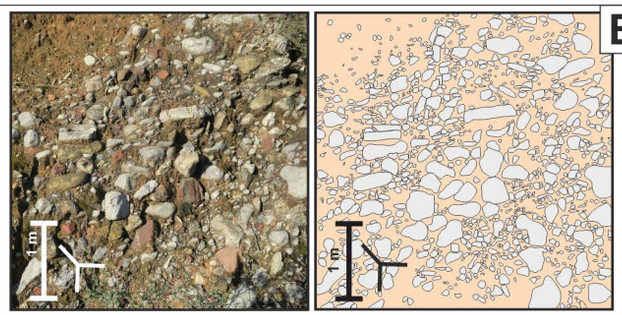

Grain size plot

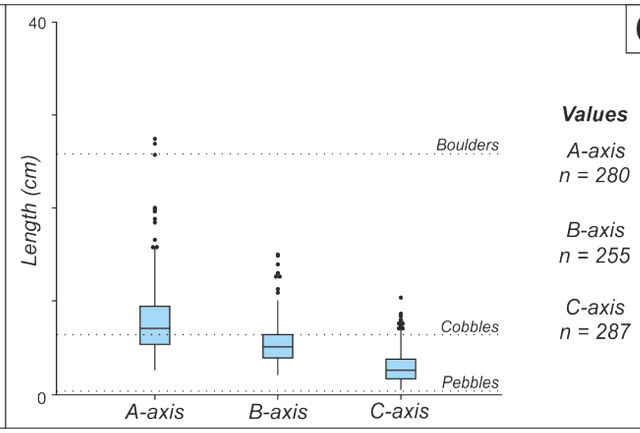

Clast shapes (Zingg)

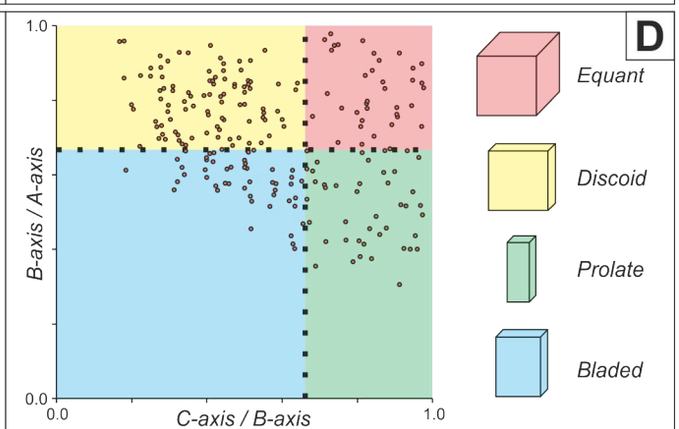

Clast textural data

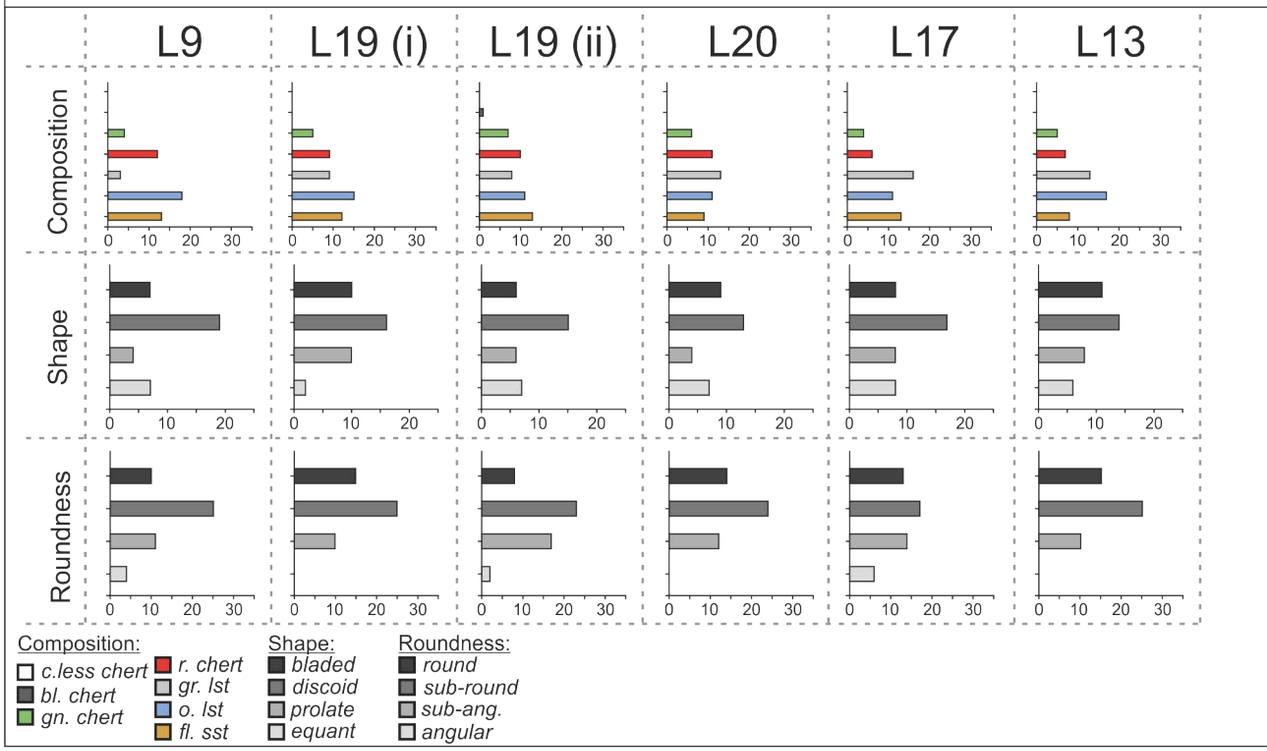

Axis orientation data

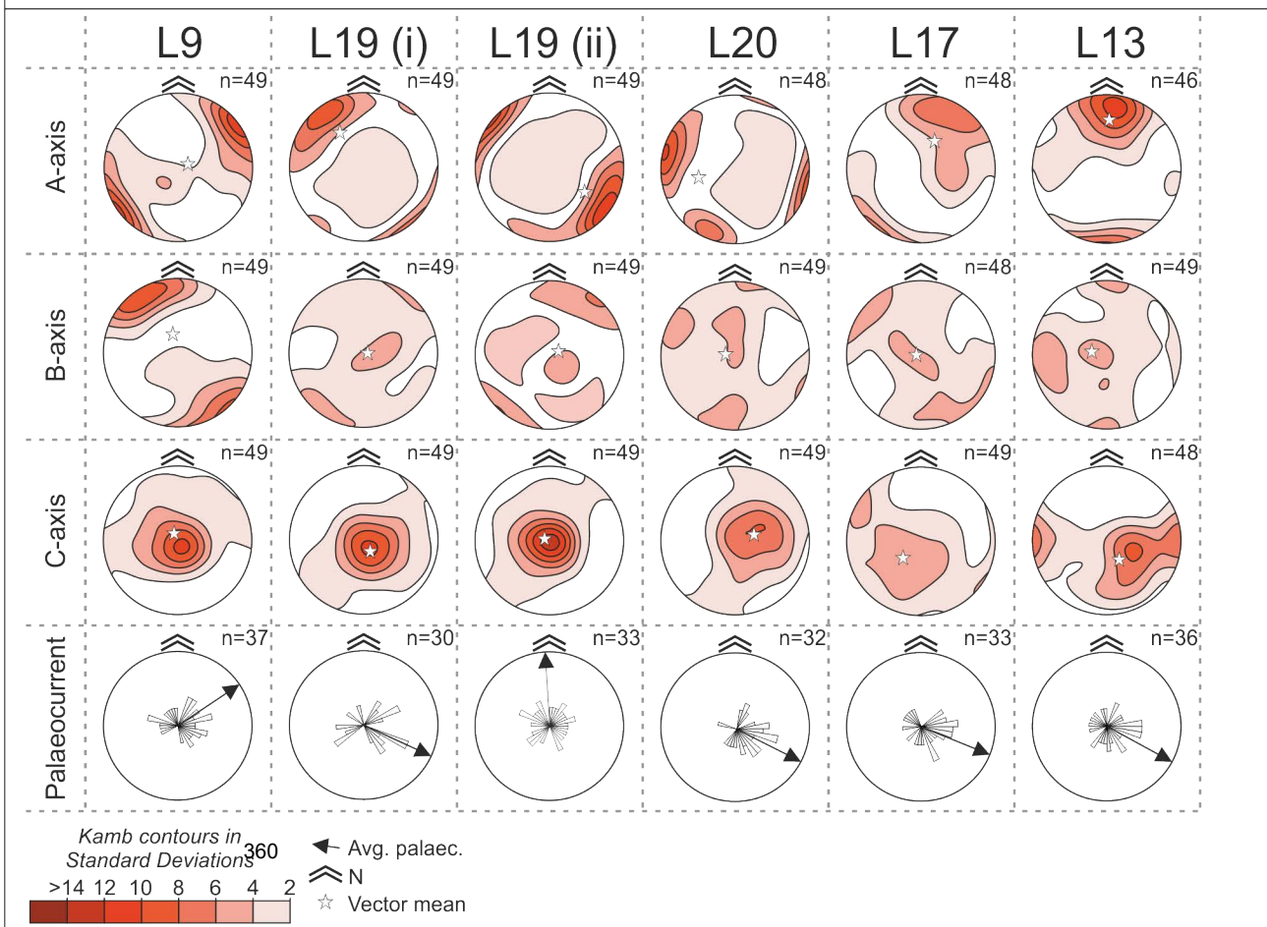

Facies B-plm

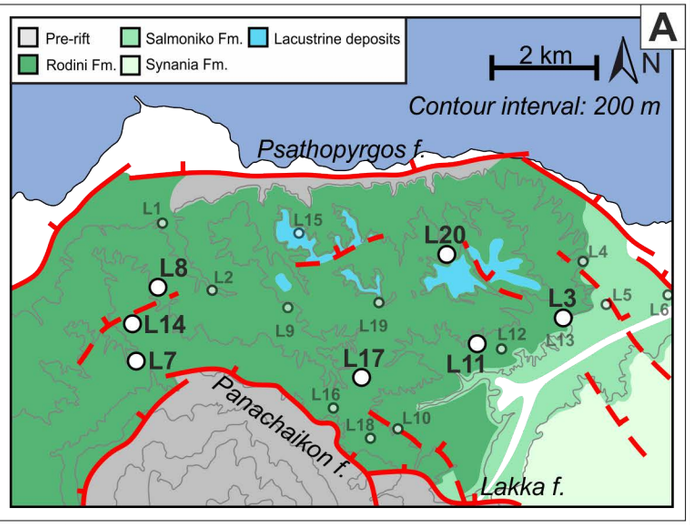

Facies images

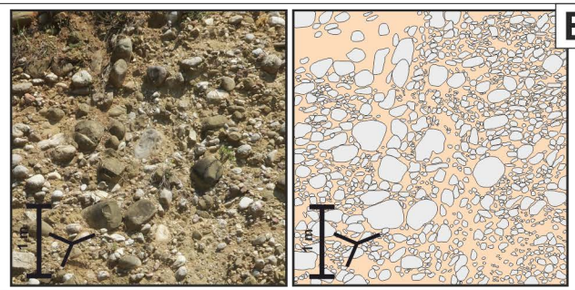

Grain size plot

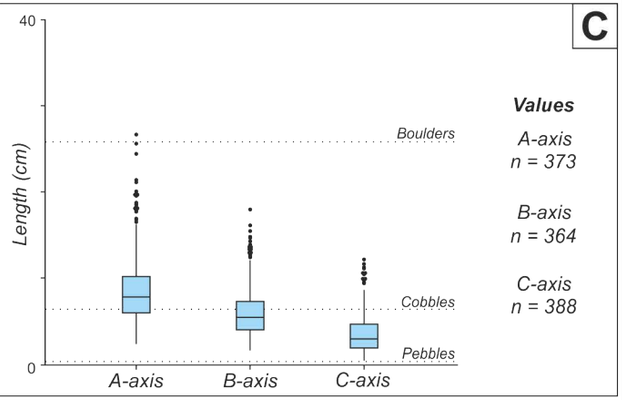

Clast shapes (Zingg)

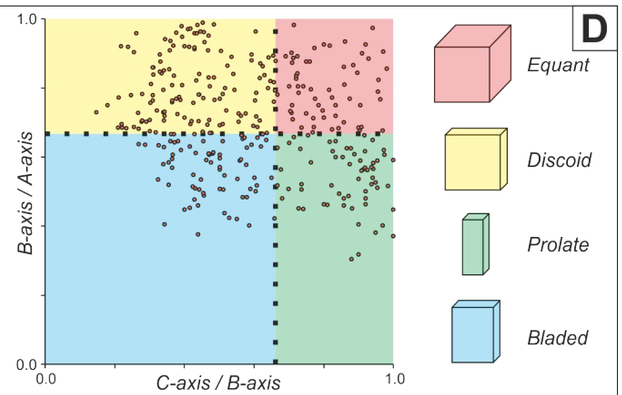

Clast textural data

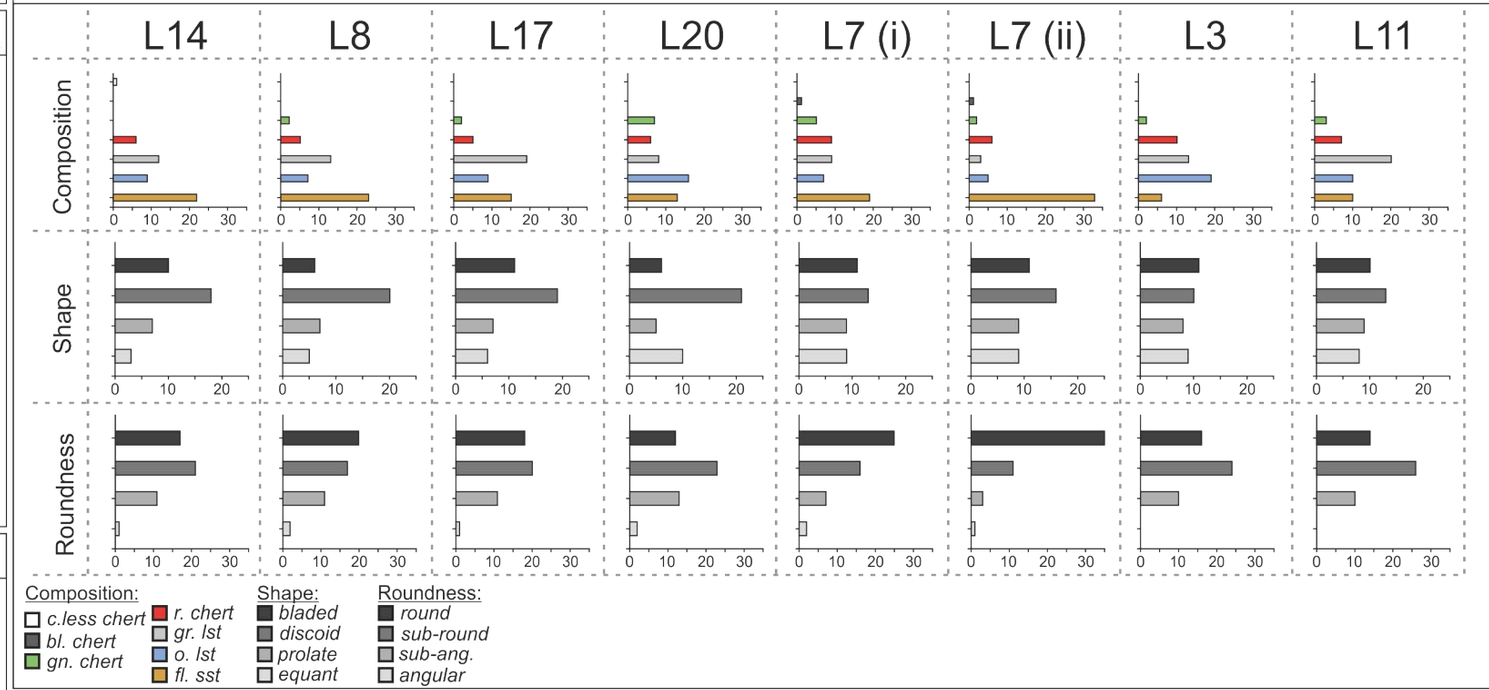

Composition:
- c.less chert
- bl. chert
- gn. chert
- r. chert
- gr. lst
- o. lst
- fl. sst

Shape:
- bladed
- discoid
- prolate
- equant

Roundness:
- round
- sub-round
- sub-ang.
- angular

Axis orientation data

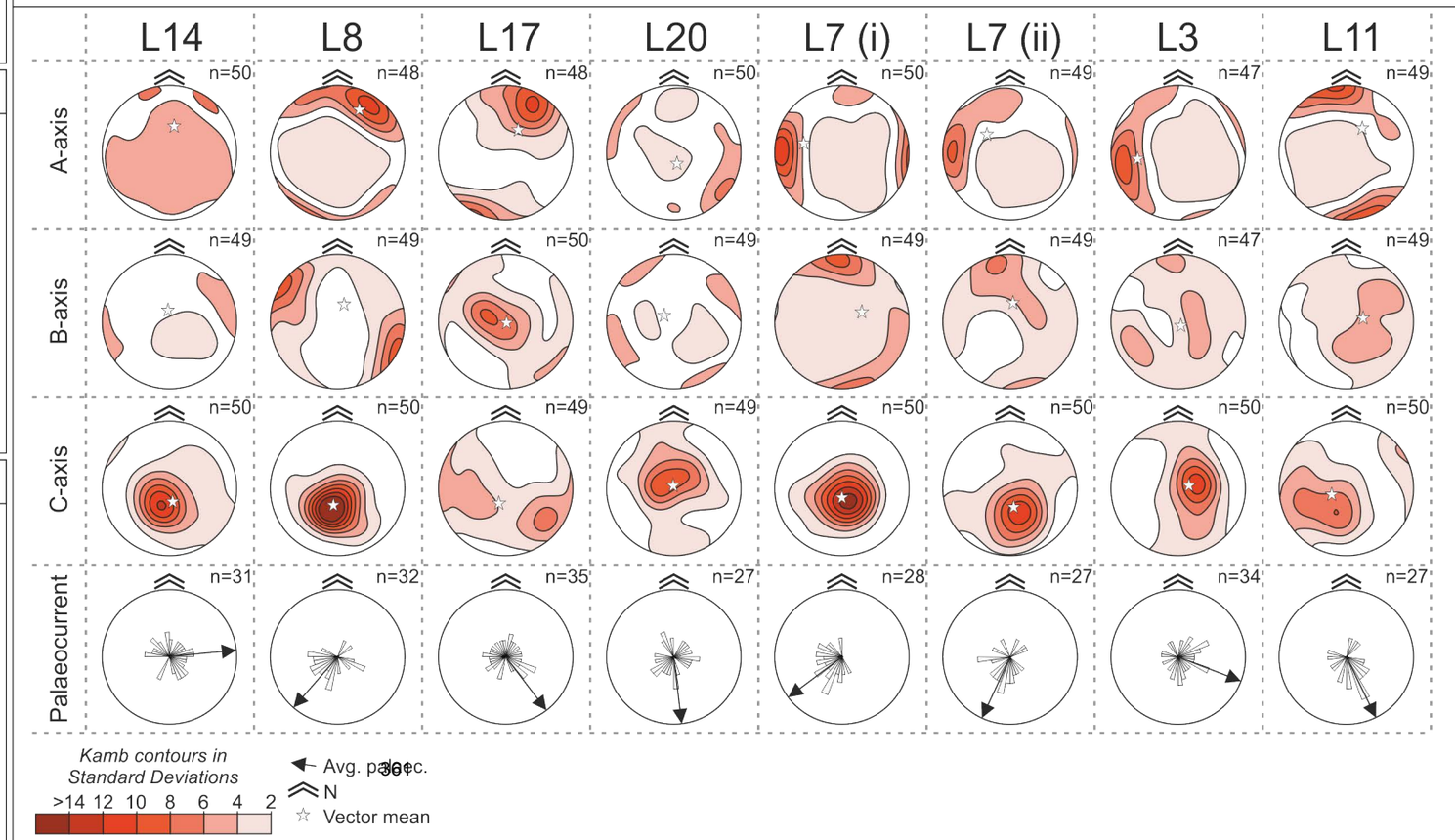

Facies B-pII

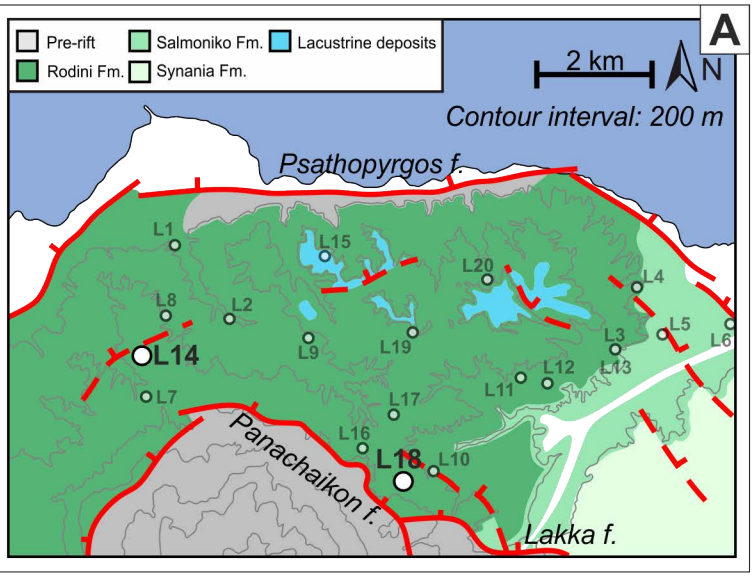

Facies images

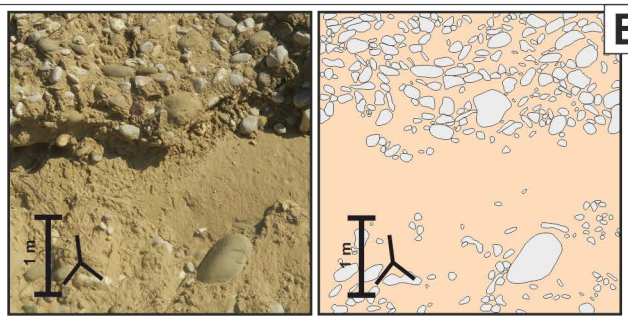

Grain size plot

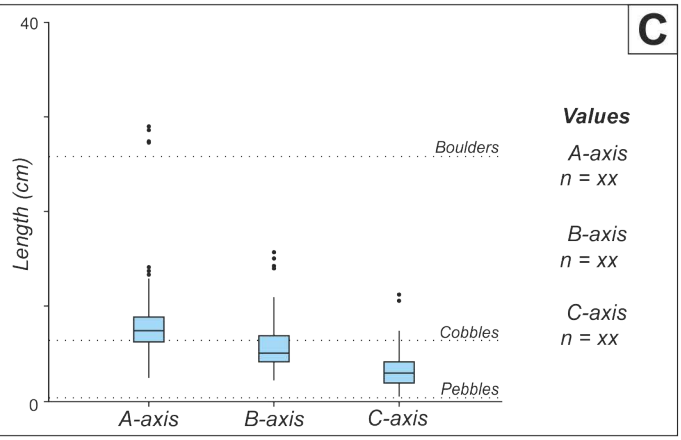

Clast shapes (Zingg)

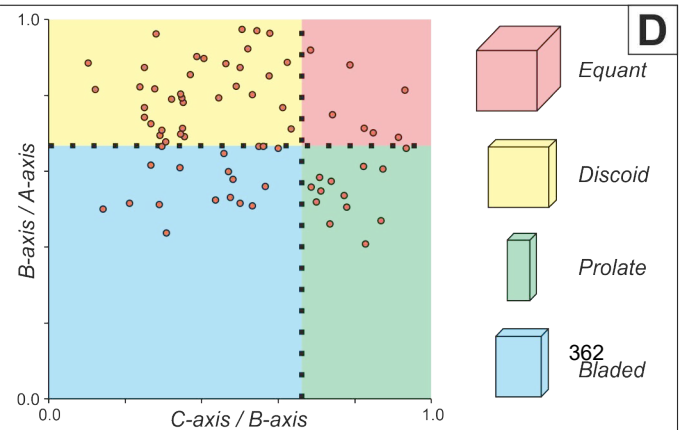

Clast textural data

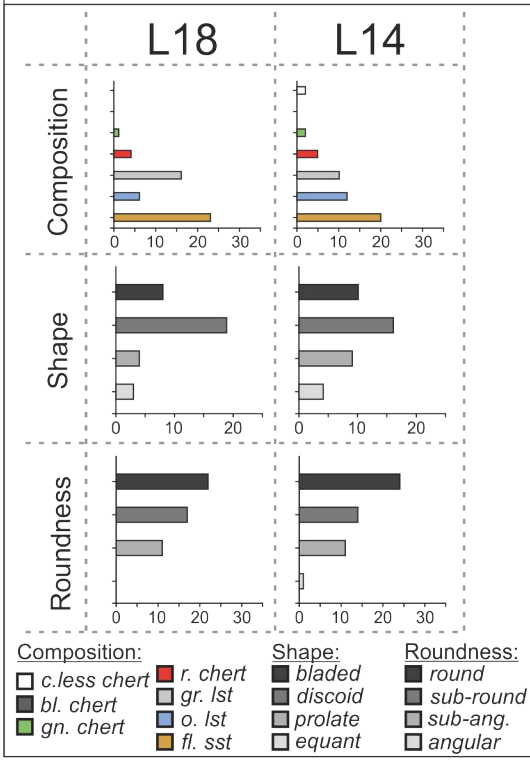

Axis orientation data

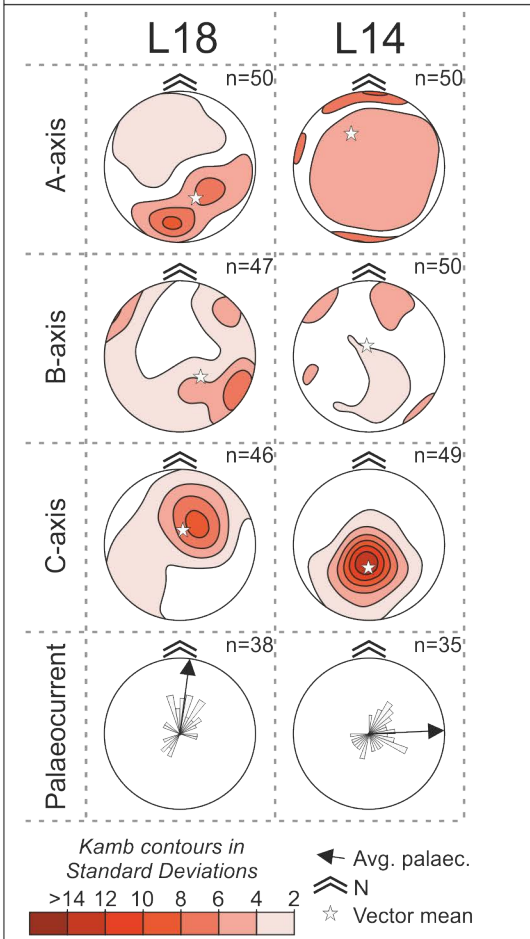

Facies C-rll

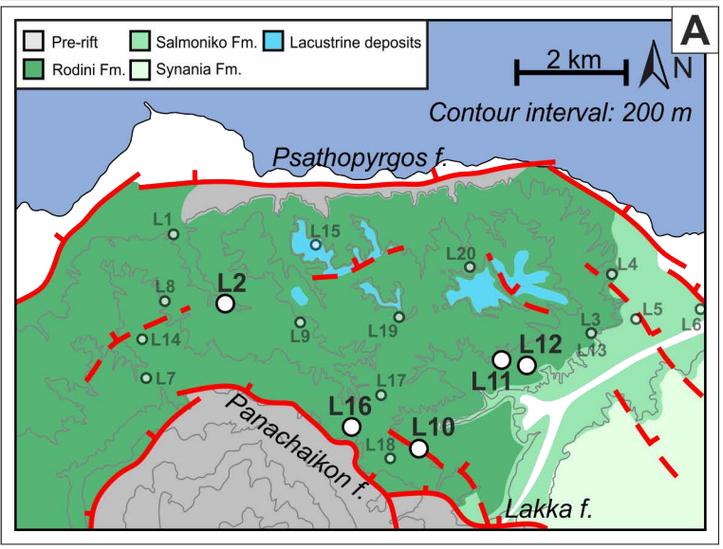

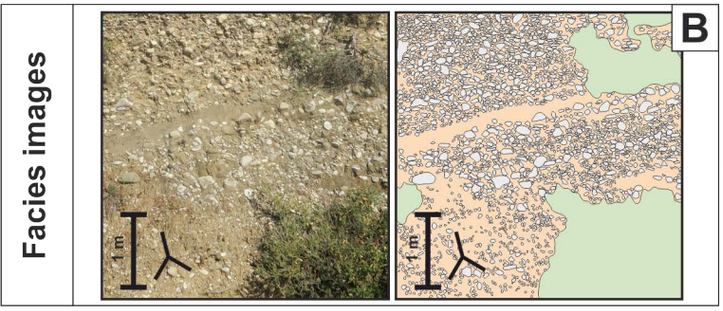

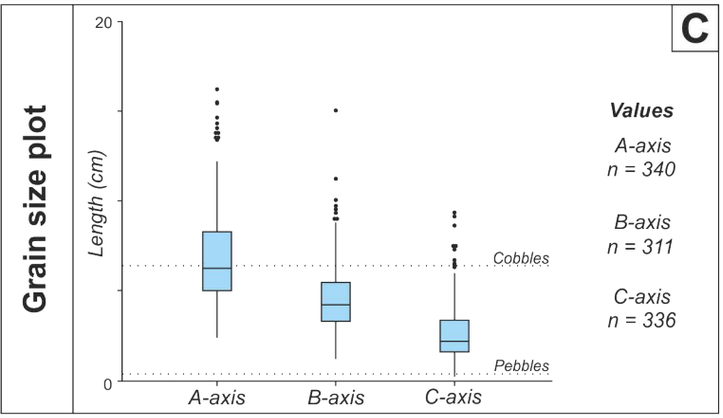

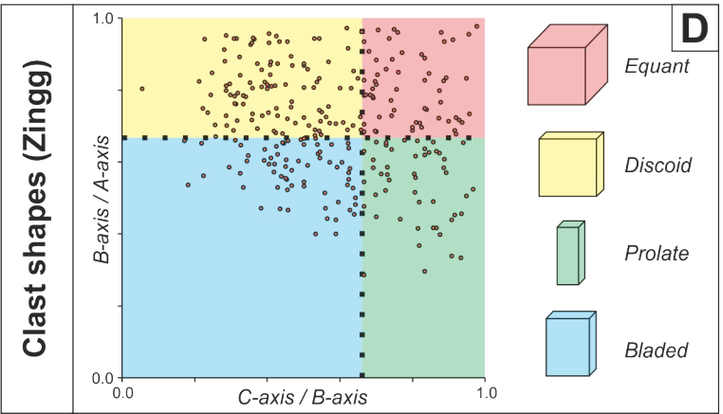

Clast textural data

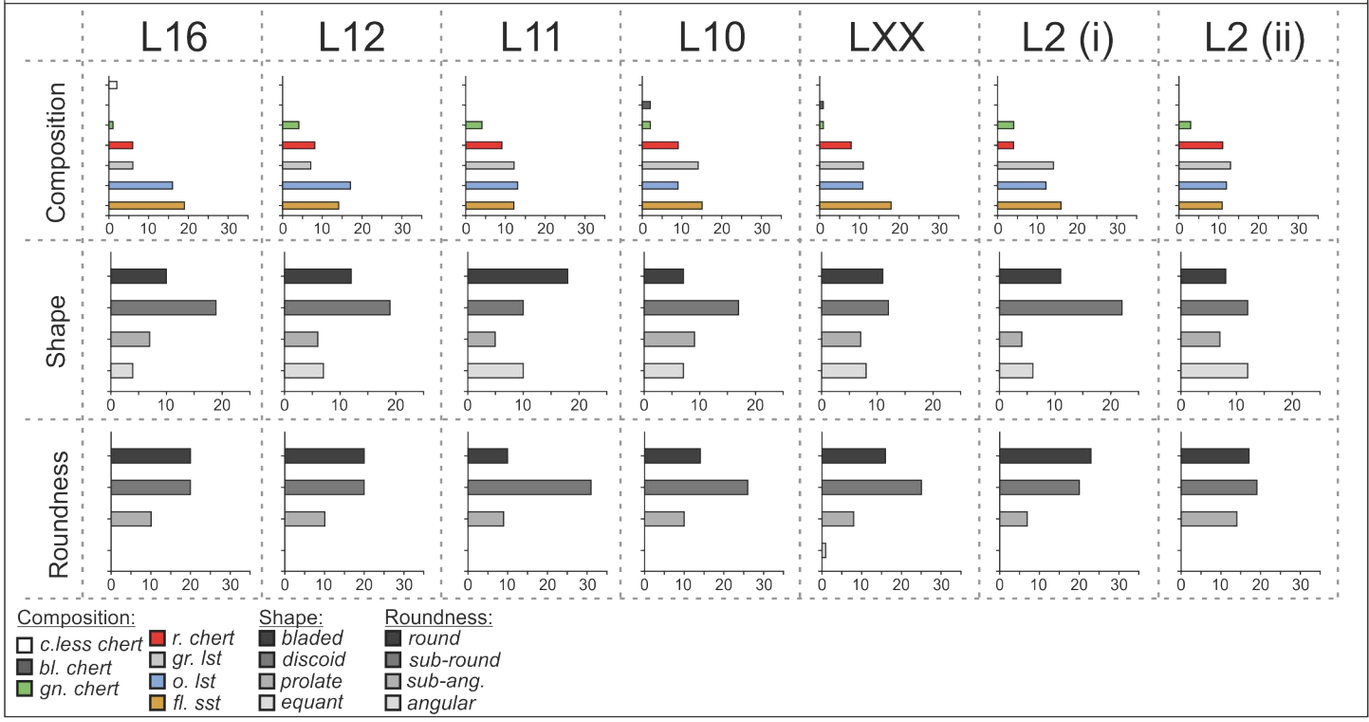

Axis orientation data

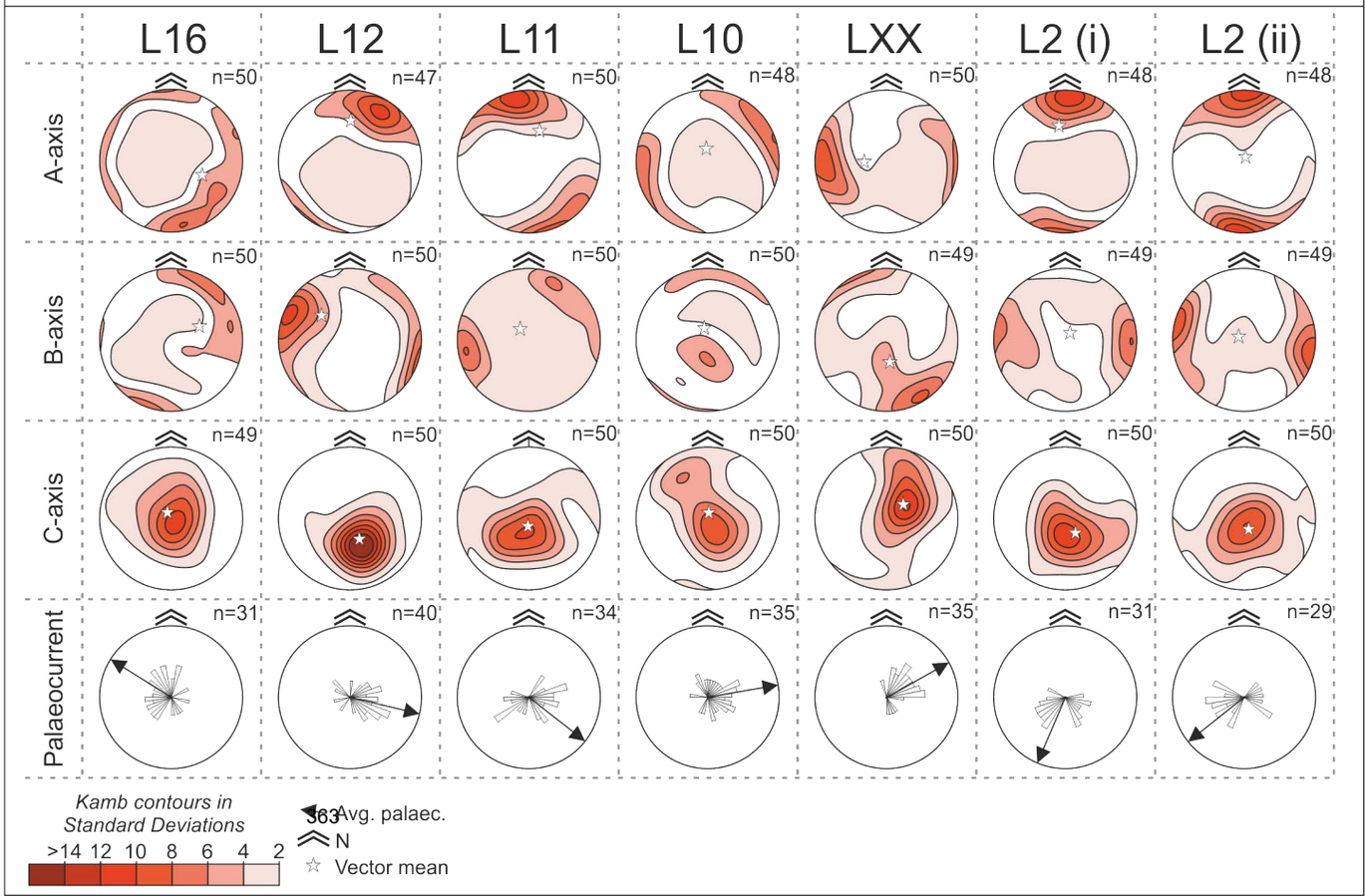

Facies C-pth

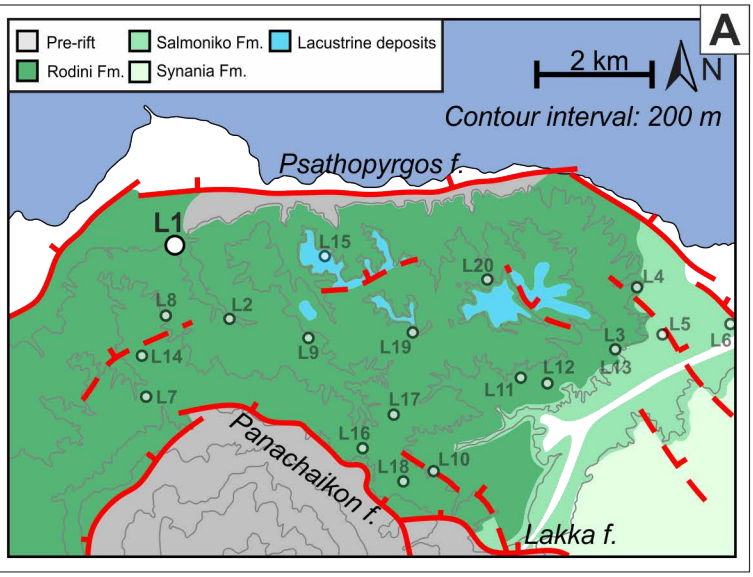

Facies images

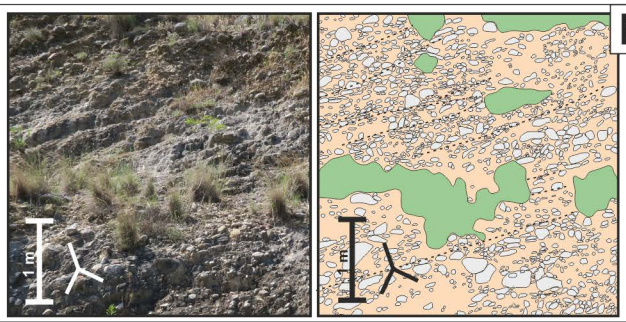

Grain size plot

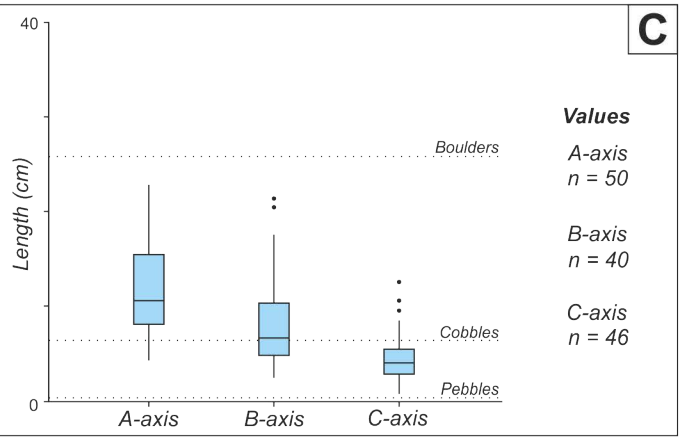

Clast shapes (Zingg)

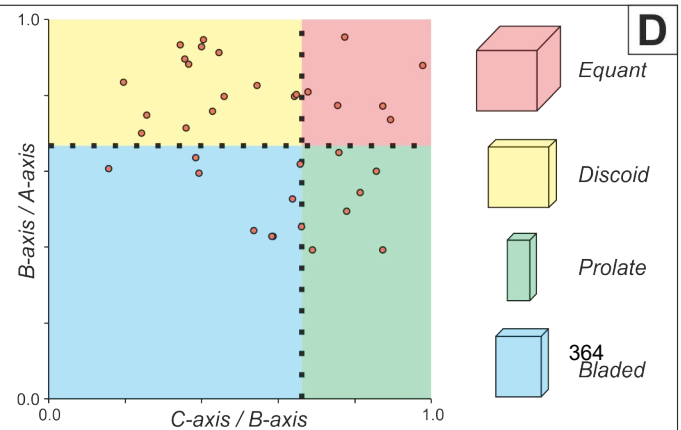

Clast textural data

E

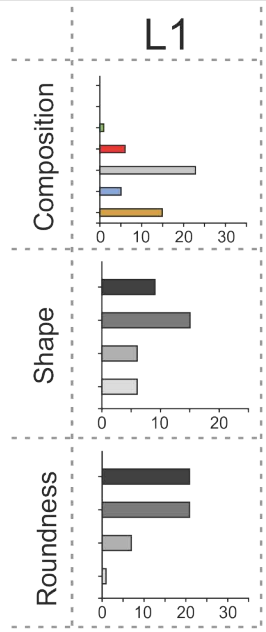

Composition:
- c.less chert
- bl. chert
- gn. chert
- r. chert
- gr. lst
- o. lst
- fl. sst

Shape:
- bladed
- discoid
- prolate
- equant

Roundness:
- round
- sub-round
- sub-ang.
- angular

Axis orientation data

F

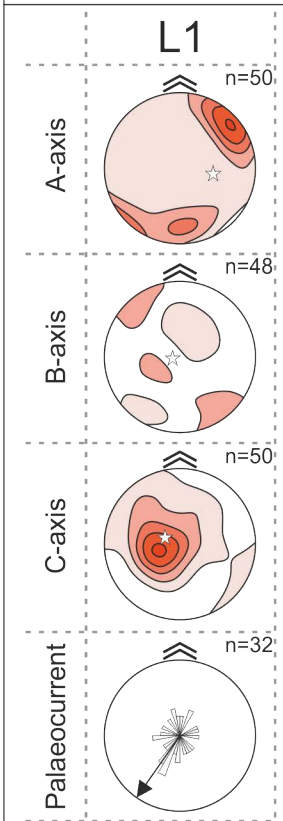

Kamb contours in Standard Deviations
>14 12 10 8 6 4 2

- Avg. palaec.
- N
- Vector mean

Facies P-wtm

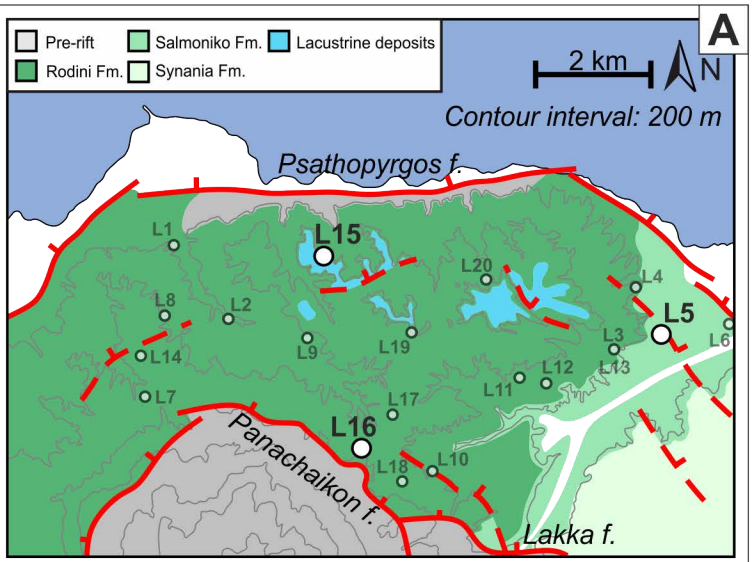

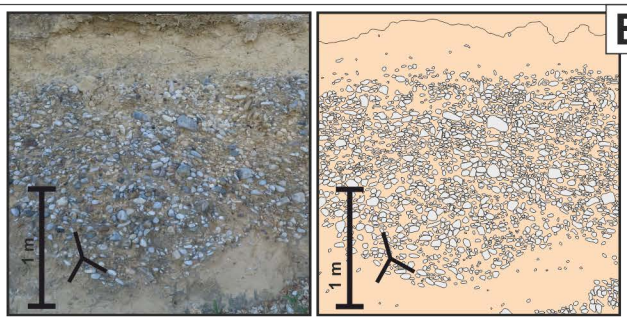

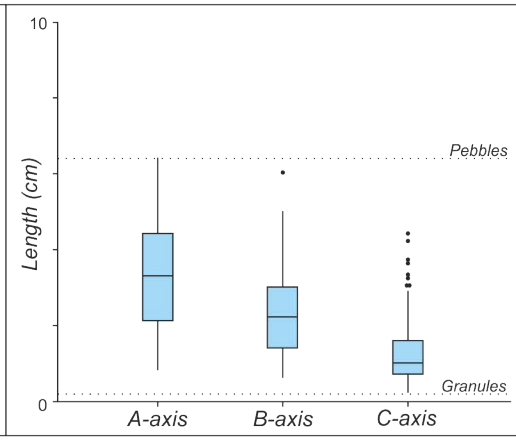

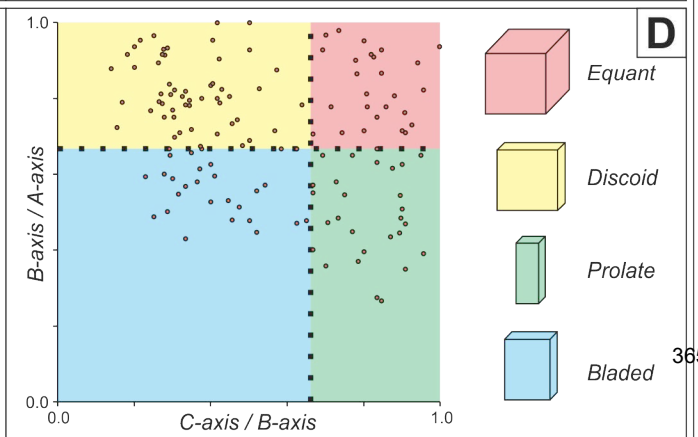

Clast textural data

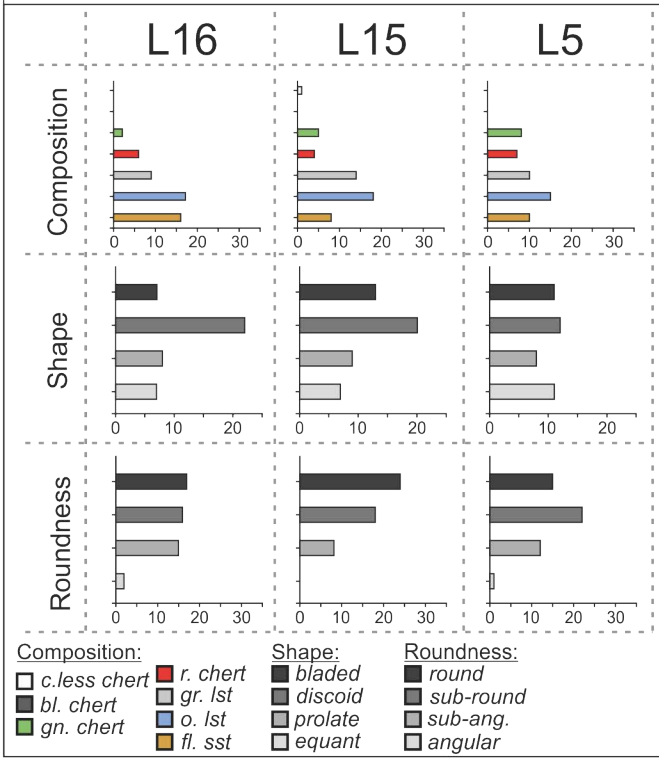

Axis orientation data

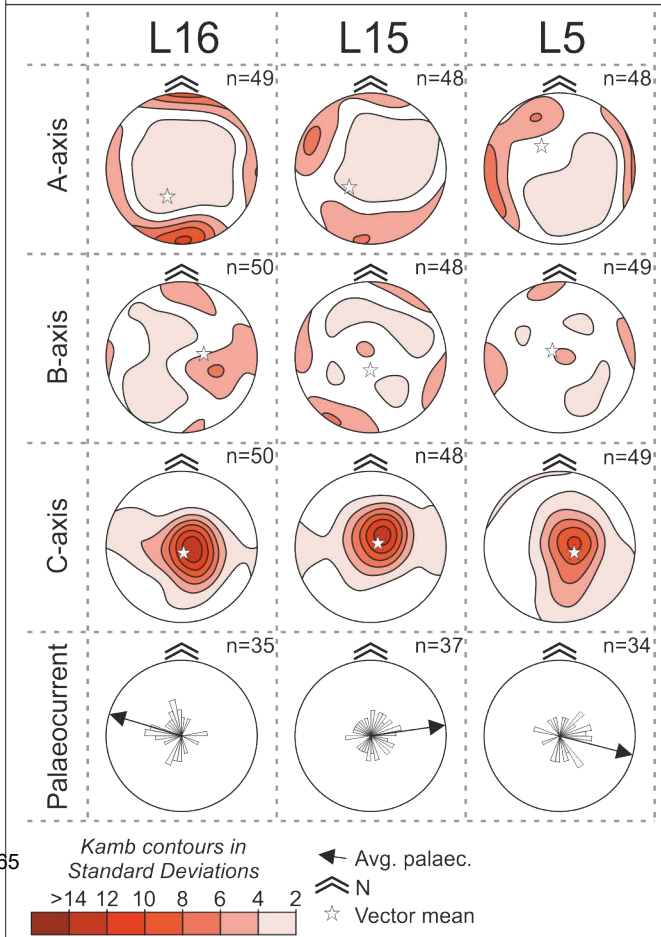

Facies B-ple

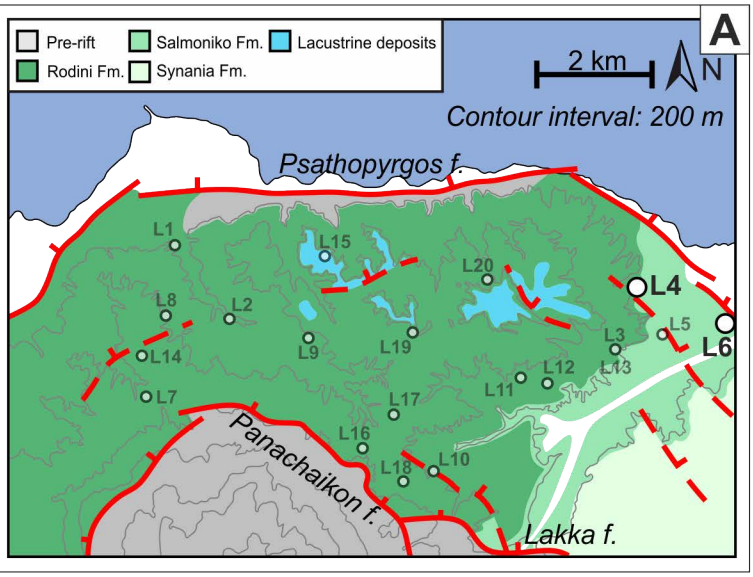

Facies images

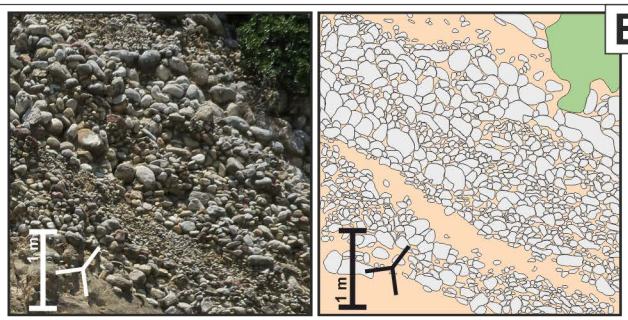

Grain size plot

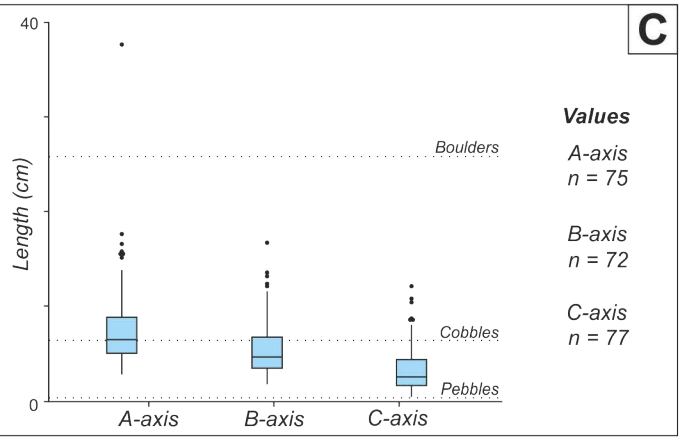

Clast shapes (Zingg)

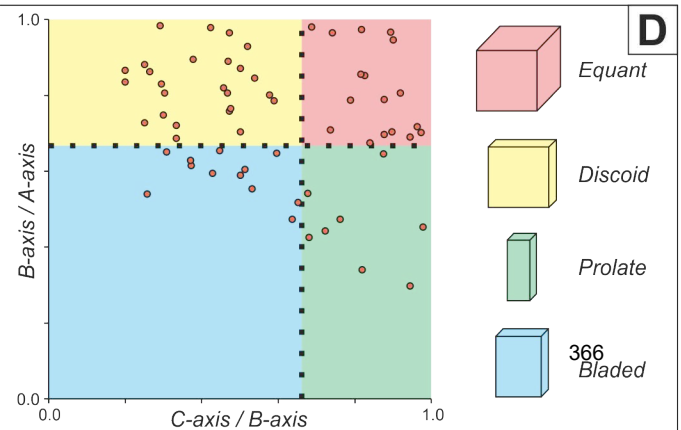

Clast textural data

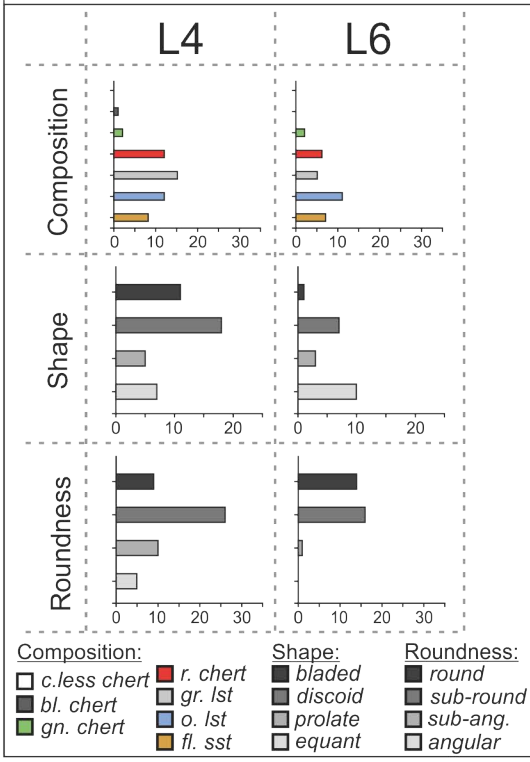

Axis orientation data